



**Study of the Interrelationship between Weld Geometry, Process  
Variables and Joint Integrity for Friction Processed AA6082-T6  
Aluminium**

**BY:**

**Darren Alton Graham Samuel**

A Thesis submitted in the full requirements of the Degree  
**Doctor of Philosophy in Engineering (Mechanical)**

To the  
**Faculty of Engineering, the Built Environment and Information  
Technology**  
At the  
**Nelson Mandela Metropolitan University**

Submitted:

10/01/2014

**Promoter:**

Prof. D. G. Hattingh

**Co-Promoter:**

Dr. A Els-Botes

### **Copyright statement**

The copy of this thesis has been supplied on condition that anyone who consults it is understood to recognise that its copyright rests with the Nelson Mandela Metropolitan University and that no extracts from the thesis or information derived from it may be published without the author's prior consent.

**I Darren Alton Graham Samuel,**

Hereby declare that this is my original work and that all sources of reference used or referred to have been recognized and documented.

Further, I have not previously in full or any part submitted this work at any other university for a degree.

Date 20/11/2014

A handwritten signature in cursive script, reading "Darren Alton Graham Samuel". The signature is written in black ink and is positioned above a horizontal dotted line. A long, thin, curved line extends from the end of the signature across the page.

Darren Alton Graham Samuel

## **Abstract**

This work presents a broad overview of the successful development of friction taper stud welding (FTSW) in 25mm thick AA6082-T6 sections. It covers the selection of geometry and process parameters, the development of data logging equipment, energy input results and interpretations.

Research was carried out to develop the FTSW process for application in 25mm AA6082-T6 sections. The development and application of the FTSW process addresses the need to fill blind holes in thick aluminium sections for the repair of incorrectly drilled holes, friction stir welding exit holes and defects in critical components. During welding, frictional torque, rotational speed, axial force, near interface temperature of the tapered hole and welding time was recorded. This data was used to calculate energy input and energy input rates throughout a weld, enabling the effect of process parameters to be linked to energy, temperature, microhardness and static joint strength. Results of preliminary experiments are included in the study that were used for the design of a process parameter test window for FTSW in AA6082-T6, as no parameters were available to indicate a starting point for the research. The effect of process parameters on the static joint strength at the base of the tapered hole are presented; using a parallel sided stud and tapered hole configuration. This addresses one of the pressing issues facing FTSW of AA6082-T6, namely the lack of bonding at the bottom of the blind hole. A final process parameter matrix is designed based on the process development welds and is presented and discussed. In addition, the use of a non-consumable heat sink was investigated to prevent the premature collapse of the stud during welding and was shown to be critically important to the FTSW of AA6082-T6.

To achieve good sidewall bonding a hole taper angle of 60° is required, this having been shown during visual evaluation of development welds. Stud taper angles between 2° and 5° less than the taper angle of the hole were identified as the range within which good FTSW can be made. With this geometry, at no stage during

welding did the body of the stud shear off from the weld interface due to softening, thereby preventing collapse of the stud and formation of poorly bonded regions at the sidewall of the hole. The absence of shearing off of the weld interface during plunge was shown to be a good indicator of appropriate geometry and can be linked to welds made with high hole and stud taper angles and high axial force ramp up rates. The large hole and stud diameter relative to the depth of the hole and the large taper angle of the hole further aid in keeping the weld nugget rotating in the hole, promoting plasticization of the sidewall. Axial force ramp up rate was found to be the main critical success factor in an AA6082-T6 FTSW. Without control of this parameter the body of the stud will heat and detrimentally soften during plunge. It was established that good FTSW in AA6082-T6 cannot be made without the use of preheat to overcome the heat dissipation during welding, and is directly linked to improved energy input characteristics. Energy input as well as energy input rate were directly linked to static tensile strength and softening in the HAZ. The angle of the stud has been related to the energy input rate limit of the stud body, with increasing stud taper angles enabling the stud to withstand a higher energy input rate, allowing the weld interface to propagate up the hole at a slower rate, promoting plasticization of the sidewall.

This study has successfully made good FTSW in 25mm thick AA6082-T6, in a 60°, 20mm deep tapered hole. Process parameters and ranges that produce FTSW exhibiting the required characteristics were identified by this study.

## **Acknowledgments**

I will start by thanking my promoter, Professor Danie G. Hattingh, for giving me the opportunity to do this research under his guidance and for the use of the equipment developed by his team of engineers at eNtsa. He has gone to great lengths to guide me in the correct path, never allowing me to wander too far from the topic and knowing just how hard to push me for this work to be a success. Without his wealth of knowledge, experience and patience this research would not have been possible.

Secondly I would like to thank my co-promoter, Dr Annelize Botes. She strove to encourage me in the right direction and spent tiresome hours encouraging and guiding me in the right direction. She was always available with advice regardless of the crisis, and I will always be grateful to her for her efforts in my research.

I would then like to thank the following people from eNtsa, Mrs Lucinda Lindsay for all her assistance during my studies, I have been far better off with her on my side during my research; Dr Ian Wedderburn for his development of the FTSW platforms used in the research and with his assistance with additional developments on the equipment; Mr Louis von Wielligh for his advice and guidance that he is never unwilling to share; Mr Dirk Odendaal for his assistance with the friction stud welding equipment and Mr Etienne Phillips for his endless assistance with setup and program development for the PDS platform; Ms Nadine Marupen for all her admin assistance, streamlining the research process.

I would also like to thank NMMU technical and laboratory staff for their support: Mr Riaan Brown; Mr Amish Lalla; Mr Jaromir Cizek; Mr Glynne Erasmus; Mr Marlon Koopman, the amount of assistance and time they offered to assist me in my work is extensive and a mere thank you hardly seems worth it.

Further, for their financial assistance, without which this research would not have been possible, I would like to thank:

- NMMU eNtsa – innovation through engineering
- NMMU RCD - Research and Capacity Development
- National Research Foundation
- NRF Technology and Human Resources Programme
- CSIR Titanium Center of Competence
- Technology Innovation Agency Technology Station Programme

Last but most certainly not least I thank my parents. Firstly for allowing me to study in the first place, making it possible for me to reach this point in my life. All my life they have supported me and have given me more than any parents could ever be asked to. They taught me to be the best I could be and have supported me regardless. For all this I thank them, the road we travelled was not always easy and the sacrifices they have made for me are countless.

---

## Table of contents

	<b>Page</b>
List of Figures .....	vii
List of Tables.....	xiii
List of Equations .....	xv
Glossary of Terms.....	xvi
 <b>CHAPTER 1</b>	
<b>INTRODUCTION TO FRICTION TAPER STUD WELDING OF AA6082-T6</b>	
1.1. Introduction .....	1
1.2. The FTSW Process.....	2
1.3. Objective .....	5
1.4. Problem Statement .....	5
1.5. Sub-Problems .....	5
1.6. Hypothesis .....	6
1.7. Delimitations .....	6
1.8. Significance of the Research .....	7
1.9. Research Methodology .....	8
1.10. Research Project Plan .....	9
1.12. Summary.....	9
 <b>CHAPTER 2</b>	
<b>REVIEW OF RELEVANT LITERATURE</b>	
2.1. Introduction to Aluminium.....	10
2.2. Summary of Relevant Literature on Friction Welding Processes .....	10
2.3. Process Parameters Applied To Friction Welding.....	14
2.3.1. Plunge Depth .....	14
2.3.2. Rotational Speed.....	16
2.3.3. Applied Axial Force during Rotation (Friction Force) .....	19
2.3.4. Applied Axial Force after Rotation (Forging Force) .....	20
2.4. Fusion Welding of Aluminium Alloys .....	21
2.4.1. TIG Welding .....	22
2.4.2. MIG Welding .....	22
2.4.3. Oxide Formation.....	22
2.4.4. Porosity Formation .....	22



---

2.5. The Need for Preheat .....	23
2.6. FTSW Process Characterisation.....	24
2.6.1. Wear Stage .....	25
2.6.2. Seizure Stage.....	26
2.6.3. Heating Stage .....	27
2.6.4. The Effect of Axial Force on the Welding Interface .....	29
2.6.5. Stopping Stage.....	30
2.6.6. Forging Stage.....	30
2.7. Process Energy and Energy Input Rate .....	30
2.8. Geometry Applied in Current FTSW Processes .....	31
2.9. Grain Boundaries and Bonding Mechanisms .....	34
2.10. Abnormal Grain Growth in Aluminium .....	35
2.11. The Use of Hardness to Characterise Friction Welded Joints.....	37
2.12. Summary.....	40
2.13. Stationary Flash Formation .....	40

### **CHAPTER 3**

#### **EXPERIMENTAL PLATFORM AND SAMPLE SETUP OF AA6082-T6 FTSW**

3.1. Introduction .....	42
3.2. Weld Material Specification.....	42
3.3. The FTSW Platform .....	43
3.3.1. Load Cell Development for FTSW Platform .....	44
3.3.2. Data Acquisition Systems.....	48
3.4. PDS Welding Platform .....	48
3.4.1. Load Cell Development for PDS Platform .....	49
3.5. Welding Procedure .....	51
3.6. Development of Plunge Depth Approximation Methodology .....	54
3.7. Near Interface Temperature Data .....	56
3.8. Tensile Samples Geometry and Preparation .....	58
3.9. Microhardness Testing.....	60
3.10. Sample Removal and Preparation .....	61
3.11. Testing Equipment.....	62
3.12. Energy Calculation.....	62
3.13. Hole Area Used at Various Points into the Weld.....	63
3.14. Residual Stress Measurements and EBSD Mapping.....	65

---

3.15. Summary of Experimental Setup .....	67
---	----

## **CHAPTER 4**

### **PROCESS DEVELOPMENT OF FTSW FOR AA6082-T6**

4.1. Introduction to the Development Process .....	68
4.2. Axial Force and Stud Taper Angle for a 20° Hole.....	68
4.2.1. Applied Axial Force for Welds TW-1 to TW-10.....	73
4.2.2. Process Torque for Welds TW-1 to TW-10 .....	74
4.2.3. Energy Input of Welds TW-1 to TW-10.....	79
4.2.4. Energy Input Rate of Welds TW-1 to TW-10.....	82
4.2.5. Summary of Welds TW-1 to TW-10.....	83
4.3. FTSW of Aluminium Torque Chart Characterization .....	84
4.4. Varying of Preheat Using a 20° Hole Taper Angle .....	86
4.4.1. Process Torque with Increasing Preheat for Welds TW-8, TW-11 and TW-12 .....	88
4.4.2. Energy with respect to Preheat for Welds TW-8, TW-11 and TW-12 .....	89
4.4.3. Energy Input Rate with respect to Preheat for Welds TW-8, TW-11 and TW-12 .....	91
4.4.4. Summary of Welds TW-8, TW-11 and TW-12.....	92
4.5. Varying of Axial Force and Stud Angle Using a 30° Hole.....	93
4.5.1. Axial Force for Welds TW-13 to TW-18.....	95
4.5.2. Process Torque for Welds TW-13 to TW-18 .....	96
4.5.3. Energy Input for Welds TW-13 to TW-18 .....	97
4.5.4. Energy Input Rate for Welds TW-13 to TW-18.....	99
4.5.5. Summary of Welds TW-13 to TW-18.....	99
4.6. The Effects of Preheat and Increased Stud Shank Diameter Using a 60° Hole .....	100
4.6.1. Process Torque for Welds TW-19 to TW-21 .....	105
4.6.2. Energy Input of Welds TW-19 to TW-21.....	106
4.6.3. Energy Input Rate for Welds TW-19 to TW-21 .....	108
4.6.4. Summary of Welds TW-19 to TW-21.....	109
4.7. Investigation of a 90° Tapered Hole.....	109
4.8. The Use of a Non Consumable Heat Sink and Increased Axial Force Ramp up Rate .....	112

---

4.8.1. Process Torque and Near Interface Temperature for Welds TW-23 and TW-24 .....	118
4.8.2. Energy Input of Welds TW-23 and TW-24.....	122
4.8.3. Energy Input Rate of Welds TW-23 and TW-24 .....	125
4.8.4. Summary of Welds TW-23 and TW-24.....	126
4.9. Conclusion of Development Welds .....	127
4.10. Investigation of Bonding at the Base of the Tapered Hole .....	129
4.10.1. Process Parameters of Parallel Welds PT-1 to PT-4.....	129
4.10.2. Applied Axial Force for Welds PT-1 to PT-4.....	132
4.10.3. Process Torque for Welds PT-1 to PT-4 .....	133
4.10.4. Energy Input for Welds PT-1 to PT-4 .....	134
4.10.5. Energy Input Rate for Welds PT-1 to PT-4.....	135
4.10.6. Tensile Data/ pull out Test for Welds PT-1 to PT-4 .....	136
4.10.7. Parallel FTSW Interface Fractures Surafces .....	139
4.10.8. Discussion of Welds PT-1 to PT-4.....	142

## **CHAPTER 5**

### **FINAL DEVELOPMENT OF THE FTSW OF AA6082-T6**

5.1. Introduction .....	144
5.2. FTSW Procedure of PDS Friction Welding Platform .....	145
5.3. The Influence of Axial Force and Rotational Speed using a 60° Hole.....	146
5.3.1. Modes of Fracture for Welds S.1 to S.4 .....	154
5.3.2. Near Interface Temperature for Welds S.1 to S.4 .....	159
5.3.3. Microhardness Measurements for Welds S.1 to S.4 .....	162
5.3.4. Residual Stress Analysis of Welds S.1 to S.4 .....	164
5.3.5. The Effect of Axial Force and Rotational Speed on Texture.....	168
5.4. The Influence of Axial Force Ramp up Rate using a 60° Hole .....	170
5.4.1. Influence of Axial Force ramp up Rate on Process Toque for Welds RR-1 to RR-4 .....	174
5.4.2. The effect of Axial Force Ramp up Rate on Energy Input for Welds RR-1 to RR-4 .....	175
5.5. Development and Testing of the Final Process Parameter Window using a 60° Hole .....	178
5.5.1. Fracture Mode Characterization and UTS for Welds FM-1 to FM-16 .....	181

---

5.5.2. Flash Formation with respect to Process Parameters and Near Interface Temperature for Welds FM-1 to FM-16 .....	183
5.5.3. Influence of Process Parameters with respect to UTS .....	185
5.5.4. Process Torque Analyses with respect to UTS, Energy and Temperature for Welds FM-1 to FM-16 .....	188
5.5.5. Energy Input Analyses with respect to Temperature and UTS ...	195
5.5.6. UTS Scatter Analyses of Typical Fracture Modes .....	204
5.5.7. Typical Microstructures of AA6082-T6 FTSW .....	209
5.5.8. Microstructure Analysis of the Fillet of the Weld .....	215
5.6. Summary .....	220

## **CHAPTER 6**

### **SUMMARY AND FUTURE WORK**

6. Summary .....	222
6.1. Recommended Future Work .....	226

### **BIBLIOGRAPHY .....**

Appendix A: Geometry for all the Holes, Studs and Removable Heat Sinks Investigated .....	232
Appendix B: Load Cell Drawings for FTSW Platform .....	242
Appendix C: Load Cell Drawings for PDS Friction Welding Platform .....	249
Appendix D: Macrographs of All Welds (Unedited) .....	263
Appendix E: Applied Axial Force Charts for all Development Welds .....	269
Appendix F: Energy Input, Process Torque and Axial Force Data .....	272
Appendix G: Process Torque Charts for Process Development Welds .....	291
Appendix H: Dye Penetration Tests for 60° Hole Taper Angle Welds .....	294
Appendix I: Tensile Test Fracture Modes .....	297
Appendix J: Logged Process Data for Welds FM-1 to FM-16 and RR-1 to RR-4 .....	301
Appendix K: Vertical and Horizontal Microhardness Charts .....	308
Appendix L: Near Interface Temperature Charts .....	314

---

Appendix M: EBSD- Band Contrast, Grain Size Distribution, and Residual Strain Maps and Grain Size Distribution Histograms .....	317
--	-----

## **PAPERS SUBMITTED DURING THIS RESEARCH**

Appendix N: Paper 1 .....	322
---------------------------	-----

***Characterization of Joint Integrity of Blind Friction Taper Stud Welds in  
the partially Supported Condition as applied to AA6082-T6***

D.A.G. Samuel<sup>\*a</sup>, Prof. D.G. Hattingh<sup>a</sup>, Prof. A. Els-Botes<sup>a</sup>

***Presented at and Published in:***

*International Friction Processing Seminar August 2011  
Nelson Mandela Metropolitan University*

Appendix O: Paper 2 .....	338
---------------------------	-----

***Development of a procedure for the filling of blind holes in thick section  
AA 6082-T6 Aluminium by Friction Hydro Pillar Processing***

D.A.G. Samuel <sup>\*a</sup>, D.G. Hattingh<sup>a</sup>, A. Els-Botes<sup>a</sup>

***Presented at and Published in:***

*International Congress Seminar November 2012  
International Institute of Welding*

Appendix P Paper 3 .....	349
--------------------------	-----

***Characterization of Tapered Friction Stud Welding Applied to AA6082-T6***

D.A.G. Samuel <sup>\*a</sup>, D.G. Hattingh<sup>a</sup>, A. Els-Botes<sup>a</sup>, A. Steuer<sup>a,b</sup>

**Awaiting Publication:**

---

<sup>a</sup> eNtsa, Faculty of Engineering, the Built Environment & Technology, Nelson Mandela  
Metropolitan University, Port Elizabeth 6031, South Africa.

<sup>b</sup>MAX IV Laboratory, Ole Römers Väg 1, Lund University, 22100 Lund, Sweden

**List of Figures**

Figure 1-1. Linked Blind FTSW in 30mmSteel (Taken at NMMU).....	2
Figure 1-2. FHPP with Nickel Tracer [11].....	3
Figure 1-3. Through Type FTSW in AA6082-T6 [4] .....	3
Figure 1-4. Stages of the FTSW Process .....	4
Figure 2-1. Through Type FTSW [10] .....	11
Figure 2-2. Aluminium Alloy FTSW .....	13
Figure 2-3. Tensile Strength vs. Friction Time [22] .....	15
Figure 2-4. Process Torque vs. Tensile Strength [13].....	15
Figure 2-5. Tensile Strength vs. Welding Time in Stainless Steel Stud Welds [23] .....	15
Figure 2-6. Extension to Fracture vs. Welding Time in Stainless Steel Stud Welds [23].....	16
Figure 2-7. Weld Nugget Tearing in Friction Stud Welding of Stainless Steel [23] .....	17
Figure 2-8. UTS vs. Peripheral Velocity for a Stainless Steel Friction Stud Weld [23].....	18
Figure 2-9. Bend Strength of RFW with increased Peripheral Velocity [14].....	19
Figure 2-10. Tensile Strength vs. Friction Pressure in AISI 304 [22].....	20
Figure 2-11 Logarithmic Plot of Diffusion Coefficient vs. Temperature [33] .....	24
Figure 2-12. Torque Stages during a Friction Weld [23] .....	25
Figure 2-13. Metallic Dust Deposited During the Wear Stage of a Friction Stud Welding Process [23].....	26
Figure 2-14. Welding Interfaces at Various Times into a RFW [13] .....	26
Figure 2-15. Through Type FTSW [4] .....	27
Figure 2-16. Increasing Equalised Torque for Stud Welds [23].....	28
Figure 2-17. The influence of Time and Axial Force on Interface Temperature [36] .....	29
Figure 2-18. Geometry Tested by Van Zyl for FTSW CM Steel [38] .....	32
Figure 2-19. Geometry used by Bulbring in the FTSW of EN-19 [5] .....	32
Figure 2-20. Geometry Used by Pinero for the FTSW of Magnesium [10].....	33
Figure 2-21. AGG at the base of a FSW in AA7075 [40].....	36
Figure 2-22. Grain Size at Temperature vs. Deformation for Pure Aluminium [44] .....	37

---

Figure 2-23. Bond Strength with Increased Radii [29].....	38
Figure 2-24. Loss of T6 Temper in AA6082 [4] .....	39
Figure 2-25. Improved Weld Quality Differentiation FTSW AISI 6082-T6 [4] ....	39
Figure 2-26. Tail of Flash Exiting the Plunging FSW Tool [45].....	41
Figure 2-27. Stationary Flash around Tool [45].....	41
Figure 3-1. FTSW Platform .....	44
Figure 3-2. Load Cell for FTSW Platform .....	45
Figure 3-3. Sectioned View of Load Cell.....	45
Figure 3-4. Sectioned View of FTSW Platform Load Cell .....	45
Figure 3-5. Strain Gauges Fitted to.....	46
Figure 3-6. Axial Force Component .....	46
Figure 3-7. Axial Component Calibration Curve for FTSW Platform .....	47
Figure 3-8. Calibration Setup for FTSW Platform Load Cell Torsional Component .....	47
Figure 3-9. Calibration Curve for FTSW Platform Load Cell Torsion Component .....	48
Figure 3-10. PDS Friction Welding Platform .....	50
Figure 3-11. Torsional Load Cell for PDS Platform .....	50
Figure 3-12. Sectioned View of PDS Platform Load Cell .....	51
Figure 3-13. Welding Setup for FTSW Platform Welds.....	52
Figure 3-14. Sectioned View of Welding Setup.....	53
Figure 3-15. AA6082-T6 FTSW on PDS Welding Platform.....	53
Figure 3-16. Plunge Depth Investigation [10].....	55
Figure 3-17. Plunge Depth Approximation Layout .....	55
Figure 3-18. Displaced Volume vs. Clearance Volume (Taken form work by Pintero [10]) .....	56
Figure 3-19. Layout of Thermocouple Holes for Near Interface Temperature Measurement.....	57
Figure 3-20. Thermocouple Hole Depths for Welds TW-23 and TW-24.....	57
Figure 3-21. Thermocouple Hole Depths for Welds S.1 to S.4, RR-1 to RR-4 and FM-1 to FM-16 .....	58
Figure 3-22. Tensile Sample Dimensions .....	59
Figure 3-23. Completed Tensile Sample Weld .....	59
Figure 3-24. Tensile Sample showing Weld Nugget .....	59
Figure 3-25. Tensile Sample showing Weld Nugget and Displaced Material ....	59

---

---

Figure 3-26. Microhardness Test Points .....	60
Figure 3-27. Microhardness Test Point Map for Welds RR-1 to RR-4 and FM-1 to FM-16 .....	61
Figure 3-28. Sample Removal with CNC Milling Machine.....	62
Figure 3-29. Energy Input in 0.1 seconds .....	63
Figure 3-30. Weld Nugget Etched, Showing Planes for Residual Stress and Vickers Microhardness Measurements .....	66
Figure 3-31. Position of EBSD Sample from Mid-Region of the FTSW.....	66
Figure 3-32. EBSD Sample Wire Cut from Sectioned Sample.....	66
Figure 4-1. Welds TW-1 to TW-10 Macrographs .....	71
Figure 4-2. Weld TW-4 with Weld Nugget Removed .....	72
Figure 4-3. Weld TW-4 Showing Bonded Regions.....	72
Figure 4-4. Applied Axial Force during Welding (Welds TW-1 to TW-10) .....	74
Figure 4-5. Seizure Torque vs. Measured Axial Force at Seizure for Welds TW-1 to TW-10 .....	75
Figure 4-6. Process Torque Charts for Welds TW-1 to TW-10 .....	77
Figure 4-7. Parallel Torque Increases after Violent Shear .....	78
Figure 4-8. The effect of Axial Force on Process Torque.....	79
Figure 4-9. Energy Input vs. Set Axial Force (Welds TW-1 to TW-10).....	82
Figure 4-10. Energy Input Rate vs. Set Axial Force (Welds TW-1 to TW-10) ...	83
Figure 4-11. FTSW Torque Curve Characterization.....	85
Figure 4-12. Welds TW-1, TW-11 and TW-12 Macrographs.....	87
Figure 4-13. Process Torque Chart for Welds TW-8, TW-11 and TW-12 .....	89
Figure 4-14. Energy Input vs. Preheat (Welds TW-8, TW-11 and TW-12).....	91
Figure 4-15. Energy Input Rate vs. Preheat (Welds TW-8, TW-11 and TW-12).....	92
Figure 4-16. Welds TW-13 to TW-18 Macrographs .....	95
Figure 4-17. Applied Axial Force during Welding (Welds TW-13 to TW-18) ....	96
Figure 4-18. Process Torque Charts for Welds TW-13 to TW-18 .....	97
Figure 4-19. Welds TW-19 to TW-21 Macrographs .....	103
Figure 4-20. Welds TW-19 to 21 (Etched in Sodium Hydroxide).....	103
Figure 4-21. Welds TW-19 to TW-21 Hole Bonding Macrographs .....	105
Figure 4-22. Localized Bond on Sidewall Interface (Located at a-a in Figure 4-21– Weld TW-19).....	105
Figure 4-23. Process Torque Curves for Welds TW-19 to TW-21.....	106
Figure 4-24. Weld TW-22 Macrograph.....	111

---



---

Figure 4-25. Process Torque Chart for Weld TW-22.....	111
Figure 4-26. Axial Force Ramp up Rate with Changes in Valve Setup .....	113
Figure 4-27. Non Consumable, Removable Aluminium Heat Sink.....	114
Figure 4-28. Welds TW-23 and 24 Macrographs .....	117
Figure 4-29. Cold Forge Defect found in Weld TW-22 (similar to weld TW-23) (Located at b-b in Figure 4-28).....	117
Figure 4-30. Process Torque, Axial Force and Temperature Curves for Welds TW-23 and TW-24 .....	120
Figure 4-31. AGG in Lower Region of Welds TW-23 and TW-24.....	125
Figure 4-32. Macrographs of Welds PT-1 to PT-4 .....	131
Figure 4-33. Applied axial Force during Welding (Welds PT-1 to PT-4).....	132
Figure 4-34. Axial Force vs. Axial Force Ramp up Rate .....	133
Figure 4-35. Process Torque for Welds PT-1 to PT-4.....	134
Figure 4-36. Filled Deformation for Welds PT-1 to PT-4 .....	136
Figure 4-37. Fracture Jig for Parallel FTSW .....	137
Figure 4-38. Fractured Parallel FTSW .....	137
Figure 4-39. Tensile Results for Parallel Welds PT-1 to PT-4.....	139
Figure 4-40. Fracture Macrographs of welds PT-1 to PT-4.....	142
Figure 5-1. Steel (EN-8) Heat Sink .....	145
Figure 5-2. Macrographs of Welds S.1 to S.4 .....	148
Figure 5-3. Flash Formation of Weld S.1 (40kN Axial Force).....	149
Figure 5-4. Flash Formation of Weld S.2 (60kN Axial Force).....	150
Figure 5-5. Flash Formation of Weld S.3 (80kN Axial Force).....	151
Figure 5-6. Flash Formation of Weld S.4 (60kN Axial Force).....	152
Figure 5-7. Dye Penetrant Testing of Welds S.1 to S.4 .....	153
Figure 5-8. Tensile Samples of Welds S.1 to S.4.....	153
Figure 5-9. Tensile Strength vs. Heat Treated Parent Plate for Welds (S.1 to S.4) .....	154
Figure 5-10. Fracture Modes of Welds S.1 and S.3 .....	155
Figure 5-11. SEM Fracture Surfaces of Welds S.1 to S.4.....	156
Figure 5-12. SEM micrograph of Point 5 x 3000 (Weld S.4) .....	158
Figure 5-13. Near Interface Temperature for Welds S.1 to S.4.....	161
Figure 5-14. Vickers Microhardness of as received and Heat Treated Parent Plate (test done at 25g).....	162
Figure 5-15. Microhardness Profiles of Welds S.1 to S.4.....	163

---

---

Figure 5-16. Residual Hoop Stress Curves for Welds S.1 to S.4 .....	167
Figure 5-17. Residual Radial Stress Curves for Welds S.1 to S.4 .....	167
Figure 5-18. Misorientation Angle for Grain Boundary Identification .....	168
Figure 5-19. All Euler Map of Weld S.1 (40kN-5000RPM) .....	169
Figure 5-20. All Euler Map of Weld S.2 (60kN-5000RPM) .....	169
Figure 5-21. All Euler Map of Weld S.3 (80kN-5000RPM) .....	169
Figure 5-22. All Euler Map of Weld S.4 (60kN-3000RPM) .....	169
Figure 5-23 Etched Tensile Samples showing Height of Final Shear Interface with respect to Axial Force Ramp up Rate Welds RR-1 to RR-4.....	172
Figure 5-24. Flash Formation of Welds RR-1 to RR-4 .....	172
Figure 5-25. Tensile Strength vs. Axial Force Ramp up Rate for Welds RR-1 to RR-4 .....	173
Figure 5-26. Weld RR-1to RR-2 Recorded Process Data.....	175
Figure 5-27. Displaced Stud Material at 0.5mm Plunge Depth .....	176
Figure 5-28. Temperature Response at the Fillet with increasing Axial Force Ramp up Rate.....	177
Figure 5-29. Near Interface Temperature Response for Welds RR-1 to RR-4	177
Figure 5-30. Fracture Modes of Welds FM-1 to FM-16 .....	182
Figure 5-31. Flash Formation of Welds FM-1 to FM-16 .....	184
Figure 5-32. Secondary Flash Formation of Weld TW-8.....	184
Figure 5-33. Near Interface Temperature Response for Welds FM-1 and FM-5 .....	188
Figure 5-34. Influence of Axial Force and Axial Force Ramp up Rate on Process Torque at 5000RPM.....	190
Figure 5-35. Near Interface Temperature Response for Welds FM-1 to FM-10 .....	191
Figure 5-36. Micrograph of the Fillet of Welds FM-1 to FM-2 and FM-9 to FM-10 .....	192
Figure 5-37. Micrograph at the Top of Welds FM-9 and FM-10 showing Lack of Fusion .....	193
Figure 5-38. Influence of Axial Force and Axial Force Ramp up Rate on Process Torque at 3000RPM.....	194
Figure 5-39. Micrograph at the Mid-Point of Welds FM-4 and FM-12 showing Lack of Fusion .....	195
Figure 5-40. Total Energy Input (Welds FM-1 to FM-16) .....	197

---

---

Figure 5-41. Change in HAZ Hardness due to Reduced Total Energy Input ..	199
Figure 5-42. Total Energy Input Rate for Welds FM-1 to FM-16 .....	200
Figure 5-43. Welding Time for Welds FM-1 to FM-16 .....	201
Figure 5-44, Contour Plot of Energy Input and Energy Input Rate vs. UTS ....	201
Figure 5-45, Contour Plot of Energy Input and Energy Input Rate at 5000RPM vs. UTS.....	203
Figure 5-46, Contour Plot of Energy Input and Energy Input Rate at 3000RPM vs. UTS.....	203
Figure 5-47, Contour Plot of Energy Input and Energy Input Rate at 5000RPM vs. Extension to Fracture.....	204
Figure 5-48, Contour Plot of Energy Input and Energy Input Rate at 3000RPM vs. Extension to Fracture.....	204
Figure 5-49. Weld FM-16 Macrograph showing the location of point (a) and (b) .....	205
Figure 5-50. 25kN/s Axial Force Ramp up Rate Weld RR-1 Bond Line of Fracture Mode 3.....	205
Figure 5-51. Bond Line of Fracture Mode 1 .....	206
Figure 5-52. Bond Line of Fracture Mode 2 .....	207
Figure 5-53. Bond Line of Fracture Mode 3 .....	207
Figure 5-54. Surface Plot of Energy Input and Energy Input Rate vs. Modes of Fracture .....	208
Figure 5-55. Microstructure of Weld FM-1 .....	211
Figure 5-56. Microstructure of Weld FM-16 .....	212
Figure 5-57. Band Contrast an Grain Boundary Map of Weld S.1 .....	213
Figure 5-58. Band Contrast an Grain Boundary Map of Weld S.4 .....	214
Figure 5-59. Typical Microstructure Types Identified at the Fillet Relative to Energy Input.....	216
Figure 5-60. Location of the Fillet in the FTSW.....	216
Figure 5-61. Localised AGG at the Fillet of all Type A and B Fillets.....	217
Figure 5-62. Residual Hoop Stress at 5000RPM .....	219
Figure 5-63. Residual Hoop Stress at 3000RPM .....	219

**List of Tables**

Table 2-1. Process Window for Through Type FTSW [4].....	12
Table 2-2. Process Parameters Used by Van Zyl [38] .....	32
Table 2-3. Process Parameters used by Bulbring [5].....	33
Table 2-4. Process Parameters used by Beamish in the FTSW of AA6082-T6 [4] .....	34
Table 3-1. Chemical Composition Specifications of AA6082 [2] [17] .....	43
Table 3-2. Distance to Weld Interface.....	61
Table 4-1. Welds TW-1 to TW-10 Parameter Constants.....	69
Table 4-2. Welds TW-1 to TW-10 Parameter Variables.....	69
Table 4-3. Results for Welds TW-1 to TW-10 .....	76
Table 4-4. Welds TW-8, TW-11 and TW-12 Parameter Variables .....	86
Table 4-5. Results for Welds TW-8, TW-11 and TW-12.....	88
Table 4-6. Welds TW-14 to TW-19 Parameter Constants.....	94
Table 4-7. Welds TW-14 to TW-19 Parameter Variables.....	94
Table 4-8. Results for Welds TW-13 to TW-18 .....	99
Table 4-9. Welds TW-19 to TW-21 Parameter Constants.....	101
Table 4-10. Welds TW-19 to TW-21 Parameter Variables.....	101
Table 4-11. Results for Welds TW-19 to TW-21 .....	108
Table 4-12. Weld TW-22 Parameter Constants .....	110
Table 4-13. Weld TW-22 Parameter Variables .....	110
Table 4-14. Results for Welds TW-22 .....	112
Table 4-15. Weld TW-23 to TW-24 Parameter Constants .....	115
Table 4-16. Weld TW-23 to TW-24 Parameter Variables.....	116
Table 4-17. Near Interface Temperature at Seizure and PSTP .....	118
Table 4-18. Near Interface Temperature Crossover Points for Welds TW-23 and TW-24 .....	120
Table 4-19. Maximum Near Interface Temperatures for Welds TW-23 and TW-24 .....	122
Table 4-20. Near Interface Cooling Rates for Welds TW-23 and TW-24 .....	122
Table 4-21. Results for Welds TW23 and TW-24.....	124
Table 4-22. Welds PT-1 to PT-4 Process Constants .....	130
Table 4-23. Welds PT-1 to PT-4 Process Variables.....	130
Table 4-24. Results for Parallel Welds PT-1 to PT4.....	135

---

Table 4-25. Tensile Data of Parent and Preheated AA6082-T6.....	138
Table 4-26. Tensile Results for Parallel Welds PT-1 to PT-4.....	139
Table 5-1. Process Parameter Constants (Welds S.1. to S.4) .....	147
Table 5-2. Process Parameter Variables (Welds S.1. to S.4) .....	147
Table 5-3. Welding Times of Welds S.1 to S.4.....	150
Table 5-4. Maximum and Minimum Recorded Microhardness in the Weld Nugget of welds S.1 to S.4.....	163
Table 5-5. Vickers Microhardness at Welding Interface for Welds S.1 to S.4 .	164
Table 5-6. Solver Results for Lattice Parameters A0 Hoop and A0 Radial .....	166
Table 5-7. Process Parameter Constants for Welds RR-1 to RR-4 .....	171
Table 5-8. Process Parameter Variables and Combinations for Welds RR-1 to RR-4 .....	171
Table 5-9. Tensile Results for Welds RR-1 to RR-4.....	173
Table 5-10. Results for Welds RR-1 to RR-4 .....	178
Table 5-11. Process Parameter Variables for Welds FM-1 to FM-16.....	180
Table 5-12. Process Parameter Variables and Combinations for .....	181
Table 5-13. Tensile Results of Welds FM-1 to FM-16.....	183
Table 5-14. UTS Results vs. Process Parameters.....	186
Table 5-15. Energy Results for Welds FM-1 to FM-16.....	198
Table 5-16. Classification of Weld Fillet Bonding.....	215

**List of Equations**

Equation 3-1. Clearance Volume .....	55
Equation 3-2. C.V.D Calculation .....	55
Equation 3-3. Energy Input .....	62
Equation 5-1. Strain .....	165
Equation 5-2. Hoop Stress .....	165
Equation 5-3. Radial Stress .....	165
Equation 5-4. Governing Limits .....	165

---

## Glossary of Terms

- **8 per. Moving Average** – A data smoothing function used to develop trend lines in Excel. The 8 is indicative that at each data point, the average of eight data points were used to smooth the data at that point. Typically the cell value before the cell in question, the cell in question and six cells after are averaged when an 8 per. Moving Average is applied.
- **AGG – Abnormal Grain Growth or Secondary Recrystallization** - The process that allows the formation of substantially large grains in a crystallographic [1]
- **Axial Force** – The axial force applied during a FTSW during plunge and forging. This term is typically used when the process has like friction and forging force during welding
- **Axial Force Ramp up Rate** – The rate at which the axially applied force build up to the set axial force during welding
- **Base Clearance/ stud and hole base hole clearance** - This is the clearance between the base of the hole and the nose of the stud
- **Burn-off** – The distance that the stud moves vertically downward after it has contacted the surface of the backing plate. This downward movement is the result of displaced plasticised material which is forced out from the weld zone. Also referred to as 'plunge depth'.
- **Clearance Angle** – The difference in the total included angle of the tapered hole and the total included angle of the tapered consumable stud
- **Cooling Time** – The time allowed for the weld to cool under a continuously applied forging force, held constant at 20seconds in this research
- **Diffusion** – The phenomenon of material transported by atomic motion
- **DRSM** - Stud Material that has not been deformed during the process of plunging
- **EBSD** – Electron Backscatter Diffraction
- **Fatigue** – A failure that occurs in a component after a period of cyclic loading in the elastic range
- **Forging Force** – The axially applied force applied during the forging/ cooling stage of a FTSW process
- **Friction Force** - The axially applied force during plunge in a FTSW process
- **Friction pressure** – The surface pressure over the face of the stud during plunge
- **Friction welding** – Term used for solid state joining processes created by a combination of frictional heat and pressure.
- **FTSW - Friction Taper Stud Weld** – A solid-state welding process used to join similar or dissimilar material by rotating a consumable tapered rod co-axially in a tapered cavity whilst under an applied load so as to generate a plasticised layer, thereby forming a bond (Developed by TWI). Can also be used for the repair of voids

- 
- **Fusion welding** – A type of welding process where melting of the base metals occur.
  - **HAZ – Heat Affected Zone.** This is the zone adjacent to the fusion zone that has not experienced melting
  - **Heat Transfer** – The phenomenon where heat passes through a medium from one point to another
  - **HMI - Human Machine Interface** – The tool by which humans interact with an electronic system
  - **Mechanical Lockup** – This is when the motor of the FTSW platform cannot overcome the frictional process torque required to complete the weld, stopping rotation
  - **Mechanical properties** – The properties of a material which indicates its suitability for mechanical applications.
  - **Microstructure** – The microscopic structure of material revealed under a microscope under a length scale of 1 – 100 micrometres.
  - **Nose Peripheral Velocity** – this is the peripheral velocity of a tapered stud as it contacts the base of the hole, before plunge has begun.
  - **Partially Supported Condition** – when a material is friction taper stud welded with no support directly below the weld interface
  - **Plastic deformation** – The permanent geometrical change of a material exerted to forces beyond its elastic limit.
  - **Plunge depth** – see ‘Burn-off distance’ Plunge depth is the distance the stud is consumed during rotation, under the axially applied load. It controls the volume of displaced plasticized material used to heat the tapered hole.
  - **Primary Flash** – This is the stud material that is plasticized and flows out of the weld during plunge
  - **Process Parameters-** The parameters that can be controlled or altered during a friction taper stud welding process
  - **Process Variables** – The process parameters that are changed between welds within a specified test matrix
  - **PSTP - Post Seizure Torque Peak** – This is the process torque reached after the seizure stage of a FTSW, normally higher than the initial seizure torque for welds made in AA6082-T6
  - **Repeatability** – In terms of a process, one test specimen will have the same mechanical properties or physical properties as another specimen if the processes were conducted using the same process parameters.
  - **Rotary Friction Welding (RFW)** – Is a process developed at TWI that utilizes local friction heating to produce continuous solid-state seams. It allows butt and lap joints to be made in low melting point materials (such as aluminium alloys) without the use of filler metals. The solid-state low distortion welds produced are achieved with relatively low costs using simple and energy-efficient mechanical equipment.
  - **Secondary Flash** - This is the plasticized plate material that flows out of the hole once sufficient heating of the plate has occurred
  - **Seizure** – Is the formation of isolated micro bonds between the welding interfaces, initiates once the surface roughness has been removed and the temperature of the fresh interface is sufficient to initiate bonding



- 
- **Seizure point** – The point during a friction welding process when the initial welding interface is in a state of shear
  - **Set pressure** – The pressure requested on the HMI.
  - **Solid-State** – A physically homogenous and distinct portion of a material system in the solid state
  - **Zener Pinning** - is the influence of a dispersion of fine elements on the drive

# CHAPTER 1

## INTRODUCTION TO FRICTION TAPER STUD WELDING OF AA6082-T6

### 1.1. Introduction

Since it was first successfully extracted by Danish physicist Hans Christian in 1825, and economically produced by the Hall-Hérault process developed in 1886 by Charles Martin Hall, aluminium has developed from a costly material afforded only by the wealthy, to the world's most widely utilized material [2] [3].

As aluminium is used more in engineering applications each year, greater demands are placed on the mechanical properties of the material, due to its application in highly stressed components and the need to reduce weight [2] [3]. This increases the need to make defect free repairs and joints in aluminium components. The friction taper stud welding (FTSW) process was developed as an alternative method for repairing through thickness and blind holes in metals. The technique has been considered as a repair procedure for critical applications where problems are encountered with fusion welding methods. A few examples of such problems are; operating in hazardous environments, welding materials that are not readily joined with conventional fusion methods and the requirement of multiple weld passes to produce a defect free weld [4] [5] [6].

The need for the FTSW process in aluminium was first made apparent by Lockheed Martin Space Systems, who are the manufacturers of the external fuel tanks for the space transportation system [3]. After development of the Weldalite® series of aluminium, Lockheed Martin were tasked with replacing the then current AL12219 tanks with the new Weldalite® type. Although the material was stronger and lighter, the alloying element utilized in its production negatively affected the materials' oxidation and weld cracking probability during repair processes. In 1995 The Welding Institute (TWI) introduced the friction plug welding process (FPWP) to Lockheed Martin for consideration. The process was a derivative from FTSW, but instead of one single tapered weld, a number of interlocking taper stud welds were made to repair a longer defect, forming the friction plug welding process, an example of which is shown in Figure 1-1 . The

through friction plug welding process optimized by Lockheed Martin produced welds typically 20% stronger than conventional TIG (tungsten inert gas) welding with improved fracture toughness. The process further produced repairs that were defect free on the first weld, unlike the current MIG (metal inert gas) welding process that often required multiple weld passes [3].

The space industry is not the only one in need of the friction taper stud welding process of aluminium. The aircraft industry, gas pipeline industry, nuclear industry and automotive industry are all in need of the process as a method of successfully repairing defects in aluminium products. This will reduce downtime, increase the life of the component due to increased repair strength and allow the joining of materials that are not easily joined or repaired by conventional welding processes. Last but not least, the FTSW process will allow for the filling of the exit hole of the now well-established friction stir welding process (FSW) in aluminium, with a plug that did not experience melting of the parent materials. An example of blind linked friction taper stud welding in steel is shown in Figure 1-1, taken at eNtsa at the Nelson Mandela Metropolitan University (NMMU).



Figure 1-1. Linked Blind FTSW in 30mmSteel (Taken at NMMU)

## 1.2. The FTSW Process

FTSW is a solid state joining technique that utilizes frictional heat generated through relative motion between two contacting friction surfaces to form a joint at the plasticization temperature, rather than melting as in a conventional fusion welding process [7]. FTSW is similar to conventional Friction Hydro Pillar Processing (FHPP), with one key variance. FHPP forms a pillar of dynamically recrystallized shear layers in a hole, while FTSW only has localised dynamic recrystallization at the interface between the hole and stud, leaving a large

percentage of the parent stud material in the hole. This is clearly shown in Figure 1-2 and Figure 1-3 for FHPP and FTSW respectively. Additionally there are two main types of FTSW, one that has a tapered hole through the plate that is to be welded, termed through type FTSW, and the second with a section of the parent plate left at the base of the hole, known as blind FTSW which will be the focus of this research.

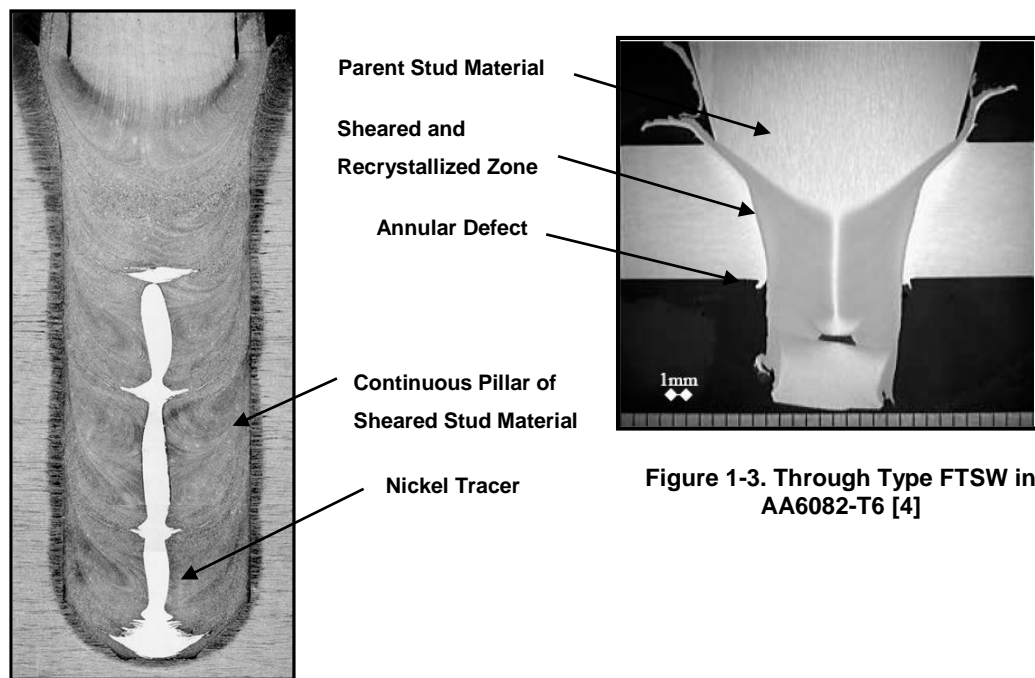


Figure 1-2. FHPP with Nickel Tracer [11]

Figure 1-3. Through Type FTSW in AA6082-T6 [4]

During a FTSW process a tapered tool is co-axially rotated in a tapered hole, with sufficient axial force to hold the welding surfaces in intimate contact, and with sufficient peripheral velocity to generate frictional heat at the weld interface. As the temperature increases to the plasticization temperature, seizure of the surfaces begins forming microbonds that are instantaneously sheared and reformed [7] [8] [9] [10]. This increases the frictional torque, inducing additional heat energy into the weld as the bonds are sheared [8] [10] [11] [12]. Once the entire surface is in a state of shear, plunge begins and layers of dynamically recrystallized stud material are deposited one on top of the other in the hole as shown in Figure 1-4 (a) and (b). As the stud is consumed, the plasticized material flows outwardly from the interface between the stud and hole as flash, removing oxides and impurities from the interface [10] [13]. The deformed stud and near interface flash contact the sidewalls of the hole, exerting an applied load due to

the hydrostatic forces flowing outwardly from the weld interface, rubbing and heating the sidewall [4] [8] [9]. The welding interface will, therefore, propagate upwards as plunge progresses, until the hole is filled and a predetermined plunge depth is reached (Figure 1-4 (c)). At this point rotation is abruptly stopped and a continuous forging force is applied to consolidate the weld (Figure 1-4 (d)). The heat necessary for the friction welding process is, therefore, supplied by the conversion of mechanical input energy to heat, which is directly dependent on the work done as a result of plastic deformation and the coefficient of friction of the material at the weld interface [7] [10]. A high integrity joint is achieved without the need for multiple weld passes, shielding gasses, a large heat affected zone or an operator with advanced welding skills. A forged solid state bond is thus formed at the interface [14].

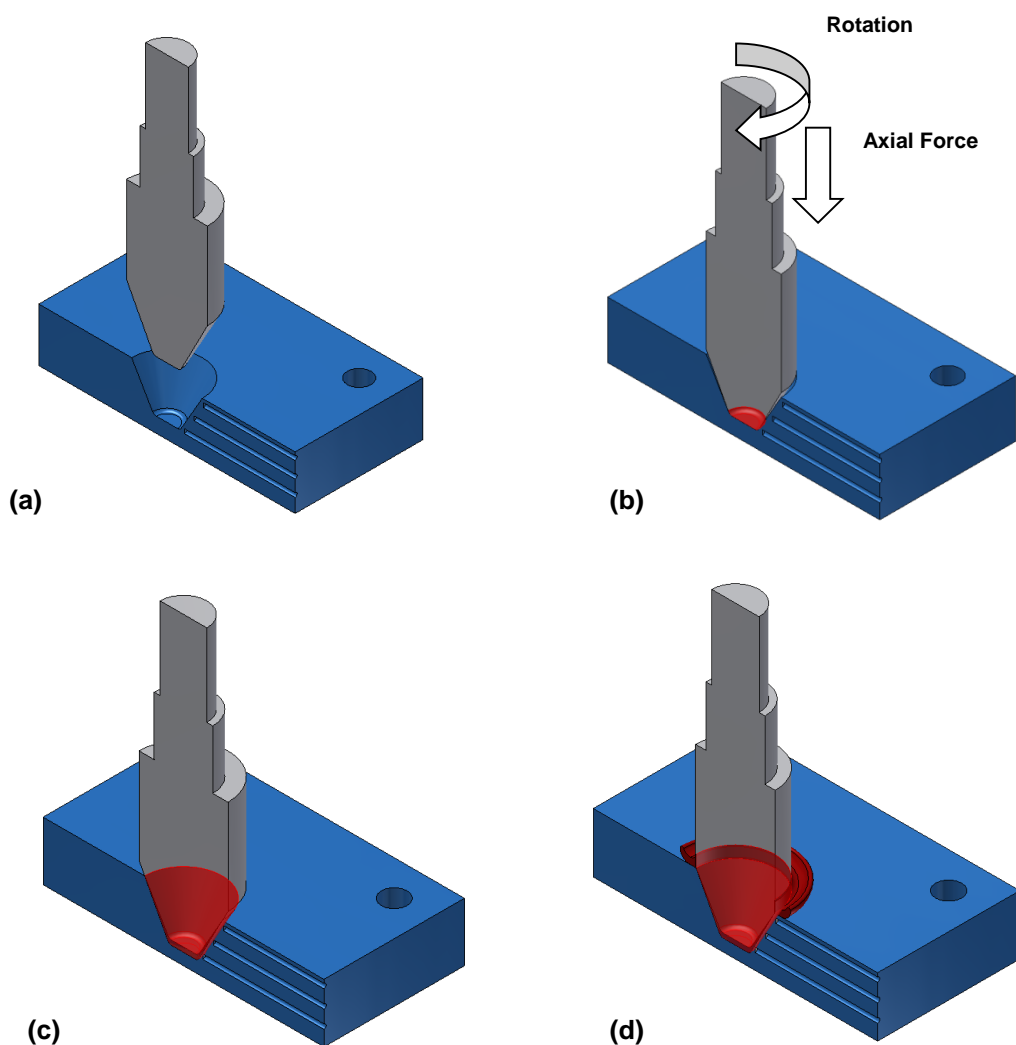


Figure 1-4. Stages of the FTSW Process

### **1.3. Objective**

The research will develop a process window to successfully produce friction taper stud welds in 25mm AA6082 – T6 plate in the partially supported welding condition. The effects of varying of process parameters on the integrity of welded joint will be investigated with respect to energy input, near interface temperature, defect population, static tensile performance and microhardness.

### **1.4. Problem Statement**

To the researcher's knowledge, at present no relative process parameters or scientific work has been conducted on blind partially supported FTSW of aluminium AA6082-T6, specifically regarding energy input during welding and process parameters to produce a good weld in aluminium 6082-T6.

The effects of geometry and process parameters in terms of energy input and near interface temperature need to be quantified with regards to defect population, static weld tensile strength and residual stress. This will allow for the evaluation of this technology as an alternative aluminium welding repair procedure for the industrial sector, and allow process parameters to be transferred between different welding platforms.

### **1.5. Sub-Problems**

#### **Sub Problem 1**

Literature and process parameter on FTSW aluminium is limited; developing an initial parameter window for the research will therefore have to be established.

#### **Sub-Problem 2**

A method of accurately measuring the process torque during welding will be necessary in order to calculate the energy input and energy input rate during welding.

**Sub-Problem 3**

Geometry for the hole and stud needs to be identified, as the high thermal diffusivity and the ability of the material to flow out of the hole with minimal sidewall pressure will change the friction welding characteristics of the process vs. that of steel [4].

**Sub-Problem 4**

A method of approximating the required plunge depth for various geometries needs to be identified in order for welds to be comparative with changes in geometry.

**Sub-Problem 5**

A process parameter window with good geometry and process parameters combinations for blind friction taper stud welding of AA6082-T6 aluminium plate is unknown and needs to be identified. A test matrix must be designed to allow for the identification of good process parameters that facilitate the study of the relationship between process parameters, energy input and joint integrity.

**Sub-Problem 6**

A common issue facing FTSW is the transfer of process parameters between welding platforms that do not have identical axial force, plunge rate and motor torque responses. This limitation will need to be addressed in order to make the FTSW of aluminium 6082-T6 commercially viable.

**1.6. Hypothesis**

The research will yield a process window for blind friction taper stud welding AA6082-T6 aluminium plate in a partially supported condition. These process parameters will be directly correlated to input energy, energy input rate and joint integrity to identify the most efficient process conditions.

**1.7. Delimitations**

- The research will only consider the welding of blind holes.
- The stud material will be restricted to AA6082-T6 in order to maintain matched base materials and hence have similar material properties.

- The process parameters which are varied in this research will be the geometry, rotational speed, axial force, axial force ramp up rate and plunge depth (commonly known as burn-off in rotary friction welding (RFW)).

### **1.8. Significance of the Research**

A need for the FTSW of aluminium as a repair procedure in pipelines, fabricated sections and castings etc. has been identified by industry, specifically the international Canadian company, Alcan. Research will be done in line with comments made by professor Mahoney at the University of Mississippi bringing forward the new repair process that will address many problems currently faced by fusion welding repair procedures.

At present defects in aluminium sections are repaired by conventional fusion welding methods. This presents the repairing of these components with many difficulties, such as the need for multiple weld passes to produce an acceptable weld, high energy consumption, the need for an inert gas shield, repairs requiring an experienced welder, difficulty in repairing short deep cracks, high preparation time and changes in material properties due to melting of the base materials and exposure to elevated temperatures. FTSW of AA6082-T6 is not susceptible to these difficulties. Acceptable repairs are typically produced in a single pass, with no melting of the base material taking place, giving a more homogeneous crystal structure and a small heat affected zone [3] [8]. No shielding gas is necessary due to the removal of oxides during plunge and to the welding action holding the welding interfaces in intimate contact, preventing oxidation. An operator with little or no welding skill can successfully make a weld once the parameters are identified for a given hole and stud profile. Short deep cracks can be easily repaired without removal of significant parent material, and further little to no joint preparation will be required once the hole is machined. The FTSW process can be applied as a repair procedure on pipes and castings where conventional welding is not allowed or suitable and to a variety of applications replacing conventional fusion welding methods.



The FTSW process however presents some disadvantages that will need to be considered before the process is applied to components in practice. Such disadvantages would include;

- The need for a specialised FTSW platform. The unit is not typically mobile unless designed for a specific application, this in turn limits the units application range and adds cost;
- The size of the FTSW platform and the need for mounting fixtures to the work piece limits the application of the FTSW process due to accessibility of the weld region;
- For most FTSW applications there are no predefined parameter for producing a good weld, and exploratory work is typically necessary to verify the weld is acceptable;
- Sufficient material below the weld is necessary in order for the stud to not punch through the bottom of the plate during the FTSW process. This is a considerable constraint in applications where lack of access prevents the mounting of a supportive structure below the weld in thin unsupported sections.

### **1.9. Research Methodology**

A thorough literature study was completed to familiarise the researcher with the FTSW process and the various friction welding processes. Literature on the friction welding and fusion welding of aluminium and its alloys was investigated. Once the literature survey was complete, the development of FTSW of AA6082-T6 followed the following stages;

- Based on literature a preliminary test matrix was designed to investigate a process parameter window and appropriate stud and hole geometries.
- From this data a final test matrix was be developed.
- Welds were carried out according to the test matrix. The joint integrity was quantified according to static performance, defect population macro/microstructure and microhardness.

- The results were analysed, process parameter, energy input and mechanical property maps were generated and near optimum welding parameters identified.
- The link between joint integrity, process parameters, energy input and energy input rate was established.
- All the results and relative data were collected and condensed into the final dissertation.

### 1.10. Research Project Plan

Activity	Start	End
Literature search, Proposal and Load Cell Development	June 2009	January 2010
Weld Trials and Analysis	February 2010	December 2012
Develop Experimental Test Matrix	January 2013	February 2013
Make Final Welds according to the Test Matrix	April 2013	June 2013
Test Samples	June 2013	August 2013
Tabulate the results	August 2013	October 2013
Analyse Final Matrix Results	October 2013	November 2013
Report write-up/ Dissertation	June 2010	January 2013

### 1.12. Summary

This chapter introduced aluminium and the demands placed on the material in typical engineering applications. The FTSW process was identified as a possible repair technique that will be applied to AA6082-T6 in this study as a solution for critical defect repair. The demand for the process is identified and various applications are acknowledged and discussed, with typical advantages of the process over rival repair techniques mentioned. The research objective was clearly identified, with the main focus aiming to develop a process window to produce good FTSW in 25mm thick plate. This section proposes a hypothesis that a process parameter window will exist for the FTSW of AA6082-T6 and that a link between process parameters, energy input and joint integrity will be established.

## CHAPTER 2

### REVIEW OF RELEVANT LITERATURE

#### 2.1. Introduction to Aluminium

Aluminium oxide is one of the most abundant materials on earth [15]. When processed into aluminium it is a light, ductile and readily worked material with good thermal and electrical properties and excellent toughness down to cryogenic temperatures (below  $-100^{\circ}\text{C}$ ), due to its face centre cubic (FCC) atomic structure [15]. It has a tenacious oxide film on the surface that provides good corrosion resistance, but prohibits ease of welding due to the high melting temperature of the oxide relative to the base material [15]. Aluminium is divided into two main categories, namely cast aluminium and wrought aluminium. Wrought aluminium is then further divided into two subcategories, heat treatable and non-heat treatable aluminium. Heat treatable alloys (which are the focus of this study) consist of aluminium-copper, aluminium-silicon-magnesium and aluminium-zinc-magnesium alloys [2] [15] [16]. They have the ability to develop high strength by age hardening (natural or artificial) after solution heat treatment [2] [15] [17]. Non heat treatable alloys are alloys based on aluminium-manganese, aluminium-silicon and aluminium-magnesium. These alloys may only be strengthened by cold working [2] [15].

Aluminium alloys present a challenge with respect to friction welding processes due to aluminium's high thermal diffusivity and low strength retention at elevated temperatures [4]. This may pose a significant limit in the FTSW of aluminium AA6082-T6 due to the relatively small displaced volume of stud material vs. the volume of plate surrounding the hole.

#### 2.2. Summary of Relevant Literature on Friction Welding Processes

To date limited work has been done on the friction taper stud welding and, to the knowledge of the researcher, no work has been published on blind taper stud welding of AA6082-T6.

Hartley [3] reviewed the use of through type friction taper stud welding as used by Lockheed Martin Space systems, shown in Figure 2-1, as a defect repair procedure. After initial development of the process at TWI, Lockheed Martin and the NASA Marshall Flight Centre in Huntsville optimized the process for the new Weldalite<sup>®</sup> aluminium series used on the Orbiter's redeveloped fuel tanks. Repairs made using Hartley's type FTSW process on the Weldalite<sup>®</sup> aluminium exhibited a 20% strength improvement over typical TIG welding, with improved fracture toughness [3].

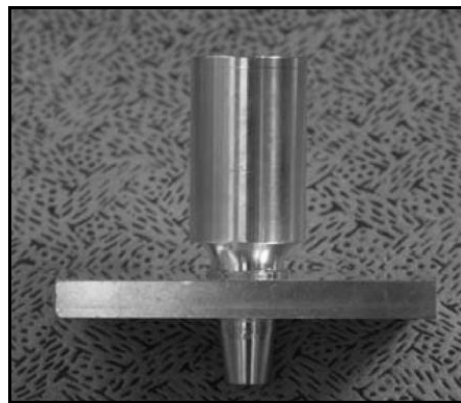


Figure 2-1. Through Type FTSW [10]

Beamish [4] researched the process of through type friction taper stud welding of 10mm AA6082-T6. The research explored the effects of friction pressure, rotational speed, plunge depth and geometry with respect to weld quality. High quality welds were achieved with optimum parameters (shown in Table 2-1) achieving 115° in a three point bend test. Frictional heating resulted in softening of the T6 temper across the heat affected zone (HAZ), with peripheral velocity shown to be a greater influence on joint quality rather than rotational speed itself, with a minimal nose peripheral velocity requirement of 1.7m/s. Beamish noted the lack of literature on the topic in the public domain and attributes the slow uptake of the process in industry to this.

When comparing the results of the three included angles of the stud and hole geometry tested by Beamish, the following conclusions could be made. With a 30° included hole taper angle, the bend test results were low, ranging between 21° and 60°. This was attributed to the ability AA6082 to plasticize and flow through a 30° extrusion die, reducing the hydrostatic forces on the walls of the hole, with the majority of the material flowing out below the weld interface. At 60°

included hole taper angle, improved joint performance was recorded, with a 90° hole included angle achieving 90° repeatedly. Beamish [4] concluded that, although process parameters plunge depth, rotational speed and axial force all play a role in the performance of the joint, none could be considered as a singular critical success factor. A critical comment made by Beamish was that in any future work on FTSW process, the investigation should include the accurate measurement of process torque to allow for the analysis of energy input and energy input rate, as this governs the microstructure and, therefore, the mechanical properties of the welded joint [4].

**Table 2-1. Process Window for Through Type FTSW [4]**

Hole Taper Angle (°)	60		90	
Bottom Hole Diameter (mm)	8	10	8	10
Plug Diameter (mm)	25			
Plug Nose Diameter (mm)	8	10	8	10
Plug Taper Angle (°)	59	59	90	90
Consumed Length Past Plate Contact (mm)	1			
Force (kN)	50-60			
Rotational Speed (RPM)	4500-5000			

Nicholas [18] completed one of the first comprehensive reports on friction hydro pillar processing, investigating tapered as well as parallel hole configurations. It was found that a tapered hole configuration performed better on materials with poor plastic flow characteristics [18]. Nicolas explains that the force applied to the sidewalls of the hole is a function of the hydrostatic behavior of plasticized materials [18] [19], correlating with Beamish [4]. Nicholas [18] further assumes that the tapered hole configuration assists with bond formation on the sidewalls of the tapered hole due to the improved normal force applied.

Mahoney et al. [20] presented a patent on a method to repair voids in aluminium alloys. The research focused specifically on the filling of exit holes for friction stir welding applications, using a FTSW process. A tapered configuration was chosen over the parallel configuration due to aluminium's reduced strength at high temperature, high thermal diffusivity and high oxidation rate [20]. Mahoney et al. used a tapered hole with ridges machined into the hole surface, as shown in Figure 2-2, with a stud included angle less than the tapered hole. The tapered sides and ridges machined into the hole typically forced only the interface of the

stud and hole to plasticize and shear. As the excess frictional heat developed by the conventional FTSW process was found to degrade the structural and metallurgical properties of aluminium, only plasticizing the ridges improved the quality of the weld, as less frictional heat was used to make the joint. The included angle of the hole was  $60^\circ$  with 72 ridges per inch machined vertically into the surface of the hole. In order to overcome stalling of the stud due to overheating of the material, a heat sink was included as part of the stud, which increased the volume of material immediately above the tapered section for heat to dissipate into, prolonging shearing of the stud material [20].

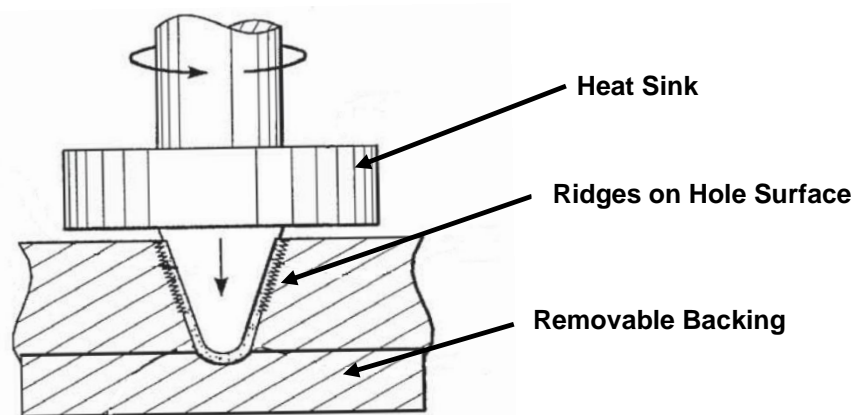


**Figure 2-2. Aluminium Alloy FTSW with Consumable Heat Sink [20]**

Mahoney et al. [20] noted that as the stud was consumed, the ridges on the surface were crushed and plasticized by the plug material. This improved local deformation and mixing of the parent materials compared to a smooth tapered wall configuration. The weld plug was found to be thoroughly bonded to the hole and that the weld consisted of fine recrystallized material. Mahoney et al. [20] overcame the problem of annular defects forming at the base of a through type FTSW found by Beamish [4] by having a backing plate with part of the tapered hole machined into it as shown in Figure 2-2. Poor bonding was found between the base of the hole and the backing plate due to reduced rubbing and subsequently reduced plasticization at the bottom of the hole. This region was, however, machined away, leaving the fully bonded region intact, though no mechanical properties are presented.

### 2.3. Process Parameters Applied To Friction Welding

There are many process parameters and conditions that influence the overall success of a friction welding process. The process parameters are the variables that can be controlled by the welding platform, and the process conditions are the variables that are material and ambient condition related. According to literature, the process parameters that influence the quality of a FTSW are;

- Plunge Depth (Burn-Off);
- Rotational Speed (Specifically Relative Velocity);
- Axial Force (friction and forging force);
- Hole and stud geometry.

Beamish [4] stated that the parameters plunge depth, rotational speed and axial force all affect the joint integrity of the FTSW, with none alone considered as the critical factor for a good FTSW, although as a guideline, high rotational speed and axial force generally produced superior welds due to more rapid heat dissipation.

#### 2.3.1. Plunge Depth

Plunge depth is the vertical upset distance (or burn-off) of the stud that is consumed during tool rotation, under the axially applied load. It governs the volume of displaced plasticized material used to heat and fill the tapered hole. The applied axial force and rotational speed during plunge influence the time required to reach a specific plunge depth, with literature typically showing the time from stud contact to the end of rotation reducing as the friction force is increased and rotational speed is decreases [8] [10] [11] [21]. When the rate of plunge is high, less time is available for grain growth and homogenisation of the weld, with low values of plunge depth found to be desirable. This is due to the reduction of total input energy and, therefore a reduced HAZ [4] [11].

Kimura et al [13] introduced a method of improving the rotary friction welding of steel by controlling the welding time, not the plunge depth. The research showed that if rotation is stopped at the point of maximum torque, the entire weld interface would be in a state of shear, indicating complete bonding. Joints with 100% static

joint efficiency in steel were achieved without the need for a plunge depth greater than the amount to achieve maximum process torque. Any additional plunge would decrease the process torque and reduce yield strength due to increased temperature, as shown in Figure 2-4. This was also found by Sahin [22], who showed that as welding time is increased, the tensile strength of the joint improved until a critical point is reached. Beyond this point any increase in welding time reduced the tensile strength of the joint as shown in Figure 2-4. These findings correlate with work by Samuel [23] on friction stud welding of stainless steel, where no improvement in tensile strength and a large reduction in extension to fracture (a measure of ductility) was noted when excessive welding time was used, as shown in Figure 2-5 and Figure 2-6 respectively.

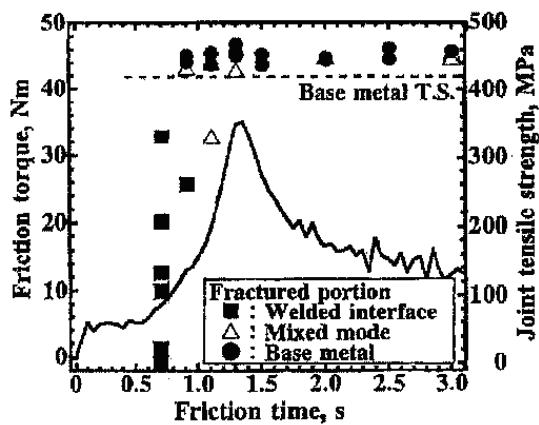


Figure 2-4. Process Torque vs. Tensile Strength [13]

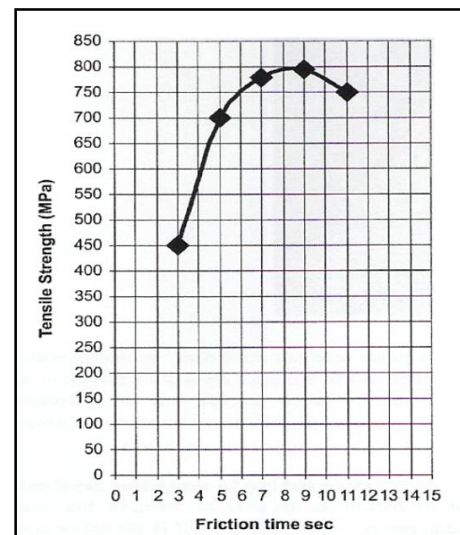


Figure 2-3. Tensile Strength vs. Friction Time [22]

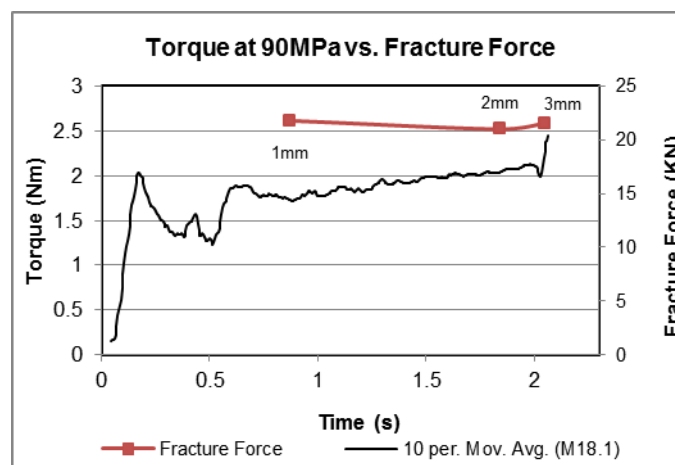


Figure 2-5. Tensile Strength vs. Welding Time in Stainless Steel Stud Welds [23]



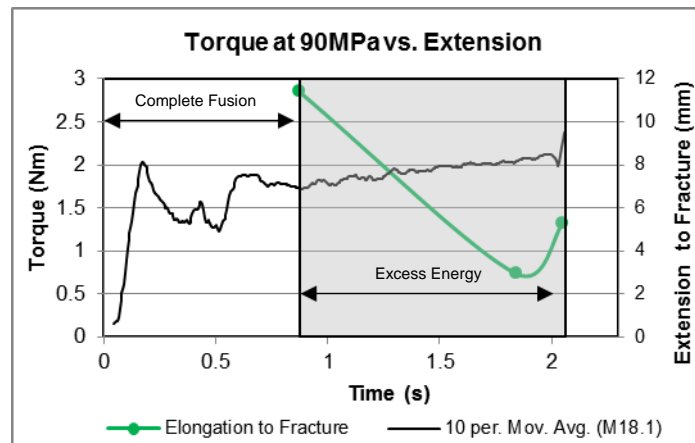


Figure 2-6. Extension to Fracture vs. Welding Time in Stainless Steel Stud Welds [23]

Beamish [4] noted that excessive plunge depth resulted in excess heating and softening of the weld nugget in through type FTSW of AA6082-T6. The study suggested that low plunge depths were beneficial as it reduced the total heat input into the aluminium, achieving successful FTSW when rotation was stopped at the point when the stud contacted the plate. The literature showed that plunge depth is critical to the completion of a FTSW, and that the amount of plunge should be minimal to minimise the effect of the welding process on the heat treatable AA6082-T6 material [4] [22].

### 2.3.2. Rotational Speed

The rotational speed and hence peripheral velocity of the welding interface during a friction welding process is generally considered to be one of the least influential process parameters, with significant changes required to influence the weld quality [10]. Literature further suggests that it is common practice to apply a constant rotational speed, reducing the number of weld tests required [4] [5] [10]. It has been noted that increases in rotational speed can make up for a lack in another process parameter, such as marginally low friction force [23]. However, this does not imply that an increase in rotational speed will give improved weld quality. The range over which changes in rotational speed has been shown to account for incorrectly selected axial force or plunge depth is limited [23]. As in RFW, there is a rotational speed range over which FTSW can be successfully made [10]. This rotational speed range is considered to be material, geometry and application specific [4] [10].

Edar et al. [7] discussed that low rotational speed increases the duration of the initial heating phase of the friction welding process [7]. This increases the time taken to reach the initial maximum torque, before plunge begins. When rotational speed is reduced, the peak torque prior to plunge increases [8] [10] [23]. This is attributed to the reduced energy input rate of low rotational speed welds, as the surrounding material has less heat to dissipate; therefore, the weld interface at seizure will be cooler, increasing the flow stress of the material and subsequently increasing the torque [23]. It is suggested that if the peripheral velocity becomes too low, the energy input rate becomes insufficient to prevent tearing of the weld interface material [10] [24]. Tearing of the interface was noted by Samuel [23] at low peripheral velocities when friction stud welding 6mm stainless steel, as shown in Figure 2-7. If the Peripheral velocity is too high, the shearing/ tearing effect at the weld interface is replaced by a polishing effect [8] [12] [25]. In this case, the thermal gradient becomes too steep, overheating the immediate weld interface material and reducing the frictional torque. This reduces the integrity of the joint as shown in Figure 2-8, by inducing rubbing instead of tearing of the welding interfaces, as documented by Vill [8]. Beamish [4] maintained that a stud nose peripheral velocity of 1.7m/s is required when welding AA6082-T6, although it will not guarantee a successful weld [4].

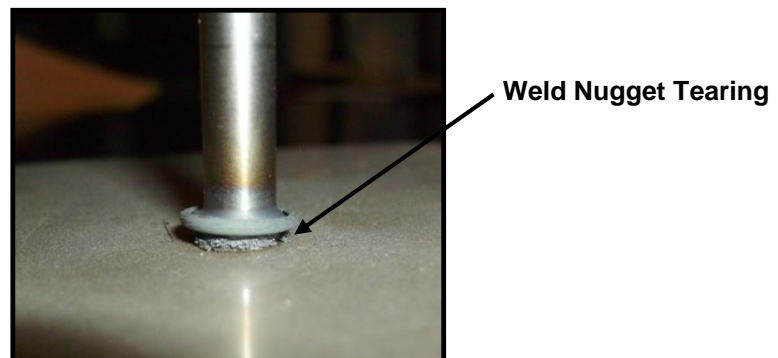


Figure 2-7. Weld Nugget Tearing in Friction Stud Welding of Stainless Steel [23]

Ahmad et al. [14] joined 15mm diameter AA6061 rod to sintered aluminium rod by RFW. Rotational speeds of 1250RPM, 1800RPM and 2500RPM were tested in the research, giving peripheral velocities of 0.98m/s, 1.41m/s and 1.96m/s respectively. At 0.98m/s a uniform grain structure was seen on both sides of the interface.

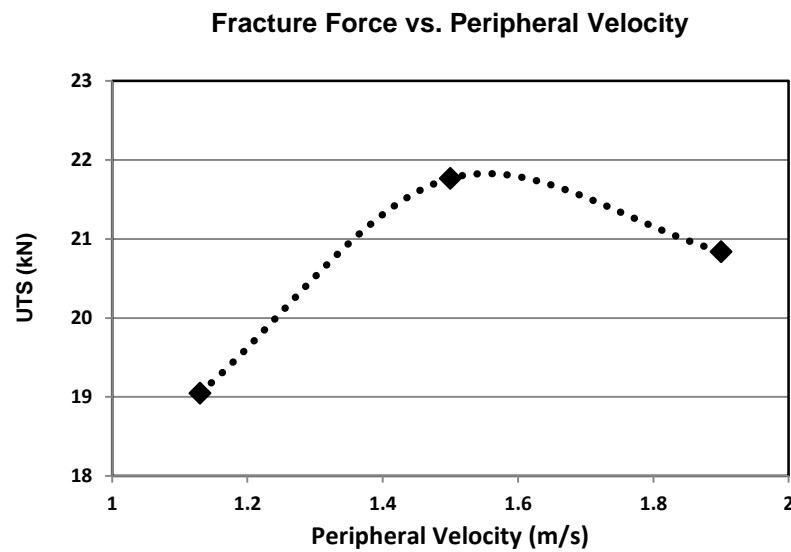


Figure 2-8. UTS vs. Peripheral Velocity for a Stainless Steel Friction Stud Weld [23]

The plastic deformation zone was not clearly visible and cracks in the un-joined regions were observed. At 1800RPM the weld interface was clear, with no lack of fusion. The flash cracks and grains were observed to be pulled in the direction of rotation due to torque stresses. At 2500RPM the AA6061 was more severely deformed by plastic deformation and frictional heat near the weld zone. The effects of rotational speed were further quantified by a bend test, the results of which are shown in Figure 2-9. The results show that the joints with the narrowest plastically deformed zone had the lowest weld integrity. With increased rotational speed, the time needed to achieve plastic deformation on the AA6061 side decreases. Therefore, the high rotational speed gave high plastic deformation, a wide plastically deformed zone, a harder weld interface and a shorter welding time [14]. This correlates with the results shown in Figure 2-8, showing peripheral velocities above 1.4m/s to be appropriate.

It is clear from literature that the stud nose peripheral velocity in a FTSW application will need to be sufficient to maintain the interface in the plasticized state, without inducing rubbing at the final shear interface. However, due to platform limitations and the sizes of the FTSW studs used, high rotational speeds will need to be maintained to minimise process torque.

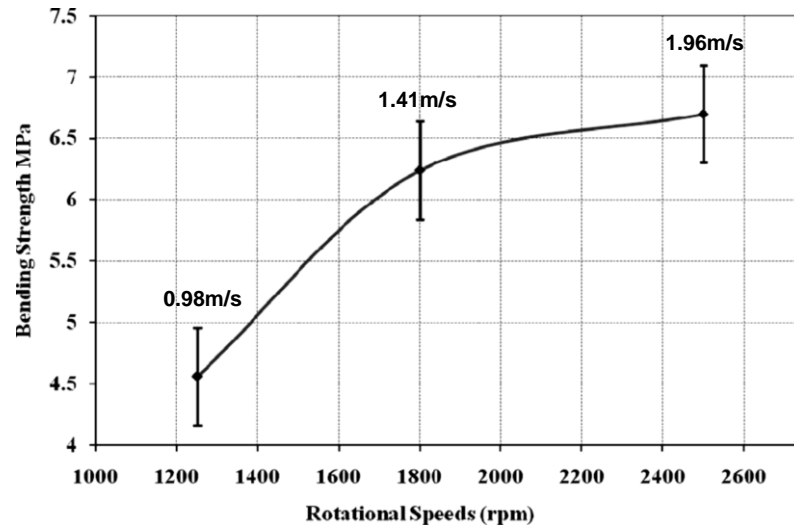


Figure 2-9. Bend Strength of RFW with increased Peripheral Velocity [14]

### 2.3.3. Applied Axial Force during Rotation (Friction Force)

Axial force applied during rotation, which is also commonly known as friction force, is the force axially applied to the consumable tool during plunge of the friction welding process. It is considered to be one of the more influential parameters in a friction welding process, and is one of the most sensitive. It is responsible for holding the weld interfaces in intimate contact with one another, with sufficient surface pressure to keep contaminants out of the weld zone, halt the formation of voids and prevent oxidation [8] [10] [12].

It has been found that higher axial force increases the upsetting rate of a friction welding process, thus shortening the heating time [10]. Mitelea et al. [26] noted that when joining heat treated 42MoCr11 steel, that changes in axial force alter the heating and cooling conditions of a RFW process. The high axial forces cause high values of localized heating to occur at the weld interface giving a steeper thermal gradient between the weld zone and surrounding material [26] [27] [28]. This means that the heat generated by friction and the energy released during the shearing of metallic bonds formed during seizure and plasticization, is used to locally heat the weld interface [10]. Therefore, if a low axial force is applied, the process time increases, allowing heat to dissipate through the material, reducing the thermal gradient, with the opposite true for high friction force. Further, increased axial force expels the weld interface material out of the joint as flash in a shorter time [4] [23]. This reduces the heat conduction in the

axial direction and creates a greater thermal gradient [10] [26]. Sahin [22] investigated the effect of increasing axial force and friction time. Sahin [22] found that there is a bell curve effect with regards to axial force as shown in Figure 2-10. If a low axial force is used, weld strength was shown to be poor. As axial force increases, so too does the tensile strength. Sahin [22] documented that tensile strength will improve with increased axial force until a process peak is reached; any further increase is shown to reduce tensile strength [22]. This shows that there is a clear axial force process window for a friction welding processes and that there is a limit to the axial force that can be applied. Literature has shown that axial force further influences the size and form of the HAZ [10]. Low force produces an almost parallel boundary, while higher force produces a double cone towards the centre of the stud [10].

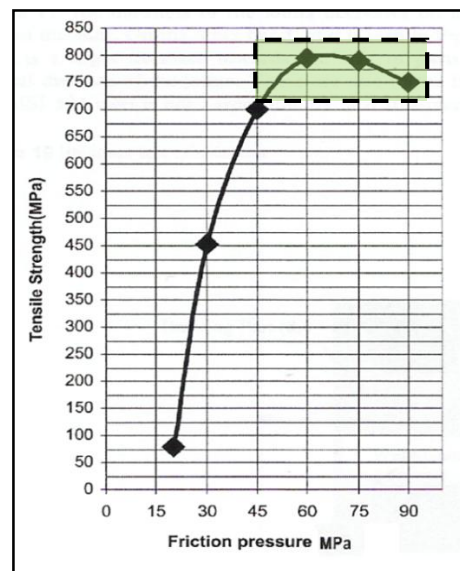


Figure 2-10. Tensile Strength vs. Friction Pressure in AISI 304 [22]

Beamish [4] found that when FTSW is applied to AA6082-T6, the axial force encourages the weld interface to move rapidly upwards to the top of the tapered hole. Insufficient force produced welds with a lack of bonding at the lower surface of the plate and upper surface flash.

#### 2.3.4. Applied Axial Force after Rotation (Forging Force)

The axial force applied to consolidate the weld once the plunge depth has been reached, is commonly known as the forging force. Mitelea et al. [26] found that if high values of forging force are utilized, the weld interface would form a bi-

concave shape [26]. If a forging force was applied that was substantially greater than the friction force, the bi-concave profile could lead to crack initiation points. This is because the outer portion is at a higher temperature than the central region in a rotary friction welding process and can support less pressure [23] [26] [29]. When the elevated forging force is applied, the softer outer region will flow out and the cooler central region will experience a far greater pressure due to the reduced area. This will cause deformation in the colder central material, causing a crack initiation region.

Based on this, the forging force will be kept the same as the friction force for the majority of this research, unless otherwise stated. This will remove a variable from the process and can be further investigated once successful welds have been achieved, if necessary. The forging force will therefore be referred to as axial force throughout this document. The forging force, when different from the friction force, can be applied in two ways, either during the stopping of rotation or once rotation has stopped. In this work, when applicable, the forging force will be applied only once rotation has stopped entirely. This will prevent excessively high stopping and terminal torques.

#### **2.4. Fusion Welding of Aluminium Alloys**

To understand and develop the FTSW process of aluminium, specifically applied to AA6082-T6, an understanding of fusion welding procedures applied to the material is necessary. This will assist in quantifying the need for the process and to establish complications that may arise that are related to both welding processes.

The fusion welding of aluminium has critical factors that influence its weld-ability, namely;

- High thermal diffusivity, making it difficult to input sufficient energy to complete the weld [15] [16].
- The presence of a tenacious surface oxide film, that if not removed from the weld can lead to lack of fusion and porosity [15].
- High solubility of hydrogen in liquid aluminium leading to the formation of porosity [15].

- Some alloys, specifically 6xxx suffer from hot cracking in the HAZ due to liquation [15].

The most popular fusion welding processes that produce high quality welds in aluminium are TIG and MIG welding [2] [16] [30].

#### **2.4.1. TIG Welding**

TIG welding is predominantly used for light gauge plate, from 0.8mm to 12.5mm, giving excellent control over penetration. It is however a relatively slow process when compared to MIG welding, achieving approximately 200mm/min [2] [16].

#### **2.4.2. MIG Welding**

MIG welding is a more economical fusion welding process when material thicknesses greater than 6mm are to be joined [2] [16]. Welding speed ranges between 500mm/min to 1000mm/min. Penetration control is difficult for thin material, with edge welds not possible and welding of thick pipe sections avoided due to the problem of penetration control [2] [16]. This is relevant, as it is difficult to make a deep, narrow MIG weld in aluminium, which is possible with FTSW.

#### **2.4.3. Oxide Formation**

Aluminium has a tough corrosion resistant oxide layer over the material surface. The oxide is strong and has a high melting temperature of approximately 2050°C [16]. The oxide has a higher density than that of the molten weld pool during fusion welding and will form at the base of the weld if not removed prior to welding [2] [15] [16] [31]. It is therefore essential that all oxides are removed from the welding interfaces before welding [16]. This may prove problematic for FTSW, as the hole is cleaned before preheating, the oxide layer therefore has time to reform before welding. Axial forces high enough to break up the oxide layer will therefore need to be applied when FTSW aluminium AA6082-T6.

#### **2.4.4. Porosity Formation**

Hydrogen formed by the breaking up of water molecules found on the material surface, is highly soluble in molten aluminium [16] [32]. This forms gas bubbles that are trapped when the weld pool solidifies [16] [32]. The hydrogen bubbles form voids, known as porosity that are detrimental to the weld [16] [30] [32].

Porosity in fusion welding is further aggravated by high cooling rates, as the weld pool solidifies too quickly for the bubbles to move to the surface. If porosity free welds are to be produced, the weld surfaces should be cleaned and the oxide layer removed before welding, as base metal cleanliness is critical [16].

### **2.5. The Need for Preheat**

The surface oxide layer that naturally forms on the surface of aluminium is porous [2] [15] [32]. This layer absorbs moisture from its surroundings, and when welded, forms hydrogen bubbles in the weld pool [15] [16] [30]. When the weld solidifies the hydrogen gas is trapped and is seen as porosity within the weld [16] [30] [32]. In fusion welding this moisture is removed by preheating the base material, effectively drying the porous oxide layer [17] [30]. In the case of FTSW aluminium, this is specifically important for the plate, as very little of the plate material is carried away with the flash (secondary flash). Consequently contaminants may be easily trapped within the weld zone.

Aluminium alloys typically have high thermal diffusivity, approximately four times that of steel [2] [17]. This cools (conducts away the heat) the filler material during fusion welding so rapidly that when thick sections are welded, fusion is occasionally not achieved [15] [31]. Therefore, depending on the geometry of the material to be welded, conventional fusion methods (specifically arc welding due to energy input being limited by the consumable electrode) may not overcome the heat dissipation rate at the weld interface [15] [31]. Additional heat is therefore needed to drive the fusion process. Preheat is applied to the plate to reduce the energy required from the electrode and reduce the thermal gradient between the weld and the plate. This increases and retains the heat at the weld interface, promoting fusion and reducing the likelihood of stress cracking in thick sections [30] [31]. Preheat further increases the diffusion coefficient and diffusion rate of aluminium, and consequently less energy will be needed for diffusion to take place as shown in Figure 2-11 [33].



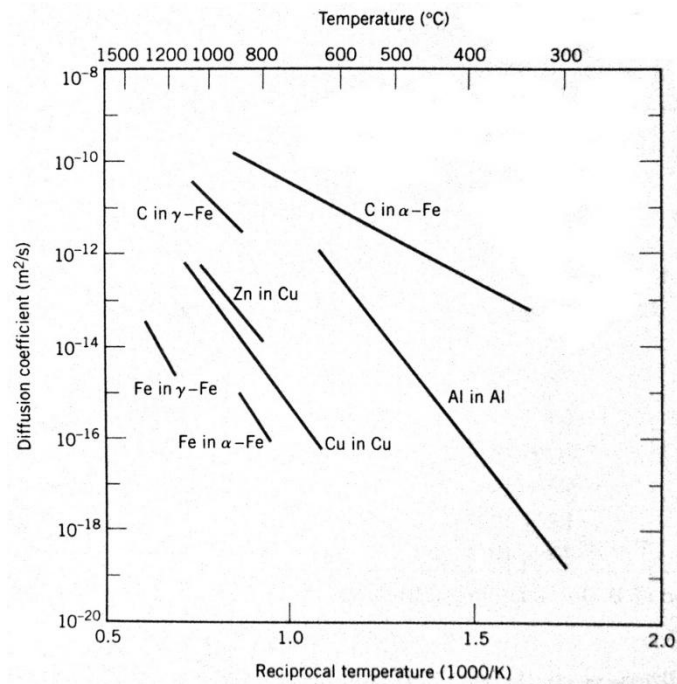


Figure 2-11 Logarithmic Plot of Diffusion Coefficient vs. Temperature [33]

This is specifically important when FTSW aluminium, for as the first bonds are formed at the base of the hole, the high thermal diffusivity of the plate material conducts heat away from the interface at a rate that may prematurely solidify the initial bonds between the plate and the stud. This could prevent contaminants on the surface of the plate flowing out of the joint with the flash and prevent bonding across the entire surface, negatively affecting the integrity of the joint. Further FTSW is expected to face similar energy input issues to fusion welding, with regards to the limit of the energy input rate sustainable of the stud. Generally preheats applied to aluminium are relatively low due to the materials low melting temperature, typically around 80°C to 120°C for plate thicknesses up to 8mm, and up to 200°C for thicker sections [15] [17] [30] [31]. As preheat is partially geometry dependant, if it is applied to FTSW of AA6082-T6, the required temperature and its effect on the process will need to be investigated before selection of the preheat temperature.

## 2.6. FTSW Process Characterisation

In order to accurately describe and explain the process of friction welding, and more specifically FTSW, the process is often divided into four stages [10] [22] [34]. Kimura et al [13] divided the process up into the wear stage, seizure stage, heating stage and forging stage, given in Figure 2-12.

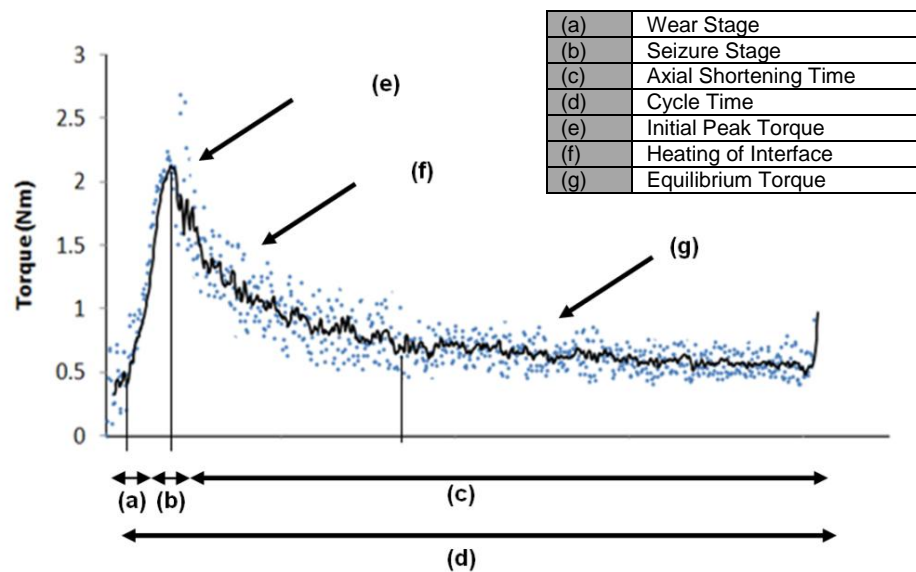


Figure 2-12. Torque Stages during a Friction Weld [23]

### 2.6.1. Wear Stage

In the first stage (wear stage) the torque is low and constant, due to surface roughness allowing only a reduced percentage of the surfaces area to be in intimate contact. These elevated regions experience high localised pressure due to the reduced area, promoting plastic deformation and flattening (or polishing) of the surfaces during rotation [10]. The wear stage, which begins at the initial contact of the interfaces, produces a smoothening effect on the surfaces where any surface roughness is effectively rubbed away [10] [13]. The surface roughness is partially smoothed by elastic and plastic deformation, with localised melting taking place in the outer regions of the weld zone [12] [35]. In many cases the material rubbed away is deposited as a metallic dust as seen on the backing plate of a friction stud weld, shown in Figure 2-13 [23].

As the surface roughness is removed, a greater portion of the weld interface makes contact, marginally increasing the frictional torque and subsequently the heat generation. According to Kimura et al. [13] [34] and Pinheiro [10] the wearing of the interface begins at the outer periphery of the welding interface where the relative velocity is at its highest and propagates inwards as seen in Figure 2-14 [10] [13]. The wearing from the periphery to the centre of rotation repeats, continually forming a fresh surface layer until sufficient heat is generated at the interface to enter the seizure stage [9] [34]. Because of this repeated

replacement of the interface layer, the heat generation in this stage is considered to be small [13]. Kimura et al. [13] documented that little to no material is consumed during the initial wear stage and that plunge only becomes significant once seizure of the weld interface begins and the initial peak torque is reached.

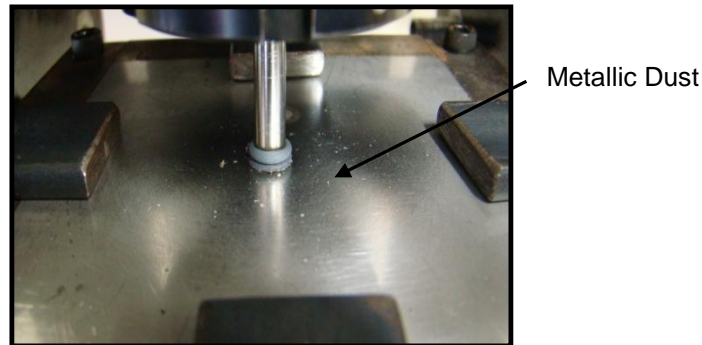


Figure 2-13. Metallic Dust Deposited During the Wear Stage of a Friction Stud Welding Process [23]

Friction time	Rotating side	Fixing side	Friction time	Rotating side	Fixing side
0.04s			0.7s		
0.11s			0.9s		
0.3s			1.1s		
0.5s					

Figure 2-14. Welding Interfaces at Various Times into a RFW [13]

### 2.6.2. Seizure Stage

Seizure, which is the formation of isolated microbonds between the welding interfaces, initiates once the surface roughness has been removed and the temperature of the fresh interface is sufficient to initiate bonding [10] [13] [34]. Kimura et al. [13] [34] noted that seizure and subsequent joining of the two materials initiated from the centre of the weld where the relative velocity is at its lowest and propagated outwards towards the periphery as seen in Figure 2-14 from 0.7 seconds onwards [13]. These microbonds are sheared during rotation,

liberating the energy stored in the deformed material as heat into the surrounding material [10] [12] [13]. This aids the formation of additional bonds at the weld interface, increasing the area in shear and process torque. This stage is, therefore, characterised by a steady climb in torque as seen in the seizure stage of Figure 2-12 [13]. The process torque reaches its peak value in a rotary friction welding process when the entire weld interface is in a state of shear. This peak is caused by the removal of oxides, surface impurities and the increase in surface area in shear at the weld interface [10] [13] [23]. Consequently the second phase is complete at the point of initial maximum frictional torque at which point axial plunge begins [13].

### 2.6.3. Heating Stage

Once the point of maximum process torque has been reached and plunge begins, the energy input into the weld is no longer used to heat the immediate weld interface and form bonds, but it forms dynamically recrystallized shear layers, or hot shears as described by Beamish [4], forming a fine grained column of material in the hole, as shown in Figure 2-15.

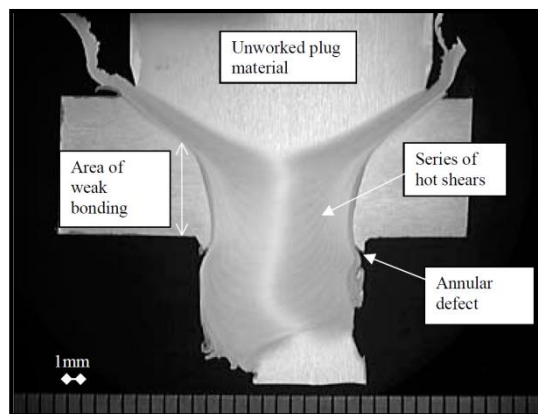


Figure 2-15. Through Type FTSW [4]

This heating of the interface and surrounding material reduces the shear strength of the material, reducing the frictional moment needed to shear the bonds at the interface, characterised by the drop in process torque [10] [13] [23]. During welding a small volume of plasticized material is forced out from the weld as flash carrying away oxides and surface impurities from the weld zone [13]. This brings fresh cold material from behind the weld interface forward to the weld interface [10] [23]. Once equilibrium is reached, the frictional torque stabilises as shown

in Figure 2-12. In RFW this equalised torque will then continue until a set value of plunge is reached and rotation is abruptly stopped.

According to Samuel [23], the equilibrium torque, shown in Figure 2-12 on page 25, at high values of axial force can begin to climb after the steady state peak torque is reached, as shown in Figure 2-16. It is characterised by a drop in process torque as the interface heats, followed by a steady climb in process torque as fresh cold material is brought forward at a greater rate than the plasticization rate. High axial force, therefore, reduces the temperature that the plasticized material will need to reach before it flows out of the weld interface, reducing the temperature of the material directly behind the weld interface and ultimately reducing the width of the band of heated material directly above the weld interface. The material brought forward to be plasticized is, therefore, at a lower temperature compared to a weld with low axial force. The reduced temperature of the plasticized material and material introduced into the welding zone increases the thermal gradient between the plasticized weld nugget and stud material, removing heat from the interface more quickly. The weld nugget, therefore, maintains a higher shear stress, increasing the process torque [23]. This climbing torque eventually equalises if sufficient friction time is allowed; however, this value has been seen to rise above the seizure torque peak, depending on the rotational speed used in the friction welding process [23]. This shows how quickly changes in axial force can alter the conditions at the weld interface and how easily a weak weld can be produced with either excessively high or low axial force.

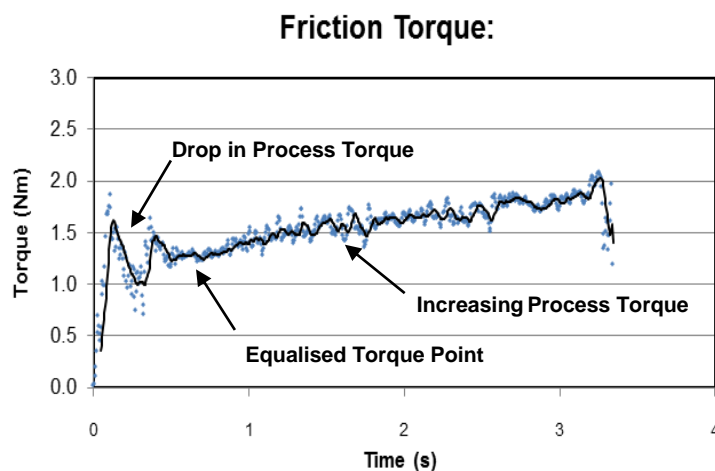


Figure 2-16. Increasing Equalised Torque for Stud Welds [23]

### 2.6.4. The Effect of Axial Force on the Welding Interface

The cooling rate, or cooling conditions, in a friction welding process are predominantly governed by the material, geometry and thermal gradient. A further contributor to the cooling rate is the effect of sensible energy stored in the flash. If high axial force is applied, the flash temperature will be high due to the high localised interface temperature and the lack of heat conduction into the surrounding parent material. Therefore, if the flash has a large mass, a large quantity of energy will be stored in it. This heat energy will then be conducted back into the weld once rotation has stopped, reducing the cooling rate within the HAZ [10]. Therefore, for the same amount of plunge depth, welds with shorter welding times generally have higher energy input rates [10]. This is demonstrated in Figure 2-17, where the effects of increasing the heating time, friction pressure and rotational speed on the interface temperature of a rotary friction weld are shown after recording it with a thermal camera [10] [36]. At high axial forces the temperature across the interface is more homogeneous, which is further improved with reduced rotational speed. This shows that in order to achieve an even temperature across the interface, the correct axial force and rotational speed are critical. Inappropriate selection will result in uneven heating and poorly bonded regions.

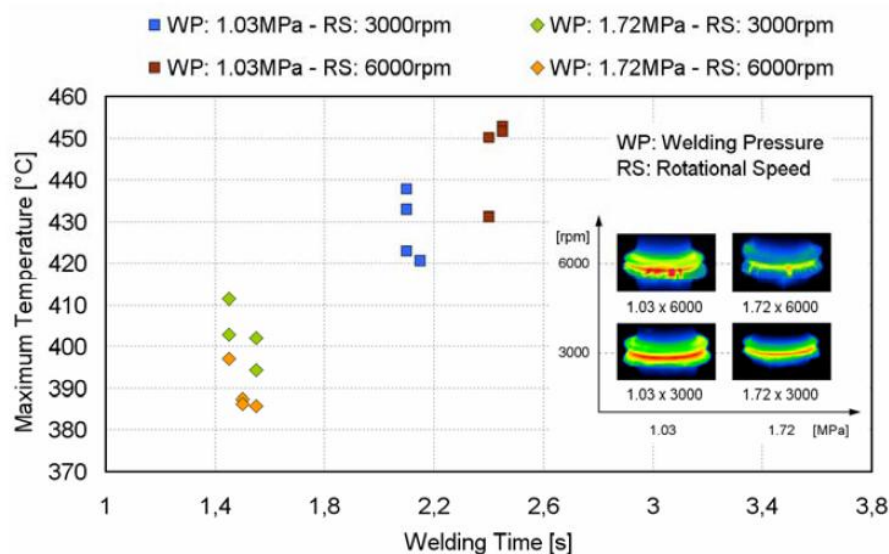


Figure 2-17. The influence of Time and Axial Force on Interface Temperature [36]

### 2.6.5. Stopping Stage

Once the pre-set plunge depth is achieved, rotation is abruptly stopped and a continuous axial force applied to consolidate the joint for a fixed cooling time, commonly 20 seconds [5] [6]. As rotation slows, the number of microbonds sheared at the interface at any point in time increases, requiring a greater torsion moment to rotate. By increasing the amount of bonds sheared per unit time, a greater quantity of heat is liberated. This additional energy causes the temperature to momentarily rise, attempting to maintain the material at the interface in a plasticized state [10]. As rotation slows further, a point is reached where the temperature at the weld interface cannot be maintained. As the material cools beyond a critical point, the shear strength of the material increases, causing the frictional moment to spike, termed the terminal torque [4]. Literature indicates that the terminal torque peak increases with stopping time [10] [23]. Eichhorn et al. [37] and Beamish [4] found the terminal torque to be unavoidable, while Kimura et al. [13] noted that the braking time had a negligible effect on the joining of a rotary friction welding process [13] [37].

### 2.6.6. Forging Stage

Once rotation has stopped, a continuous forging force is applied to consolidate the joint. The interfaces are brought closer together, reducing atomic distance, producing metallic bonds [10]. As the material cools, static recrystallization begins [10]. Once recrystallization is complete, and the weld zone has dropped below 200°C, the forging force is released and the welding process is complete. In literature the forging force used is predominantly higher than the friction force; however, research by Kimura et al. [13] shows that successful welds can be produced without an elevated forging force.

## 2.7. Process Energy and Energy Input Rate

The amount of energy and the rate of energy input into a FTSW governs the microstructure of the weld and, therefore, the mechanical properties of the joint [4].

Beamish [4] recorded friction torque during two welds during work on FTSW of AA6082-T6, and used the data to calculate the energy input rate and total energy

input during a weld. The results showed that the two welds, both with a HAZ width greater than 5.8mm and having the same peripheral velocity, but with different axial forces, (30kN and 50kN respectively), failing at 30° and 90° respectively in a bend test, with the results suggesting that a certain energy input is required to plasticise the material filling the tapered hole [4]. Beamish [4] stated that access to such information would be invaluable in results interpretation, and would provide a means of comparing welds made in different materials. Further; this information would allow for parameters to be predicted for different materials and geometries [4]. Beamish [4] suggests that there is a number of ways to express the heat input of a weld, but recommends considering the amount of energy per unit hole interface area. However, due to lack of data, was unable to verify this, but hypothesizes that for a through type FTSW the requirement will be greater than 22J/mm<sup>2</sup>. Though limited, the observation by Beamish regarding the lack of knowledge and data regarding energy input and energy input rate identifies the need for energy data during FTSW, and will form the main body of this research.

### **2.8. Geometry Applied in Current FTSW Processes**

Due to the lack of knowledge and published work on the FTSW process and more specifically, blind FTSW applied to aluminium, few sources of accurate weld data could be identified. This reduced the body of work that could be used to establish a preliminary process window for the FTSW of AA6082 – T6 aluminium. The following summarises the hole and stud configurations known to the researcher, that were used to make successful friction taper stud welds in a variety of materials, that contributed to the initial geometry process window selection, used and/or tested in this research.

Nicholas [18] and [19] assumes that a tapered hole configuration will assist sidewall bonding due to the increased applied force on the tapered surface. The greater the angle of the hole, the more of the applied load is transferred to the sidewalls [19]. Therefore, the more ductile the material, the greater the required taper angle of the hole and stud [18] [19]. Nicholas [19] further stated that investigations into the effects of taper angle with respect to bond quality have not been significantly reported.



Van Zyl [38], using Chromium-Molybdenum (10CrMo910) made blind friction taper stud welds using a stud and hole included angle of  $15^\circ$  and  $20^\circ$  respectively to fill a 25mm deep hole in his research on modelling of heat distribution during FTSW. The stud and hole configuration utilized in Van Zyl's research is shown in Figure 2-18, utilising a constant set of process parameters, shown in Table 2-2.

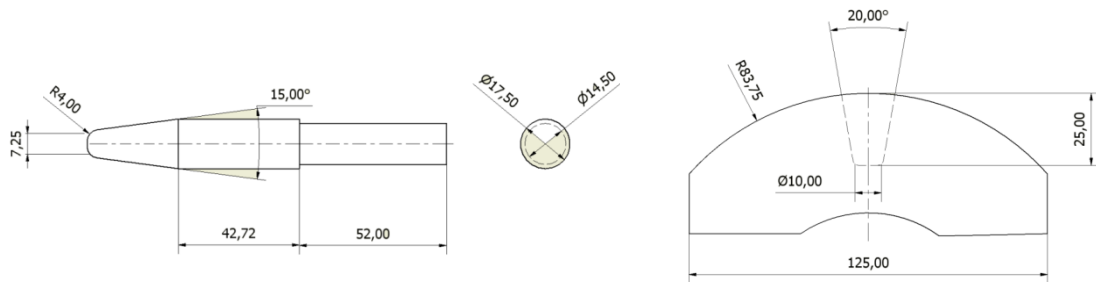


Figure 2-18. Geometry Tested by Van Zyl for FTSW CM Steel [38]

Table 2-2. Process Parameters Used by Van Zyl [38]

Axial Force (kN)	17.78
Rotational Speed (RPM)	4950-5000
Consumable Length	15
Cooling Time (s)	20

Bulbring [5] using AISI 709M40 (EN 19) made successful blind friction taper stud welds using the same stud and hole included angles as Van Zyl [38]. The stud and hole configuration used is shown in Figure 2-19. The size of the stud and hole base diameter was however enlarged, compared to that of Van Zyl, to increase the nose peripheral velocity and to reduce the volume of material required to fill the clearance between the stud and hole. The process parameters that achieved the best tensile strength are given in Table 2-3.

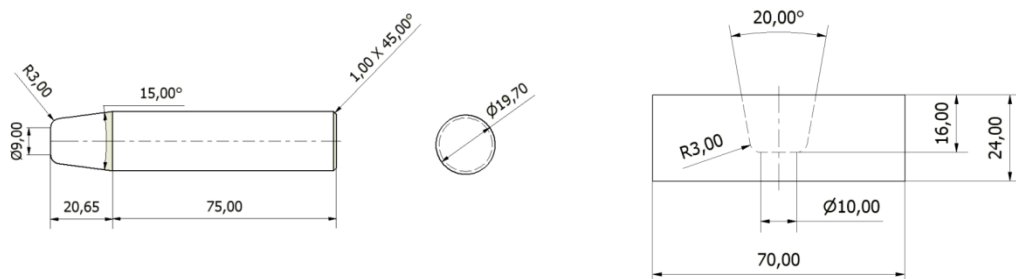
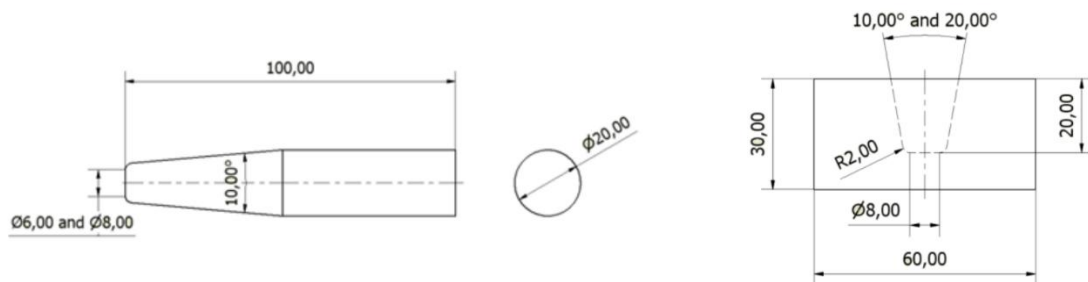


Figure 2-19. Geometry used by Bulbring in the FTSW of EN-19 [5]

**Table 2-3. Process Parameters used by Bulbring [5]**

Parent material UTS ( MPa)	975
Max average UTS (MPa)	895
Rotational Speed (RPM)	6000
Friction/ Forging Force (kN)	11.7
Cooling Time (s)	20
Consumable Length (mm)	9

Pinheiro [10] made blind FTSWs in AZ91D – T6 Magnesium, using hole included angles of  $10^\circ$  to  $20^\circ$  with base diameter combinations of 6mm and 8mm. A stud taper angle of  $10^\circ$  was used, with hole base diameter combinations of 6mm and 8mm. The hole and stud configurations used in the research are shown in Figure 2-20. A final selection using a  $10^\circ$  included stud angle, 6mm stud nose diameter,  $20^\circ$  hole included angle and 6mm hole base diameter was chosen for the joining AZ91D – T6 Magnesium. This was however deviated from during additional research with alternative stud materials, however these changes are not relevant to this study. Pinheiro [10] suggested that within this configuration, minor defects were not expected even at the sidewall due to the high horizontal component created by the taper angle of the hole and stud configuration.

**Figure 2-20. Geometry Used by Pinero for the FTSW of Magnesium [10]**

Beamish [4] made through type FTSWs in AA6082 – T6 aluminium. Due to aluminium's ability to extrude, the stud and hole included taper angles tested were  $30^\circ$ ,  $60^\circ$  and  $90^\circ$  respectively for through type FTSW. The process parameter combination that achieved  $90^\circ$  in a bend test is given in Table 2-4. As can be seen, the stud and hole included angle is greater than with blind FTSW, and significantly less plunge depth. The low consumable length is attributed to the small volume required to fill the clearance volume at  $1^\circ$  included angle difference.

**Table 2-4. Process Parameters used by Beamish in the FTSW of AA6082-T6 [4]**

Stud Included Angle (°)	59
Hole Included Angle (°)	60
Stud Diameter (mm)	25
Stud Nose Diameter (mm)	10
Hole Base circle Diameter (mm)	10
Plate Thickness (mm)	10
Friction/ Forging Force (kN)	40
Rotational Speed	5000
Peripheral Velocity (m.s <sup>-1</sup> )	2.62
Consumable Length (mm)	1
Bend Test (°)	90

The survey of FTSW geometries applied in literature indicate that a 20° tapered hole is appropriate for FTSW, and as it was successfully applied by Pinero [10] in the FTSW of Magnesium, this will serve as an appropriate starting point. However as aluminium AA6082-T6 has a high thermal diffusivity and low strength retention at elevated temperature as mentioned by Beamish [4], the angle may need to be increased considerably. This will, however, need to be investigated with preliminary testing, as sufficient relative data is not currently available.

Axially applied forces and rotational speeds appear to be within the operating range of the FTSW platform currently available. However, as no relative process data is available, this will need to be verified by preliminary testing. One of the biggest gaps in data noted in this review is on the rate at which the axially applied load is applied during the start of the weld and the effect this has on the FTSW process. This may or may not be relevant to the process, but will ultimately be recorded to verify its effect.

### **2.9. Grain Boundaries and Bonding Mechanisms**

In friction welding, the term grain refinement is a key advantage of the process, where grain refinement is achieved by the breaking down and dynamic recrystallization of large grains into smaller ones during welding. Recrystallization is defined by Mittemeijer [39] as the process that changes the crystal orientation of a polycrystalline structure, is accompanied by a release of stored strain energy [1] [39]. By reducing the size of the grains in a given unit of material, the grain boundary area is effectively increased. A grain boundary is

the misalignment or mismatch separating groups of aligned atoms in crystallographic structures, classified into high and low angles with respect to their relative orientation, they are essentially defects in the structure [1] [33] [39]. Atoms are not regularly bonded along the grain boundary interface [33]. This forces the bonds to stretch over a greater distance, causing an incomplete state of chemical bonding and distortion, storing energy [1] [39]. The stored energy between the grains is termed grain boundary energy, and causes the grain boundary to be more reactive than the grain itself [1] [33] [39]. The grain boundary energy is effectively concentrated energy; therefore, a material will naturally tend to form grains that minimise the grain boundary area around a single grain, thus energy will need to be added to grow larger grains [39]. As there is less grain boundary area in a coarse grain structure than in a fine one, there will be less grain boundary energy per unit volume, excluding the effect of deformation. Known as the Hall-Petch relationship, it follows that a material with finer grains has a higher yield strength, as there is more grain boundary area to resist dislocations, [1] [33] [39]. Humphery [1] found that the relationship applied to most alloys with grain sizes larger than  $5\mu\text{m}$  with  $0.2\mu\text{m}$  validated recently for aluminium, typically of the medium strength age hardening type as in the case of AA6082.

### **2.10. Abnormal Grain Growth in Aluminium**

The process that allows the formation of substantially large grains in a crystallographic structure is known as Abnormal Grain Growth (AGG) or secondary recrystallization [1]. Restriction of grain boundaries to a limited number of grains causes the grains to grow, consuming the surrounding grains [39] [40] [41].

Charit and Mishra [40] observed AGG during post weld annealing of AA7075 friction stir welds, attributed to changes in process parameters. The formation of AGG was found to be related to the formation of unstable microstructures (distorted microstructures with higher dislocation densities and strain/grain boundary energy) between the shear layers within the stir zone [40] [41]. The mechanism, therefore, consumes small high energy grains, replacing them or growing them into fewer larger, low boundary energy, grains [39] [40]. Grest et al. [42] found that in two dimensional models that anisotropy (changes in

distribution) in the grain boundary energy can promote abnormal grain growth, yielding microstructures vastly different from the norm. Microstructures with large grains and high mobility tend to grow, while small grains with high mobility tend to shrink [42]. Srolovitz et al. [43] further theoretically showed anisotropy in strain energy between grains (grain boundary energy) to promote AGG [43].

#### Highly Plasticized Region

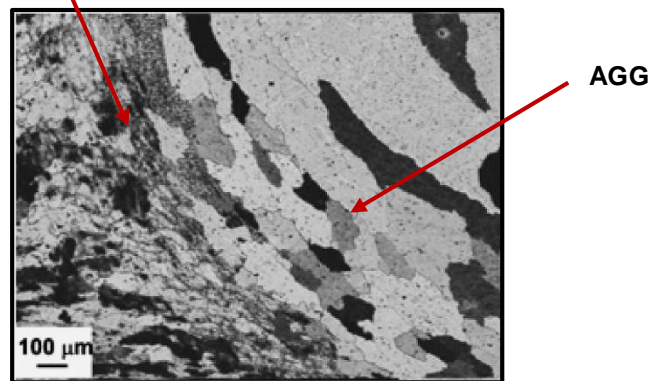


Figure 2-21. AGG at the base of a FSW in AA7075 [40]

When a material is annealed, the normal process followed is recovery, recrystallization, and grain growth [1] [39]. Charit and Mishra [40], found that when highly plastically deformed (highly strained grain boundary) material is annealed, AGG forms in the highly stressed regions/shear planes (shown in Figure 2-21), accompanied by a release of energy by the destruction of grain boundaries of the surrounding grains [39]. A grain (or grains) with high angle boundaries and hence high grain boundary energy surrounded by grains with low angle boundaries (low grain boundary energy) that have stopped growing due to the loss of driving force, will be consumed by the high energy/high angle grain boundary grains, forming AGG [1] [39] [41].

***“Therefore abnormal grain growth cannot occur in an ideal grain assembly”*** [1] page 369.

The activation of AGG in unstable (highly deformed) microstructures is dependent on input energy/temperature [1] [39] [40] [41] [44]. Sato et al. [41] reported that AGG occurs at high temperature, specifically when this temperature is higher than the maximum temperature during processing [41]. The onset of AGG (Secondary Recrystallization) is conveniently displayed for pure aluminium

in Figure 2-22, highlighting the sudden onset of AGG with highly plasticised/ deformed material at increased temperature.

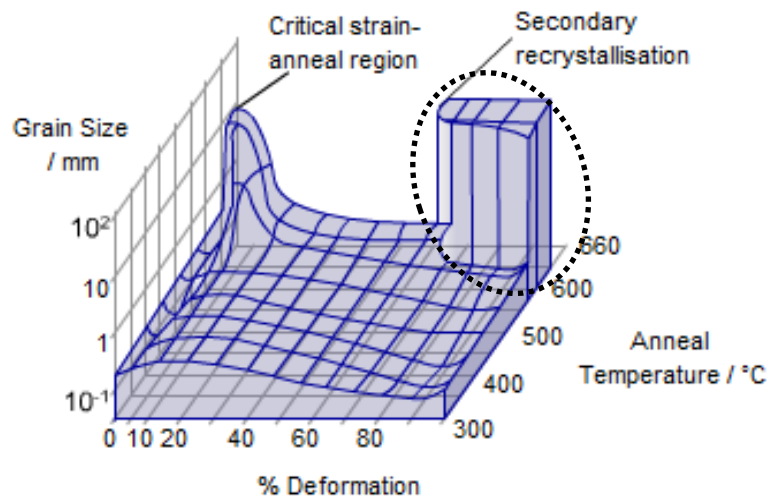


Figure 2-22. Grain Size at Temperature vs. Deformation for Pure Aluminium [44]

This could be a particular concern for the FTSW of aluminium, as in the first stages of the process, the deposited material is highly plasticized (deformed). The high cooling rate at the beginning of the process may lock the grains in a highly unstable matrix. Heat energy input in the later stage of the weld may conduct to the lower region of the weld, possibly activating the process in the highly stressed regions.

### 2.11. The Use of Hardness to Characterise Friction Welded Joints

Mitelea et al. [26] found that in a RFW process on 42MoCr11 QT heat treatable steel, the outer region of the interface showed reduced hardness compared to the central region of the same weld. This was attributed to axial heat conduction near the periphery of the interface being less than towards the centre and to heat stored in the flash, slowing the cooling rate at the periphery. This correlates with the heat distribution seen in Figure 2-17. Yu-lai et al. [29] also found that in rotary friction welding of Nodular Cast Iron to AISI1050 Aluminium, the energy input and temperature distribution in the radial direction differs due to changes in relative velocity, thus influencing the energy input rate across the interface [29]. This change in energy was found to influence the strength distribution of the weld interface by forming Fe<sub>x</sub>Al<sub>y</sub> intermetallic compounds in the outer peripheral region of the weld. Initially the bond strength increased with increased radii, then at

approximately 2mm dropped off dramatically as shown in Figure 2-23, showing the effect that excessive relative velocity can have on a friction welding process, and further also shows the effect of energy input and energy input rate. The work of Yu-lai et al. [29] appears to oppose the work of Mitelea et al. [26] who accounts for the large HAZ and subsequently tempering of the peripheral region on reduced axial heat conduction towards the periphery.

Based on previous work on friction stud welding [23] it is the researcher's opinion that both theories play a part in the process. The energy input rate, and thus the energy input, will be greater at the periphery, increasing the temperature at the periphery and the heat dissipation requirement to maintain stud integrity. Furthermore, the heat dissipation will be reduced due to reduced conduction and poor heat flow due to convection from the outer walls of the stud to the ambient air.

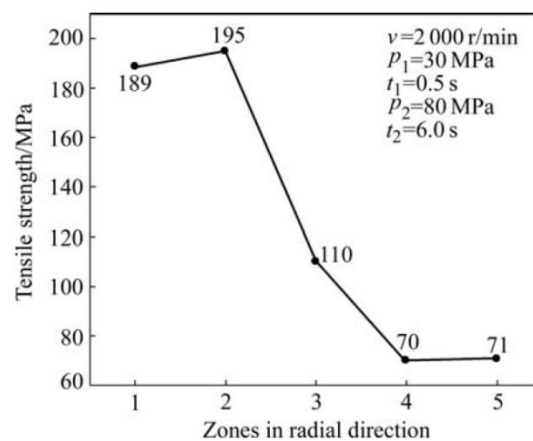


Figure 2-23. Bond Strength with Increased Radii [29]

Beamish [4] states that when joining AA6082-T6 the frictional heating caused by the rotation of the plug against the hole, results in a loss of hardness across the HAZ, or rather a loss of the T-6 temper as indicated in Figure 2-24 [4] [17]. Some failures revealed that the welds had failed due to an exhaustion of ductility in a very small softened heat affected region, not at the weld interface [4].

Beamish [4] constructed hardness profiles from ten AA6082-T6 aluminium FTSW samples, representing "good and bad" welds at the five different hole geometry configurations. Measurements were taken along the centre line of the plate, using a Vickers hardness machine with 1.5mm spacing and a 2.5kg load. The

results did not provide differentiation between a good and bad weld, showing the thermal conditions at the weld interface to be the same for all tested welds.

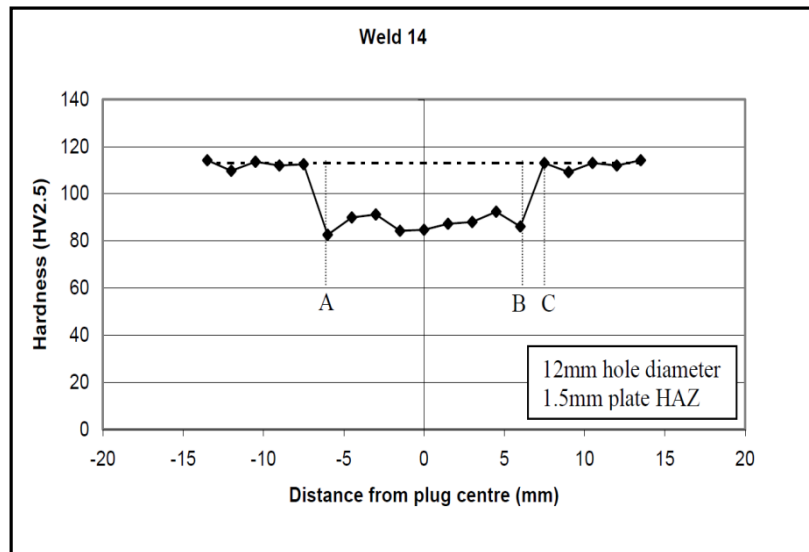


Figure 2-24. Loss of T6 Temper in AA6082 [4]

Instead Beamish [4] found an improved determination method of weld quality, comparing the width of the plate HAZ with the relative peripheral velocity after allowance was made for changes in stud diameter. This gave a process window for good welds as shown in Figure 2-25. This is an indication that the failures of the welds made by Beamish [4] were not due to softening of the parent plate, but lack of bonding. Though there may not have been any substantial voids, there may have been only minimal plasticization of the parent plate, giving shallow shearing, as discussed by Vill [8]. This is a likely explanation for the lack of microhardness response with poor quality welds.

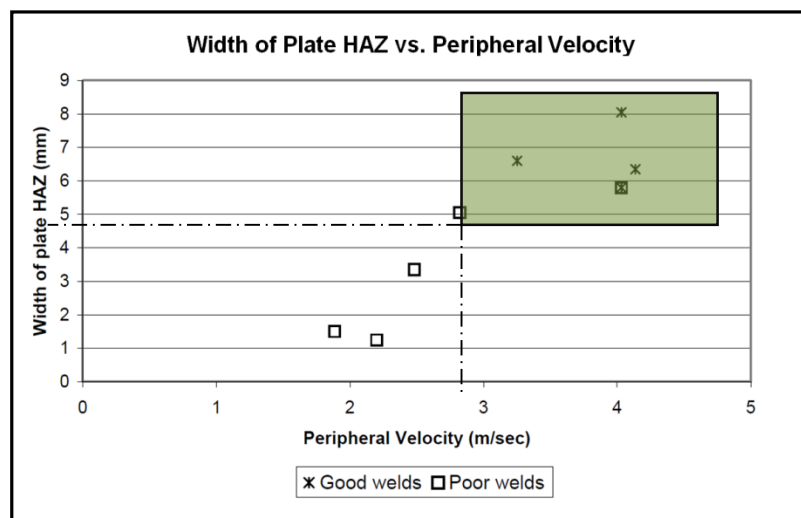


Figure 2-25. Improved Weld Quality Differentiation FTSW AISI 6082-T6 [4]



### 2.12. Summary

The survey of relative literature has identified the current state of FTSW development with respect to hole and tool geometry, with all relevant data identified. Process parameters have been identified that will assist in the design of a development weld matrix. To the researcher's knowledge at the time, no available data for the blind FTSW of AA6082-T6 was available, with little geometry data available that was specifically applied to AA6082-T6.

It is clear that for the successful development of the process of FTSW of AA6082-T6, process torque, axial force and near interface temperature will need to be measured. This will give access to critical energy and energy input data that are currently not available. This data will allow a deeper understanding of the process, and assist in the interpretation of results.

The literature indicates that the successful FTSW of aluminium will be achievable, though many issues such as high thermal diffusivity, low strength at high temperature and oxide formation will need to be overcome.

### 2.13. Stationary Flash Formation

Nunes et al. [45] investigated the frictional torque and plunging force required in a friction stir welding process. The experimentation was simplified by not moving the tool forward and only considering the frictional torque at various depths into the material. The parameters which varied were rotational speed and plunge rate. This makes their investigation applicable to FTSW and FHPP, with the main difference being that in FSW a non-consumable tool is used and in the case of FTSW the tool and hole are tapered. However, the flow of material away from the weld interface at initial contact and out of the joint as flash is assumed to be similar.

The tail, shown in Figure 2-26 shows the first material to flow out of the joint as flash, as the tool is plunged into the material. It thus serves as a record of the thickness of the fine grained region extruded from the disc of plasticized material below the tool, as the plunge depth increases. Nunes et al. [45] states that the tail or flash is easily visible and does not rotate with the tool, with only the region

directly below the tool pin rotating as indicated in Figure 2-27. Shear, therefore, takes place between the rotating disc and the stationary non-recrystallized material [45]. As the tool descends, material enters the rotating disc to be dynamically recrystallized and forced out of the rotating region and up towards the surface as a stationary column, as shown in Figure 2-27. Nunes et al. [45] state that it is only possible to verify that the upper region or visible region of the flash is stationary during welding, and that the state of the region as the material leaves the rotating disc and bends upwards, is not known.

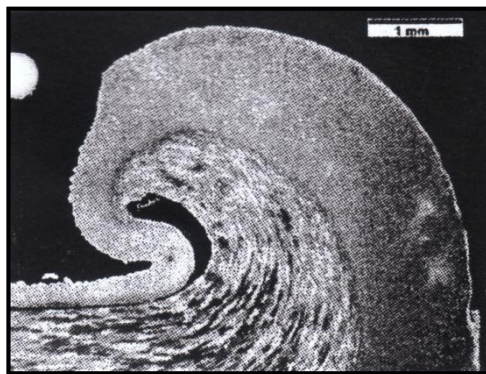


**Figure 2-26. Tail of Flash Exiting the Plunging FSW Tool [45]**

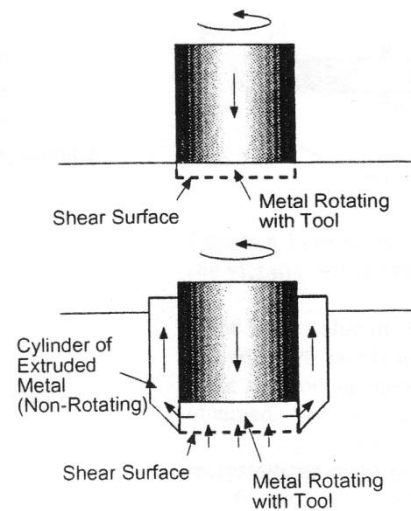


**Figure 2-27. Stationary Flash around Tool [45]**

Although Nunes et al. [45] suggest that the cylinder of flash leaving the weld region is stationary, it is hypothesised that there is a transition period between the time when the material is within the rotating disc and when it becomes stationary and flows up and out of the joint as flash. If this were to be applied to a FTSW process, this would bring the material into contact with the stationary wall of the tapered hole, causing friction between the flash material and the stationary tapered hole wall, slowing its rotation until a point is reached where the material is stationary. The stationary flash point theory will be applied in the plunge depth approximation, discussed in experimental setup and applied in this research.

---

## CHAPTER 3

### EXPERIMENTAL PLATFORM AND SAMPLE SETUP OF AA6082-T6 FTSW

#### 3.1. Introduction

In this chapter, the plate and consumable stud material used for this research study will be discussed, also highlighting its typical applications. The FTSW platform used for the first section of the research will be introduced with a brief summary of its specifications. The axial force and process torque load cell designed by the researcher for the development of FTSW of AA6082-T6 is introduced and explained, showing the calibration of the system and the data acquisition equipment. The then recently commissioned (Late 2012) PDS friction welding platform that was used in the final stage of the research as a replacement welding platform is introduced with a brief summary of specifications and key improvements. The custom load cell designed by the researcher for measuring process torque is introduced and its key components explained. A method of approximating the required plunge depth is presented, allowing for changes in geometry to not require preliminary plunge depth investigations prior to welding. This allows for a constant plunge depth factor to be applied to all welds, thus removing a variable from the process development study. The quantification of joint quality and the equipment used are presented and discussed.

#### 3.2. Weld Material Specification

The material used in this study is AA6082-T6, for both the plate and consumable stud, giving matched base materials. It is an Al-Si-Mg based, medium strength alloy (proof strength  $\pm 290$  MPa) that is moderately heat treatable [2]. It is typically used in stressed structural members and has good machinability, weld ability, formability and anti-corrosive properties [2] [46]. Further it is a material commonly friction stir welded, further highlighting the need for a process to fill the hole left by the stirring tool at the end of the process. All final development welds were taken from the same sheet/ length of round bar, excluding the four welds sent to the European Synchrotron Research Facility (ESRF) for residual stress measurements. The accepted chemical composition specification for AA6082-T6 is given in Table 3-1.

Table 3-1. Chemical Composition Specifications of AA6082 [2] [17]

Element	Wt. %
Si	0.7-1.3%
Fe	<0.5%
Cu	<0.1%
Mn	0.4-1.0%
Mg	0.6-1.2%
Zn	<0.2%
Ti	<0.1%
Cr	<0.25%
Al	Balance

### 3.3. The FTSW Platform

The first stage of the research was done on a portable continuous drive type FTSW platform at Nelson Mandela Metropolitan University (NMMU), shown in Figure 3-1. The system allows two stage control of rotational speed, axial force and plunge depth, with isolated forging force and cooling time control. The system, however, has no suitable data logging system for plunge depth, axial force, rotational speed and process torque. Furthermore, the plunge rate of the platform and, therefore, the axial force ramp up rate, are governed by the flow rate of the axial force hydraulic system. This makes the axial force ramp up rate an outcome that is process parameter and geometry dependant for the development work completed in this research.

The FTSW platform has the following operating ranges;

- Axial force range **0.72 - 32kN**
- Speed range **0 – 6000RPM**
- Plunge depth range **0.56 - 98 mm**
- Plunge depth increments **0.5 mm**
- Maximum process torque sustainable **±60Nm**
- Peak process torque achievable **100Nm**

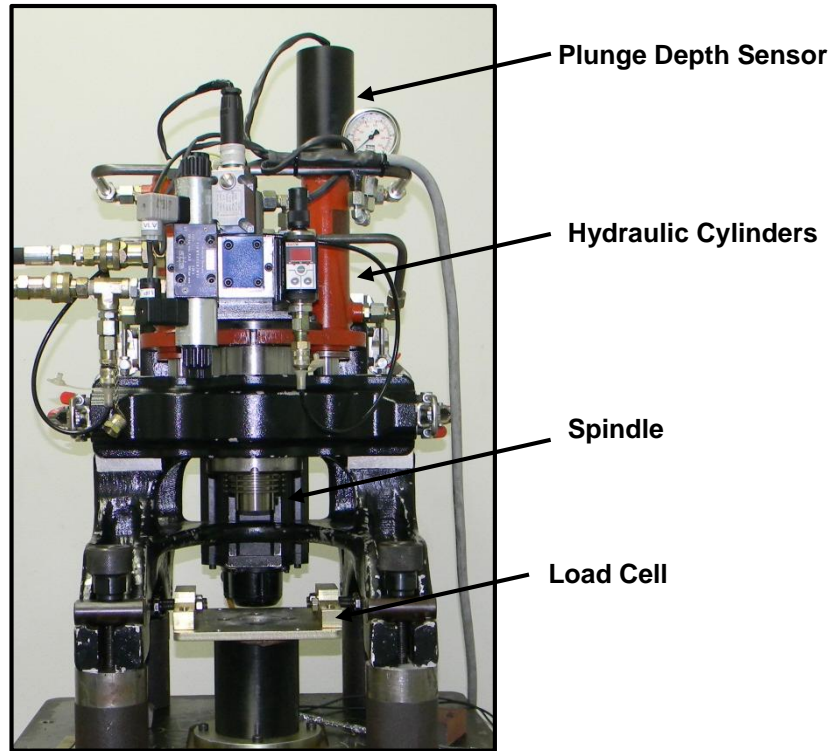


Figure 3-1. FTSW Platform

### 3.3.1. Load Cell Development for FTSW Platform

In order to record the dynamic axial force and process torque during welding, a custom load cell was developed to fit below the spindle, axially in line with rotation. As the proportions of the axially applied load was significantly higher than the proportions of the process torque expected during welding, and considering the stability requirements of the FTSW process, it was decided to isolate the axial and torsional load cell components of the load cell. This was similar to the load cell designed by the researcher for stud welding development utilising the same welding platform in previous work [23]. To separate the axial force and torsional component, the axial component was mounted on free rotation axial thrust bearings, with the torsional component located in the centre. The torque component is fixed to the axial component by two torque rings, with a claw coupling preventing any axial movement being transferred to the torque component.

The load cell with mounting plate is shown in Figure 3-2 and shown sectioned in Figure 3-3. The components are labelled in Figure 3-4, showing the isolation of the axial and torsional components.

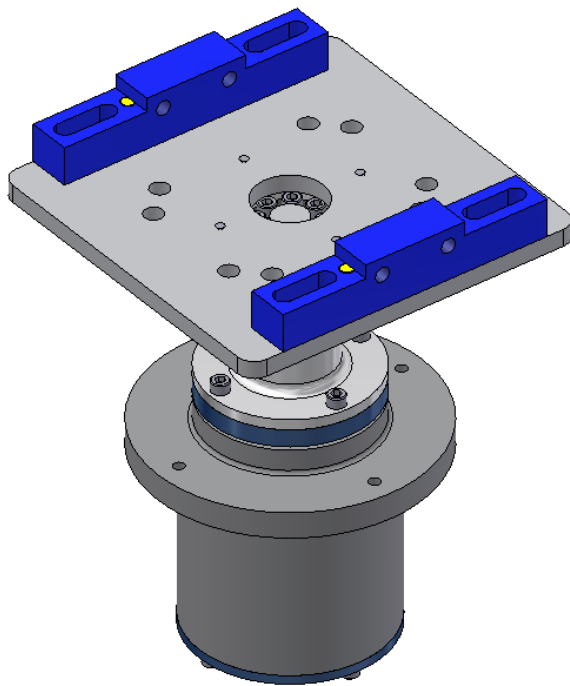


Figure 3-2. Load Cell for FTSW Platform

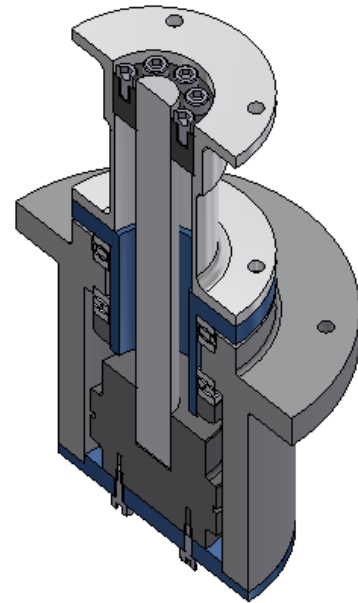


Figure 3-3. Sectioned View of Load Cell

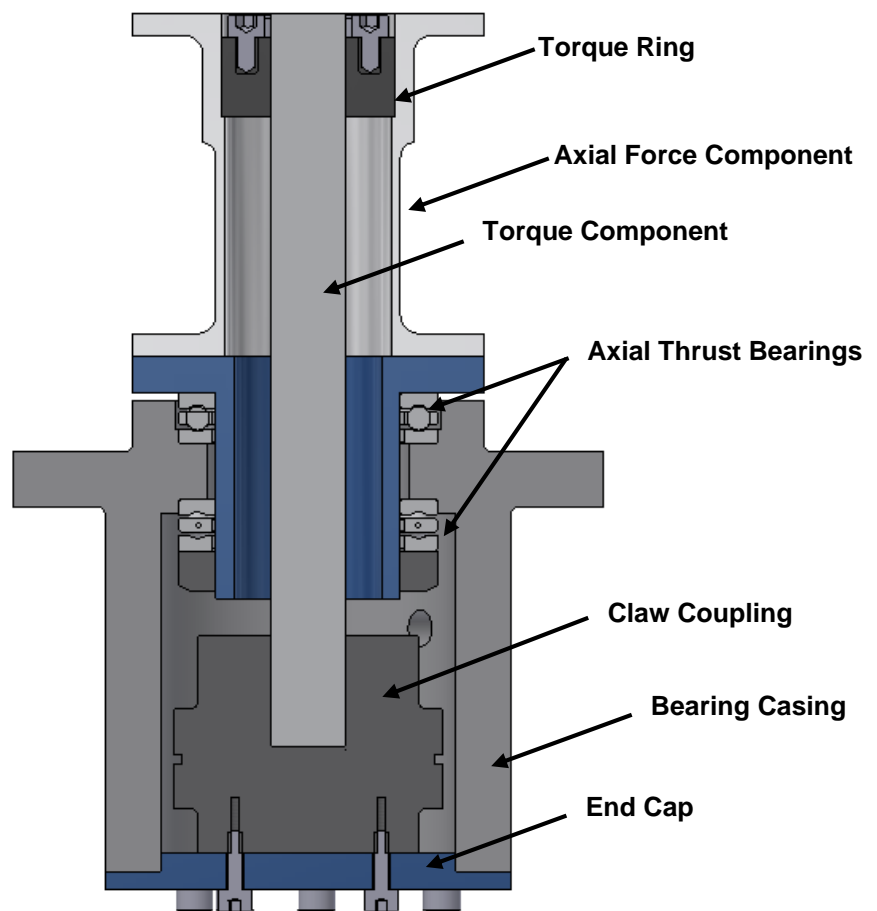


Figure 3-4. Sectioned View of FTSW Platform Load Cell

Strain gauges were fixed to the reduced section of the axial and torsional component, example given in Figure 3-5. Full bridge strain gauge setups were used in both axial and torsion setups to allow for Poisson's ratio and thermal changes expected during welding. In operation the system was earthed with the welding platform, data logging system and power supply to prevent noise induced by the motor when welding. Once assembled, the load cell had to be calibrated axially and in torsion. An Instron - 8801 tensile tester was used to calibrate the axial component, with five runs done and averaged, with the setup shown in Figure 3-6. The results of the calibration are given in Figure 3-7, with the equation used to convert the recorded strain induced on the axial component to axial force.



**Figure 3-5. Strain Gauges Fitted to Axial Force Component**



**Figure 3-6. Axial Force Component Calibration Setup**

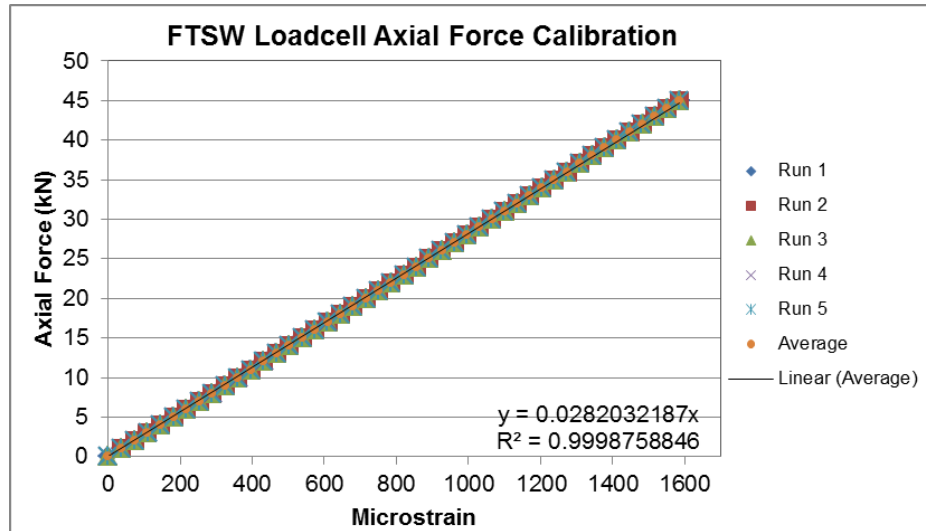


Figure 3-7. Axial Component Calibration Curve for FTSW Platform

The torsional component was calibrated using a pulley and known measured weights with three runs loading up and three runs loading down, with the average curve and average equation given in Figure 3-9. The equation was used to convert recorded strain to process torque. This was then used to calculate energy input and energy input rate. The setup for the torsional component calibration is shown in Figure 3-8.

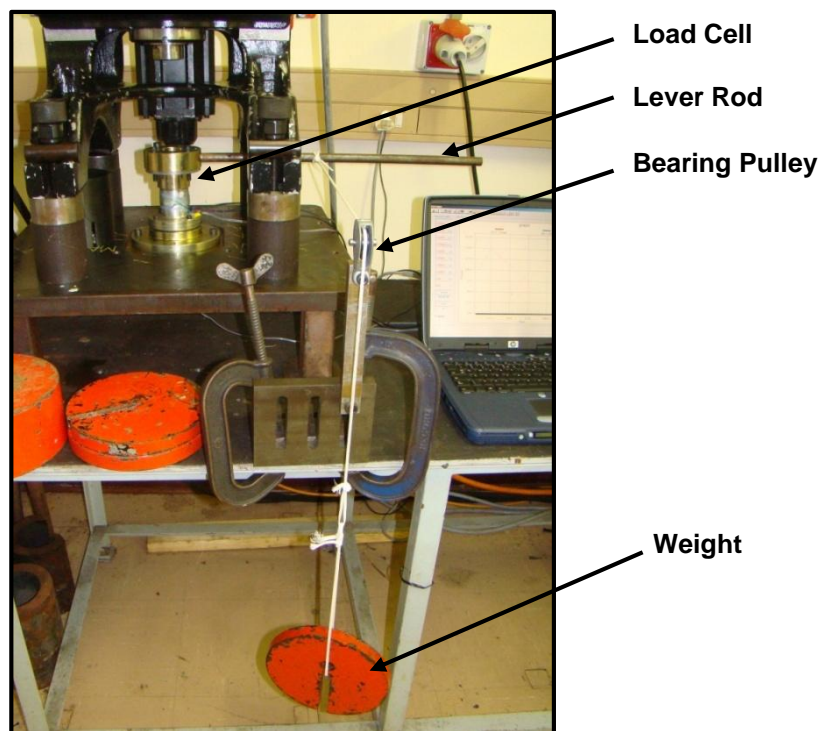


Figure 3-8. Calibration Setup for FTSW Platform Load Cell Torsional Component



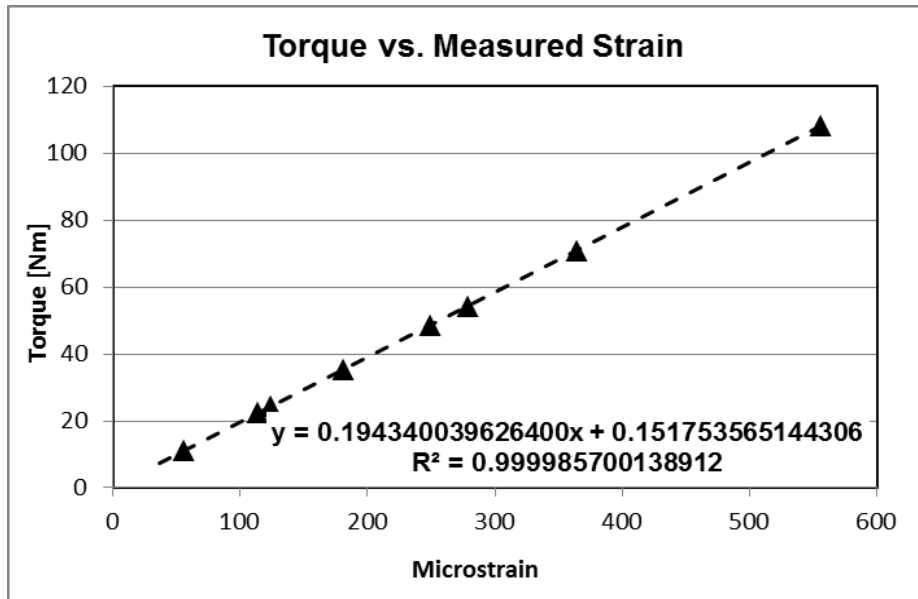


Figure 3-9. Calibration Curve for FTSW Platform Load Cell Torsion Component

### 3.3.2. Data Acquisition Systems

As the FTSW platform did not have the functionality to measure and record data from the load cell, an external “Spider 8” amplifier was used. It allowed axial force and process torque to be recorded at a rate of 250Hz, all development welds conducted on the FTSW platform were recorded at rates of 100Hz, 200Hz or 250Hz, with the selection based on predicted welding time due to limits of the Spider 8 on board memory buffer.

Temperature data for development welds that were done on the FTSW platform used a “Temp Point” data acquisition system with N-Type thermocouples. Measurements were taken at 10Hz, the maximum recording rate of the system.

### 3.4. PDS Welding Platform

During this study the eNtsa engineers developed an advanced friction processing platform called the PDS, shown in Figure 3-10, purpose built for process development. Being available only during the final stages of this study, as commissioning was late 2012, it was only used for the final set of welds once the process window was identified.

It is a continuous drive system, with direct spindle drive. It allows full control of stud plunge rate, axial force ramp up rate and spindle speed. The platform has

built-in data logging that records spindle speed, plunge depth and applied axial force during welding at a rate of up to 1000Hz, and currently has the additional capability for the logging of four external inputs such as thermocouples and load cells. This platform further has a self-alignment function allowing centring of the hole and stud with a repeated four point touch cycle.

The PDS platform has the following operating ranges;

- |                                      |                    |
|--------------------------------------|--------------------|
| • Axial force range                  | <b>0.5-100kN</b>   |
| • Speed range                        | <b>0 – 9000RPM</b> |
| • Plunge depth increments            | <b>0.01 mm</b>     |
| • Maximum process torque sustainable | <b>±200Nm</b>      |
| • Peak process torque achievable     | <b>500Nm</b>       |
| • Axial force ramp up rate (tested)  | <b>200kN/s</b>     |
| • Axial plunge rate                  | <b>1000mm/min</b>  |

#### 3.4.1. Load Cell Development for PDS Platform

As the PDS friction welding platform did not have the capacity to accurately measure the process torque during welding, a torsional load cell was developed by the researcher for the platform as shown in Figure 3-11. The load cell consisted of a set of axial thrust bearings and a centralising needle roller bearing that allowed free rotation of a torque arm during welding. The frictional moment exerted by the stud was therefore translated through the torque arm and was measured at the end point by a standard 59M/2kN HBM axial force transducer shown in Figure 3-11, that was isolated by two rose joints. The rose joints were damped from movement and vibration by four O-Rings located between washers at the mounting bolts. The axial force transducer was supplied calibrated and was interfaced with the PDS data acquisition system via the supplied HBM amplifier. A sectioned view of the torsional load cell is given in Figure 3-12, showing the location of the bearings in the bearing case. The full drawing set for the PDS torsional load cell is given in Appendix C.

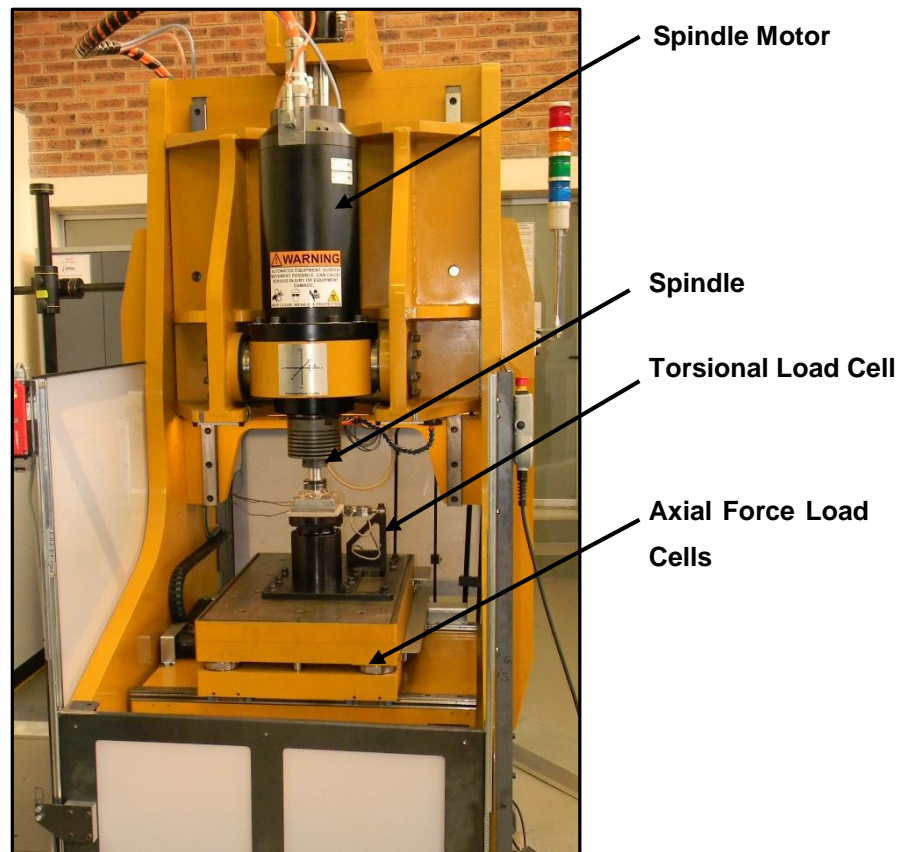


Figure 3-10. PDS Friction Welding Platform

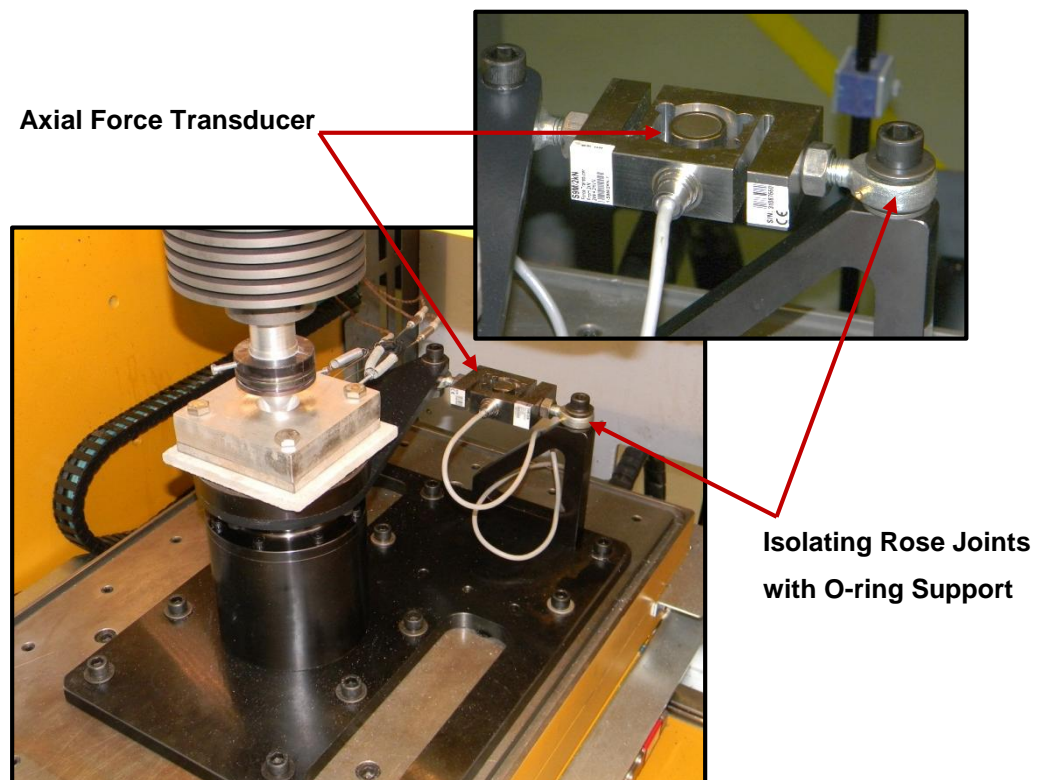


Figure 3-11. Torsional Load Cell for PDS Platform

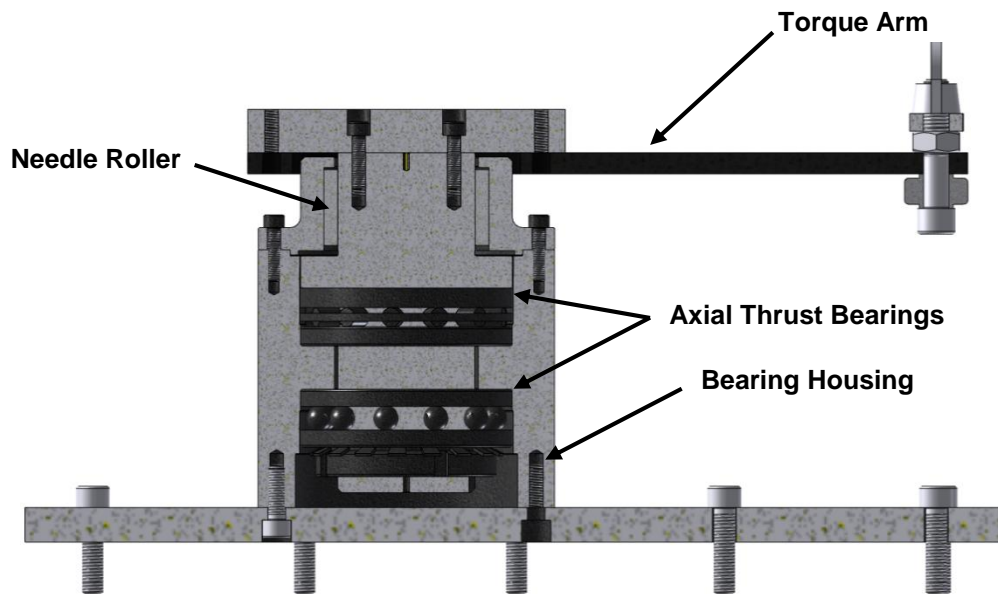


Figure 3-12. Sectioned View of PDS Platform Load Cell

### 3.5. Welding Procedure

The welding procedure for the process development phase of the research was as follows, with the setup of the block on the load cell shown in Figure 3-13. The hole and stud are cleaned using degreaser and scotch bright to remove surface oxides, oil and dirt. The samples are then chemically cleaned with acetone prior to welding or preheat. A centring stud is fitted into the spindle of the FTSW platform that has a tapered section larger than the exit diameter of the tapered hole in the plate. The plate with the tapered hole is fitted onto the load cell, either preheated or at room temperature depending on welding parameters. The plate is placed on top of an 8mm thick section of AA6082-T6 plate with a 30mm hole in the centre, which is placed on top of a 10mm thick section of Nad-500, thermal insulator. The 30mm hole, shown in Figure 3-14, represents the un-supported welding condition as would be found in a typical application. The size of the hole was based on the initial exit diameter of the tapered hole in the plate. The spindle is moved down until the tapered section of the alignment stud centres the tapered hole to the rotation axis of the spindle. The cross braces and side braces are fastened and the spindle is retracted. The alignment stud is removed and the tapered stud inserted. The stud is cleaned a final time with acetone before the spindle is lowered and the stud is moved into the hole, approximately 10mm off the bottom.

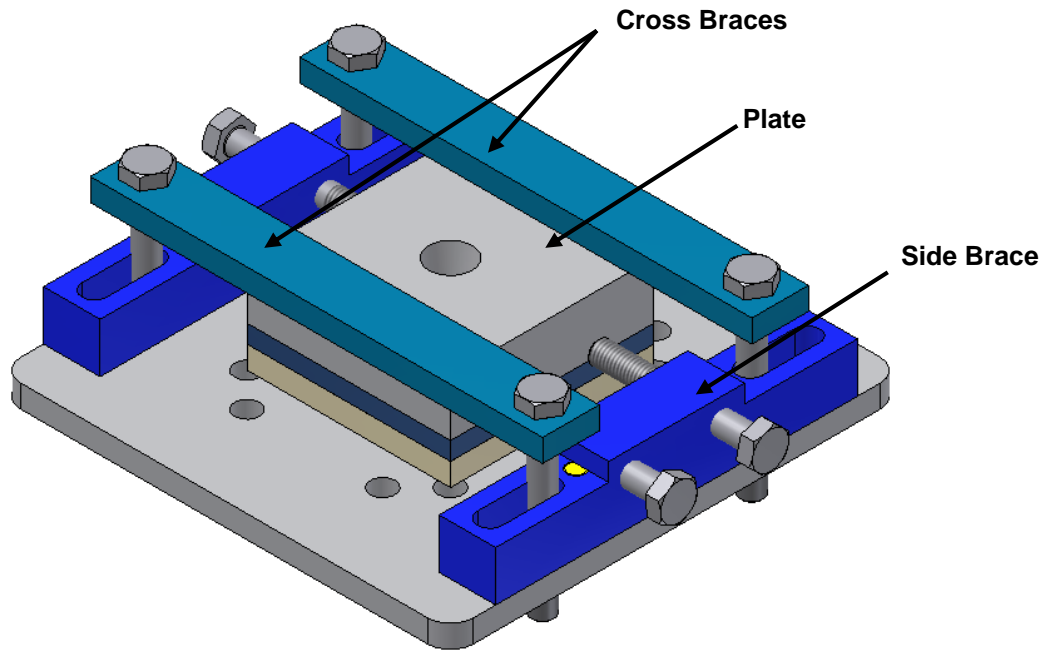


Figure 3-13. Welding Setup for FTSW Platform Welds

The data logging for axial force, process torque and temperature is started and balanced. The welding cycle is then started. The stud will move to the bottom of the hole and probe the surface at the set welding force. When the set axial force is reached this position is used as the zero reference point to determine the plunge depth. The spindle retracts 20mm and waits for the start command, giving time to abort the weld if any anomalies are noted. When the command is given, the motor spins up to the set rotational speed and once it is achieved begins to move axially into the hole at the plunge rate of the platform. Once the stud contacts the bottom of the hole, the plunge rate reduces as the axial force builds up. If the platform can maintain the consumption rate of the stud material, the set axial force will be reached during rotation. Once the set plunge depth is reached, rotation is abruptly stopped and a continuous axial force (forging force) is applied. In this research, most of the welds are made with a forging force equal to the axial force applied during welding, as discussed in section 2.3.4 on page 20. The weld is allowed to cool for 20 seconds before the forging force is released. The data logging is then stopped and the weld removed from the FTSW platform. For welds that use studs with like hole and stud base diameters, the actual stud is used to align the hole, not the alignment stud.

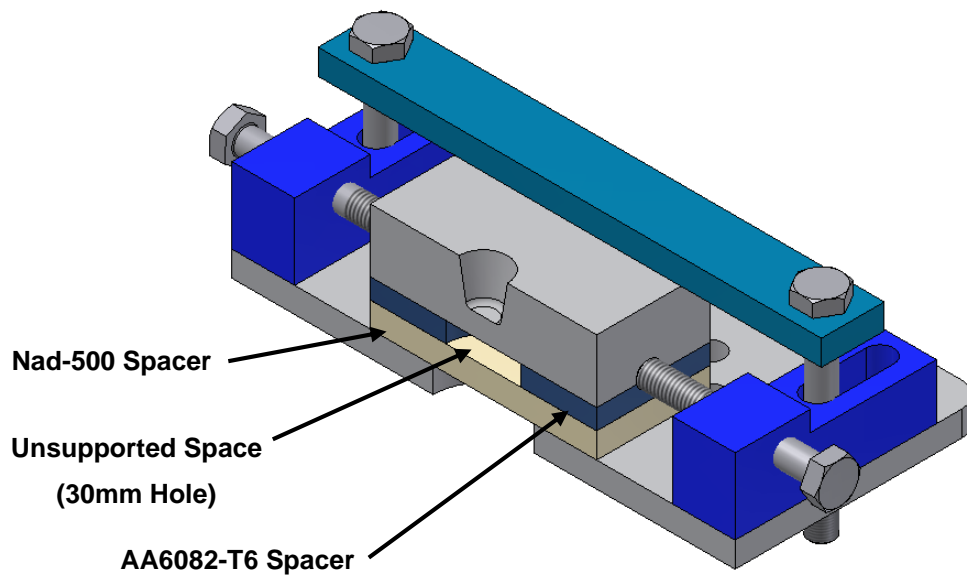


Figure 3-14. Sectioned View of Welding Setup

Figure 3-15 shows the weld setup on the PDS friction welding platform that was used in the last phase of the research. The figure shows the plate with the machined tapered hole mounted on top of the torsional load cell. The three springs are holding three N-Type thermocouples in their respective holes, under a continuous load for continuous contact during welding. All the welds made on the PDS platform have a 10mm EN-8 plate between the aluminium plate and the Nad-500 for support of the weld nugget, as the partially supported condition was abandoned due to plunge control issues due to deformation of the plate, complicating the control of low plunge depth welds.

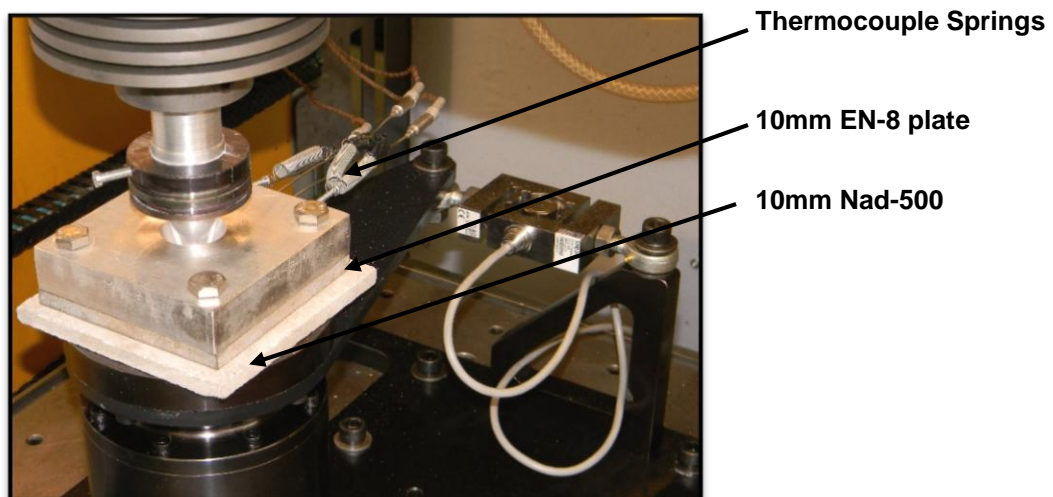


Figure 3-15. AA6082-T6 FTSW on PDS Welding Platform

### 3.6. Development of Plunge Depth Approximation Methodology

As the plunge depth has been identified as a critical parameter in the literature of friction welding and more specifically when it is applied to heat treatable aluminium alloys, a method to determine an appropriate plunge depth for a given geometry is needed. This will allow for a quantifiable value to be assigned to the varying plunge depths required with changes in stud and hole geometries, removing a variable from the testing matrix.

For shearing, and therefore bonding, to take place on the sidewall of the hole during FTSW, relative velocity is needed between the two rubbing surfaces. Therefore, as the weld interface moves up the tapered hole, the wall becomes progressively more heat saturated. As the material leaving the weld interface is initially rotating, combined with the hydrostatic force exerted by the material on the side of the tapered hole, bonding above the initial weld interface occurs. This is shown in Figure 3-16 in the plunge depth investigation done by Pinero [10] in Figure 3-16. Therefore, there is rotation of the flash material above the weld interface, and the longer the process runs, the more heat saturated the walls of the hole become, increasing the height of bonding above the welding interface. This is how bonding and plasticization is found above the weld interface and above the point where the sidewall of the stud has contacted the side of the hole.

Based on the stationary flash observation presented by Nunes [45] and the volume of displaced material at a 12mm plunge depth used by Pinero [10], the displaced volume vs. clearance volume factor approximation was developed, shown in Figure 3-17 and calculated using Equation 3-1 and Equation 3-2. The results are plotted in Figure 3-18, showing the tapered hole to have been filled by 3.8mm plunge depth and the rotation to have been stopped at a displaced volume vs. clearance volume of approximately 18 times. This is therefore the approximate ratio required to fill the hole and bring the rotating flash into contact with the sidewall of the plate. This needed verification and was subsequently tested and shown to be successful during the first set of development welds. The plunge depth approximation was therefore maintained throughout the FTSW research on AA6082-T6.

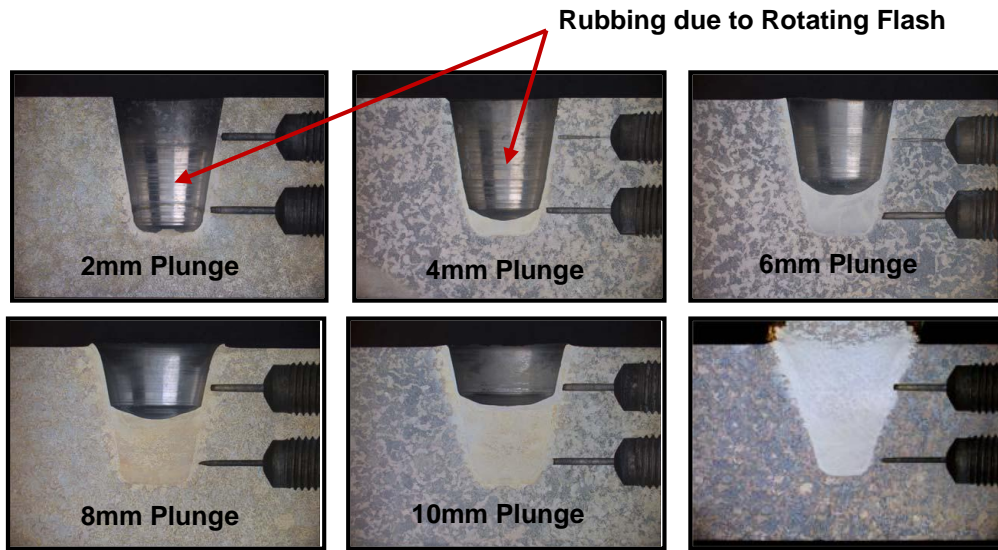


Figure 3-16. Plunge Depth Investigation [10]

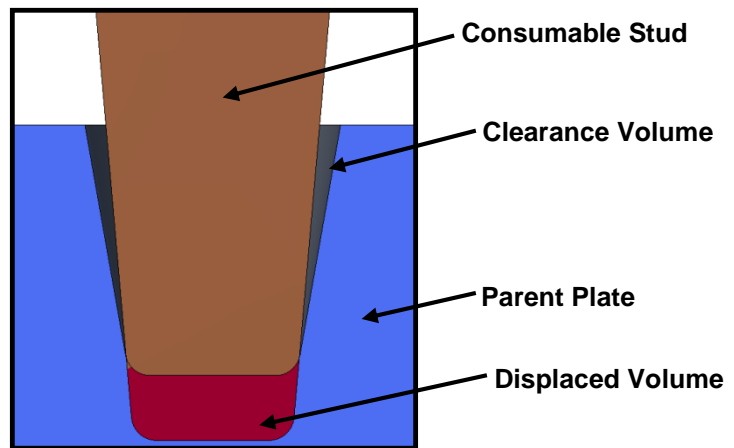


Figure 3-17. Plunge Depth Approximation Layout

$$V_c = V_h - V_{sh} \quad \text{Equation 3-1. Clearance Volume}$$

$$C.V.D = V_d/V_c \quad \text{Equation 3-2. C.V.D Calculation}$$

$V_c$ =Clearance Volume

$V_h$ =Volume of Empty Hole

$V_d$ =Volume Displaced

$V_{sh}$ =Volume of Stud at Depth



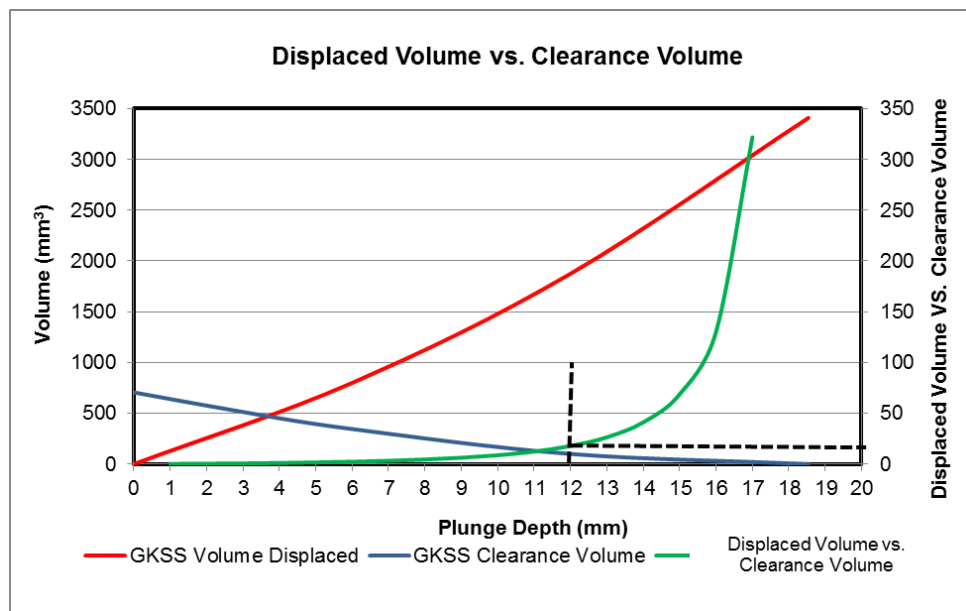


Figure 3-18. Displaced Volume vs. Clearance Volume (Taken form work by Pinero [10])

### 3.7. Near Interface Temperature Data

Near interface temperature was measured to investigate the effect of changes in process parameters and geometry on the temperature experienced in the plate material, adjacent to the tapered hole. Three holes, 2 millimetres in diameter, were CNC drilled on the front of each block as shown in Figure 3-19. Temperature was measured using three N-Type Thermocouples, held in place with springs to keep the heat sensitive points in intimate contact with the bottom of the hole; the setup is shown in Figure 3-15. The sampling rate used for the process development welds was 10Hz, as this was the maximum rate of the Temp Point data acquisition system, with the final welds done on the PDS friction welding platform sampled at 200Hz. The first utilised temperature measurements were taken in 18mm deep welds with the location of the thermocouples near the top of the hole, at the midpoint in the hole and at the fillet at the base of the hole, as shown in Figure 3-19. The thermocouples were positioned 1.5mm from the welding interface at depths of 2mm, 7.5mm and 13mm as shown in Figure 3-20, for all 18mm deep welds.

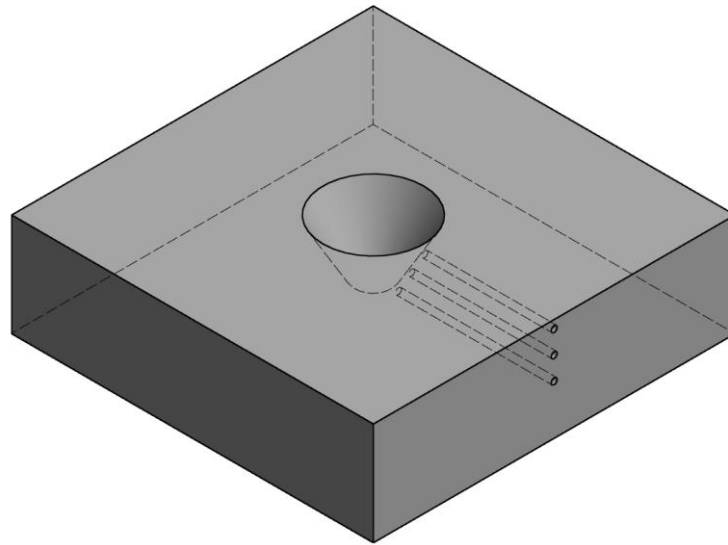


Figure 3-19. Layout of Thermocouple Holes for Near Interface Temperature Measurement

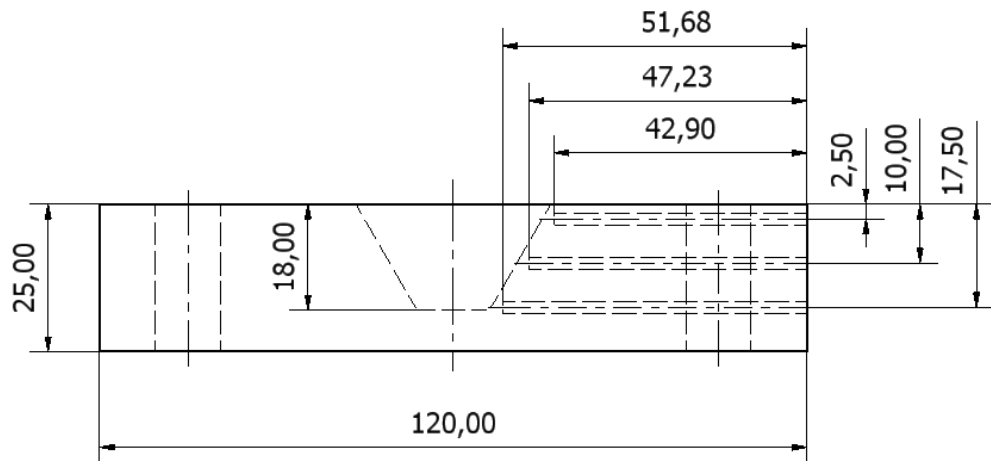


Figure 3-20. Thermocouple Hole Depths for Welds TW-23 and TW-24

When the research was moved from the FTSW platform to the PDS friction welding platform, the depth of the tapered hole was increased from 18mm to 20mm, to align with the project's initial specifications as the PDS platform had the capability to accommodate the size increase. The depths of the thermocouple holes were increased to 2.5mm, 10mm and 17.5mm as shown in Figure 3-21. The distance from the interface was also increased from 1.5mm to 2mm in order to prevent thermocouples lodging in the holes during welding due to the increased axial force applied by the PDS friction welding platform.

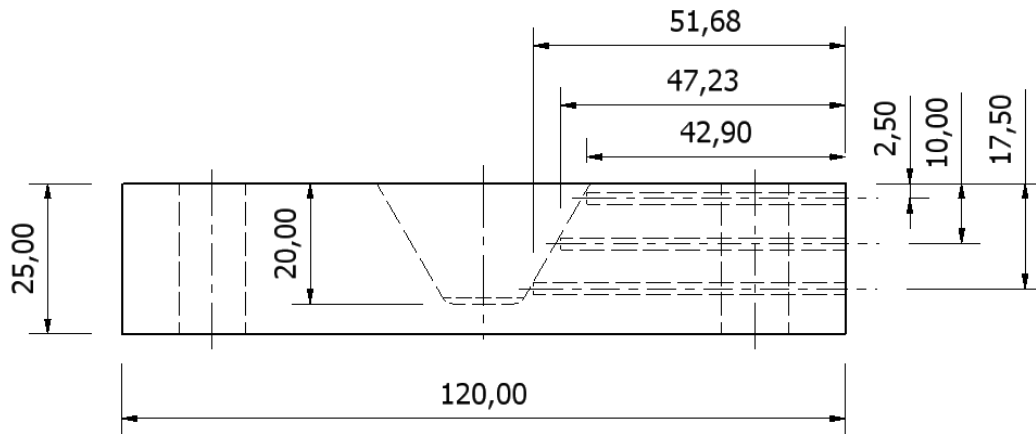


Figure 3-21. Thermocouple Hole Depths for Welds S.1 to S.4, RR-1 to RR-4 and FM-1 to FM-16

### 3.8. Tensile Samples Geometry and Preparation

To test the sidewall bonding of the aluminium FTSW weld nugget, one single tensile sample from each weld will be prepared. The dog bone profile will be cut vertically (with respect to Z) incorporating as much of the weld nugget as possible. The width of the sample will be as wide as the base diameter of the hole, giving a reduced section of 12.5mm. The sample is then machined according to the ASTM e8m standard, giving tensile sample geometry as shown in Figure 3-22. The completed FTSW is shown in Figure 3-23 after welding. The stud is first removed by band saw, then, to remove any flash cracks, 0.5mm is machined off the top surface of the plate leaving a 24.5mm high sample. The dog bone profile is then machined with the weld nugget located in the mid region of the sample as shown in Figure 3-24. Once the dog bone profile is machined, the ligament at the base of the hole will be machined away, removing 5.5mm off the bottom of the sample. This will remove the entire weld ligament, base defects, and give a parallel sided specimen which focuses on the sidewall bonding of the FTSW. Figure 3-25 shows the tensile sample after machining and removal of the weld ligament, highlighting the region of displaced material due to plunge. All tensile samples are CNC milled at NMMU to ensure geometry consistency with full flood cooling, preventing any post weld heating due to the machining process.

One tensile sample per parameter combination was tested, which required two welds to be made with each process parameter combination, one for sectioning and the other for tensile testing. The tensile sample welds were made using a longer plate, compared to the square samples used for sectioning, and without

the thermocouple holes in order to accommodate the length of the tensile sample, as shown in Appendix A. All the tensile sample welds were tested in the rolling direction of the plate and were taken from the same sheet to ensure consistency.

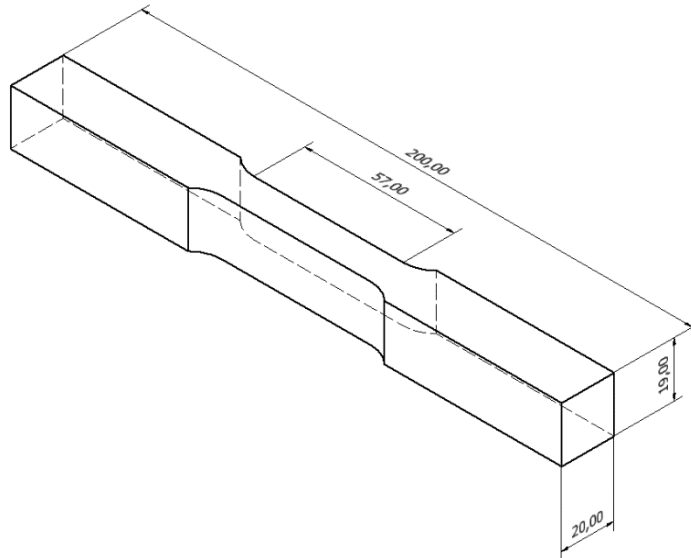


Figure 3-22. Tensile Sample Dimensions

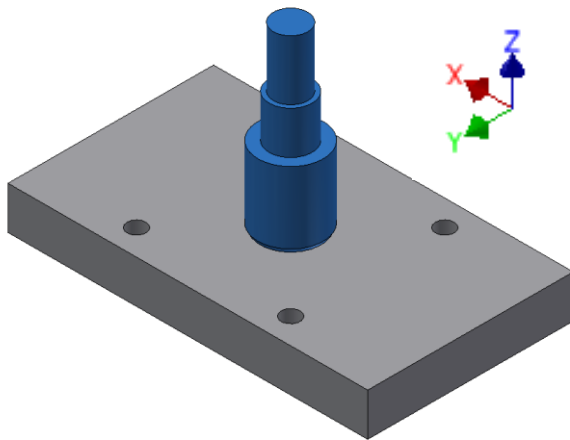


Figure 3-23. Completed Tensile Sample Weld

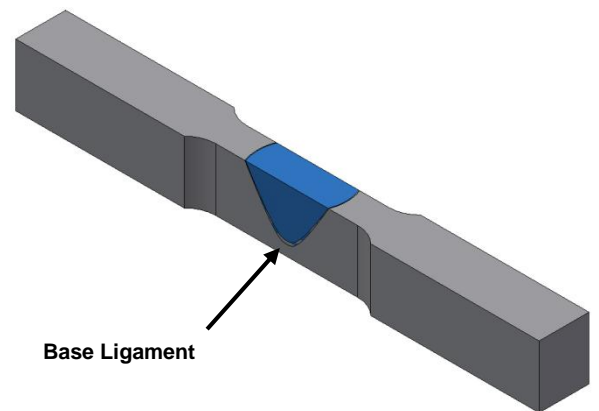


Figure 3-24. Tensile Sample showing Weld Nugget

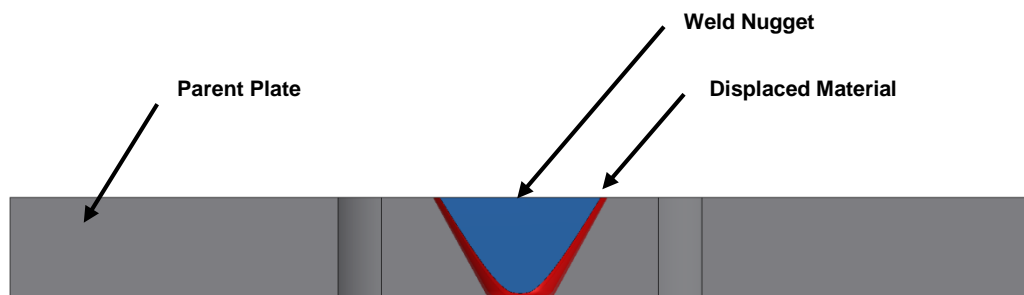


Figure 3-25. Tensile Sample showing Weld Nugget and Displaced Material

### 3.9. Microhardness Testing

Microhardness testing was done on all welds that were welded on the PDS welding platform, using a FM-ARS 9000 automatic microhardness tester, applying a 50g load. Welds made with severe void formation, poor tensile strength at low axial force ramp up rates and high thermal saturation of the block at low axial forces, were not evaluated.

All welds were tested as shown in Figure 3-26 except for welds S.1 to S.4, which are discussed in the relevant section. Three horizontal test lines were done at 5mm, 12.5mm and 20mm depths into the plate, investigating the hardness profiles at the top, middle and bottom zones of the weld. One vertical microhardness test line was done along the centre of the weld to identify any significant vertical changes in weld nugget microhardness, as shown in Figure 3-26.

As the weld is considered symmetrical, all hardness tests were done on one half of the weld nugget only, with the test points shown in Figure 3-27. The spacing between test points was 1mm for the horizontal lines and 0.5mm for the vertical line. The spacing along the horizontal line was reduced to 0.2mm for the 2mm before and 2mm after the weld interface, with the location of the weld interface relative to the height of testing in the plate given in Table 3-2.

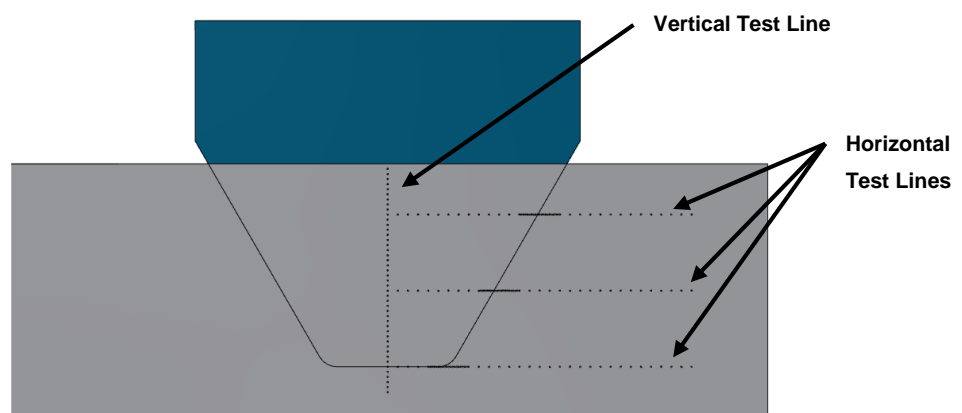


Figure 3-26. Microhardness Test Points

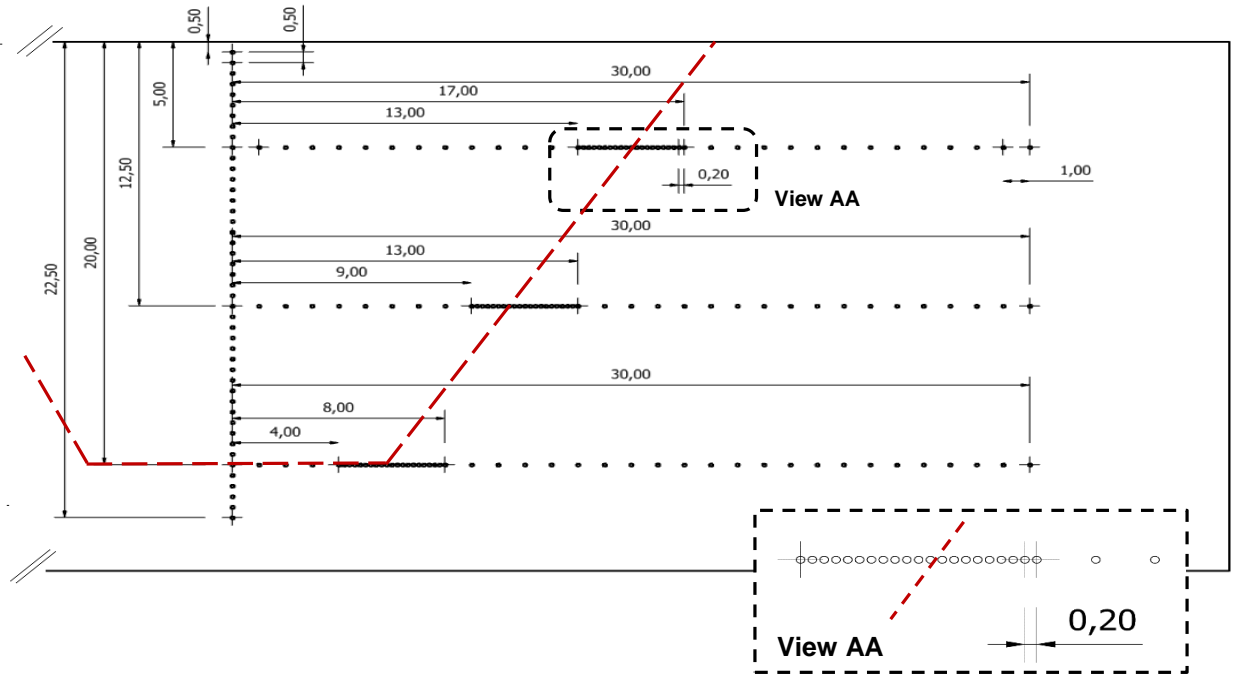


Figure 3-27. Microhardness Test Point Map for Welds RR-1 to RR-4 and FM-1 to FM-16

Table 3-2. Distance to Weld Interface

Top Line (5mm Below Surface)	14.815mm
Middle Line (12.5mm Below Surface)	10.485mm
Bottom Line (20mm Below Surface)	5.000mm

### 3.10. Sample Removal and Preparation

Once the RR-1 to RR-4 and FM-1 to FM-16 welds were completed, the top section of the stud was removed and the samples mounted in a fixture jig in a 3 axis CNC milling machine. The macrograph/hardness sample was then machined out of the plate as shown in Figure 3-28. Full flood cooling was used during machining to prevent heating of the material with multiple small step full depth machining passes done on the final face to ensure minimal deformation due to machining. This also ensured a parallel sample for microhardness testing. Samples were then ground and polished for hardness testing, before final polishing to 1µm and etching in modified Poulson’s reagent.

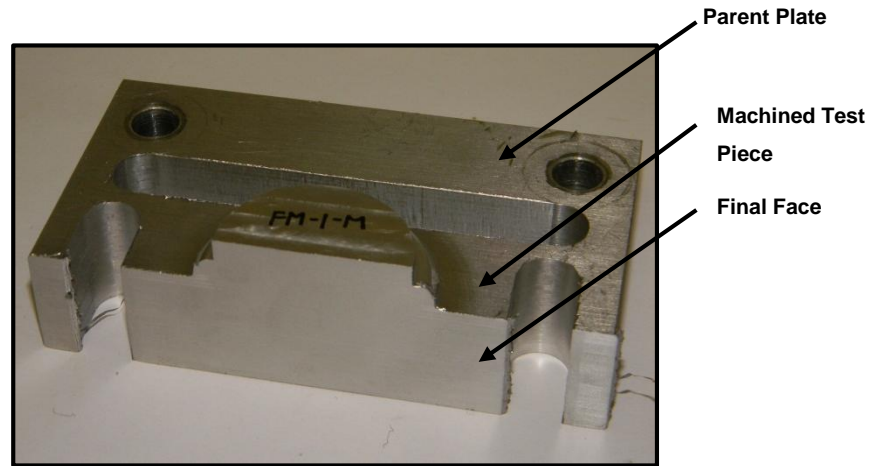


Figure 3-28. Sample Removal with CNC Milling Machine

### 3.11. Testing Equipment

All hardness tests were done on a FM – ARS 9000 automatic microhardness tester. Macros were taken using a Zeiss Stereo Discovery V12 Axiovision camera or a Nikon L110 Camera. Tensile testing of welds S.1 to S.4 and RR-1 to RR-4 was done on an Avery 7110 DCJ tensile tester, at an extension rate of 2 millimetres per minute. Welds PT-1 to PT-4 and welds FM-1 to FM-16 were tested on an Instron - 8801 tensile tester at an extension rate of 2mm per minute.

### 3.12. Energy Calculation

One of the main objectives of the research is to calculate the energy input and energy input rate into the welds during rotation. The energy is calculated from the process torque curve, using rotational speed and the sampling time as the interval.

$$Energy (J) = \sum_{End\ Time}^{Start\ Time} \left( \frac{[2 \times \pi \times RPM \times Torque]}{60} \right) \times Time\ Interval \quad \text{Equation 3-3. Energy Input}$$

The energy input (work done by the stud) up to a point into a weld is therefore the sum of the energy inputs per time interval (Data Acquisition Sampling Rate). For example the energy input to 0.1 seconds is the total amount of energy under the process torque curve to that point, using Equation 3-3 to calculate energy per time interval, shown in Figure 3-29. Therefore, the area under the curve at 0.1 seconds into the weld will contain the sum of 20 samples if a sampling rate of 200Hz was used.

The energy input of all welds will be referenced to the area of the hole to make the results of various geometries comparative, giving a  $J/mm^2$  unit. The volume of displaced material is not used as there will be no displaced material to reference the energy to before plunge begins, the  $J/mm^2$  is, therefore, the simplest approach that can be applied to almost any point in the weld. In the study, all values of energy input and energy input rate are referred to in this way; however, true energy inputs at various points into the weld are given in Appendix F for all welds for reference.

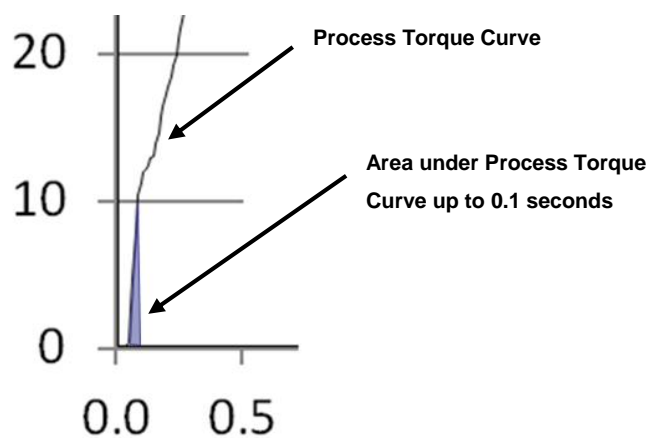


Figure 3-29. Energy Input in 0.1 seconds

### 3.13. Hole Area Used at Various Points into the Weld

The FTSW process was broken up into various stages, identified as important by literature and the researcher. These were energy input at 0.1 seconds, 1 second, seizure, post seizure torque peak (PSTP), and energy input total. The final analysis gives the total energy input to the point where plunge depth was reached and once rotation had stopped.

The energy input into the weld during the first 0.1 seconds and to seizure is taken over the base area of the hole, or the area in contact with the stud during the rubbing phase. As this area is known and constant, this energy can be cross referenced to other hole geometry configurations in this study. This value is only the area in contact. However, if like base and stud diameters are used, the area of the fillet is included.



The energy at 1 second into the weld will be taken over the entire surface of the tapered hole. Though the hole will not be filled by this time for many weld configurations, as the data logging system is not capable of determining the real time position of the stud in the hole, there is no method to quantify the position of the welding interface; therefore, this is the only satisfactory analysis for the scenario. The value, therefore, compares the energy input in the first second of the weld, to quantify changes in process parameters. This does not however imply that the depicted value of energy has been evenly distributed across the entire hole surface.

The energy to the post seizure torque peak (PSTP) shows the amount of energy put into the weld by the point where maximum process torque is reached. This point indicated the point when the greatest amount of surface area is in shear, with minimum temperature at the interface. This correlates with the point at which the displaced stud material is approximately equal to the clearance volume between the stud body in the hole and the sidewall. As an example, for the 15° stud the hole is filled at approximately 3.45mm plunge. The PSTP occurred 1.4 seconds into the weld for weld TW- 5, corresponding with a plunge depth of 1.8mm to 2 millimetres from the welding platform's position logging system. This is not considered an accurate system, as the data acquisition rate is 1Hz, and it is not considered to be accurate to measure the plunge depth at such low rates, considering the weld is only 4.3 seconds long and that the first data point is not at the weld start but at the start of motion. Taking into account that at three seconds (the next data point) the plunge depth had reached 4.5mm and that at the deflection of the platform under low loads is not known, it is going to be assumed that the plunge depth of 3.45mm was achieved at the PSTP point and that the maximum area is in shear. Therefore the energy input to the PSTP will be considered over the entire surface of the tapered hole throughout the study. The total energy input into the weld is taken to have been distributed over the surface of the hole. All welds were complete and no lack of fill was noted in any weld.

### 3.14. Residual Stress Measurements and EBSD Mapping

Due to collaboration between the distinguished Professor Danie Hattingh at eNtsha, Nelson Mandela Metropolitan University, Port Elizabeth, and Professor Axel Steuwer at MAX IV Laboratory, Forskningsstrateg, Lund University, four FTSW samples were sent to the European Synchrotron Research Facility (ESRF) in Grenoble France for residual stress measurements to be taken in the weld nugget zone and surrounding material. The welds were returned and sectioned, with one half analysed by Electron Backscatter Diffraction (EBSD) at the mid region of the bond line and the other polished and etched for further analysis. The EBSD testing was done by Dr Jacques O' Connell, at the Centre for High Resolution Electron Microscopy at Nelson Mandela Metropolitan University, Port Elizabeth.

The synchrotron residual stress data and EBSD data is developed and presented by the researcher and is discussed to the best of the researcher's knowledge, however a detailed analyses of the results will be conducted in a following paper, co-authored by Professor Axel Steuwer who is an expert in the field of synchrotron residual stress measurements and EBSD data analyses, as this field of work falls outside the current competent knowledge of the researcher.

The four welds made for the analysis were of the first to be done on the PDS welding platform at NMMU, and these welds therefore did not utilise the soft touch down as discussed above, as this functionality was added to the PDS control system as a consequence of these welds. The welds instead used the maximum plunge rate of 1000mm/min, striving to achieve the axial force ramp up rate specified, at which point the system changes into force control and maintains the set axial force ramp up rate and axial force specified. The new welding platform had proved capable of filling 20mm deep holes using a base diameter of 10mm, which was the original target depth and size specified for the research, with dimensions given in Appendix A.

The residual stress and Vickers microhardness testing were done at 5mm, 12.5mm and 20mm depths into the plate, starting at the mid-point of the weld nugget and moving outwards towards the edge of the plate. Residual stress

measurements were taken at 1mm intervals for the full 60mm length of the plate, as surface strain measurements were needed to calculate  $d_0$  for the material. Vickers microhardness readings were taken at 0.5mm intervals, to a distance of 50mm from the weld centre, as shown in Figure 3-30.

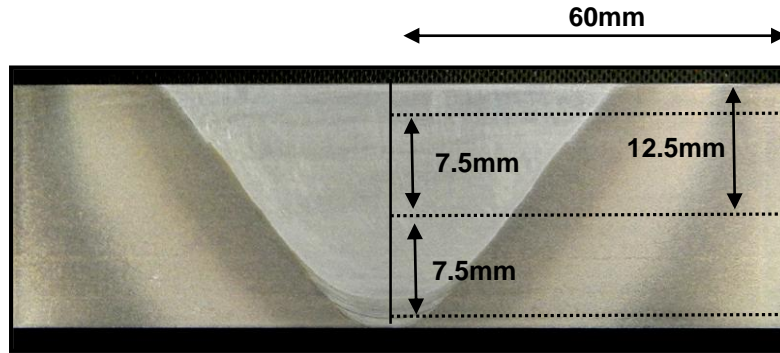


Figure 3-30. Weld Nugget Etched, Showing Planes for Residual Stress and Vickers Microhardness Measurements

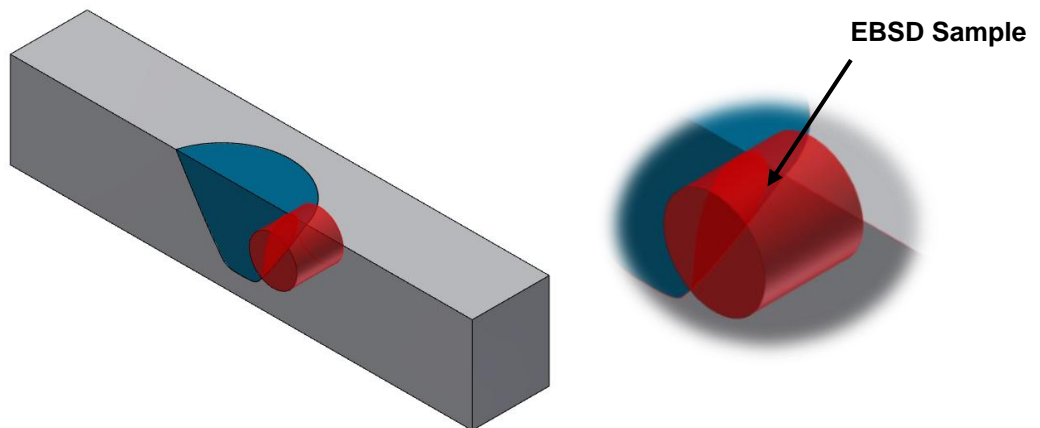


Figure 3-31. Position of EBSD Sample from Mid-Region of the FTSW

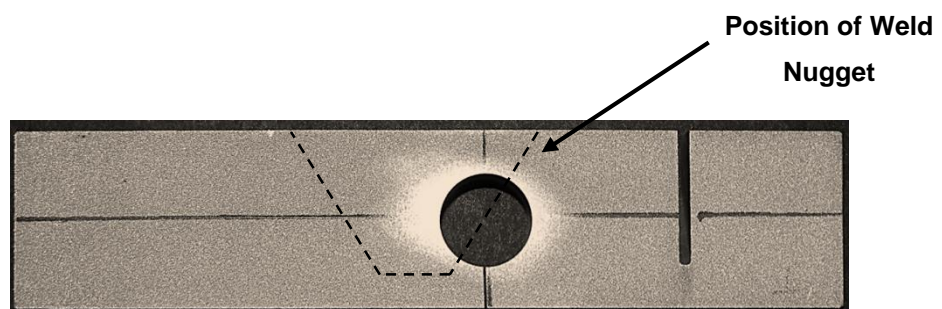


Figure 3-32. EBSD Sample Wire Cut from Sectioned Sample

A 12mm diameter cylinder was wire cut from of a 15mm thick section from the opposing side of the weld for EBSD analyses, as shown in Figure 3-31. The sample was taken from the mid-region of the weld as shown in Figure 3-32, as this typically is a region of poor bonding in aluminium FTSW.

The plunge depth was set to 3mm for these welds, as a starting point, with the theoretical 18 times displaced volume vs. clearance volume being 1.8mm. This was to account for rapid displacement of material during the first moments of welding with the relatively high axial force ramp up rate, as this had not been previously tested.

### **3.15. Summary of Experimental Setup**

The information highlighted and discussed in this chapter is critical for the repeatability of results found in the chapters to follow, and to further understand the calculation of the approximate plunge depth and energy input calculations. The equipment used in the research is identified with all the relevant machine specifications given. The development and calibration of custom load cells for the FTSW platform and PDS platform are presented and discussed with the working drawings given in Appendix B and C. For successful repeatability of the results presented in this research, it is critical that the identical procedures are followed.

---

## CHAPTER 4

### PROCESS DEVELOPMENT OF FTSW FOR AA6082-T6

#### 4.1. Introduction to the Development Process

The following sections guide the development of the FTSW process, as it was applied to 25mm thick AA6082-T6 plate. The development test matrixes follow on from one another as the process and equipment are developed to form a window in which FTSW can be made, before a final set of welds are investigated.

The sections consist of matrixes that will focus on;

- The effect of axial force;
- The influence of stud taper angle;
- The influence of hole taper angle;
- The need for preheat;
- The use of a non-consumable heat sink;
- The effect of axial force ramp up rate.

For the development study welds, the effect of these parameters is quantified by Macro defect analysis. Voids and general lack of bonding are identified, characterized and correlated with the recorded axial force, process torque and input energy. Selected welds are used to investigate the near interface temperature during welding by the use of thermocouples imbedded into the plate near the interface. An initial process parameter window needed to be identified before a test matrix could be designed for the FTSW research on AA6082 – T6. This was predominantly due to the lack of knowledge and known research on the process and more specifically, its application to aluminium and its alloys.

#### 4.2. Axial Force and Stud Taper Angle for a 20° Hole

As a starting point, the tapered stud geometry was investigated with varying axial force. The hole taper angle, stud and hole base diameters, rotational speed and forging time were kept constant as given in Table 4-1. The geometries are based on the literature of Van Zyl [38], D Bulbring [5], Pinheiro, [10], K Beamish [4], and

equipment capabilities. The rotational speed was chosen as the maximum that the platform would maintain while keeping close to the 5000 and 4000RPM used by Beamish [4] and Pinheiro [10] respectively. The hole taper angle of 20° was based on the work of Van Zyl [38], Bulbring [5] and Pinheiro [10], who suggested it to be appropriate for blind FTSW in similar thickness plate. The stud angle was designed to cover the change in angle applied by Beamish [4], Van Zyl [38], Bulbring [5] and Pinheiro [10]. The applied cooling time of 20 seconds was found to be sufficient for the weld to cool to approximately 180°C, which is approximately the aging temperature of the material. The geometry selected and process parameter combinations are given in Table 4-1 and Table 4-2 respectively.

**Table 4-1. Welds TW-1 to TW-10 Parameter Constants**

Rotational Speed (RPM)	5200
Cooling Time (s)	20
Clearance Volume vs. Displaced Volume Factor	18
Hole Area (mm <sup>2</sup> )	1 192.23
Base Area (mm <sup>2</sup> )	78.54

**Table 4-2. Welds TW-1 to TW-10 Parameter Variables**

Weld No:	Hole Depth (mm)	Stud Taper Angle (°)	Hole Taper Angle (°)	Hole Base Diameter (mm)	Stud Base Diameter (mm)	Plunge Depth (mm)	Axial Force (kN)	Stud Material Displaced During Plunge (mm <sup>2</sup> )
TW-1	20	10	20	10	9	16	15	2 803.9
TW-2	20	15	20	10	9	7.5	15	1 247.1
TW-3	20	18	20	10	9	4.5	15	688.0
TW-4	20	10	20	10	9	16	5	2 803.9
TW-5	20	15	20	10	9	7.5	5	1 247.1
TW-6	20	18	20	10	9	4.5	5	688.0
TW-7	20	10	20	10	9	16	30	2 803.9
TW-8	20	15	20	10	9	7.5	30	1 247.1
TW-9	20	18	20	10	9	4.5	30	688.0
TW-10	20	15	20	10	9	2+8	5-30	1 961.1

Once sectioned, polished and etched, it was found that all welds made using a 5kN axial force, had large voids within the weld nugget, with little or no mixing of the plate and stud material visible as shown in Figure 4-1 for Welds TW-1 to TW-3. Increased axial force to 15kN reduced the weld nugget voids and 30kN closed them, but did not entirely eliminate them. This shows that insufficient axial force was applied during welding. The most visually acceptable weld in this test matrix was weld TW-8. The weld showed localised bonding on the sidewalls with small voids between the shear layers in the lower region that had been mostly closed by the axial force during consolidation.

The weld nugget, was found to be divided in two main zones, separated by a shear layer; Zone 1 taken as below the shear layer and Zone 2 taken as above the shear layer. It should be noted at this point that the shear layer that is observed between Zone 1 and Zone 2 is not the final shear interface. Voids were formed on this layer for all welds, specifically the 5kN and 15kN combinations, reducing with increased axial force. The level at which the shear layer forms in the hole lowers with increased axial force, highlighted in Figure 4-1 for welds TW-2, TW-5 and TW-8. For example, the shear layer for TW-2 is near the surface and that of TW-8 is near the bottom of the hole. The position of this shear layer is a critical part of the FTSW of aluminium, as the sidewall bonding in Zone 2 is visually superior to that of Zone 1, and all voids within the weld nugget body are formed in Zone 1 regardless of the applied axial force. Therefore the lower Zone 1 in the tapered hole, the less volume of material available to form voids within the weld nugget. This indicates that in FTSW of AA6082-T6, as the stud rubs on the bottom of the hole during the first moments of the weld, heat conducts axially up the stud, softening it. As the stud begins to plunge, heat is conducted away from the weld zone into the plate, causing the weld interface to propagate upwards rapidly, as the stud material could not support the load. This reduces the rubbing time on the sidewalls of the hole during plunge, and hence the sidewall temperature needed to plasticize the interface.

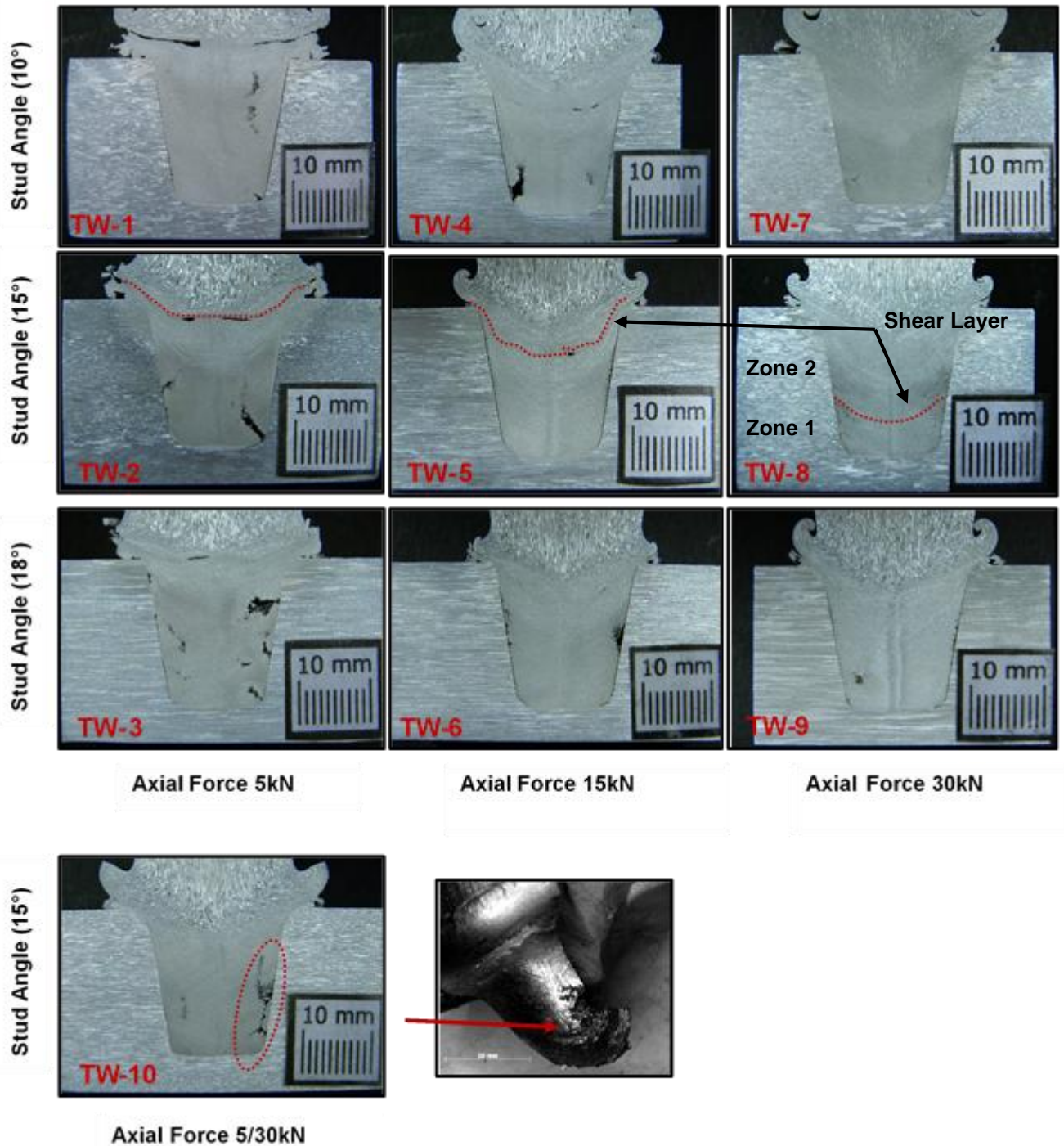


Figure 4-1. Welds TW-1 to TW-10 Macrographs

Figure 4-2 and Figure 4-3 show weld TW-4, a 15kN axial force weld with the stud removed. The dull region near the base and upper portion of the hole indicate bonding, while the reflective mid-region (area of Zone 1 as shown Figure 4-1) indicate lack of bonding, as this is the finish of the machined hole. At a point into the weld, the plate begins to warm, slowing down the conduction of heat into the plate from the weld interface. The stud, which is now softening further, shears under the increased axial load and frictional moment, causing the interface. The



zone that is now formed, referenced as Zone 2 in Figure 4-1, is formed above this shear interface, under a higher axial force and sidewall temperature, promoting bonding. Positioning and/or removal of this interface is critical to the success of an AA6082-T6 FTSW.

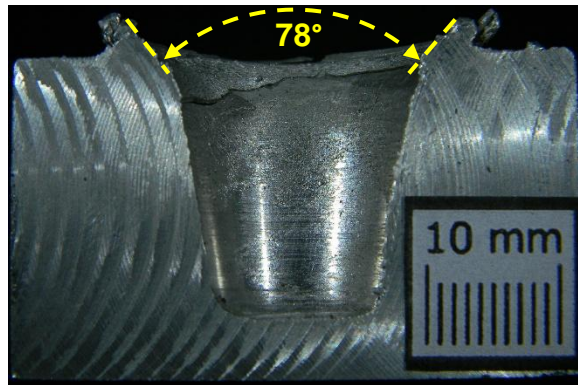


Figure 4-2. Weld TW-4 with Weld Nugget Removed

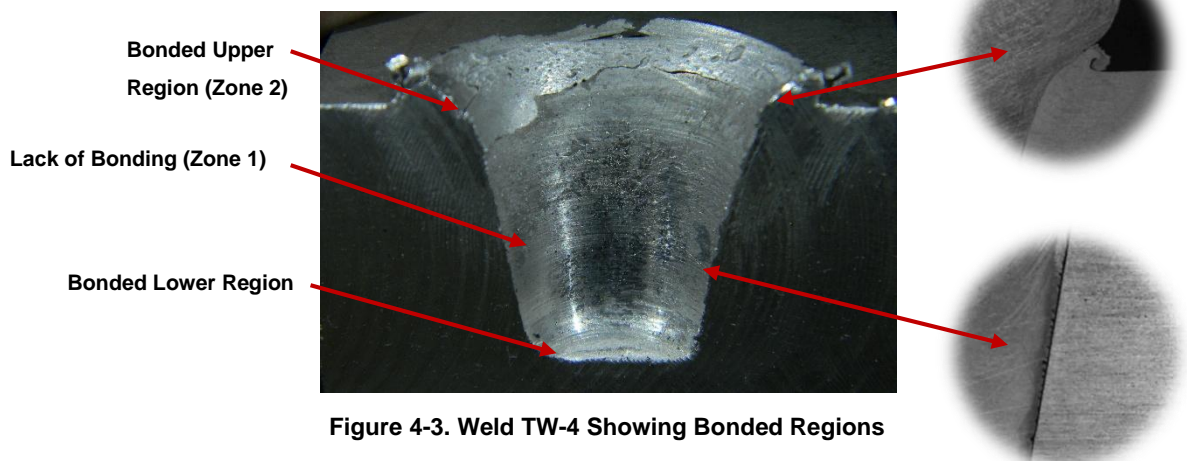


Figure 4-3. Weld TW-4 Showing Bonded Regions

Poor bonding was identified for all welds in Zone 1, with most having limited localised bonds between the weld nugget and the sidewall of the hole. This very poorly bonded zone is formed due to the high thermal diffusivity of the material. As the stud rubs on the bottom of the hole and begins to heat, bonds begin to form at the weld interface. These bonds are instantaneously sheared and reproduced, releasing heat. This corresponds with the work of Pinheiro [10] and Kimura et al. [13] who discuss the formation of these bonds during a friction welding process. However, it appears from these welds that AA6082, due to the material's high thermal diffusivity and low strength retention at elevated temperature, as these bonds are formed, the heat within the bond, maintaining it

in a plasticized state, is dissipated into the cold plate. This solidifies the bond, forcing the heated material directly above to shear due to its low strength retention, forming a new shear layer directly above the previous one. Therefore, at the base of the hole, there appears to be mainly localised bonds towards the periphery and a column of dynamically recrystallized stud material (DRSM), deposited one layer on top of the other, filling the hole, with only a few localised bonds securing Zone 1 to the sidewall of the hole. Mitelea et al. [26] explained that increases in axial force, expel the weld interface material out of the joint as flash in a shorter time [4] [23]. This reduces the heat conduction in the axial direction and creates a greater thermal gradient [23] [26]. To reduce heating of the stud, a higher axial force must be applied, to reduce heating in the axial direction; however, the stud will need to be capable of supporting the load.

The stud taper angle of  $15^\circ$  appears to give the most visually acceptable weld combination. A  $10^\circ$  clearance angle ( $10^\circ$  stud) appears to allow the flash to travel out too easily, while a  $2^\circ$  clearance ( $18^\circ$  stud) retains the flash and prevents rotation of the stud (This will be discussed later). The two stage weld, TW-10, shows no advantage over the single stage welds. The researcher's hypothesis that a weld with low initial axial force that ramps to a higher axial force, would allow the initial interface to rub and heat while the high secondary force would promote sidewall bonding and prevent weld nugget voids, was found to not be valid for the geometry and equipment setup used at this time. A variation of this approach is applied in future welds, with a more advanced control system. In this weld (TW-10), the body of the stud merely softened during the first stage and collapsed as force increased in the second stage, giving the large central void as shown in Figure 4-1. This initial rubbing is crucial to the FTSW of aluminium; however, considerable work will need to be done and precise control systems put into place to improve the base bonding and prevent stud collapse.

#### **4.2.1. Applied Axial Force for Welds TW-1 to TW-10**

The recorded axial force data showed that the FTSW platform was unable to reach the set axial force at the plunge rate of the stud, as shown in Figure 4-4. This gave a low axial force ramp up rate of approximately 3.6kN/s to 16.6kN/s taken to the seizure point, given in Appendix G. Welds done at 5kN achieved the set axial force due to low stud consumption rates; however, 15kN and 30kN welds

achieved a maximum of 10.5kN and 18kN to 22kN respectively. Appendix E for welds TW-1 to TW-10 shows that increased stud taper angle further increased the achieved axial force in the first phase of the weld. The axial force was higher with the larger stud taper, as the stud body consumed slower, allowing the system to apply more force. The axial force charts as well as the applied axial force at various critical points into the weld are given in Appendix E and F respectively, for all welds. This shows the sensitivity of the FTSW platform to changes in plunge rate and set axial force. The axial force applied during welding will, therefore, require monitoring for all development welds.

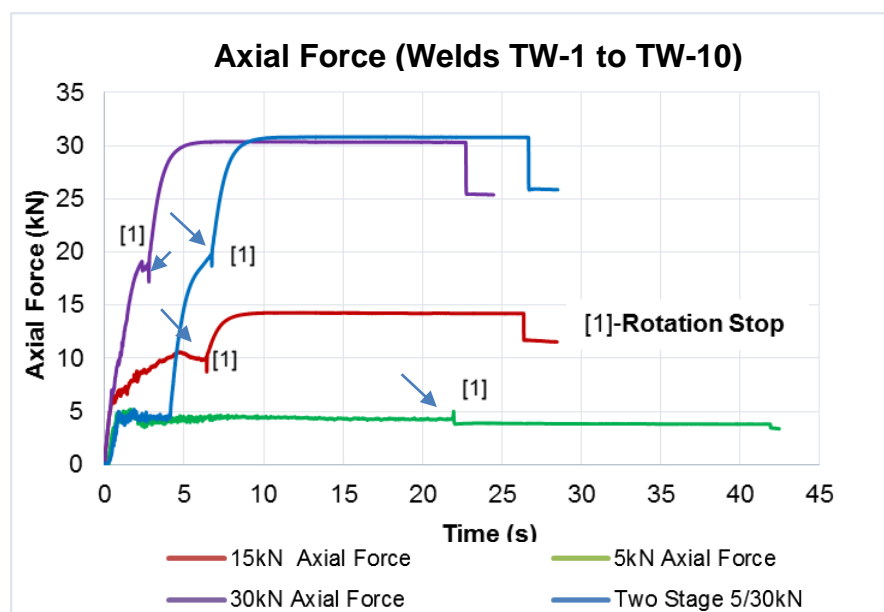


Figure 4-4. Applied Axial Force during Welding (Welds TW-1 to TW-10)

#### 4.2.2. Process Torque for Welds TW-1 to TW-10

The seizure stage is considered a critical point in the friction welding process of aluminium with regards to bonding at the base of the hole due to the high thermal diffusivity of the material. It is thought that the sooner this point is reached, or the higher the torque measured at that point, the more work is done in a shorter time on the interface. This reduces heat conduction away from the welding interface into the plate.

The process torque at seizure shown in Figure 4-5, is indicative that increased axial force directly increases the process torque exerted on the tool. Seizure, which is defined as the point at which maximum torque is achieved as the stud begins to be consumed by shearing, is characterized by an abrupt change in the

steady state of torque increase, highlighted in insets of Figure 4-6 (a), (b) and (c). The time at which seizure was reached for this matrix was 0.35 seconds to 0.6 seconds, given in Table 4-3. There was little to no change in the time to seizure as the axial force ramp up rate was the same for all welds, and none had reached the set force by this time. Table 4-3 shows that as the set axial force increased, the axial force ramp rate to seizure increased, corresponding with changes in time to seizure. This is not a phenomenon of the welding process, but a system control issue. With a greater set force, a higher pressure is generated on either side of the hydraulic proportional valve, giving greater control.

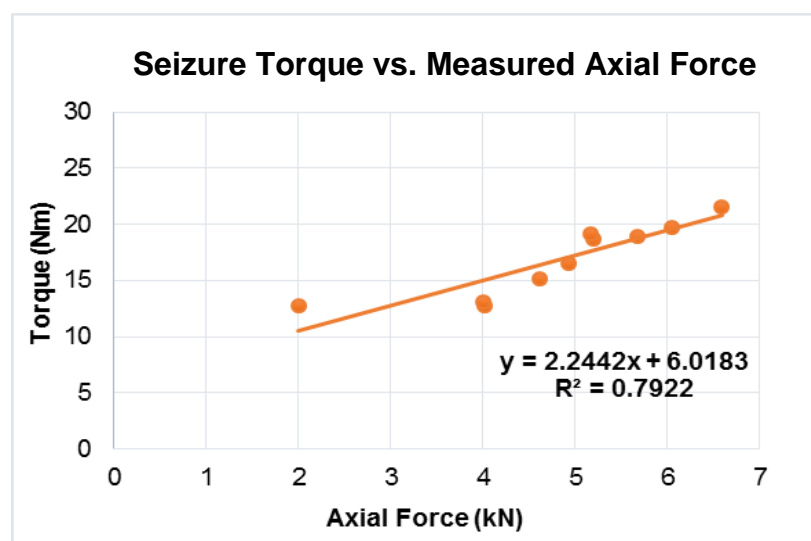


Figure 4-5. Seizure Torque vs. Measured Axial Force at Seizure for Welds TW-1 to TW-10

The process torque, increased with increased axial force for all welds, as shown in Figure 4-5 and given separately for all welds in Appendix G. Although the point up to seizure remained approximately constant, the effect after the point of seizure changed significantly. All 5kN welds with a 10° and 15° stud taper, showed that torque to dropped off after seizure as is the case for a conventional rotary friction weld reaching equilibrium [13] [9]. Welds using an 18° stud and/ or an axially applied load of 15kN or 30kN showed an increase in process torque after seizure (post seizure torque). The 18° studs repeatedly achieve the highest post seizure torque as shown in Figure 4-6, with reductions in stud angle reducing the torque. The maximum process torque after the seizure stage will be referred to as the Post Seizure Torque Peak (PSTP) from this point in the research and is shown in insets of Figure 4-6 for 15kN and 30kN welds.

Table 4-3. Results for Welds TW-1 to TW-10

Weld No:	Stud Taper Angle (°)	Welding Time (s)	Time to Seizure (s)	Energy Input at 0.1s (J/mm <sup>2</sup> )	Energy Input at Seizure (J/mm <sup>2</sup> )	Energy Input at 1s (J/mm <sup>2</sup> )(W/mm <sup>2</sup> )	Energy Input to PSTP (J/mm <sup>2</sup> )	Total Energy Input (J/mm <sup>2</sup> )	Energy Input Rate at 0.1s (W/mm <sup>2</sup> )	Energy Input Rate at Seizure (W/mm <sup>2</sup> )	Energy Input Rate at PSTP (W/mm <sup>2</sup> )	Total Energy Input Rate (W/mm <sup>2</sup> )	Axial Force at Plunge Depth (kN)
TW-1	10	24.4	0.45	2.1	21.0	4.5	7.2	92.4	20.7	49.0	14.1	3.8	3.1
TW-2	15	21.9	0.60	2.0	21.6	4.7	7.7	112.1	19.9	59.1	4.6	5.1	4.2
TW-3	20	19.9	0.50	1.3	19.7	7.3	8.4	101.6	13.4	47.9	6.7	5.1	3.4
TW-4	10	6.4	0.40	1.8	22.0	6.7	15.7	61.6	18.3	52.4	8.8	9.6	9.9
TW-5	15	4.3	0.38	2.1	35.4	7.3	12.1	41.8	20.7	57.5	8.6	9.7	10.0
TW-6	20	3.7	0.38	2.0	23.9	7.9	10.3	36.3	19.9	52.6	8.8	9.9	12.0
TW-7	10	4.4	0.35	2.4	24.3	7.3	13.2	46.8	24.1	69.3	8.9	10.7	15.5
TW-8	15	2.8	0.40	2.6	24.0	8.8	9.4	31.0	26.0	60.0	8.2	11.0	19.7
TW-9	20	2.4	0.40	1.6	24.4	10.6	9.7	32.1	16.4	61.0	10.0	13.2	23.0
TW-10	15	6.7	0.55	0.8	7.8	4.2	8.7	41.6	7.8	26.9	4.8	6.2	18.6

The increase in process torque after the seizure stage is thought to be influenced by two factors, namely;

- Increased stud angle increases the volume of stud material behind the shear interface that heat is dissipated into, increasing the studs ability to resist shear;
- Less clearance between the stud and hole prevents the flash from exiting the hole, the flash therefore locks between the two surfaces and causes additional rubbing and hence a larger friction moment. This increase in torque was noted by Pentz [47], who investigated the effect of clearance between the hole and tool during FHPP.

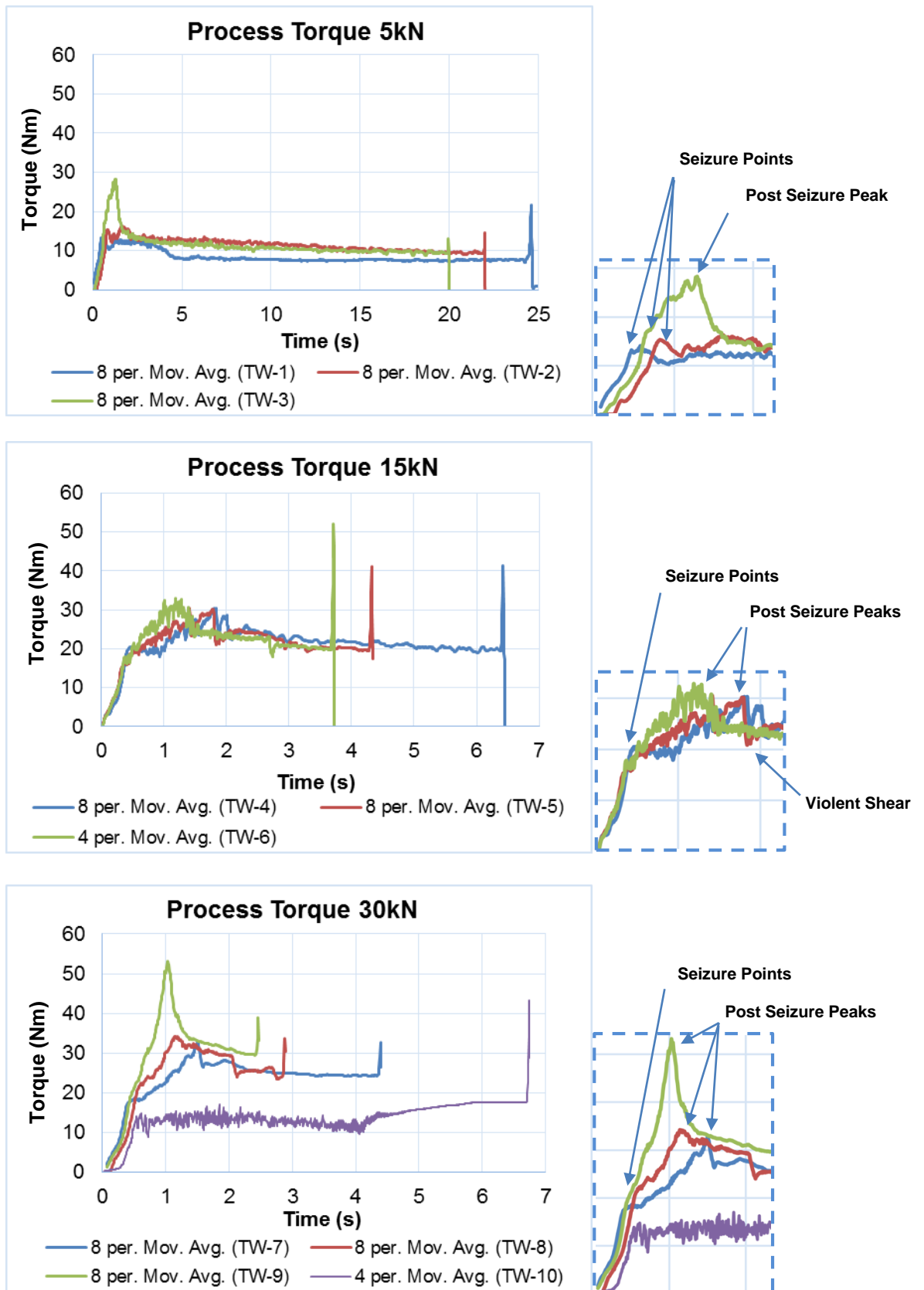


Figure 4-6. Process Torque Charts for Welds TW-1 to TW-10

**\*Note:** All process torque charts are expressed as 8 per. Mov. Avg. This indicates that an 8 per moving average was applied to the process torque data in order to smooth out noise from the spindle motor drive. All development weld torque charts are displayed in this way.

The additional rubbing generates extra heat in the stud body, softening it. This is thought to affect the way the material shears after the PSTP, during equalizing of the process torque. The softening of the stud body causes a tipping point to be reached in the process where the softened material behind the weld interface cannot maintain the energy input required to drive the plasticized state at the weld interface. When this point is reached, the interface shears off and is seen as a sudden drop in process torque. For the purposes of this research this will be termed violent shear and will be characterized by a sudden drop in process torque during the equalization stage of the process torque curve that begins to recover at approximately the same slope as the climb to seizure stage, as shown in Figure 4-7. These violent shears have been an indication of good bonding/ appropriate process parameters in previous work [23]. The weld with the best visual appearance, weld TW-8, had a substantial shear mid-way through the equalization stage, shown in Figure 4-6.

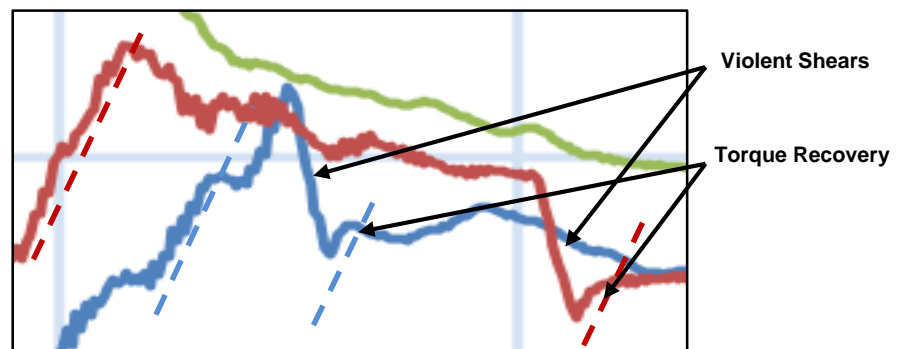


Figure 4-7. Parallel Torque Increases after Violent Shear

Axial force is shown to be the main contributing parameter in a FTSW process with regards to the torque exerted on the tool during rotation, as shown in Figure 4-8, highlighting the direct relationship between axial force and process torque. The chart displays the process torques for 30kN welds TW-7, TW-8 and TW-9 with respect to the measured axial force. The data shows that with increased axial force, the process torque increases to a point. As equilibrium of the process torque begins, the increase in torque with respect to increasing axial force reduces, as seen in Figure 4-6. The chart verifies that with increased stud angles, a greater torque is applied to the stud for the same axial force above 9.3kN axial force. Below 9.3kN axial force, all welds set to weld at 30kN had not yet reached the PSTP stage of the welding process, indicating why the process torques are

crossed below the 9.3kN point. The hole is not filled and only portions of the interfaces are rubbing. Due to changes in flow characteristics out of the weld with smaller taper angles, more material is displaced at lower forces and in a shorter time. Therefore, before the axial force reaches approximately 9.3kN, weld TW-7 has displaced more material than TW-9 for the same axial force, increasing the torque due to increased sidewall contact and hence shear interface footprint.

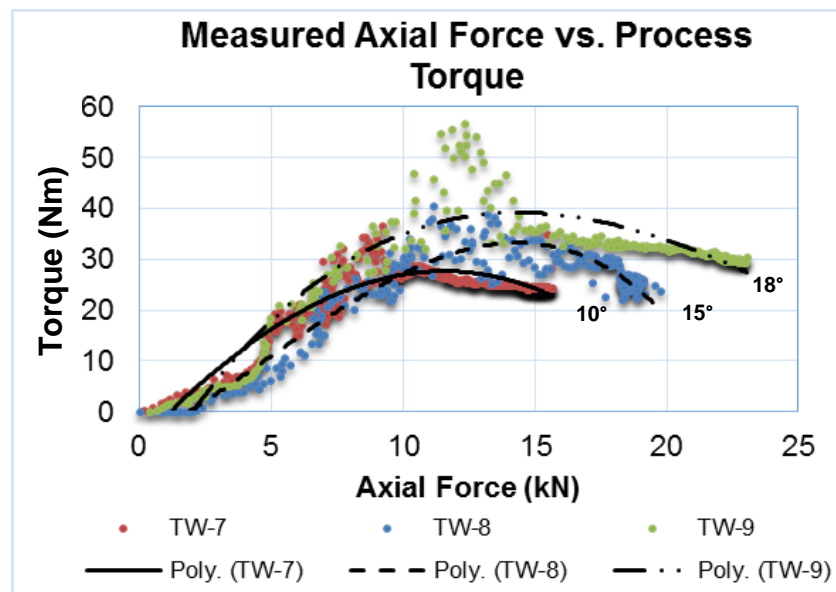


Figure 4-8. The effect of Axial Force on Process Torque

#### 4.2.3. Energy Input of Welds TW-1 to TW-10

The energy input into the welds was analysed to assist with additional characterization of the welds. As the friction moment increases so does the area under the process torque curve to that point, increasing the energy input at a constant rotational speed. Therefore, a greater amount of energy or work done, is put into the weld per unit time. All energy data, including the input energies at various points into the weld with and without considering the area of the tapered hole, and relevant axial forces are given in Appendix F.

The energy input at seizure remained constant as expected, with an average of 22.4J/mm<sup>2</sup>, deviating with 6.7J/mm<sup>2</sup> (Table 4-3 and Appendix F). As this is the seizure point and the stud had not yet begun to plunge, the area in shear is considered to be the area of the base of the hole. The energy to seizure will also



remain constant if the boundary conditions are identical. In the case of welds TW-1 to TW-10, no geometry or material change took place. As the parameters governing energy input were fixed until 5kN axial force was reached at approximately 0.3 seconds into the weld, any changes in energy were related to system control and surface roughness.

Energy input at 1 second into the weld was found to increase marginally with increased axial force by an average of  $1.8\text{J/mm}^2$  and  $1.6\text{J/mm}^2$  from 5kN to 15kN and from 15kN to 30kN axial force welds respectively, showing the direct link between axial force and the energy input in the first 1 second (Table 4-3). Increased stud angles were shown to increase the energy input into the weld at 1 second by  $0.6\text{J/mm}^2$ ,  $1.4\text{J/mm}^2$  and  $2.7\text{J/mm}^2$  for  $10^\circ$ ,  $15^\circ$  and  $18^\circ$  studs respectively as the set axial force was increased from 15kN to 30kN, highlighting the increased effect on energy input with increased stud taper angle. If the geometry of the visually best weld is analysed ( $15^\circ$  stud) for 15kN and 30kN axial forces vs. 5kN axial force (Weld TW-2, TW-5 and TW-8), the increase in energy input at 1 second is  $2.6\text{J/mm}^2$  and  $4.1\text{J/mm}^2$ , showing increased axial force to correspond directly with increased energy input in the first 1 second. This indicates that there is a minimum amount of energy input required in the first moments of the weld in order to control the formation of Zone 1 and successfully plasticize the plate at the bottom of the tapered hole, as this zone is formed predominantly in the first moments of welding. The energy input during this time is therefore critical, with the data indicating that more energy is beneficial in reducing the height of the shear interface between Zone 1 and Zone 2.

The energy to the PSTP shows the input energy into the weld up to the maximum torque point, before equalization begins. It is thought that the shorter the time needed to reach this point, and the more energy put into the weld to this point, the better the weld in the lower region. The energy to the PSTP for welds TW-1 to TW-10 range from  $7.2\text{J/mm}^2$  to  $15.7\text{J/mm}^2$ , with a downward trend towards increased stud angle Table 4-3. The energy input does not highlight any reasons for the improvement in weld TW-8. The only indicator is that TW-8 was formed at one of the highest axial forces and highest axial force ramp rates, reducing the time for the heat generated at the weld interface to dissipate into the plate (Appendix F), increasing local plasticization and bonding. The force ramp rate to

PSTP increased with increasing stud angle due to lower stud consumption rates. This increased the axial force applied at that point, increasing the torque and hence energy input, given in Appendix F. The time to PSTP appears to reduce with increasing stud angle and axial force, Appendix F. As only the 5kN welds reached the set force by the PSTP, the only notable changes in time and energy input to the PCTP is between the 5kN welds and the 15kN and 30kN combined. This highlights the effect that axial force has on the process as a governing parameter. The changes in energy input for the 15kN and 30kN welds are probably due more to axial force changes induced by the slow response and inconsistency of the control system than changes in geometry. This will need to be investigated at a later stage with a more precise control system for the force ramp up rate.

The total input energy, given in Table 4-3 stayed constant for 5kN welds and drops for 15kN and 30kN welds with increasing stud angle and axial force. This indicates that 5kN is inefficient, verified by its smooth process torque curve (Figure 4-6). The stud rubs on the softened material, for the axial force is insufficient to push out the material as flash. This is confirmed by the extended weld times of 5kN welds, given in Table 4-3, as the heat generated at the interface dissipated predominantly into the plate over the extended welding time and not used to form the joint. For the 15° studs the total energy input was 112.1J/mm<sup>2</sup>, 41.8J/mm<sup>2</sup> and 21J/mm<sup>2</sup> for 5kN, 15kN and 30kN welds, correlating with the applied axial force. This shows that the total energy to form the weld nugget reduces with increased axial force for all geometry combinations, as shown in Figure 4-9. Increased stud taper angle required less total energy to complete, as less material escapes out of the joint as flash, and less material is displaced to fill the hole. This shows that with increased axial force, the welding interfaces are held in more intimate contact, promoting diffusion bonding. The shearing effect begins to strive towards adiabatic shear, improving the efficiency of the weld and aligning with violent shear as seen in weld TW-8.

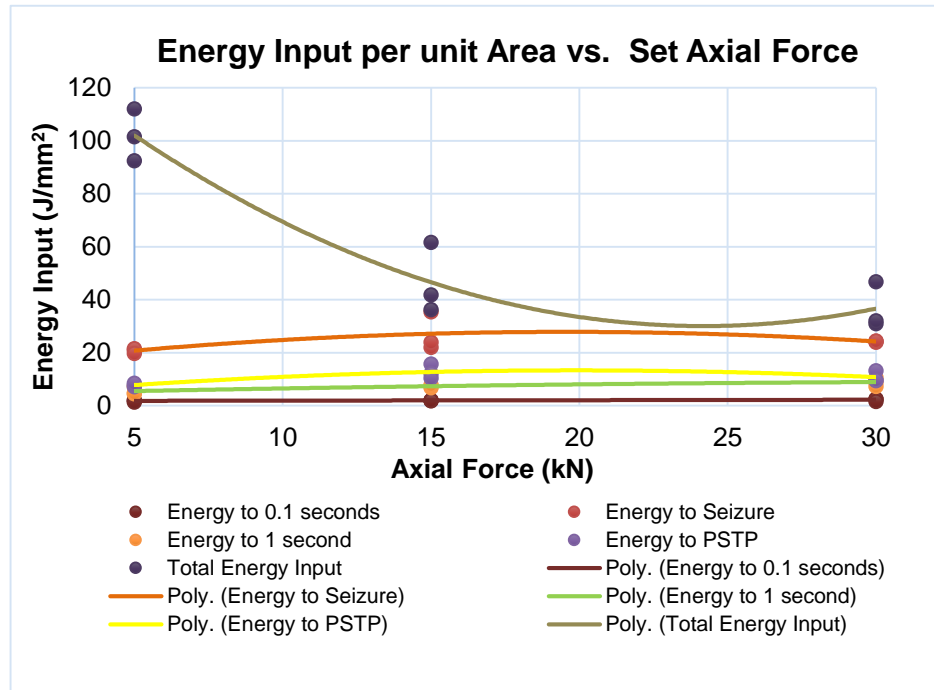


Figure 4-9. Energy Input vs. Set Axial Force (Welds TW-1 to TW-10)

#### 4.2.4. Energy Input Rate of Welds TW-1 to TW-10

The energy input rate into the welds was analysed to identify if the changes in geometry and process parameters were evident in relation to weld quality. The energy input rate to seizure increased with increased set axial force. This was not expected as no boundary conditions were changed. This change is attributed to increases in applied axial force due to improved hydraulic system control at higher set axial forces (Appendix F). The energy input rate to seizure was the highest overall, as the most amount of energy was used at the interface to form the joint, not consume and heat the stud as clearly shown in Figure 4-10. This increase is reflected in the reduced size of Zone 1 in the 30kN set axial force welds.

The rate of total energy input into a weld was found to not change significantly with stud geometry, but rather with applied axial force, linking the rate directly with axial force as shown in Figure 4-10. If welds TW-2, TW-5 and TW-8 are compared, the improvement with increasing total energy input rate is clear (Figure 4-1 and Table 4-3); therefore, higher axial force gives a higher energy input rate. This focuses the input energy on a narrower band of material at the interface, causing localised heating and plasticization, rather than low energy

input rates that allow the heat generated at the interface to conduct away into the plate.

The results of the energy data shows that changes in geometry, though reflective in the torque and, therefore, energy and energy input rate cannot alone distinguish between a visually good and bad weld, if incorrect geometry is chosen. However, it is thought that a good weld can be identified and imperfections highlighted using energy, if the geometry used is known to be good.

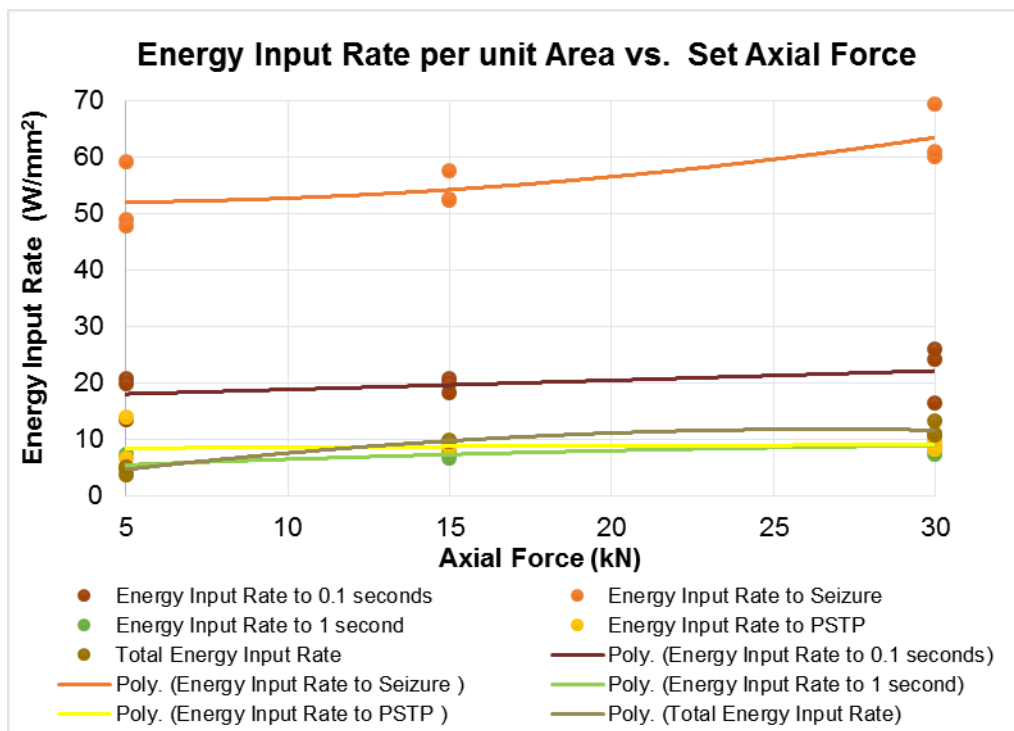


Figure 4-10. Energy Input Rate vs. Set Axial Force (Welds TW-1 to TW-10)

#### 4.2.5. Summary of Welds TW-1 to TW-10

This section, although showing the effect of increasing axial force and taper stud angle, did not achieve welds with visually good sidewall bonding. The best weld, TW-8 had only localised bonds in this region, and the weld nugget could be forcefully removed from the plate. The upper bonded region was characterized by deformation, shown in Table 4-2. The deformation of the hole increased the taper angle significantly to approximately  $78^\circ$ , showing that a larger angle was needed to transfer the axially applied load and hence hydrostatic forces to the surface of the hole. This would prevent the plasticized stud material flowing out without sufficiently rubbing the sidewall. The deformation also shows that the

block was significantly heated by the time the weld interface reached the top surface, as the deformation of the plate was caused at relatively low forces. This indicates that a method of slowing the heat conduction away from the weld and retaining stud integrity is needed to allow sufficient heating of the mid-region, where conduction is multi directional.

Some key observations made in this section regarding how aluminium reacts to FTSW process, what the effect of axial force is, what is the influence of the stud taper angle, and what direction should be taken in the next stage of development process are;

- Axial force is the most significant parameter in a friction welding process;
- Insufficient axial force caused large voids within the body of the weld nugget;
- Welding time reduces with increased axial force;
- Increase axial force directly increases the rate of energy input into a weld;
- Increased energy input in the first 1 second of welding improves weld quality in the lower region of the weld if appropriate geometry is chosen;
- A higher axial force ramp up rate gave the most visually sound weld with the least amount of poor bonding at the base of the hole (the smallest Zone 1 as shown in Figure 4-1);
- The control system of the FTSW platform will need to be reconsidered, to give more control of the axial force during welding and to achieve the set axial force.

### **4.3. FTSW of Aluminium Torque Chart Characterization**

During analysis of welds TW-1 to TW-10 and many of the following welds, an observation was made regarding the process torque curve. Conventionally in a rotary friction welding process, the torque curve, as discussed by Kimura et al [13] and Andrews and Beamish [9], has an initial rubbing stage, followed by a seizure stage. The seizure stage ends at the point of maximum torque, and as

rotation continues, the interfaces heats and the torque drops off until equilibrium is reached. The process continues until a set amount of material is displaced and rotation is stopped. The stopping stage is characterized by an abrupt climb in torque (terminal torque) as rotation is slowed, caused by the interface beginning to solidify, as power input drops.

This was found to not be the case for FTSW of aluminium AA6082-T6. As shown in Figure 4-11, the process torque curve continues to climb after seizure, indicated as the post seizure torque stage (c) in Figure 4-11, separated by a brief dip as plunge begins. This increasing process torque is caused by the increase in weld interface footprint, high axial force and flash trapped between the hole and the stud rubbing causing additional drag in welds with small (less than 5°) hole/stud tapered differences. Due to the tapered geometry of the hole, as the shear interface moves up, the shear area increases. There is, therefore, a second climb in process torque after the seizure point. This reaches a maximum point, termed the post seizure torque peak (PSTP), after which the torque drops reaching an equilibrium state due to filling of the hole and thermal saturation of the weld region. The process then follows the conventional trend of equalised torque followed by the terminal torque spike as rotation is stopped.

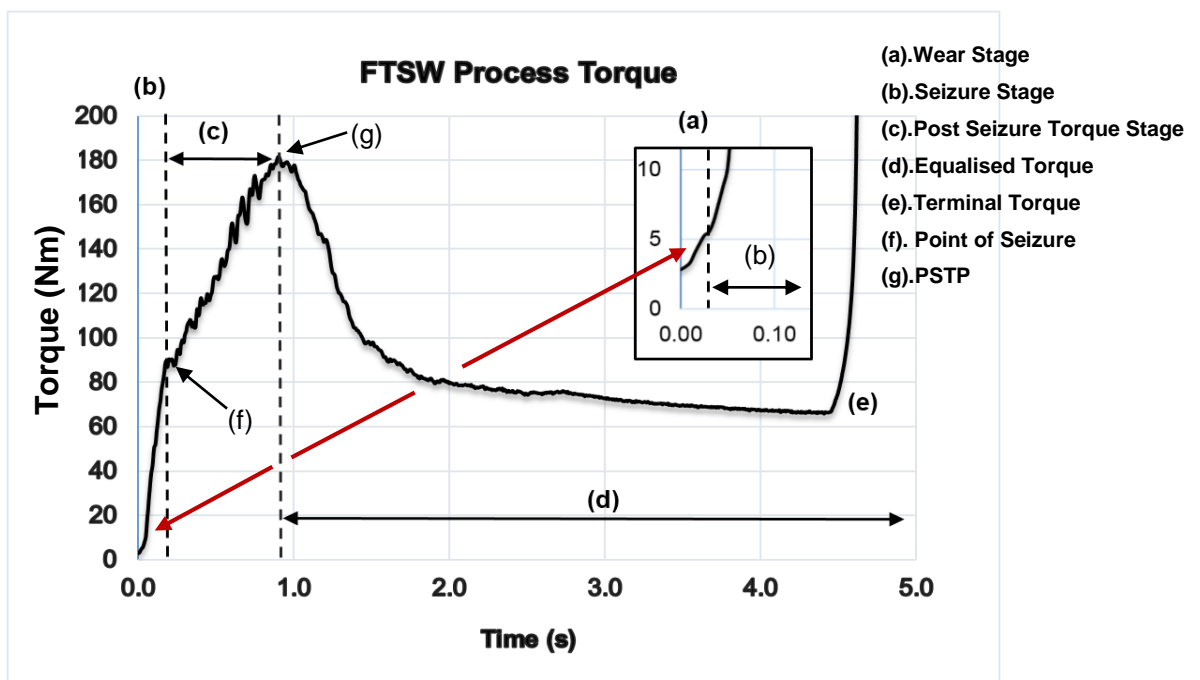


Figure 4-11. FTSW Torque Curve Characterization

#### 4.4. Varying of Preheat Using a 20° Hole Taper Angle

The next step in the development of FTSW of AA6082-T6 was to reduce the conduction of heat away from the welding interface, specifically in the lower regions. This was aimed at improving sidewall and base bonding. The geometry and process constants were kept the same as welds TW-2, TW-5 and TW-8, given in Table 4-1. A 30kN axial force was chosen as no benefits were found for reduced axial force welds. A 15° stud was selected as it gave the most satisfactory results in welds TW-1 to TW-10 using a 20° tapered hole. The parameter combinations are given in Table 4-4. Weld TW-8 is compared with Welds TW-11 and TW-12. Weld TW-8 has no preheat, where weld PW-11 was preheated to 250°C and PW-12 to 500°C (uncontrolled atmosphere). This was the preheat temperature when the block was removed from the oven. The average cooling of the block between removal from the oven at 200°C and the start of welding was approximately 60°C. A true welding surface temperature for weld PW-10 can be assumed to be between 100°C and 150°C. Before clamping a surface reading of 390°C was recorded for weld TW-11, and welding followed shortly at approximately 350°C.

Table 4-4. Welds TW-8, TW-11 and TW-12 Parameter Variables

Weld No:	Hole Depth (mm)	Stud Taper Angle (°)	Hole Taper Angle (°)	Hole Base Diameter (mm)	Stud Base Diameter (mm)	Plunge Depth (mm)	Axial Force (kN)	Stud Material Displaced during Plunge (mm <sup>2</sup> )	Preheat Temperature (°C) (Oven Temperature)
TW-8	20	15	20	10	9	7.5	30	1 247.1	22
TW-11	20	15	20	10	9	7.5	30	1 247.1	250
TW-12	20	15	20	10	9	7.5	30	1 247.1	500

Welds TW-8, TW-11 and TW-12 are shown in Figure 4-12. The most significant change with increasing preheat is the additional amount of stud not dynamically recrystallized at the top of the hole, the size of the thermo mechanically affected zone (TMAZ) of the plate and stud and the amount of deformation at the top of

the plate, highlighted in Figure 4-12. The degree of preheat did not change the depth of Zone 1 as expected, nor improve the bonding in Zone 1. The mixing at the base of the hole for weld TW-12 is improved, though approximately 3.5mm of plate deformation at the base was measured. This shall be a consideration in application with regards to controlling the plunge depth and breaking through of the stud during welding. The 250°C preheat weld showed improved sidewall bonding in the upper region to the depth of the final shear interface. The 500°C preheat gave good sidewall bonding in the upper half of the hole, in line with the final shear interface of the stud, this includes Zone 2. The sectioned half of weld TW-12 could not be broken out of the hole by applying a direct lateral force to the stud, as the stud failed above the top surface of the plate when the attempt was made, indicating good bonding. The improved bonding in the upper region of welds TW-11 and TW-12 was accompanied by an increased hole taper angle due to plate deformation. Weld TW-12 was the first weld to give an indication that good bonding was possible with FTSW of AA6082-T6. It is critical to note at this point that preheat directly increases the amount of stud in the hole and reduces the volume of stud material between the final shear interface and Zone 1. This is important as in order to produce a good FTSW the removal of Zone 1 and Zone 2 will be essential as the results to this point indicate that the strongest bonds are adjacent the final shear interface.

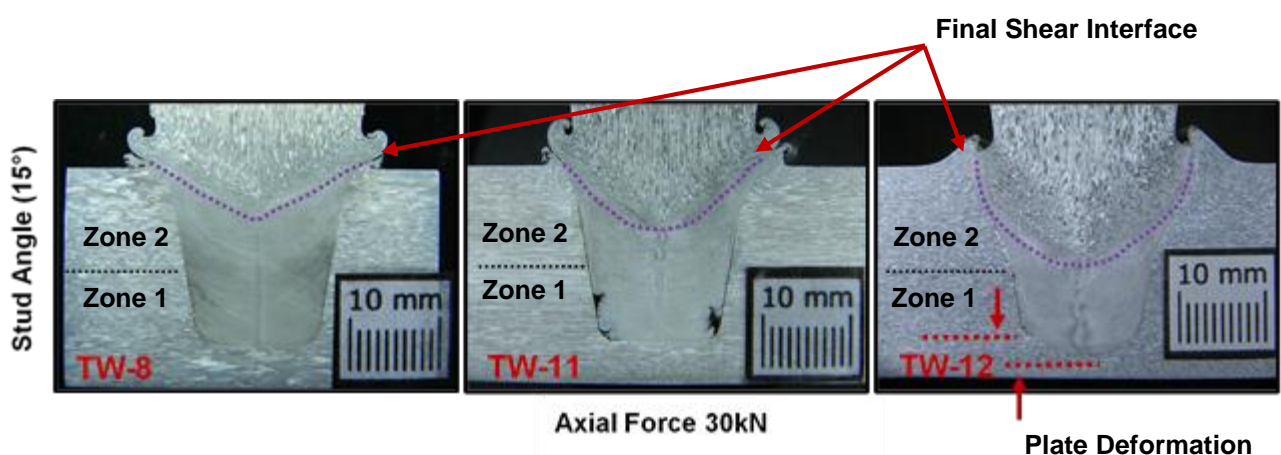


Figure 4-12. Welds TW-1, TW-11 and TW-12 Macrographs



#### 4.4.1. Process Torque with Increasing Preheat for Welds TW-8, TW-11 and TW-12

The process torque curves are given in Figure 4-13, for welds TW-8, TW-11 and TW-12, with all tabulated data given in Appendix F and all torque curves given individually in Appendix G. The use of preheat was found to increase the welding time as shown in Table 4-5. The welding time is seen to increase by 0.6 seconds and the seizure time to reduce by 0.08 seconds. The seizure torque reduced with preheat from 24Nm to 12.1Nm with a 250°C preheat and further to 7Nm with a 500°C preheat. The equalized torque remained constant at 25Nm after 2.2 second into the weld, for all welds. With increased preheat the magnitude of the violent shear experienced as torque equalized increased, indicating the stud sheared more abruptly as clearly seen in Figure 4-13. The drop in seizure torque and post seizure torque is explained by the heat retained within the weld zone with preheat. The heat retentions soften the parent plate material, allowing it to shear more easily. The bonds formed at the interface therefore remain plasticized longer as the heat generated due to rubbing and shearing of the interface bonds is not conducted away into the plate as fast. This is beneficial as it allows the bottom of the hole to rub and plasticize more effectively and promotes better processing of the material in the bottom region of the hole.

**Table 4-5. Results for Welds TW-8, TW-11 and TW-12**

Weld No:	Welding Time (s)	Time to Seizure (s)	Energy Input at 0.1s (J/mm <sup>2</sup> )	Energy Input at Seizure (J/mm <sup>2</sup> )	Energy Input at 1s (J/mm <sup>2</sup> )(W/mm <sup>2</sup> )	Energy Input to PSTP (J/mm <sup>2</sup> )	Total Energy Input (J/mm <sup>2</sup> )	Energy Input Rate at 0.1s (W/mm <sup>2</sup> )	Energy Input Rate at Seizure (W/mm <sup>2</sup> )	Energy Input Rate at PSTP (W/mm <sup>2</sup> )	Total Energy Input Rate (W/mm <sup>2</sup> )	Axial Force at Plunge Depth (kN)
TW-8	2.82	0.40	2.60	24.0	8.8	9.4	31.0	26.0	60.0	8.2	11.0	10.3
TW-11	2.96	0.35	2.71	16.3	6.6	12.6	32.4	27.1	46.5	8.8	10.9	8.2
TW-12	3.42	0.08	4.96	3.4	6.4	12.4	36.5	49.6	43.0	8.7	10.7	9.0

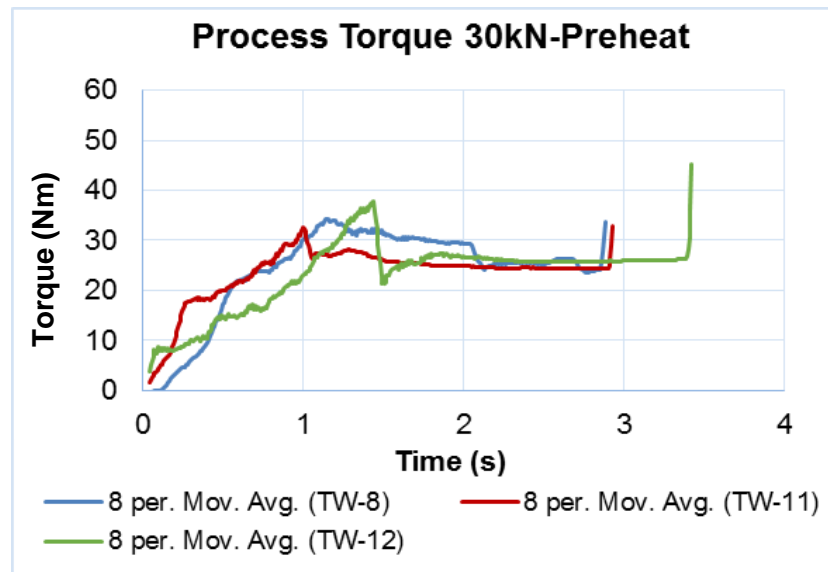


Figure 4-13. Process Torque Chart for Welds TW-8, TW-11 and TW-12

This is important as it shows that with preheat the initial interface reaches a state of shear faster and is under less shear stress. This means that the nose of the stud did less work on the interface before the interface reached the seizure stage, as part of the heat required for bonding at the interface is then supplied by preheat. The energy put into the weld by the stud up to the seizure stage is therefore directly focussed on plasticizing the interface at the bottom of the hole. The stud body will, therefore, have retained more integrity due to reduced thermal saturation and be unlikely to prematurely shear, promoting rubbing. This is shown by the improved mixing at the base of the hole for weld TW-12.

#### 4.4.2. Energy with respect to Preheat for Welds TW-8, TW-11 and TW-12

The energy input in the first 0.1 second of the weld doubled with preheat of 500°C as shown in Figure 4-14 and Table 4-5. During this initial period, preheat allowed more energy to be put into the weld by promoting the rubbing away of the surface roughness. This allowed bonds to form at the interface in less time; thus reducing the time for heat to conduct axially up the stud. The stud will, therefore, rub sufficiently on the base of the hole before the weld interfaces shear and the next shear layer is generated. This is clearly evident by the mixing of the plate and stud material at the base of the hole, shown in Figure 4-12.

The energy input to seizure reduced from  $24\text{J/mm}^2$  to  $3.4\text{J/mm}^2$  as shown in Table 4-5 and Figure 4-14. Less work was therefore needed to be done by the stud in order for the welding interface to reach a state of seizure. If less work is done by the stud, less heat will be generated to conduct up the stud. This indicates that less energy input with reduced time to seizure is beneficial at the base of the weld, providing seizure was successfully reached. This is due to the high thermal conductivity of aluminium, as the stud cannot heat the plate material at the base of the hole sufficiently for it to soften and plasticize before the stud begins to be consumed. As aluminium has a specific heat of  $0.88\text{kJ.kg K}$  vs. that of steel, which is  $0.49\text{kJ.kg K}$  and a thermal conductivity of  $180\text{W.mK}$  vs. steels  $43\text{W.mK}$ , with an approximate plasticization temperature for aluminium of  $450^\circ\text{C}$  and mild steel of  $1230^\circ\text{C}$ , the energy needed to plasticize aluminium vs. mild steel, taking room temperature to be  $22^\circ\text{C}$ , is  $376\text{kJ.kg}$  and  $592\text{kJ.kg}$  respectively. Therefore, an aluminium weld will generate 0.64 times the heat energy of steel for the same displaced volume, and will conduct it away 4.2 times faster. This, along with poor strength retention at high temperature, makes it problematic for the aluminium stud to adequately heat the base of the hole without preheat as the stud will overheat and collapse.

The energy input in the first 1 second of welding was seen to reduce marginally with preheat between welds TW-8 and TW-11 and then remain constant for weld TW-12. The reduction in energy input is thought to be due to the elevated block temperature reducing the conduction of heat away from the weld during plunge. This keeps the weld zone at higher temperatures and hence lower shear stress, preventing cooling of the flash as it travels out the hole, reducing rubbing and sidewall plasticization. The energy input in the first 1 second has been shown to be directly linked to the formation height of Zone 1; therefore, as these welds all have similar Zone 1 formation heights it follows that the energy input in the first 1 second should be similar for all welds, however it is critical to increase the energy input at 1 second in order to minimise the formation height of Zone 1.

The input energy input to the PSTP increased with preheat, but was the same for both  $250^\circ\text{C}$  and  $500^\circ\text{C}$  preheat as shown in Figure 4-14. This is thought to be due to the severe deformation of the hole of weld TW-12. The energy input to

PSTP will be investigated further in other welds before any conclusions are proposed; however, it appears to be predominantly affected by axial force and hence axial force ramp up rate.

The total energy input increased with increasing preheat temperature, not significantly when compared to the effect of axial force, but consistently. This is thought to be a function of the increased welding time, which is influenced by the deformation of the hole seen in Figure 4-12, increasing the surface area, and to the slowed forming and axial propagation of shear layers, as heat conduction is slowed with preheat.

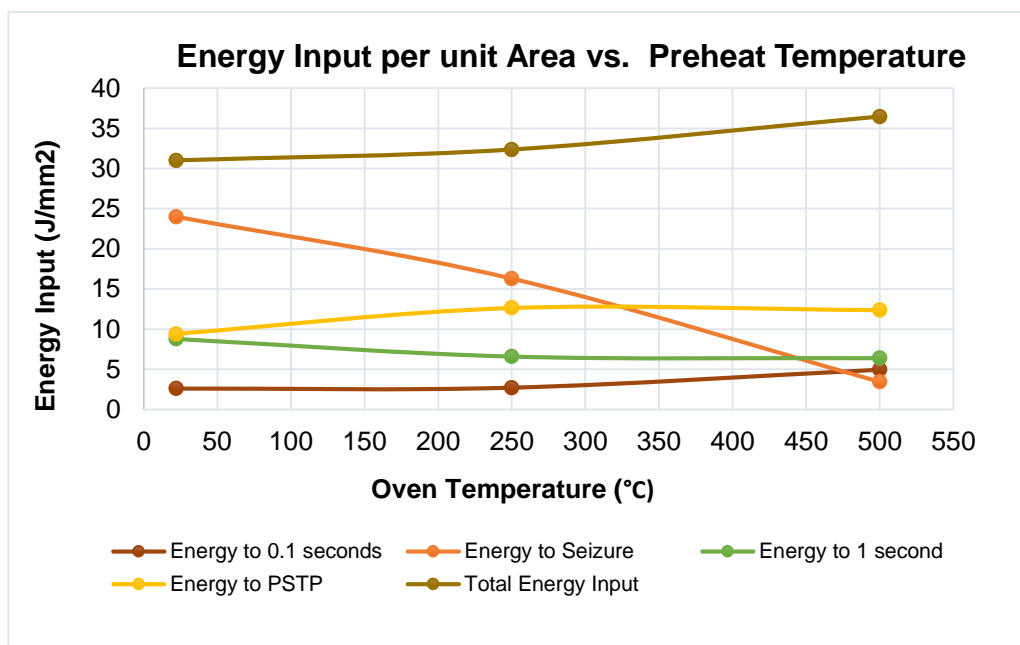


Figure 4-14. Energy Input vs. Preheat (Welds TW-8, TW-11 and TW-12)

#### 4.4.3. Energy Input Rate with respect to Preheat for Welds TW-8, TW-11 and TW-12

The energy input rate at 0.1 seconds increased from  $26\text{J/mm}^2$  to  $49.6\text{J/mm}^2$  with  $500^\circ\text{C}$  preheat (Table 4-5 and Figure 4-15). This may be a reason for the high deformation at the base of the hole, as the material softened locally before heat could be conducted away, promoting the good mixing at the base interface of weld TW-12.

The rate of energy input at seizure was lower with preheat as the torque reduced and the time to seizure reduced from 0.4 seconds to 0.1 seconds. The stud,

therefore, had to do less work per unit time to achieve seizure. This is important, for the lower the energy input rate on the stud, the less the chance of stud collapse.

The energy input at 1 second, PSTP and total energy input into the weld appears to not be affected by preheat. However, as these are time dependant and the plate experienced significant deformation, this will be investigated further in other welds. The energy input data results highlight the improvements at the base of the hole with preheat. All energy input data is given in Appendix F.

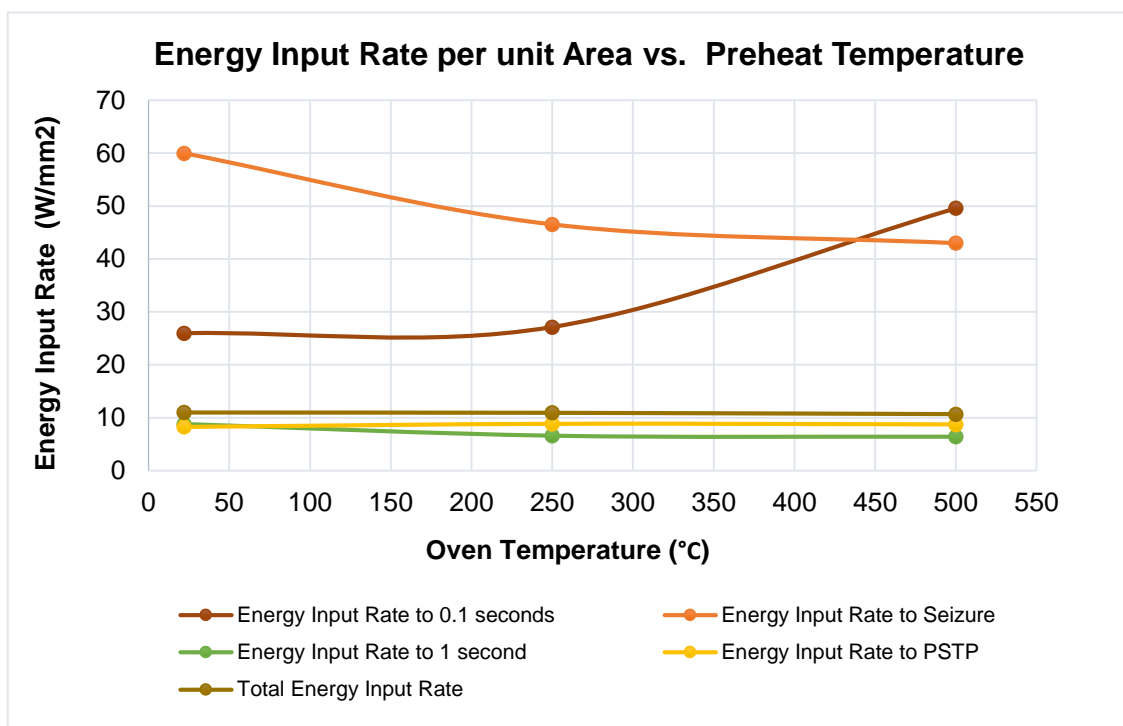


Figure 4-15. Energy Input Rate vs. Preheat (Welds TW-8, TW-11 and TW-12)

#### 4.4.4. Summary of Welds TW-8, TW-11 and TW-12

With an oven preheat temperature of 250°C, there was little to no noticeable improvement in sidewall bonding, except near the top of the weld. With a 500°C preheat temperature the sidewall bonding between the weld nugget and plate was significantly improved. There is good bonding at the base of the hole with mixing of the base materials. Preheat did not improve the lack of sidewall bonding in Zone 1, which correlated with no change in energy input in the first 1 second of welding. The occurrence and formation height of zone one will therefore need to be controlled by increasing the axial force applied in the first 1

second, requiring an increased axial force ramp up rate, which will be investigated later in the research. Increased preheat changed the shape of the final shear interface from a pointed shallow profile shown in Figure 4-12 (TW-8) to a rounded interface much deeper into the weld, shown in Figure 4-12 (TW-12). It appears that having a more unprocessed stud in the hole assists with sidewall bonding. This is partially explained by Nunes et al. [45] who states that the flash is easily visible during plunge of a FSW tool, and does not appear to rotate with the tool. There is therefore, a region of flash in the tapered hole, near the interface only, that rotates, then, over a distance, stops. Therefore, the more stud there is in the hole, the better the final shear interface follows the profile of the hole and the narrower the distance between the rotating stud and the sidewall of the hole. This promotes rotation in the highly plasticized material and improves sidewall bonding.

This section has clearly identified that preheat is a critical success factor for the FTSW of AA6082-T6, and that it significantly influenced the energy input and energy input rate during welding. Furthermore, this section has highlighted that a method of slowing the stud consumption rate during welding is essential to achieve good bonding in the lower region and minimise the formation of Zone 1.

#### **4.5. Varying of Axial Force and Stud Angle Using a 30° Hole**

The influence of increasing the angle of the tapered hole needed to be investigated, as this would increase the normal force exerted on the side walls of the hole and give a greater volume of material above the weld interface. Though Beamish [4] had already established that taper angles of up to 90° were beneficial for good sidewall bonding for through type FTSW, this was not certain for blind FTSW Welds. As large taper angles are problematic due to the frictional torque required to drive the stud during plunge and the increased axial force needed to forge the weld with the larger stud shank, a hole taper angle of 30° was chosen. This will be tested with 20°, 25° and 28° stud angles, with the expected optimum being a 5° difference between hole and stud. Axial force levels of 15kN and 30kN will be tested, with tests at 5kN abandoned due to void formation. No preheat was applied to identify if the angle of the hole and the additional cross-sectional area of the stud would allow rotation and prevent plunge long enough to achieve

bonding. The process constants are given in Table 4-6 and the process variables and combinations tested in Table 4-7.

**Table 4-6. Welds TW-14 to TW-19 Parameter Constants**

Rotational speed (RPM)	5200
Cooling Time (s)	20
Clearance Volume vs. Displaced Volume Factor	18
Hole Area (mm <sup>2</sup> )	1 313.22
Base Hole Area (mm <sup>2</sup> )	78.54

**Table 4-7. Welds TW-14 to TW-19 Parameter Variables**

Weld No:	Hole Depth (mm)	Stud Taper Angle (°)	Hole Taper Angle (°)	Hole Base Diameter (mm)	Stud Base Diameter (mm)	Plunge Depth (mm)	Axial Force (kN)	Stud Material Displaced During Plunge (mm <sup>2</sup> )
TW-14	20	20	30	10	9	9.5	15	1 965
TW-15	20	25	30	10	9	5	15	950
TW-16	20	28	30	10	9	3.5	15	696
TW-17	20	20	30	10	9	9.5	30	1950
TW-18	20	25	30	10	9	5	30	950
TW-19	20	28	30	10	9	3.5	30	696

Macrographs for welds TW-13 to 18 are given in Figure 4-16. Welds showed little overall improvement vs. welds using a 20° hole taper and no preheat. Weld TW-16, TW-17 and TW-18 showed improved sidewall bonding in the upper third of the joint vs. 20° welds made at 30kN axial force, showing an improvement with the increased hole taper angle. All 15kN welds had no sidewall bonding for the full depth of the hole and a clearly distinguishable final shear layer separating Zone 1 and 2, specifically weld TW-14.

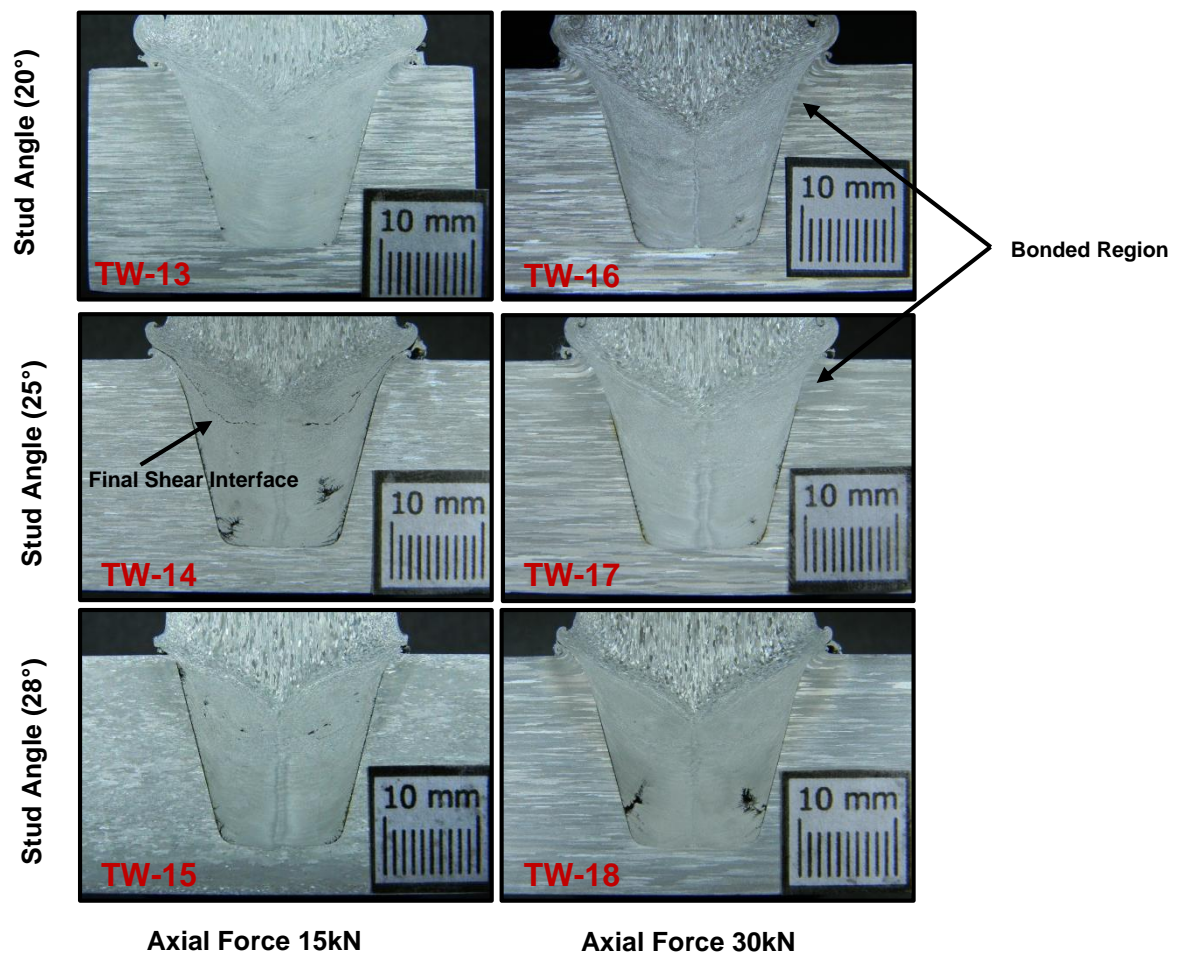


Figure 4-16. Welds TW-13 to TW-18 Macrographs

#### 4.5.1. Axial Force for Welds TW-13 to TW-18

Axial force data for welds TW-13 to TW-18 is shown in Figure 4-17. Data shows that for all welds the set axial force was not achieved. 15kN and 30kN axial force welds achieved approximately 14kN and 24kN applied axial force respectively, considerably more than the 10.5kN and 18kN-22kN achieved using the 20° hole geometry. This gave a force ramp rate to seizure of 7.6kN/s to 11.1kN/s. This showed that the larger stud was able to resist shear longer and, therefore, consume slower, allowing the hydraulic system to apply more force at the plunge rate of the stud. Axial force Charts as well as the applied axial force at various critical points into the weld is given in Appendix E and F respectively, for all welds.



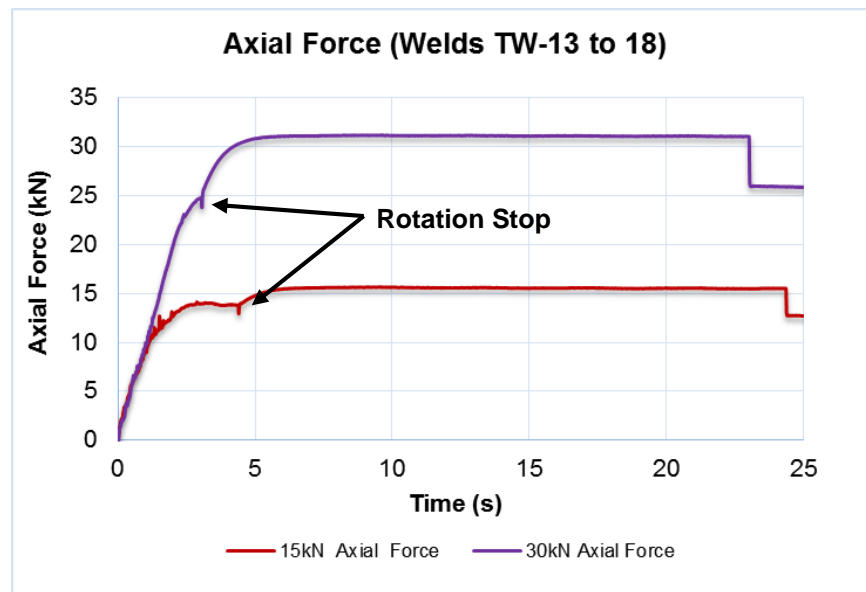


Figure 4-17. Applied Axial Force during Welding (Welds TW-13 to TW-18)

#### 4.5.2. Process Torque for Welds TW-13 to TW-18

The process torque for welds TW-13 to TW-18 is given in Figure 4-18. All welds showed a climb in process torque after seizure. Increases in axial force shortened the welding time and increased the PSTP as shown in Figure 4-18 and Appendix F, and given in Appendix G. The most prominent feature of the torque curves is the occurrence of violent shears during welding and there is direct correlation to weld quality. All welds with voids within the body of the weld nugget did not experience violent shear. Welds TW-16 and TW-18 were visually superior, with bonding in the upper regions, no visible final shear interface and minimal voids within the lower region of the weld nugget (Zone 1). Both welds experienced violent shear with TW-16 having two small ones and TW-17 one large shear. The profile being similar but scaled up from that of weld TW-8, the visually best 20° tapered hole weld without preheat, and TW-12 the visually best 20° hole weld with preheat.

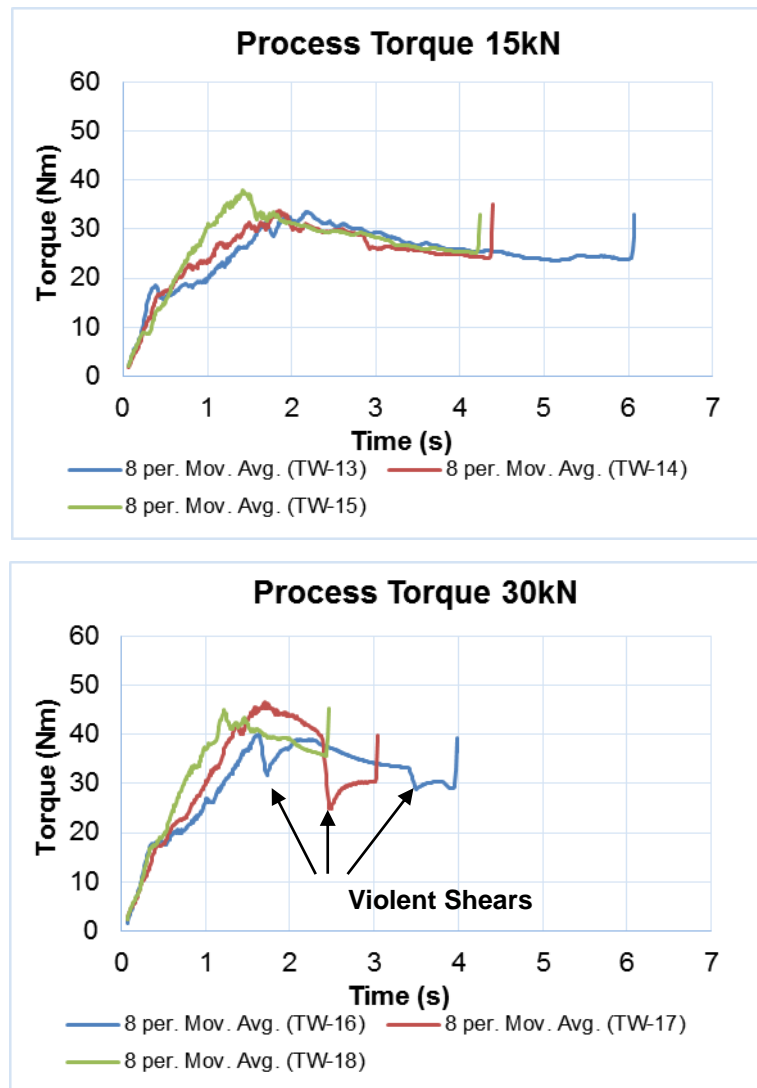


Figure 4-18. Process Torque Charts for Welds TW-13 to TW-18

#### 4.5.3. Energy Input for Welds TW-13 to TW-18

Energy input up to 0.1 seconds was similar to welds TW-4 to TW-8 as expected, given in Table 4-8, with an average increase of only  $0.8\text{J}/\text{mm}^2$ . This is not considered a noteworthy difference in energy, but the change may be triggered by the interface dissipating heat into the larger body of the stud.

The energy input at seizure showed no correlation to joint quality and did not change as shown in Table 4-8, except for a drop in energy to seizure for weld TW-15. The lack of correlation is a clear indicator that without preheat the energy input by the stud will not necessarily influence the formation of a good weld. Seizure for weld TW-15 was reached in 0.2 seconds, a shorter time than

considered normal for this geometry and setup, approximately 0.32 seconds to 0.43 seconds. Further, considering that weld TW-18 had the correct time to seizure of 0.3 seconds and is essentially the same welding process up to 0.75 seconds into the weld as weld TW-15, weld TW-15 is considered an outlier. As the axial force ramp rate is approximately 7.6kN.s to 16.5kN.s for the platform at seizure and that the recorded ramp rates to seizure given in Table 4-8 are within normal range for weld TW-15, the stud reached seizure in less than normal time without reasonable explanation from the data acquisition system. There is currently no reasonable explanation for this other than possible stud misalignment during setup or marginal unnoticed difference in geometry.

The energy input at 1 second was constant for all welds, with an overall increase in energy input with increased stud taper angles as shown in Table 4-8, correlating with welds TW-4 to TW-9. The increase in hole angle to 30° appears to have no effect on the energy input at 1 second vs. that of a 20°.

Energy input up to PSTM reduced with increased stud taper angles as before and increased with the higher axial force when compared to previous welds due to the decelerated stud consumption rate. This highlights the dependence of input energy on the applied axial force. The axial force at PSTM did not change between welds as shown in Appendix F, hence the correlation between energy inputs. Appendix F shows the energy input to 1 second and PSTM without taking the area of the hole into account. When welds TW-1 to TW-10 and welds TW-13 to TW-18 are compared there is no increase in input energy at 1 second with the increased hole taper angle. Energy input at PSTP however had an average increase of 1.52 times, due to the increase in hole angle.

Total energy input reduced with increased stud angle, as less material was displaced during plunge as given in Table 4-7. Increased axial force further reduced the total energy input. However, this could not be linked to changes in the appearance of the welds. It is thought that more control of the axial force is needed from the welding platform in order to precisely compare changes in geometry, this will be addressed later. Further, higher axial force limits appear to be necessary for the process.

Table 4-8. Results for Welds TW-13 to TW-18

Weld No:	Welding Time (s)	Time to Seizure (s)	Energy Input at 0.1s (J/mm <sup>2</sup> )	Energy Input at Seizure (J/mm <sup>2</sup> )	Energy Input at 1s (J/mm <sup>2</sup> )(W/mm <sup>2</sup> )	Energy Input to PSTP (J/mm <sup>2</sup> )	Total Energy Input (J/mm <sup>2</sup> )	Energy Input Rate at 0.1s (W/mm <sup>2</sup> )	Energy Input Rate at Seizure (W/mm <sup>2</sup> )	Energy Input Rate at PSTP (W/mm <sup>2</sup> )	Total Energy Input Rate (W/mm <sup>2</sup> )	Axial Force at Plunge Depth (kN)
TW-13	6.07	0.34	2.9	26.2	6.4	19.7	63.0	29.1	78.3	9.2	10.4	12.7
TW-14	4.40	0.34	2.4	22.1	6.8	16.4	45.8	24.1	65.4	9.1	10.4	12.9
TW-15	4.24	0.20	2.8	9.6	7.1	12.8	46.7	28.3	47.8	9.1	11.0	13.4
TW-16	3.99	0.25	2.8	15.1	7.1	15.5	49.5	28.4	60.5	9.7	12.4	23.5
TW-17	3.05	0.37	2.9	25.5	7.5	18.6	39.5	29.2	69.9	11.1	12.9	23.8
TW-18	2.46	0.3	2.6	20.9	9.0	12.4	32.9	25.9	69.8	10.3	13.4	23.6

#### 4.5.4. Energy Input Rate for Welds TW-13 to TW-18

The energy input rate at 0.1 second, and PSTM were constant (excluding weld TW-15), with changes directly linkable to applied axial force in Appendix G. The effect of increased stud taper angle increased the energy input, showing the larger stud body to dissipate heat at a greater rate, enabling the welding interface to maintain a higher energy input rate.

#### 4.5.5. Summary of Welds TW-13 to TW-18

The visually best welds without voids in the weld nugget had significant violent shears during plunge in the equalized torque phase of their process torque curves. As with previous welds this seems to be an indication of weld quality. The energy input rates did not significantly change as the boundary conditions remained the same. This group of welds highlights that energy at the start of the weld is not changed with the increase of hole angle. The increase in angle did, however, show that a stud with a large taper angle, consumes slower, allowing the system to apply a greater axial force as the demands on the hydraulic system was reduced with slower motion. This increase in force changed the input energy and energy input rate.

From this it is clear that the angle of the tapered hole as noted by Beamish [4] is critical to sidewall bonding and will need to be significantly increased in order to make a substantial improvement.

#### **4.6. The Effects of Preheat and Increased Stud Shank Diameter Using a 60° Hole**

Previous welds and literature showed that a larger hole taper angle is needed to improve sidewall bonding. The angle of the hole was, therefore, further increased to 60°. No clearance between the base diameters of the hole and stud was selected, as to keep the maximum amount of material within the plasticized zone. Furthermore, it was theorised that if the flash could be held in the weld region for longer and the least amount of plunge possible was used that would be necessary to fill the hole, the body of the stud would experience less heat conduction and would rotate longer against the sidewall before collapse.

To achieve this, the base diameter of the hole and stud were made equal and a 1° difference in hole and stud taper angles used to minimise flash formation. This would serve to slow material flow, reducing heat loss out of the weld that would have been carried by the flash. Though this is a smaller difference in angle than previously identified as appropriate, it was thought that the small amount of displaced material required to fill the hole would not allow the stud to soften, promoting stud rotation. As the exit diameter of the hole increased with the 60° hole, so theoretically would the process torque. As the welding platform was limited in its torque capacity and considering the possibility of mechanical lockup due to the reduced clearance, the weld geometry was scaled down. The depth of the hole was reduced to 14mm and the base diameters of the hole and stud reduced to 6mm as given in Appendix A, while the plate thickness was maintained at 25mm. The three welds discussed are aimed at identifying the effect of increased hole taper angle with respect to preheat and maintaining rotation of the stud as long as possible. This is purely an effort to improve sidewall bonding, not specifically exercising practical process parameters as will be seen by the excessive plunge depths applied of up to 6mm, when the required amount is theoretically 0.3mm.

Weld TW-14, TW-15 and TW-16 investigated the use of a 60° hole taper and 59° stud configuration in order to verify the need to use a larger hole angle as mentioned by Beamish [4], combined with the need for preheat as indicated by development welds conducted to this point. Weld TW-14 had no preheat, TW-15 was preheated to an oven temperature of 250°C and TW-16 had the same preheat procedure as weld TW-15 but utilised a 30mm stud shank diameter instead of the normal 25mm. Weld TW-14 used a 3mm plunge depth. This is approximately 2 mm past the 18 times fill factor for this geometry, but testing showed the stud collapsed prematurely above the plate. The total energy input for these welds is, therefore, not comparative between welds or reflective of the geometry. Weld TW-15 uses a 4mm plunge to further maintain rotation and TW-16 a 6mm plunge with the 5mm larger stud shank. The additional stud material would ideally act as a heat sink, maintaining rotation. The process constants and process combinations for welds TW-14 to TW-16 are given in Table 4-9 and Table 4-10 respectively.

**Table 4-9. Welds TW-19 to TW-21 Parameter Constants**

Rotational speed (RPM)	5200
Cooling Time (s)	20
Clearance Volume vs. Displaced Volume Factor	NA
Hole Area (mm <sup>2</sup> )	880.5
Base Area (mm <sup>2</sup> )	78.54

**Table 4-10. Welds TW-19 to TW-21 Parameter Variables**

Weld No:	Hole Depth (mm)	Stud Taper Angle (°)	Hole Taper Angle (°)	Hole Base Diameter (mm)	Stud Base Diameter (mm)	Plunge Depth (mm)	Axial Force (kN)	Stud Material Displaced During Plunge (mm <sup>2</sup> )	Preheat Temperature (°C) (Oven Temperature)	Preheat Temperature (°C)
TW-19	14	59	60	6	6	3	30	N/A	22	22
TW-20	14	59	60	6	6	4	30	N/A	250	170-180
TW-21	14	59	60	6	6	6	30	N/A	250	170

Welds TW-19 to TW-21 were sectioned, polished and etched in modified Poulson's reagent as shown in Figure 4-19, then reworked and re-etched in sodium hydroxide as shown in Figure 4-20 to identify the HAZ and final shear interface.

Figure 4-19 and Figure 4-20 show preheat to lower the final shear interface between welds TW-19 and TW-20, reducing the height of the dynamically recrystallized column of material in the hole. Weld TW-21 has the same final shear interface height as TW-20, showing preheat to be the parameter controlling this height, not plunge depth. The increased plunge can be recognized by the excessive outwards flow of the stud above the plate as it collapsed due to thermal saturation in welds TW-20 and TW-21. Preheat appears to change the way the primary flash forms and flows out of the weld during FTSW. As seen in Figure 4-19 no preheat gives the typical curling flash as commonly seen in FTSW in steel [10] [38] [47]. Welds with preheat appear to flow horizontally outwards, not curl upwards. Previously the upwards curling was thought to be beneficial; however this does not appear to be the case for aluminium AA6082-T6. With preheat the energy input in the top region of the hole appears to saturate the block. This prevents heat conducting away from the welding interface into the plate, increasing the temperature at the interface (this will be investigated with thermocouples at a later stage). This will cause a greater thermal gradient between the welding interface and stud body; hence the material flowing out as flash possesses less strength due to retained heat. This, combined with the greater depth of the final shear interface appears to prevent the curling of the primary flash, and may be useful in predicting weld quality. Additionally the body of the stud above the plate swells under the applied axial force during the last stage of the weld, as seen in Figure 4-19 for weld TW-21. This makes it impossible to accurately use small plunge depths, for as the body of the stud swells, the stud shortens. This indicates to the control system that the plunge depth has been achieved, prematurely stopping rotation. A method of retaining this outwards expansion is, therefore, essential for future welds, further highlighted by Mahoney et al [20], who used a consumable heat sink to prevent this on smaller welds, but with limited success.

The larger stud used in weld TW-21 showed clear improved sidewall bonding, though the excessive welding time caused grain growth between shear layers in the lower region of the weld and the stud plate interface at the bottom of the hole, shown at inset of weld TW-21 in Figure 4-19. This is similar to the abnormal grain growth (AGG) found by Charit and Mishra [40] and Sato [41] in friction stir welds with post weld heat treatment.

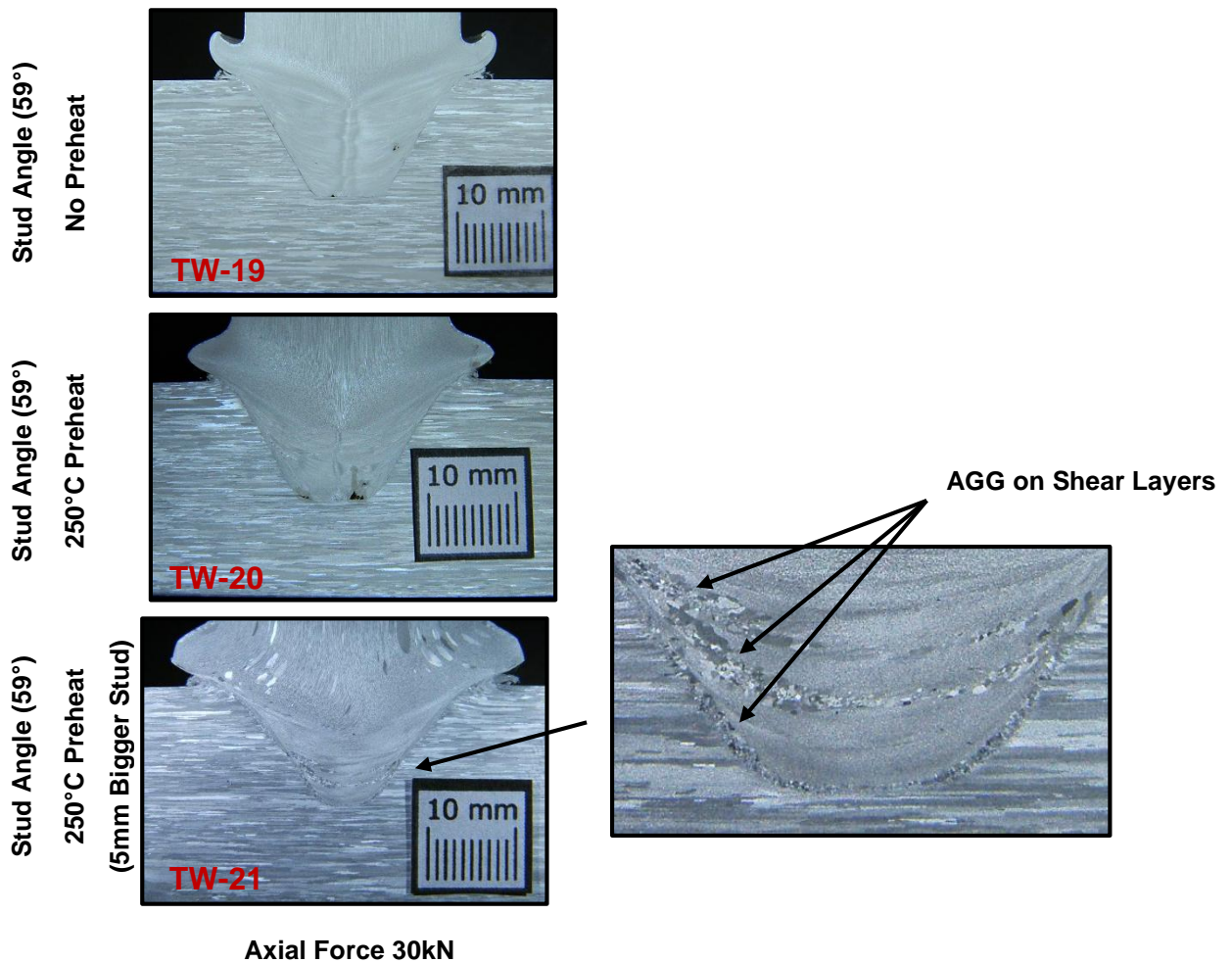
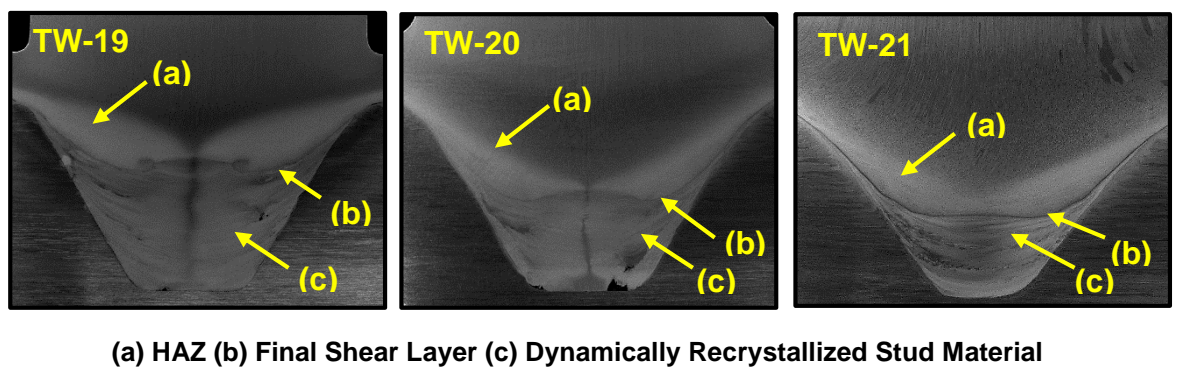


Figure 4-19. Welds TW-19 to TW-21 Macrographs



(a) HAZ (b) Final Shear Layer (c) Dynamically Recrystallized Stud Material

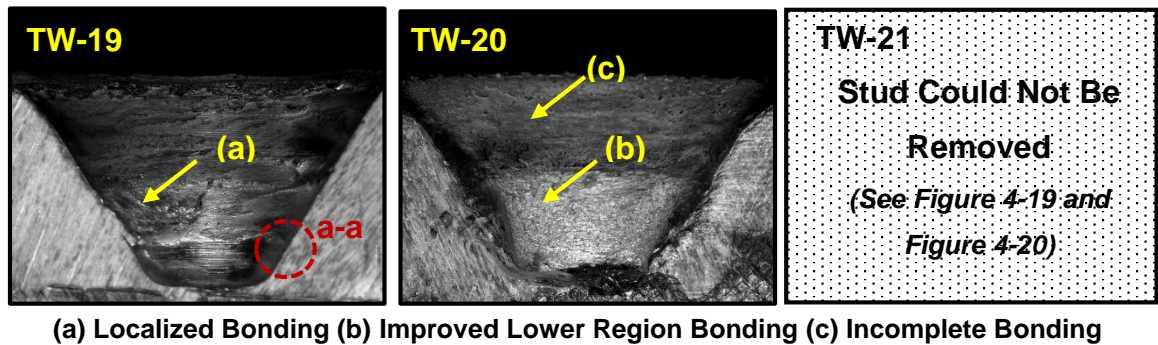
Figure 4-20. Welds TW-19 to 21 (Etched in Sodium Hydroxide)



The formation of a Zone 1 and Zone 2 as discussed in Section 4.2 on page 68 is indistinguishable. As the two zones were formed due to the rapid collapse of the stud, combined with material flowing between the rotating stud body and hole, when a geometry with no base diameter clearance was used with sufficient axial force and hole/stud taper angle to support the axial load, the stud did not collapse in the hole.

Figure 4-21 shows the hole after the stud was broken out of the sectioned weld by applying a lateral shock load to the stud for welds TW-19 and TW-20. Weld TW-21 could not be removed, indicating improved bonding. Weld TW-19 clearly shows locally bonded regions between the machining marks on the sidewall of the hole as highlighted in Figure 4-22, with the least bonding falling within the lower quarter of the weld. As zone 1 is defined as the level at which bonding of the sidewalls initiates, as previously shown in Figure 4-1, Figure 4-2 and Figure 4-3 on page 72, there is little to no Zone 1 formed in these welds. The bonding in the lower region of weld TW-19 may be localised with machining marks between them, but it is present regardless. This shows the stud did not collapse prematurely, but also could not rub and plasticize the plate sufficiently to bond fully. When the plate was preheated for weld TW-20, the bonding in the lower region of the block improved significantly as shown in Figure 4-21, with considerably more effort required to remove the weld nugget.

A line of improved bonding is visible in the lower half of the weld, with no machining marks visible in the upper region. A larger plunge depth could not be used to increase the bonding in the upper region due to collapse of the stud material above the plate due to thermal saturation. This led to the selection of a larger stud, in order to maintain rotation. Weld TW-21 used the same weld setup as weld TW-20, with a 5mm larger stud shank diameter. This allowed a plunge depth of 6mm to be achieved at the point of stud collapse, improving bonding in the upper region.



(a) Localized Bonding (b) Improved Lower Region Bonding (c) Incomplete Bonding

Figure 4-21. Welds TW-19 to TW-21 Hole Bonding Macrographs

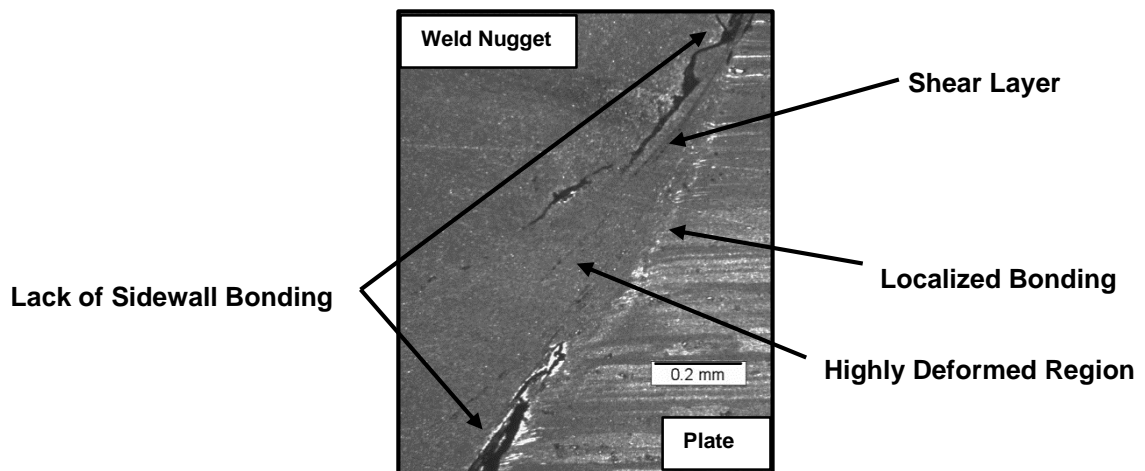


Figure 4-22. Localized Bond on Sidewall Interface (Located at a-a in Figure 4-21– Weld TW-19)

#### 4.6.1. Process Torque for Welds TW-19 to TW-21

The process torque curves for welds TW-19 to TW-21 are given in Figure 4-23, with the high plunge depths applied to these welds clearly shown to extend cycle times. The most significant characteristic of this group of welds is that no violent shears were recorded during the equalised torque stage, showing the stud material is able to sustain the process torque. Shearing is instead found distributed around the PSTP for preheated welds, and is more substantial and occurs over a narrower band (compacted shearing) for weld TW-21 as highlighted in inset of Figure 4-23. The close packing of the shears as seen in Figure 4-23 for weld TW-21 vs. those found in weld TW-20, show that the band of softened material directly above the weld interface narrows with the increased stud shank diameter. The occurrence of the shears themselves in weld TW-20 and TW-21 indicate points in the process where the welding interface could not be maintained, shearing and reforming. The crystallographic structure of the shear

interfaces in these regions is, therefore, highly deformed (anisotropic), with the closer pack shears indicating further plastic deformation. Weld TW-21 shows two distinct process torque shears that can be correlated with the bands of AGG seen in Figure 4-19 highlighting the location of the shear planes.

Weld TW-20 had voids at the base of the hole, as seen in Figure 4-19. This is a characteristic of a preheated weld with the inability of the stud to maintain rotation at the initial interface, as shear occurs prematurely without sufficient plasticization. Similar voids were seen in weld TW-11, which were removed with increased preheat, whereas the voids in weld TW-20 were removed by the larger stud shank. Weld TW-20 and TW-21 experienced 12Nm to 14Nm of torque respectively at 0.1 seconds, whereas TW-19 only experienced 1.5Nm. The stud for weld TW-20, therefore, sheared a larger section before the welding interface propagated upwards, creating the void due to lack of plasticization of material and axial force. The trend is indicative of preheat increasing the process torque at 0.1 seconds as given in Appendix F.

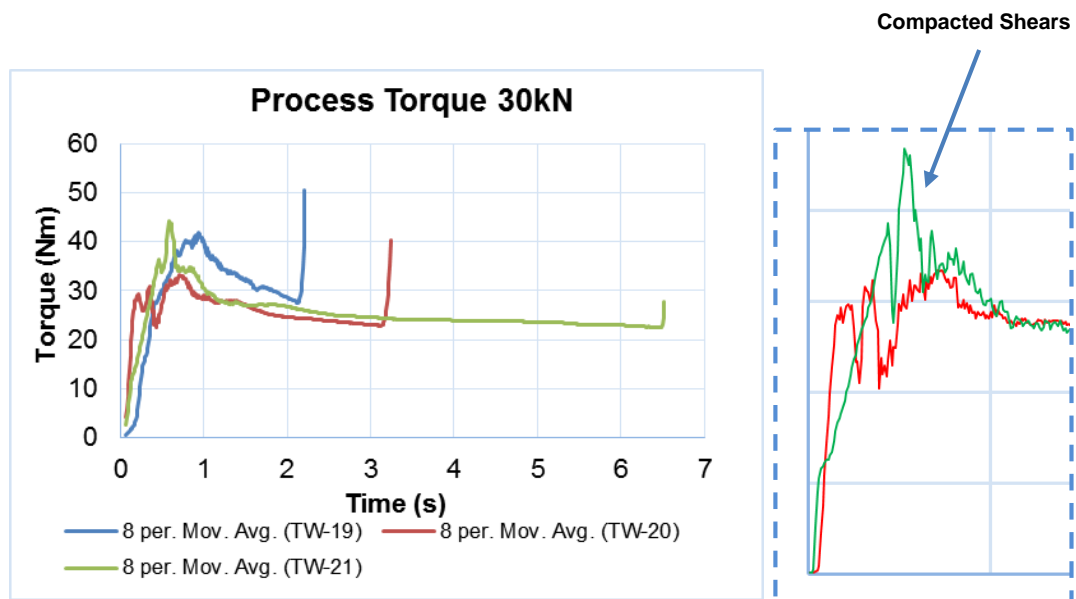


Figure 4-23. Process Torque Curves for Welds TW-19 to TW-21

#### 4.6.2. Energy Input of Welds TW-19 to TW-21

Energy input was specifically evaluated to identify the effect of preheat and the increase in stud diameter, given in Table 4-11 and Appendix G. Energy input in the first 0.1 seconds of welding increased with preheat, and increased further with the larger stud. This further increase was initially thought to be incorrect, as the tapered section of the stud had not geometrically changed; only the shank was

larger with the intent to maintain rotation in the later stages of the weld. However, the data indicates that the energy input increased with the axial force applied being similar for both preheated welds; therefore, the only explanation is the effect of the larger stud. If weld TW-20 in Figure 4-19 is examined, a void is visible at the base of the weld that is removed in weld TW-21. The applied axial force is the same for both welds; however,  $1.9\text{J}/\text{mm}^2$  or 48% more energy was put into the weld by this time, indicating that the build-up of localised bonds across the welding interface had rapidly increased. This is due to the stud material maintaining integrity while rubbing, allowing additional plasticization. In previous welds it was found that if the stud consumed too rapidly, the interface would deposit material above purely localised bonds formed at the interface, creating voids. The increased diameter of the stud, therefore, reduced the width of the band of softened material behind the welding interface, increasing the thermal gradient. This maintains the shear stress of the material directly behind the welding interface, maintaining stud rotation. This is verified by the closely packed shears in weld TW-21, as the softened band narrows, the recovery from shear will be faster, bringing the shears closer together. It is clear from this, that maintaining stud integrity and hence plasticising the interface material sufficiently, is a key requirement for the process.

The energy input to seizure reduces with increased preheat and further reduced with the larger stud as given in Table 4-11. This follows the trend of welds TW-8 to TW-12, that show the same reduction of input energy to seizure with increased preheat, with TW-12 and TW-21 both reaching  $3.4\text{J}/\text{mm}^2$ , the larger stud body appears to compensate for the reduced preheat.

Energy input at 1 second remained constant which followed trends previously noted that the energy in the first 1 second is governed by the axial force and axial force ramp up rate. Energy to PSTP reduced with preheat, and further reduced with the larger stud. The time to the PSTP reduced from 0.87 seconds to 0.71 seconds with preheat and further to 0.54 seconds with increased stud size, further verifying the increased thermal gradient due to the larger stud body.

The total energy input, though not applicable to the geometry in this section due to increasing plunge depth, increased from 36kJ to 43kJ for weld TW-19 and TW-

20 and then doubled to 89.7kJ for weld TW-21. The additional 46.7kJ of energy was input into the weld by rubbing at the top of the hole, as the hole was already filled by 4mm plunge, verified by the final shear interfaces of weld TW-20 and TW-21 ending at the same height in the weld, as shown in Figure 4-20. The additional heat conducted to the highly deformed shear layers in the lower region of the weld, initiating AGG. The formation of AGG in weld TW-21 highlights that the temperature at the bottom of the weld did not reach the same temperature as the final shear interface, as heat was conducted away too quickly, locking the material at the shear interfaces in an unstable plasticized state [41].

**Table 4-11. Results for Welds TW-19 to TW-21**

Weld No:	Welding Time (s)	Time to Seizure (s)	Energy Input at 0.1s (J/mm <sup>2</sup> )	Energy Input at Seizure (J/mm <sup>2</sup> )	Energy Input at 1s (J/mm <sup>2</sup> )(W/mm <sup>2</sup> )	Energy Input to PSTP (J/mm <sup>2</sup> )	Total Energy Input (J/mm <sup>2</sup> )	Energy Input Rate at 0.1s (W/mm <sup>2</sup> )	Energy Input Rate at Seizure (W/mm <sup>2</sup> )	Energy Input Rate at PSTP (W/mm <sup>2</sup> )	Total Energy Input Rate (W/mm <sup>2</sup> )	Axial Force at Plunge Depth (kN)
TW-19	2.28	0.23	1.0	9.0	17.1	13.9	N/A	10.1	39.2	16.0	N/A	22.0
TW-20	3.24	0.11	4.0	5.3	16.4	9.1	N/A	39.7	48.5	12.7	N/A	24.2
TW-21	6.51	0.06	5.9	3.4	18.1	8.4	N/A	59.1	56.0	15.6	N/A	25.5

#### 4.6.3. Energy Input Rate for Welds TW-19 to TW-21

The energy input rate as 0.1 seconds increased from 10.1J/mm<sup>2</sup>, to 39.7J/mm<sup>2</sup> with preheat and further to 59.1J/mm<sup>2</sup> as the stud shank diameter increased. This same trend is found with the energy input rate to seizure, just at a lower gradient. The larger stud allows a higher energy input rate to be maintained without losing integrity (Maintaining Shear Stress) of the material at or behind the interface. The heat is instead conducting axially up the stud and dissipated into the larger volume of material. Though the time to PSTP was found to reduce along with input energy to PSTP, the rate of energy input did not change significantly. It appears that a fixed rate of energy input is applied as the hole is filled and is not significantly affected by preheat as previously noted, with an overall average of 10.55J/mm<sup>2</sup> for all welds done to this point in the research.

#### 4.6.4. Summary of Welds TW-19 to TW-21

This section reinforces the need to maintain stud integrity during welding in order to sufficiently plasticize the material at the interface, by maintaining rotation for the longest time possible without stud collapse occurring. The 60° tapered holes gave improved side wall bonding throughout, with or without preheat, showing the effect of increased axial forces, and the ability to resist shear.

Preheat itself was found to change the way in which the primary flash forms during welding, with preheated welds flowing horizontally outwards, not curling upwards. The curling of the primary flash, previously thought to be an indicator of good process parameters is shown to not apply to AA6082 FTSW. Violent shear, previously shown as an indicator of improved sidewall bonding did not occur during these welds, but was replaced by shearing distributed around the PSTP. These shears served as highly deformed initiation sites for AGG when additional total energy input was applied, indicating the lower region of the hole was cooler than the interface higher up in the weld due to thermal saturation of the plate.

The size of the stud shank was found to directly increase the energy input during the first stages of the weld, and maintain a higher energy input rate. This increase correlated with improved weld quality.

#### 4.7. Investigation of a 90° Tapered Hole

To complete the investigation of the effect of increasing the hole taper angle, a 90° hole configuration was tested. Due to material stock size and welding platform limitations a 25mm stud shank diameter was maintained as given in geometry Appendix A. The depth of the hole was limited to 8.5mm to prevent the exit diameter of the hole becoming too large, increasing the process torque beyond the limits of the welding platform. Rotational speed was maintained at 5200RPM and a 1° difference in stud and hole taper angle was tested with like stud and hole base diameters, as given in Table 4-12 and Table 4-13. As the exit diameter of the hole was similar to previous welds, a 30kN axial force was retained with the same preheat procedure as weld TW-21 maintained. As with welds TW-19 to TW-21 the plunge depth is increased to 3mm in an attempt to

compensate for swelling of the stud body during welding, when approximately 0.2mm was needed to fill the hole.

**Table 4-12. Weld TW-22 Parameter Constants**

Rotational speed (RPM)	5200
Cooling Time (s)	20
Clearance Volume vs. Displaced Volume Factor	N/A
Hole Area (mm <sup>2</sup> )	654
Base Area (mm <sup>2</sup> )	65.2

**Table 4-13. Weld TW-22 Parameter Variables**

Weld No:	Hole Depth (mm)	Stud Taper Angle (°)	Hole Taper Angle (°)	Hole Base Diameter (mm)	Stud Base Diameter (mm)	Plunge Depth (mm)	Axial Force (kN)	Stud Material Displaced During Plunge (mm <sup>2</sup> )	Preheat Temperature (°C) (Oven Temperature)	Preheat Temperature (°C)
TW-22	8.5	89	90	6	6	3	30	N/A	250	106

As shown in Figure 4-24, visually good sidewall and base bonding was achieved, with a predominantly flat final shear interface near the top of the hole. When the attempt was made to remove the stud from the sectioned hole, failure occurred between the stud and final shear interface, leaving the weld nugget intact. As the final shear interface is a region of high plastic deformation due to the stopping, and hence terminal torque applied at the end of the weld, and that the relatively flat final shear interface reduced the area of the final shear interface, failure was highly likely to propagate through this region. The initiation site for failure was located at the stress concentration points between the primary and secondary flash, shown in inset of Figure 4-24.

The process torque for the 90° hole followed the same trend as seen in 60° tapered hole welds, achieving no violent shears in the equalized region of the process torque curve. Shears are instead distributed around the PSTP region, seen in Figure 4-25. This is a good indicator that the nose of the stud shears due to the steep change in stud angle and small clearance between the hole and stud.

The welds tested up to this point have shown shearing in the PSTP region in welds with less than 5° difference in hole and stud angle.

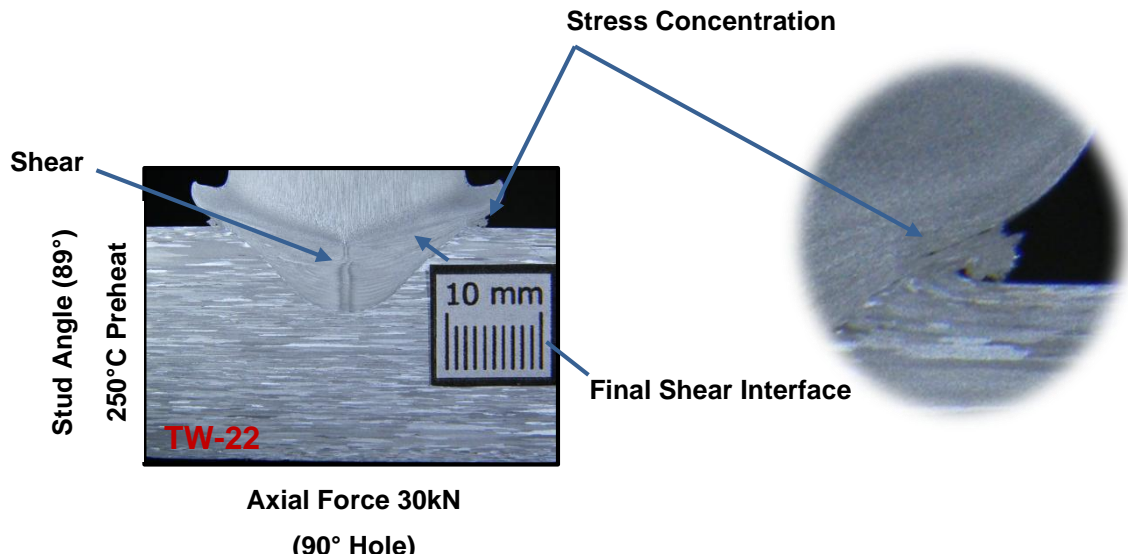


Figure 4-24. Weld TW-22 Macrograph

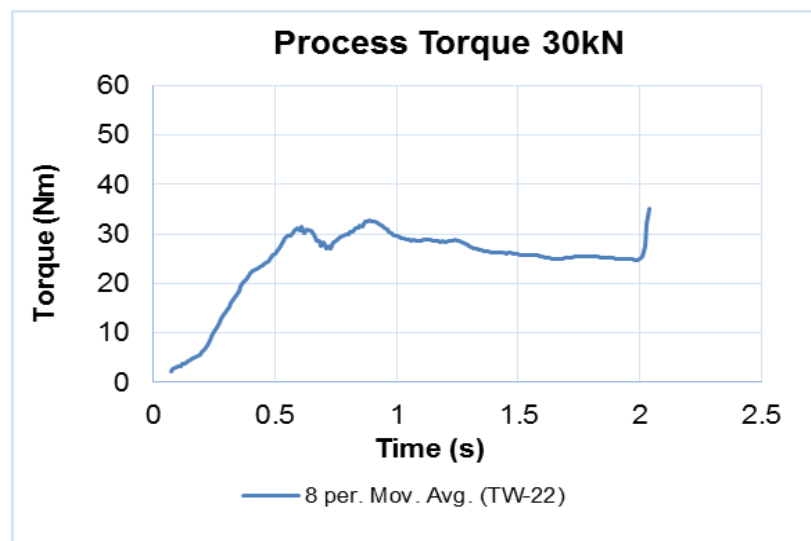


Figure 4-25. Process Torque Chart for Weld TW-22

The energy input at 0.1 seconds, seizure, PSTM and total energy input are comparative to all previous welds, with the increase in taper angle to 90° only giving a substantial change in energy input at 1 second into the weld, achieving 18.5J/mm<sup>2</sup>, the highest at this stage in the research, given in Table 4-15. The energy input at 1 second is mainly increased by larger hole taper angles, and a small difference is hole and stud taper angles. It is not clear if this is beneficial, and will be further investigated.



The 90° tapered hole configuration showed promise in this development weld; however, the 90° hole geometry was not perused further. This was based on the size of the exit hole needed to achieve acceptable hole depths and the consideration that the final shear interface was near the top of the hole for this weld, indicating that the success of a significantly larger stud was unlikely.

**Table 4-14. Results for Welds TW-22**

Weld No:	Welding Time (s)	Time to Seizure (s)	Energy Input at 0.1s (J/mm <sup>2</sup> )	Energy Input at Seizure (J/mm <sup>2</sup> )	Energy Input at 1s (J/mm <sup>2</sup> )(W/mm <sup>2</sup> )	Energy Input to PSTP (J/mm <sup>2</sup> )	Total Energy Input (J/mm <sup>2</sup> )	Energy Input Rate at 0.1s (W/mm <sup>2</sup> )	Energy Input Rate at Seizure (W/mm <sup>2</sup> )	Energy Input Rate at PSTP (W/mm <sup>2</sup> )	Total Energy Input Rate (W/mm <sup>2</sup> )	Axial Force at Plunge Depth (kN)
TW-22	2.04	0.11	2.6	3.0	26.9	14.6	41.14	20.2	9.9	17.2	25.7	21.2

As the research is aimed at repairs approximately 20mm deep, if such a large taper angle were implemented, a 51mm diameter stud would be required. Such a large diameter would overcome the torque capacity of the FTSW platform and further require an applied axial force unachievable with accessible equipment, limiting the application. Based on this, it was decided to use a 60° hole taper angle as the standard taper angle for the FTSW of aluminium, with geometry changes made only to stud taper angles.

#### **4.8. The Use of a Non Consumable Heat Sink and Increased Axial Force Ramp up Rate**

The results of welds TW-1 to TW-22 show the axial force ramp up rate of the FTSW platforms to be unsuitable for the FTSW of aluminium, due to high material consumption rates reducing the axial force. As this is shown to be critical throughout the FTSW process, the axial force ramp up rate, and hence feed rate of the FTSW platform, was increased to better suit the process. The proportional

valve and hydraulic pump were swapped out to give a higher, more repeatable tool feed rate, and hence force ramp up rate. The change in ramp rate is compared in Figure 4-26, with Valve 1 and Valve 2 representing the old and new configuration respectively. The results show the ramp up rate to 12kN for all welds regardless of geometry that achieved 12kN or higher axial force during welding. As the consumption rate of the stud material affects the axial force ramp rate with the existing servo hydraulic control system, all welds were included to express a representative axial force ramp up rate. The average force ramp up rate increased from 8kN/s to 28.2kN/s at 12kN axial force with the standard deviation ranging between 2.7 and 2.8kN/s. For further reference, the axial force curves for all welds are given in Appendix E with axial force and axial force ramp rates at specific points during welding given in Appendix F.

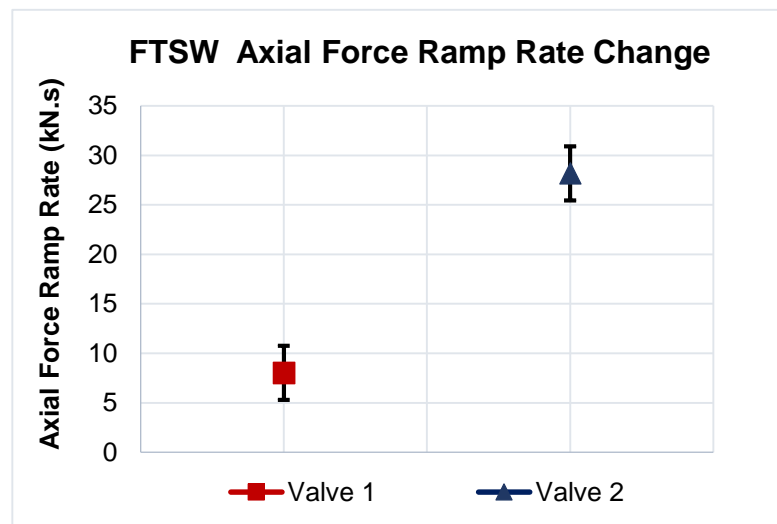


Figure 4-26. Axial Force Ramp up Rate with Changes in Valve Setup

The geometry and process parameter combinations investigated to this point highlight a major issue facing the successful FTSW of AA6082-T6, maintaining rotation of the stud during plunge due to aluminium's high thermal diffusivity and low strength retention at elevated temperature. This reduced rubbing on the sidewalls and prematurely stopped the weld due to stud swelling. To prevent this, a removable AA6082-T6 heat sink was fitted to the shank of the stud as shown in Figure 4-27. This would conduct heat energy away from the stud nose and shank area, maintaining the material integrity and preventing the stud from swelling (premature collapse). The heat sink is a snug fit on to the shank of the stud, held in position 3mm above the tapered section of the stud with a single

grub screw, with the geometry given in Appendix A. To ensure good heat transfer, thermal paste (Austerlitz WPN 10 Electronic Thermal Compound) was placed between the heat sink and the stud to ensure maximum and consistent thermal contact.

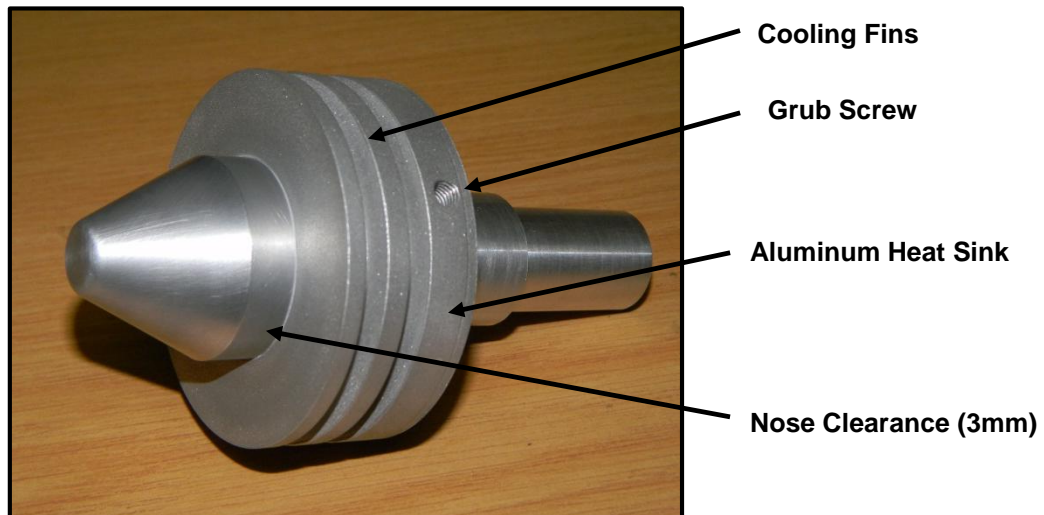


Figure 4-27. Non Consumable, Removable Aluminium Heat Sink

Two welds were designed to test the increased axial force ramp up rate of the platform, and the influence of the removable heat sink. The hole depth was increased to 18mm to adapt the geometry in stages to the target depth of 20mm, with the geometry given in Appendix A. As process torque is related to the area in shear, the increased hole depth to 18mm (4mm deeper) gave a larger hole exit diameter and hence shear area. This caused the process torque to increase such that the FTSW platform was unable to maintain a constant rotational speed. As this would skew the energy calculation and repeatability of the welds, the rotational speed was reduced to 5000RPM from 5200RPM, bringing the servo motor speed closer to its performance peak. The base diameter of the hole and stud was increased to 9mm from 6mm, as a step towards the ideal 10mm base diameter, restricted by unobtainable process torques with the 10mm base diameter welds spiking to 95Nm, stalling the welding platform.

To prevent the stud ramming into the plate due to the high plunge rate setup, the axial force was staged into a low and high axial force procedure. The low force was set for 12kN with a plunge depth of 0.5mm and the high force was set to 20kN with a 1.5mm plunge depth. This was 0.4mm higher than the calculated

plunge needed to fill the hole to an 18 times clearance volume vs. displaced volume factor; however, as the first 0.5mm would take place at a relatively low force, the material was thought to be highly plasticized at the nose of the stud and would flow out of the weld easily with the sudden change in force. The total plunge was therefore increased to 2mm, with the 12kN stage acting to soften the initial contact and reduce the PSTP to a maintainable limit, as at high axial forces such as 30kN the rapid climb in axial force would push flash out from the welding interface that was insufficiently heated. This caused mechanical lockup as the flash would rapidly dissipate heat into the relatively cold block and stud, solidifying and entangling between the hole walls and rotating stud. These staged welds prevented mechanical lockup during welding for the development investigations into the use of a heat sink and increased axial force ramp up rate.

No preheat was used in these welds in order to remove a variable from the analysis and to investigate if the heat sink could overcome the need for preheat. The taper angle of the stud was reduced to 55° to reduce process torque by increasing the clearance for the flash to move in, preventing mechanical lockup as identified in welds TW-2, TW- 4 and TW-7. The increased taper angle also require more plunge to fill the hole, displacing more material. As temperature at the interface of a friction weld is related to the strength of the weld, temperature data is a key aspect to the understanding of the process and the effects of parameter and boundary conditions [7] [11] [20]. To investigate this, the near interface temperature was measured at depths of 2mm, 9mm and 17.5mm, with a wall clearance of 2mm between the end of the thermocouple and the sidewall of the hole, as given in Appendix A. The process constants and variables are given in Table 4-15 and Table 4-16 respectively.

**Table 4-15. Weld TW-23 to TW-24 Parameter Constants**

Rotational speed (RPM)	5000
Cooling Time (s)	20
Clearance Volume vs. Displaced Volume Factor	Approximately 18
Hole Area (mm <sup>2</sup> )	1509.3
Base Area (mm <sup>2</sup> )	135.4

Table 4-16. Weld TW-23 to TW-24 Parameter Variables

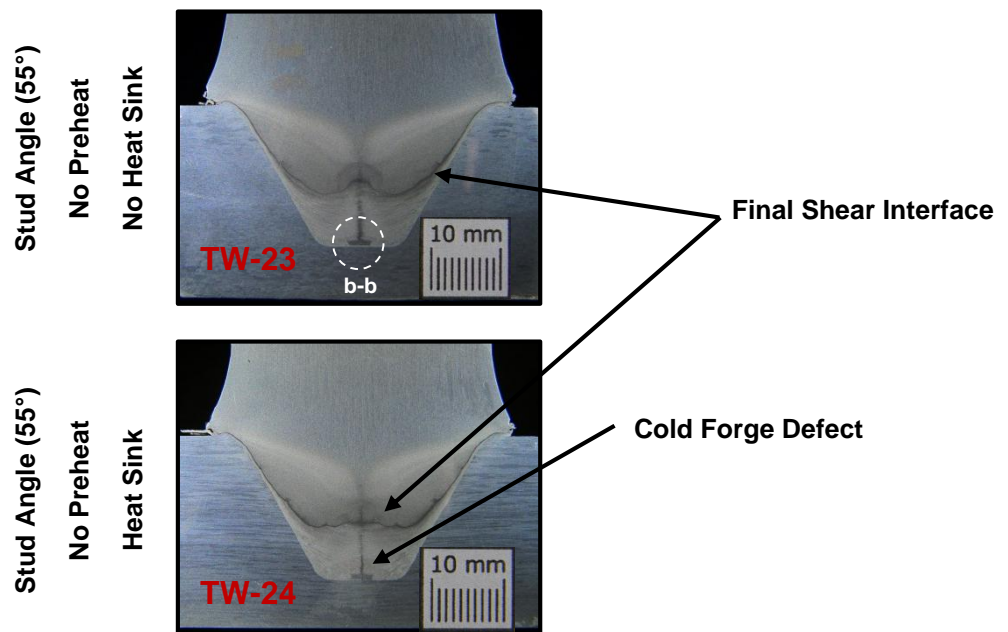
Weld No:	Hole Depth (mm)	Stud Taper Angle (°)	Hole Taper Angle (°)	Hole Base Diameter (mm)	Stud Base Diameter (mm)	Plunge Depth (mm)	Axial Force (kN)	Stud Material Displaced During Plunge (mm <sup>2</sup> )
TW-23	18	55	60	9	9	0.5-1.5	12-20-30	890
TW-24	18	55	60	9	9	0.5-1.5	12-20-30	890

The macrographs for the sectioned welds are given in Figure 4-28. The most significant visual change between welds is the profile of the final shear interface. Weld TW-23 has a curved profile with an elevated central region, whereas weld TW-24 has a relatively flat final shear interface, highlighted in Figure 4-28. This profile was noted by Mitelea et al. [26], who based it on increases in axial force after rotation had stopped. This shows how the heat sink extracts heat from the outer region of the weld, maintaining stud integrity and preventing the distortion of the profile during forging. This flattening of the final shear interface was seen in welds TW-20 and TW-21 where TW-21 had a larger stud shank, acting as a heat sink.

Both welds show no voids on the sidewalls and fillet of the weld, though weld TW-24 showed more plate deformation, and therefore superior intermingling of the base material in the upper half of the weld. A cold forge defect was found at the base of both welds, approximately 3mm wide, near the central region where angular velocity strives towards zero, shown in Figure 4-29. The void consisted of layers of plastically deformed material, compacted on top of one another. Undeformed stud material (UDSM) is visible directly above the defect, with the original draw lines of the stud material still visible, serving as an indicator of how cold this region was during formation.

Both welds show a final shear interface that is relatively low in the hole, approximately mid depth. As preheat reduces the height of the final shear interface as seen in welds TW-8 to TW-12 and TW-19 to TW-21, the increased axial force ramp up rate has a similar effect, increasing sidewall rubbing and plasticization.

The use of the heat sink increased the welding cycle time from 15.1 seconds to 23.06 seconds, effectively maintaining stud integrity 53% longer, further rubbing and plasticization of the sidewalls of the hole.



Axial Force Stages of 12/ 20 and 30kN

Figure 4-28. Welds TW-23 and 24 Macrographs

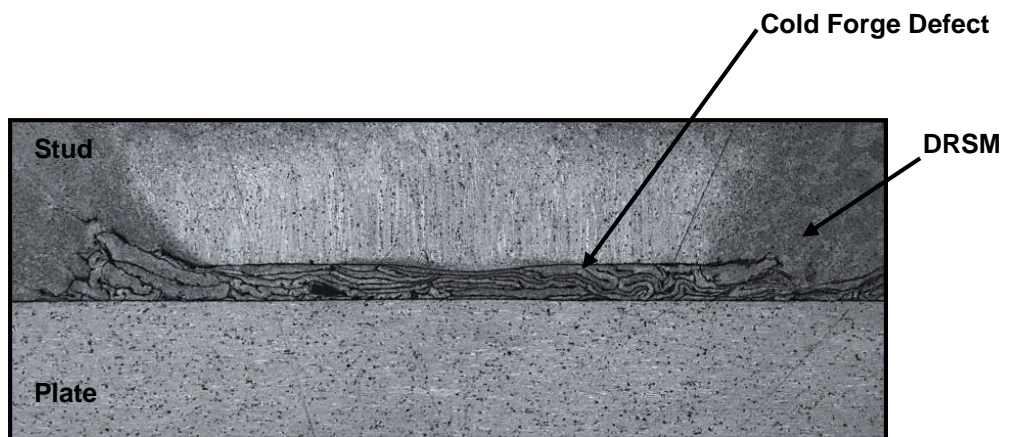


Figure 4-29. Cold Forge Defect found in Weld TW-22 (similar to weld TW-23) (Located at b-b in Figure 4-28)

#### 4.8.1. Process Torque and Near Interface Temperature for Welds TW-23 and TW-24

The heat sink did not influence the time to seizure, with welds TW-23 and TW-24 having seizure times of 0.15 seconds and 0.12 seconds respectively. The times were consistent with preheated welds such as TW-11 and TW-20, showing the increased axial force ramp up rate to reduce the time to seizure, similar to the effect of preheat. The process torque recorded at seizure for weld TW-23 and TW-25 was 34.1Nm and 37.4Nm respectively, not a significant difference but still indicating a higher torque and, therefore, higher heat conduction away from the welding interface.

The PSTP increased from 48.72Nm to 59.6Nm, with no change in time to PSTP, as given in Table 4-21 and Appendix F. This shows the stud to be cooler at the interface, with the heat energy conducting into the heat sink. This is verified in Table 4-17 showing the interface temperature at the bottom of the hole to reduce from 47.9°C to 25.6°C at seizure, and from 116.5°C to 74.9°C at the PSTP with the use of a heat sink. No violent shears or shears in the PSTP region occurred as seen in Figure 4-30. Instead, welds consisted of fine continuous shears occurring throughout the weld, indicating the rate that fresh cool material is brought forward to the welding interface vs. the shearing torque at the welding interface, balanced. This is indicative that the band of softened material behind the weld interface narrows with increased axial force ramp up rate, as expected.

**Table 4-17. Near Interface Temperature at Seizure and PSTP**

	TW-23 (No Heat Sink)		Energy Input (J)	TW-23 (Heat Sink)		Energy Input (J)
	Time (s)	Temperature (°C)		Time (s)	Temperature (°C)	
<b>Seizure (Approximate)</b>						
Top Thermocouple	0.2	<b>24.0</b>	2062.7	0.2	<b>23.8</b>	1445.5
Middle Thermocouple	0.2	29.8		0.2	23.9	
Bottom Thermocouple	0.2	47.9		0.2	25.6	
<b>PSTP (Approximate)</b>						
Top Thermocouple	1.3	57.4	26536.3	1.4	29.7	31598.1
Middle Thermocouple	1.3	92.1		1.4	56.0	
Bottom Thermocouple	1.3	116.5		1.4	74.9	

The torque curves shown in Figure 4-30 smooth out as the 20kN axial force stage begins. This shows that the increase in axial force and axial feed rate brings material forward fast enough to maintain the weld interface in a state of shear without the material behind the stud interface shearing due to softening. The heat sink did not significantly influence the time taken to consume the first 0.5mm of the stud, remaining consistent at 11.35 seconds and 11.11 seconds for welds TW-23 and TW-24 respectively. However, the time taken to complete the weld once the second axial force stage was applied, increased from 15.1 seconds to 23.6 seconds as shown in Figure 4-30.

As temperature is a critical parameter in solid state welding, specifically with regards to atomic diffusion, the near interface temperature is analysed with respect to axial force ramp up rate and the use of a heat sink to maintain stud integrity [1] [7]. Edar et al. recorded up to 400°C at the central interface of a RFW of Aluminium 1050 to AISI 304. Pinheiro [10], recorded up to 427°C at the top thermocouple of magnesium FTSW, while noting a decrease in temperature to 361°C for the thermocouple 11mm lower in the weld. It is, therefore, expected that temperatures in the region of 400°C will be recorded near the interface if welds with good sidewall bonding are achieved, with lower temperatures in the lower region of the weld.

The process temperature curves are plotted in Figure 4-30 for welds TW-23 and TW-24. The curves follow one on from the other, starting at room temperature with the bottom thermocouple heating first, followed by the middle and finally the top thermocouple as the heat and welding interface travels up the hole. The data shows that both welds experience lower interface temperatures during the initial stage of welding. This low temperature is caused by the thermal gradient between the welding interface and the block, as the block is cold at the start of the weld and conducts heat energy generated at the interface away rapidly. As the process continues, the block temperature increases, reducing the thermal gradient. In this way, the top region of the hole has the lowest thermal gradient, which is further restricted by the air boundary at the top of the plate. As the welding interface moves past a thermocouple point, the climb in temperature at



that level begins to drop and is overtaken by the thermocouple further up the hole, indicated as crossover points in insets of Figure 4-30 and given in Table 4-18.

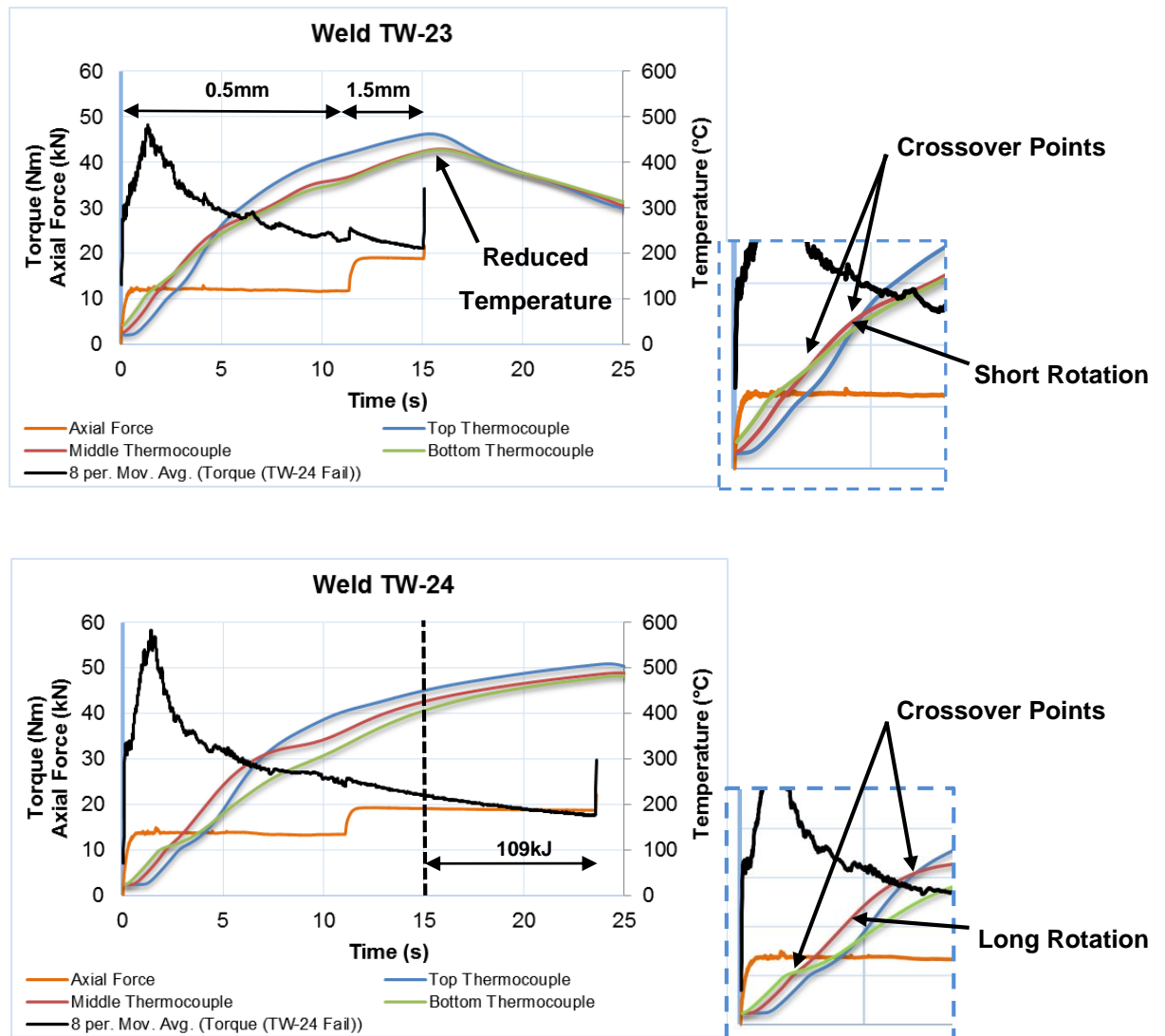


Figure 4-30. Process Torque, Axial Force and Temperature Curves for Welds TW-23 and TW-24

Table 4-18. Near Interface Temperature Crossover Points for Welds TW-23 and TW-24

	Weld TW-23		Weld TW-24	
	Time (s)	Temperature (°C)	Time (s)	Temperature (°C)
Middle Crosses Bottom Thermocouple	2.7	161	2.3	108
Top Crosses Middle Thermocouple	4.7	249	7.1	311

The results show the heat sink to reduce the temperature of the crossover point at the bottom of the hole. Therefore the heat energy is conducted away from the interface at a higher rate than with the heat sink, correlating with increased

recorded process torques. Table 4-18 shows the welding interface to have propagated past the bottom thermocouple when the plate interface temperature is 88°C and 203°C colder than the temperatures experienced at the midpoint of the weld, for TW-23 and 24 respectively. Therefore, with a heat sink, the lower regions of the weld is more plastically deformed as indicated by the increased process torque, and was formed at lower temperatures as shown in Table 4-17 likely to cause high residual stress zones between the hole and the DRSM.

The use of the heat sink increased the crossover temperature between the top and middle thermocouple, and more importantly increases the time to crossover from 4.7 seconds to 7.1 seconds. The heat sink, therefore, increased the near interface temperature at the middle and bottom of the hole by the end of the weld, as the block was more thermally saturated, reducing the thermal gradient and cooling rate. This shows that the heat sink assisted the stud material to maintain rotation and increase plasticization of the stud and plate material in the central region of the weld by 51%. Therefore, although the heat sink removes heat energy from the interface, rotation is maintained sufficiently long for a higher temperature to be reached in the mid region of the weld. This assists in overcoming the lack of sidewall rubbing and plasticization in the mid region of the weld as seen in Figure 4-2 on page 72.

The maximum near interface temperatures and time of occurrence are given in Table 4-19 for welds TW-23 and TW-24. The data shows that the maximum temperatures reached at the bottom of the hole are lower than that reached at the top for both welds, as expected due to conduction through the plate and the relative distance from the final shear interface [7] [10] [11]. The increased energy input and hence thermal saturation of the block with the use of a heat sink is clearly shown in Figure 4-30 for weld TW-24, by the equalization of the temperature curves and their parallel profiles past 15 seconds welding time. The temperature curves do not join together for weld TW-23, as the interface had propagated past the mid region so rapidly that the surrounding material remained cool, as discussed above. Therefore, the lower regions of the weld will experience a significantly higher temperature at the end of the weld than experienced during formation of the shear layers.

**Table 4-19. Maximum Near Interface Temperatures for Welds TW-23 and TW-24**

	TW-23		TW-24		$\Delta$ Time (s)	$\Delta$ °C
	Time (s)	Temperature (°C)	Time (s)	Temperature (°C)		
Top Thermocouple	15.4	464.7	24.2	510.0	8.8	45.2
Middle Thermocouple	15.9	430.5	24.6	490.1	8.7	59.6
Bottom Thermocouple	15.9	428.8	24.8	483.0	8.9	54.2

The cooling rates once rotation had stopped are given in Table 4-20 at the three thermocouple interfaces. The data shows that the use of a heat sink reduced the overall cooling rate of the block, more significantly in the top and mid region. The cooling rates at the bottom, middle and top of the hole, therefore, reduce and remain constant, independent of depth. Not only does the heat sink increase the maximum temperatures experienced at the interface, but also the time temperature is retained.

**Table 4-20. Near Interface Cooling Rates for Welds TW-23 and TW-24**

Weld TW-23					
	Max Temperature (°C)	End Temperature (°C)	$\Delta$ °C	$\Delta$ Time (s)	Interface Cooling Rate (°C/s)
Top Thermocouple	464.0	327.8	136.2	8.1	<b>16.9</b>
Middle Thermocouple	430.5	333.8	96.2	8.1	<b>12.0</b>
Bottom Thermocouple	428.8	338.0	90.0	8.1	11.2
Weld TW-24					
Top Thermocouple	510.0	328.0	181.0	23.2	7.8
Middle Thermocouple	490.0	330.0	160.0	23.2	6.9
Bottom Thermocouple	483.0	332.0	151.0	23.2	6.5

#### 4.8.2. Energy Input of Welds TW-23 and TW-24

Energy input was found to be significantly influenced by the use of a heat sink and the increased axial force ramp up rate. As expected the energy input in 0.1 seconds did not change with the use of a heat sink as this point in the weld is predominantly concerned with the rubbing away of surface roughness and oxides [7].

The input energy at 0.1 seconds did, however, increase with the increased axial force ramp up rate applied. When comparing welds TW-23 and TW-24 that have energy inputs of 9.5J/mm<sup>2</sup> and 9.8J/mm<sup>2</sup> at applied axial forces of 5.9kN and

5.6kN respectively, to previous welds such as TW-12 and TW-21 that have energy inputs of  $5\text{J/mm}^2$  and  $5.9\text{J/mm}^2$  at axial forces of 1.73kN and 1.6kN respectively, the improvement in input energy due to increasing the axial force ramp up rate is clear, more so considering welds TW-12 and TW-21 were preheated. This shows the influence of the applied axial force on energy input and process torque, highlighting the necessity to control the axial force ramp up rate, as Weld TW-23 and TW-24 had 58.7kN/s and 56.2kN/s axial force ramp up rates respectively, while welds TW-22 and TW-21 had 15.8kN/s and 17.3kN/s axial force ramp up rates respectively.

The energy input at seizure dropped from  $15.2\text{J/mm}^2$  to  $10.7\text{J/mm}^2$  accompanied by a reduced time to seizure with the use of the heat sink, correlating with the reduced temperature recorded at the bottom the hole in Table 4-17 on page 118. This shortened time to seizure was also noted between welds TW-20 and TW-21 where TW-21 had a larger stud body acting partially as a heat sink, correlating with less energy input to seizure. Preheat and increased stud diameters were previously shown to reduce the seizure torque, accompanied by a significant reduction in axial force due to high material consumption rates associated with preheat. The axial force for welds TW-23 and TW-24 were 7.9kN and 6.5kN respectively, showing the increased axial force ramp up rate to improve the applied axial force and maintain seizure torque, as given in Appendix F.

The energy input to PSTP increased with the use of the heat sink as the slope of the torque curve from seizure to the PSTP increased by  $9^\circ$  and the PSTP increased as reflected in Figure 4-30 on page 120 and Appendix F. As the temperature was lower at the bottom of the weld with the use of a heat sink with a greater amount of input energy, the energy will have been conducted into the heat sink. If the welding interfaces are visualized with the heat generated at the shear interface splitting between the plate and the stud, and the stud is maintained at a lower temperature, the heat transfer from the interface will be higher towards the stud body. This will require more driving energy to reach the same point in the welding process.

Table 4-21. Results for Welds TW23 and TW-24

Weld No:	Welding Time (s)	Time to Seizure (s)	Energy Input at 0.1s (J/mm <sup>2</sup> )	Energy Input at Seizure (J/mm <sup>2</sup> )	Energy Input at 1s (J/mm <sup>2</sup> )(W/mm <sup>2</sup> )	Energy Input to PSTP (J/mm <sup>2</sup> )	Total Energy Input (J/mm <sup>2</sup> )	Energy Input Rate at 0.1s (W/mm <sup>2</sup> )	Energy Input Rate at Seizure (W/mm <sup>2</sup> )	Energy Input Rate at PSTP (W/mm <sup>2</sup> )	Total Energy Input Rate (W/mm <sup>2</sup> )	Axial Force at Plunge Depth (kN)
TW-23	15.1	0.15	9.5	15.2	12.1	17.6	155.8	94.9	99.6	13.2	10.3	21.6
TW-24	23.1	0.12	9.8	10.7	13.65	20.9	228.3	98.0	89.0	15.2	9.7	18.7
TW-24 (Fail)	41.4	x	x	x	x	x	350.6	x	x	x	x	x

The total energy input increased significantly from 155.8J/mm<sup>2</sup> to 228.3J/mm<sup>2</sup> with the welding time increasing from 15.1 seconds to 23.1 seconds. This is due to two aspects of the weld; the heat sink removing heat energy from the interface slowing the propagation of the welding interface up the hole, and achieving the correct plunge depth by preventing stud shank swelling and hence collapse. In total the use of a heat sink allowed an additional 72J/mm<sup>2</sup> or 109kJ of energy to be put into the weld as indicated in Figure 4-30. The energy input into the welds by 15.1 seconds (the welding time for weld TW-23) was 155.8J/mm<sup>2</sup> and 168J/mm<sup>2</sup> for welds TW-23 and TW-24 respectively, showing the dissipating of heat energy due to the heat sink to increase the energy input as discussed, with minimal changes to the near interface temperatures at this time in the weld.

AGG was found at the base of the welds, as shown in Figure 4-31 (a) and (b). As these regions are formed under high shear stresses and hence have highly distorted crystal lattices, combined with the pinning effect of the stretched grains of the plate restricting grain boundary migration, these areas are highly susceptible regions to AGG. The heat energy conducting into the weld from the final shear interface, therefore, raised and maintained the temperature in these regions sufficiently to initiate AGG. Figure 4-31 (a) and (b) show that the use of a heat sink significantly increased the volume of AGG formed, with weld PW-23 having only localized AGG on the sidewalls and weld TW-24 having AGG along

the entire base of the hole. The additional  $72\text{J}/\text{mm}^2$  of input energy of weld TW-24 was the driving energy for the additional AGG, giving a  $54.2^\circ\text{C}$  higher peak temperature at the bottom of the hole, and significantly lower cooling rate as given in Table 4-20.

The direct influence of total energy input and temperature can be further highlighted by Figure 4-31 (c). The image shows a weld, identical to TW-24 that was welded at  $12\text{kN}$  axial force for the full  $2\text{mm}$  plunge (this was due to a failure in the plunge depth sensor). This extended the welding time to  $41.4$  seconds and pushed the total energy input up to  $350\text{J}/\text{mm}^2$  (an additional  $122.3\text{J}/\text{mm}^2$ ). This drove the formation of significantly more AGG in the lower region of the weld.

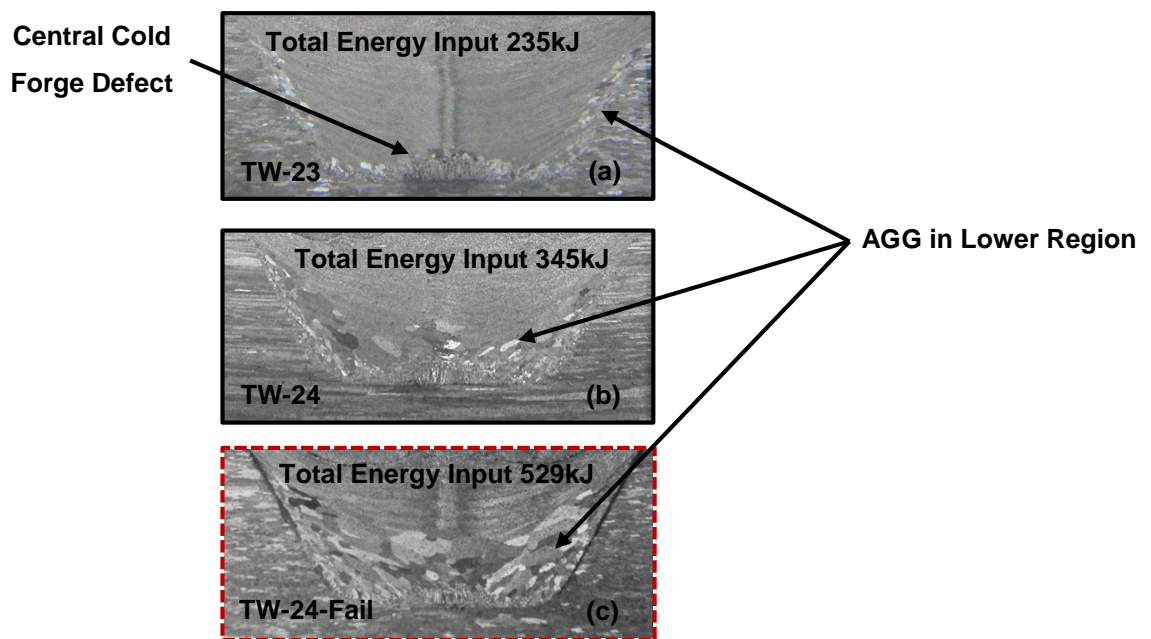


Figure 4-31. AGG in Lower Region of Welds TW-23 and TW-24

#### 4.8.3. Energy Input Rate of Welds TW-23 and TW-24

The energy input rate at  $0.1$  seconds was similar for both welds, with the use of the heat sink showing no influence. The increased axial force ramp up rate, however, significantly increased the energy input rate to  $94.9\text{W}/\text{mm}^2$ , when compared to all previous welds with the maximum being  $59.1\text{W}/\text{mm}^2$  for weld TW-21, a preheated weld with a larger stud shank. Therefore, preheat and axial force ramp up rate affect the rate of energy input in the first  $0.1$  seconds into the weld, with values above  $49\text{W}/\text{mm}^2$  having visually superior bonding at the initial interface. However, the results also show that if the stud is unable to conduct the

heat energy away at a high enough rate, a void is formed at the bottom interface as seen in welds TW-11 and TW-20, as shown in Figure 4-12 on page 87 and Figure 4-19 on page 103 respectively.

The energy input rate at seizure and PSTP was not influenced by the use of a heat sink. The increased axial force ramp up rate increased the energy input rate to seizure, compared with the highest previously achieved being  $78.3\text{W}/\text{mm}^2$ , for weld TW-13. The energy input rate to PSTP did not change with axial force ramp up rate, and was consistent for all welds, with the biggest changes seen in previous welds with increased hole taper angles.

Energy input and energy input rate at 1 second was the same for both welds, with previous results showing axial force and preheat to govern the results as found in all previous welds. The total energy input rate remained constant for both welds, ranging from  $10.3\text{W}/\text{mm}^2$  to  $9.7\text{W}/\text{mm}^2$  for welds TW-23 and TW-24. The results were similar to all previous welds, with the maximum energy input rate recorded by this point in the research being  $20.2\text{W}/\text{mm}^2$ , using a  $90^\circ$  tapered hole. The data indicates that there is a limiting rate at which the overall energy input rate can be maintained. This is thought to be a fundamental limit induced by the conduction of heat through the 25mm thick plate, as changes in geometry, axial force and preheat show no significant influence. The only notable changes in total energy input rate are with exceptionally low axial forces such as welds TW-1, TW-2 and TW-3 that had total energy input rates of  $3.8\text{W}/\text{mm}^2$ ,  $5.11\text{W}/\text{mm}^2$  and  $5.1\text{W}/\text{mm}^2$  respectively, as given in Appendix F.

#### **4.8.4. Summary of Welds TW-23 and TW-24**

A near interface temperature of  $464^\circ\text{C}$  was recorded near the top of the weld with no heat sink fitted and  $510^\circ\text{C}$  with, correlating with the increased total energy input recorded. The near interface temperature at the bottom of the weld was measured as low as  $108^\circ\text{C}$ , low for good atomic diffusion to take place and significant plate plastic deformation [7] [33]. These welds further identify the need for preheat to be applied to the process in order to raise the temperature in the lower region, promoting diffusion and plastic deformation (plasticization).

The use of a heat sink was shown to be essential in the FTSW of aluminium 6082-T6, as it maintained the integrity of the stud and prevented swelling of the stud shank. This made it possible to control the true plunge depth more accurately, and achieve the maximum amount of plasticization. By extracting the heat energy conducting axially up the stud, the heat sink maintained rotation and plasticisation at the mid region of the hole, significantly increasing the near interface temperature and therefore bond strength in this region.

The additional heat energy put into the weld by preventing the swelling of the stud shank initiated additional AGG in the lower regions of the weld. As this area is formed under high stresses, the temperature at which the shear layers are formed will need to be increased, as AGG only occurs when post formation temperatures are exceeded [1] [39] [43]. This may be increased by the use of preheat, though any excess energy may cause more grain growth if not controlled. In future tests involving preheat, the plunge depth will need to be precise and minimal to prevent AGG. The near interface temperature was found to be lower at the base of the hole, with the use of a heat sink, further stressing the microstructure. Therefore, although the use of a non-consumable, removable heat sink has been found essential to the FTSW process, it negatively affects the initial bonding at the base of the hole with respect to the measured sidewall temperature.

The increased axial force ramp up rate improved the sidewall bonding throughout the weld, reducing the height of the TMAZ and preventing the body of the stud warming to the point of violent shear. The increased axial force ramp up rate reduced the amount of rubbing and plasticization occurring at the bottom central region of the hole, forming a cold forge defect in the low relative velocity region. The balance of required axial force ramp up rate vs. base rubbing (initial interface warming) will, therefore, need to be controlled; however, the FTSW platform did not have this control capability available at the time of investigation and will need to be considered at a later stage.

#### **4.9. Conclusion of Development Welds**

The process development welds presented in this chapter laid the foundation for FTSW AA6086-T6, identifying key process points and enabling the development



to move from development to testing. One of the key observations made during the preliminary test welds is one of the large issues facing FTSW currently, the difficulties experienced when transferring process parameters for identical geometries between different FTSW platforms. In testing it was shown that changes in applied axial force during welding dramatically change the energy input and energy input rates into the weld, affecting the quality of the weld. The applied axial force is controlled by the applied axial force ramp up rate of the system, and, therefore, the tool travel speed. As shown, the static axial force ramp up rate vs. applied axial force is nonlinear, and is reduced with increased tool travel speed (plunge rate). As these two variables cannot be individually controlled on the current FTSW platform, it will be difficult to repeat the welds and get identical results with a different welding platform that does not have an identical axial force response. Therefore, to make FTSWs that are transferable between welding platforms, the plunge rate and axial force ramp up rate will need to be controlled independently. The changeover to the PDS FTSW platform will allow for this control.

Preheat was shown to be essential to the FTSW of aluminium 6082-T6, as the high thermal diffusivity and low strength retention at elevated temperatures prevent the relatively small amount of displaced and plasticized stud material from sufficiently heating the plate, in order to achieve good bonding.

The use of a removable heat sink on the stud shank was shown to be unavoidable in the FTSW process, as it is the only option available to prolong the propagation of the shear interface in the hole, allowing heating and plasticization of the mid region of the weld. The heat sink was also shown to be critical in controlling plunge depth, by prevention of stud body swelling, prematurely stopping the weld.

The taper angle of the hole was shown to need to be a minimum of  $60^\circ$  to maintain stud integrity, and apply a greater normal force on the sidewalls during plunge, promoting bonding.

In order to further the investigation, the process torque capacity of the welding platform will need to be increased, as welds attempted at 30kN repeatedly stall the motor, with only one 30kN weld on the FTSW platform completing at a

preheat of 140°C. This weld failed at 90.7MPa. As this was below the limits known to be achievable from the parallel FTSW, the low force welds were abandoned, favouring the new PDS FTSW platform, with axial force capacities of up to 100kN.

A key parameter not noted in literature at the time of the research, was the influence of axial force ramp up rate. It has been shown in this section to dramatically influence the formation of the weld nugget. Further it is now known to be the leading reason why many optimised process parameters noted in literature are not easily and directly transferable to other FTSW platforms.

#### **4.10. Investigation of Bonding at the Base of the Tapered Hole**

The preliminary welds made to this point investigated the effect of process parameters, geometry and preheat on the visual appearance of FTSW of AA6082-T6. As the appearance of sidewall bonding improved with regions of localized bonds and highly plastically deformed zones seen along the sidewall interface and the removal of all large voids within the weld nugget, it was necessary to quantify the quality of the bond at the base of the tapered hole before proceeding to higher axial forces to further improve sidewall bonding. Due to aluminium's high thermal diffusivity, heat is dissipated at a rate that prohibits bonding at the initial interface at the bottom of the hole, creating one of the largest issues facing FTSW of aluminium 6082-T6, lack of bonding at the base of the hole. A test matrix was designed to investigate only the effect of preheat and rotational speed on the bonding at the base of the hole. The 60° tapered hole was maintained and the tapered section of the stud removed leaving only a parallel sided stud. The hole depth was retained at 18mm with a 10mm base diameter and 2mm fillet, giving an overall stud shank diameter of 14mm. The parallel sides of the stud made it possible to quantify only the effects of process parameters on the bonding at the base of the hole, while maintaining identical thermal boundary conditions.

##### **4.10.1. Process Parameters of Parallel Welds PT-1 to PT-4**

The rotational speeds selected were 5000RPM and 3000RPM, giving 1.6m/s and 2.6m/s peripheral velocity respectively of the flat face of the stud. The selection was based on work by Beamish [4] who discussed that lower rotational speeds

with higher axial forces will produce good welds and recommending a minimum nose peripheral velocity of approximately 1.7m/s, and successful aluminium to cast iron RFW made at 3200RPM with a peripheral velocity of 2.48m/s by Edar et al. [7].

Preheat was investigated, with the plate being heated to 200°C and allowed to cool to 140°C  $\pm$ 2°C before welding started. This allowed for setup and ensured consistency. This temperature was based on the maximum time needed for setup without heating the block beyond 200°C in the oven, proving effective in previous preheated test welds. The process constants are given in Table 4-22 with the process variables and weld combinations given in Table 4-23.

**Table 4-22. Welds PT-1 to PT-4 Process Constants**

Cooling Time (s)	20
Clearance Volume vs. Displaced Volume Factor	N/A
Plunge Depth (mm)	2
Hole Area (mm <sup>2</sup> )	1592.5
Base Area (mm <sup>2</sup> )	156.9

**Table 4-23. Welds PT-1 to PT-4 Process Variables**

Weld No:	Hole Depth (mm)	Stud Taper Angle (°)	Hole Taper Angle (°)	Hole Base Diameter (mm)	Stud Base Diameter (mm)	Preheat Temperature (°C) (Oven Temperature)	Preheat Temperature (°C)	Axial Force (kN)	Rotational Speed (RPM)
PT-1	18	0	60°	10	10	0	0	30	5000
PT-2	18	0	60°	10	10	250	140	30	5000
PT-3	18	0	60°	10	10	0	0	30	3000
PT-4	18	0	60°	10	10	250	140	30	3000

The sectioned macrographs of welds PT-1 to PT-4 are given in Figure 4-32. Visually the most significant changes are the influence of rotational speed on the formation of the weld nugget and flash. Welds made at 5000RPM have distinct primary and secondary flash formation, with the primary flash traveling more uniformly up the stud with preheat as seen in Figure 4-32 (b), compared to Figure

4-32 (a). Welds made at 3000RPM have no distinct primary or secondary flash; instead, the weld consists of only a weld nugget consisting of dynamically recrystallized stud material, with a TMAZ that is substantially higher in the hole than in welds made at 5000RPM, as shown in Figure 4-32 (c) and (d). This indicates that at 3000RPM the temperature at the periphery is cooler and the flash is not flowing out of the weld, but is cooling and forming shear layers. As heat builds up at the periphery, moving to the central region of the stud with time, high rotational speeds rub the outer regions instead of tearing and plasticizing [10] [13] [23]. For the same quantity of plunge, higher temperatures were recorded on the backing plate below the weld zone in previous work on stainless steel stud by the researcher, when RPM was increased past a critical point [23]. Showing the rubbing action to heat the plate, not actively form the joint, as discussed by Vill [8], [23]. It is not clear if this is beneficial with regards to the tapered section of the weld with respect to the parallel sided studs, however the removal of the primary and secondary flash reduces the stress concentration between the stud and plate which is beneficial for stud welding, though in application for FTSW with the stud trimmed after machining, this is not a concern [23]. Preheated welds all had deformation of the plate at the fillet, indicating that sufficient temperature was achieved at the interface to cause severe plastic deformation, shown in Figure 4-32 (b) and (d).

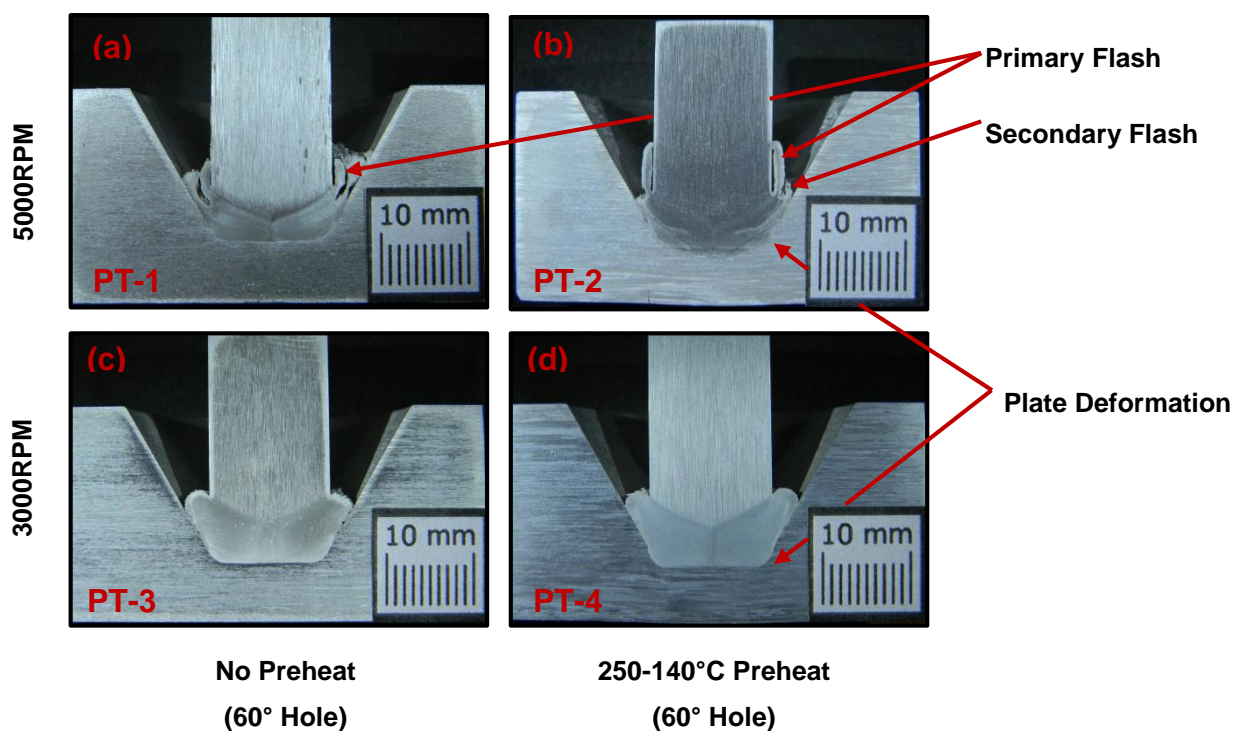


Figure 4-32. Macrographs of Welds PT-1 to PT-4

#### 4.10.2. Applied Axial Force for Welds PT-1 to PT-4

The axial force applied during welding did not achieve the set value before plunge depth was reached and rotation stopped as shown in Figure 4-33. As the volume of the stud body behind the welding interface has been directly linked to the rate of plunge, the high energy input rate cannot be maintained by the uniform profiled stud body, causing consumption rates (average of 300mm/min) that the welding platform cannot maintain. The axial force response for all welds follow the same profile, showing the improved control and stability of the revised system. It is clear from Figure 4-33 that the interface reached the plasticized state at approximately 0.2 seconds, as the steady state of climb plateaued, identifying the initiation of plunge and high plunge rates, verified by the longest time to seizure being 0.15 seconds. Once rotation stopped, the 30kN forging force was reached in 0.5 seconds, giving an axial force ramp rate of 15kN/s. As the static axial force ramp up rate of the current FTSW platform is nonlinear, and influenced by plunge rate and axial force as shown in Figure 4-34, it is clear that at 12.5kN the axial force ramp up rate could have been as high as 74.8kN/s if the stud were stationary. However as it is lower, the stud is plunging during consolidation of the weld. This nonlinearity is an issue affecting repeatability when alternating between welding platforms that will be addressed later in the research.

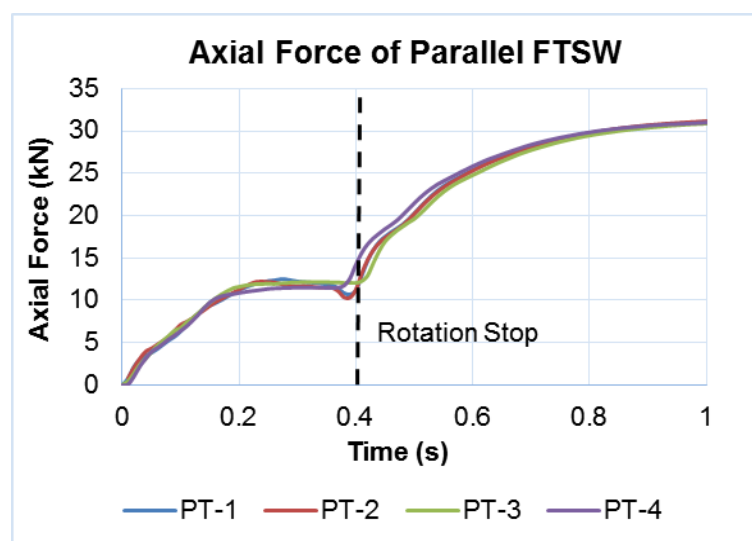


Figure 4-33. Applied axial Force during Welding (Welds PT-1 to PT-4)

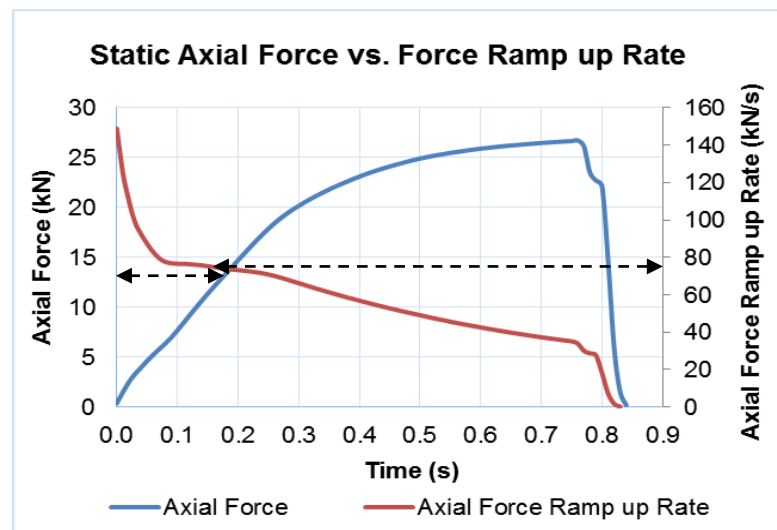


Figure 4-34. Axial Force vs. Axial Force Ramp up Rate

#### 4.10.3. Process Torque for Welds PT-1 to PT-4

The process torque for welds PT-1 to PT-4 is given in Figure 4-35. As there is no tapered stud body to increase the shear area once plunge begins, the maximum torque is the seizure torque for welds PT-1 to PT-4, with the recorded values of seizure torques and axial force ramp up rates corresponding with welds TW-23 and TW-24 (high ramp up rate configuration).

Reduced rotational speed increased the seizure torque as expected, due to the energy input at the interface maintaining a plasticized state of shear [8] [10] [23] [5]. The time taken to reach seizure increased, due to the lower rotational speed reducing the energy input rate and increasing the total energy input to seizure, discussed later. For both rotational speeds, the slope of the climb in process torque increased with preheat as previously noted in Section 4.8.1 on page 118, showing less rubbing to be needed and a quicker rate of interface bond generation with preheat.

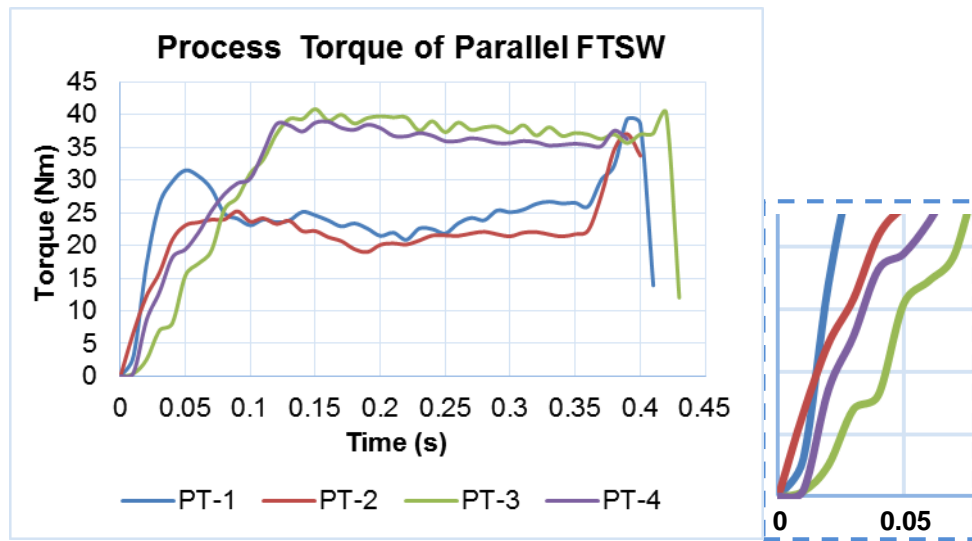


Figure 4-35. Process Torque for Welds PT-1 to PT-4

#### 4.10.4. Energy Input for Welds PT-1 to PT-4

The energy input results are summarised in Table 4-24. For detailed results of energy input, axial force and process torque refer to Appendix F. Energy input at 0.1 seconds into the weld ranges from  $8\text{J/mm}^2$  to  $6.7\text{J/mm}^2$  at 5000RPM and  $3.8\text{J/mm}^2$  to  $4.6\text{J/mm}^2$  at 3000RPM, consistent with welds TW-23 and TW-24.

As energy input in the first 0.1 seconds into the weld has been shown to increase with preheat, the increase in energy input for weld PT-1 vs. PT-2 is believed to be due to rubbing between the primary and secondary flash that do not travel uniformly up the stud as seen in Figure 4-32 (a) on page 131, characterised by the change in process torque profile shown in Figure 4-35. The energy input to 0.25 seconds decreases with rotational speed. The energy input to seizure increased with reduced rotational speed, as the time to seizure increased and the process torque increased. More energy was therefore put into the interface before plunge began, with 3000RPM welds. As the applied axial force ramp up rate was the same for all welds at seizure, the energy is input under the same surface contact conditions as seen in Figure 4-32, there is substantially more plastic deformation of the plate at the fillet with preheated, 3000RPM welds.

Table 4-24. Results for Parallel Welds PT-1 to PT4

Weld No:	Welding Time (s)	Time to Seizure (s)	Energy Input at 0.1s (J/mm <sup>2</sup> )	Energy Input at Seizure (J/mm <sup>2</sup> )	Energy Input at 0.25s (J/mm <sup>2</sup> )	Total Energy Input (J/mm <sup>2</sup> )	Energy Input Rate at 0.1s (W/mm <sup>2</sup> )	Energy Input Rate at Seizure (W/mm <sup>2</sup> )	Energy Input Rate at 0.25s (W/mm <sup>2</sup> )	Total Energy Input Rate (W/mm <sup>2</sup> )	Axial Force at Plunge Depth (kN)
PT-1	0.41	0.05	8.0	4.6	19.5	33.8	80.0	91.8	78.0	82.5	12.5
PT-2	0.40	0.05	6.7	3.4	17.3	29.3	66.5	68.4	69.4	73.3	12.2
PT-3	0.43	0.13	3.8	5.3	15.5	27.4	37.7	42.2	61.8	63.7	12.3
PT-4	0.39	0.15	4.6	6.11	15.9	25.0	46.0	40.7	63.4	64.0	11.5

The plastic deformation and bonding at the fillet is clearly shown in Figure 4-36. Welds made without preheat showed no plate deformation, regardless of rotational speed, with only localised bonds forming along the interface. Preheated welds clearly show severe plate deformation as indicated by the original position of the fillet, shown in Figure 4-36 (b). Lower rotational speeds increasing the penetration of the plastic deformation, as highlighted in Figure 4-36 (d), correlating to higher energy inputs to seizure and time to seizure. The stud material at the fillet in Figure 4-36 (c) shows parallel deformation bands caused by the high torque at seizure, and high cooling rates into the cold plate.

#### 4.10.5. Energy Input Rate for Welds PT-1 to PT-4

The energy input rate at 0.1 econds and siezure almost halved at 3000RPM as given inTable 4-24. The recorded energy input rates at 5000RPM are almost identical to the recorded energy input rates of welds TW-23 and TW-24, showing correlation and consistency with previous welds. Therefore, the reduced energy input rate and extended time to seizure put in sufficient energy to reach seizure; however, additional energy had to be put in to account for heat energy dissipation with the extended cycle time to seizure. This energy is clearly used to plastisize the plate when preheat is applied, reducing the thermal gradient.



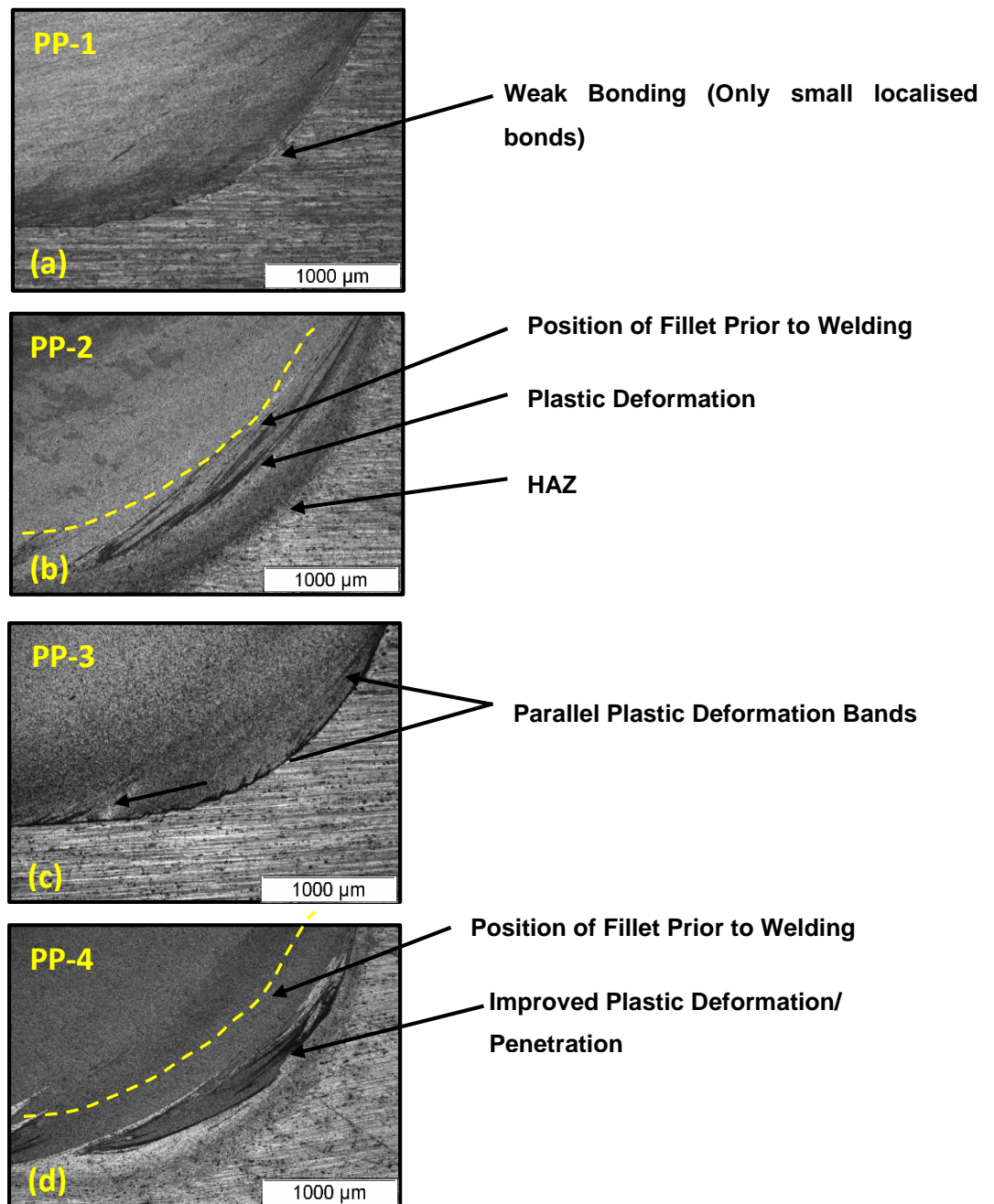


Figure 4-36. Filled Deformation for Welds PT-1 to PT-4

#### 4.10.6. Tensile Data/ pull out Test for Welds PT-1 to PT-4

Welds PT-1 to 4 were repeated and tested axially in a tensile jig, shown in Figure 4-37, using an Instron - 8801 tensile tester. The samples were pulled at 2mm/min until fracture, as shown in Figure 4-38, and the UTS (Ultimate Tensile strength) recorded.

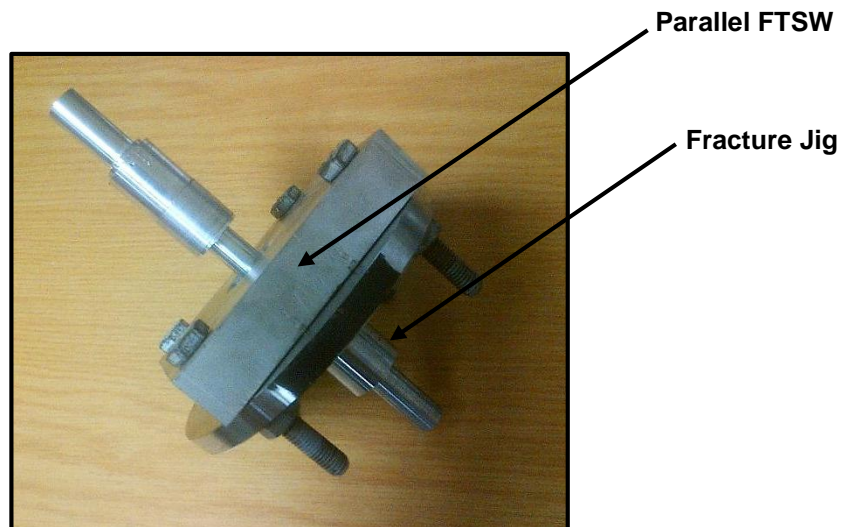


Figure 4-37. Fracture Jig for Parallel FTSW

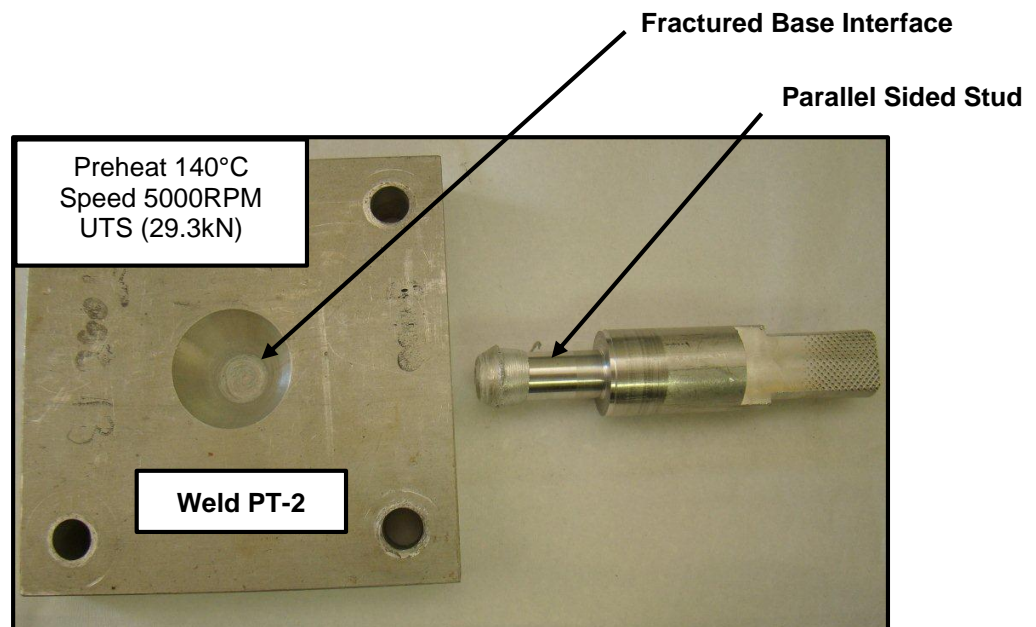


Figure 4-38. Fractured Parallel FTSW

In order to quantify the performance of the welded joints, the maximum achievable joint strength needed to be determined. Parent tensile samples were machined according to the ASTM E8M standard as discussed in experimental setup. It was necessary to test the effect of preheat and the effect of the near interface temperatures experienced during welding. Two parent plate samples were tested in each condition, as received condition without preheat achieving, 200°C preheat and 500°C heating, all taken in the rolling direction. The results for all conditions are given in Table 4-25.

The first two samples were tested in the as received condition. The second two samples were heated to 200°C, identical to all preheat conditions, remaining in the oven for 1 hour. The samples were then removed and allowed to cool naturally to room temperature. The third pair of samples were heated identically to 200°C, allowed to cool to room temperature and then heated to 500°C, taking approximately 15min heating time. Once at temperature the samples were removed and allowed to cool naturally to room temperature. This was the closest representation of the thermal cycle experienced by the preheated FTSW material achievable by the researcher at the time, taking near interface temperature data from welds TW-24 as reference. The results, given in Table 4-25, show the parent plate to achieve 309MPa, the 200°C preheat to achieve 300.6MPa and the 500°C welds to achieve 170.46MPa.

**Table 4-25. Tensile Data of Parent and Preheated AA6082-T6**

Sample Number	Heating Stage 1	Time at Stage 1 (h)	Heating Stage 2	Time at Stage 2 (h)	Sample Width (mm)	Sample Height (mm)	UTS (kN)	Average (kN)	Percentage of Parent	UTS Stress (MPa)
U-1.1	x	x	x	x	12.7	19.2	74.5	75.2	100.0	<b>309.1</b>
U-1.2	x	x	x	x	12.6	19.1	75.8			
U-2.1	200	1	x	x	12.6	19.1	72.4	72.7	96.7	<b>300.7</b>
U-2.2	200	1	x	x	12.7	19.1	73.0			
U-3.1	200	1	500	Approximately 0.15	12.7	19.2	41.4	41.4	55.0	<b>170.5</b>
U-3.2	200	1	500	Approximately 0.15	12.6	19.1	41.3			

The UTS results are given in Figure 4-39 and Table 4-26. The tensile results clearly show the increased tensile strength with preheat and rotational speed. Preheat increased UTS from 45.5MPa to 117.2MPa at 5000RPM and from 79.8MPa to 162.4MPa. As this is close to the 170.5MPa achieved by the heat treated parent plate, this was identified as a good weld. These results show that the reduced energy input rate at 3000RPM and extended time to seizure, while maintaining the surface pressure across the interface produces superior welds. Kimura et al. [13] show that in rotary friction welds, the process should be stopped past the torque peak; therefore, judging from Figure 4-35, the process could have been stopped at 0.2 seconds, to prevent overheating of the stud material.

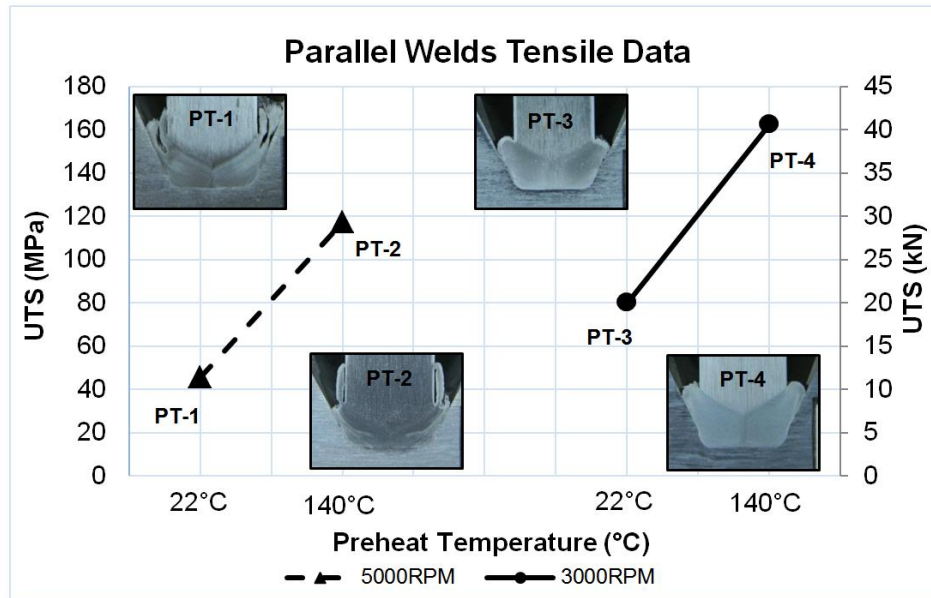


Figure 4-39. Tensile Results for Parallel Welds PT-1 to PT-4

Table 4-26. Tensile Results for Parallel Welds PT-1 to PT-4

Weld No:	UTS (kN)	UTS (MPa)
PT-1	11.4	45.5
PT-2	29.4	117.2
PT-3	20.0	79.8
PT-4	40.7	162.4

#### 4.10.7. Parallel FTSW Interface Fractures Surafces

The fracture surfaces were analyzed to identify changes with respect to UTS. The macgraphs of the fracture surfaces are given in Figure 4-38, showing the hole and stud fracture surfaces respectively.

The fracture surfaces show that at 5000RPM without preheat, the surface has a rotary smear effect consisting of a layer of locally plasticized material that was pulled between the welding interfaces. As the heat generated at the interface conducted away immediately into the cold plate with only small traces of localised bonding, the highly deformed layer was locked in place, before additional shear layers were deposited above as shown in Figure 4-40 (a) and (e), achieving only 45.5kN UTS. Reduced rotational speed broke up the rotary smear defect and initiated a band of small localised bonds at 2/3 the diameter of the stud face, corresponding with an increased UTS of 79.8kN.

The formation of this band was noted by Crossland [35] and Meyer [11], who indicate the band to consist of a thin plasticised layer of sheared material. This correlates with the reduced energy input rate to seizure, and extended time to seizure of weld PT-3, allowing the heat generated at the interface to begin heating the plate material before the initiation of plunge. Figure 4-40 (e) and (f) clearly show more plasticization of the interfaces to be present in the rotating stud. This was noted in work by Eichhorn [37] and Meyer [11], though without rationale. In the case of parallel FTSW it is thought to be due to the centrifugal effect of the rotating member assisting the hydrodynamic movement of materials and oxides to the periphery, and the difference in thermal condition, allowing the stud to be at a higher temperature than the plate. In both non preheated welds, machining marks are still visible at the periphery of the studs and hole, indicating the low amount of plasticization at the periphery.

With preheat the entire fracture surface is seen to be dull and torn, indicating bonding across the majority of the interface, with welds made at 3000RPM, showing deeper and less localised fractures, shown in Figure 4-40 (b) and (f) and (d) and (h), correlating with the increased UTS for Welds PT-2 and 4 of 117.2MPa and 162.4MPa respectively.

The effect of rotational speed on energy input and its influence on the appearance of the fracture surface is explained by the polishing effect. At high rotational speeds, the deep shearing across the welding interface which is needed to provide high plastic deformation is replaced by a polishing action [8] [12]. The deformation rate of the interface is unsustainable by the material, reducing the formation of bonds and therefore the rate of bonds sheared at the interface. Therefore, to reach the plasticized state at the interface, a longer rubbing time is needed at higher rotational speeds [10], correlating with the recorded energy input, seizure times and energy input rates recorded.

An observation made with regards to the fracture surfaces of welds PT-1 to PT-4 is that in all cases the stud pulled away from the plate, leaving stud material deposited in the hole. Vill [8] states that when welding a T-section (a friction stud weld onto a plate) the stud has poorer mechanical properties than the plate, due

to changes in thermal gradients vs. conventional RFW, overheating and weakening the stud material [8]. This reduction of stud body strength in T-section welds was noted in previous work by Samuel [23] when welding AISI 316 studs to AISI 304L plate. As the geometry of the tapered hole prevents additional plunge from improving the initial interface conditions, as the hole begins to fill and layers of material build up, the interface of a FTSW will need the maximum amount of plastic deformation in the longest time, without initiating plunge, to ensure good initial interface bonding at the base of the hole. The lower energy input rate and extended time to seizure at 3000RPM, therefore, improved bonding by promoting plastic deformation and therefore bonding at the interface.

As seen in Figure 4-40 (b) the central region of the fracture surface still shows an area of unaffected interface giving reduced bonding at the low relative velocity region of the weld, caused by changing heat inputs across the interface [7] [48]. This central region is approximately 3mm across, corresponding with the cold forge defect seen in Figure 4-29 on page 117.

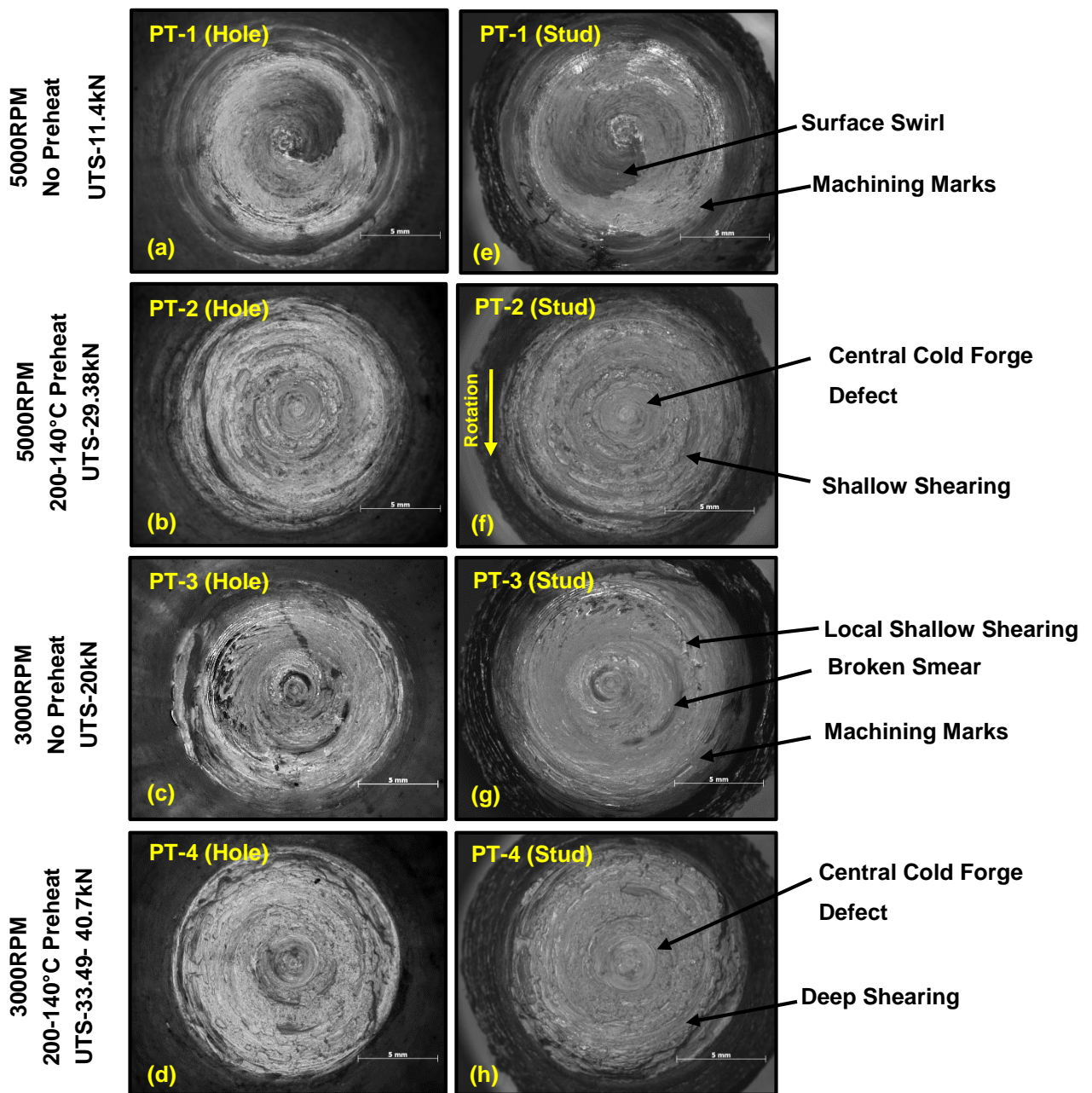


Figure 4-40. Fracture Macrographs of welds PT-1 to PT-4

#### 4.10.8. Discussion of Welds PT-1 to PT-4

The energy input at seizure drops with the removal of the stud tapered section, highlighting the heat sink effect of the tapered section of the stud and heat sink itself. Energy input rate at seizure is consistent with welds TW-23 and TW-24, reducing with rotational speed. The reduced energy input rate combined with increasing the time to seizure of 3000RPM parallel FTSW allowed time for the stud to rub and heat the plate before the weld interface propagated up the hole. This heat increased the depth of plasticization, producing the deeper shears

---

found at the weld interface. The cold forge defect in the central region of the hole was not removed by preheat or rotational speed changes. This defect was only removed with exceptionally high preheat temperatures and low axial force ramp up rates. However, this was problematic as discussed, for it allowed the stud body to heat and soften, negatively influencing sidewall bonding. Lastly, it is clear that without a stud material with a higher melting temperature, preheat is unavoidable in the FTSW of AA6082-T6.



---

## CHAPTER 5

### FINAL DEVELOPMENT OF THE FTSW OF AA6082-T6

#### 5.1. Introduction

Once development of the geometry and process parameter window was complete, identified in the previous chapter, the decision was made to move the research to the then recently commissioned (late 2012) PDS friction welding platform at NMMU, shown in Figure 3-10 on page 50. The platform is significantly larger than the FTSW platform previously used, with process torques maintainable up to 200Nm and axial force capabilities of 100kN. The platform has superior hydraulic control vs. the previous FTSW platform used in this research at NMMU. It allowed the stud plunge rate, axial force ramp up rate and applied axial force to be controlled simultaneously. This removed the nonlinearity of the previous FTSW platform, presented in Figure 4-34 on page 133.

The move to the new welding platform presented the researcher with the question of what axial force ramp up rate was appropriate to apply to the FTSW of AA6082-T6. As the previous platform gave no control of this and the archived rate was a function of the stud plunge rate and flow rate of the hydraulic pump. This would need to be investigated prior to the design and welding of the final test matrix.

This section will mainly consists of;

- Development of a new welding procedure for the PDS friction welding platform;
- The influence of axial force and rotational speed is investigated on four FTSW, identifying the axial force window for the process. The welds are additionally analysed with respect to residual stress measurements made at the European Synchrotron Radiation Facility (ESRF) and texture maps from Electron Backscatter Diffraction (EBSD);
- The influence of axial force ramp up rate is investigated, identifying optimum parameter limits for the final test matrix;

- Design and testing of a 4x2 (16 combinations) final test matrix, investigating the effects of changes in axial force ramp up rate, axial force, rotational speed and stud taper angle geometries;
- Summary of the investigation and findings.

The welds are quantified with respect to dye penetrant crack testing, macro analysis, selected micro analysis, microhardness and static tensile testing. The results are correlated to process torque, process energy, energy input rate and near interface temperature.

The AA6082-T6 heat sink, though successfully used in previous welds was replaced by a steel (EN-8) heat sink, as the swelling (radial) force of the collapsing stud stretched the heat sink, preventing removal and reuse. The steel heat sink shown in Figure 5-1, maintained the external geometry of the aluminium heat sink, however with an internal diameter increase to 38mm to accommodate a larger stud shank. In testing, no notable differences in input energy and near interface temperature were found by the researcher to indicate any negative effects of the steel heat sink.



Figure 5-1. Steel (EN-8) Heat Sink

## 5.2. FTSW Procedure of PDS Friction Welding Platform

As the PDS platform had additional control of axial force ramp up rate and was a fully programmable system, the welding was done in the following order. The block or plate with the machined tapered hole is fixed by four bolts to the torque load cell. The platform then performs and repeats an automatic four point centre finding process that was previously done manually. The bottom of the hole is

then probed at the set axial force and the coordinates of the bottom of the hole under the set load recorded and used as the reference point for determining plunge depth, accounting for deflection of the system at high (80kN) axial forces. The stud is then retracted and rotation of the spindle initiated. Once the set rotational speed is achieved, the spindle plunges in free air at 20mm/min until an axial force reaction response of 500N is measured by the load cells in the welding bed. This changes the control system to force control, following the requested axial force ramp up rate up to a limit of 1000mm/min. This soft touch eliminates the ramming effect high axial force ramp up rates cause at the start of the weld, preventing mechanical lockup. Once the plunge depth has been achieved, rotation is stopped at the maximum braking capacity of the platform, varying depending on rotational speed and resistance caused by the stud. The axial force is then applied for 20 seconds as before, forging the weld as before.

Due to the relatively high axial force (up to 80kN) applied during welding, the partially supported welding setup was abandoned, as at such high forces, the plastic deformation of the plate at the bottom of the hole was significant enough to critically reduce the plunge depth. A 10mm EN-8 backing plate was therefore mounted below the AA6082-T6 plate as shown in Figure 3-15 on page 53. This fully supported the load and prevented any deformation of the aluminium plate. The backing plate was preheated with the aluminium plate to ensure as little heat dissipated into the backing plate as possible. A 10mm section of Nad-500 thermal insulation was fitted between the load cell and backing plate to prevent heat from conducting into the body of the load cell, as shown in Figure 3-15.

### **5.3. The Influence of Axial Force and Rotational Speed using a 60° Hole**

Axial forces of 40kN, 60kN and 80kN were tested at 5000RPM and an additional weld 60kN weld done at 3000RPM. This covers axial forces above what was previously achievable, and shown to be insufficient, and utilises the axial force upper limit of the PDS welding platform. The axial force ramp up rate was set to 75kN/s as identified as appropriate in welds TW-23 and TW-24 at 0.1 seconds. This will be investigated and optimised in the next set of welds, as this is purely a hypothesised starting point. The finalised welding constants are given in Table 5-1, with the process variables and parameter combinations given in Table 5-2. Near interface temperature was recorded during welding, with all welds

preheated to a temperature of 200°C for no longer than 60 minutes, with all welds starting when the near interface temperature was 140°C ± 5°C. Process torque was not recorded for these welds, as this functionality was not yet developed.

**Table 5-1. Process Parameter Constants (Welds S.1. to S.4)**

Cooling Time (s)	20
Clearance Volume vs. Displaced Volume Factor	N/A
Hole Area (mm <sup>2</sup> )	1840.98
Base Hole Area (mm <sup>2</sup> )	156.9
Axial Force Ramp up Rate (kN/s)	75

**Table 5-2. Process Parameter Variables (Welds S.1. to S.4)**

Weld No:	RPM	Plunge Depth (mm)	Axial Force (kN)	Preheat (°C) (Oven-Weld Temperature)	Stud/ Hole Angle (°)
S.1	5000	3	40	200-140	55/60
S.2	5000	3	60	200-140	55/60
S.3	5000	3	80	200-140	55/60
S.4	3000	3	60	200-140	55/60

The macrographs of welds S.1 to S.4 are given in Figure 5-2. The welds show the upper region of the tapered hole to change angle, indicating high amounts of plastic deformation. All welds showed varying amounts of AGG at the base of the hole, initiating at the fillet. Low axial force welds (40kN) had more AGG than high axial force welds, with 80kN only having localised AGG at the bottom of the hole at the fillet. Reduced speed to 3000RPM initiated a continuous band of AGG along the entire base of weld S.4, corresponding with the formation of highly distortion, unstable crystallographic structures in this region.

The formation of the primary and secondary flash was analysed to identify key visual indicators that may differentiate between good and bad welds, and the effect axial force and rotational speed play with regards to formation. Weld S.1 had heavily cracked primary flash, with only localised secondary flash formation,

sporadically distributed around the periphery of the hole, as shown in Figure 5-3. This shows that the plate did not heat sufficiently, or the axial force was insufficient to cause deformation and hence plastic flow. The cracking of the primary flash is likely due to low energy input rates and high welding time at 40kN axial force, allows the flash to cool. Therefore, as the periphery of the primary flash expands with plunge, the flash begins to crack due to loss of plasticity of the material at low temperature.

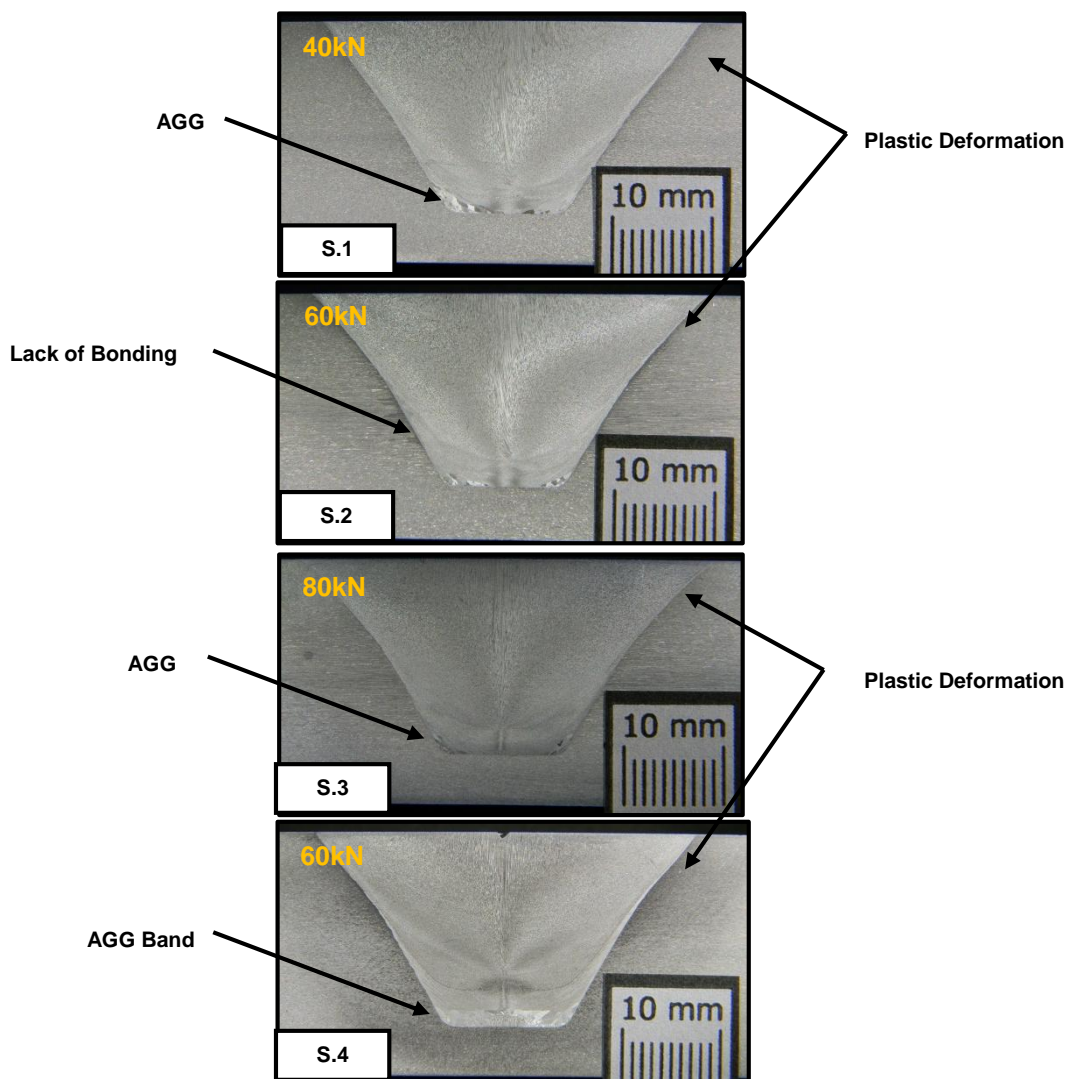


Figure 5-2. Macrographs of Welds S.1 to S.4

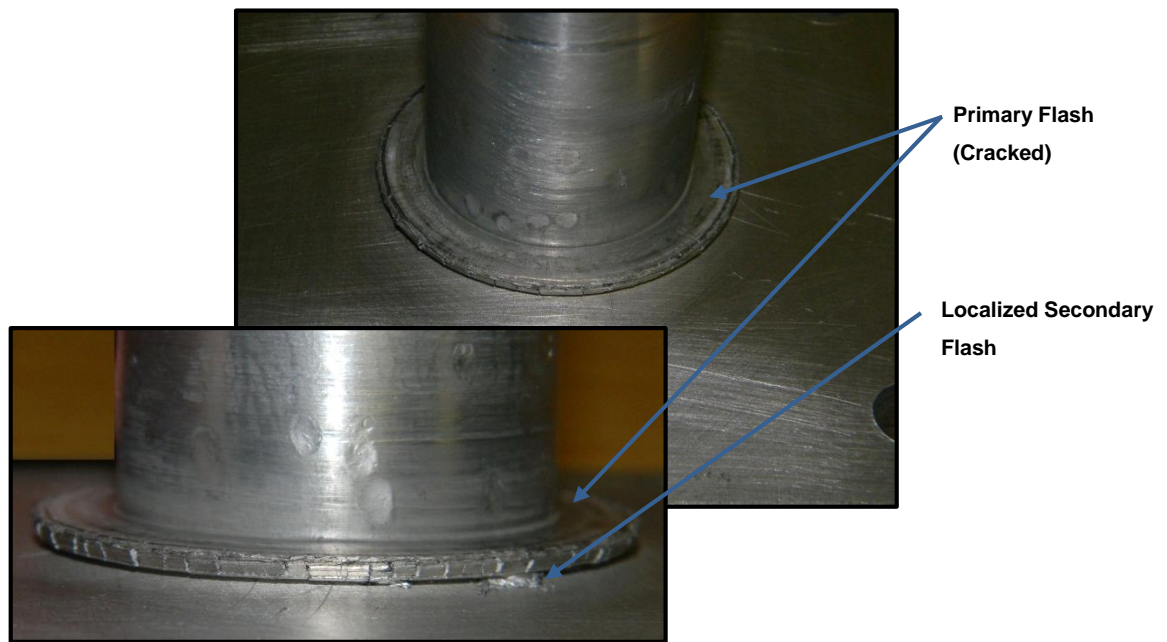


Figure 5-3. Flash Formation of Weld S.1 (40kN Axial Force)

Weld S.2 showed no cracks in the primary flash, and formed a heavily deformed secondary flash as the plate curled due to thermal saturation as shown in Figure 5-4. The upper region of the secondary flash showed expansion cracking as seen in the primary flash of weld S.1. This is as expected, for the increased axial force shortens the welding time as given in Table 5-3, increasing the energy input rate. This maintains the primary flash in a sufficiently plasticised state to allow for expansion, and as the plate is sufficiently heated in the upper region to plastically deform, secondary flash is formed. As the plate dissipates heat, the secondary flash cools rapidly and cracks due to radial expansion. This shows that the high axial forces are beginning to plastically deform the upper region of the plate, promoting good bonding and deep penetration; however, the flash indicated that additional axial force is needed.

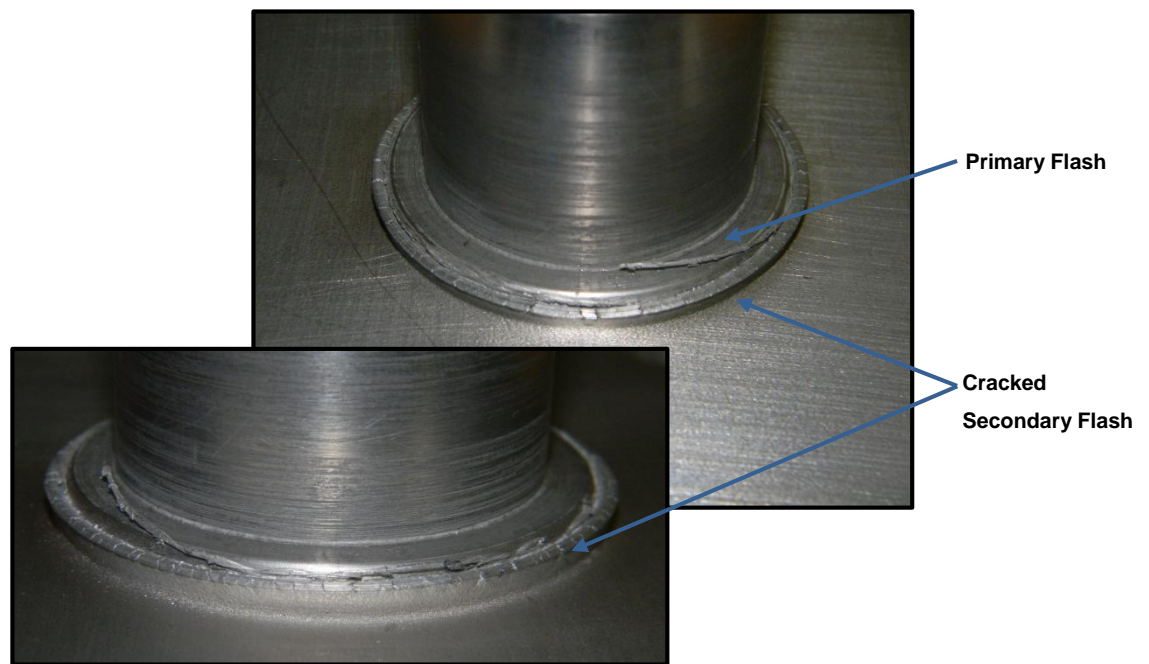


Figure 5-4. Flash Formation of Weld S.2 (60kN Axial Force)

Table 5-3. Welding Times of Welds S.1 to S.4

	Welding Time (s)
S.1	35.37
S.2	8.40
S.3	6.06
S.4	9.23

Weld S.2 showed a well-developed primary and secondary flash with significant plastic deformation of the plate as seen in Figure 5-5. No cracking of the primary or secondary flash occurred, with a smooth transition between the two flash formations. This shows that the upper region of the plate was hotter during formation. It is thought that this is the ideal flash formation for aluminium, as the materials are hot and highly plasticized.

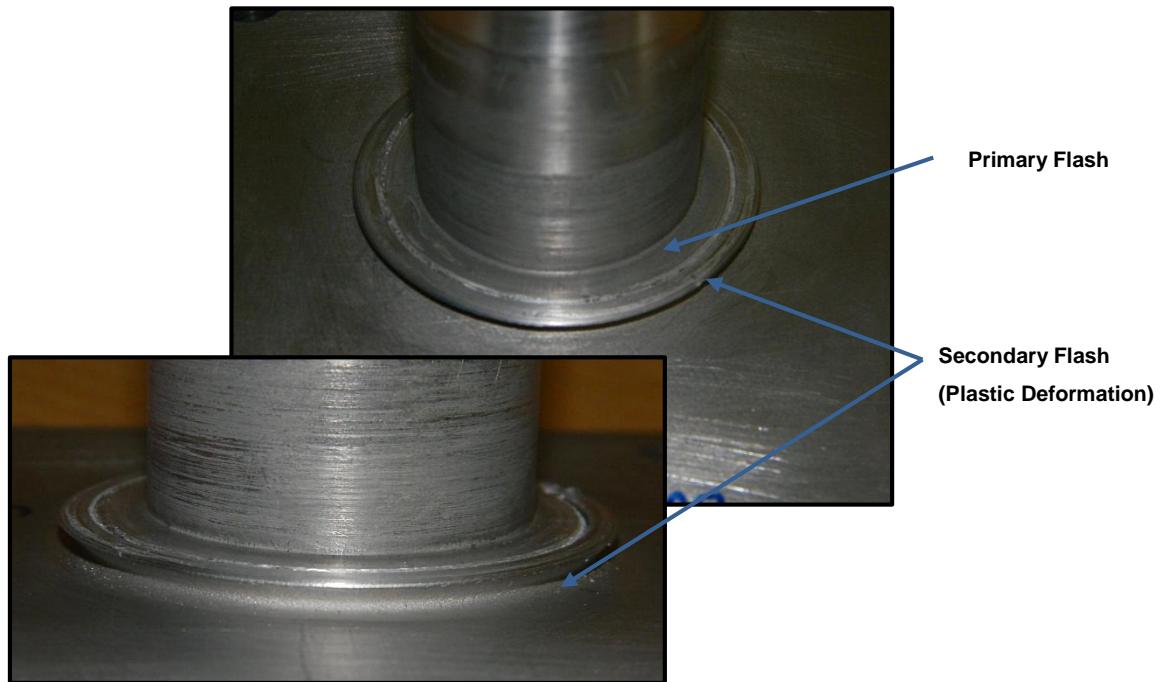


Figure 5-5. Flash Formation of Weld S.3 (80kN Axial Force)

When the rotational speed was reduced to 3000RPM in weld S.4, the formation of the secondary flash reduced and is similarly sparsely located around the periphery as was seen in weld S.1 shown in Figure 5-6. There is no plate deformation and the transition between the two flash formations is sharp. No expansion cracks in the primary flash could be seen, with the step indicating the position of the heat sink forming higher above the plate as before. As noted, reduced rotational speed reduced the welding time, and hence reduces the energy input rate into the weld. This shows that the reduced energy input rate did not sufficiently heat the upper region of the plate, but was sufficient to heat the stud. This may be improved with variations in the axial force ramp up rate.



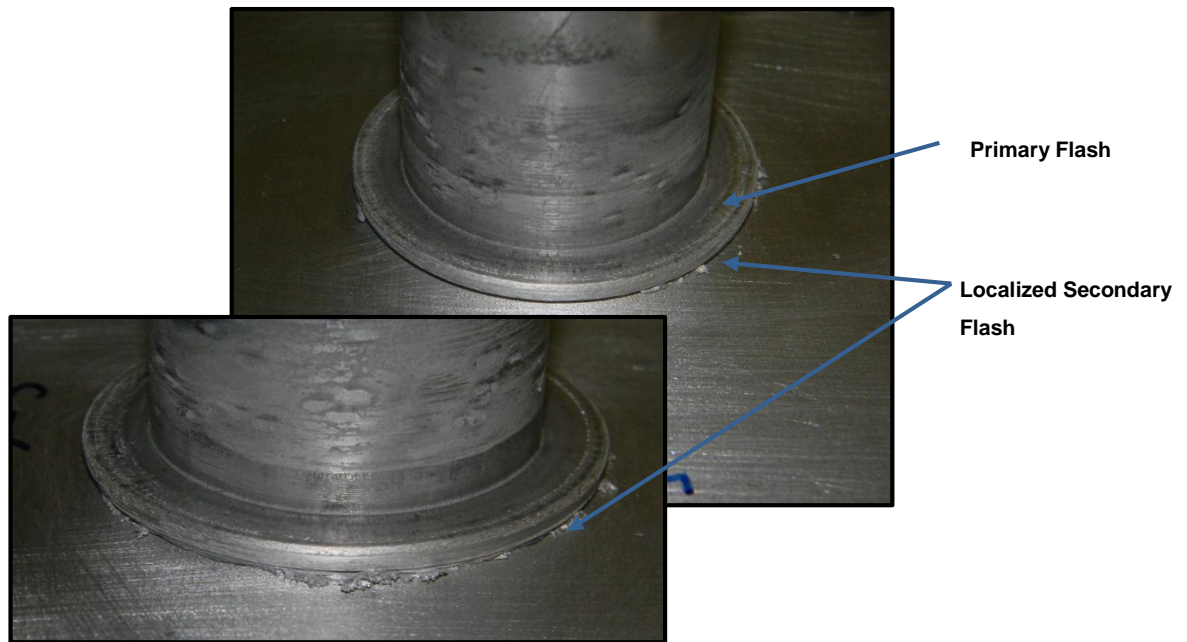


Figure 5-6. Flash Formation of Weld S.4 (60kN Axial Force)

The sectioned welds were polished, etched and dye penetrant tested to identify lack of bonding. The macrographs of the dye penetrant tests are given in Figure 5-7, with macrographs for all welds tested from this point given in Appendix H. The results show Weld S.1 to have only a small localised void in the lower region of the sidewall. Weld S.2 has a significantly larger sidewall void, propagating to the mid-point of the weld. Weld S.3 has a reduced sidewall void compared to S.2, but has a cold forge defect at the base of the hole. Weld S.4 shows no sidewall voids, however, with a larger cold forge defect. This indicates that Welds S.1 and S.4 have the least voids formed along the sidewall bond line. The fracture force analyses will identify if this is a suitable indicator of the static strength of the weld. Four repeat welds were made for tensile testing, as discussed in the experimental setup, shown in Figure 5-8.

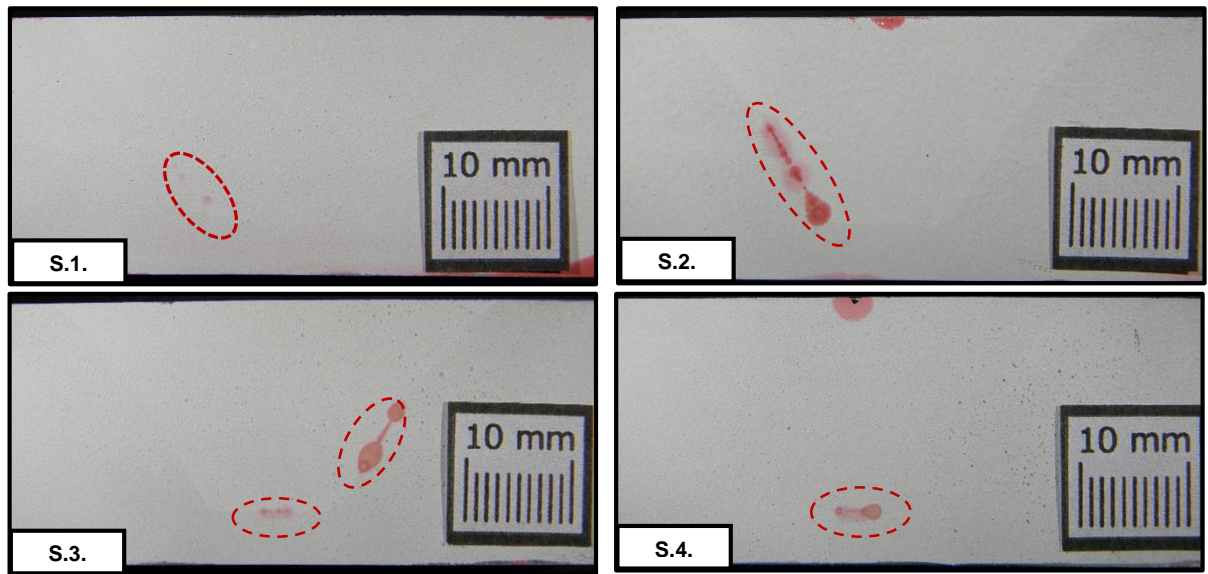


Figure 5-7. Dye Penetrant Testing of Welds S.1 to S.4



Figure 5-8. Tensile Samples of Welds S.1 to S.4

The recorded UTS for welds S.1 to S.4 are shown in Figure 5-9, with the UTS of the as received and preheated material and heat treated parent material included. The relationship of increasing axial force is near linear with 80kN achieving 95% of the heat treated parent material and 52.5% of the as received parent material UTS. The Weld done at 3000RPM achieved 24.8% higher than its S.2 counterpart, indicating that superior bonding was achieved at identical axial forces. The results show that near heat treated parent material strengths are achievable and that high axial forces promote good bonding. The results further show that the selection of 75kN/s axial force ramp up rate was appropriate, giving successful welds, though undoubtedly requiring development which is addressed

in the next set of welds. It is predicted that if the trend of the 5000RPM welds is extrapolated for the 3000RPM weld, joint strengths in the range of 200MPa are achievable.

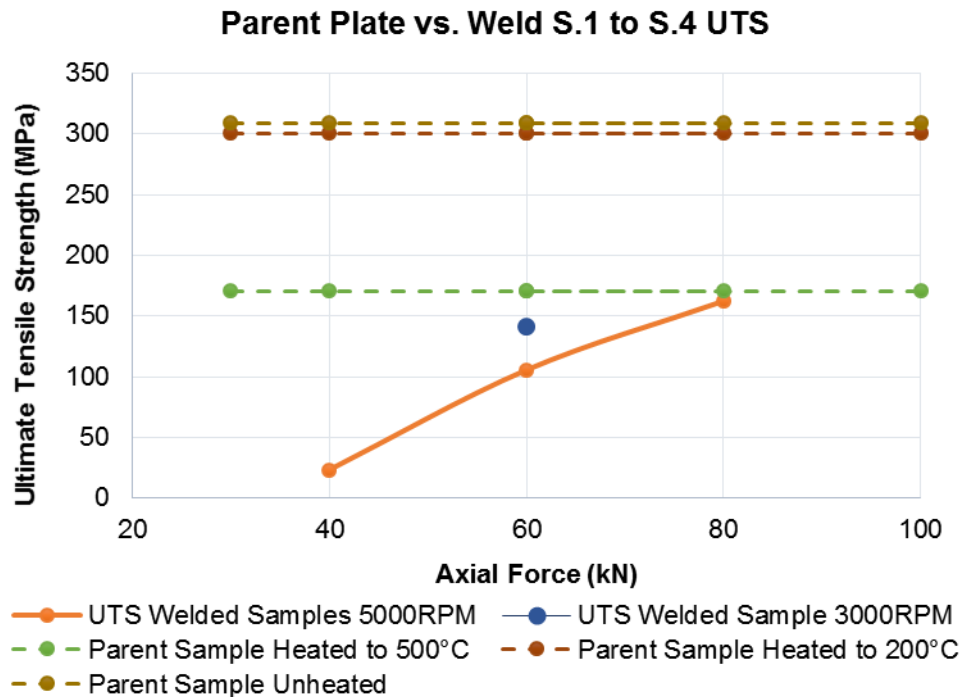


Figure 5-9. Tensile Strength vs. Heat Treated Parent Plate for Welds (S.1 to S.4)

### 5.3.1. Modes of Fracture for Welds S.1 to S.4

The welds all failed along the bond line between the plate and weld nugget, with only limited and localised amounts of plastic deformation visible, as shown in Figure 5-10. No samples showed necking, indicating all failures were a type of brittle fracture. Surprisingly, Weld S.1 did not show any significant lack of fusion in the dye penetrant tests that failed at 23.4MPa vs. S.2, which showed significantly more lack of fusion and achieved 105.6MPa UTS. The Fractures of all welds made from this point are given in Appendix I.

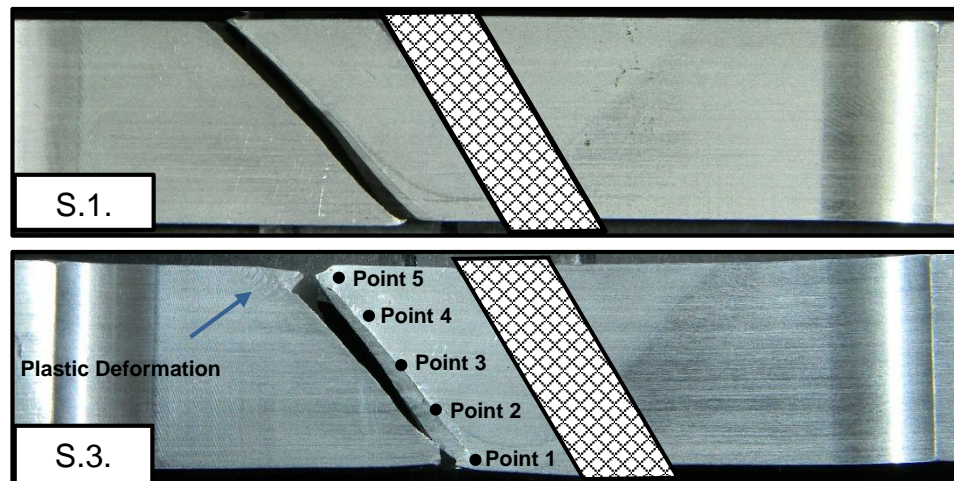


Figure 5-10. Fracture Modes of Welds S.1 and S.3

#### 5.3.1.1. Fracture Surfaces of Welds S.1 to S.4

SEM micrographs of the fracture surfaces on the side of the weld nugget were taken at five points starting and ending on the upper and lower surface respectively. Point 1 is, therefore, positioned at the bottom of the hole and point five at the top, with three equally spaced intermediate points as shown in Figure 5-10. The micrographs were taken using 15kV at a magnification of X1500. The fracture surfaces of welds S.1 to S.4 are given in Figure 5-11. The objective of the fracture surface analyses was to identify if oxide formation and contaminants concentrated along the fracture surface could be linked to joint strength and process parameters, focusing on the influence of axial force and rotational speed.

##### 5.3.1.1.1. Weld S.1

The bottom of the hole (Point 1 and 2) in Figure 5-11 for Weld S.1 showed oxide smearing, identified by dull regions that shows lack of bonding. The mid region of the weld (Point 3) showed localised bonding, covered with oxide. Point 4 shows a breakup of the oxide layer; however, with a dark patch of unbroken oxide present on the left. Point 4 shows traces MVC and breaking up of the oxide layer; however, it shows a general lack of bonding. This corresponds with the tensile results, showing this to have been a poor quality weld, achieving 7.5% of the parent UTS.

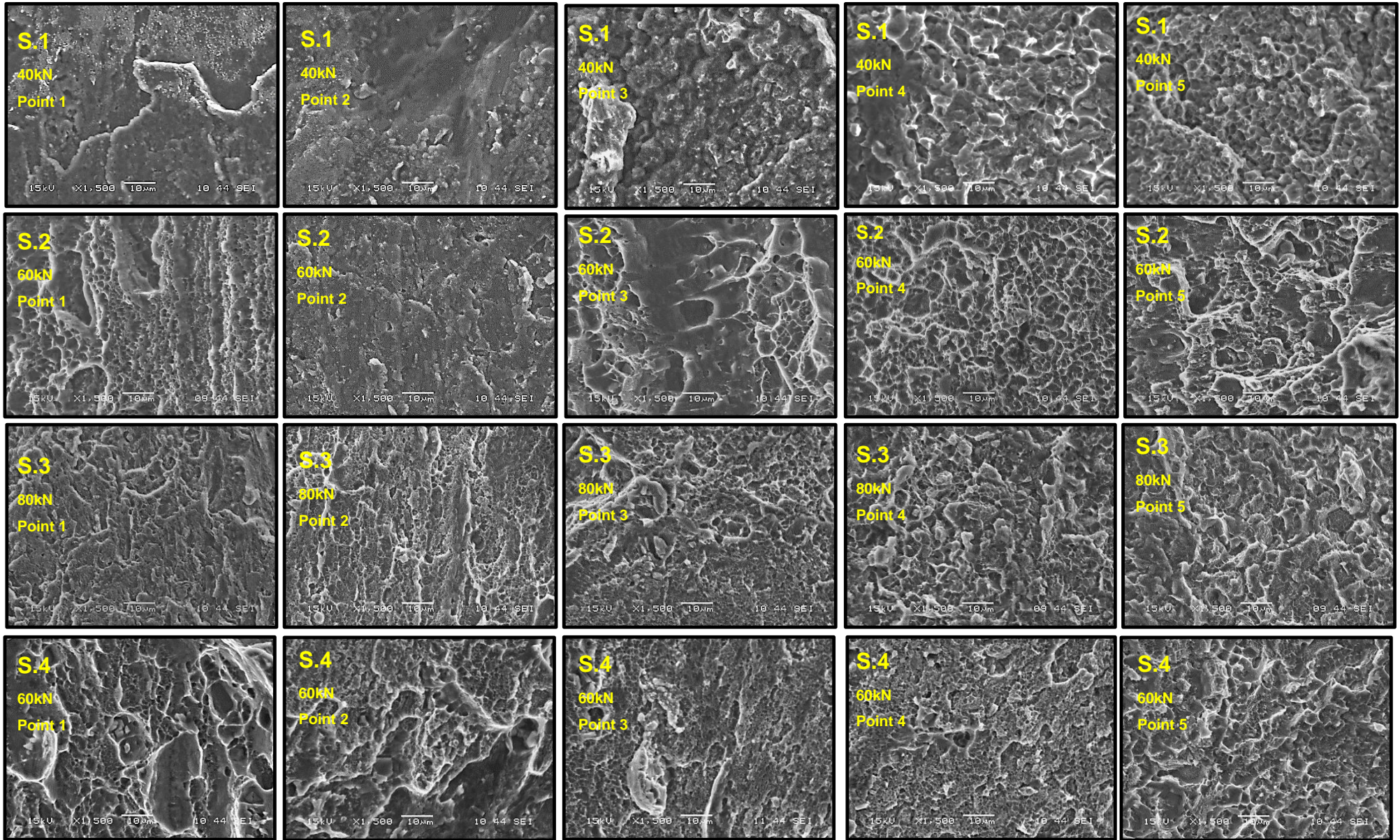


Figure 5-11. SEM Fracture Surfaces of Welds S.1 to S.4

#### 5.3.1.1.2. *Weld S.2*

The bottom of the hole (point 1) in Figure 5-11 shows breakup of the oxide layer and the occurrence of MVC, indicating bonding and ductile fracture, with the formation of the cup and cone elongated in the direction of the applied load (load is 30° out of plane with the 60° tapered hole). Point 2 shows a dull interface with unbroken surface oxide, having only a few points of localised bonding. Point three shows breaking up of the surface oxide layer and MVC with the cup and cone elongated in the pulling direction. Point 4 shows 100% MVC across the surface, with cup and cone formations formed in the pulling direction, indicating good bonding. This corresponds with the plate deformation seen in the secondary flash formation shown in Figure 5-4 on page 150. The top region of the weld at point 5 shows MVC at X1500, corresponding with expansion cracking observed in Figure 5-4 on page 150, linking the plastic deformation of the plate in the upper regions to bonding at the interface. This weld shows typical lack of bonding, an unbroken surface oxide layer and surface tearing commonly seen in friction welds that form under insufficient axial force, achieving 34.16% parent material UTS. This is still well below the estimated joint strength of approximately 60% parent material; however, the improvement of a 60kN axial force weld over a 40kN weld is clearly shown, with increases in UTS reflected on the fracture surfaces. It is unclear whether higher axial force ramp up rate will address the issue but as the axial force is reached in 0.6 seconds, vs. the 8.4 second welding time, it is unlikely to play any further role past the formation of the weld at the bottom of the hole at such a low applied axial force.

#### 5.3.3.2.3. *Weld S.3*

All the fracture surface points in Figure 5-11 for weld S.3 show breaking up of the oxide layer, with no dull patches or smearing visible. Good homogeneous bonding is archived at point 1 with bands of MVC located around oxide bands at point 2. This is the first weld to show MVC in this region, correlating with the dye penetrant testing that shows no fillet voids in this region. Point 3 was 100% bonded, showing unevenly sized zones of MVC. Point 4 and 5 show 100% bonding with near homogeneous MVC occurring, giving cup elongation in the pulling direction, corresponding with the near perfect formation of the primary and secondary flash as shown in Figure 5-5. The influence of the increased

occurrence of MVC and the breaking of surface oxides are clearly reflected in the tensile data with weld S.4 achieving 52.5% parent material UTS, with the most significant changes occurring in the lower half of the weld. As noted previously with the formation of Zones 1 and 2 at low axial forces, the stud body overheats and collapses just past seizure, leaving a poorly bonded region directly above the fillet as discussed in Section 4.2 from page 68.

#### 5.3.1.1.4. Weld S.4

Point 1 in Figure 5-11 for Weld S.4 has MVC located between dull regions of broken oxide, indicating localised lack of bonding. This area falls within the band of AGG noted at the base of Weld S.4 in Figure 5-2 on page 148. Point 2 consists of bands of small MVC with the lower right section showing a dark patch of unbroken surface oxide. Point 3 has continuous small MVC with no large dark oxide patches. The oxide layer is broken up in this area with good overall bonding. Point 4 shows deposits of broken surface oxides, with small MVC at X3000. Point 5 shows small regions of MVC, surrounded by oxide regions, as shown in Figure 5-12 at X3000. This links the lack of plastic deformation and hence lack of formation of the secondary flash to reduced tensile strength, with this weld achieving 45.4% parent UTS vs. its 5000RPM weld S.2 counterpart. 3000RPM is clearly shown to improve the bonding in the lower regions of the hole, with increased UTS for the same axial force during welding. This decreased tensile strength may be overcome with higher axial forces and increased axial force ramp up rate.

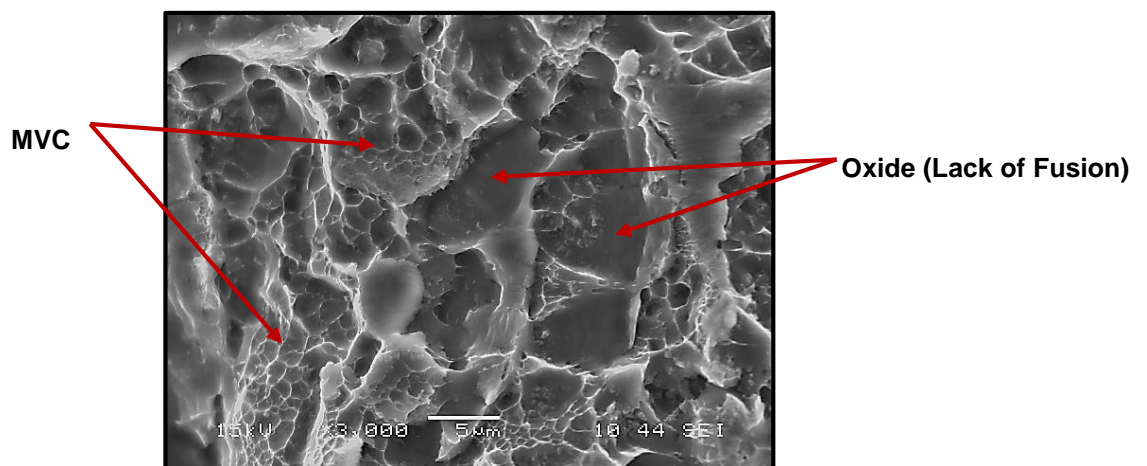


Figure 5-12. SEM micrograph of Point 5 x 3000 (Weld S.4)

Overall this investigation links the formation of the primary and secondary flash to the fracture surfaces at the top two points of the weld, and can be used as a process indicator, although not definitive of overall joint quality. The increased axial force was shown to break the tenacious oxide layer in the tapered hole, improving overall bonding. The formation of fine MVC was shown to correspond with plastic deformation noted at point 5 in Weld S.3, verifying the link to weld quality.

### **5.3.2. Near Interface Temperature for Welds S.1 to S.4**

The near interface temperature during welding is shown in Figure 5-13 for Welds S.1 to S.4. The recorded temperatures were comparative across all welds within the first 8 seconds, with increased welding force not significantly influencing the maximum temperature. The 40kN weld achieved a marginally higher overall temperature, however, past the 10 seconds welding time the additional heat was generated at the surface due to rubbing at low forces, verified by the slow post rotation cooling rate of the plate and the temperature curves running parallel from 10 seconds welding time.

Increased axial force significantly increased the temperature response in the mid region of the weld, with the time taken for the middle thermocouple to register an increase in sidewall temperature, reducing and giving a steeper temperature increase gradient (more direct heat input), as shown in Figure 5-13 for Welds S.1 and S.2. At 80kN axial force the bottom and middle temperature response overlap as shown in Figure 5-13 for Weld S.3. The middle region of the weld, therefore, heats sooner due to reduced response time, allowing the mid region to be at a higher temperature for a longer period of time. This is evident in the fracture surfaces showing the increased bonding in this region, with the breaking of the surface oxides and MVC formation. This is critical as the mid region generally has the lowest bonding due to low interface heat generation and rubbing, with the heat carried away in three directions. Therefore, the higher the temperature and the sooner this temperature is reached, the greater the possibility of achieving good bonding, as heat and pressure together are needed to break the surface oxide to form diffusion bonds.



In welds made above 40kN axial force, the overall peak temperature was shown to be in the middle of the weld. Indicating that this region is still rotating and has not stalled with the increased axial force and high axial force ramp up rates applied to the welds. The effect of changes in rotational speed do not appear to alter the response of the bottom and middle weld temperature; however, the top thermocouple responds sooner as shown in Figure 5-13. The three temperature responses near overlap from the start, indicating the interface moved up quickly, without allowing time for the plate to heat, correlating with primary and secondary flash formation and fracture surface analysis. This may be advantageous at higher axial forces and axial force ramp up rates.

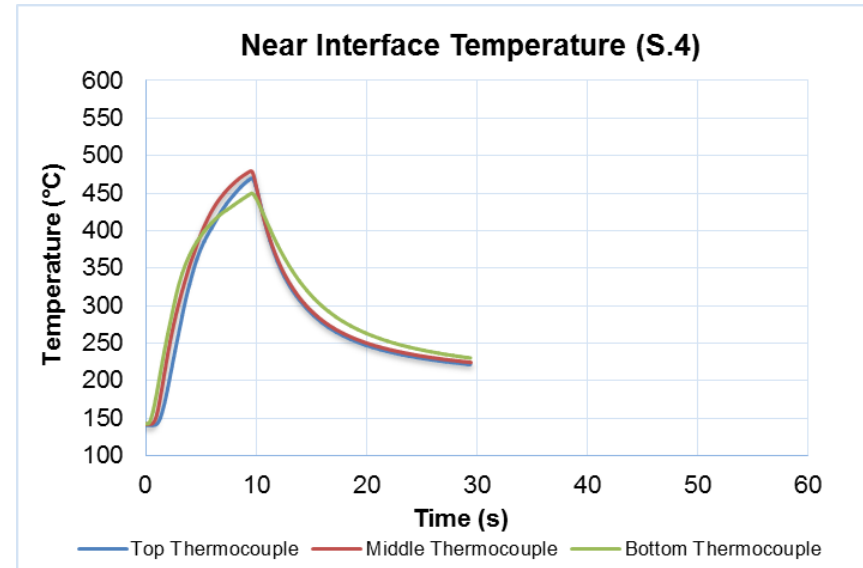
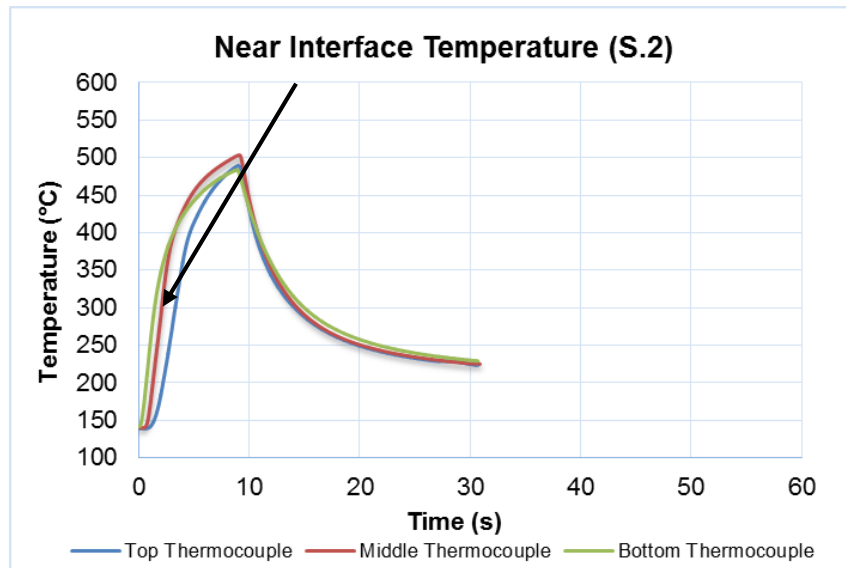
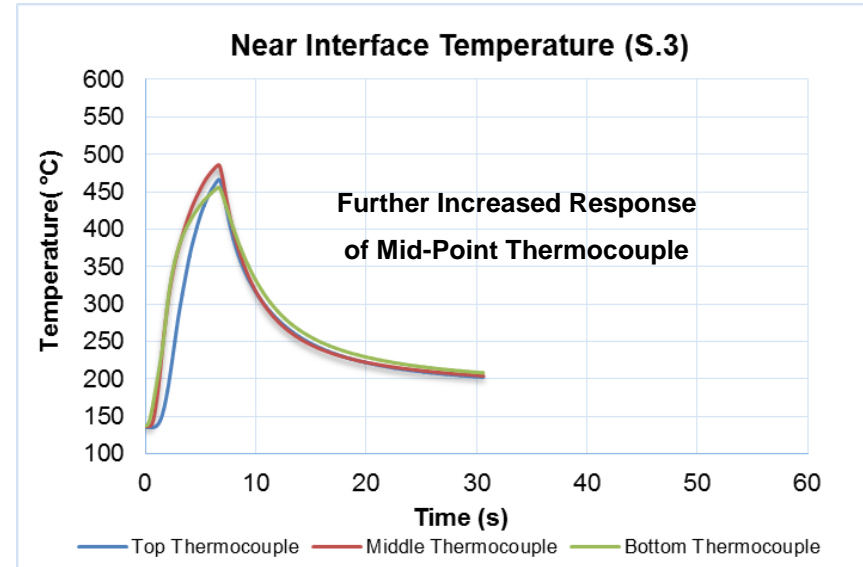
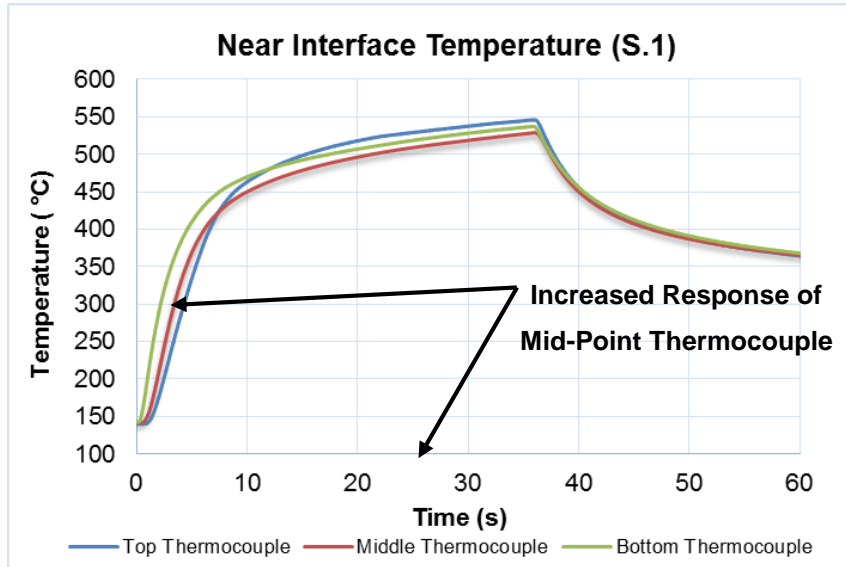


Figure 5-13. Near Interface Temperature for Welds S.1 to S.4

### 5.3.3. Microhardness Measurements for Welds S.1 to S.4

Figure 5-14 shows the Vickers microhardness readings of the as received and heat treated parent material. The 200°C preheat reduced the average hardness by 5.5%, correlating with the 2.8% drop in UTS. The 500°C heat treatment reduced the average hardness by 56.8% corresponding to the 44.85% drop in UTS, validating the link between hardness and UTS [2].

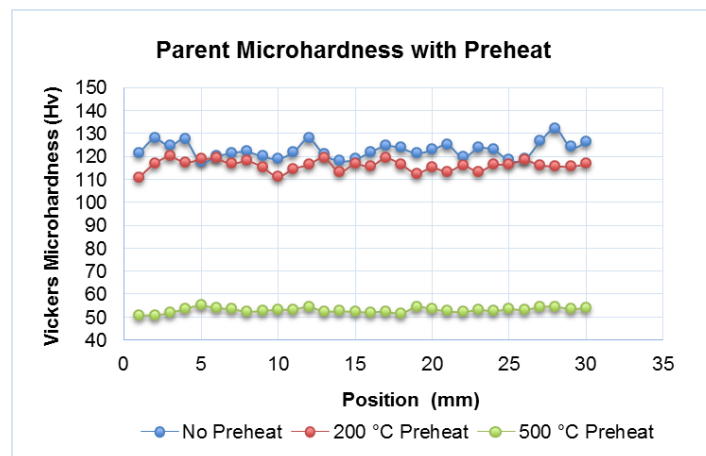


Figure 5-14. Vickers Microhardness of as received and Heat Treated Parent Plate (test done at 25g)

The microhardness profiles are given for Welds S.1 to S.4 in Figure 5-15. Weld S.1 was found to be almost fully softened due to the extended cooling time and slow cooling rates. Reducing the welding time prevented this, as all welds made above 40kN axial force began to recover to near parent plate hardness towards the edge of the plate. For Welds S.2 to S.4 the minimum hardness values are found in the HAZ, beyond the weld sidewall interfaces, marked in Figure 5-15. Therefore, the interface is not the softest zone in the weld. The weld nugget showed hardness ranging between 75HV and 108HV which is similar to the 94HV of the parent stud material. The dynamically recrystallized material making up the weld nugget is, therefore, approximately as hard as the parent stud material with the T-6 temper intact, showing the increased material properties due to the friction processing and grain refinement. The microhardness in the mid region of Weld S.2 and S.3 were the only two to show reduced hardness at the interface, possibly because the region experienced the highest interface temperature past the point at which the interface travelled past the middle thermocouple point.

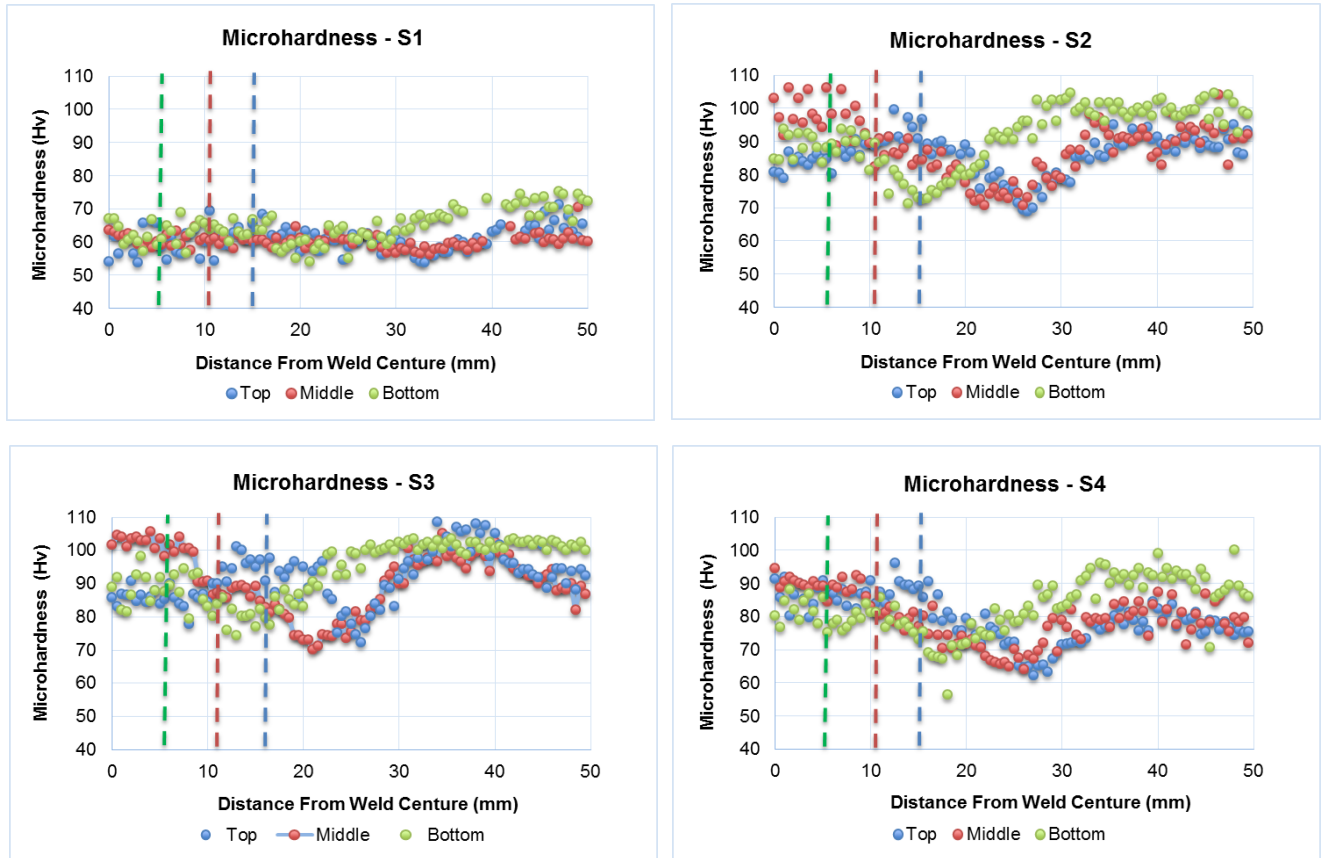


Figure 5-15. Microhardness Profiles of Welds S.1 to S.4

Table 5-4 shows the significant effect of increased welding force on the maximum and minimum hardness, found within the weld nugget. The maximum recorded values ranged from 70.2HV to 108.6HV with axial forces of 40kN to 80kN respectively. It also shows the minimum hardness increased with increasing axial force and reduced with rotational speed, correlating with the reduced formation of AGG with increased axial force and the band of AGG formed at the base of weld S.4 at reduced rotational speed.

Table 5-4. Maximum and Minimum Recorded Microhardness in the Weld Nugget of welds S.1 to S.4

	S1	S2	S3	S4
Maximum (HV)	75.1	106.3	108.6	100.2
Minimum (HV)	53.7	69.0	70.2	56.3

The microhardness values at the interface between the plate and the weld nugget are given in Table 5-5. The effect of increasing axial force on interface hardness is clear, increasing directly with increased force. The effect of AGG is not

identified as the levels of hardness tested omit the lower region if the weld and focus along the base of the hole. Hardness values close to that of parent plate are again recorded, indicating the integrity of the joint with respect to hardness. This indicated that the achievable joint strength far surpasses that which has to this point been achieved, as Weld S.3 had near identical UTS to the heat treated parent plate, however Weld S.3 had significantly higher hardness values throughout. This shows that that the lack of joint integrity is due to unbounded regions at the interface, as the FTSW process did not soften the weld zone as severely as the annealing heat treatment process applied in Figure 5-14. This is verified by the dye penetrant testing and fracture surface analysis results. It was further observed that Weld S.1 had interface hardness equal to the 500°C heat treated parent sample, yet failed well below the 170.46MPa achieved by the parent sample. Therefore, though there were no visible voids in the dye penetration test, grain interaction (interface bonding) was poor in certain regions, giving a poor joint due to insufficient axial force to produce bonding. Therefore, welds with significantly higher tensile properties can be achieved if the bonding across the interface is improved, with the microhardness data indicating that the HAZ will be the weakest point, which according to hardness chart of AA6063-T6 will be in the range of 210MPa, based on hardness values recorded in the HAZ [2].

**Table 5-5. Vickers Microhardness at Welding Interface for Welds S.1 to S.4**

	Distance to Interface	Data Point Used	Hardness (S1)	Hardness (S2)	Hardness (S3)	Hardness (S4)
	(mm)	(mm)	(HV)	(HV)	(HV)	(HV)
Top	14.815	14.5	60.5	94.19	97.14	88.24
Middle	10.485	10.5	60.3	82.44	86.52	81.27
Bottom	5	5	59.07	83.63	91.84	85.68

#### **5.3.4. Residual Stress Analysis of Welds S.1 to S.4**

The Synchrotron measures residual strain and hence stress by measuring the distance between atoms. This is then converted to strain by the standard strain calculation given in Equation 5-1. However, a reference A0 radial and A0 hoop is needed, which is effectively the original spacing of an un-deformed material in the radial and hoop orientation. As no reference parameter of A0 was available, as an un-welded section of plate was not scanned, an A0 Hoop and A0 Radial

lattice parameter was assumed as the average lattice spacing of all the points recorded in the hoop orientation during testing only, giving a starting point of 4.051996.

$$\varepsilon = \frac{A - A_0}{A_0} \quad \text{Equation 5-1. Strain}$$

Assuming the strain values to be the principal strains, the preliminary stress hoop and radial were calculated using Equation 5-2 and Equation 5-3 respectively. This gave the hoop and radial stress relative to the assumed reference  $A_0$  parameters. To calculate the true lattice parameter for hoop and radial strain the following assumptions were made:

- The sum of all the hoop stresses are assumed to be equal to zero,
  - The final radial stress value, taken on the side of the plate were assumed to equal zero and
  - The sum of the radial and hoop stresses were assumed to equal zero.
- These governing limits are displayed in Equation 5-4 .

$$\sigma_{hoop} = \frac{F}{(1-\nu^2)} \times [\varepsilon_{hoop} + \nu\varepsilon_{radial}] \quad \text{Equation 5-2. Hoop Stress}$$

$$\sigma_{Radial} = \frac{F}{(1-\nu^2)} \times [\varepsilon_{Radial} + \nu\varepsilon_{hoop}] \quad \text{Equation 5-3. Radial Stress}$$

$$\begin{aligned} \sum \sigma_{hoop} &= 0 \\ \sigma_{radial}(surface) &= 0 \\ \sum \sigma_{hoop} + \sigma_{radial} &= 0 \end{aligned} \quad \text{Equation 5-4. Governing Limits}$$

With these governing limits, Solver in Excel was used to find the closest match for  $A_0$  hoop and  $A_0$  radial, with the results given in Table 5-6. Good results were obtained with a standard deviation of 18.1MPa in surface radial stress remaining after solving, with minimum and maximum radial stresses at the surface of the plate between the three levels of testing of -14.72 to 10.8MPa, giving appropriate lattice parameters. The residual radial and hoop stress plots for welds S.1 to S.44 are given in Figure 5-17 and Figure 5-16 respectively.

Table 5-6. Solver Results for Lattice Parameters A0 Hoop and A0 Radial

A0 Hoop	4.054564
A0 Radial	4.047178
$\sum\sigma$ hoop (MPa)	0
$\sum\sigma$ radial (MPa)	0
$\sigma$ radial Max (MPa)	10.8
$\sigma$ radial Min (MPa)	-14.762

The results show that the maximum radial stress points are located within the central region of the stud, with the stress shown to strive to zero towards the outer surface of the plate, as expected. High force welds such as S.3 have higher radial stresses in the central region of the stud, indicating high plastic deformation. Further no radial stresses appeared to be detrimental in magnitude to the welds; however, high radial stresses in the central region correspond with higher weld UTS. This may be an indicator that the weld experienced the least amount of rubbing and, therefore, excess heat energy, following the same trend as microhardness, dipping towards the central region of the weld. The offset of the top radial stress for Welds S.2 and S.3 is, therefore, induced by the offset of the temperature response at lower rotational speeds. The near overlapping temperature response gave near overlapping hoop stress response, identifying a possible link between temperature response, UTS, microhardness and hoop stress. However, energy input data was not available for these welds for further confirmation.

The hoop stress for 40kN welds was found to be neutral, corresponding with the microhardness values and thermal saturation of the plate. The excessive input heat relieved any stress induced by the welding process. The hoop stress plots show that welds with good UTS have elevated hoop stress at the weld centre and weld interface, approximately above 50MPa. A drop in the central hoop stress is seen for Weld S.3, corresponding with the un-cracked formation of the primary and secondary flash, indicating softening and relieving by thermal saturation.

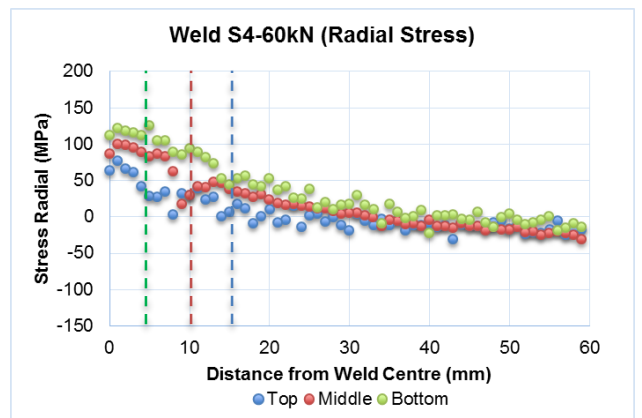
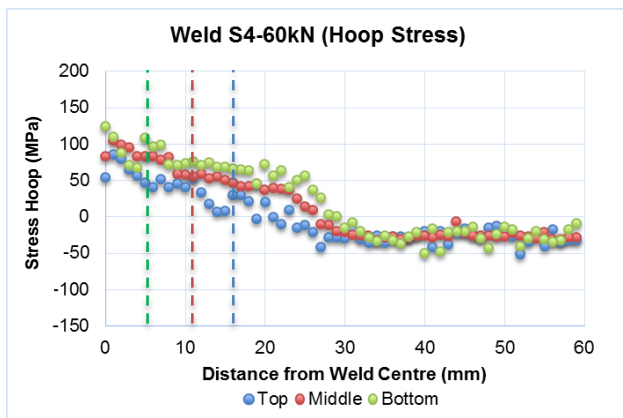
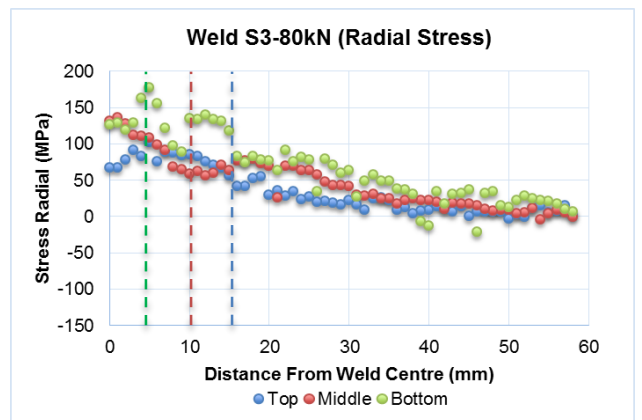
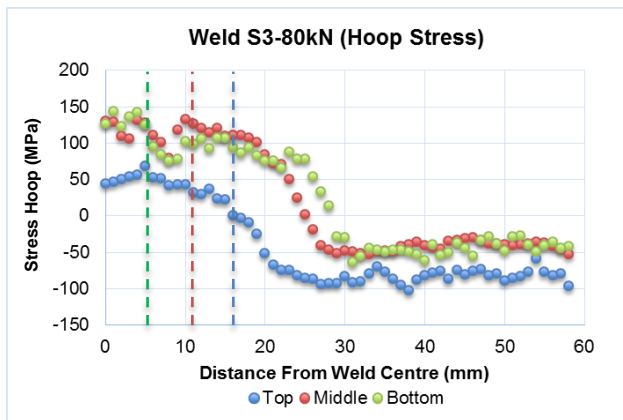
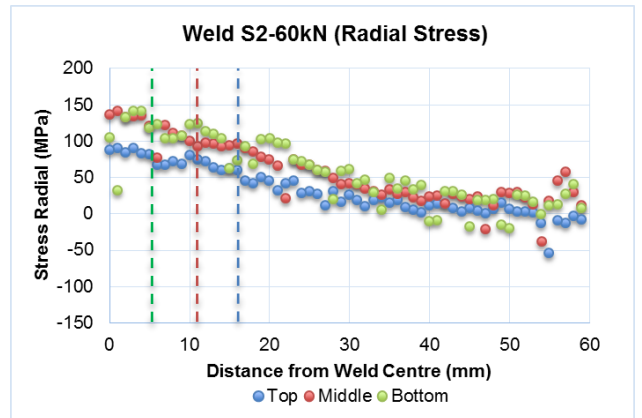
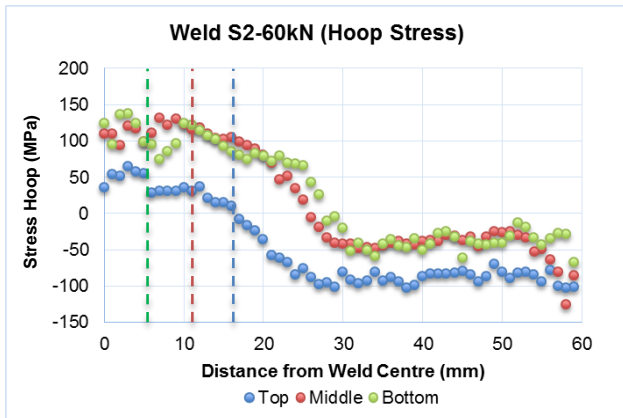
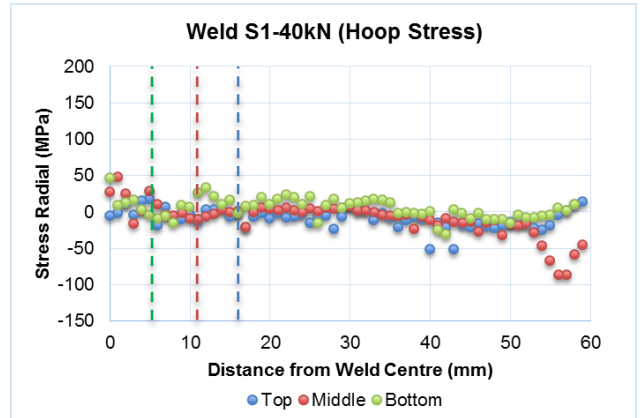
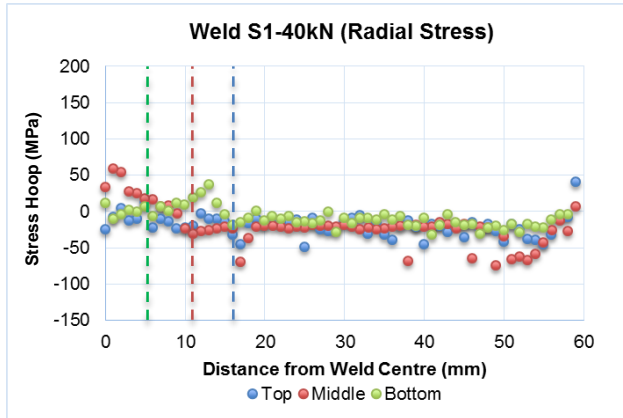


Figure 5-17. Residual Radial Stress Curves for Welds S.1 to S.4

Figure 5-16. Residual Hoop Stress Curves for Welds S.1 to S.4



### 5.3.5. The Effect of Axial Force and Rotational Speed on Texture

EBSD was used to develop texture Maps, grain size maps and residual strain maps and grain size maps as methods to quantifying the effect of FTSW at the bond line between the parent plate and weld nugget in the mid region of the hole. The definition of grains and, therefore, grain boundaries is a function of the misorientation between crystallographic lattices. A Misorientation angle of  $8^\circ$  was identified for Welds S.1 to S.4 as shown in Figure 5-18. This omitted the noise within the spectrum while maintaining the peaks identified as grain boundary orientations.

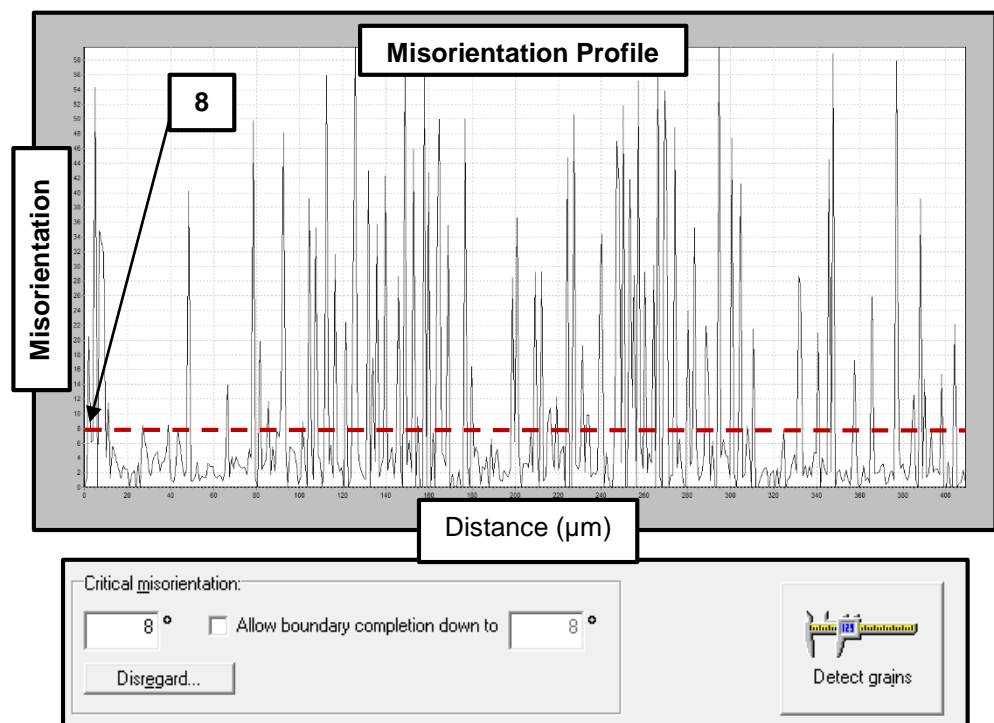


Figure 5-18. Misorientation Angle for Grain Boundary Identification

The all Euler maps with Band Contrast for Welds S.1 to S.4 are given in Figure 5-19 to Figure 5-22. The band contrast maps, residual strain maps, grain size maps are given in Appendix M for reference. The results show significant grain refinement at the weld interface with increased axial force, with less grain refinement and a more homogeneous interface produced at reduced rotational speed, shown in Figure 5-22 and Appendix M. Low axial force welds show no preferred grain orientation, while high force and low rotational speed show a distinct orientation at the interface between the weld nugget and flash. Significant

grain growth can be seen in the parent plate for weld S.1, showing the dramatic affect welding times as high as 35 seconds has on an AA6082-T6 FTSW.

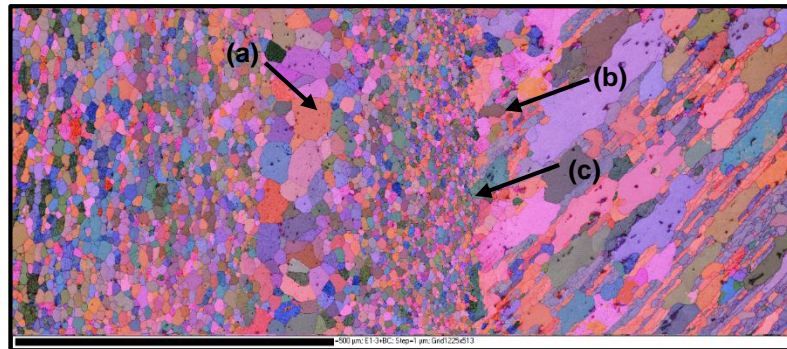


Figure 5-19. All Euler Map of Weld S.1 (40kN-5000RPM)

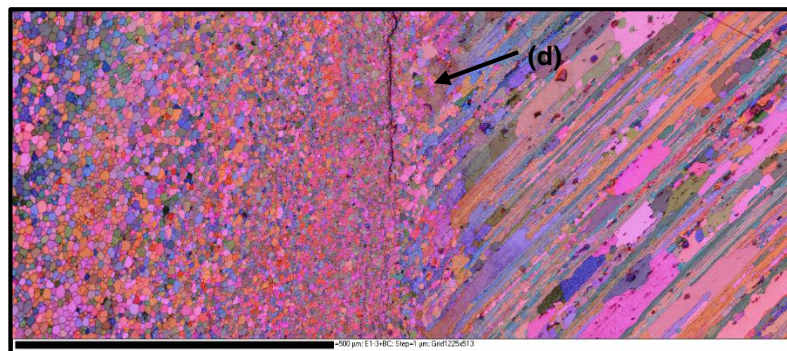


Figure 5-20. All Euler Map of Weld S.2 (60kN-5000RPM)

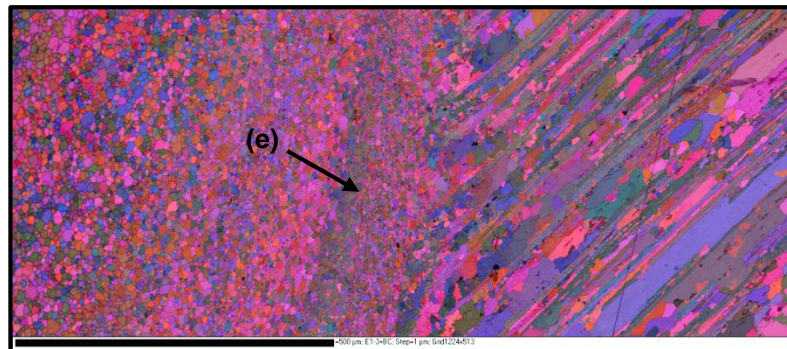


Figure 5-21. All Euler Map of Weld S.3 (80kN-5000RPM)

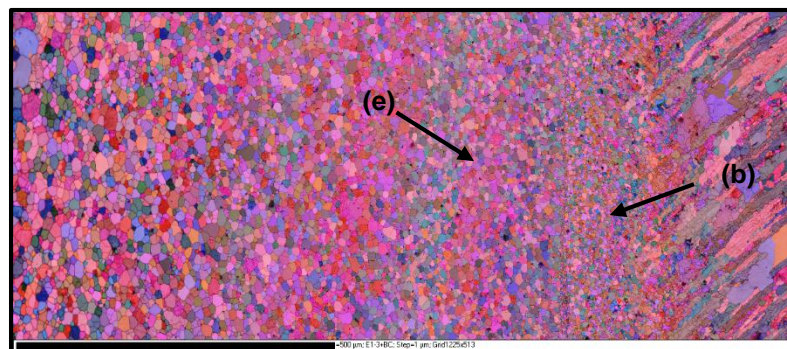


Figure 5-22. All Euler Map of Weld S.4 (60kN-3000RPM)

(a) Weld Nugget Flash Interface (b) Parent Plate Flash Interface (c) Flash  
(d) Fine Poorly Bonded Grains (e) Preferred Orientation Band

#### 5.4. The Influence of Axial Force Ramp up Rate using a 60° Hole

Axial force ramp up rate has been identified as the most critical parameter in an AA6082-T6 FTSW process, with the required rate seen to be material dependant. The work done in the previous section on Welds S.1 to S.4 identified that 75kN/s axial force ramp up rate is an appropriate starting point for the successful FTSW in AA6082-T6, as good welds were achieved. The welds further identified that the maximum joint integrity considered possible had not been reached, as all fractures were at the weld interface, not in the detrimentally over-aged HAZ. As the analyses of all the FTSW made to this point have shown axial force ramp up rate to be at the critical success parameter for FTSW of AA6082-T6 and that so little data is available for reference in literature, a test matrix of four welds was designed and tested to identify the window of the axial force ramp up rate for the successful FTSW of AA6082-T6.

The lowest axial force ramp up rate tested was 15kN/s, based on visually acceptable Welds TW-11, TW-12 and TW-21 which had an average ramp up rate of 16.3kN/s at 0.1 seconds. The second axial force ramp up rate tested was 45kN/s, located approximately between 16.3kN/s and the previously defined as appropriate 75kN/s. The 75kN/s axial force ramp up rate was included as the welding procedure was changed from this point forward in the research to having a soft start setup as discussed, and due to the reduced rotational speed selected for these tests. The highest axial force ramp up rate was determined experimentally by testing the limits of the PDS platform. It was found that at 120kN/s axial force ramp up rate and 80kN axial force, the process torque exceeded the capacity of the motor. Therefore, the axial force ramp up rate was limited to 110kN/s as the envisaged final test matrix appeared to be accomplishable at this limit. The rotational speed was reduced to 3000RPM, as it gave superior joint performance to 5000RPM at the same axially applied load. The axial force was held constant at 60kN, as this had produced good welds in previous tests, allowing the focus of these welds to be the axial force ramp up rate. The plunge depth was reduced to 2mm, as disproportionate flash formation, upper surface plate deformation and excessive AGG formation in Welds S.1 to S.4 had shown a plunge depth of 3mm to be excessive. The tests done from this point use the 18 times displaced volume vs. clearance volume factor as reference

for the plunge depth. The true plunge according to the calculation is 1.8mm; however, the plunge is rounded to 2mm to account for any small changes in deflection (as 0.2mm was found to be the variation in deflection readings at equal loads of 60kN on the PDS welding platforms). The process constants are given in Table 5-7 and the process parameter variables and combinations given in Table 5-8.

**Table 5-7. Process Parameter Constants for Welds RR-1 to RR-4**

Cooling Time (s)	20
Clearance Volume vs. Displaced Volume Factor	18
Base Area (mm <sup>2</sup> )	156.9
Hole Area (mm <sup>2</sup> )	1840.9

**Table 5-8. Process Parameter Variables and Combinations for Welds RR-1 to RR-4**

Weld No:	Rotational Speed	Plunge Depth (mm)	Axial Force (kN)	Axial Force Ramp up Rate (kN/s)	Preheat (°C) (Oven-Weld Temperature)	Stud\ Hole Angle (°)
RR-1	3000	2	60	15	200-140	55/60
RR-2	3000	2	60	45	200-140	55/60
RR-3	3000	2	60	75	200-140	55/60
RR-4	3000	2	60	110	200-140	55/60

The most visually apparent influence of increasing the axial force ramp up rate is the formation height of the final shear interface, seen in Figure 5-23. Increased axial force ramp up rate reduced the formation height from 16.6mm to 4.2mm when increasing from 15kN/s to 110kN/s. Furthermore, the reduced plunge depth prevented the development of a solid band of AGG at the base of the weld nugget, with only localised AGG seen at the fillet for axial force ramp up rates of 45kN/s and higher. The reduced plunge depth was found sufficient to form secondary flash as seen in Figure 5-24, with only a marginal increase noted between high and low axial force ramp up rates. This was expected as the secondary flash formation is predominantly dependent on the axial force, as shown in Section 5.3 on page 146. Dye penetrant tests showed no sidewall voids for all welds, with

only cold forge defects visible at the base of the hole for all but Weld RR-4 as given in Appendix H. The improved secondary flash and lack of void formation shows the improvement in weld quality with the soft touch welding setup, with Weld RR-3 achieving superior secondary flash to weld S.4, though RR-3 had 1mm less plunge depth, identifying the touch force as an additional critical parameters that will need to be quantified in future research.

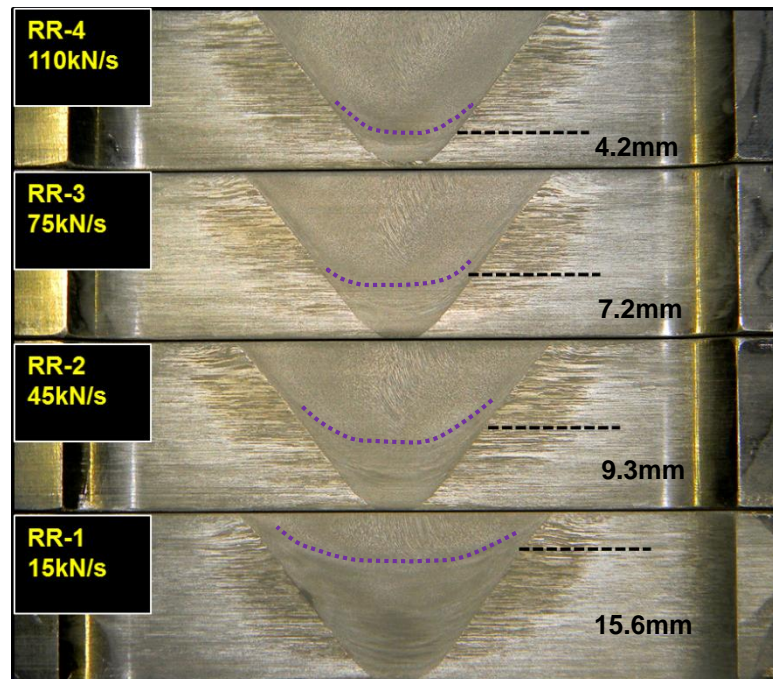


Figure 5-23 Etched Tensile Samples showing Height of Final Shear Interface with respect to Axial Force Ramp up Rate Welds RR-1 to RR-4

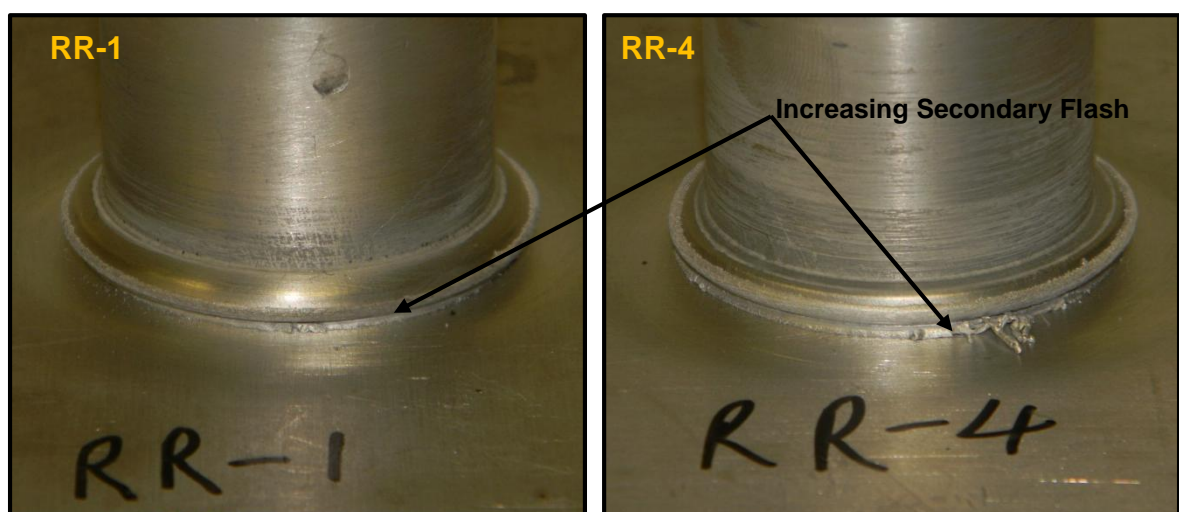


Figure 5-24. Flash Formation of Welds RR-1 to RR-4

The tensile results of Welds RR-1 to RR-4 are given in Figure 5-25. The results show that increased static joint integrity is directly linked to increased axial force ramp up rate. This confirms that this is the most influential control parameter in a FTSW in AA6082-T6, as 195MPa UTS was achieved at 110kN/s vs. the 59MPa UTS at 15kN/s. This test shows that without control of the axial force ramp up rate and free air plunge rate of the stud, successful FTSW in AA6082-T6 is not possible. The results further show that tensile strengths above that of the fully annealed parent material is attainable, as discussed in Section 5.3. The tabulated results for UTS of welds RR-1 to RR-4 are given in Table 5-9.

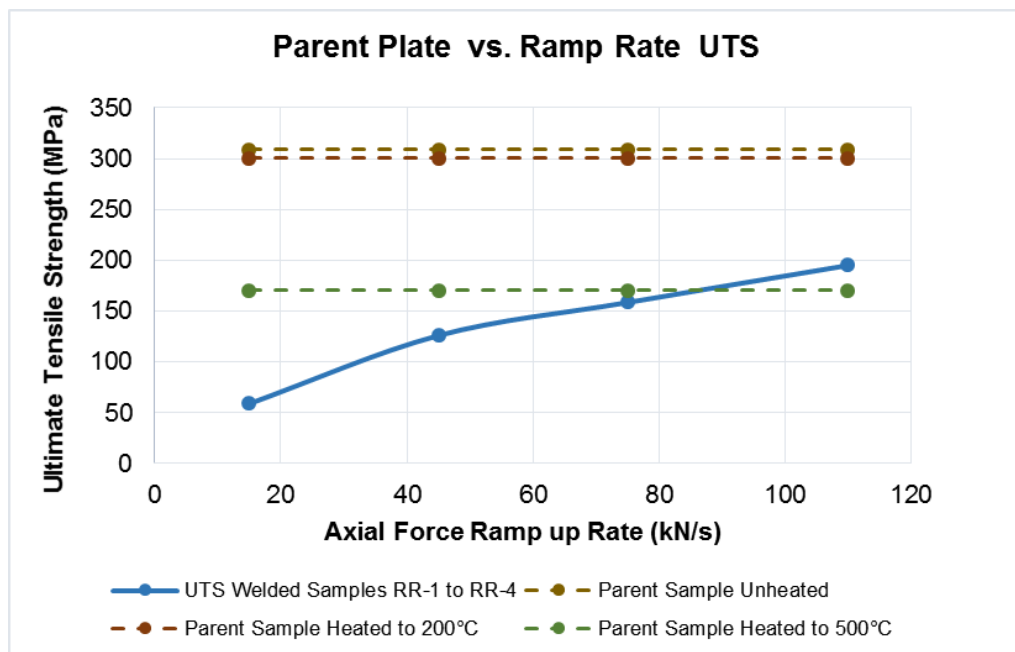


Figure 5-25. Tensile Strength vs. Axial Force Ramp up Rate for Welds RR-1 to RR-4

Table 5-9. Tensile Results for Welds RR-1 to RR-4

Weld No:	UTS (MPa)
RR-1	59.0
RR-2	126.0
RR-3	191.2
RR-4	195.0

#### **5.4.1. Influence of Axial Force ramp up Rate on Process Torque for Welds RR-1 to RR-4**

The process torque, applied axial force, plunge depth and rotational speed are given for welds RR-1 to RR-4 in Figure 5-26. For reference for all charts displaying plunge depth from this point forward, it must be noted that the plunge depth curve must not be interpreted as accurate until the set axial force has been reached. This is because of deflection in the welding platform. As the axial force is applied the system registers plunge depth as the frame of the system deflects. Once the set axial force has been reached, the frame will hold its position and the plunge depth can be considered accurate. For reference the deflection for the PDS welding platform is approximately 1.1mm at 60kN axial force, with a deviation of approximately 0.1mm.

Increased axial force ramp up rate directly increases the slope and magnitude of the process torque curve to PSTP as shown in Figure 5-26, with the time to PSTP reducing from 2.06 seconds to 1.13 seconds as given in Appendix F. This shows axial force to reduce the width of the heated band of stud material above the welding interface as previously noted in Chapter 3, by increasing the axial force in the first moments of welding. This brings cold material forward to the weld interface, causing the increased process torque. This is the mechanism that drives the reduced formation height of the final shear interface in the hole at high axial force ramp rates, as welding time is seen to remain constant. Welding time is, therefore, only axial force, rotational speed and geometry dependant.

No violent shears at the PSTP were noted, with reduced axial force ramp up rate welds experiencing shearing during the climb to PSTP, specifically evident in Weld RR-1. The manifestation of these sluggish shears are a clear indication that the applied axial force is insufficient. The process torque at seizure increased from 19.2 to 77.8Nm for welds RR-1 to RR-4, showing the axial force ramp up rate and hence increased applied axial load to play a critical role in bringing cold material forward as discussed. This rate needs to be sufficient to maintain high process torque during plunge, preventing the shearing during the climb to the PSTP of weld RR-1 in Figure 5-26. The high process torque promoted plastic deformation of the plate at the weld interface, promoting

penetration. It was noted that the equalised process torque was the same for all RR welds (Approximately 60Nm). Also it was found that the process torque only equalised once the set axial force was achieved and a continuous axial force was applied, and that welds RR-2 to 4 achieve equalised torque at approximately the same time (2.8 seconds to 3 seconds). This is at approximately 0.65mm plunge for the three welds and is the point at which the hole is filled with flash.

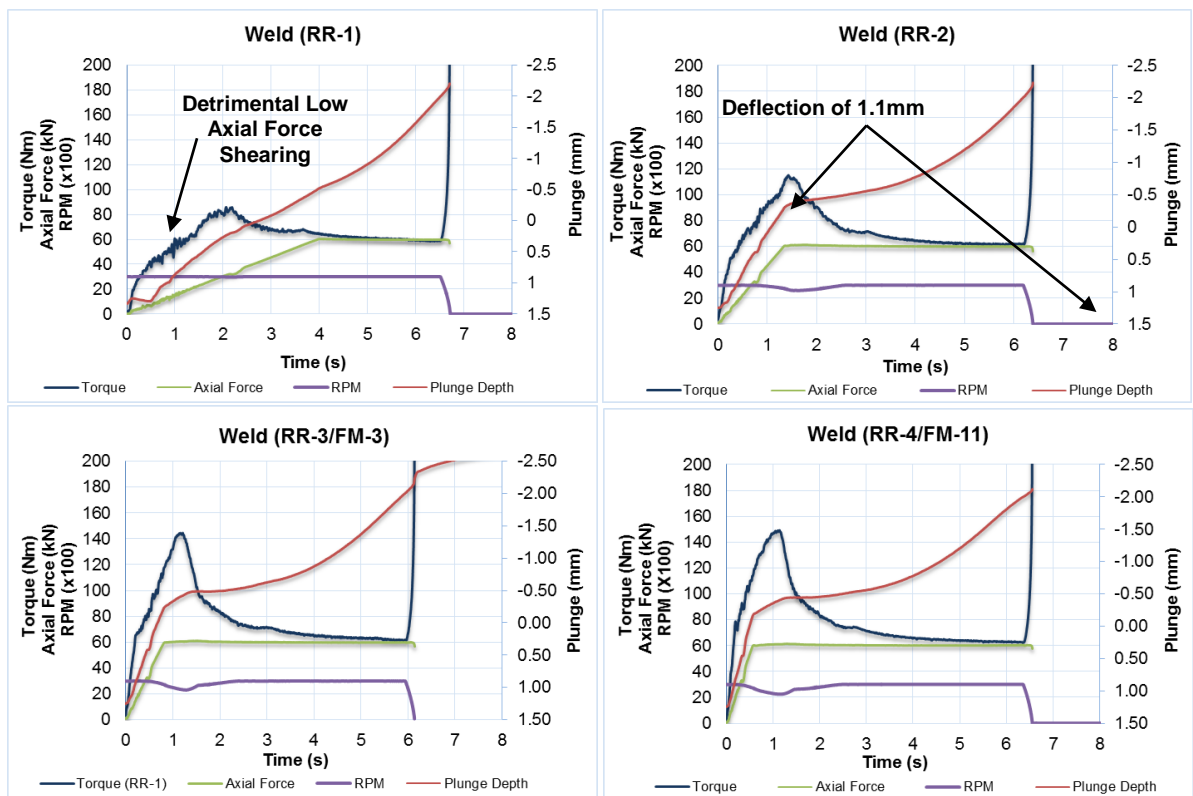


Figure 5-26. Weld RR-1to RR-2 Recorded Process Data

#### 5.4.2. The effect of Axial Force Ramp up Rate on Energy Input for Welds RR-1 to RR-4

The analysis of energy input given in Table 5-10 showed that increased axial force ramp up rate directly increased the energy input at 0.1 seconds, seizure, PSTP and total energy input, corresponding with the increased tensile strength noted. The energy input at 0.1 seconds increased from  $1.3\text{J/mm}^2$  to  $4.5\text{J/mm}^2$ , directly correlating with improvements recorded in Welds TW-1 to TW-22, identifying  $4.5\text{J/mm}^2$  to be the required energy input at 0.1 seconds for welds made at 3000RPM. It was expected that the total energy input would decrease with increases axial force ramp up rate; however, this was not found to be the case as shown in Table 5-10. The process torque in Figure 5-26 is shown to



increase while welding time remains constant. Therefore, welding time is found to be purely a function of axial force and not axial force ramp up rate. This is thought to be related to the magnitude of the equalised process torque curve, as increased axial force increases the equalised process torque as seen in previous welds. The process torque curve is also seen to equalise at approximately 3 seconds for welds RR-1 to RR-4 at a plunge depth of approximately 0.5mm, which has stud sidewall contact that is still low in the tapered hole at this point as shown in Figure 5-27. As the weld time and time to process torque equalization are similar for the four welds, a similar amount of input energy is put into the weld after the equalization point for all axial force ramp up rates. This shows axial force ramp up rate to have no effect on the point at which process torque equilibrium is reached, only effecting the energy input up to the equalised torque point. This occurrence of this point is, therefore, a function of the material and boundary conditions of the weld, not geometry or process parameter.

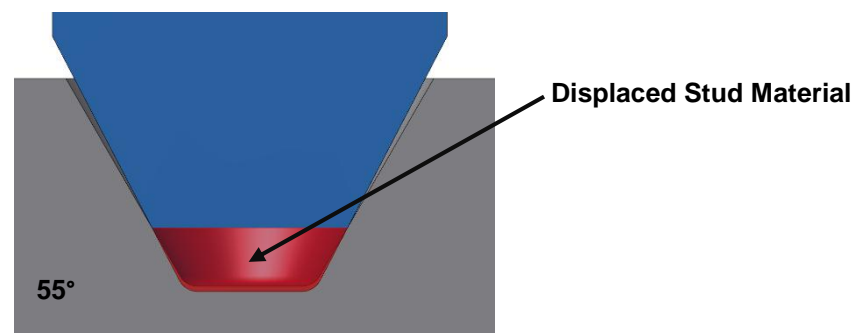


Figure 5-27. Displaced Stud Material at 0.5mm Plunge Depth

This is a critical observation as increased axial force applies a greater amount of energy into the same volume of displaced stud material for the first 3 seconds of the weld. This energy is therefore applied more directly and is converted to more localised heat that plasticizes and bonds the lower region of the plate, verified by the increase in near interface temperature response at the bottom of the hole with increased axial force ramp up rate as seen in Figure 5-28.

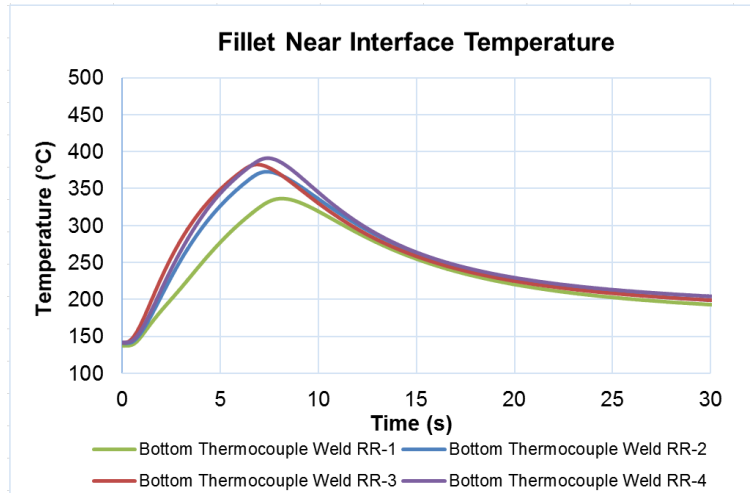


Figure 5-28. Temperature Response at the Fillet with increasing Axial Force Ramp up Rate

The near interface temperature of the plate in the mid and upper region is shown to not be influenced by axial force ramp up rate as seen in Figure 5-29, correlating with the occurrence of the equalised torque point. As the same amount of energy is put into the weld after 3 seconds, and the majority of the temperature response occurs post 3 seconds welding time, it follows that the axial force ramp up rate is not influential of the temperature in the upper region.

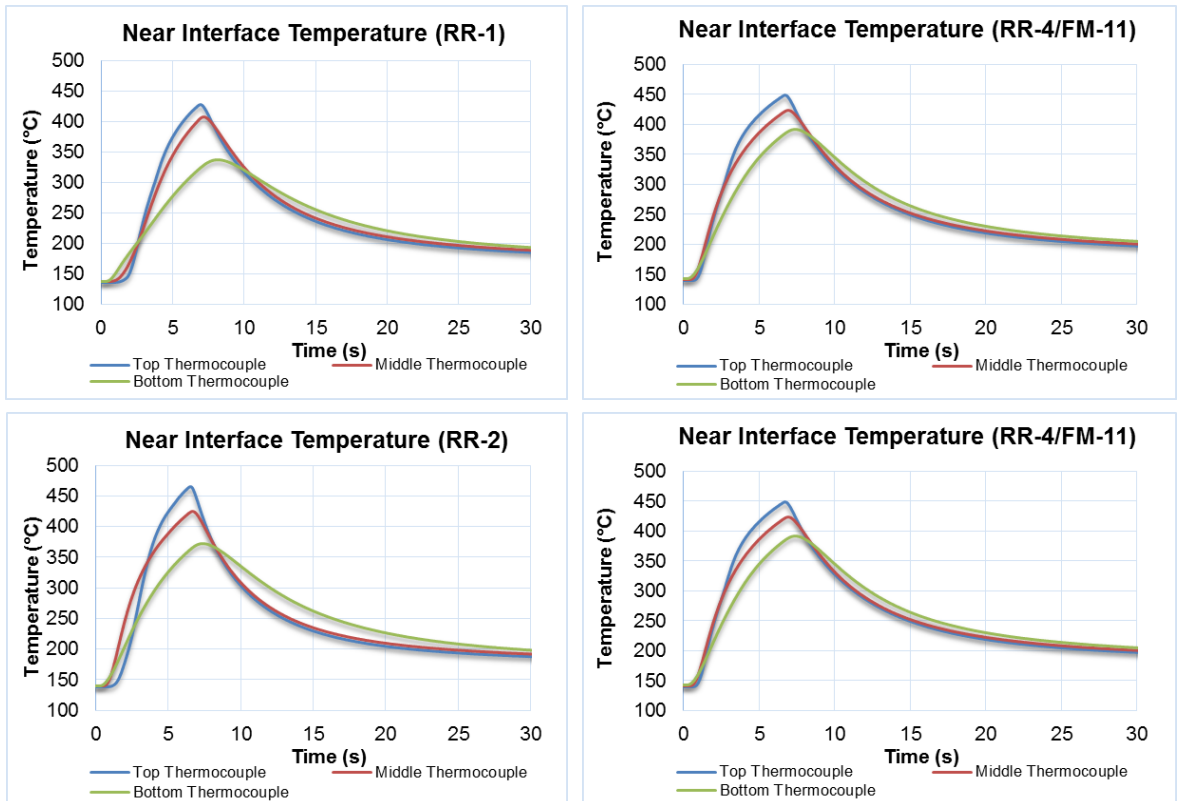


Figure 5-29. Near Interface Temperature Response for Welds RR-1 to RR-4

Increasing axial force ramp up rate is seen to increase the energy input rate throughout the weld, as shown in Table 5-10, showing energy input rates at various critical times into the weld. As this defines the energy that will be liberated at each shear of the dynamically recrystallized weld nugget, it follows that increased energy input rates input more direct energy that is applied over a small volume of material, promoting additional localised plasticization. This forces energy to be used for bonding, not heating the plate, as seen in Figure 5-29. For Welds RR-1 to RR-4, 14.8W/mm<sup>2</sup> to 75.5W/mm<sup>2</sup> was achieved at 0.1 seconds into the weld. As the increased energy input rate increases the input energy to locally deform (wear away) the surface roughness, the additional energy increases the bonding at the base of the hole as the heat has no time to conduct into the surrounding material, before layers of dynamically recrystallized stud material are deposited above the weld interface.

**Table 5-10. Results for Welds RR-1 to RR-4**

Weld No:	Welding Time (s)	Time to Seizure (s)	Torque at Seizure (Nm)	Energy Input at 0.1s (J/mm <sup>2</sup> )	Energy Input at Seizure (J/mm <sup>2</sup> )	Energy Input at 1s (J/mm <sup>2</sup> )(W/mm <sup>2</sup> )	Energy Input to PSTP (J/mm <sup>2</sup> )	Total Energy Input (J/mm <sup>2</sup> )	Energy Input Rate at 0.1s (W/mm <sup>2</sup> )	Energy Input Rate at Seizure (W/mm <sup>2</sup> )	Energy Input Rate at PSTP (W/mm <sup>2</sup> )	Total Energy Input Rate (W/mm <sup>2</sup> )	Forge Plunge Depth (mm)
RR-1	6.5	0.115	19.2	1.3	1.7	4.0	18.9	69.9	13.3	14.8	9.2	10.7	0.8
RR-2	6.2	0.250	51.0	2.9	14.7	10.4	17.3	75.2	28.6	58.7	12.1	12.2	0.9
RR-3	5.9	0.210	65.1	3.6	14.6	13.5	17.5	76.2	36.3	69.7	14.4	12.8	0.8
RR-4	6.4	0.185	77.8	4.5	14.0	15.3	17.4	82.7	45.2	75.5	15.4	13.0	0.7

### 5.5. Development and Testing of the Final Process Parameter Window using a 60° Hole

The results of Welds S.1 to S.4 and RR-1 to RR-4 clearly identified the operating window for the final stage of process development with regards to axial force ramp up rate, axial force and rotational speed. Axial force ramp up rate is identified as the most critical parameter to control during FTSW of AA6082-T6.

A minimum of 60kN/s has been identified to be crucial for the proposed material. Values of axial force ramp up rate of 45kN/s were found to achieve only 41% of the parent plate UTS (126MPa) which is well below the required weld requirement. Axial force is found to be the most influential process parameter in an AA6082-T6 FTSW with changes in axial force directly controlling the welding time. For the proposed hole geometry, relatively high axial force requirements were identified with a minimum axial force of 60kN shown to be necessary as welds made at 40kN axial force achieved only 8% of the parent plate UTS (23.3MPa). 60kN axial force achieved 34.16% to 61.9% of the parent plate UTS (105.6MPa to 191.2MPa). Rotational speed of 3000RPM, when compared to 5000RPM, was found to increase the static joint strength by 33% (34.8MPa), while also increasing the required process torque necessary to produce the weld from 115.2Nm to 149.5Nm. The upper limit of the rotational speed parameter was, therefore, identified to be 5000RPM.

Development welds showed that the clearance angle between the tapered hole and the tapered stud influenced the process torque curve, energy input and sidewall bonding of the weld. This is, therefore, an important geometric parameter to consider when FTSW is applied to AA6082-T6. Studs with included taper angles of more than 5° less than the tapered hole were found to allow flash to travel between the hole and stud body too easily, substantially reducing sidewall rubbing. A difference in stud taper of less than 2° less than the tapered hole was found to significantly increase the PSTP by preventing the flash from moving out of the hole, while also displacing insufficient stud material during plunge to promote good sidewall bonding of a 20mm deep hole with no stud and hole base clearance. The four process parameters mentioned above all contribute considerably to producing a good weld. Therefore, all will be considered in the final investigation, as critical interactions may not be realised if any of the parameters are omitted. The maximum and minimum parameter levels are therefore identified and tested, giving four parameters with two levels (16 combinations).

The upper and lower limits of the process parameters were selected as follows;

- The axial force ramp up rate limits were chosen as 75kN/s and 110kN/s. These produce good welds, with 110kN/s shown to be the limit for 80kN welds;
- The upper and lower axial force levels were chosen as 60kN and 80kN respectively, with both giving good static joint strength and 80kN being at the operating limit of the of the PDS welding platform;
- The maximum rotational speed was identified as 5000RPM, with the lower rotational speed as 3000RPM. The lower speed limit produced welds with superior static joint strength for the same applied axial force. Lower rotational speeds were not investigated as the sharp increase in process torques would exceed the capability of the PDS friction welding platform for the proposed geometry;
- The selected stud taper angle limits are 55° and 58°. Stud taper angles between 55° and 59° have been tested in development work for the 60° tapered hole, with 55° shown to repeatedly produce welds with good static strength characteristics. A 58° stud was selected as it would require a plunge depth of 0.8mm which is well within the achievable 0.1mm tolerance of the PDS friction welding platform.

The process constants are given in Table 5-11, with the process variables and combinations tested in the final study given in Table 5-12. Note that for reference, all process torque, rotational speed, plunge depth and axial force curves for welds FM-1 to FM-16 are given in Appendix J, with tabulated data given in Appendix F.

**Table 5-11. Process Parameter Variables for Welds FM-1 to FM-16**

Cooling Time (s)	20
Clearance Volume vs. Displaced Volume Factor	18
Hole Area (mm <sup>2</sup> )	156.9
Base Hole Area (mm <sup>2</sup> )	1840.98
Hole Taper Angle (°)	60
Preheat (Oven Temperature/ Weld Temperature) (°C)	200/140

**Table 5-12. Process Parameter Variables and Combinations for Welds FM-1 to FM-16**

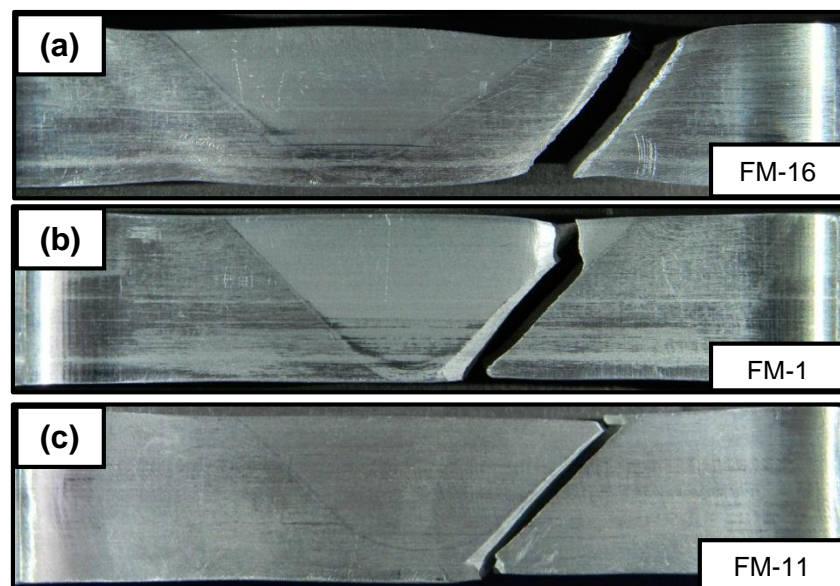
Weld No:	Stud Taper Angle (°)	Rotational Speed	Displaced Stud Material (mm <sup>3</sup> )	Plunge Depth (mm)	Axial Force Ramp up Rate (kN/s)	Plunge Depth (mm)	Axial Force (kN)
FM-1	55	5000	969.70	2.0	75	2	60
FM-2	55	5000	969.70	2.0	75	2	80
FM-3	55	3000	969.70	2.0	75	2	60
FM-4	55	3000	969.70	2.0	75	2	80
FM-5	58	5000	405.78	0.8	75	2	60
FM-6	58	5000	405.78	0.8	75	2	80
FM-7	58	3000	405.78	0.8	75	2	60
FM-8	58	3000	405.78	0.8	75	2	80
FM-9	55	5000	969.70	2.0	110	2	60
FM-10	55	5000	969.70	2.0	110	2	80
FM-11	55	3000	969.70	2.0	110	2	60
FM-12	55	3000	969.70	2.0	110	2	80
FM-13	58	5000	405.78	0.8	110	2	60
FM-14	58	5000	405.78	0.8	110	2	80
FM-15	58	3000	405.78	0.8	110	2	60
FM-16	58	3000	405.78	0.8	110	2	80

### 5.5.1. Fracture Mode Characterization and UTS for Welds FM-1 to FM-16

The dye penetrant testing of Welds FM-1 to FM-16 showed that the process parameter window developed for the final stage of the research produced welds with no sidewall or fillet voids between the tapered hole and weld nugget as seen for all the welds in Appendix H. Typically all welds showed a cold forge defect/lack of fusion at the base of the hole, with the exception of Weld FM-1 and FM-9 due to high values of total energy input and long welding time closing the void. Though the dye penetrant test did not show voids at the base of these welds, lack of fusion was observed under optical microscopy. This shows that increased axial force, axial force ramp up rate and the implementation of the soft start welding procedure produced FTSW in AA6082-T6 with superior sidewall bonding vs. the conventional setup applied to welds S.1 to S.4 that did not use the soft start and previous FTSW platform. As no sidewall voids were noted by

dye penetrant testing or optical microscopy, all macrographs are presented for welds FM-1 to FM-16 in Appendix D.

Tensile samples for Welds FM-1 to FM-16 were found to fracture in three modes, parent fracture (Mode 1), mixed mode fracture (Mode 2) and interface fracture (Mode 3), with examples of each shown in Figure 5-30, and all fracture macrographs given in Appendix I. Of the 16 process parameter combinations tested, ten failed in the parent material, four failed mixed mode and two failed at the interface. All welds achieved between 181.72MPa to 230.05MPa UTS, giving 58.8% to 77% of the as received parent material UTS. This exceeded the expectations of the researcher as welds with above 60% parent UTS had seemed unlikely in development work. The geometry and process parameter window designed for the final analysis was, therefore, well within the optimum process parameter window for producing FTSW in AA6082-T6 with good static joint performance. The tensile results for all welds are given in Table 5-13, with the welds with the highest UTS being parent material fractures. These welds all extended 6.7mm to 8.4mm before fracture, indicating a ductile tough material, vs. interface and mixed mode fractures that range from 2.3mm to 3.6mm. The amount of plastic deformation achieved with changes in fracture mode is clearly seen in Figure 5-30.



(a). Parent Fracture (Mode 1). (b). Mixed Mode Fracture (Mode 2).  
(C). Interface Fracture (Mode 3)

Figure 5-30. Fracture Modes of Welds FM-1 to FM-16

Table 5-13. Tensile Results of Welds FM-1 to FM-16

Weld Number	Recorded UTS (kN)	Recorded UTS (MPa)	Percentage Parent UTS	Percentage Heat Treated Parent UTS	Distance to Max Load (mm)	Distance to Fracture (mm)	Failure Modes
FM-1	43.7	181.7	58.8	106.6	2.4	3.6	2
FM-2	47.4	197.2	63.8	115.7	3.3	4.5	2
FM-3	45.7	191.2	61.8	112.1	3.0	3.1	3
FM-4	54.4	225.2	72.8	132.1	7.5	10.4	1
FM-5	50.0	208.1	67.3	122.1	x	X	3
FM-6	52.2	217.5	70.4	127.6	7.8	10.0	1
FM-7	52.5	218.7	70.8	128.3	8.4	10.7	1
FM-8	53.4	221.7	71.7	130.1	7.4	9.3	1
FM-9	52.5	214.9	69.5	126.1	7.1	9.5	1
FM-10	53.1	220.5	71.3	129.3	7.3	9.6	1
FM-11	46.8	194.3	62.9	114.0	3.2	3.5	3
FM-12	47.1	195.9	63.4	114.9	3.0	3.6	2
FM-13	51.0	211.9	68.6	124.3	7.7	9.3	1
FM-14	53.1	220.6	71.4	129.4	8.2	10.6	1
FM-15	51.2	212.5	68.7	124.6	6.7	9.1	1
FM-16	57.5	238.0	77.0	139.6	5.9	6.4	1

### 5.5.2. Flash Formation with respect to Process Parameters and Near Interface Temperature for Welds FM-1 to FM-16

The plastic deformation of the upper surface plate as shown in Figure 5-31 (a) and (b) is similar for Welds FM-14 and FM-1 with Weld FM-14 having a 38.75MPa higher UTS than weld FM-1. This was a typical observation with respect to the flash formation of Welds FM-1 to FM-16, as the flash formation for these welds does not show any indication of joint integrity, as near optimum process parameters combinations were selected. If Welds FM-1 to FM-16, Welds RR-1 to RR-4 and Welds S.1 to S.4 are compared, the formation of a continuous flow of secondary flash is shown to be critical to produce a good complete FTSW in AA6082-T6, however cannot be used as the singular deciding feature. This is further demonstrated in Figure 5-32, which clearly shows a continuous ring of secondary flash formation on Weld TW-8. The weld which is discussed in



Chapter 3 had near appropriate axial force, rotational speed and plunge depth, however had little to no sidewall bonding due to low axial force ramp up rate, lack of preheat and incorrect hole and stud taper angles. From welds S.1 to S.4 and RR-1 to RR-4 it was shown that axial force ramp up rate is not influential in the formation of secondary flash, but is predominantly dependant on high axial force and rotational speed, corresponding with the flash formation of weld TW-8. The previous tests in this chapter further show that the formation of radial flash cracks are a good indication of excessive rotational speed and axial force parameter selection. As Welds FM-1 to FM-16 all have a continuous ring of secondary flash, it can be stated that all the welds were made using process parameter combinations that perform above the limits that can be judged by primary and secondary flash formation characteristics.



Figure 5-31. Flash Formation of Welds FM-1 to FM-16

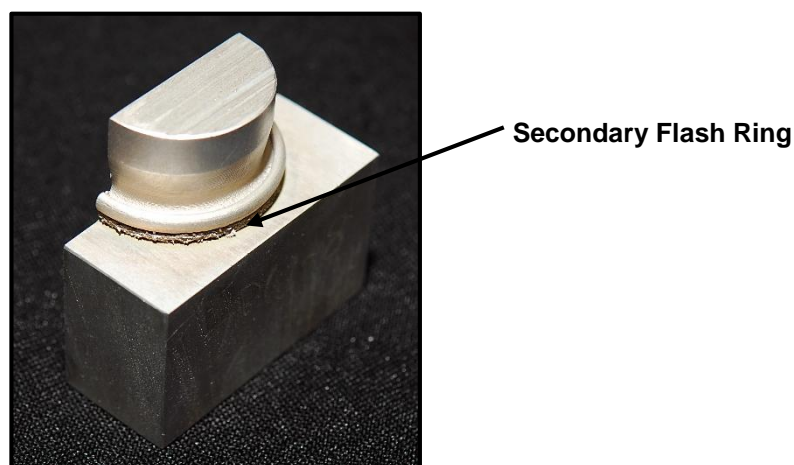


Figure 5-32. Secondary Flash Formation of Weld TW-8

A remarkable indicator, noted only in the flash formation of Weld FM-16, is the occurrence of good secondary flash formation around the periphery of the stud with no upper surface plate deformation. This weld experienced 248.9 °C near interface temperature at the top of the hole, which is a relatively low temperature compared to similar Weld FM-15 that reached 430°C at the top of the hole. This significant drop in maximum near interface temperature at the top of the hole is caused by a large reduction in rotational speed during welding, experienced repeatedly by Weld FM-16 and its tensile sample counterpart due to high process torques of  $\pm 500\text{Nm}$ . The reduced rotational speed and hence peripheral velocity near the top of the hole improve mixing at the interface and produces less excess energy due to reduced rubbing of the interfaces. This shows that a continuously reducing rotational speed in proportion to the increasing stud diameter during plunge will produce a superior weld, as was suggested by Thomas and Nicholas [49]. This is a possible direction for future development in FTSW of AA-6082-T6. The process torque curves and rotational speeds recorded during welding are given in Appendix J for all FM welds.

Though not fully conclusive, the visual assessment approach presented in this section is a critical judging method for welds in application or preliminary studies, as welds with incorrect axial force, rotational speed and plunge depth can be identified.

### **5.5.3. Influence of Process Parameters with respect to UTS**

Understanding the influence of process parameters on the static strength of the joint is critical to the selection of good process parameters that achieve the desired joint quality for the application and that suit the welding equipment available. The average, maximum, minimum and scatter of the measured UTS are given with respect to the high and low process parameter levels for Welds FM-1 to FM-16 in Table 5-14. The table is, therefore, an indicator of the average joint performance achieved with respect to the specified process parameter, considering the influence of all the weld combinations.

Table 5-14. UTS Results vs. Process Parameters

	Low	High
Speed	3000RPM	5000RPM
<b>Average</b>	<b>212.55</b>	<b>206.54</b>
<i>Max</i>	238.05	220.62
<i>Min</i>	191.16	181.72
Range	46.89	38.9
Axial Force	60kN	80kN
<b>Average</b>	<b>203.99</b>	<b>215.59</b>
<i>max</i>	218.73	238.05
<i>min</i>	181.72	195.89
Range	37.01	42.16
Ramp Rate	75kN/s	110kN/s
<b>Average</b>	<b>208.79</b>	<b>214.07</b>
<i>max</i>	225.16	238.05
<i>min</i>	181.72	194.3
Range	43.44	43.75
Stud Angle	55°	58°
<b>Average</b>	<b>208.78</b>	<b>219.06</b>
<i>max</i>	225.16	238.05
<i>min</i>	181.72	208.08
Range	43.44	29.97

From Table 5-14, the following observations with regards to the influence of process parameters of FTSW made in AA6082-T6 can be made;

- High rotational speed welds were shown to produce weaker joints overall than low rotational speed welds, with low rotational speed producing the strongest weld (FM-16).
- High axial force achieved the highest average UTS overall and the highest UTS for weld FM-16, achieving 19.4MPa higher than the strongest low force weld.
- High axial force ramp up rate achieved the highest average UTS and highest UTS. Though an axial force ramp up rate reduction from 110kN/s to 75kN/s reduced the maximum UTS by 12.9MPa, previous work on welds RR-1 to RR- 4 showed reductions in axial force ramp up rate to rapidly reduce to a critical value, below which no currently achievable process parameter alterations known to the researcher will produce a

good weld. This lower limit has been found to be approximately 45kN/s as shown in Figure 5-25 on page 173.

- A high stud angle gave the highest average UTS, highest UTS and highest minimum UTS, with seven out of eight parent material (Mode 1) fractures occurring with a 58° stud and three out of eight parent fractures with the 55° stud. This is predominantly due to increased energy input rates, reduced welding time and the retention of flash in the space between the stud and hole which encourages sidewall rubbing and plasticization. This is clearly displayed by the near identical near interface temperature response of welds FM-1 and FM-5 shown in Figure 5-33. This is significant as weld FM-1 displaced 969.7mm<sup>3</sup> of stud material and weld FM-9 displaced 405.78mm<sup>3</sup> of stud during plunge. Therefore as both welds had similar energy inputs and similar heating and cooling curves, the reduced displaced material for weld FM-5 experienced a greater input energy per unit of displaced stud material volume, hence increasing sidewall plasticization and increasing the joint strength from 181.7MPa to 208.08MPa.

In all cases, the strongest weld made at the parameter level producing the welds with the lower average UTS, is stronger than the weakest weld of the parameter level producing the strongest weld. This shows that the process parameter levels produce overlapping results. This is important, as depending on application, a high force weld with low rotational speed may fall outside the operating window of the FTSW platform available as it may be a platform with low axial force and high speed capability as is typical for mobile FTSW platforms intended for use on steels.

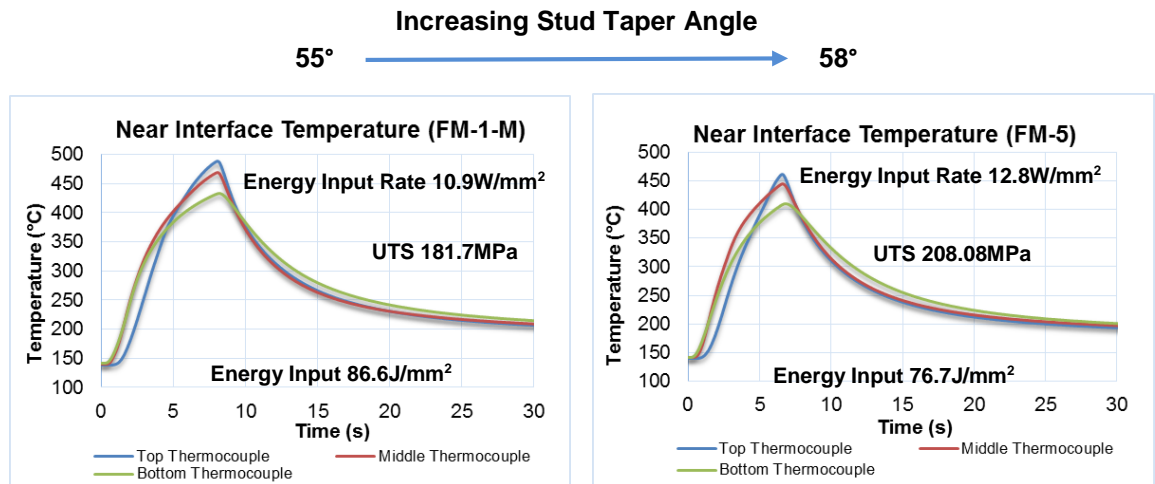


Figure 5-33. Near Interface Temperature Response for Welds FM-1 and FM-5

#### 5.5.4. Process Torque Analyses with respect to UTS, Energy and Temperature for Welds FM-1 to FM-16

The process torque recorded during welding has been discussed extensively up to this point in the research, with Weld RR-3 and RR-4 achieving what is considered to be ideal process torque curves. To this point no welds with high axial force ramp up rate and high axial force produced welds that experienced violent shears and shearing at the PSTP as seen in low axial force ramp up rate Welds TW-5, TW-7 to TW-8, TW-11 to TW-12, TW-16 to TW-17 and TW-20 to TW-22. Therefore, a good indicator of appropriate stud taper angle, axial force ramp up rate and stud strength retention (maintaining rotation of the stud in the hole) is the complete omission of violent shears and shearing at the PSTP. The process torque curves for Welds FM-1 to FM-16 showed that no violent shears or PSTP shearing occurred for all combinations tested. All the process torque curves for Welds FM-1 to FM-16 are given in Appendix J.

Reduced rotational speed increased the maximum process torque (PSTP) significantly. As discussed above in flash formation, process torques as high as 500Nm were recorded at the PSTP for high axial force, high axial force ramp up rate, high stud taper angles and low rotational speed welds. The reduction from 5000RPM to 3000RPM was found to increase the PSTP from a range of 51.4Nm to 64.3Nm to a range of 144.6Nm to 500Nm, showing rotational speed to have the most significant influence on the PSTP, correlating with process development

welds in Chapter 4 and Welds RR-1 to RR-4 in the current Chapter. As an example, Welds FM-8 and FM-6 have a UTS of 221.72MPa and 217.46MPa respectively. The increase in rotational speed reduced the joint strength by 1.92% while the maximum torque requirements reduced from 170.6Nm to 61.3Nm respectively. This is a 64% reduction in maximum torque. All process torque curves and tabulated torque and energy data is given in Appendix J and Appendix F respectively.

The analysis of the process torque curves for Welds FM-1 to FM-16 show that the magnitude and time of the PSTP could not be linked to static joint integrity, but rather to the omission of violent shears and PSTM shears. The main observation that can be linked to static joint integrity with respect to the profile of the process torque curve is the duration of the equalised torque stage. Welds with reduced joint integrity typically experienced an equalised process torque for an extended period of time. Figure 5-34 shows the shortening of welding time with increased axial force from 60kN to 80kN, between Welds FM-1 and FM-2 and Welds FM-9 and FM-10. The 33% increase in axial force is shown to reduce the welding time by 3.5 seconds and 2.7 seconds between Welds FM-1 and FM-2 and Welds FM-9 and FM-10 respectively. The increase in axial force ramp up rate is shown to reduce the welding time between Weld FM-1 and FM-9 by 0.7 seconds and have no significant effect between Weld FM-2 and FM-10. This was also observed in the analysis of axial force ramp up rate for Welds RR-1 to RR-4.

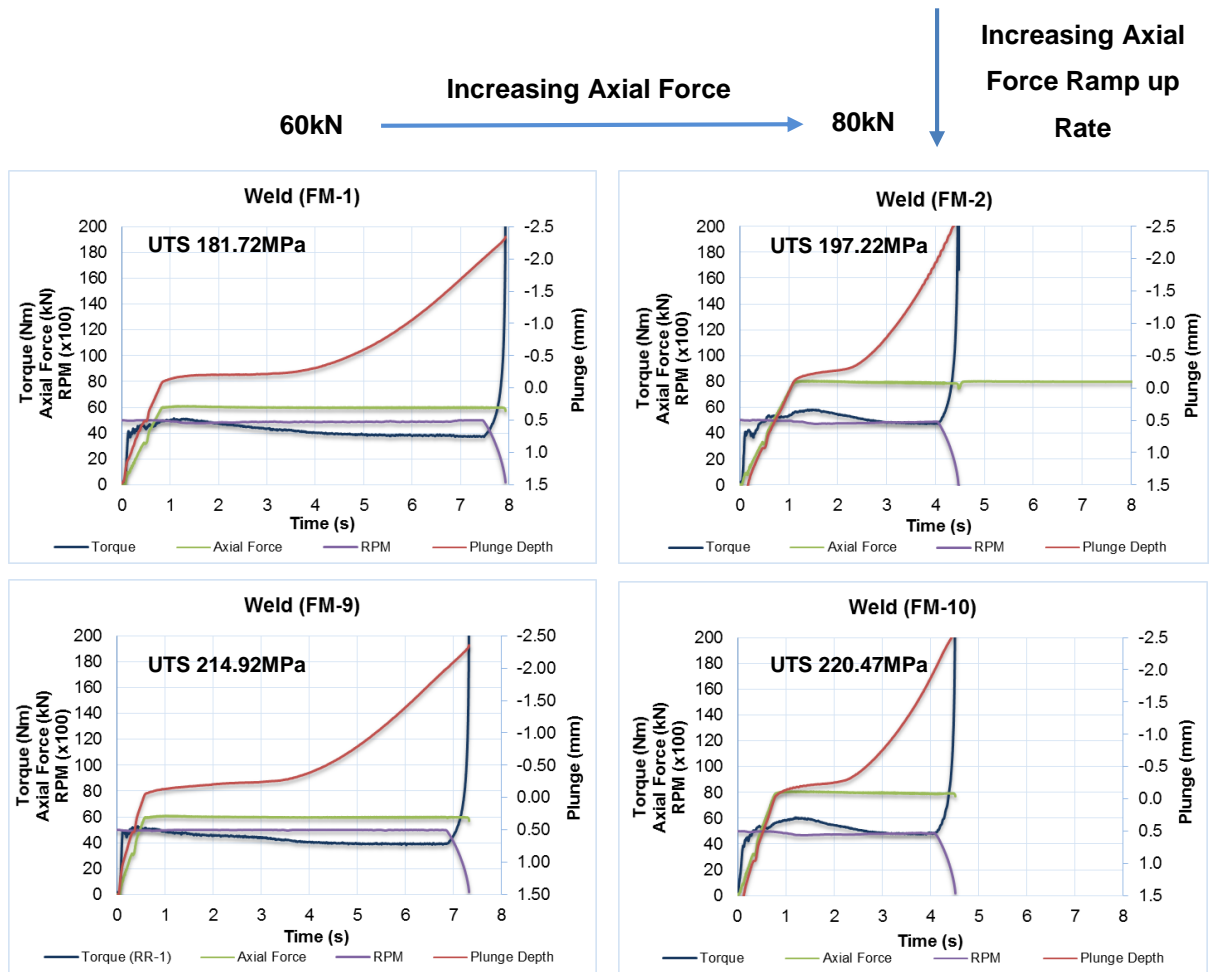


Figure 5-34. Influence of Axial Force and Axial Force Ramp up Rate on Process Torque at 5000RPM

If the near interface temperature response of Welds FM-1 and FM-2 are compared it is clear that the increase in axial force reduced the temperature response of the bottom thermocouple as shown in Figure 5-35. This shows that the increase in axial force caused the lower portion of the stud to bond and the welding interface to move up excessively fast due to overstressing the material at the nose of the stud. If the area of the nose of the stud is considered, the stress exerted at the bottom of the hole at the interface at the PSTP is 382MPa and 510MPa for Welds FM-1 and FM-2 respectively. As the material heats, the stress experienced by the nose of the stud is unsustainable and forces the shear interface to move up rapidly until a more sustainable interface stress is reached. This is characterised by a sudden reduction of energy input and energy input rate to the PSTP for Welds FM-1 and FM-2 from 12.8J/mm<sup>2</sup> to 7.9J/mm<sup>2</sup> and 11.9W/mm<sup>2</sup> to 5.3W/mm<sup>2</sup> respectively, this causes a significant drop in temperature at the bottom thermocouple as seen in Figure 5-35.

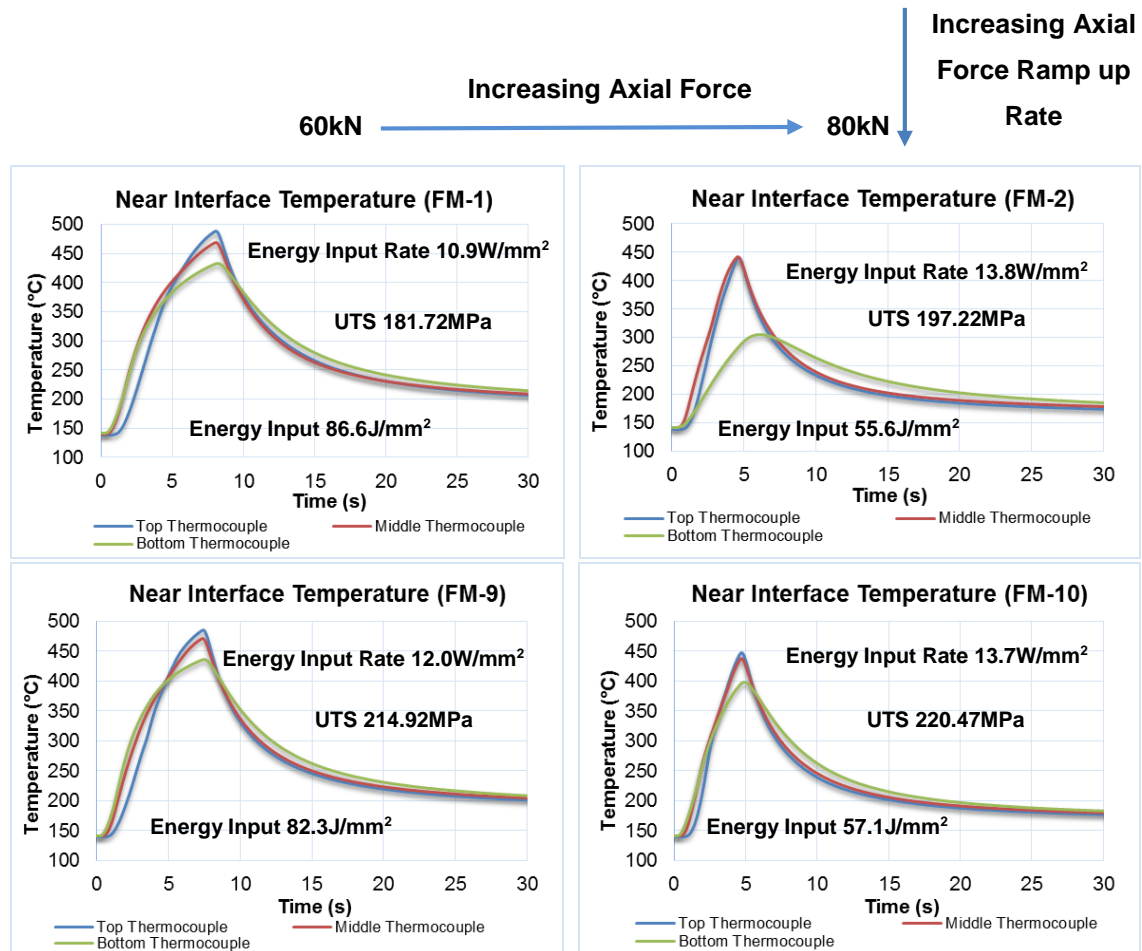


Figure 5-35. Near Interface Temperature Response for Welds FM-1 to FM-10

The effect of low temperature at the base of the hole is clearly evident at the fillet of the weld, shown in Figure 5-36. The plastic deformation and bonding at the fillet is reduced with increased axial force between welds FM-1 and FM-2, corresponding with the low temperature response. The plastic deformation of the plate is shown to increase with axial force ramp up rate between welds FM-2 and FM-10. This corresponds with observations noted when testing axial force ramp up rate on the near interface temperature at the fillet. This shows that increased axial force and axial force ramp up rate improves the static strength of the weld up to a limit, beyond which the bonding at the base of the weld is reduced with excessive interface pressure.



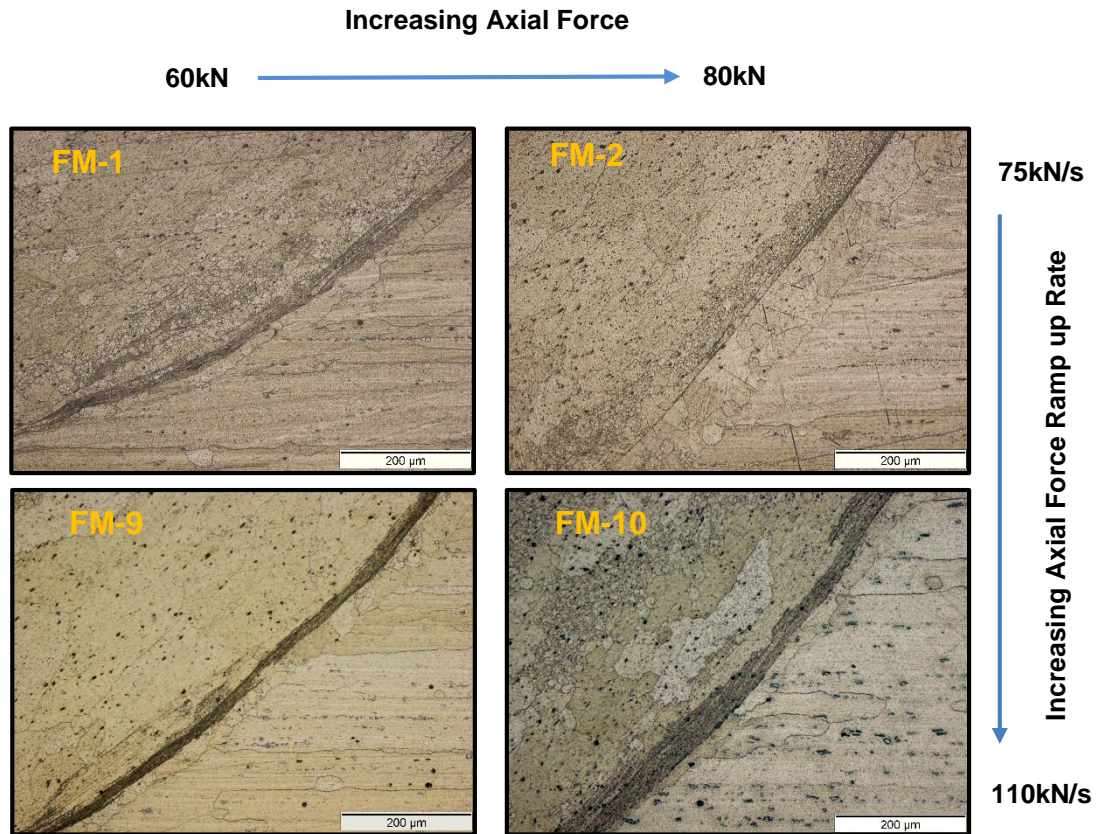


Figure 5-36. Micrograph of the Fillet of Welds FM-1 to FM-2 and FM-9 to FM-10

This is not highlighted in the tensile test data as 0.5mm of the fillet is removed when the tensile sample is machined, and the increased axial force ramp up rate considerably improves the sidewall bonding in the top region of the hole as shown in Figure 5-37. Weld FM-9 clearly has lack of bonding between the plate and weld nugget, while weld FM-10 has a more homogeneous interface. This increased bonding improves the overall static integrity of the joint. This shows that a sloped axial force ramp up rate is needed to fully optimise the efficiency of the joint. The microstructure of the fillet is discussed in more detail with respect to energy input further on.

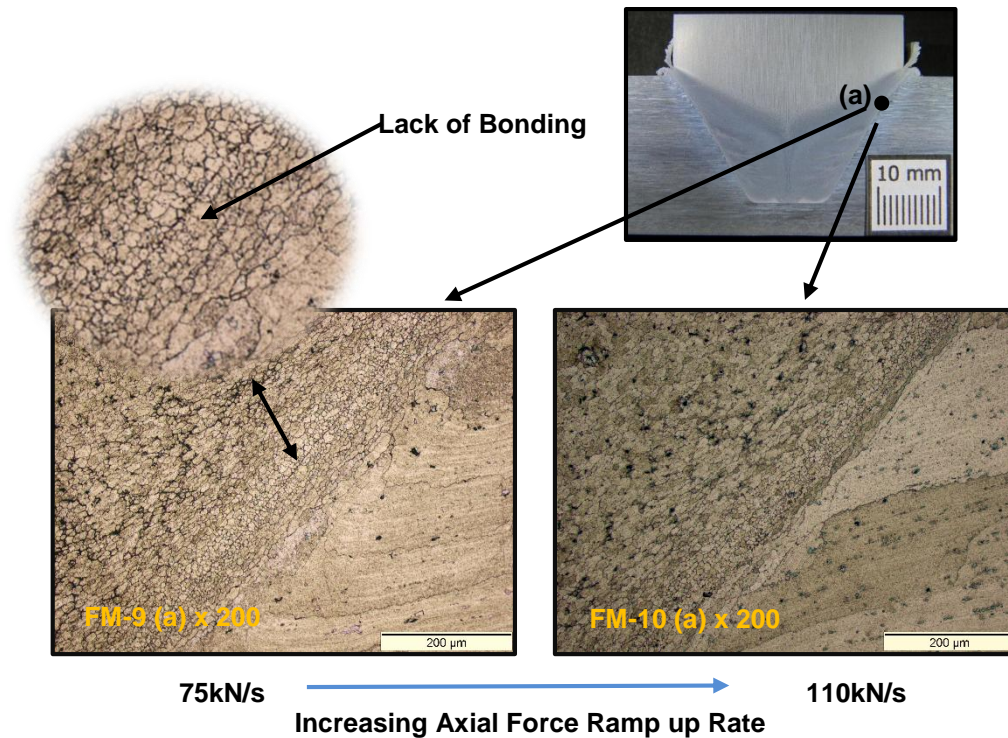


Figure 5-37. Micrograph at the Top of Welds FM-9 and FM-10 showing Lack of Fusion

The results show that increased axial force ramp up rate, improves the performance of the weld, until a critical point is reached where any further increase in axial force ramp up rate reduces the overall UTS and hence performance of the joint. This is seen between Welds FM-4 and FM-12, which are both high axial force welds made at 3000RPM. Figure 5-38 clearly shows the increased UTS between Welds FM-3 and FM-4 as the axial force increased from 60kN to 80kN, with the welds achieving 191.96MPa and 225.16MPa respectively. When the axial force ramp up rate was increased from 75kN/s to 110kN/s at 80kN axial force, the achieved UTS reduced to 195.89MPa for weld FM-12. This is the only combination to exhibit this reduced tensile strength with increased axial force ramp up rate. The occurrence is characterised in the process torque curve by the near omission of an equalised torque stage for Weld FM-12 in Figure 5-38. The curve shows that as the interface had reached the equalised torque stage, the plunge depth was reached and rotation stopped. This caused lack of bonding in the central region of the hole as seen in Figure 5-39. The lack of fusion in the central region is explained by energy input rates at the PSTP going from  $14.4\text{W}/\text{mm}^2$  to  $16.1\text{W}/\text{mm}^2$  for Welds FM-4 and FM-12 respectively. This shows that the  $55^\circ$  stud could not maintain an energy input

rate above  $14.4\text{W/mm}^2$  at 3000RPM. This shows the crest of the bell curve for axial force ramp up rate for a  $55^\circ$  stud at 3000RPM, where ramp up rate above  $75\text{kN/s}$  and values below  $45\text{kN/s}$  produce weaker welds. This gives an energy input rate range to the PSTP of  $12.1\text{W/mm}^2$  to  $14.4\text{W/mm}^2$  for 3000RPM welds using a  $55^\circ$  stud.

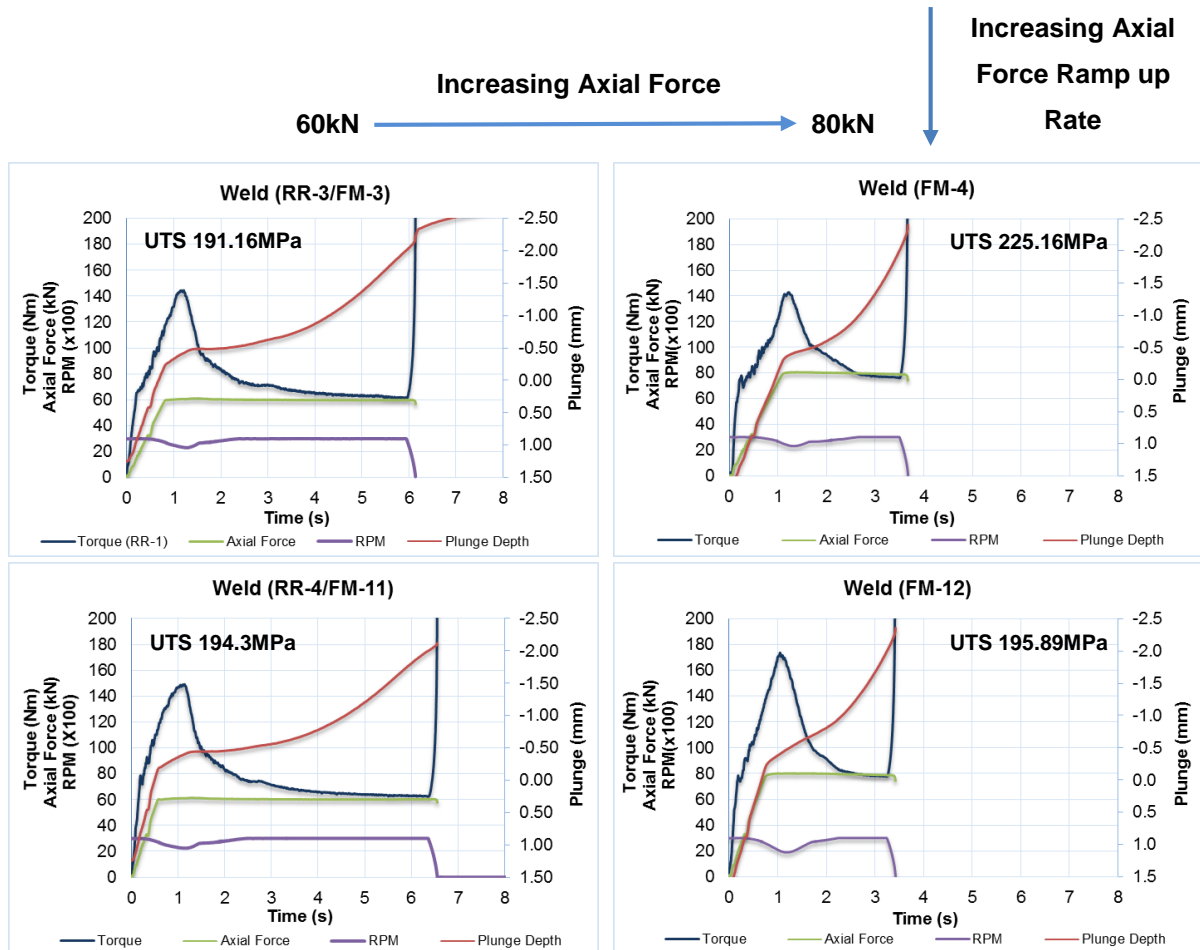


Figure 5-38. Influence of Axial Force and Axial Force Ramp up Rate on Process Torque at 3000RPM

The collapse of the stud body at 3000RPM under high axial force ramp up rates is prevented by increasing the taper angle of the stud. This increases the ability of the nose of the stud to support the axially applied load, as seen between Welds FM-8 and FM-16. Welds made at 3000RPM and using a  $58^\circ$  stud all had parent material Mode 1 fractures with energy input rates at the PSTP between  $14.7\text{W/mm}^2$  and  $17.1\text{W/mm}^2$  with  $17.1\text{W/mm}^2$  (Weld FM-16) having the highest static strength for both  $75\text{kN/s}$  and  $110\text{kN/s}$  axial force ramp up rate welds. This shows the  $55^\circ$  stud angles to be more suited to  $80\text{kN}$  axial force and  $75\text{kN/s}$  axial force ramp up rate at 3000RPM and  $110\text{kN/s}$  at 5000RPM, with rotational speed

only changing the UTS by 4.7MPa for welds FM-10 and FM-4 respectively. These welds have near identical energy input rates to the PSTP and end of the weld. This shows that increased rotational speed can be used to compensate for low axial force ramp up rate within a limited parameter window.

Similar trends are seen between all welds when similar parameters with different axial force and axial force ramp up rates are compared. All the process torque curves and tabulated torque and energy data is given in Appendix J and Appendix F respectively for reference. Process torque is therefore a good indicator of appropriately chosen process parameters, and can be used to verify that a weld has completed in the manner expected, however alone does not enable clear determination of a good weld.

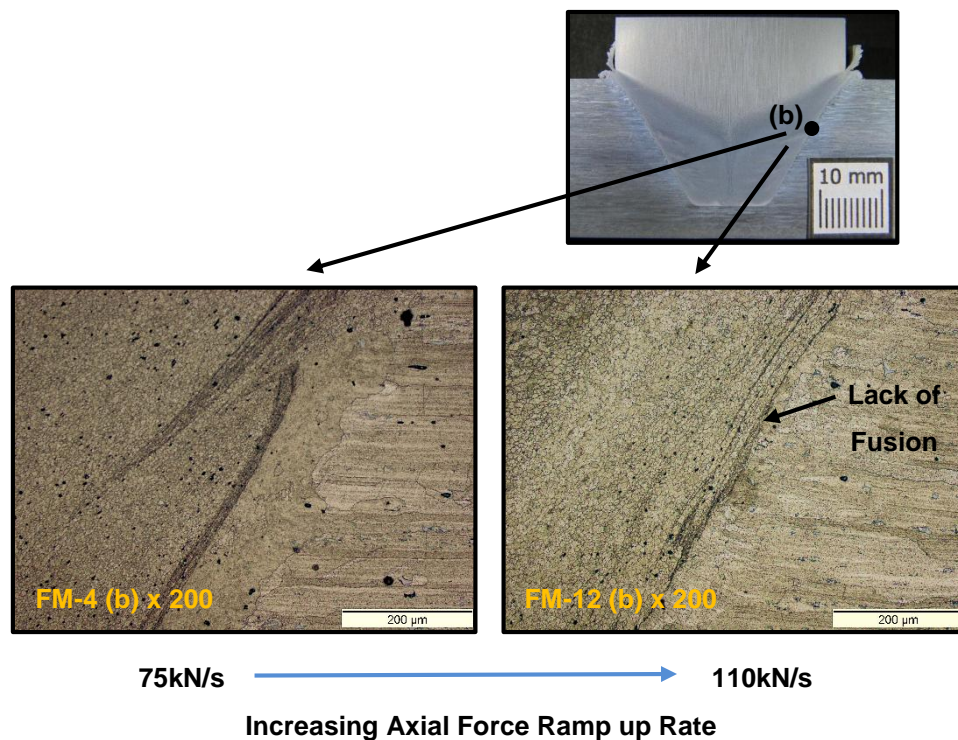


Figure 5-39. Micrograph at the Mid-Point of Welds FM-4 and FM-12 showing Lack of Fusion

### 5.5.5. Energy Input Analyses with respect to Temperature and UTS

Due to improvements made in data logging during welding, the energy input for Welds FM-1 to FM-16 was calculated up to the point at which plunge depth was reached and to the point at which rotational speed reached zero. As no link could be identified between differences in energy input to plunge depth and to the point of rotation stop, only energy input to plunge depth will be considered in this section and will be referred to as the total energy input. The plunge depth during

stopping of the motor, the motor stopping time and the plunge depth during forging were also recorded in this section. As no link between plunge depth during stopping, stopping time and plunge depth during forging were identified with respect to UTS, the results are not discussed. The results are, therefore, presented as reference for repeatability of results for Welds FM-1 to FM-16 in Appendix F. To ensure repeatability of this work, similar results will need to be achieved in order to simulate a similar welding environment.

The energy input analyses of the final set of welds identify that the energy input to 0.1 seconds, 1 second and to the PSTP have no influence on the static strength of the weld once appropriate parameters of axial force ramp up rate are selected. The effect of axial force ramp up rate in Section 5.3 showed that minimum values of energy input and energy input rate up to the PSTP are critical in the formation of a good welds as shown in Table 5-13, with the total energy input rate shown to not be affected by axial force ramp up rate. The results of Welds FM-1 to FM-16 show that for an axial force ramp up rate above 75kN/s, changes in energy input to the PSTP has no significant effect on the UTS of the joint as seen between welds FM-1 and FM-9 in Table 5-14 and Appendix F. These welds have identical process parameters with FM-1 and FM-9 having axial force ramp up rates of 75kN/s and 110kN/s respectively. The welds have similar input energy up to the PSTP; however, Weld FM-1 has a UTS of 181.72 and Weld FM-9 a UTS of 214.92MPa. As axial force ramp up rate has little effect on the total energy input, the key difference in joint strength lies within the welding time and hence total energy input rate for changes in axial force ramp up rate. Further, changes in process parameters at or above 75kN/s axial force ramp up rate that cause significant changes in the energy input and energy input rates up to the PSTM show no correlation to the UTS of the joint. This is as expected, as the energy input to the PSTP predominantly controls the quality of the weld in the lower region, of which 0.5mm is machined away during machining of the tensile sample.

Figure 5-40 shows the UTS of the three fracture mode types of welds FM-1 to FM-16. The results clearly show low values of total energy input ( $21.8\text{J}/\text{mm}^2$ ) to correlate with high strength welds, with high total energy input values (above  $60\text{J}/\text{mm}^2$ ) to correlate with lower strength welds. The separation of the fracture

modes shows that all Mode 1 fractures closely follow the correlation that reduced total energy input increases the UTS of the HAZ. Increased total energy input is therefore characterised by softening of the parent plate adjacent to the weld nugget in the HAZ. Welds FM-13 and FM-14 clearly show the influence of energy input on microhardness in Figure 5-41. Weld FM-13 has an energy input of  $80.1\text{J/mm}^2$  and Weld FM-16 had an energy input of  $21.8\text{J/mm}^2$ , 3.67 times less total energy input for the same geometry and plunge depth. The parent material hardness in the HAZ is clearly seen to decrease.

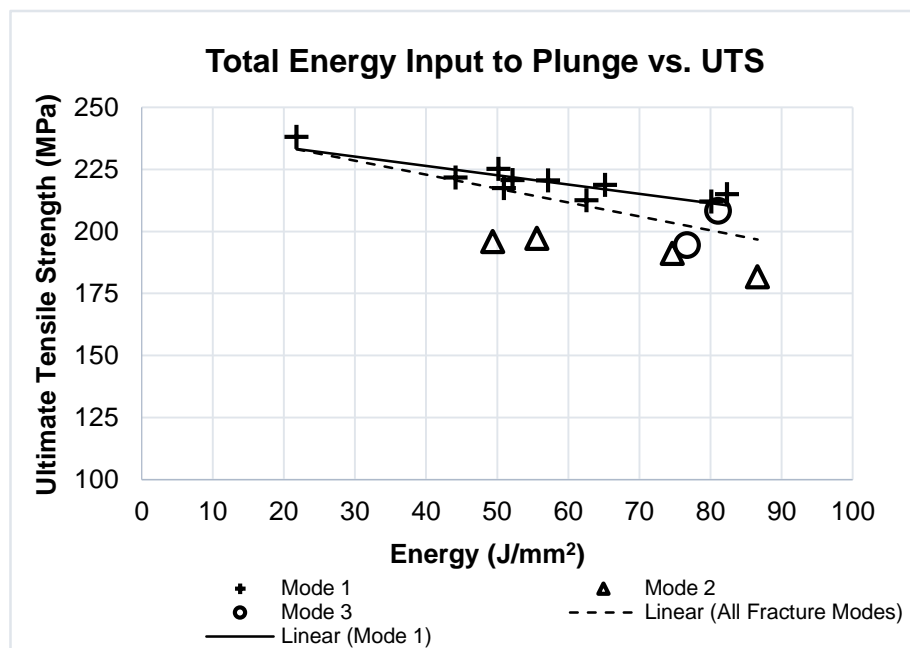


Figure 5-40. Total Energy Input (Welds FM-1 to FM-16)

Table 5-15. Energy Results for Welds FM-1 to FM-16

Weld No:	Energy Input at 0.1s (J/mm <sup>2</sup> )	Energy Input Rate at 0.1s (W/mm <sup>2</sup> )	Energy Input at 1s (J/mm <sup>2</sup> ) (W/mm <sup>2</sup> )	Time to Seizure (s)	Torque at Seizure (Nm)	Energy Input at Seizure (J/mm <sup>2</sup> )	Energy Input Rate at Seizure (W/mm <sup>2</sup> )	Time to PSTP (s)	PSTMP (Nm)	Energy Input to PSTP (J/mm <sup>2</sup> )	Energy Input Rate at PSTP (W/mm <sup>2</sup> )	Welding Time	Total Energy Input (J/mm <sup>2</sup> )	Total Energy Input Rate to Plunge Depth (J/mm <sup>2</sup> )	Energy Input to Stop (J/mm <sup>2</sup> )	Total Energy Input Rate to Stop Depth (J/mm <sup>2</sup> )	UTS (MPa)	Distance to Fracture (mm)
FM-1	4.4	44.1	11.8	0.13	39.6	5.2	41.1	1.1	51.4	12.8	11.9	7.5	86.6	10.9	90.9	12.2	182	3.6
FM-2	4.5	45.0	12.7	0.11	41.5	5.9	53.4	1.5	58.6	7.9	5.3	4.0	55.6	13.8	76.2	12.4	197	4.5
FM-3	3.6	36.3	13.5	0.24	65.1	14.6	69.8	1.2	144.6	17.5	14.4	5.9	74.6	12.6	82.7	12.6	191	3.1
FM-4	3.5	35.4	13.5	0.20	75.5	14.6	73.2	1.2	142.8	17.6	14.4	3.5	50.2	14.4	51.2	14.9	225	10.4
FM-5	6.4	64.3	14.3	0.10	34.0	6.4	64.2	0.5	64.3	5.8	11.9	5.9	76.7	12.8	60.5	13.5	208	x
FM-6	5.8	58.4	13.9	0.12	42.8	7.9	65.6	0.3	61.3	3.9	11.4	3.5	51.0	14.7	76.7	12.8	217	10.0
FM-7	1.9	18.8	15.9	0.19	79.5	11.9	63.6	1.0	184.8	14.9	15.6	4.8	65.2	13.6	84.4	12.3	219	10.7
FM-8	3.7	37.5	16.2	0.21	88.1	18.3	87.1	1.0	170.6	15.8	16.0	2.8	44.2	15.6	64.2	13.9	222	9.3
FM-9	3.5	35.3	12.9	0.11	46.3	5.1	46.4	0.4	52.4	4.8	11.2	6.8	82.3	12.0	86.9	11.9	215	9.5
FM-10	6.6	65.8	13.7	0.11	37.6	7.9	71.5	0.8	56.7	10.6	13.2	4.1	57.1	13.7	55.5	14.4	220	9.6
FM-11	4.5	45.2	15.3	0.19	77.8	14.0	75.5	1.1	149.5	17.4	15.3	6.4	81.1	12.8	66.9	13.5	194	3.5
FM-12	4.0	40.2	15.9	0.19	78.4	15.3	80.7	1.1	173.7	17.0	16.1	3.2	49.4	15.2	62.1	14.0	196	3.6
FM-13	8.1	81.5	14.4	0.12	39.7	10.1	84.5	0.6	59.3	7.8	13.6	6.4	80.1	11.7	57.2	14.7	212	9.3
FM-14	7.8	77.6	15.5	0.18	54.9	20.6	114.2	0.8	63.6	11.6	14.7	3.5	52.2	15.1	46.1	15.3	221	10.6
FM-15	4.3	43.2	17.5	0.18	89.6	15.0	85.9	0.9	181.8	15.4	17.0	4.4	62.5	14.1	52.0	14.1	212	9.1
FM-16	3.6	36.2	17.8	0.20	90.2	17.9	89.4	1.3	500.0	21.8	17.1	1.4	21.8	15.2	21.8	15.2	238	6.4

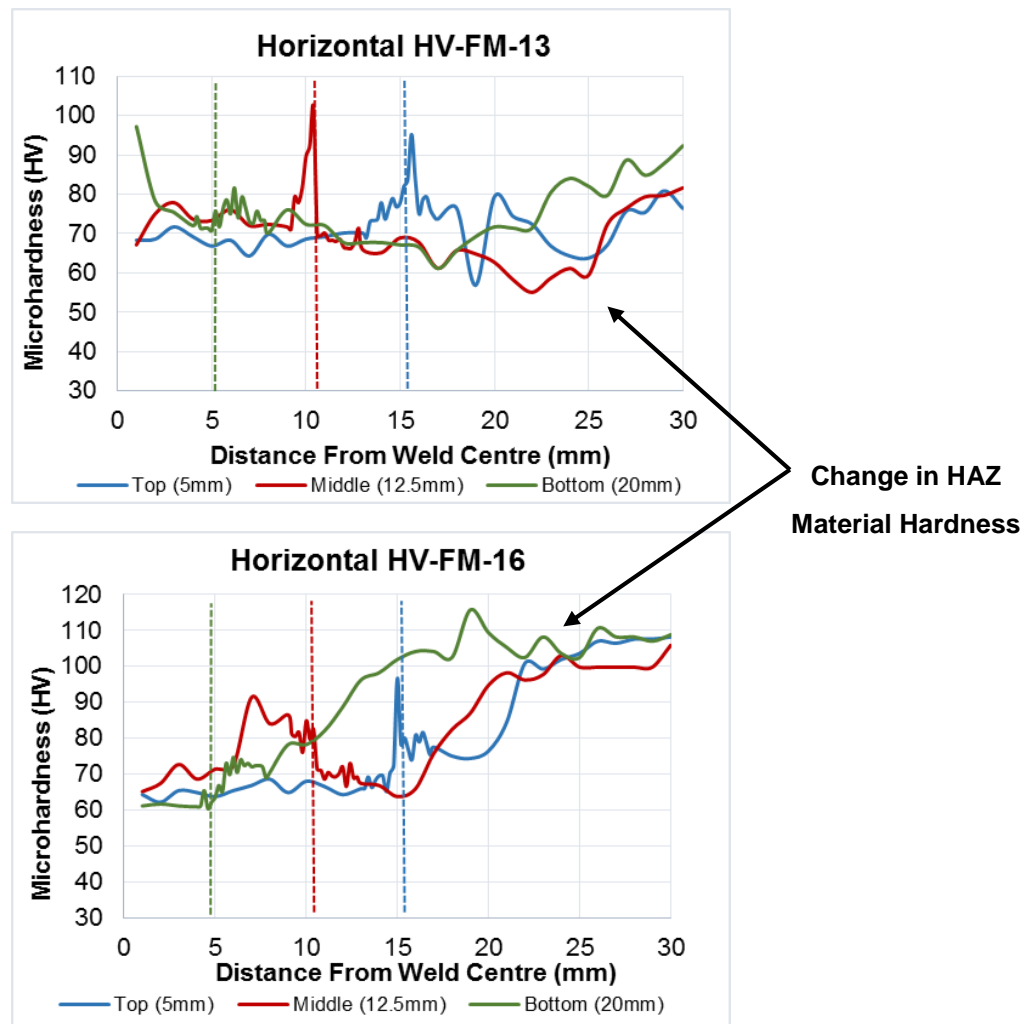


Figure 5-41. Change in HAZ Hardness due to Reduced Total Energy Input

A similar trend exists with respect to energy input if all fracture modes are considered; however, there is considerable scatter with no correlation to microhardness at the weld interface for fracture Modes 2 and Mode 3. This is shown clearly in the microhardness profiles of Welds FM-1 and 2 in Appendix K. The welds are shown to have weld interface hardness higher than the adjacent parent material, though failure occurred on the bond line. This shows that welds with mixed mode and interface failures are inferior due to poor bonding at the interface, not strength reduction due to softening. This is as expected as EBSD results showed significant grain refinement at the bond line, following the Hall Petch effect with respect to joint strength. All microhardness profiles for Welds FM-1 to 16 are given in Appendix K for reference.



The total energy input rate for welds FM-1 to FM-16 shows that there is a clear trend of increasing energy input rate vs. increasing UTS as shown in Figure 5-42. Energy input rates as low as 11W/mm<sup>2</sup> and 12W/mm<sup>2</sup> typically achieve 210MPa while energy input rates above 15W/mm<sup>2</sup> give welds above 200MPa. As in the case with total energy input, the effect of increasing energy input rate produces a near linear correlation to UTS as expected when only Mode 1 fractures are considered. This verifies that welds with high energy input rates and low energy inputs have the smallest HAZ which is critical when welding heat treatable aluminium.

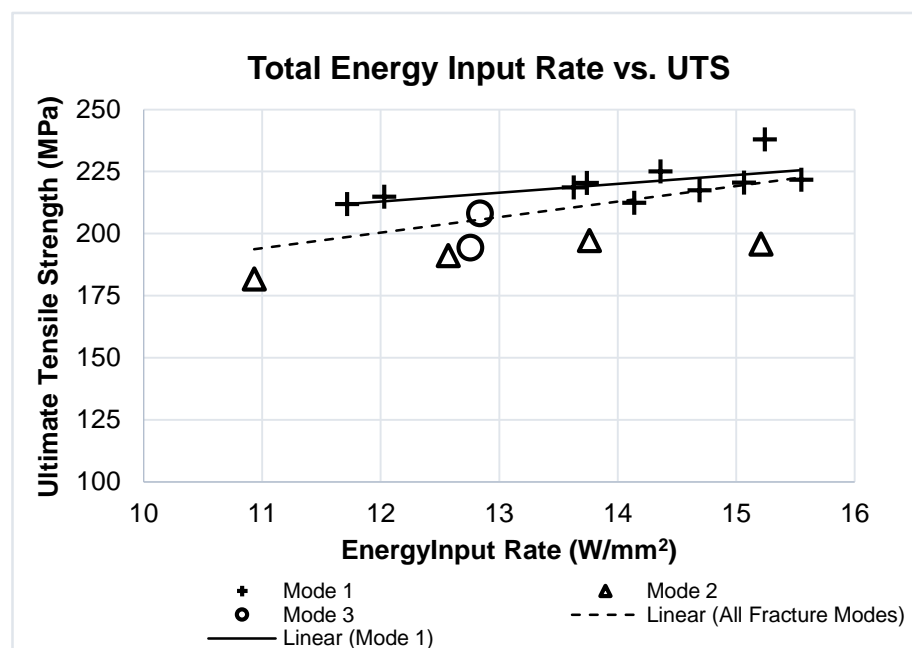


Figure 5-42. Total Energy Input Rate for Welds FM-1 to FM-16

As high energy input rates reduce the heat conduction into the plate, preventing softening, it therefore follows that there is a direct link between UTS and welding time. Welds with low total energy input and high energy input rates typically have short welding times, usually around 4 seconds. The influence of reduced welding time vs. UTS is shown in Figure 5-43, with a clear trend showing reduced welding time to directly improve joint integrity. There is, therefore, strong evidence that a direct link exists between energy input and energy input rate on the integrity of the welded joint if Mode 1 failures are considered. A similar link is shown to exist for all fracture modes, though with significant scatter as process parameter combinations move outside their respective operating window.

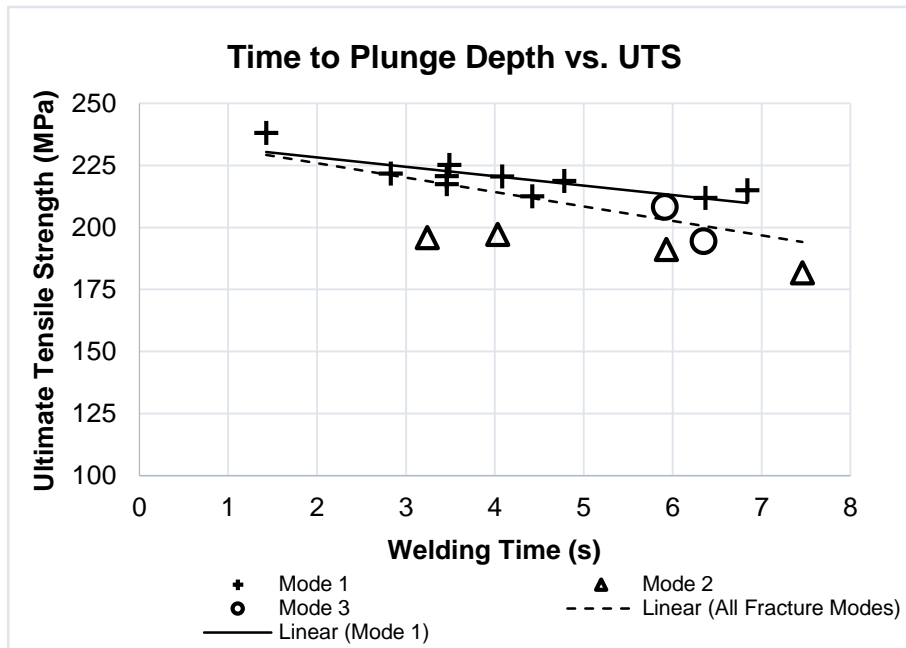


Figure 5-43. Welding Time for Welds FM-1 to FM-16

The effect of energy input and energy input rate discussed above is summarised in a contour plot to graphically display the interaction of energy input and energy input rate. This is displayed for all parameters in Figure 5-44. The plot clearly shows that a total energy input of less than 35J/mm<sup>2</sup> applied at an energy input rate of 14W/mm<sup>2</sup> to 16W/mm<sup>2</sup> will produce a weld with good static joint strength with above 60% parent material UTS. Total energy input above 60J/mm<sup>2</sup> is shown to reduce joint integrity over the entire energy input rate range.

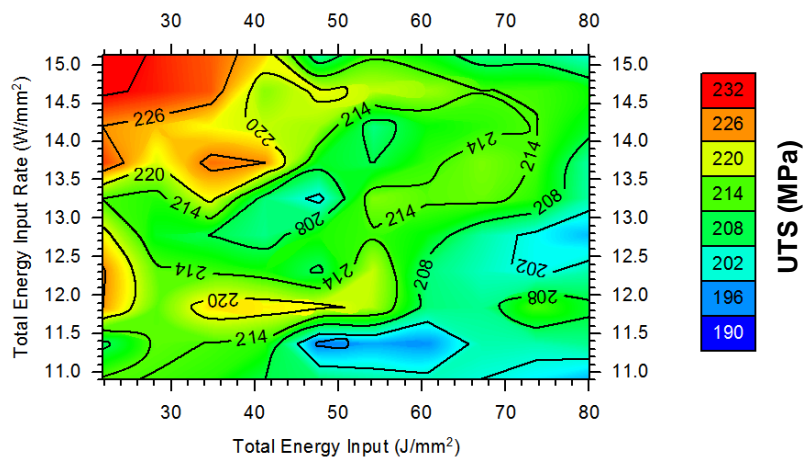


Figure 5-44, Contour Plot of Energy Input and Energy Input Rate vs. UTS

As rotational speed has a significant effect on the total energy input and the energy input rate, the contour plots were separated into welds made at 5000RPM and 3000RPM in Figure 5-49 and Figure 5-46 respectively. The results show Figure 5-44 to be a good representation of the energy input and energy input rate for Welds FM-1 to FM-16. Welds made at 5000RPM are clearly shown to produce good welds in a high integrity band indicated in Figure 5-49. The formation of the high integrity band shows that energy input rate is able to compensate for energy input within limits, with the general trend that more total energy input will be accompanied by increased energy input rate. Welds made at 3000RPM are shown to produce good welds with a lower total energy input and higher energy input rate than 5000RPM welds, with the statically strongest weld made at  $21.8\text{J/mm}^2$  and  $15.2\text{W/mm}^2$  as shown in Figure 5-50. This makes 3000RPM the more efficient rotational speed parameter with the highest static joint strength.

The toughness and hence extent of parent material softening of the welds is of interest, as it identifies welds that are more likely to fail suddenly at the bond line, or plastically deform before failure in the parent material. To quantify this the distance traveled by the jaws of the tensile testing platform at the point of fracture was recorded. After fracture the samples were inspected for slipping of the jaws, as no slip was noted for all welds; the results are given in Table 5-15. The results are summarised in contour plots for 5000RPM and 3000RPM welds in Figure 5-47 and Figure 5-48 respectively. The results clearly show that welds with high total energy input are made at 5000RPM, producing welds with high average extension to fracture, with no parent material fracture (Mode 1) welds produced that extended less than 9.31mm to fracture. Welds made at 3000RPM required less total energy input and have shorter welding times, corresponding with the drop in parent material hardness observed between Welds FM-16 to FM-13 in Figure 5-41. The drop in total energy input from  $80.1\text{J/mm}^2$  to  $21.8\text{J/mm}^2$  reduced the extension to fracture from 9.46mm to 6.4mm, corresponding to the lower near interface temperatures recorded and a narrower near interface temperature curve profile.

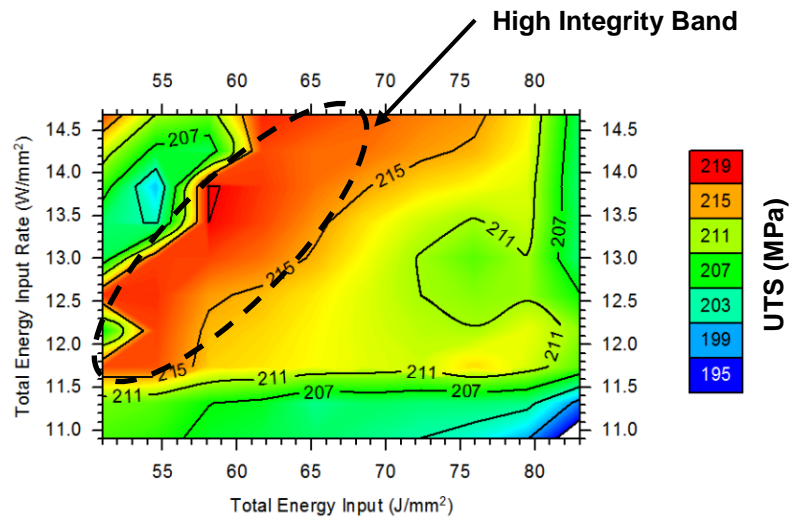


Figure 5-45, Contour Plot of Energy Input and Energy Input Rate at 5000RPM vs. UTS

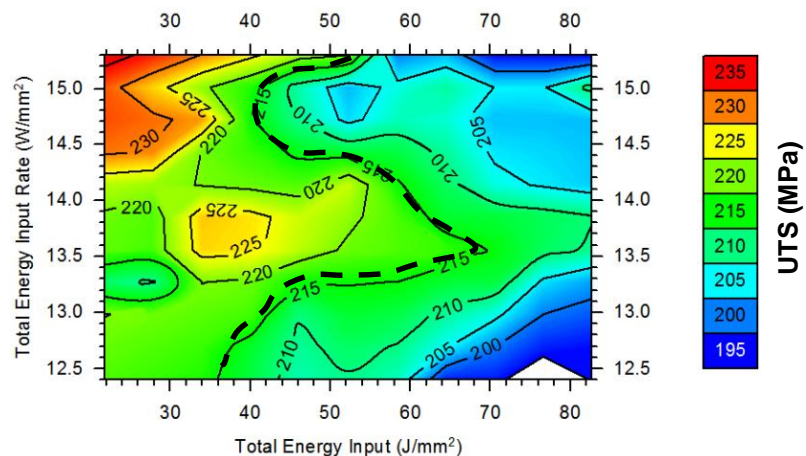


Figure 5-46, Contour Plot of Energy Input and Energy Input Rate at 3000RPM vs. UTS

The analysis of the UTS contour plots clearly shows the interaction of energy input and energy input rate, with the common trend showing good welds to be made at total energy inputs between 21.8J/mm<sup>2</sup> and 65J/mm<sup>2</sup>. The contour plots also clearly show that good welds can be produced within an energy input and energy input rate window, giving a suggestion of the energy input requirement and tolerance to produce a good weld. This is critical in application, as this can be used as a guide to predict weld quality if energy input and energy input rates are known. Welds made at 3000RPM were shown to be significantly more efficient than 5000RPM welds, requiring 58% less total energy input to produce a good weld, however requiring significantly higher process torques as a consequence which may be a concern for onsite application.

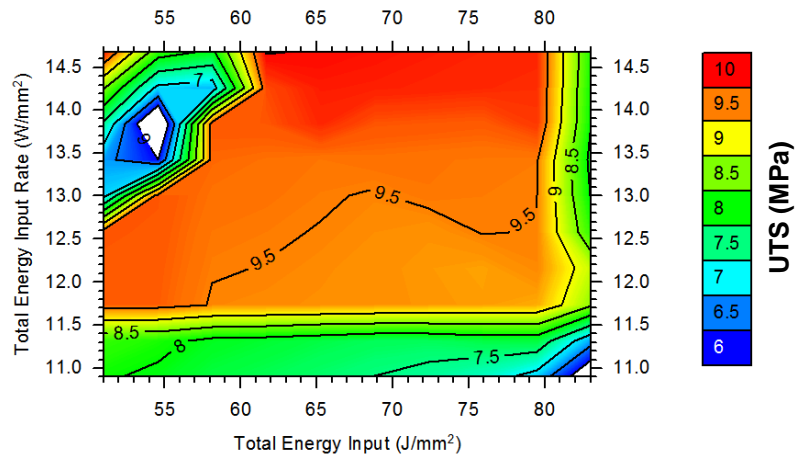


Figure 5-47, Contour Plot of Energy Input and Energy Input Rate at 5000RPM vs. Extension to Fracture

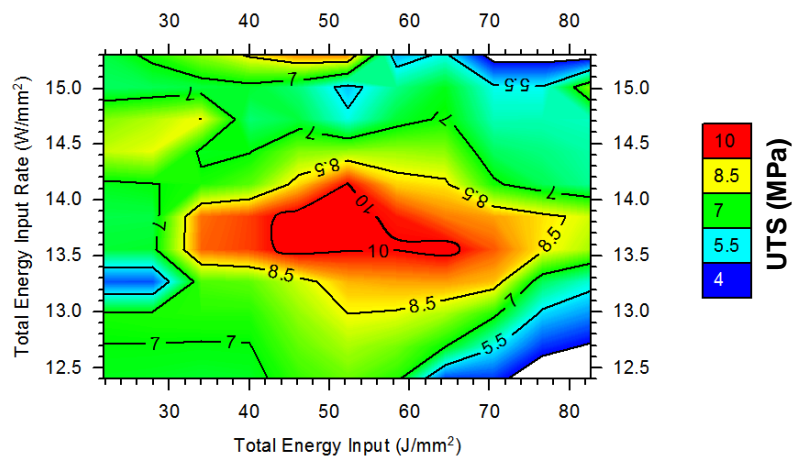


Figure 5-48, Contour Plot of Energy Input and Energy Input Rate at 3000RPM vs. Extension to Fracture

### 5.5.6. UTS Scatter Analyses of Typical Fracture Modes

To identify possible explanations for the scatter in the UTS results with respect to energy input trends when all fracture modes are included in the analyses, the microstructure at the weld interface was investigated to identify if second phases formed during welding or lack of bonding influenced the UTS of the weld that is not evident with respect to energy data. Figure 5-49 shows the location of the points analysed, with the focus on the top and midsection of the weld interface. All welds are investigated in the etched condition as lack of fusion was not clearly identified in the polished condition for welds that failed with relatively low UTS. Bonding will, therefore, be identified with respect to plastic deformation of the plate and a homogeneous weld interface of dynamically recrystallized grains with no clear bond line.

The first weld interface analysed is Weld RR-1. This weld was made with an axial force ramp up rate of 15kN/s, achieving the lowest UTS of all welds tested using the soft start welding procedure at 60kN axial force. This weld will serve as a clear indicator of weak sidewall bonding, to be referenced against the interfaces of the three fracture mode types identified in Welds FM-1 to FM-16, as the weld failed in Mode 3 fracture, with a UTS of only 59MPa.

The micrographs for Weld RR-1, given in Figure 5-50 (a) and (b), show a clear straight bond line at point (a) with no evident plastic deformation of the plate, showing a clear bond line between the plate and weld nugget. This weld clearly identifies poor bonding without the formation of voids along the sidewall of the hole.

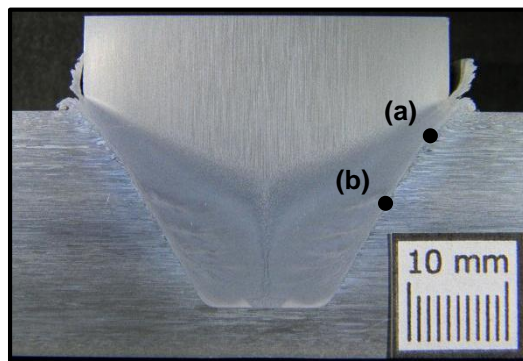


Figure 5-49. Weld FM-16 Macrograph showing the location of point (a) and (b)

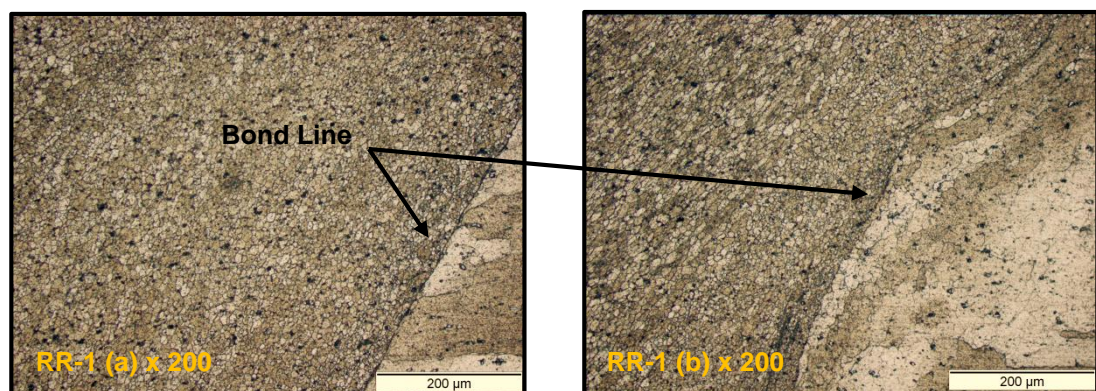


Figure 5-50. 25kN/s Axial Force Ramp up Rate Weld RR-1 Bond Line of Fracture Mode 3

Fracture Mode 1 (Parent Material Fracture) is shown for weld FM-14 and FM-16 in Figure 5-51. These welds represent the best 5000RPM and 3000RPM welds

that failed in the parent plate. Weld FM-14 shows good mixing of the plate and stud material with high levels of plastic deformation in the upper region of the plate. Dynamic recrystallization is seen at the interface as shown in the inset of Weld FM-14 (a) in Figure 5-51, with no visible bond line, indicating good bonding. The mid-region of Weld FM-14 shows a dark band along the bond line, with good mixing of the parent plate and stud and high amounts of plate plastic deformation. Weld FM-16 shows no distinguishable bond line at the top of the weld, with the characteristic deep tearing of low rotational speed welds forming a near homogeneous interface with high amounts of plastic deformation of the plate clearly visible. The mid-region of the weld shows a section of isolated second phase particles formed at the interface that is broken up and mixed with the parent plate and stud material. High amounts of plastic deformation, with dynamically recrystallized grains are clearly visible, as with Weld FM-14. These fracture types typically achieved 238MPa to 211.9MPa UTS, correlating with the noted good bonding and high amounts of plate plastic deformation. These features clearly represent good bonding at the interface, with respect to UTS.

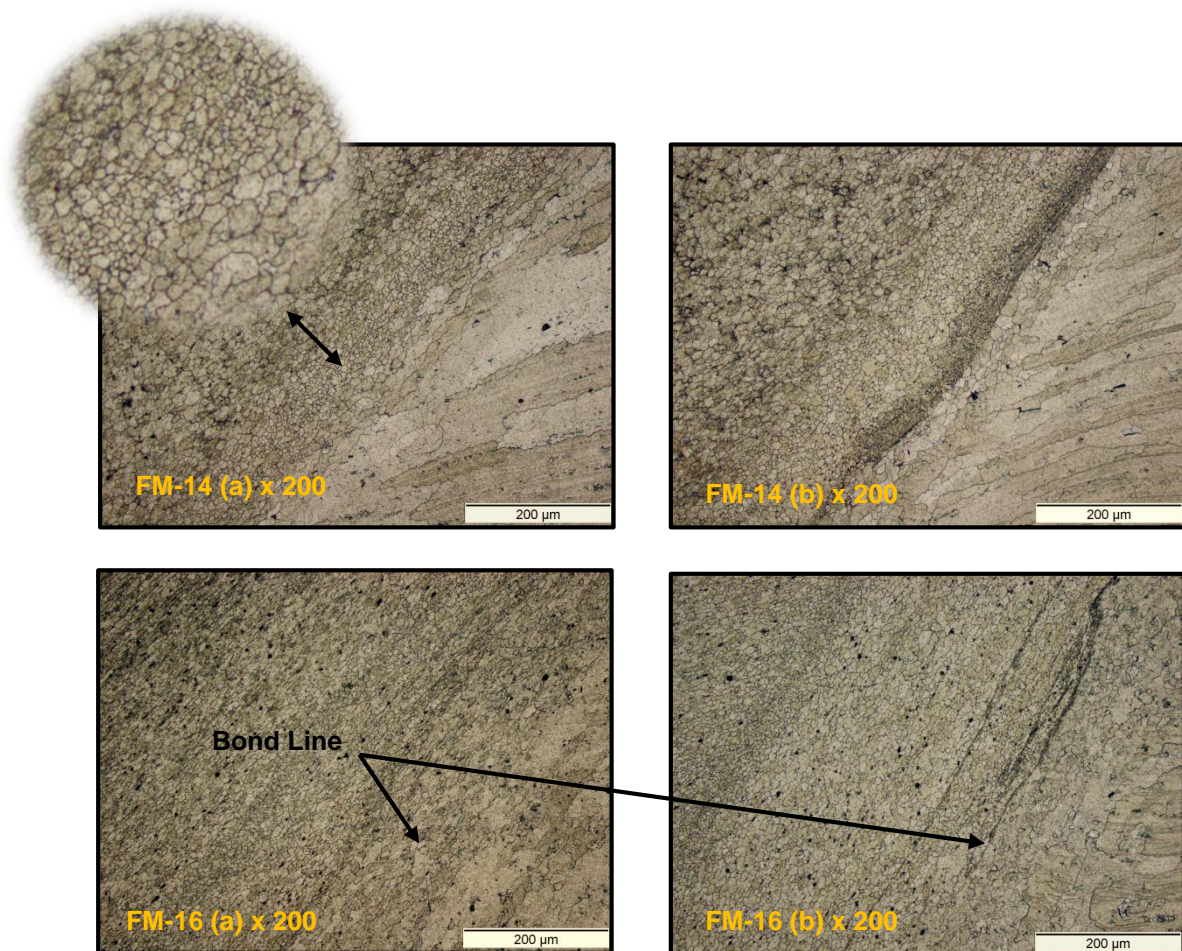


Figure 5-51. Bond Line of Fracture Mode 1

Figure 5-52 shows the weld interfaces of Weld FM-1. This represents the worst weld made in the final weld matrix that failed in fracture Mode 2. It is clear that there is little to no plastic deformation of the plate, a clearly distinguished bond line is visible and non-homogeneous dynamic recrystallization at the interface, with the plate left predominantly unaffected. These welds typically achieve between 197.5MPa and 181.7MPa, correlating with the poor bonding noted.

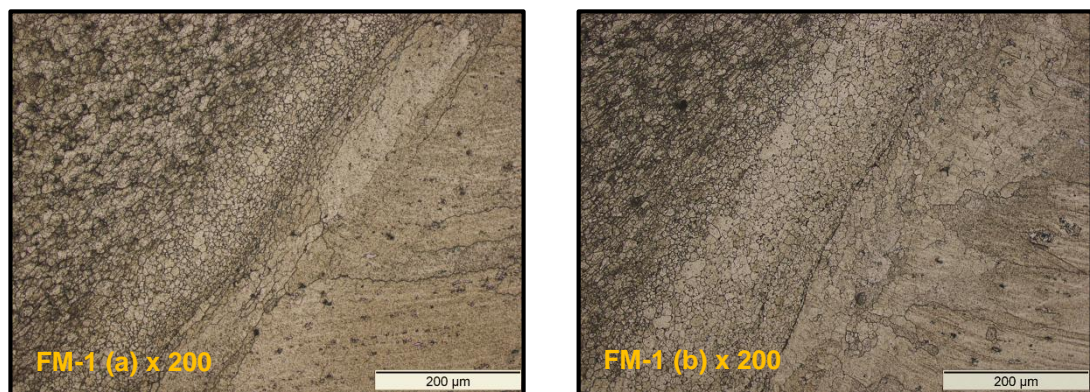


Figure 5-52. Bond Line of Fracture Mode 2

Figure 5-53 shows the weld interface of Weld FM-5. This weld represents the typical microstructure of welds that fractured in Mode 3. The weld has a dark continuous band of precipitates in the mid region of the weld, at point (b), with good plastic deformation of the plate. Typically this fracture mode is found at low axial force and rotational speeds of 5000RPM. Although these welds failed purely on the interface, fracture Mode 3 welds were not significantly weaker than fracture Mode 2, typically achieving between 208.08MPa and 194.3MPa.

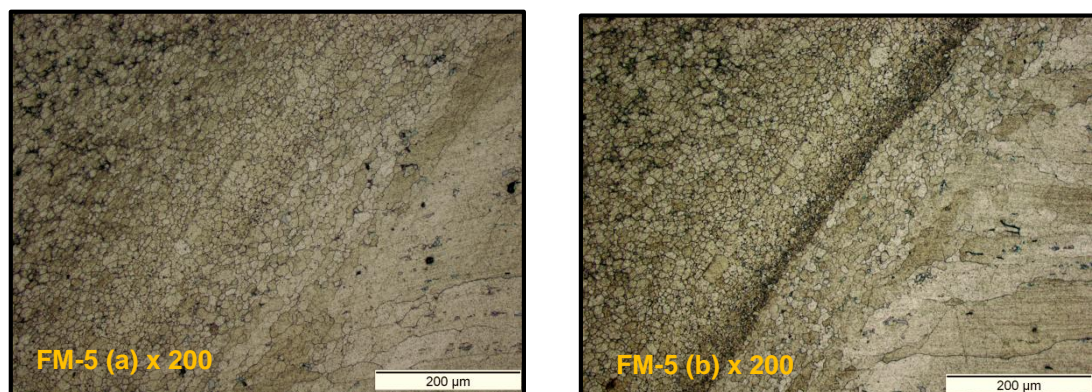


Figure 5-53. Bond Line of Fracture Mode 3



The interface analyses of the three main fracture modes showed that Mode 1 fractures typically have a near indistinguishable weld interface, with high amounts of plate plastic deformation and dynamically recrystallization of the plate material at the interface. Mode 2 and three fractures typically have less plastic deformation of the plate and have unbroken bands of precipitates along the bond line. The precipitates appear to form under specific conditions; therefore, their formation may not only be parameter dependent, but energy, temperature and time dependant. Figure 5-54 shows that Mode 3 fractures are concentrated around a total energy input of 60J/mm<sup>2</sup> to 80J/mm<sup>2</sup> and total energy input rate of 13W/mm<sup>2</sup>. The welding times for Welds FM-1 to FM-16 show that Mode 1 fractures occur for welding times between 1.4 seconds and 6.8 seconds, Mode 2 fractures between 4 seconds and 7.5 seconds and Mode 3 fractures between 5.9 seconds and 6.4 seconds. This indicates that the formation of precipitates is energy and time dependant and as clearly shown in Figure 5-54 are concentrated at specific total energy input, total energy input rate and weld time locations. The formation of precipitates, combined with specific process parameter and geometry combinations that applying excessive surface pressure during welding, account for the scatter in UTS noted with regards to the energy analyses. This is an important observation and characteristic of FTSW of AA6082-T6 that requires further analyses by a metal scientist.

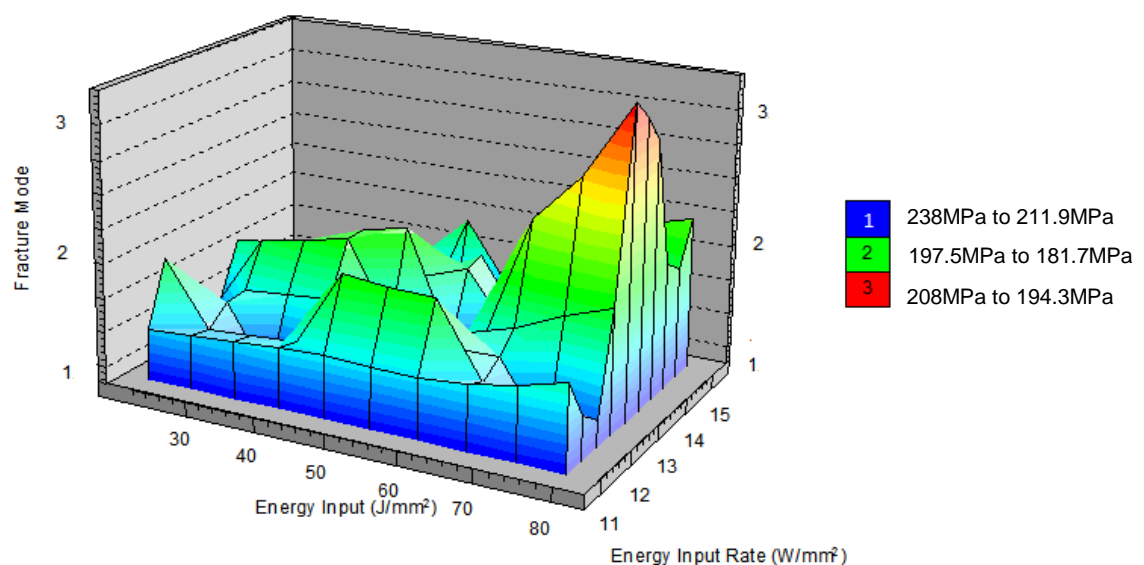


Figure 5-54. Surface Plot of Energy Input and Energy Input Rate vs. Modes of Fracture

### 5.5.7. Typical Microstructures of AA6082-T6 FTSW

Optical microscopy analyses of welds FM-1 to FM-16 were conducted to identify voids, lack of bonding and any microstructural anomalies that occurred with changes in process parameters that would correspond with joint integrity. The welds were analysed at X50 and X200, with the hypothesis that voids unidentifiable at these magnifications are insignificant to the static strength of the weld, with a more detailed analysis not considered necessary as it is outside the requirements for the development process and scope of this study.

No voids were found between the weld nugget and the sidewalls of the tapered hole for Welds FM-1 to FM-16 as verified by the dye penetrant testing. Cold forge defects were found at the base of the hole for all welds as identified by the dye penetration tests and as discussed in previous work. Therefore, the use of preheat and the soft touch welding procedure did not remove the defect, though welds with higher energy inputs to 0.1 seconds and seizure did show improved bonding, with the most bonding in this region noted for weld FM-1, due to high total energy input consolidating the joint. These voids were typically 3mm in diameter, similar to welds TW-23 and TW-24.

Figure 5-55 and Figure 5-56 show the microstructures at the top, middle, fillet and central base region of the weld for Welds FM-1 and FM-16 respectively. They represent the welds with the lowest and highest UTS in the final set of welds. These two welds are also situated at opposing sides of the process parameter and energy input window, showing the direct link between input energy, process parameters and microstructure. Weld FM-1 has low axial force, low axial force ramp up rate, low stud taper angle and high rotational speed, while weld FM-16 has high axial force, high axial force ramp up rate, high stud taper angle and low rotational speed. Weld FM-1, therefore, has 3.97 times more total input energy and 28% less total energy input rate than weld FM-16, with the energy and process torque data for all the welds given in Table 5-15 on page 198.

Weld FM-1 in Figure 5-55 shows a clearly distinguished bond line at point (a) and (b), with the zone between the parent plate and weld nugget, which is essentially

flash locked in the clearance between the stud and hole during plunge, and is seen to etch lighter than the surrounding material. This was typical for most welds with welding times above 3 seconds. The variance in etching is likely caused by changes in material properties due to the shearing and dynamic recrystallization process during welding, triggering the formation of various precipitates under the strain and strain rates exerted on the plasticized material during welding at the extended welding times of low energy input rate welds. The band of light etching corresponds with bands of preferred grain orientation seen in Figure 5-22. Lack of bonding was identified between the lightly etched flash material and the dynamically recrystallized stud material, shown in the inset of Figure 5-55 (b) X50. The bonding between the flowing flash material and the stud is, therefore, significantly reduced at low energy input rates, compared to the bonding noted between the plate and the flash. The explanation for this is not entirely clear; however, the occurrence and intensity of this poorly bonded region is reduced with increased axial force and axial force ramp up rate. With the interface found to be near indistinguishable with energy inputs below  $51\text{J/mm}^2$  and energy input rates above  $15\text{W/mm}^2$ , this shows the sensitivity of process parameter selection for FTSW in AA6082-T6, as incorrectly selected process parameters that give low energy input rates are likely to produce welds that fail between the flash and the weld nugget, rather than between the flash and parent plate. This lack of bonding is shown to be eliminated with increased axial force, increased stud angle and reduced rotational speed as shown in Figure 5-56.

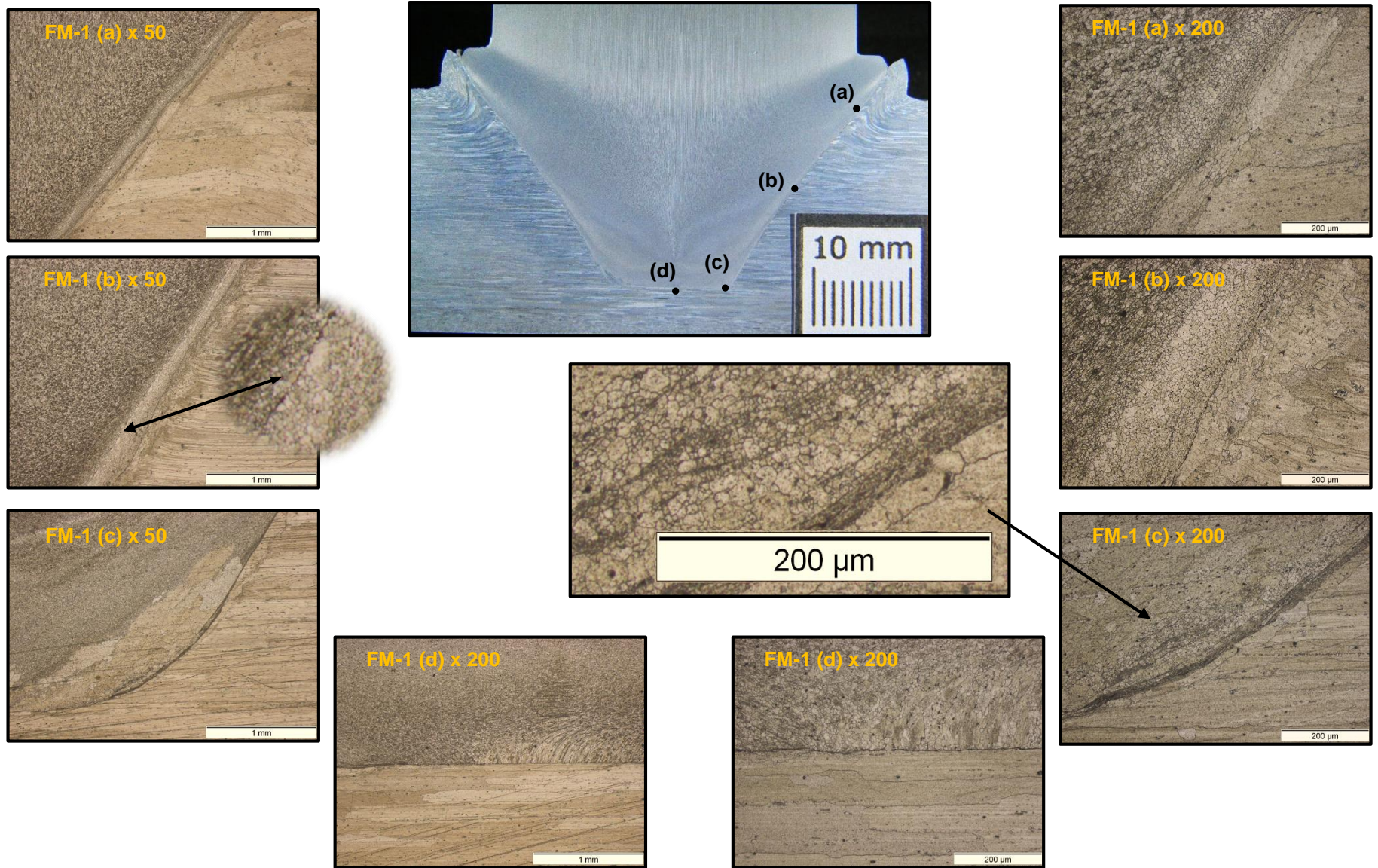


Figure 5-55. Microstructure of Weld FM-1

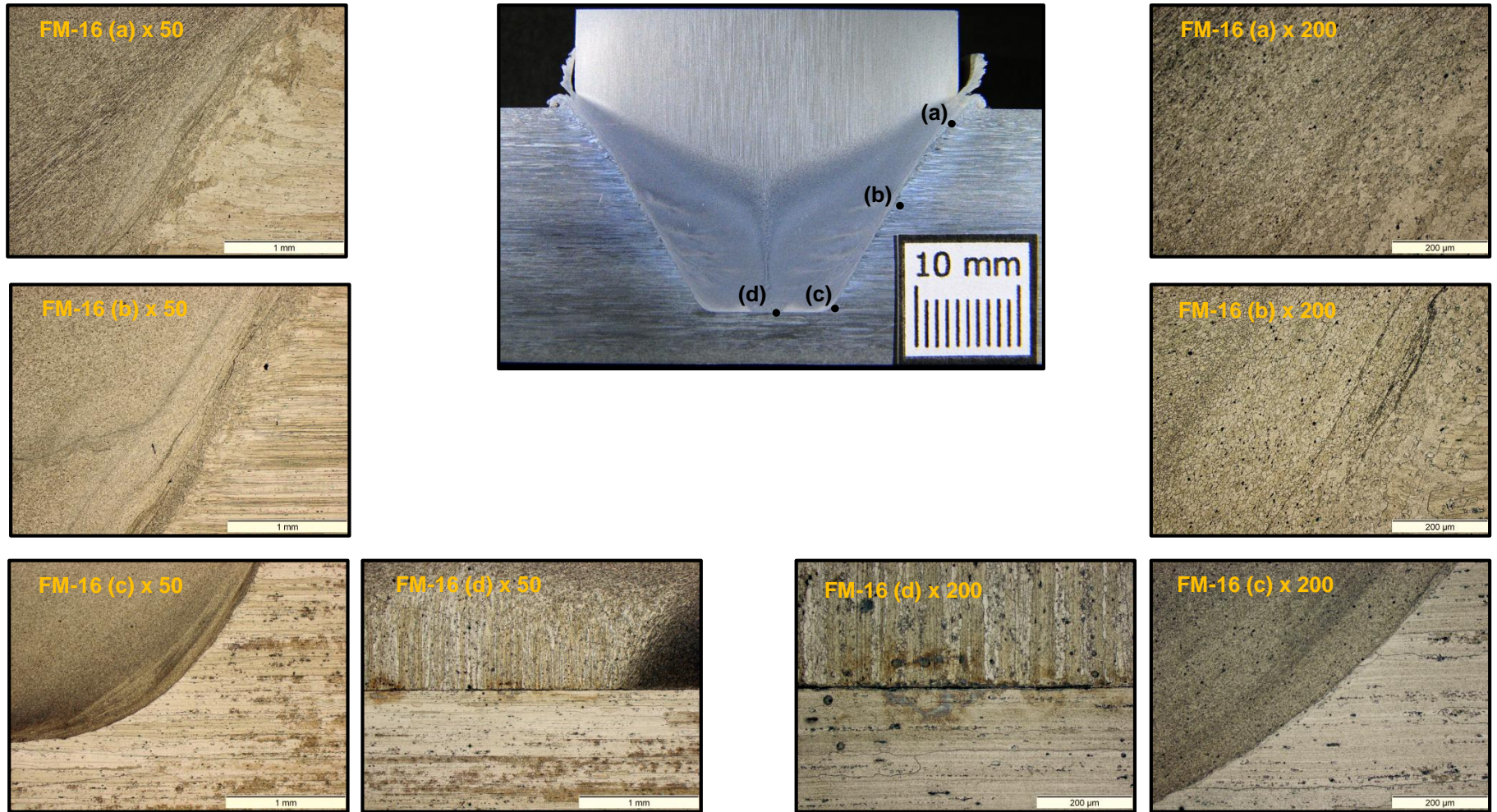


Figure 5-56. Microstructure of Weld FM-16

The formation of these large grains between the flash and weld nugget and their significant reduction in size is clearly shown in the band contrast/ grain boundary maps of Welds S.1 and S.4 shown in Figure 5-57 and Figure 5-58 respectively. These figures represent the mid region of the welds at approximately point (b) in Figure 5-55. The grain boundaries are defined by a misorientation angle of  $8^\circ$  for both Welds S.1 and S.4. These welds use axial forces of 40kN and 80kN and rotational speeds of 5000RPM and 3000RPM respectively. This reduces the welding time from 35.3 seconds to 9.7 seconds respectively for Welds S.1 to S.4. The maps show excessively large grains distributed along the boundary between the flash and weld nugget of weld S.1, correlating with a six fold decrease in UTS between Welds S.4 and S.1. The formation of these large equiaxed grains can be directly related to low axial force, high rotational speed and high welding time as these large grains are seen to disappear with the opposing process parameters as seen between Welds FM-1 and FM-16. The grain formation at the weld nugget/ flash interface is so sensitive to energy input and welding time that the large grains formed in weld S.1 were significantly reduced for weld S.4 and in fact were the smallest grains formed at the interface. The width of the flash band is also seen to narrow considerably and consists of significantly finer grains with reduced welding time and rotational speed, showing high energy input rate to drive the formation of the fine grains and a narrow flash band. There is, therefore, a direct link to the size of these grains, process parameters and energy input.

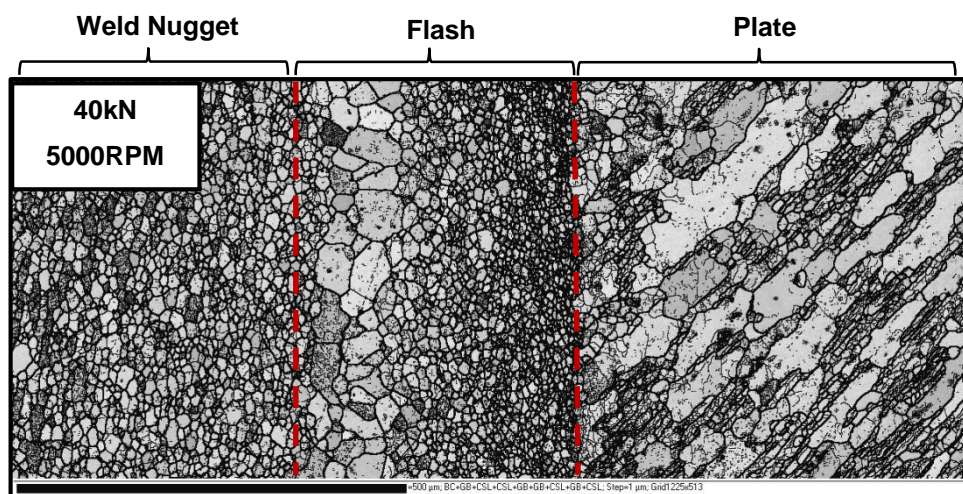


Figure 5-57. Band Contrast and Grain Boundary Map of Weld S.1

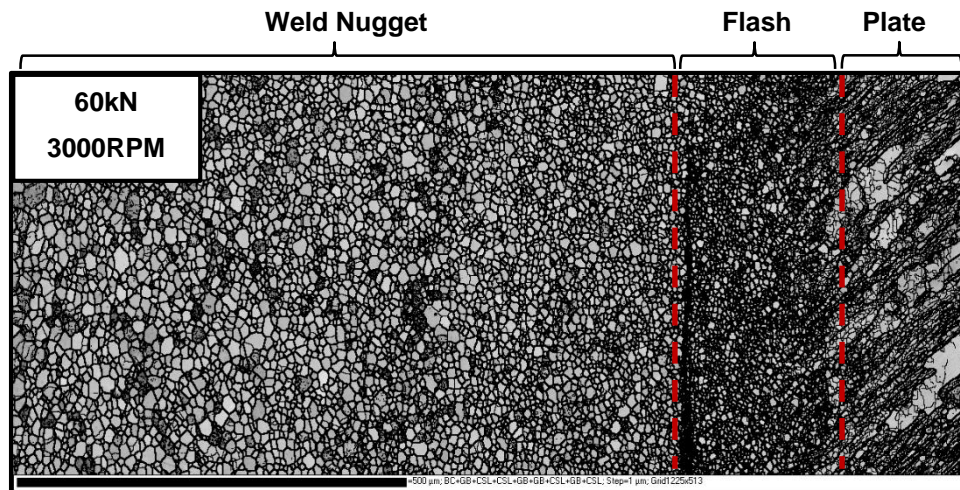


Figure 5-58. Band Contrast and Grain Boundary Map of Weld S.4

This shows how critical the selection of good process parameters is on the FTSW of AA6082-T6, as changes significantly affect the size of the grains formed and the static strength of the joint. This was linked directly to process parameters and energy input, with a clear trend that high energy input rate, and low total energy input forms fine grains at the weld interface that are superior to the large grains of the parent material in the HAZ, allowing failure of good welds in the parent plate HAZ. The analysis of the cold forge defect at the base of the hole shows that it is not removed over the entire process parameter window range investigated. The next step to improve the bonding in this region is to allow a small clearance between the stud and the hole. This will improve the flow of flash around the fillet in the first moments of the weld, forcing the central region to plasticize, for the stud material is clearly left intact as shown in Figure 5-56 (d) X200. The entrapment of the flash in the lower region is responsible for the highly deformed and unstable crystal lattice formed at the fillet that is susceptible to AGG. A small clearance will allow the flash to flow around the fillet, heating and plasticizing the material in the region. As shown in development welds, clearance between the hole and the stud of 1 mm is excessive and reduces sidewall rubbing and plasticization considerably as additional plunge is required that heats the stud and reduces rotation at the welding interface, eventually leading to premature stud collapse. A smaller clearance of approximately 0.1mm to 0.2mm is estimated to address the problem.

### 5.5.8. Microstructure Analysis of the Fillet of the Weld

The analyses of welds RR-1 to RR-4 showed that a minimum energy input of  $4.6\text{J/mm}^2$  at 3000RPM and  $6.7\text{J/mm}^2$  at 5000RPM was necessary to achieve bonding between the base of the hole and the weld nugget. This is similar to the energy input requirements identified to produce a good bond at the base of the hole in parallel FTSW PT-1 to PT-4. As expected, no trend between energy inputs in the first 0.1 second of the weld was found with respect to the recorded UTS of the welds. As the quality of the joint cannot be quantified at this point, the interface between the parent plate and stud at the fillet will be investigated to identify characteristics of good welds.

To identify trends in the microstructure with respect to energy input and process parameters the welds were grouped according to energy input during the first 0.1 seconds. They are divided into three groups, namely Type A, B and C, representing high, medium and low energy input as shown in Table 5-16. The microstructures at the fillet of all the welds within each range were then observed to identify typical characteristics that identify the fillet types. The point of observation is located at the fillet as indicated in Figure 5-60, with the typical microstructures at the fillet shown over the energy input range defining the fillet type, giving two examples per fillet type. Data from all the development welds has shown that good base and hence fillet bonding is achieved between  $5\text{J/mm}^2$  and  $10\text{J/mm}^2$  for 5000RPM welds and at approximately  $4\text{J/mm}^2$  for 3000RPM welds. The number of occurrences of the type of fillet at the respective process parameter level as well as the seizure torque and achieved UTS ranges per fillet type are specified in Table 5-16.

**Table 5-16. Classification of Weld Fillet Bonding**

	Type A	Type B	Type C
Energy Input Range at 0.1 s ( $\text{J/mm}^2$ )	5.8 – 8.1	4 - 4.5	1.9 - 3.7
Weld Numbers in Range	FM-6, 5, 10, 14, 13	FM-12, 15, 1, 2, 11	FM-7, 9, 4,16, 3, 8
Rotational Speed	5/5 at 5000RPM	2/5 at 5000RPM	1/6 at 5000RPM
Axial Force	2/5 at 60kN	3/5 at 60kN	2/6 at 60kN
Axial Force Ramp Rate	2/5 at 75kN/s	2/5 at 75kN/s	4/6 at 75kN/s
Stud Angle	1/5 at 55°	4/5 at 55°	3/6 at 55°
UTS (MPa)	208 to 220.6	181.7 to 212.4	225.1 to 191.1
Seizure Torque (Nm)	37.6 to 54	39.6 to 89.6	46.3 to 90.2



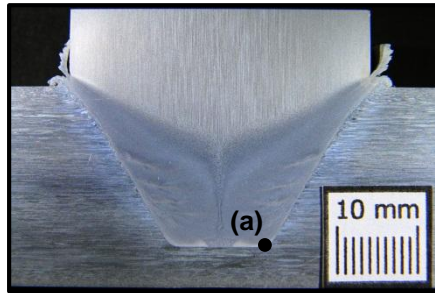
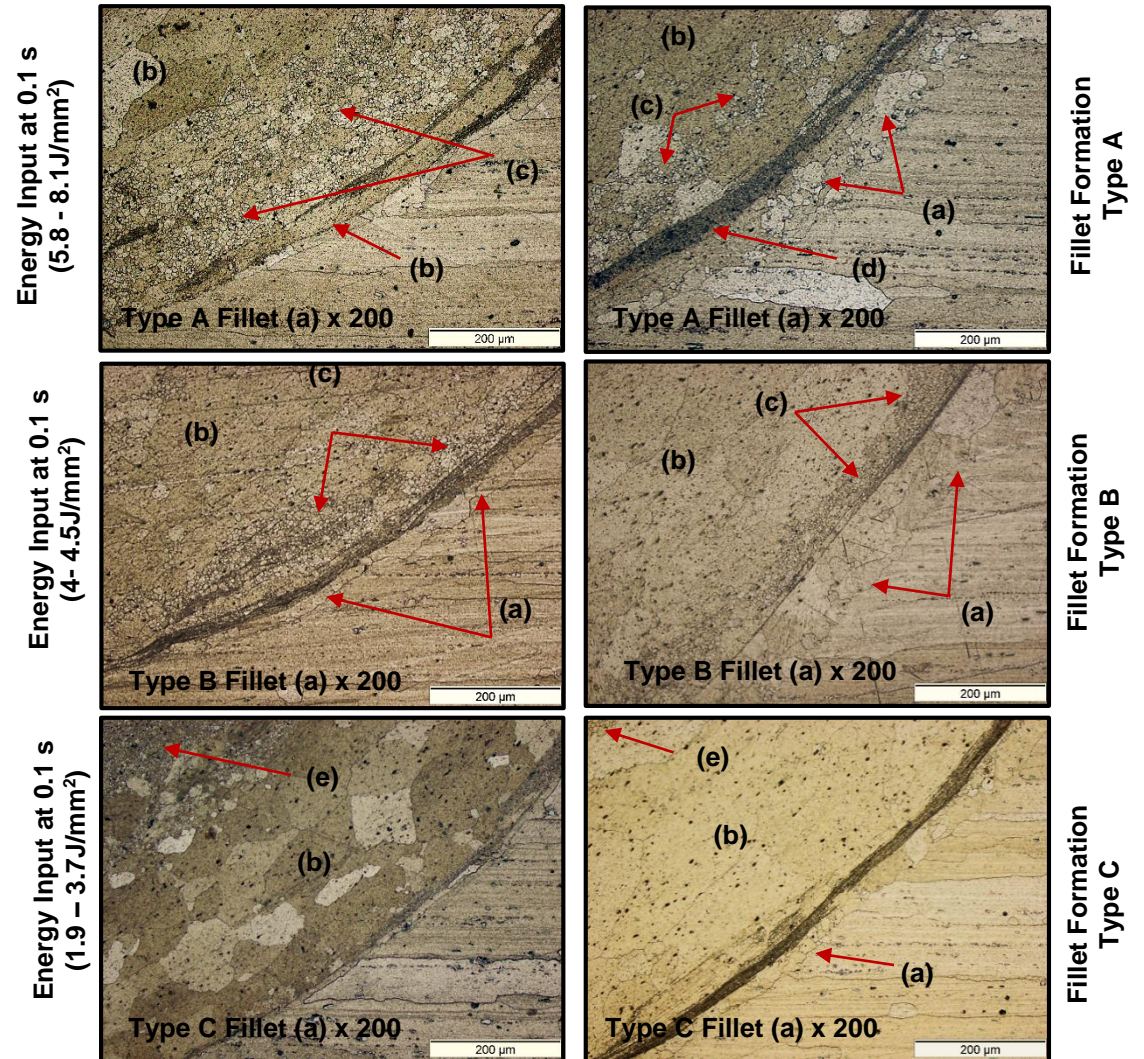


Figure 5-60. Location of the Fillet in the FTSW



(a) Plate Plastic Deformation and Grain Growth (b) AGG (c) Fine Grain Bands (d) Precipitate Band (e) Fine Dynamically Recrystallized Stud Material

Figure 5-59. Typical Microstructure Types Identified at the Fillet Relative to Energy Input

The microstructure for type A fillets is shown to have localised AGG at the fillet of all welds as shown in Figure 5-61, with plastic deformation and recrystallization of the plate clearly evident. There is no distinct bond line, with no welds showing voids or lack of fusion. The welds mostly showed the retention of fine grains in bands offset from the weld interface into the stud material. The AGG was, therefore, located at the bond line, followed consecutively by a band of fine grains, a narrow band of AGG and finally the fine grained dynamically recrystallized stud material.

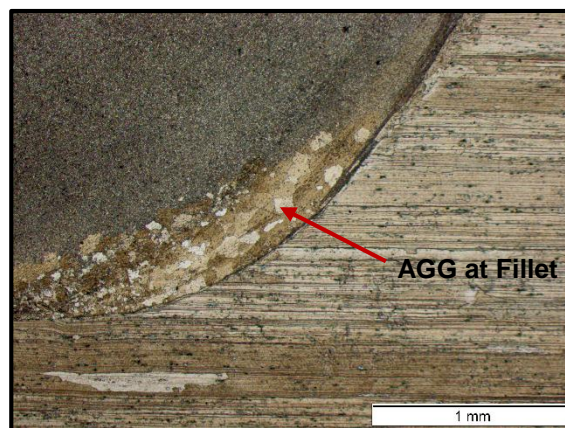


**Figure 5-61. Localised AGG at the Fillet of all Type A and B Fillets**

Type B fillet microstructures were found to also all have AGG localised at the fillet, with a band of fine grains at the interface commonly observed. The fine grains are followed by a band of AGG in the stud material before transition to the dynamically recrystallized stud material. The most significant difference between type A and type B fillets is the movement of the fine grain band to the bond line.

Type C fillets have AGG at the fillet for 4 of the 6 welds, with the remaining two having no AGG at all. No type C fillets retained fine grains between the dynamically recrystallized stud and the weld interface. These welds typically had less plastic deformation of the plate, with less recrystallization of the plate at the bond line. These welds show that welding times below 3 seconds with total energy input rates above  $15.2\text{W/mm}^2$  do not form AGG at all. Welds that did not form AGG at the fillet also both had maximum near interface temperatures below  $400^\circ\text{C}$ , linking energy input, energy input rate, low near interface temperature and time to the formation of AGG.

The separation of the three fillet types clearly show that process parameters and geometry that cause high energy input in the first 0.1 seconds of the weld produces welds with localised AGG at the fillet. The fine grains seen in fillet type A and type B are fragmented remains of the initial dynamically recrystallized microstructure formed as the interface moved up in the hole in the beginning stages of the weld. These fragmented remains appear to not have had sufficiently distorted crystallographic structures to drive the formation of AGG. This was seen previously in the material adjacent to the fillet and shear interfaces in the body of the weld nugget of weld TW-21. AGG is located at the fillet of the tapered hole because this region experienced high normal forces at initial contact at the start of the process as there is no clearance between the hole and stud. This promotes the formation of a highly distorted and unstable crystallographic structure that are susceptible to AGG.

The main key parameter separating type A fillets and Type B fillets is that type A fillets are formed only at 5000RPM and with four out of five using 58° studs, while three out of five type B fillets are formed at 3000RPM with four out of five formed with a 55° stud. This shows the occurrence of AGG and the distribution and location of the fragmented fine grain bands to be peripheral velocity, material flow and geometry dependant. High rotational speeds have been shown to increase the width of the heated band of material behind the welding interface, causing zones of dynamically recrystallized stud material that have crystallographic microstructures that are less distorted and hence less susceptible to AGG, forming the separating zones between the AGG bands seen in Weld TW-21. The relieving of the stressed crystal structure at the weld interface of 5000RPM welds is seen in the residual hoop stress measurements of Weld S.2, shown in Figure 5-62. The reverse trend is seen for Weld S.4 in Figure 5-63, which is an identical weld to S.2 with a rotational speed reduction to 3000RPM. The interface is clearly seen to retain more residual hoop stress. As AGG forms strain free grains, it follows that areas with high residual stress consist of the original dynamically recrystallized material, while areas with low residual stress are areas affected by AGG.

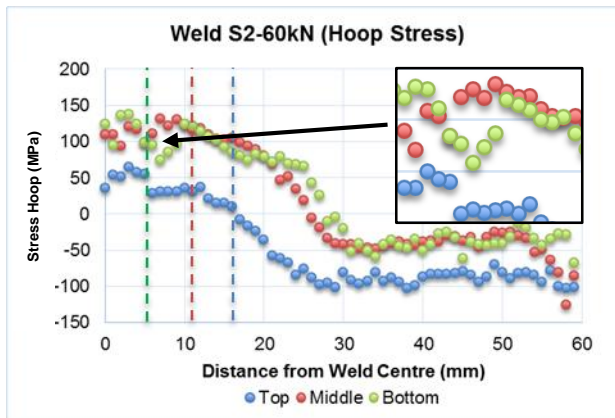


Figure 5-62. Residual Hoop Stress at 5000RPM

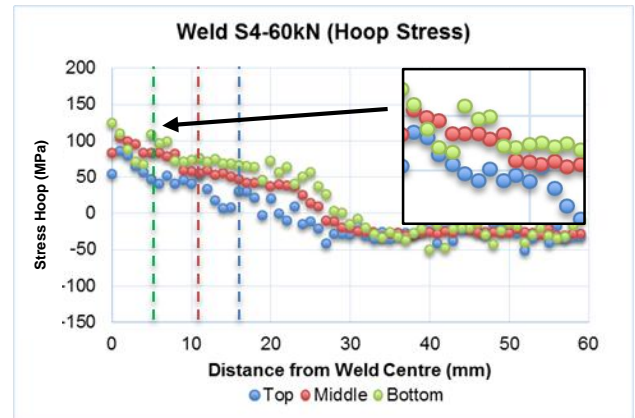


Figure 5-63. Residual Hoop Stress at 3000RPM

The analysis of the fillets show that high total energy input and extended welding times cause AGG at the fillet. This is detrimental to the integrity of the joint as large unstressed grains with low grain boundary areas are weak and allow the propagation of cracks. The results are, however, not clearly conclusive as to which fillet type is more suitable for the process of FTSW of AA6082-T6 as the achieved UTS is constant for all fillet types. However, based on the study of the bond strength at the base of the hole in Welds PT-1 to PT-4, and the micrographs presented above it is the researcher's opinion that the static strength of the base of the hole is superior for 3000RPM welds; however, type C fillets appear to have less plastic deformation of the plate, which may be an indication of weaker bonds than those of type A fillets. For a weld to have a higher energy input at any point in time, the shear stress at the interface would need to have been higher before and up to that point. This would form a more distorted structure that would be susceptible to AGG if exposed to sufficient post formation temperature. This is why high energy inputs are prone to AGG. The higher shear stresses at the interface would promote plastic deformation of the plate, which is seen to typically be greater for fillet type A which is an indication of increased bonding. It is unclear at which point increases in energy input at 0.1 seconds begin to be detrimental to the weld; however, it is clear that values below  $3\text{J/mm}^2$  are insufficient. It may be that energy inputs in the first 0.1 seconds as high as  $8.1\text{J/mm}^2$  would be preferred if the AGG could be prevented, either by cooling of the block below the tapered hole once plunge began, or continuously reducing the rotational speed to optimise the total energy input to a point below which the base of the hole

heats to the activation temperature required for AGG. This will need further investigation, and will be considered in future work.

The data presented in this section shows conclusively that welds with no AGG can only be made if the welding times are kept below 3 seconds, high axial force and axial force ramp up rate is used, a rotational speed of 3000RPM is maintained, a stud taper angle of 58° is used and, most critically, a total energy input in the first 0.1 seconds below 3.7J/mm<sup>2</sup> must be achieved.

### **5.6. Summary**

This chapter has gone through the procedure of process development applied to the successful FTSW of AA6082-T6, producing welds with 77% parent material UTS. The effect of axial force, axial force ramp up rate, stud taper angle and rotational speed are presented with respect to static joint strength, modes of fracture, microhardness and typical bond line microstructures. These are related to energy input, energy input rate and near interface temperature during welding in order to present the reader with a broad perspective of the influence of process parameters in an AA6082-T6 FTSW.

This section presents approaches for identifying a good high integrity weld once appropriate geometry has been identified by observing the formation of the secondary flash. Though not fully conclusive, the visual assessment approach presented is a critical judging method for welds in application or preliminary studies, as welds with incorrect axial force, rotational speed and plunge depth can be identified.

Near ideal energy inputs and energy input rates are identified for the geometry presented in this study, identifying a window within which good welds can be produced. This is considered an important analyses as the process parameters required to produce the best welds made in this study, may be beyond the operating limits of available friction welding platforms. This work presents the reader with the relative information to select process parameter's that suit the available welding equipment and that will meet the desired weld quality, within limits.

Residual stress data is presented, showing no apparent detrimental residual stresses to be formed over a range of applied axial forces and rotational speeds. All Euler Maps, band contrast maps, residual strain maps and grain size maps generated using EBSD are presented for these welds for reference, with high axial force welds showing grain refinement and preferred orientation for high force, high strength welds.

The dynamically recrystallized stud material making up the weld nugget is shown to be approximately as hard as the parent stud material with the T-6 temper intact. This shows the increased material properties due to friction processing and grain refinement, indicating that with a more efficient process parameter's, it may be possible to achieve welds with more than 77% parent material UTS.

## CHAPTER 6

### SUMMARY AND FUTURE WORK

#### 6. Summary

According to the hypothesis, the purpose of this research was to develop a process parameter window for the blind FTSW of AA6082-T6 plate in a partially supported condition, and that a correlation existed between joint integrity, energy input and energy input rate, as stated below.

#### *Hypothesis*

*The research will yield a process window for blind friction taper stud welding AA6082-T6 aluminium plate in a partially supported condition. These process parameters will be directly correlated to input energy, energy input rate and joint integrity to identify the most efficient process conditions.*

This research has fulfilled this goal and has proved the hypothesis to be true. A process parameter window does exist for the samples tested, within which successful FTSW in AA6082-T6 can be made, achieving 77% of the parent material UTS, which is higher than was initially hypothesised by the researcher, due to AA6082-T6 being a heat treatable aluminium. A direct link between process parameters, energy input and energy input rate was established, with energy input and energy input rates at various times into the FTSW shown to give a clear indication of the expected joint integrity.

The only deviation from the initial hypothesis was the abandonment of welding in the partially supported condition. This was due to significant plastic deformation of the bottom surface of the plate, affecting the accurate control of the plunge depth. This will not be of specific concern in this application, as once the appropriate process parameters are selected, the weld can be time controlled, rather than plunge depth controlled.

A successful methodology for calculating the plunge depth required for various geometries in a FTSW in AA6082-T6 has been developed by comparing the

clearance volume in the hole with the displaced volume of the stud. This methodology was shown to be applicable for vastly diverse hole and stud geometries, with a clearance volume vs. displaced volume factor of 18 shown to be appropriate for the material, if a heat sink was fitted to the shank of the stud to prevent swelling of the stud body. All welds in the final test matrix that followed this methodology were shown to be complete and have little to no AGG in the lower regions of the weld. During the plunge depth methodology investigation, the effect of using a plunge depth below the 18 times fill factor was tested. The setup for this weld was the same as for Welds S.2, with no soft touch at the start of the weld. This weld used a plunge depth of 1.7mm instead of the 3mm used for Weld S.2. With this reduction in plunge depth, the UTS for the weld fell from 105.6MPa to 30.48MPa. Considering that only 2mm of plunge was needed to reach the 18 times fill factor, and that a similar weld using the soft start setup and a 2mm plunge depth achieved an UTS of 181.72MPa, the change in plunge depth detrimentally affected the weld. This shows how critical the control of plunge depth is for FTSW with large taper angles.

A hole and stud geometry has been identified, that produce good welds, with a minimum hole angle of  $60^\circ$  shown to be required. The accompanying  $55^\circ$  and  $58^\circ$  stud angles showed that this geometry eliminated the formation of violent shears during welding and gave good bonding in the mid region of the hole.

Data logging equipment has been developed and presented for the accurate measurement of process torque during the FTSW process, allowing for energy input and energy input rate at various times into the weld to be calculated. This has allowed a new approach for in the development of FTSW with respect to energy input and has furthered the fundamental understanding of the process. Process torque is shown to be a good indicator of appropriately chosen process parameters, and can be used to verify that a weld was completed in the manner expected; however, individually does not enable clear determination of a good weld, without the selection of appropriate hole and stud geometries.

The identification of a good weld is shown to be supported by the analyses of energy input and energy input rate, which clearly shows a trend with regards to static joint strength. It is shown to be critical that geometry and energy input rate



are considered together when analysing the energy data of a FTSW, as energy input alone can be ambiguous. An excellent example of this is the energy data from Weld TW-8 and Weld FM-16. Weld FM-8 has a total energy input of  $32.1\text{J/mm}^2$  and an energy input rate of  $13.2\text{W/mm}^2$  while Weld FM-16 has a total energy input of  $21.8\text{J/mm}^2$  and an energy input rate of  $15.2\text{W/mm}^2$ . These welds would appear similar with respect to total energy input and energy input rate, however Weld TW-8 has no notable sidewall bonding, while Weld FM-16 was the weld with the highest joint integrity made during this investigation, achieving 77% parent material UTS. The key difference between these welds lies in the taper angles of the hole and stud, with Weld TW-8 having a hole angle of  $20^\circ$  and Weld FM-16 a hole angle of  $60^\circ$ . This analogy aims to highlight that it is critical when analysing the energy data of a FTSW, to take into account geometry, for energy analyses cannot be directly related to static joint strength if appropriate geometry is not predetermined for the material.

This research has shown that the full control of axial force ramp up rate and tool free air plunge rate is essential for the successful FTSW of AA6082-T6. This allows for a brief rubbing phase at the base of the hole before the initiation of plunge, before the system changes to a pure axial force control setup. This rubbing stage allows critical heating time at the base of the hole, promoting rubbing away of the surface roughness, and preventing mechanical lockup of the stud, while being brief enough to not detrimentally heat the body of the stud.

Axial Force ramp up rate is further shown to be the most critical process parameter in an AA6082-T6 FTSW. Without control of this parameter above  $45\text{kN/s}$ , no good welds can be produced in this material, regardless of geometry and other process parameter choices. When axial force ramp up rates below  $45\text{kN/s}$  are applied, the body of the stud will heat and detrimentally soften during the axial force ramp up rate stage and cause the stud to prematurely collapse as the axial force becomes too high for the softening material to support. This will reduce the energy input in the first stages of the weld, which will decrease rubbing and hence plasticisation of the sidewall. The final shear interface will form higher in the tapered hole, which is shown to give low near interface temperature response at the bottom of the hole, and poor overall static weld strength characteristics due to poor bonding. The axial force ramp up rate is further found

to be material dependant, not geometry, as FTSW in steel is typically successfully achieved with axial force ramp up rates in the order of 15kN/s to 25kN/s.

The influence of using a removable heat sink was investigated and is presented in this study, with the results showing the use of the heat sink to be unavoidable when FTSW is applied to AA6082-T6, without significant swelling and eventual collapse of the stud nose and shank. The collapse of the stud will prevent rotation of the stud body in the tapered hole and hence plasticization of the surface of the hole. Further, the heat sink was shown to increase the total energy input capability of the stud by 47%.

Preheat of 140°C was shown to contribute to bonding by allowing for more energy to be put into the weld during the first stage of the process, and to reduce the conduction of the heat generated during welding away from the weld interface, promoting plasticization. As a final verification of the influence of preheat, the best 55° stud weld (Weld FM-4) was repeated without preheat. Weld FM-4 with preheat achieved an UTS of 225.2MPa and Weld FM-4 made without preheat achieved an UTS of 148MPa. This is a significant drop in UTS that cannot be overcome with any process parameter changes when using like stud and plate materials.

Energy input maps have been developed that show the locations of ideal energy input and energy input rates. The data shows that for good welds an approximate total energy input of 55J/mm<sup>2</sup> is needed, at an average energy input rate of 13W/mm<sup>2</sup> to 14W/mm<sup>2</sup>. Total energy inputs between 65J/mm<sup>2</sup> and 80J/mm<sup>2</sup> were found to fail repeatedly at the weld interface, typically at reduced static UTS.

One of the large issues facing FTSW and its implementation in industry currently is complications with transferring known good process parameters between dissimilar welding platforms. This issue has been addressed in this research by identifying the critical success factor, axial force ramp up rate and the need for its linearity over a wide range of plunge rates. This parameter was non-adjustable and non-linear on the initial FTSW platform, making it difficult to transfer results to the PDS friction welding platform as the non-linear axial force ramp up rate is not easily repeatable. The work has shown that if the boundary conditions for the

weld are similar and the same axial force ramp up rate is used (governing within  $\pm 5\text{kN/s}$ ), identified good welding parameters can be confidently transferred between two friction welding platforms.

The process development stage of this research has identified that there is a critical stud size relationship between the thickness of the plate, the depth of the hole and the diameter of the stud. This means that for a 20mm deep hole in 25mm thick AA6082-T6, a nose diameter for the stud would be recommended as 10mm. If the nose diameter is reduced significantly, the body of the stud will not be capable of generating the necessary energy input and energy input rate to overcome the dissipation of heat into the plate.

### 6.1. Recommended Future Work

- The cold forge defect at the base of the hole needs to be addressed, possibly by using a small clearance of approximately 0.1mm to 0.2mm between the base diameter of the stud and the base diameter of the plate. This will reduce the risk of forming AGG at the fillet of the weld, further improving the joint integrity.
- Welds made with continuously reducing rotational speed should be considered in order to maintain a constant peripheral velocity at the welding interface during plunge. This has been shown to be beneficial to the joint static strength in this work, and if appropriately controlled with respect to the plunge depth, may reduce excessive softening in the HAZ and promote deep tearing of the weld interface during the FTSW process instead of rubbing. This will further minimise the plastic deformation of the plate and total energy input as shown in this study, leading to the formation of more efficient welds with above 77% parent material UTS. Due to the increase in process torque with reducing rotational speed, it may not be ideal to keep the peripheral velocity constant as the process torque may exceed the limits of the welding platform. If this is the case, a reduced and controlled rotational speed should then be considered.
- It would be ideal to divide the axial force ramp up rate into two stages, namely the axial force ramp up rate before the initiation of plunge and the axial force ramp up rate during plunge. This will allow control of the applied

axial force and hence the pressure between the welding interfaces throughout the welding process. If this is then taken a step further and the axial force ramp up rate is made dependant on plunge depth, the pressure between the welding interfaces during welding can be optimised. This will prevent the situation where excessive axial force is applied during plunge, preventing poorly bonded regions caused by premature stud collapse.

- The most successful welds made in this study should be repeated and the welding times verified for repeatability. This will allow similar welds to be made based on welding time and not plunge depth. This is not necessarily a more accurate control method but it will allow the FTSW of AA6082-T6 to be applied in the partially supported condition, as plastic deformation at the bottom surface of the plate will not reduce the welding time and volume of displaced stud material.
- The static tensile strength between Welds FM-1 to FM-16 did not deviate significantly for changes in energy input and energy input rate. It is therefore recommended that good parameters be selected from the test matrix and are fatigue tested as this will highlight the effect of changes in energy input.
- A method of tensile testing the bond strength at the base of the hole when having the tapered section of the stud in place during welding, needs to be considered. This will allow process parameters to be selected that give good base and sidewall bonding and represent a complete weld.
- A thorough analysis of the precipitates and phases formed along the bond line for different process parameter and energy input values needs to be conducted. This will allow the process parameters that are presented to be further optimised.
- An alternative heat sink design needs to be investigated, possibly one that splits in half with retaining bolts. This will reduce machining time as maintaining the tight tolerance for the heat sink fitment over the body length of the stud is troublesome. Also, this will make it easier to remove the heat sink once the weld is complete, as the softening of the stud tends to lock the heat sink to the stud body on welds with long welding times.

**BIBLIOGRAPHY**

- [1] F. J. Humphreys and M. Hatherly, *Recrystallization and Related Annealing Phenomena*, 2nd ed., Oxford UK: Elsevier, 2004.
- [2] S. Malan and A. Paterson, *Introduction to Aluminium*, Aluminium Federation of South Africa, 1993.
- [3] P. Hartley, "Friction Plug Weld Repairs for the Space Shuttle External Tanks," *Welding and Metal Fabrication*, 2000.
- [4] K. Beamish, "Friction taper plug welding of 10mm AA6082-T6," The Welding Institute, Cambridge, 2003.
- [5] D. L. Bulbring, "Characterization of Friction taper Stud Weld Properties as applied to AISI 4140 High Tensile Alloy Steel," Port Elizabeth, 2008.
- [6] D. G. Hattingh, D. L. Bulbring, A. Els-Botes and M. N. James, "Process Parameter Influence on Performance of Friction Taper Stud Welds in AISI 4140 steel," *Elsevier - Materials & Design*, vol. 32, no. 6, pp. 3421-3430, February 2011.
- [7] P. A. Eder, P. N. Francisco, Y. A. Chen and C. d. S. Euclides, "Experimental Determination of Temperature During Rotary Friction Welding of AA1050 Aluminium with AISI 304 Stainless Steel," *J. Aerosp. Technol. Manag.*, São José dos Campos, vol. 4, no. 1, pp. 61-67, January-March 2012.
- [8] V. I. Vill, "Welding Metals By Friction," Ohio, 1960.
- [9] R. Andrews and K. Beamish, "Characterisation of and guidelines for rotary friction welding of common metallic engineering materials," The Welding Institute (TWI), Cambridge, 2005.
- [10] G. A. Pinheiro, "Local Reinforcement of Magnesium Components by Friction Processing: Determination of Bonding Mechanisms and Assessment of Joint Properties," Helmholtz, 2008.
- [11] M. Meyar, "Friction Hydro Pillar Processing - Bonding Mechanism and Properties," Geesthacht, 2003.
- [12] V. I. Vill, *Friction Welding of Metals*, New York: Feinholds Publishing Corporation, 1962.
- [13] M. Kimura, K. Seo, M. Kusaka and A. Fuji, "Observation of joining phenomena in friction stage and improving friction welding method," *JSME*, vol. A/36/3, pp. 384-390, 2003.
- [14] M. N. Ahmad, M. B. Uday, H. Zuhailawati and A. B. Ismail, "Microstructure and mechanical properties of alumina-6061 aluminium alloy joined by friction welding," *Metal and Design (Elsevier)*, vol. 31, pp. 670-676, August 2009.
- [15] AFROX, 2013. [Online]. Available: [http://www.afrox.co.za/internet.global.corp.zaf/en/images/Section%2012%20-%20Welding%20Consumables%20-%20Aluminium266\\_27347.pdf](http://www.afrox.co.za/internet.global.corp.zaf/en/images/Section%2012%20-%20Welding%20Consumables%20-%20Aluminium266_27347.pdf). [Accessed 06 June 2010].
- [16] ALFED, 2013. [Online]. Available: [http://www.powerofaluminium.com/page.asp?node=86&sec=Fusion\\_Welding\\_](http://www.powerofaluminium.com/page.asp?node=86&sec=Fusion_Welding_). [Accessed 05 June 2010].

- [17] aalco, 2013. [Online]. Available: <http://www.azom.com/article.aspx?ArticleID=2813> . [Accessed 2 February 2010].
- [18] E. Nicholas, "Friction Processing Technologies," *TWI Welding in the World*, vol. 47, no. 11/12, 2003.
- [19] E. D. Nicholas, "Friction Hydro Pillar Processing," in *11th Annual North American Welding Research Conference - Advances in Welding Technology*, 1995.
- [20] M. Mahoney, N. Taylor, W. Bingel, F. Long, R. A. Spurling and G. S. Steele, "Method to Repair Voids in Aluminium Alloys". United States of America Patent 5,975,406, 2 November 1999.
- [21] P. Drews and J. Schmidt, "Steuerung des Reibschweißvorganges zum Erzielen eines vorbestimmten Endmaßes," *Zeitschrift für industrielle Fertigung, Springer Verlag (Journal of Industrial Manufacturing)*, vol. 68, pp. 387-393, 1978.
- [22] M. Sahin, "An investigation into joining of austenitic-stainless steels (AISI 304) with friction welding.," *Assembly automation*, vol. 25, no. 2, pp. 140-145, 2005.
- [23] D. Samuel, Masters Disertation/ Characterization of Joint Integrity of Friction Stud Welding As Applied To Aisi 304l Stainless Steel, Port Elizabeth: Nelson Mandela Metropolitan University, 2009.
- [24] V. V. Satyanarayana, G. M. Reddy and T. Mohandas, "Dissimilar metal friction welding of austenitic-ferritic stainless steels.," *Journal of Materials Processing Technology*, vol. 160, pp. 128-137, 2005.
- [25] V. G. Voinov, "Mechanism of Joint Formation in Friction Welding," *Welding Production*, vol. 15, pp. 8-13, 1968.
- [26] I. MITELEA, A. MOSILA and B. RADU, "The Role of Axil Pressure for Friction Welding of QT Heat Treated Components," *ANNALS of the ORADEA UNIVERSITY (Fascicle of Management and Technological Engineering)*, pp. 1049-1056.
- [27] W. Hofmann and L. Thome, "Einige Einflußgrößen auf das Reibungsschweißen von Stahl und von Aluminium," *Schweißen und Schneiden*, vol. 17, no. 05, pp. 194-199, 1965.
- [28] C. R. Ellis, "Continuous Drive Friction Welding in Mild Steel," *Welding Journal*, pp. 183-197, 1972.
- [29] S. Yu-Lai, L. Yao-hui, Z. Xian-yong, Y. Si-rong and Z. Ying-bo, "Strength Distribution at Interface of Rotary-Friction-Welded Aluminium to Nodular Cast Iron," *Transactions of Nonferrous Metals Society of China*, pp. 14-18, 2007.
- [30] M. Renshaw, The Welding of Aluminium Castings, Gauteng: on behalf of The Aluminium Federation of Southern Africa (AFSA), 2004.
- [31] BOC, 2007. [Online]. Available: <http://www.bocworldofwelding.com.au/media/pdf/file/library/WOWLibrary-Preheating%20of%20materials-Consumables.pdf>. [Accessed 03 November 2010].
- [32] Alcotec, 2013. [Online]. Available: <http://www.alcotec.com/>. [Accessed 05 June 2010].
- [33] W. D. Callister, *Materials Science and Engineering - An Introduction*, 6th ed., W. Anderson, K. Hepburn, K. Santor , K. G. Kincheloe, S.

- Malinowski, S. Wight and R. Wiemann, Eds., United States of America: John Wiley & Sons, Inc., 2003.
- [34] M. Kimura, H. Inoue, M. Kusaka, K. Kaizu and A. Fuji, "Analysis Method of Friction Torque and Weld Interface Temperature during Friction Processing of Steel Friction Welding," *Journal of Solid Mechanics and Materials Engineering*, vol. 4, no. 3, pp. 401-413, 2010.
- [35] B. Crossland, "Friction Welding-Recommended Practices for Friction Welding," *Contemporary Physics*, vol. 12, no. 6, pp. 559-574, 1971.
- [36] G. A. Pinheiro, C. G. Pankiewicz, C. A. Weis Olea, J. F. Dos Santos and K. U. Kainer, "Effects of Welding Conditions on Microstructural Transformations and Mechanical Properties in AE42HP Friction Welded Joints," in *3rd Workshop on Recent Advances in Friction Welding and Allied Processes*, Dubrovnik, 2007.
- [37] F. Eichhorn and R. Schaefer, "Beitrag zu den Vorgängen an der Verbindungsstelle beim," *Schweißen und Schneiden*, vol. 20, no. 11, pp. 563-570, 1968.
- [38] C. Van Zyl, Masters Dissertation- Analysis and Modelling of Temperature Distribution During the Friction Taper Stud Welding of 10CrMo910, Port Elizabeth: Nelson Mandela Metropolitan University, 2008.
- [39] E. J. Mittemeijer, Fundamentals of Materials Science, Stuttgart: Springer, 2010.
- [40] I. Charit and R. S. Mishra, "Abnormal grain growth in friction stir processed alloys," *ELSEVIER (Scripta Materialia)*, Vols. 58 (367-371), 2008.
- [41] Y. S. Sato, H. Watanabe, S. H. Park and H. Kokawa, "Grain growth in friction stir welded Al alloy 1100," in *5th International Symposium on Friction Stir Welding*, Metz, France,, 2004.
- [42] G. S. Grest, M. P. Anderson, D. J. Srolovitz and A. D. Rollet, "Abnormal Grain Growth in Three Dimensions," *Scripta Metallurgica et Materialia*, vol. 24, pp. 661-665, January 1990.
- [43] D. J. Srolovitz, G. S. Grest and M. P. Anderson, "Computer simulation of grain growth - V. Abnormal Grain Growth," *Acta Metallurgica*, vol. 33, no. 12, pp. 2233-2247, December 1985.
- [44] F. J. Humphreys and M. Hatherly, 2013. [Online]. Available: <http://aluminium.matter.org.uk/content/html/eng/default.asp?catid=69&pageid=2060294757>. [Accessed 08 11 2013].
- [45] A. Nunes, J. McClure and R. Avila, "Torque and Plunge Force During the Plunge Phase of Friction Stir Welding," *ASTM International*, pp. 241-245, 2006.
- [46] S. Missori and A. Sili, "Mechanical behaviour of 6082T6 aluminium alloy welds," *Metallurgical Science and Technology*.
- [47] W. G. Pentz, Development of repair procedure for rotor steelmaterial (26NiCrMoV145) by Friction Hyde Pillar Processing (Masters Thesis), Port Elizabeth: Nelson Mandela Metropolitan University, 2012.
- [48] Y.-L. SONG, Y.-h. LIU, X.-y. ZHU, S.-r. YU and Y.-b. ZHANG, "Strength Distribution at interface of rotary-friction-welded aluminium tp nodular cast iron," in *Transformation of Nonferrous Metals Society of China (Jilin University)*, Changchun China, 2008.

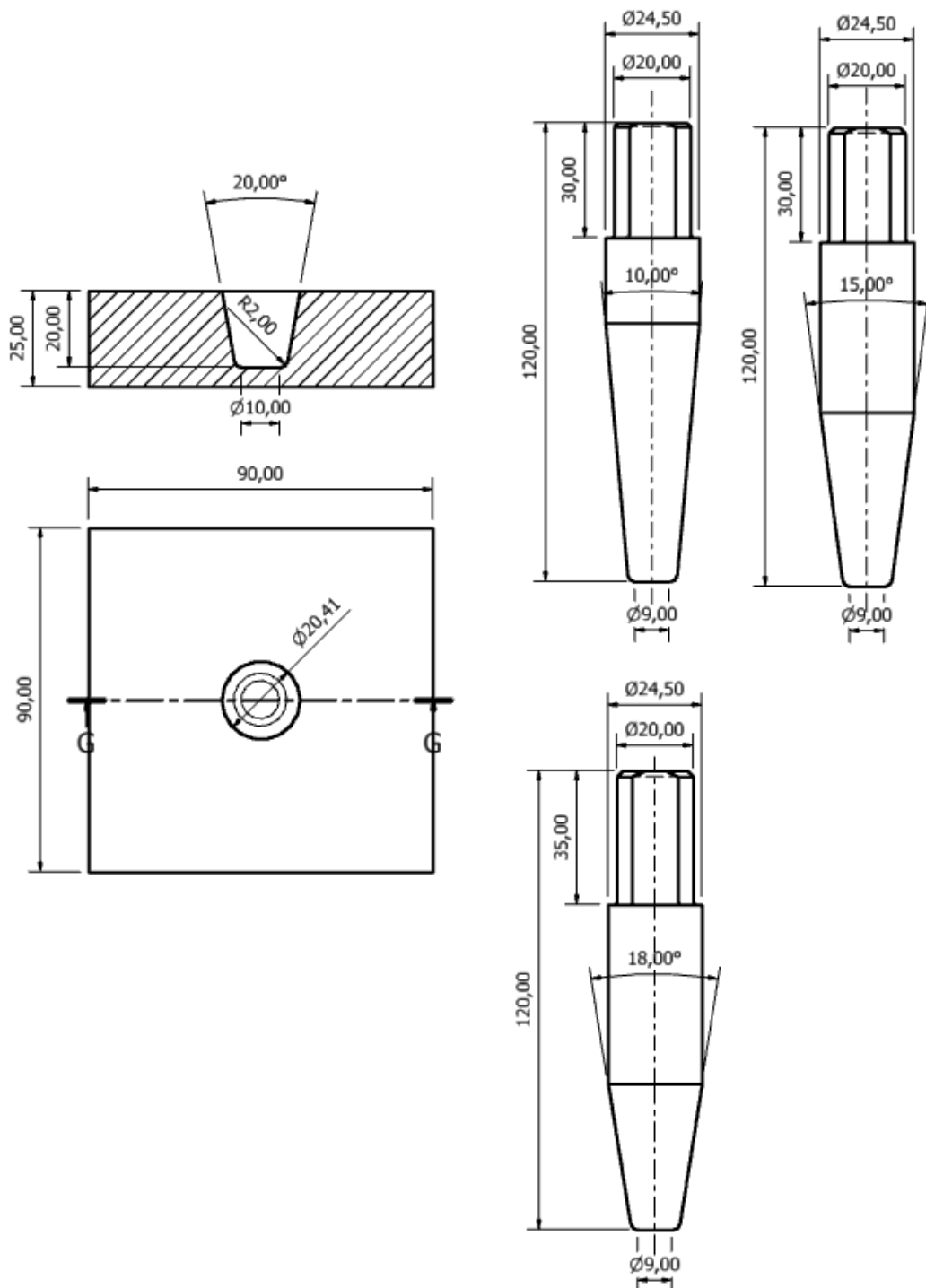
- [49] W. M. Thomas and E. D. Nicholas, "Emerging friction joining technology for stainless steel and aluminium applications," in *Productivity Beyond 2000: IIW Asian Pacific Welding Congress*, Auckland, New Zealand, 1996.
- [50] A. W. S. Abstract, "<http://www.nctfrictionwelding.com/process.php>," 2008. [Online]. [Accessed 27 2 2008].
- [51] E. P. Alves, F. Neto P, Y. A. Chen and E. Castorino da Silva, "Experimental Determination of Temperature During Rotary Friction Welding of AA1050 Aluminium with AISI 304 Stainless Steel," *J. Aerosp. Technol. Manag.*, São José dos Campos, vol. 4, no. 1, pp. 61-67, March 2012.
- [52] S. Missori and A. Sili, "Mechanical Behaviour of 6082-T6 aluminium alloy welds," *Metallurgical Science and Technology*, vol. 18, no. 1, 2000.



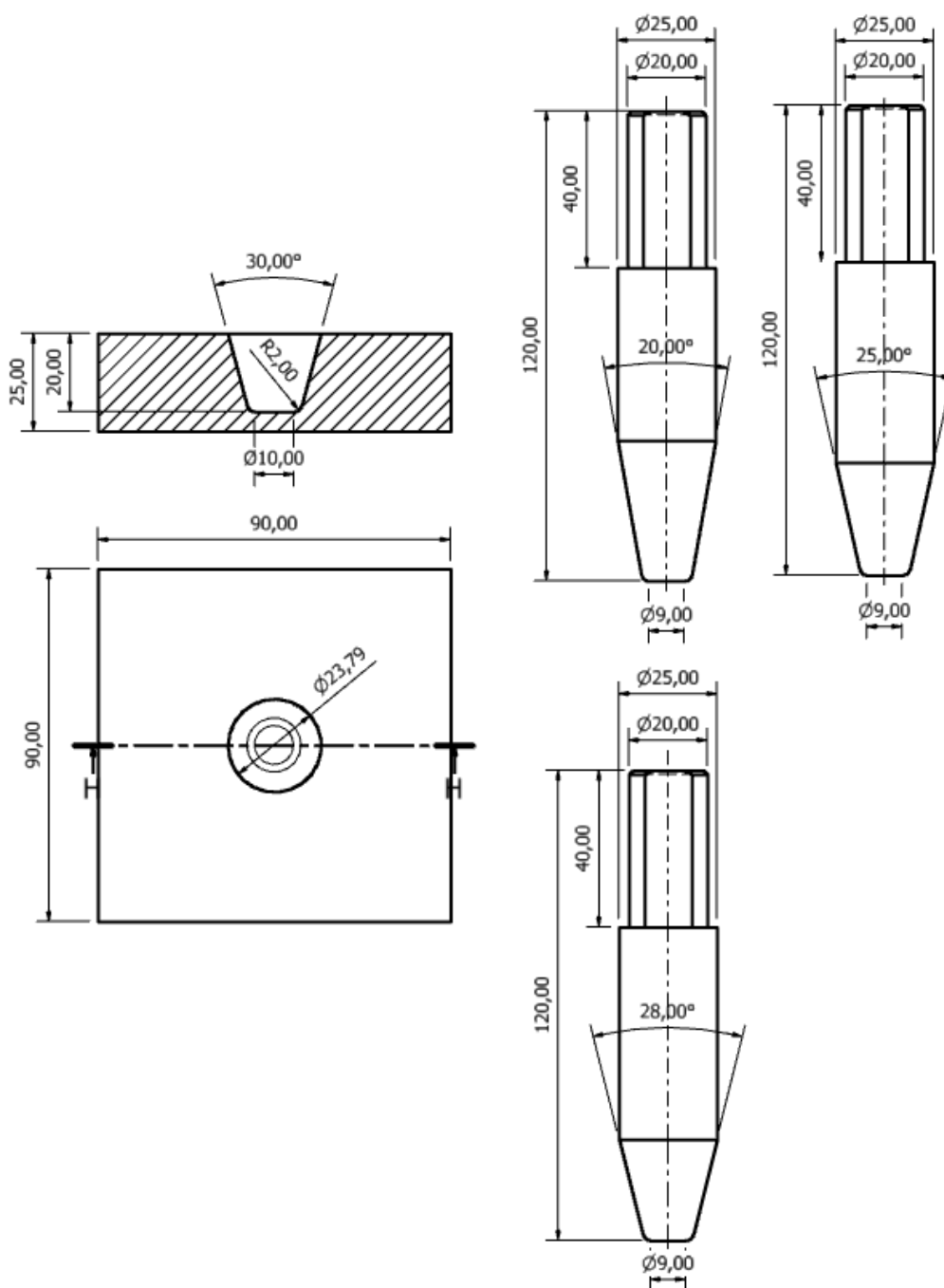
## Appendix A

## Geometry for all the Holes. Studs and Removable Heat Sinks Investigated

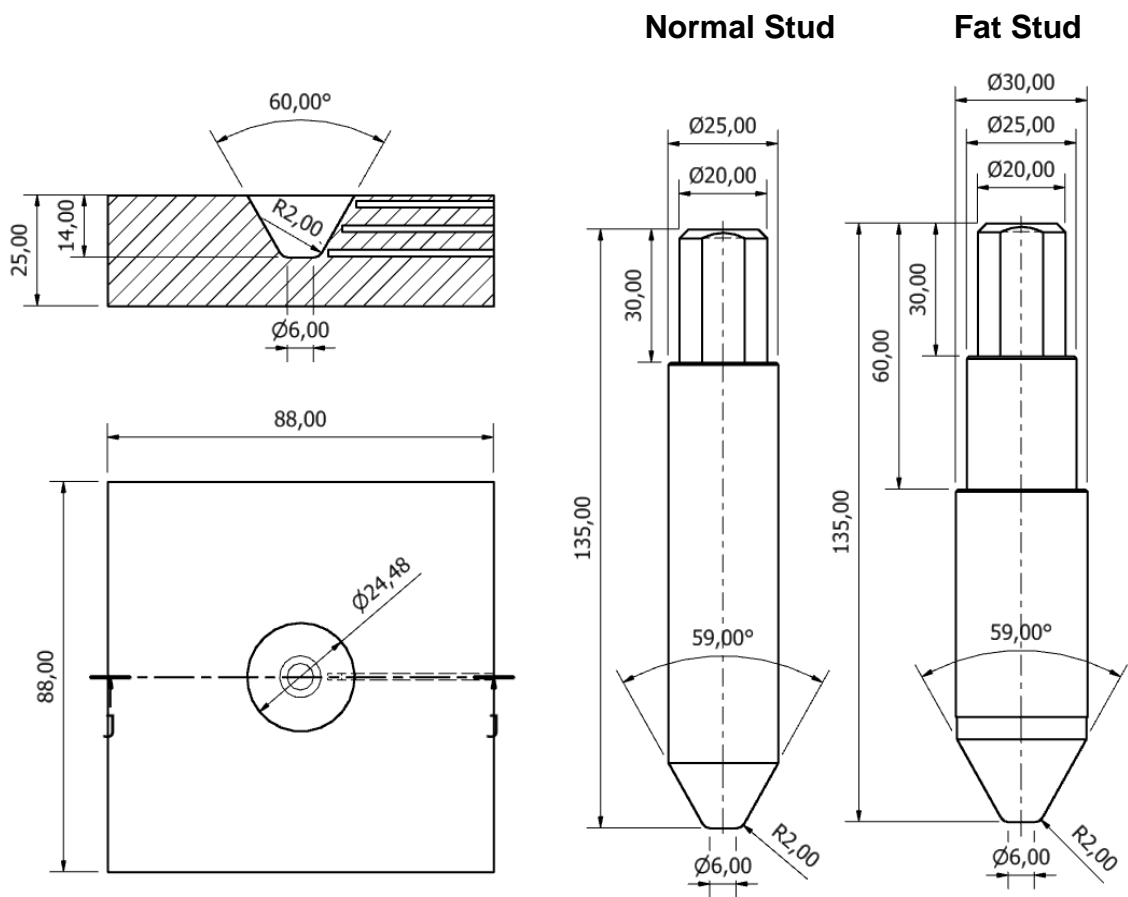
## Geometry for Welds TW-1 to TW-12 and TW-11 and TW-12



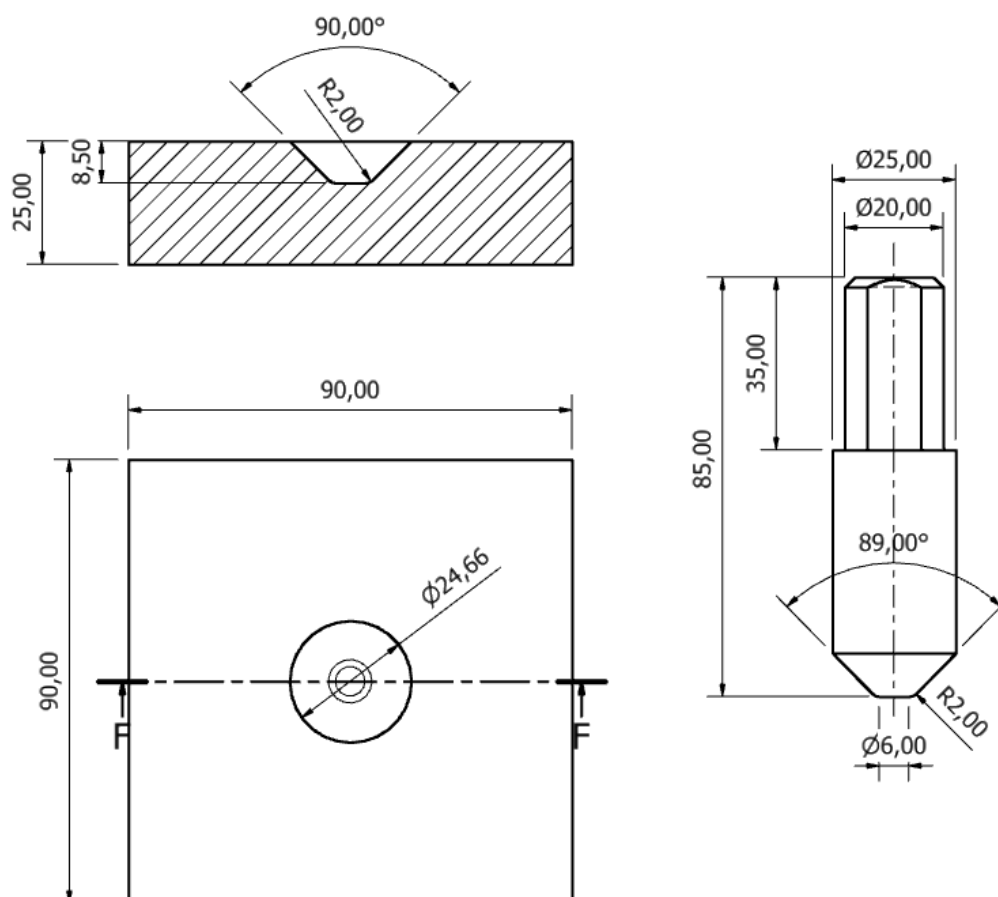
## Geometry for Welds TW-13 to TW-18



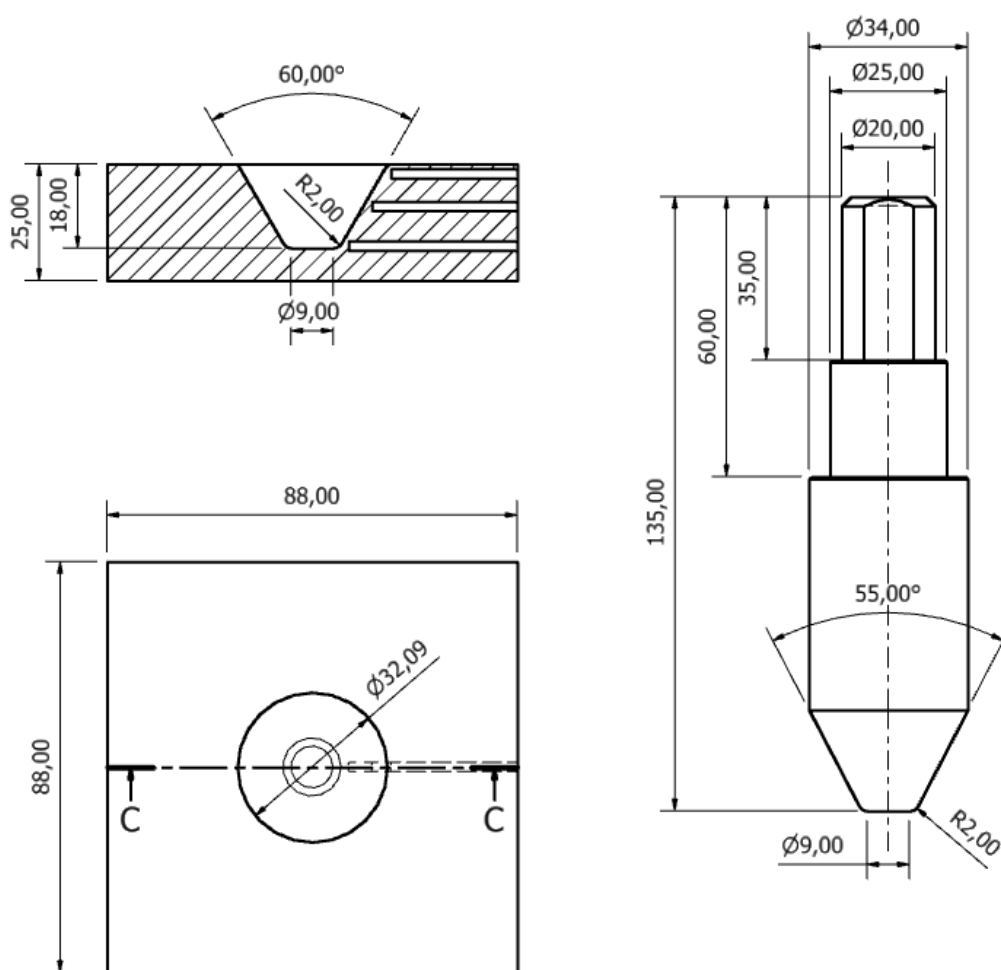
## Geometry for Welds TW-19 to TW-21

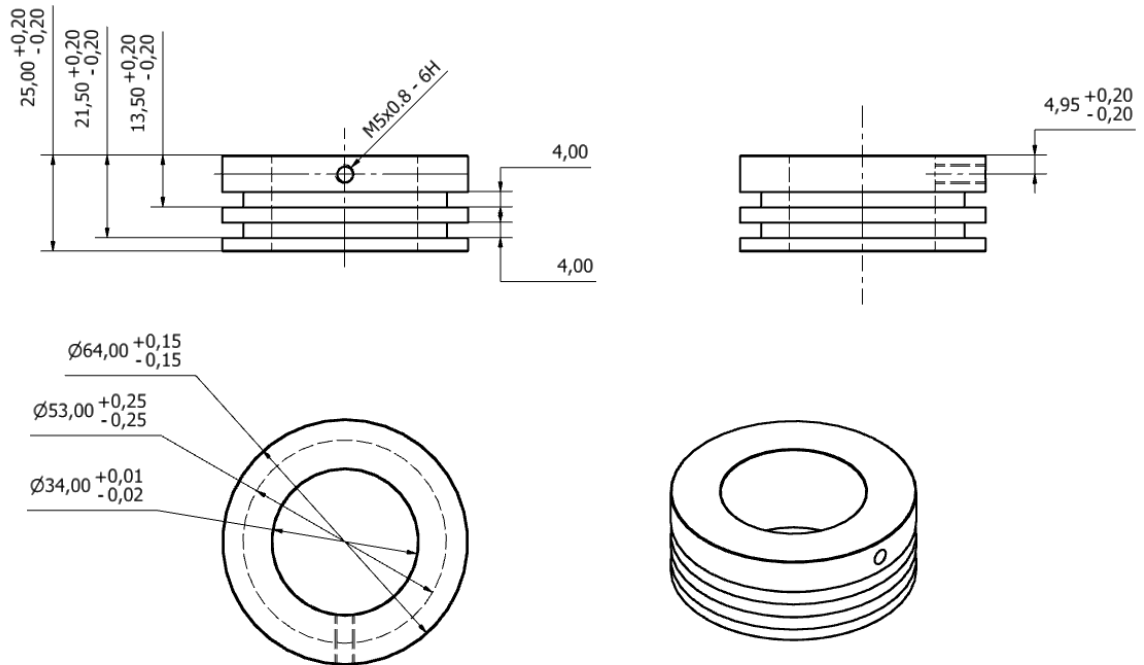


## Geometry for Weld TW-22

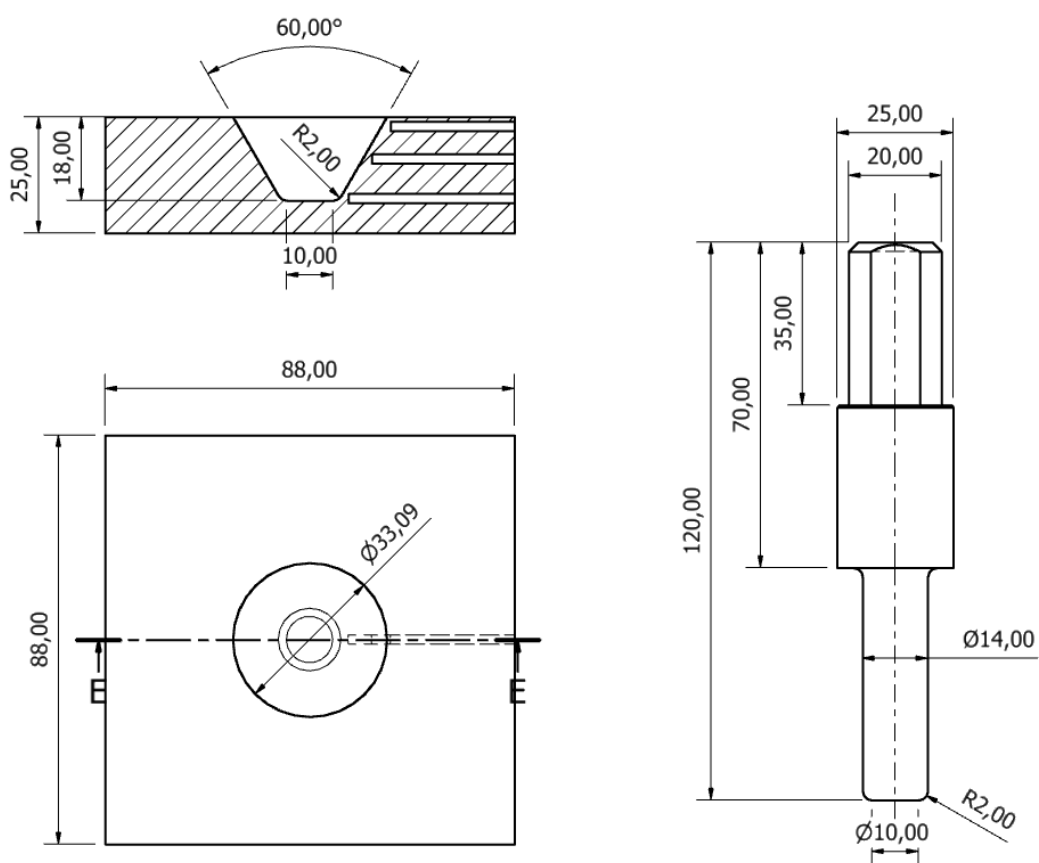


## Geometry for Welds TW-23 and TW-24

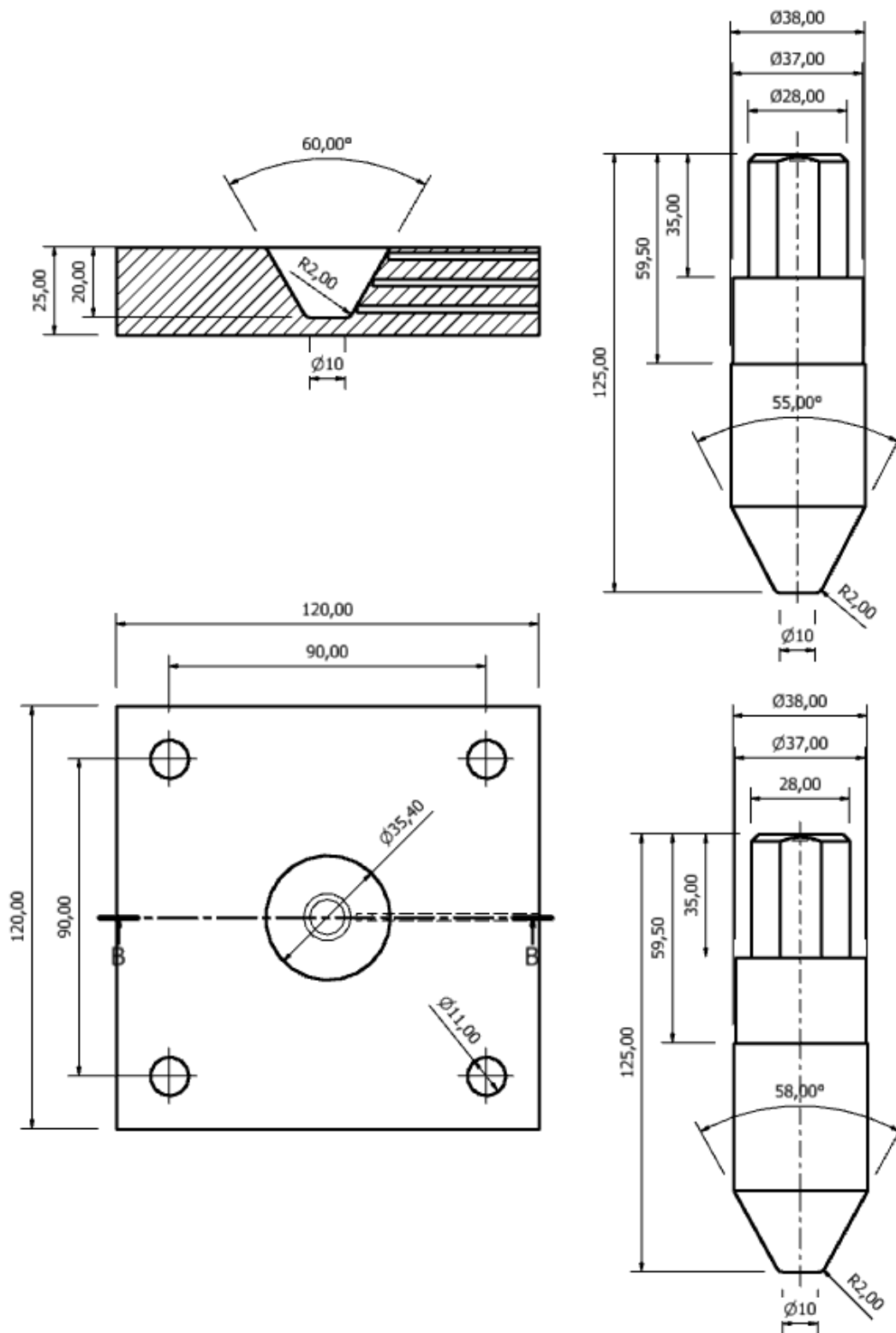


**Geometry for Removable Heat Sink for Development Welds**

## Geometry for Welds PT-1 to PT-2

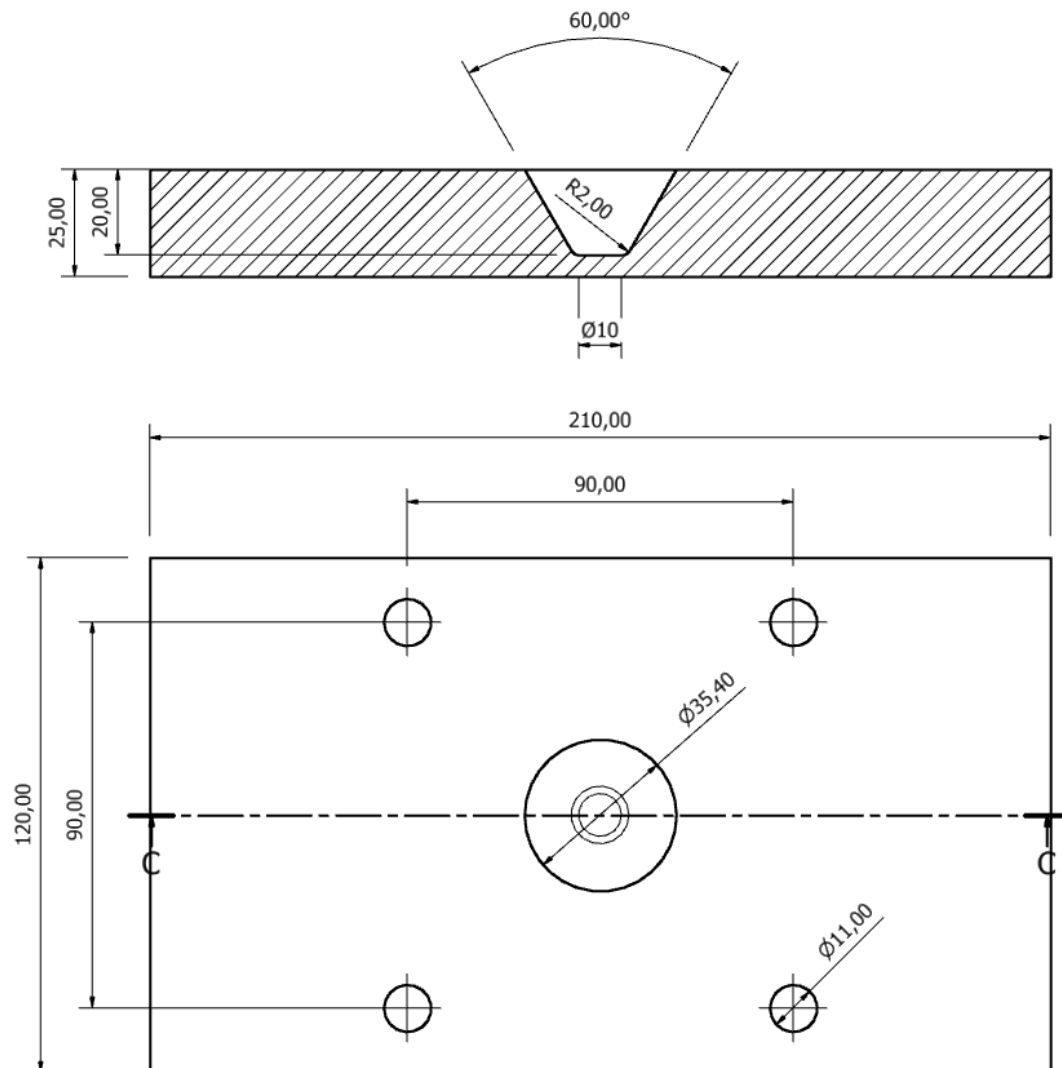


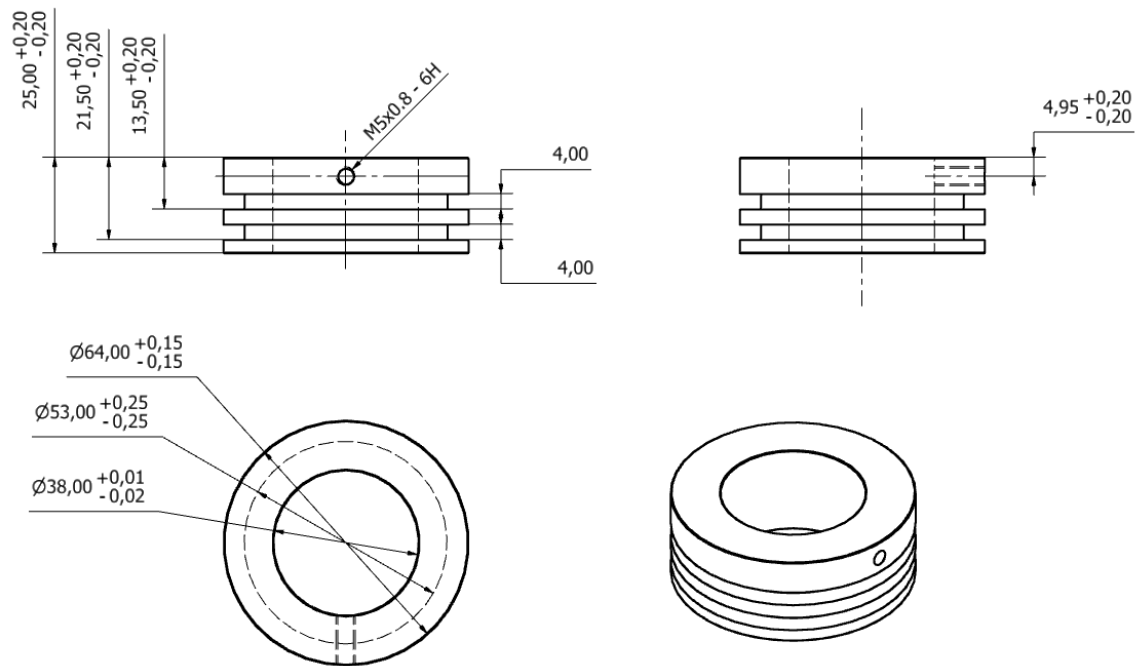
## Geometry for Welds FM-1 to FM-16





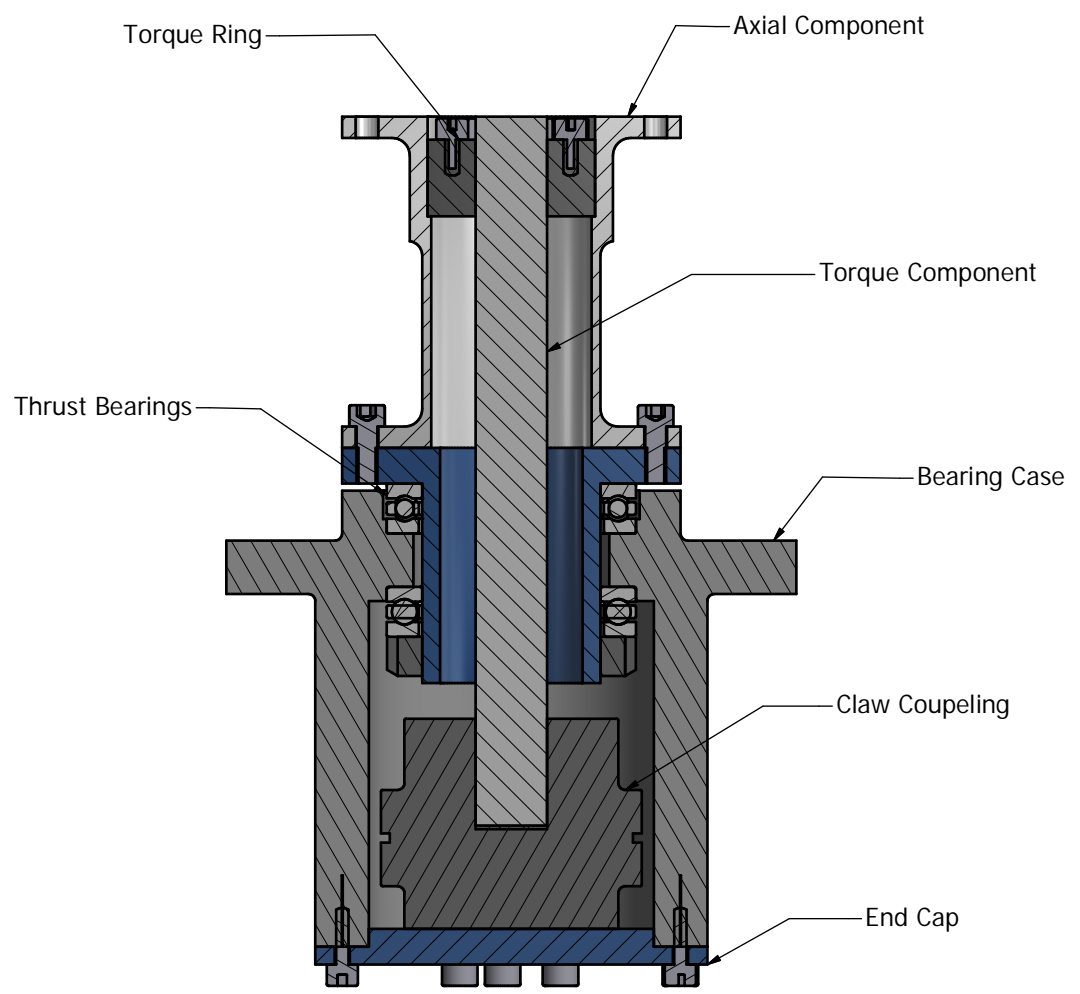
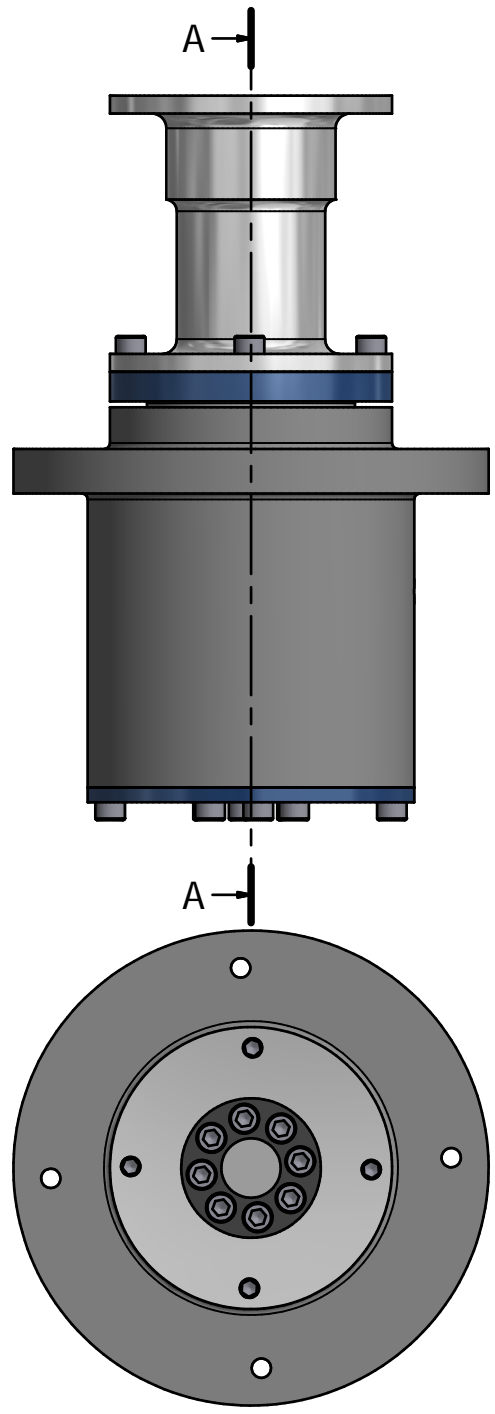
## Geometry for Tensile Welds FM-1 to FM-16



**Geometry for Removable Heat Sink for Welds FM-1 to FM-16**

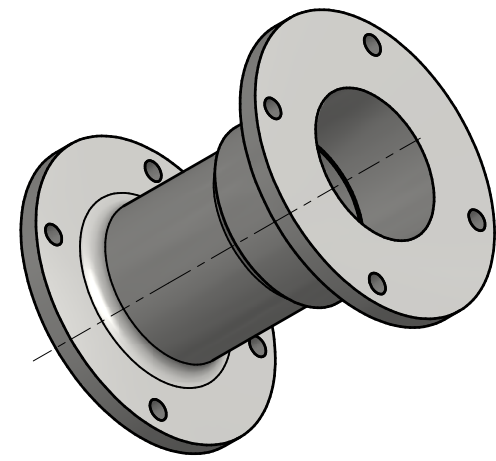
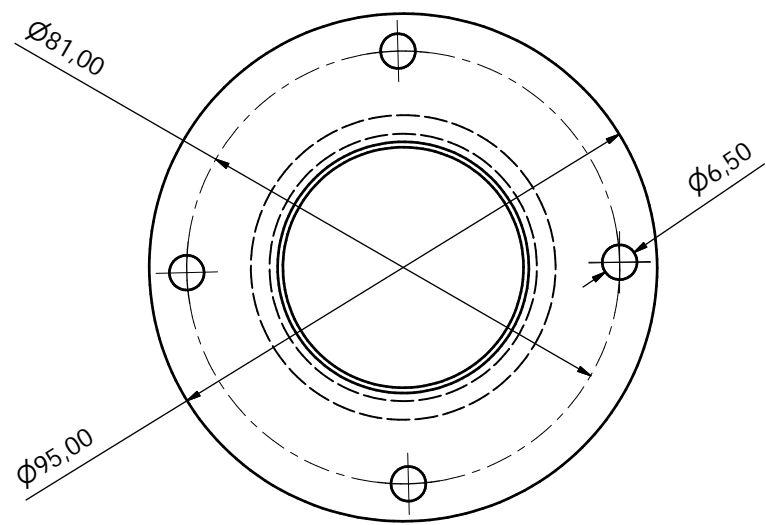
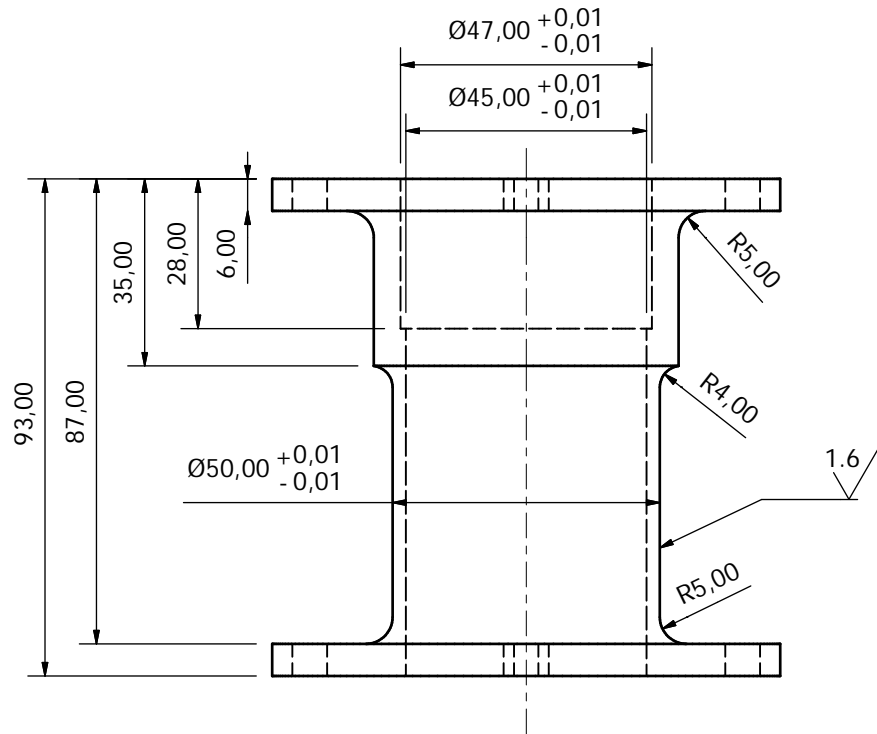
**Appendix B**

**Load Cell Drawings for FTSW Platform**

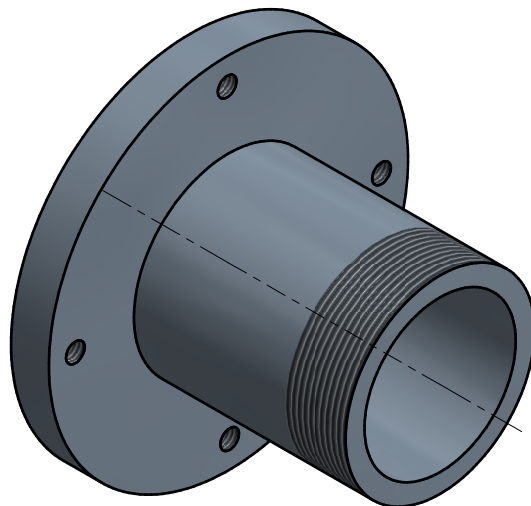
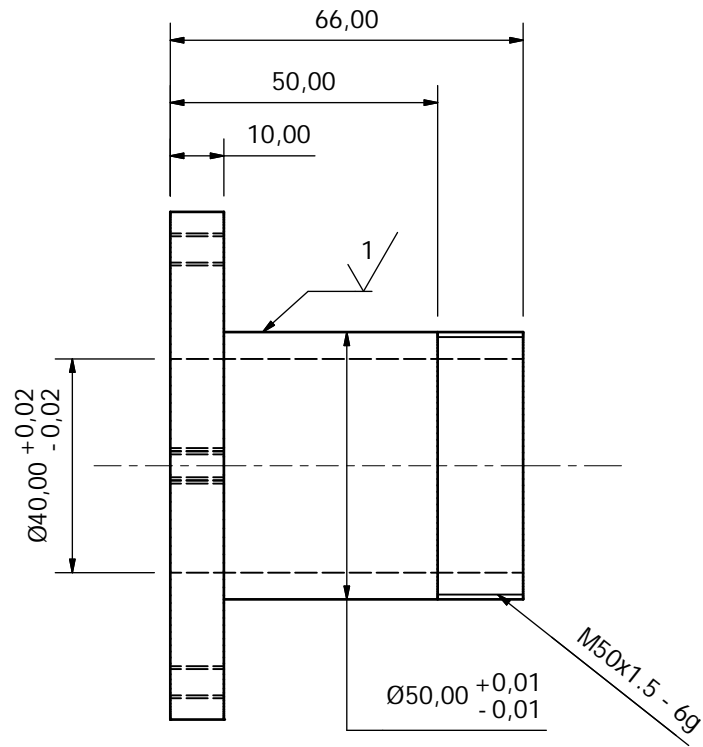
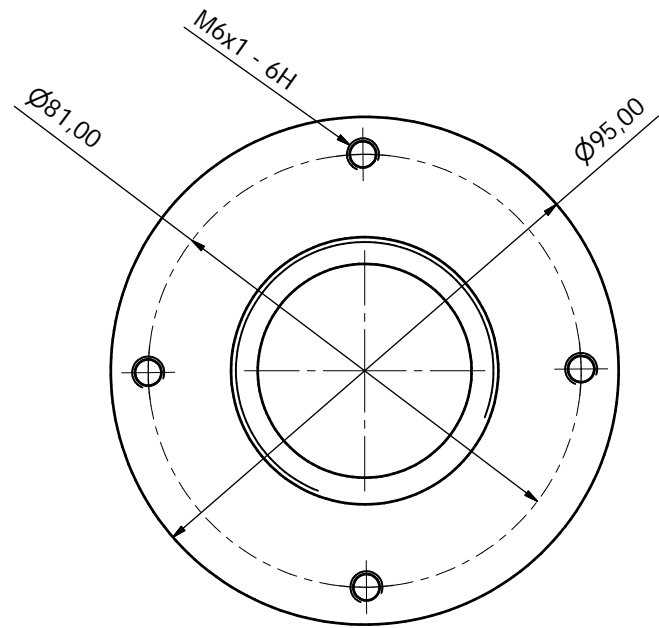


View A-A ( 1 :1.5 )

Designed by Darren	Checked by	Approved by	Date 2014/01/02	Sheet A3	Date 2014/01/02	
<b>eNtsa</b>			Complete Assembly			
			FTSW Platform Load Cell		Edition	Sheet 1 / 6



Designed by Darren	Checked by	Approved by	Date 2014/01/02	Sheet A3	Date 2014/01/02	
<b>eNtsa</b>			Axial Force Component (EN-19)			
			FTSW Platform Load Cell		Edition	Sheet 2 / 6



Designed by Darren	Checked by	Approved by	Date Sheet A3	Date 2014/01/02	
<b>eNtsa</b>			Bearing Shaft (EM-8)		
			FTSW Platform Load Cell		Edition

6 5 4 3 2 1

D

D

C

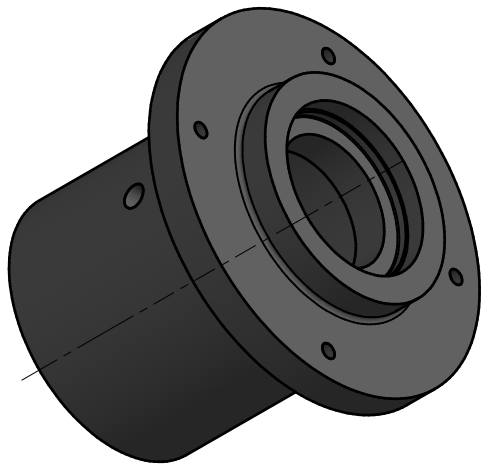
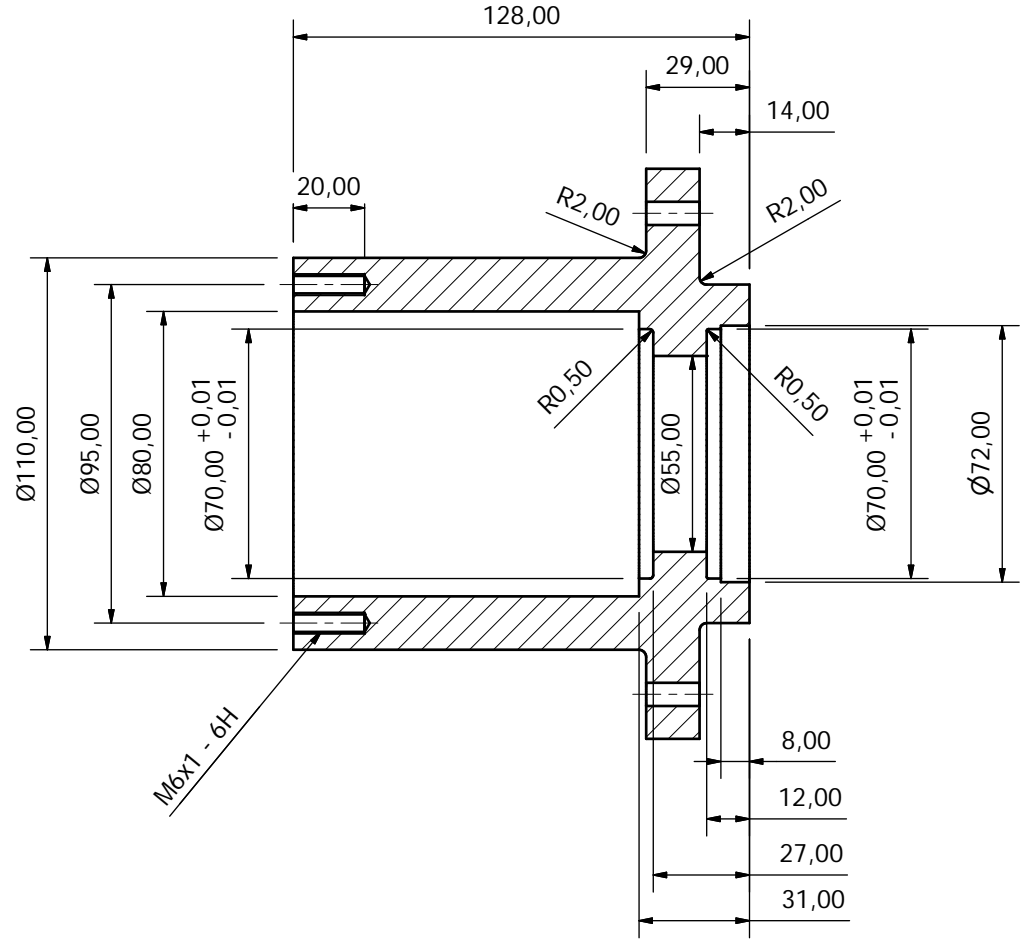
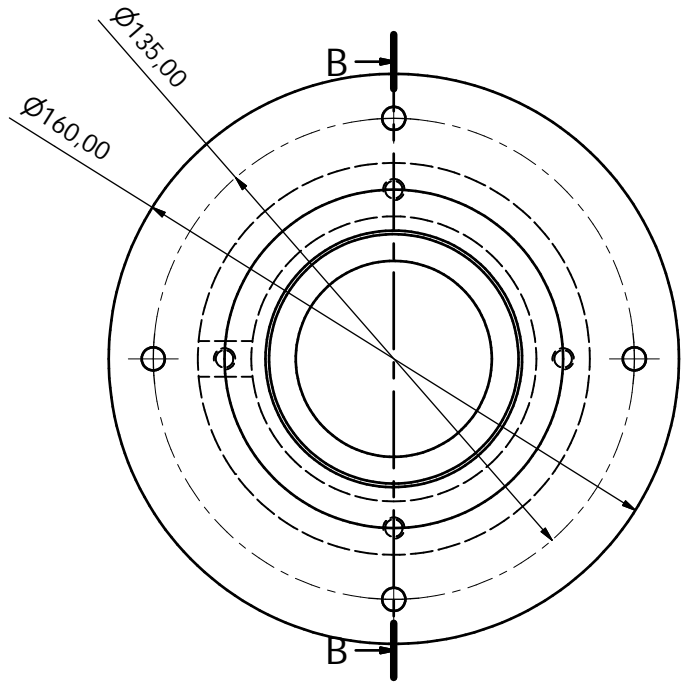
C

B

B

A

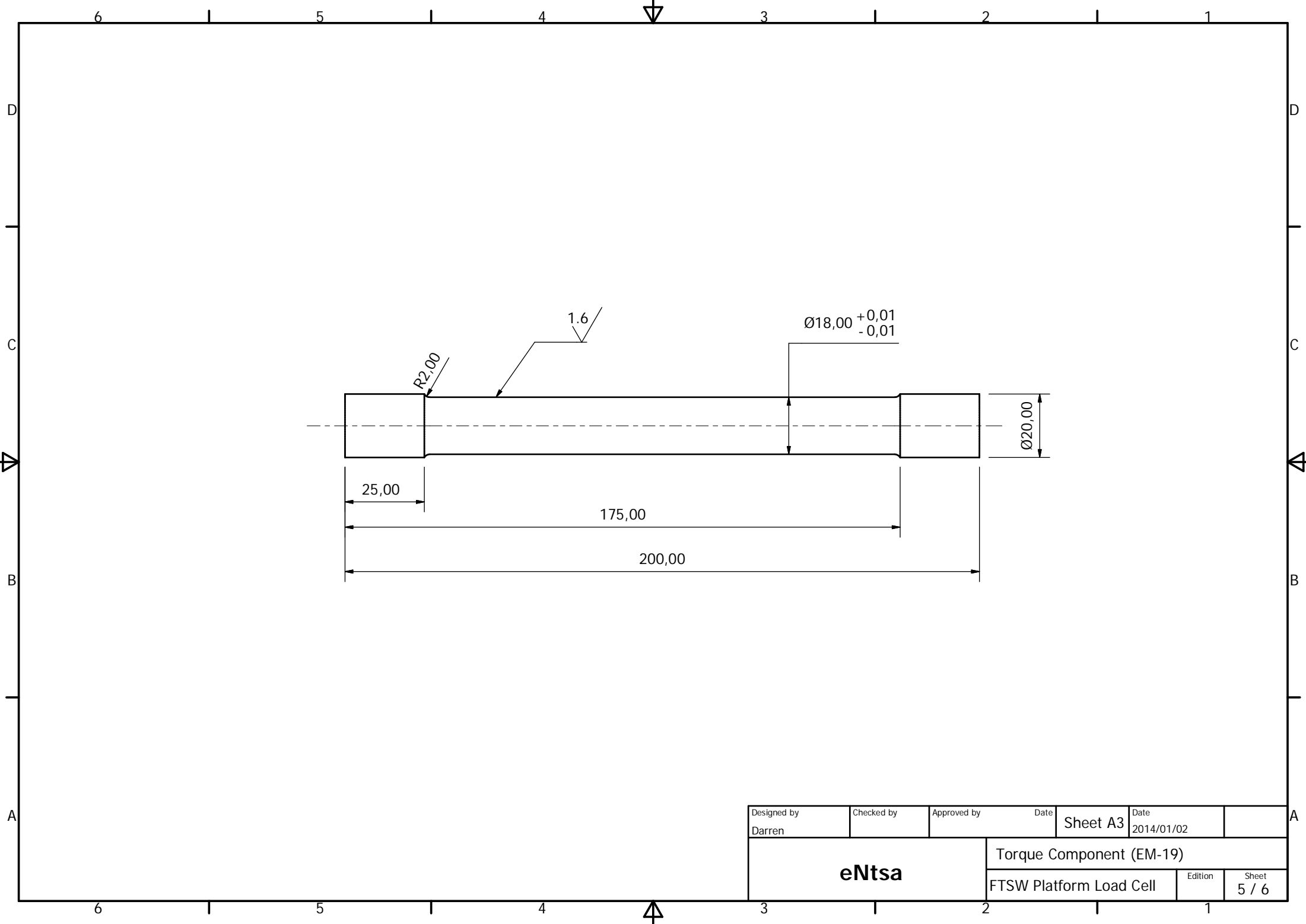
A



View B-B ( 1 : 1.5 )

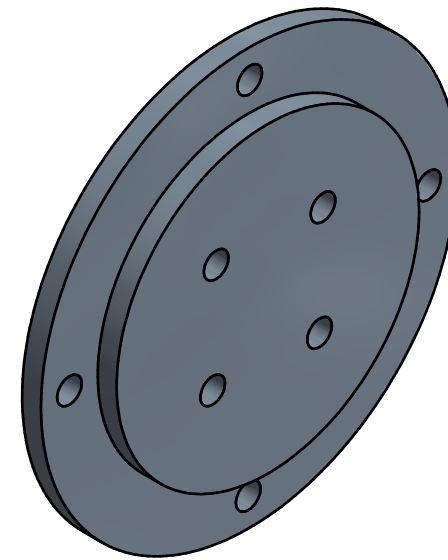
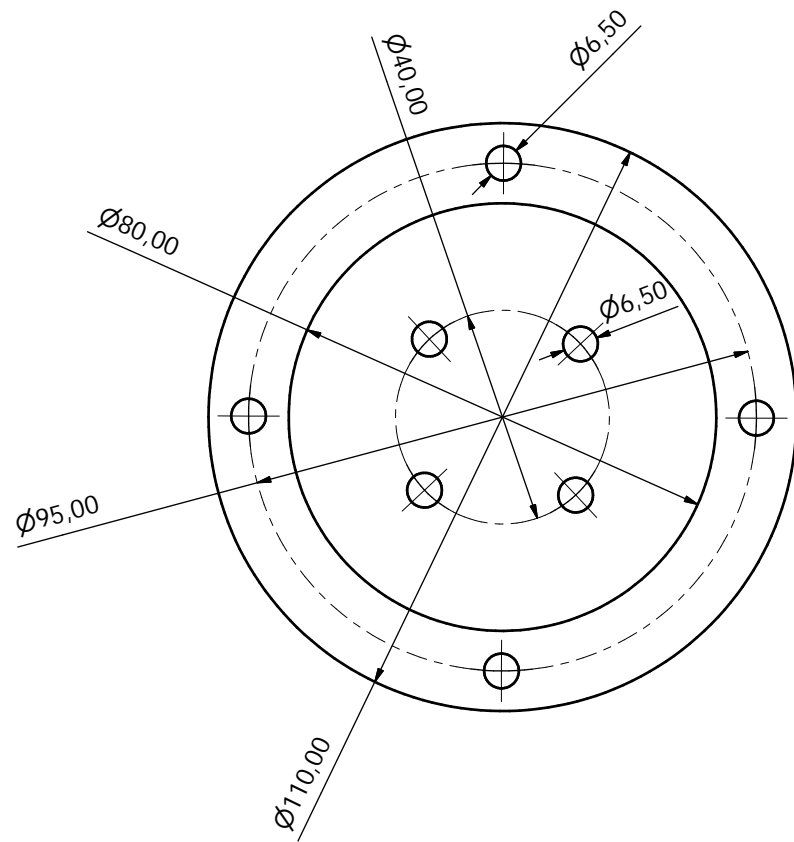
Designed by Darren	Checked by	Approved by	Date	Sheet A3	Date 2014/01/02	
<b>eNtsa</b>			Bearing Casing (EM-8)			
			FTSW Platform Load Cell		Edition	Sheet 4 / 6

6 5 4 3 2 1



Designed by Darren	Checked by	Approved by	Date 2014/01/02	Sheet A3	Date 2014/01/02	
<b>eNtsa</b>			Torque Component (EM-19)			
			FTSW Platform Load Cell		Edition	Sheet 5 / 6

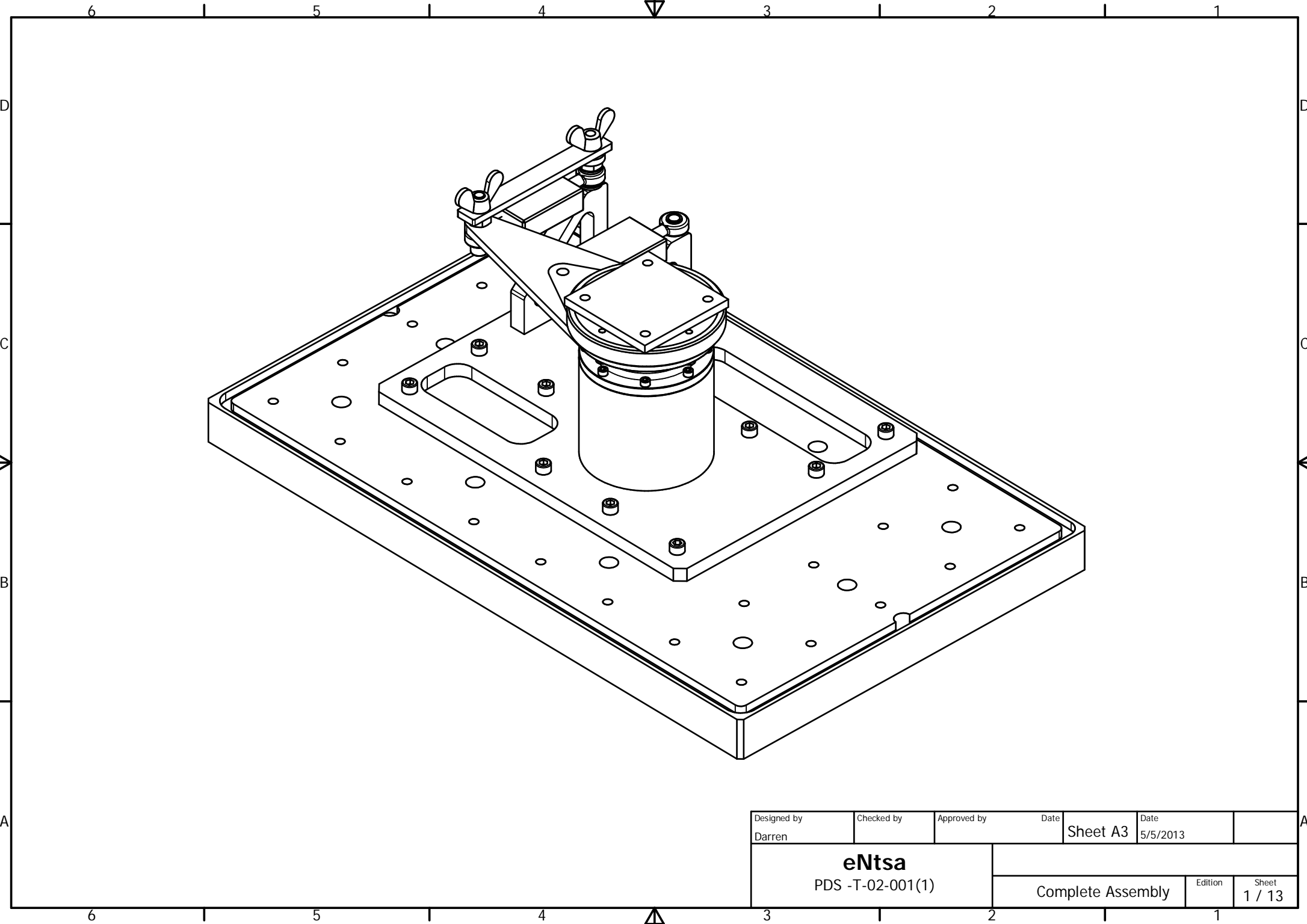




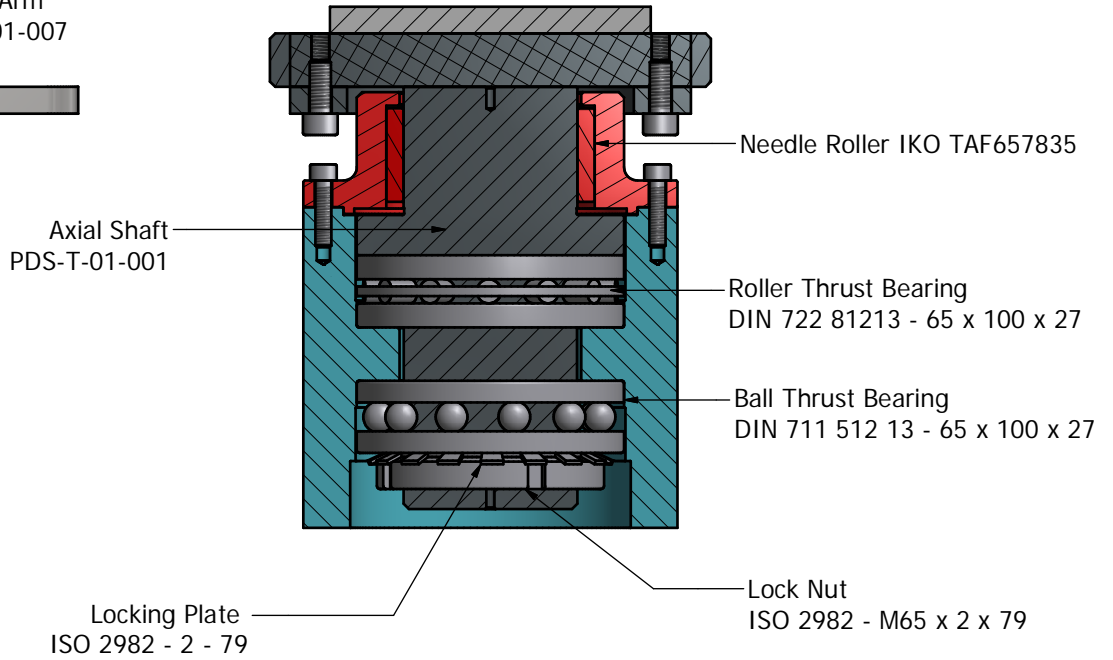
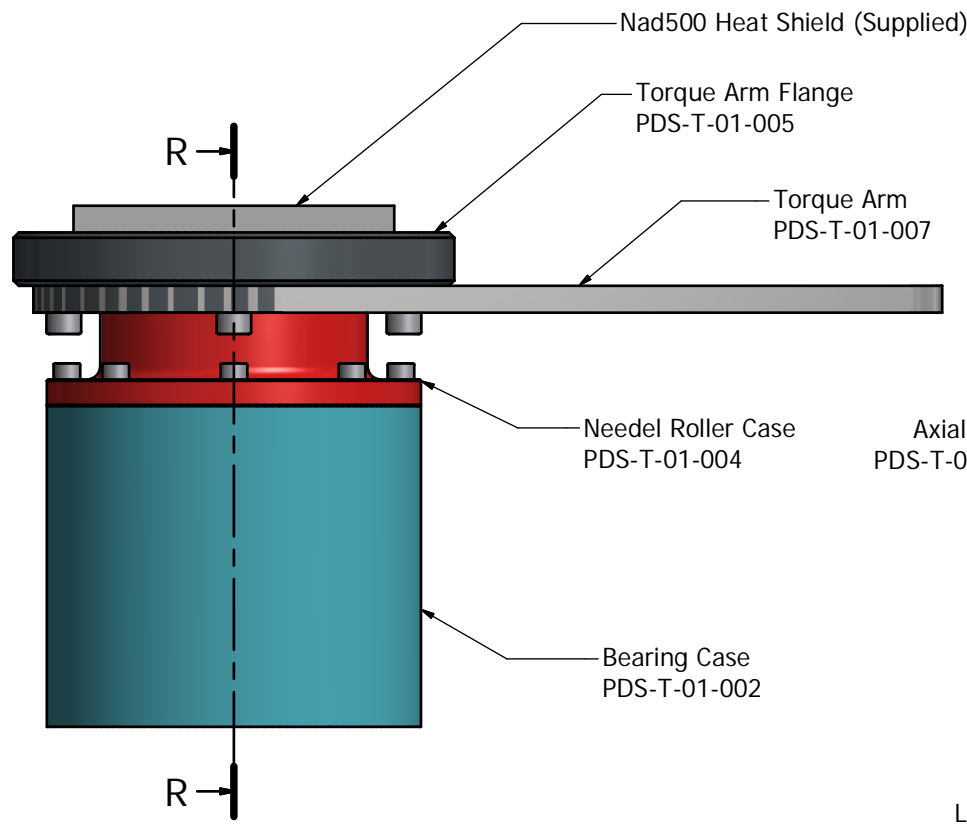
Designed by Darren	Checked by	Approved by	Date	Date 2014/01/02
<b>eNtsa</b>		Load Cell Cap (EM-8)		
		FTSW Platform Load Cell	Edition	Sheet 6 / 6

**Appendix C**

**Load Cell Drawings for PDS Friction Welding Platform**

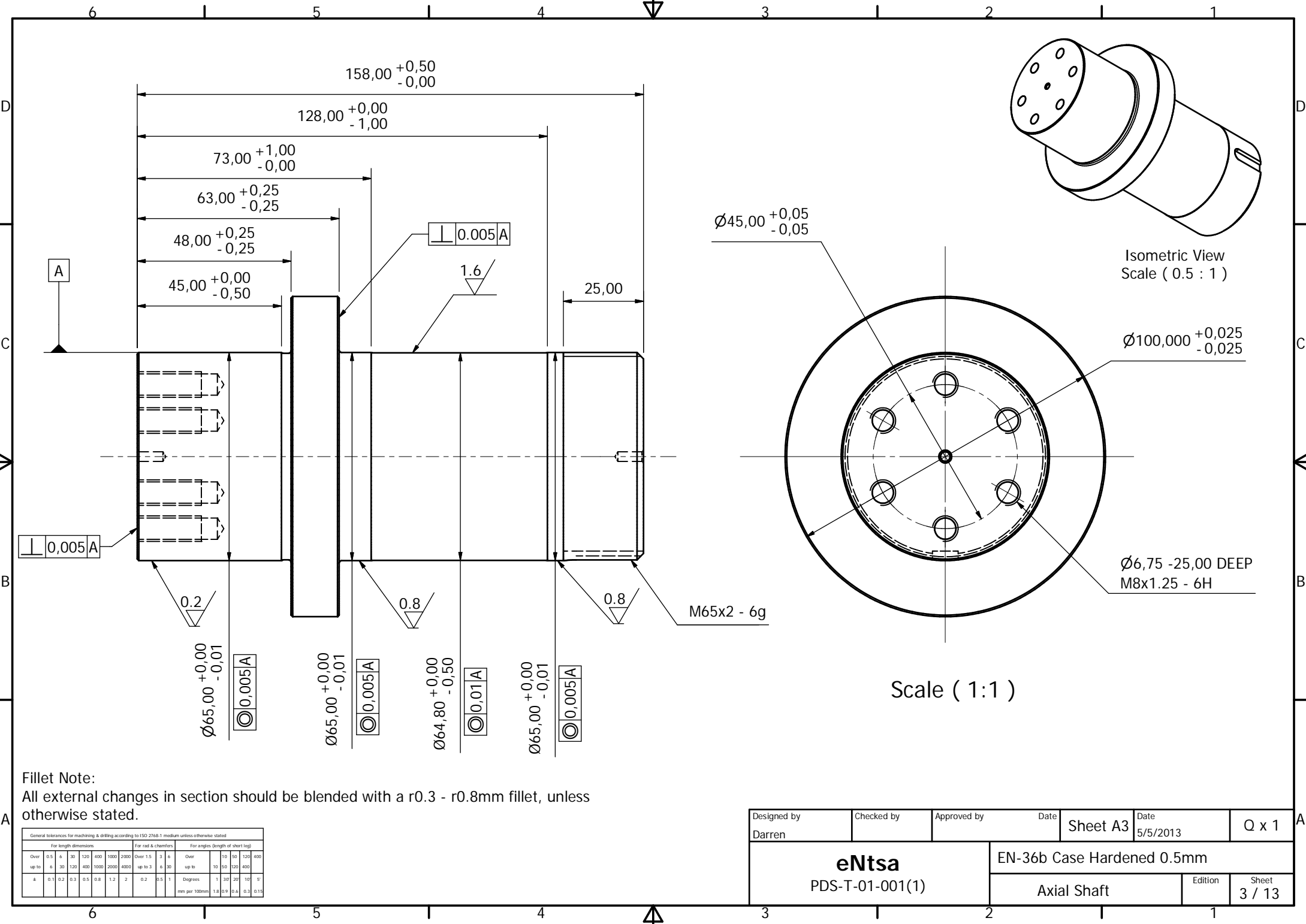


Designed by Darren	Checked by	Approved by	Date Sheet A3	Date 5/5/2013	
<b>eNtsa</b> PDS -T-02-001(1)			Complete Assembly		Edition
					Sheet 1 / 13



Section View R-R Scale ( 0.5 : 1 )

Designed by Darren	Checked by	Approved by	Date	Sheet A3	Date 5/5/2013	
<b>eNtsa</b> PDS-T-02-002(2)			Bearing Head Assembly		Edition 1.0	Sheet 2 / 13

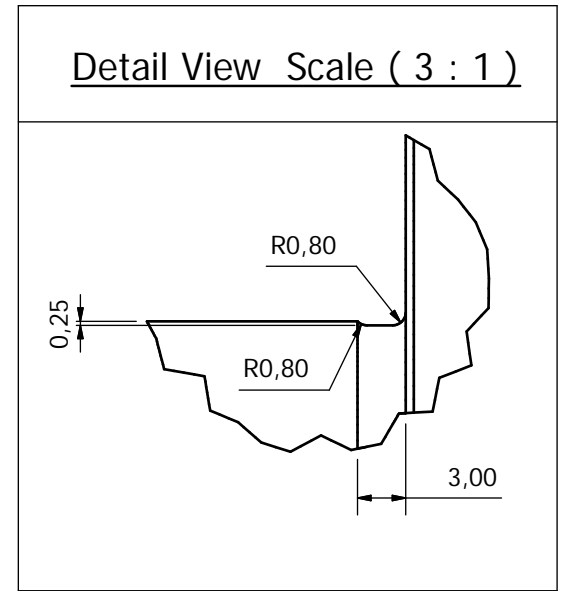
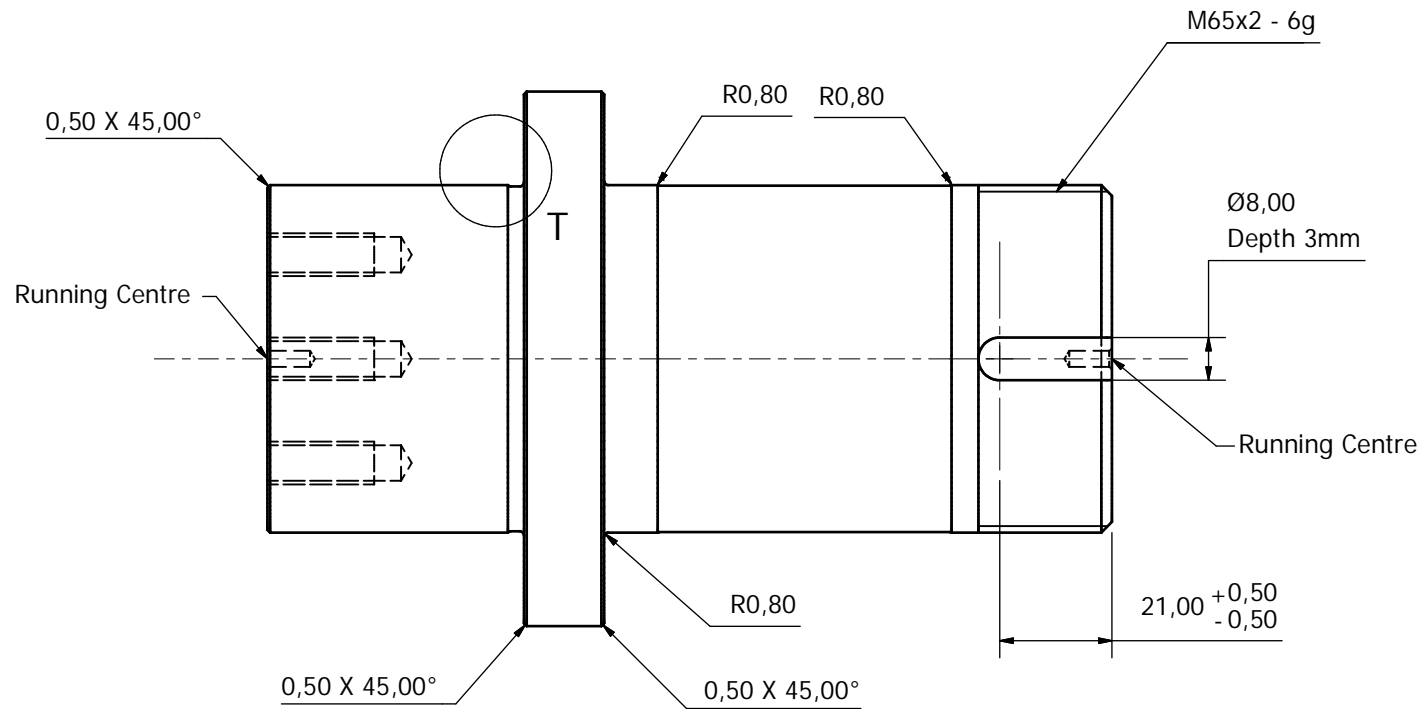


**Fillet Note:**  
 All external changes in section should be blended with a r0.3 - r0.8mm fillet, unless otherwise stated.

General tolerances for machining & drilling according to ISO 2768-1 medium unless otherwise stated															
Over up to	For length dimensions				For radii & chamfers				For angles (length of short leg)						
	0.5	3	120	400	1000	2000	Over 1.5 up to 3	3	6	10	50	120	400		
±	0.1	0.2	0.3	0.5	0.8	1.2	0.2	0.5	1	Degrees	1	30'	20'	10'	5'
										mm per 100mm	1.8	0.9	0.4	0.3	0.15

Designed by Darren	Checked by	Approved by	Date	Sheet A3	Date 5/5/2013	Q x 1
<b>eNtsa</b> PDS-T-01-001(1)			EN-36b Case Hardened 0.5mm			
			Axial Shaft		Edition	Sheet 3 / 13

Fillet Note:  
All external changes in section should be blended with a r0.3 - r0.8mm fillet, unless otherwise stated.

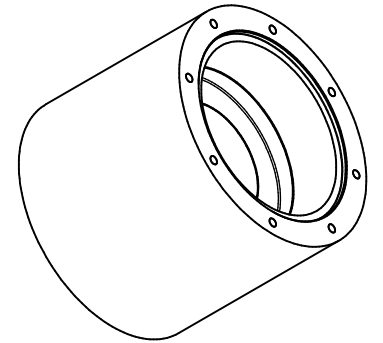


Scale ( 1 : 1 )

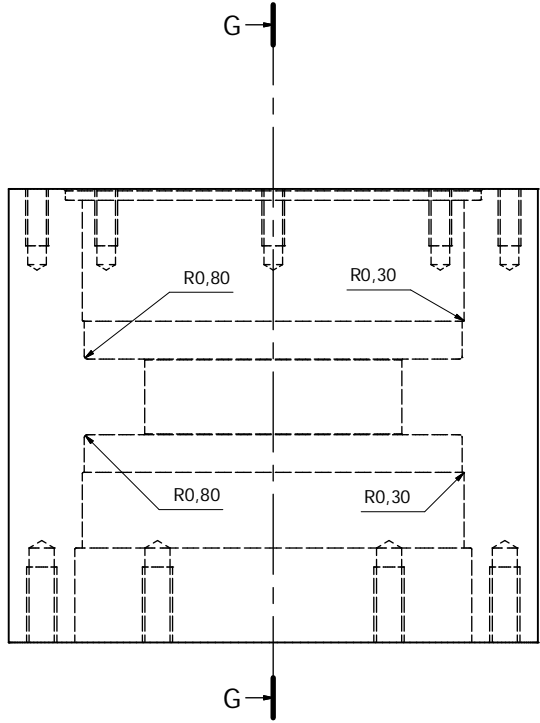
General tolerances for machining & drilling according to ISO 2768-1 medium unless otherwise stated																
Over up to	For length dimensions					For radii & chamfers			For angles (length of short leg)							
	0.5	6	30	120	400	1000	2000	Over 1.5 up to 3	3	6	10	50	120	400		
±	0.1	0.2	0.3	0.5	0.8	1.2	2	0.2	0.5	1	Degrees	1	30'	20'	10'	5'
											mm per 100mm	1.8	0.9	0.6	0.3	0.15

Designed by Darren	Checked by	Approved by	Date	Sheet A3	Date 5/5/2013	Q x 1
<b>eNtsa</b> PDS-T-01-001(2)			EN-36b Case Hardened 0.5mm			
			Axial Shaft		Edition	Sheet 4 / 13

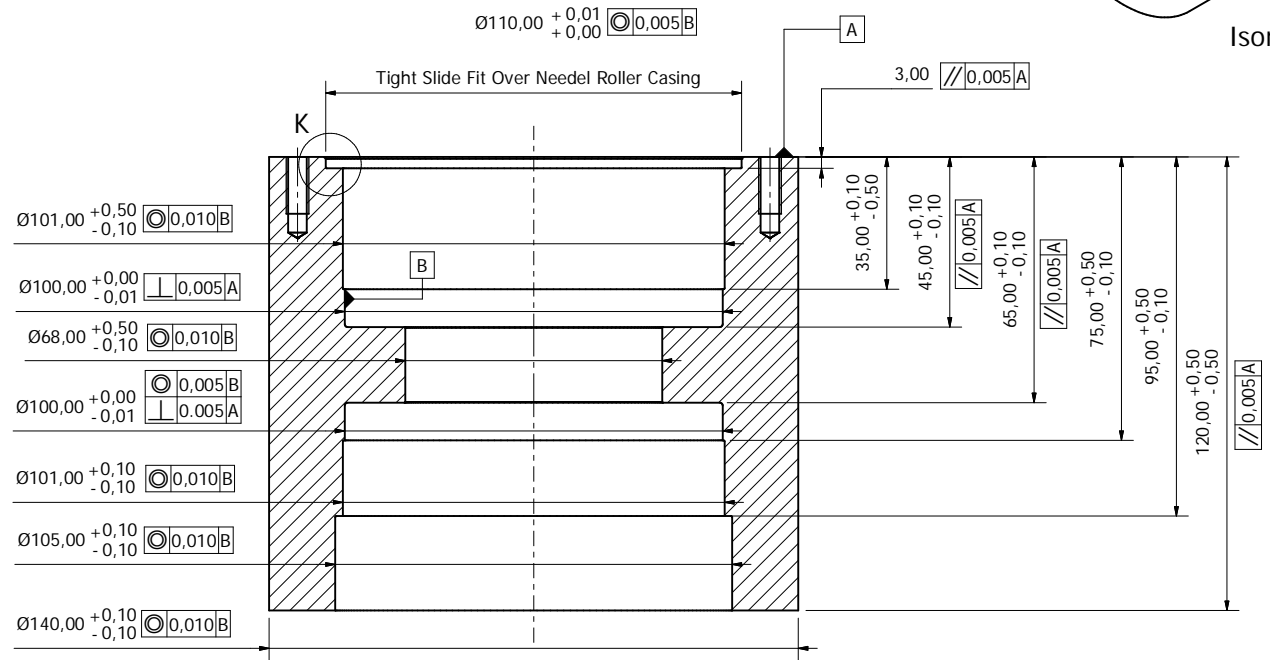
**Fillet Note:**  
 All internal changes in section should be blended with a r0.3 - r0.8mm fillet, unless otherwise stated.



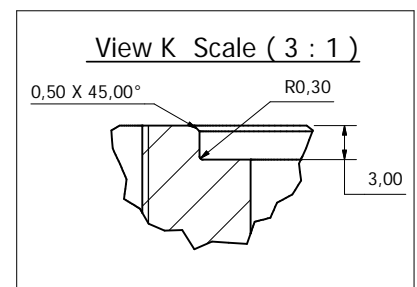
Isometric View



Scale ( 1 : 1 )



Section View G-G Scale ( 1 : 1 )

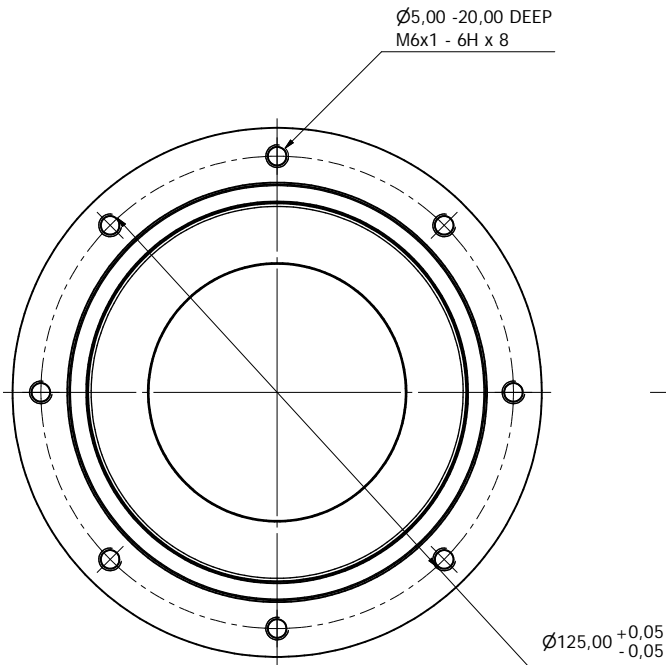


View K Scale ( 3 : 1 )

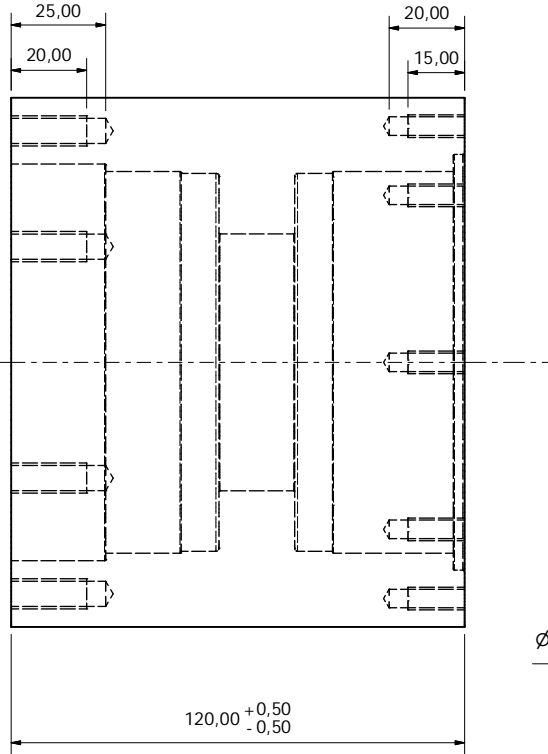
General tolerances for machining & drilling according to ISO 2768-1 medium class (otherwise stated)		Surface texture (Ra)	
Class	Deviation	Symbol	Value
AS	±0,15	Sa	3,2
AK	±0,10		1,6
AM	±0,07	Sm	0,8
AN	±0,05		0,4
AV	±0,03	0,2	

Designed by Darren	Checked by	Approved by	Date	Sheet A2	Date 5/5/2013	Q x 1
<b>eNtsa</b> PDS-T-01-002(1)			EN-8 (BMS) Blackened			
			Bearing Case		Edition 1 Sheet 5 / 13	

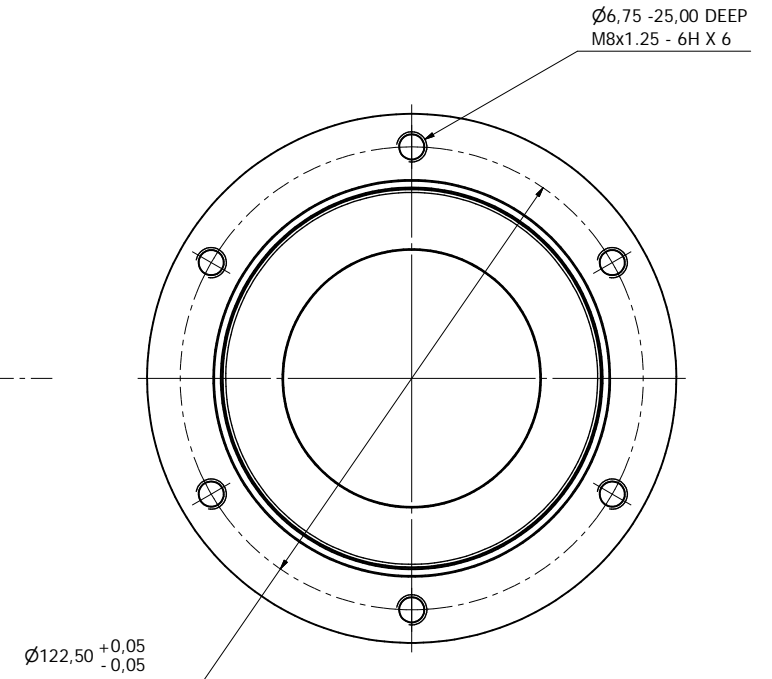
**Fillet Note:**  
**All internal changes in section should be blended with a r0.3 - r0.8mm fillet, Unless otherwise stated.**



Top View (Locating Holes For Needle Roller Case)



Scale ( 1 : 1 )



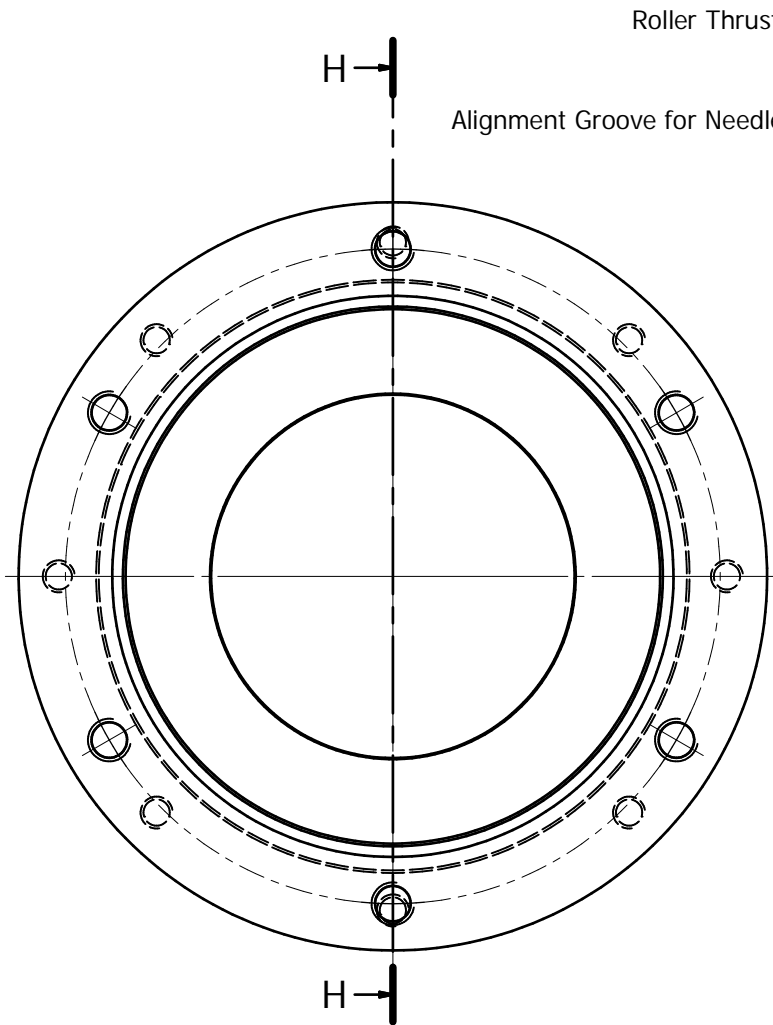
Bottom View (Locating Holes For Base Plate)

Drill		Tap		Reamer		Bore		Hole		Hole		Hole	
Code	Size	Code	Size	Code	Size	Code	Size	Code	Size	Code	Size	Code	Size
4	01	02	0.3	0.5	0.8	1.2	2	52	35	1	20	20	30
mm per 100mm													

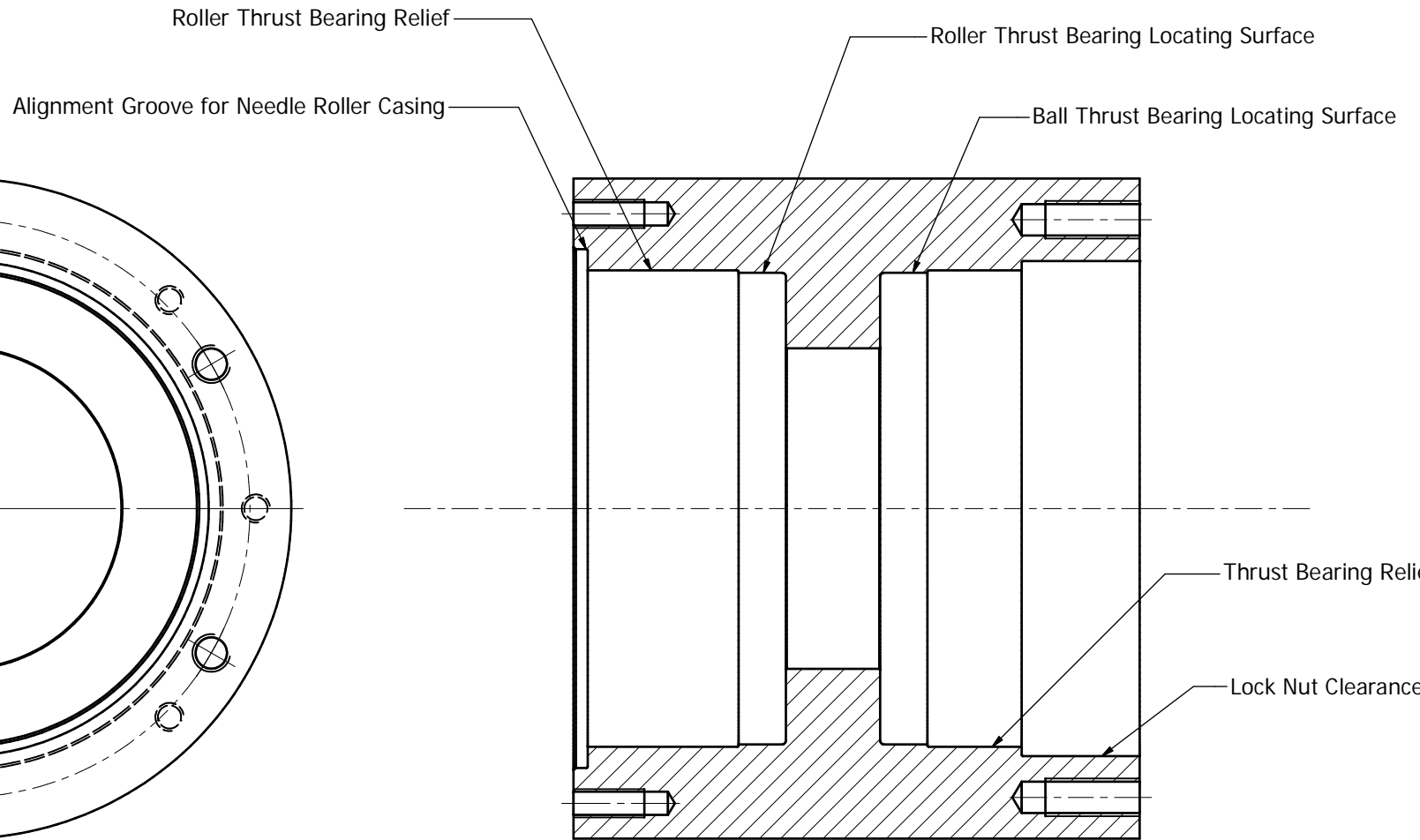
Designed by Darren	Checked by	Approved by	Date	Sheet A2	Date 5/5/2013	Q x 1
<b>eNtsa</b> PDS-T-01-002(2)			EN-8 (BMS) Blackened			
			Bearing Case	Edition	Sheet 6 / 13	



Fillet Note:  
 All internal changes in section should be blended with a r0.3 - r0.8mm fillet, unless otherwise stated.



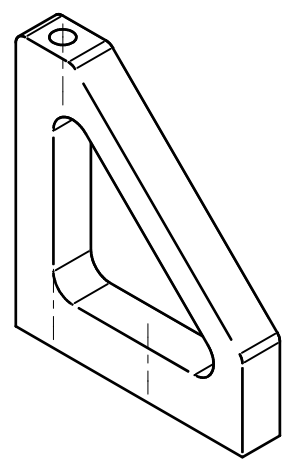
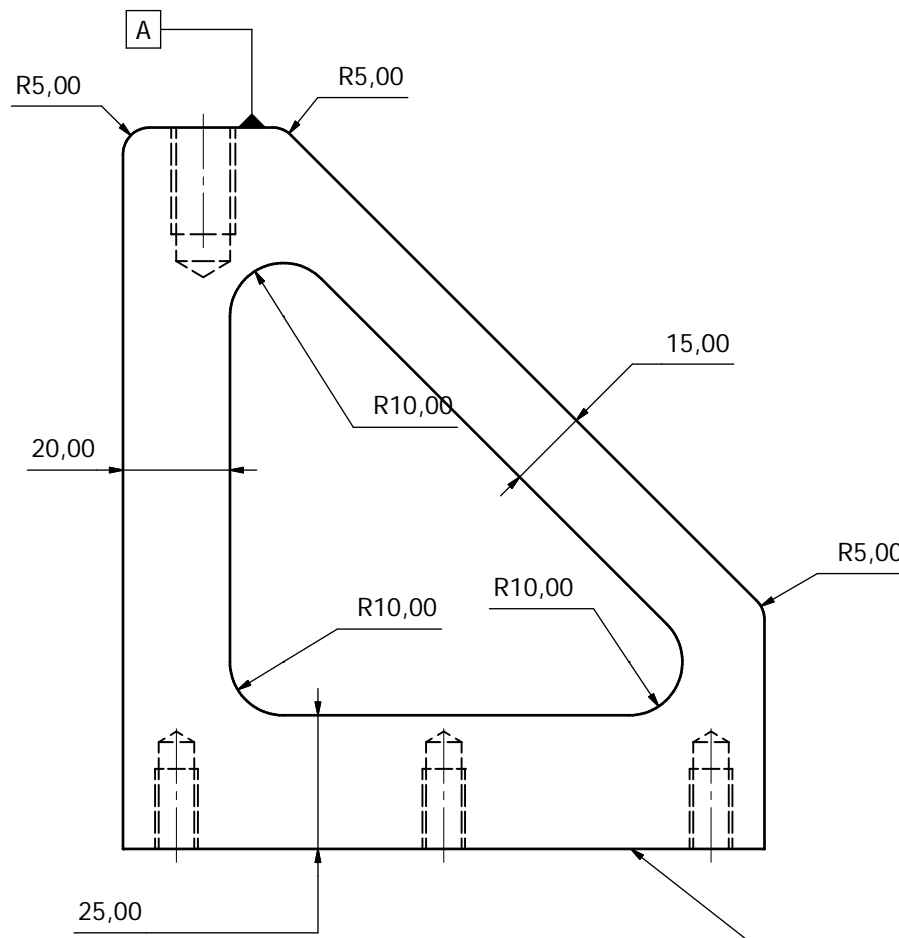
Scale ( 1 : 1 )



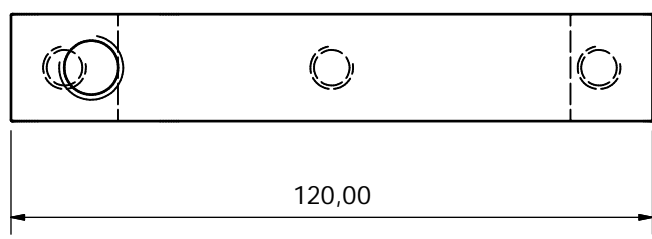
Section View H-H Scale ( 1 : 1 )

General tolerances for machining & drilling according to ISO 2768-1 medium unless otherwise stated																
	For length dimensions						For radii & chamfers			For angles (length of short leg)						
	Over	up to	Over	up to	Over	up to	Over	up to	Over	up to	Over	up to				
±	0.1	0.2	0.3	0.5	0.8	1.2	2	0.2	0.5	1	Degrees	1	30	20	10	5
											mm per 100mm	1.8	0.9	0.6	0.3	0.15

Designed by Darren	Checked by	Approved by	Date	Sheet A3	Date 5/5/2013	Q x 1
<b>eNtsa</b> PDS-T-01-002(3)			EN-8 (BMS) Blackened			
			Bearing Case			Edition



Isometric View



120,00

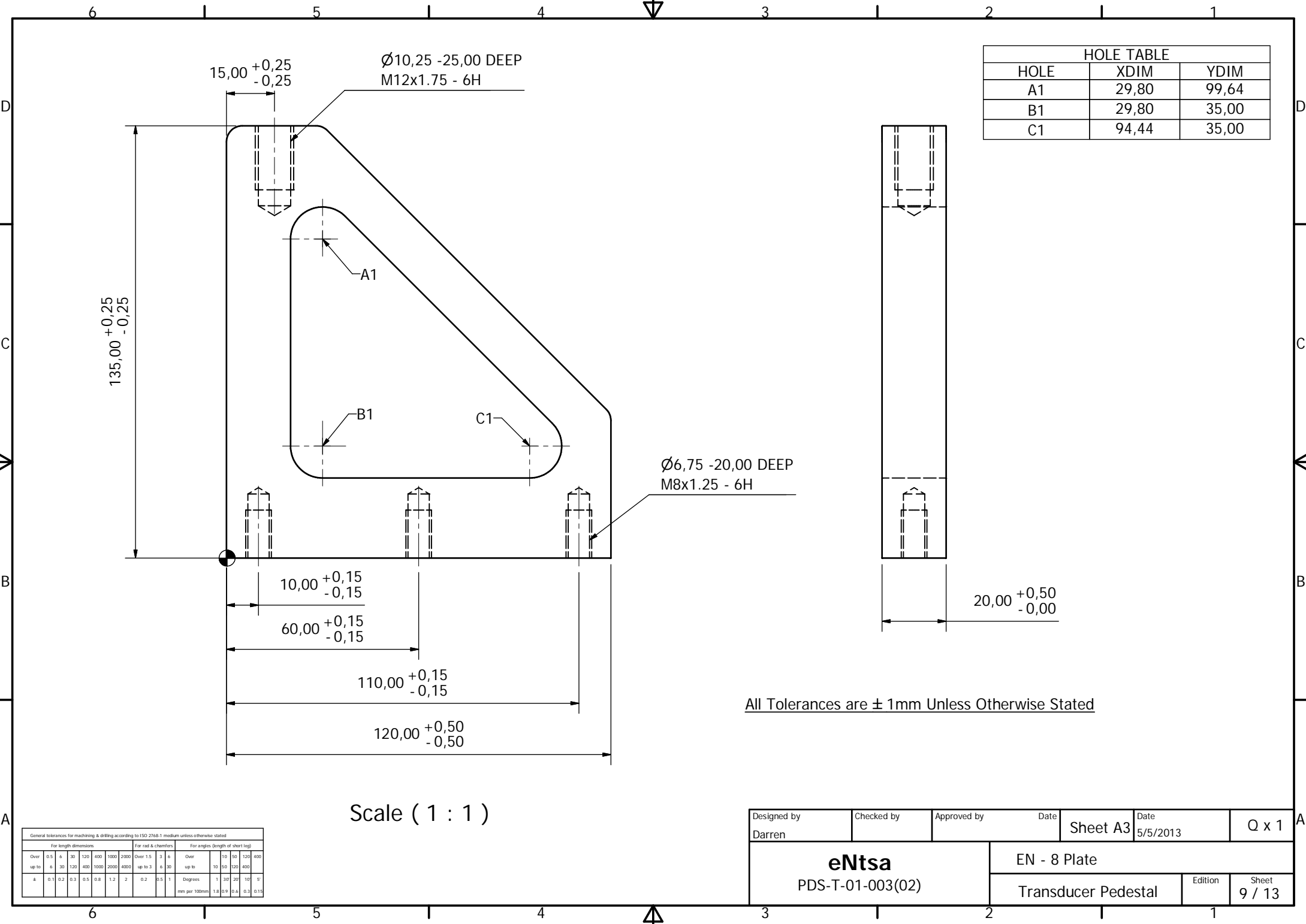
//0,05A

All Dimensions are ± 1mm Unless Otherwise Stated

Scale ( 1 : 1 )

General tolerances for machining & drilling according to ISO 2768-1 medium unless otherwise stated															
	For length dimensions					For radii & chamfers			For angles (length of short leg)						
	Over	up to	Over	up to	Over	up to	Over	up to	Over	up to					
±	0,1	0,2	0,3	0,5	0,8	1,2	2	0,2	0,5	1	1	30'	20'	10'	5'
	mm	mm	mm	mm	mm	mm	mm	mm per 100mm	mm	mm	mm	mm	mm	mm	mm

Designed by Darren	Checked by	Approved by	Date	Sheet A3	Date 5/5/2013	Q x 1
<b>eNtsa</b> PDS-T-01-003(01)			EN - 8 Plate		Edition	Sheet 8 / 13
			Transducer Pedestal			



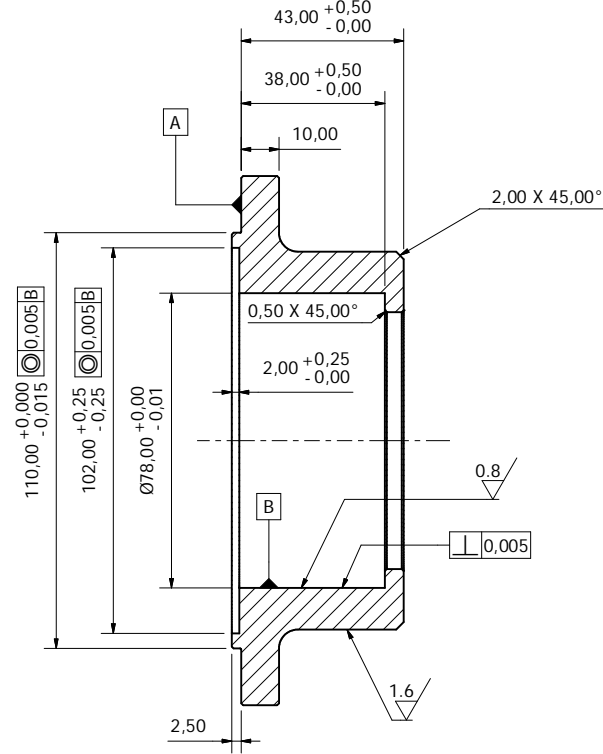
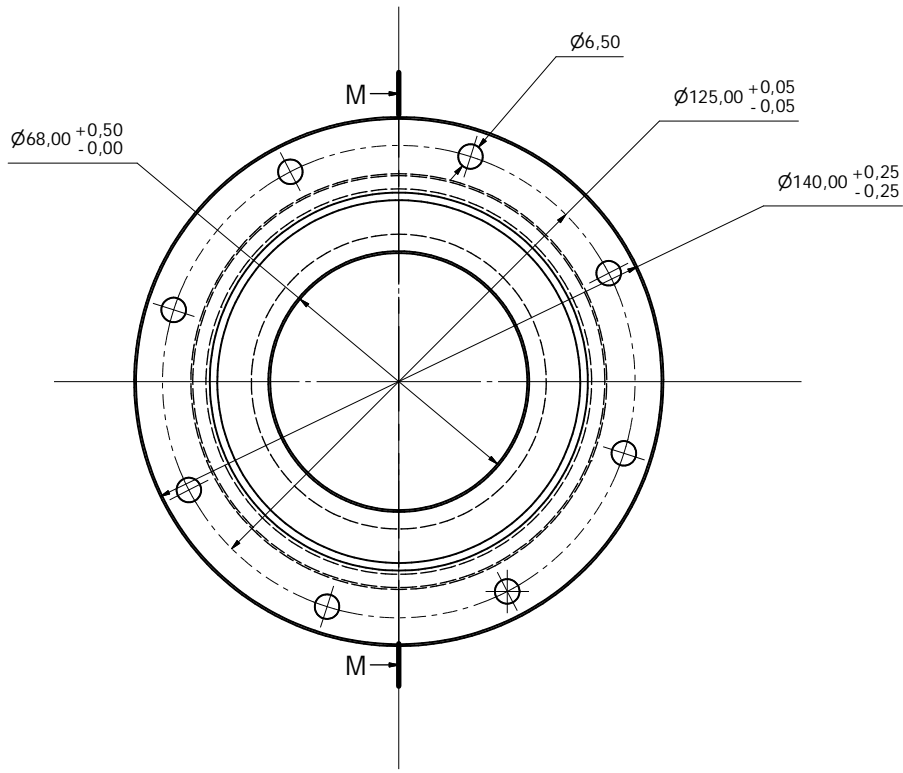
HOLE TABLE		
HOLE	XDIM	YDIM
A1	29,80	99,64
B1	29,80	35,00
C1	94,44	35,00

All Tolerances are ± 1mm Unless Otherwise Stated

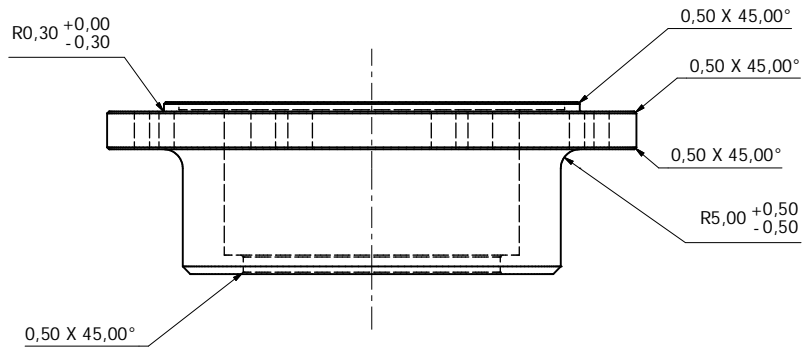
Scale ( 1 : 1 )

General tolerances for machining & drilling according to ISO 2768-1 medium unless otherwise stated											
	For length dimensions					For radii & chamfers			For angles (length of short leg)		
	Over	up to	Over	up to	Over	up to	Over	up to	Over	up to	
±	0.1	0.2	0.3	0.5	0.8	1.2	2	0.2	0.5	1	5
	6	30	120	400	1000	2000	4000	1	30	100	5
	6	30	120	400	1000	2000	4000	1	30	100	5
	mm per 100mm	1.8	0.9	0.6	0.3	0.15					

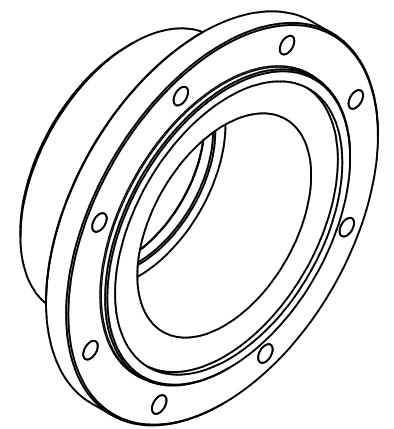
Designed by Darren	Checked by	Approved by	Date	Sheet A3	Date 5/5/2013	Q x 1
<b>eNtsa</b> PDS-T-01-003(02)			EN - 8 Plate			
			Transducer Pedestal		Edition	Sheet 9 / 13



Section View M-M Scale ( 1 : 1 )



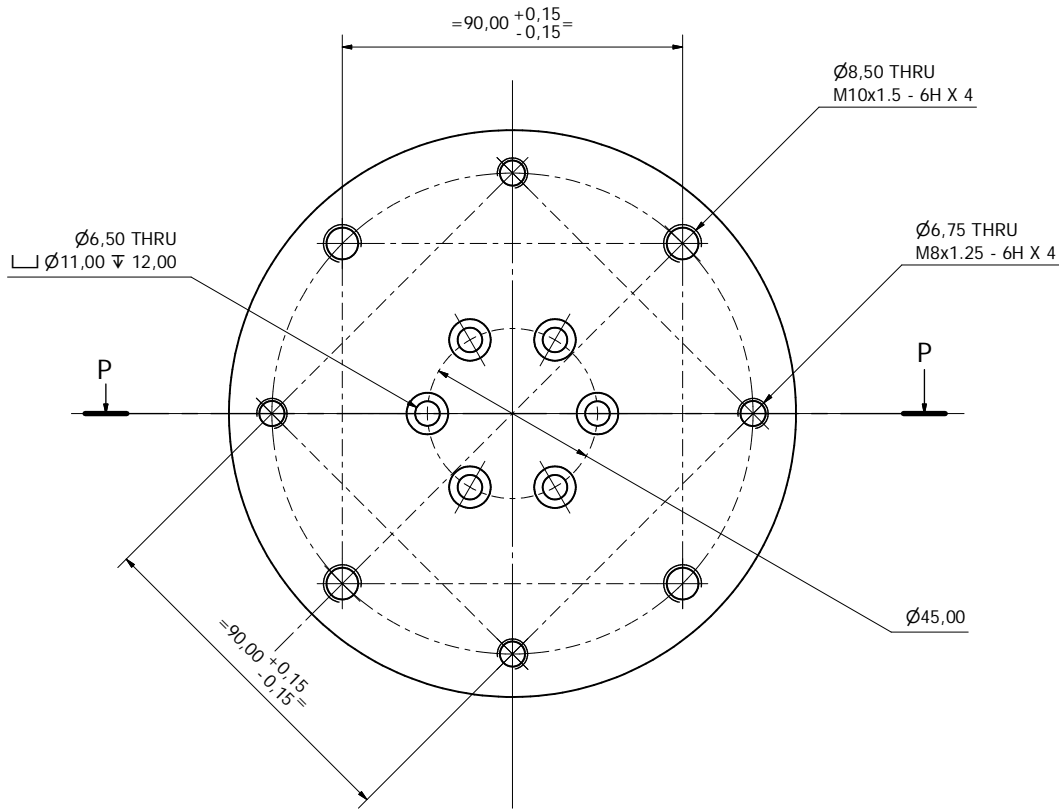
Scale ( 1 : 1 )



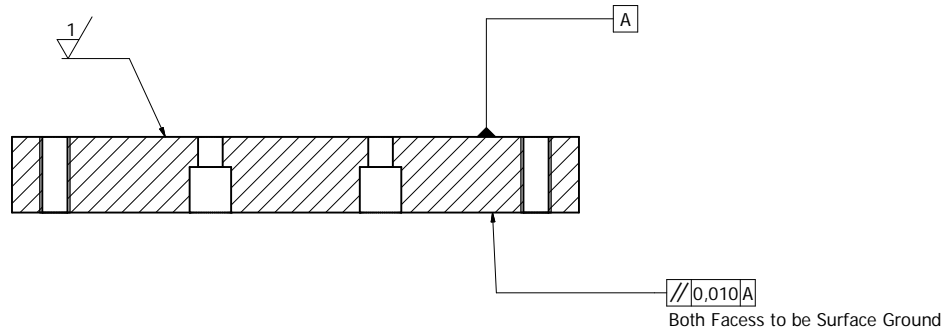
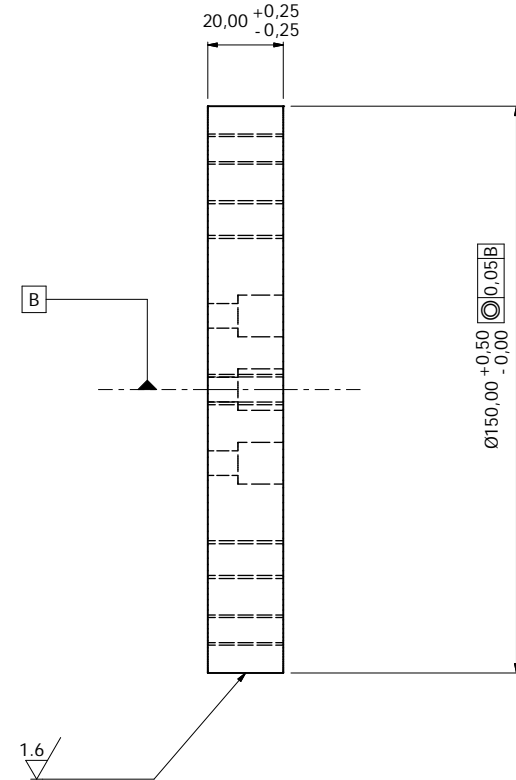
Isometric View

Class	1	2	3	4	5	6	7	8	9	10	11	12	13	14	15	16	17	18	19	20									
0,01	0,02	0,03	0,04	0,05	0,06	0,07	0,08	0,09	0,10	0,12	0,15	0,20	0,25	0,30	0,40	0,50	0,60	0,80	1,00	1,20	1,50	2,00	2,50	3,00	4,00	5,00	6,00	8,00	10,00

Designed by Darren	Checked by	Approved by	Date	Sheet A2	Date 5/5/2013	Q x 1
<b>eNtsa</b> PDS-T-01-004(1)			EN-8 (BMS) Blackened			
			Needle Roller Case	Edition	Sheet 10 / 13	



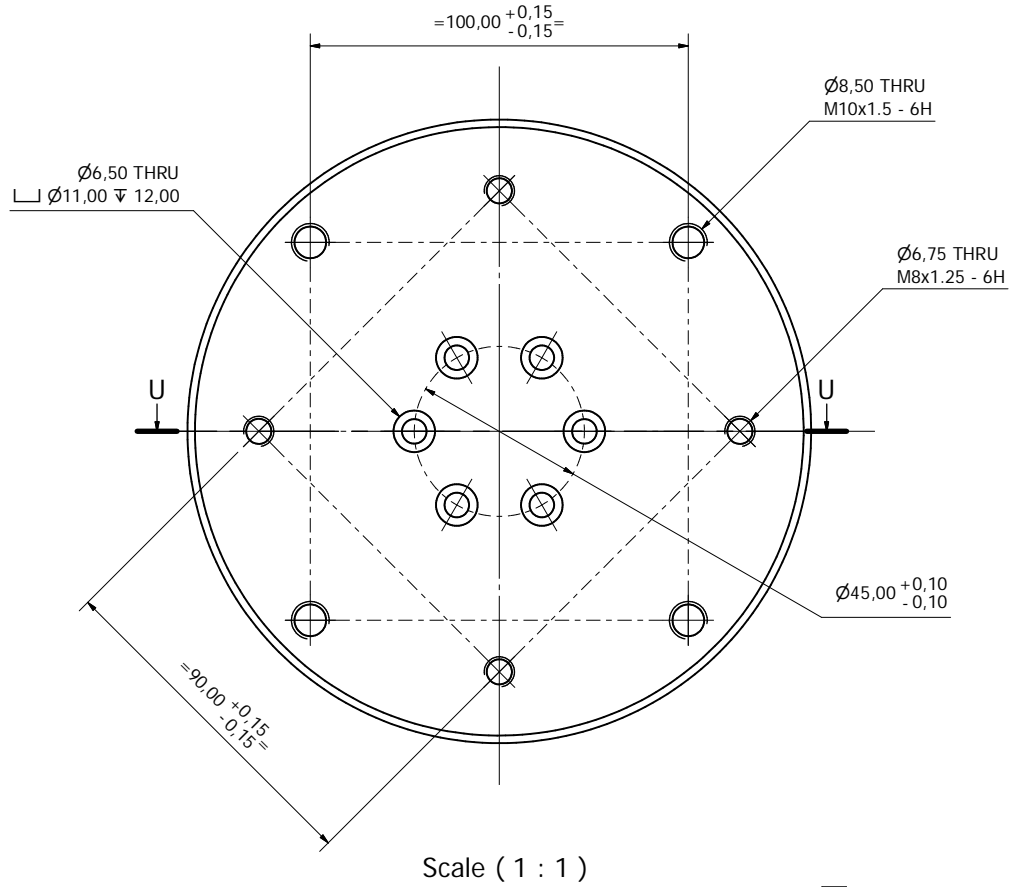
Scale ( 1 : 1 )



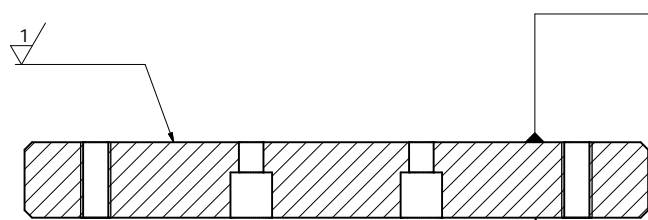
Section View P-P Scale ( 1 : 1 )

Drill		Tap		Reamer		Bore		Hole		Hole		Hole	
Code	Code	Code	Code	Code	Code	Code	Code	Code	Code	Code	Code	Code	Code
4	01	02	03	04	05	06	07	08	09	10	11	12	13

Designed by Darren	Checked by	Approved by	Date	Sheet A2	Date 5/5/2013	Q x 1
<b>eNtsa</b> PDS-T-01-005(1)			EN-8 (BMS) Blackened			
			Torque Arm Flange		Edition	Sheet 11 / 13

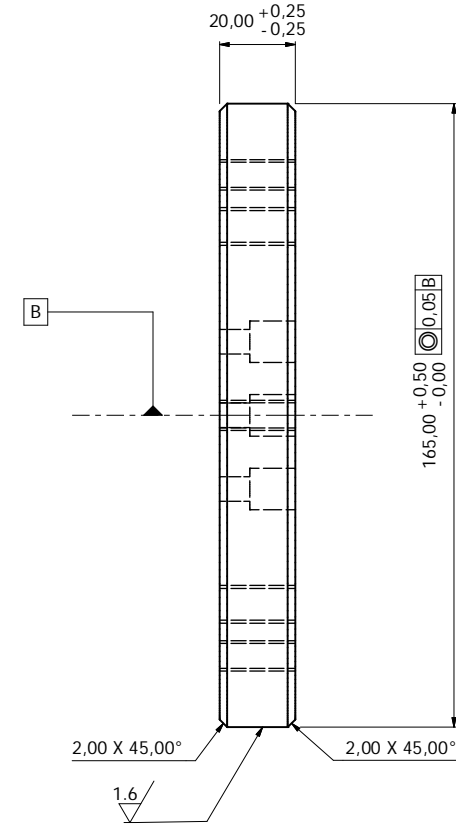


Scale ( 1 : 1 )



Section View U-U Scale ( 1 : 1 )

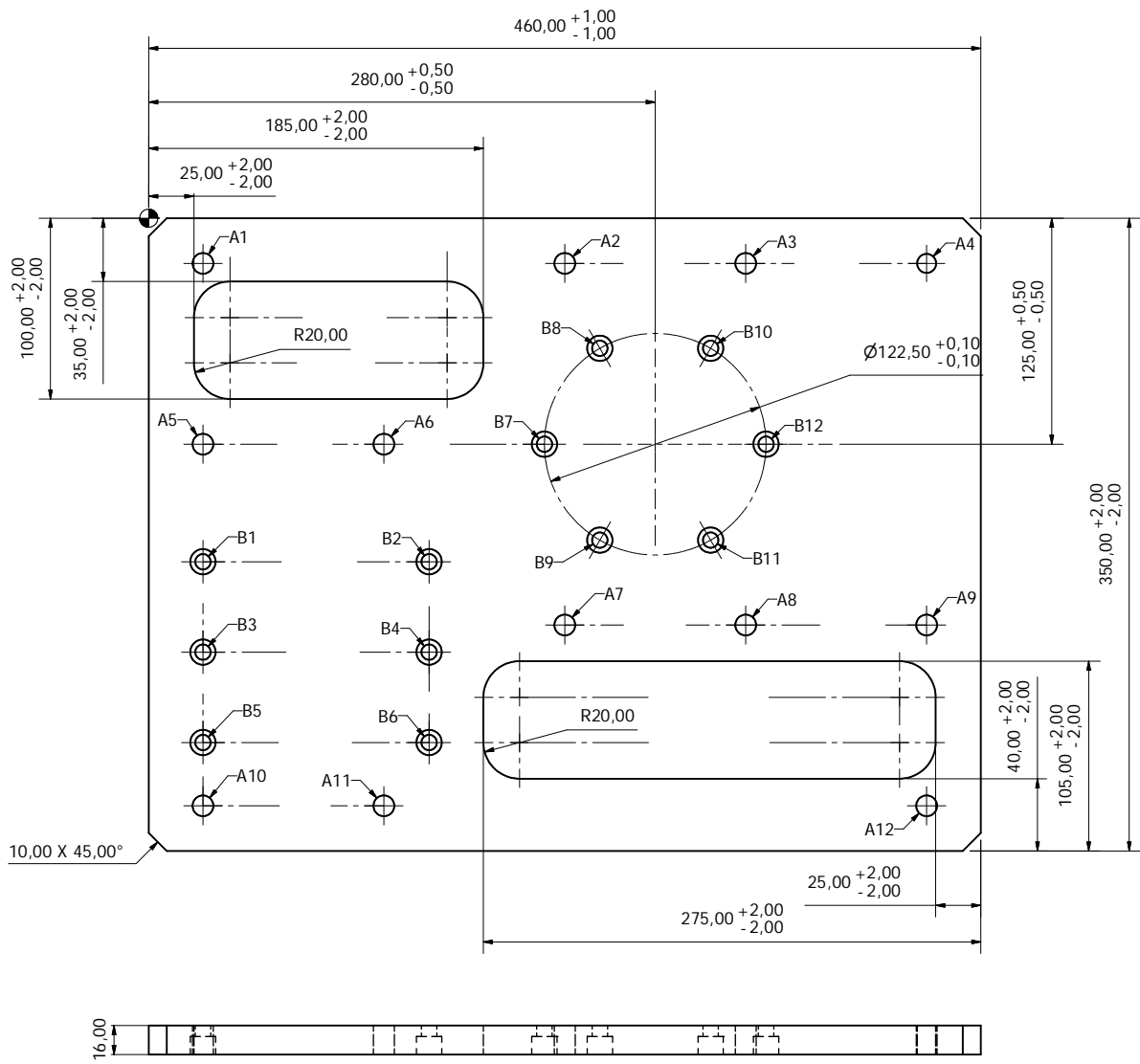
$\sqrt{\sqrt{0,01|A}}$   
Both Faces to be Surface Ground



$2,00 \times 45,00^\circ$   $2,00 \times 45,00^\circ$

1.6

Designed by Darren	Checked by	Approved by	Date 5/5/2013	Date 5/5/2013	Q x 1
<b>eNtsa</b> PDS-T-01-007(1)			EN-8 (BMS) Blackened		
			Torque Arm Flange 2	Edition	Sheet 12 / 13



HOLE TABLE			
HOLE	XDIM	YDIM	DESCRIPTION
A1	30,00	-25,00	Ø11,50 THRU
A2	230,00	-25,00	Ø11,50 THRU
A3	330,00	-25,00	Ø11,50 THRU
A5	30,00	-125,00	Ø11,50 THRU
A6	130,00	-125,00	Ø11,50 THRU
A7	230,00	-225,00	Ø11,50 THRU
A8	330,00	-225,00	Ø11,50 THRU
A9	430,00	-225,00	Ø11,50 THRU
A10	30,00	-325,00	Ø11,50 THRU
A11	130,00	-325,00	Ø11,50 THRU
A12	430,00	-325,00	Ø11,50 THRU
A4	430,00	-25,00	Ø10,50 THRU
B1	30,00	-190,00	Ø8,50 THRU └┘ Ø14,00 ▽ 10,00
B2	155,00	-190,00	Ø8,50 THRU └┘ Ø14,00 ▽ 10,00
B3	30,00	-240,00	Ø8,50 THRU └┘ Ø14,00 ▽ 10,00
B4	155,00	-240,00	Ø8,50 THRU └┘ Ø14,00 ▽ 10,00
B5	30,00	-290,00	Ø8,50 THRU └┘ Ø14,00 ▽ 10,00
B6	155,00	-290,00	Ø8,50 THRU └┘ Ø14,00 ▽ 10,00
B7	218,75	-125,00	Ø8,50 THRU └┘ Ø14,00 ▽ 10,00
B8	249,37	-71,96	Ø8,50 THRU └┘ Ø14,00 ▽ 10,00
B9	249,37	-178,04	Ø8,50 THRU └┘ Ø14,00 ▽ 10,00
B10	310,62	-71,96	Ø8,50 THRU └┘ Ø14,00 ▽ 10,00
B11	310,62	-178,04	Ø8,50 THRU └┘ Ø14,00 ▽ 10,00
B12	341,25	-125,00	Ø8,50 THRU └┘ Ø14,00 ▽ 10,00

All Hole Positions Have a Vertical and Horizontal Tolerance of ± 0.25 From Datum  
 Break all sharp edges

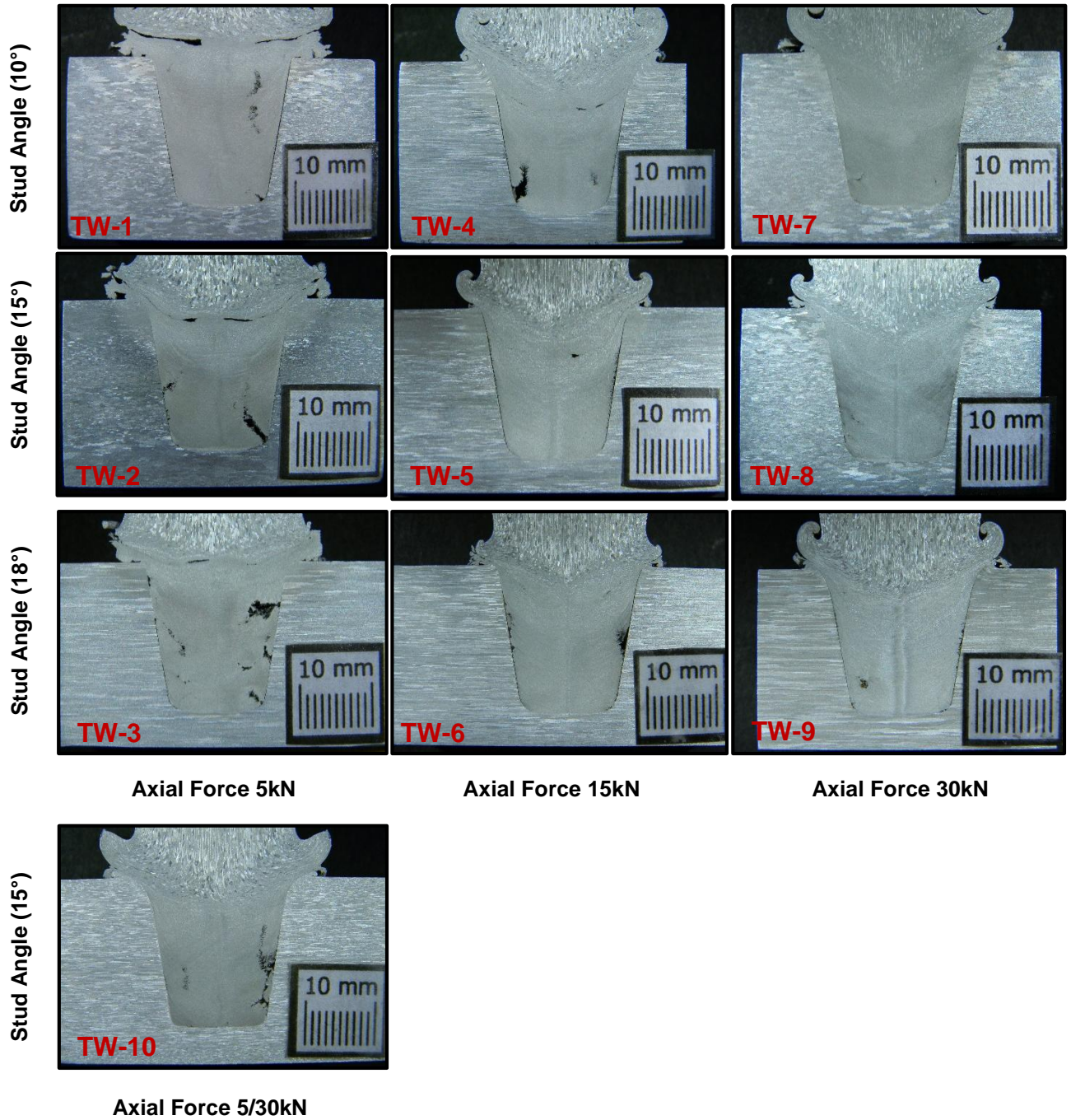
Scale ( 1 : 2 )

Class	Q1	Q2	Q3	Q4	Q5	Q6	Q7	Q8	Q9	Q10	Q11	Q12	Q13	Q14	Q15	Q16	Q17	Q18	Q19	Q20	
1	0,1	0,15	0,2	0,3	0,4	0,5	0,6	0,7	0,8	0,9	1,0	1,2	1,5	2,0	2,5	3,0	4,0	5,0	6,0	8,0	10,0

Designed by Darren	Checked by	Approved by	Date	Sheet A2	Date 5/5/2013	Q x 1
<b>eNtsa</b> PDS-T-01-006(1)			EN-8 (BMS)			
			Base Plate		Edition	Sheet 13 / 13

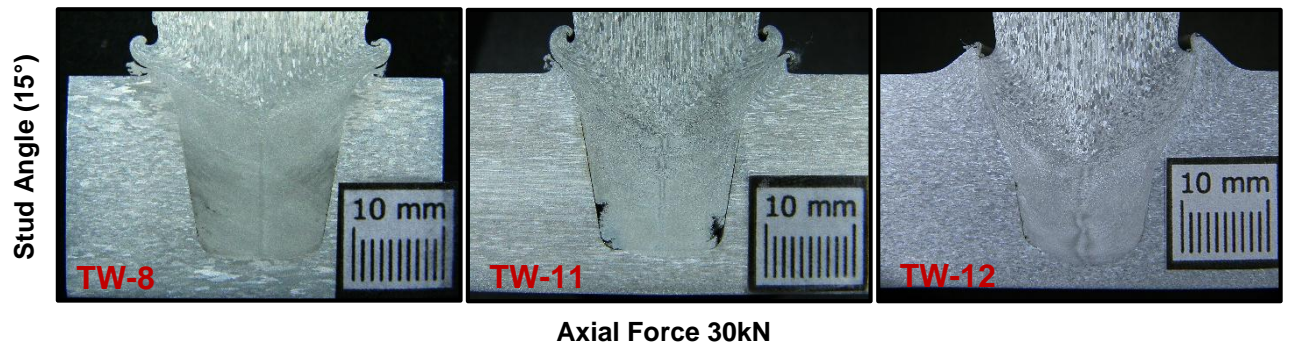
Appendix D

Macrographs (Welds TW-1 to TW-10)

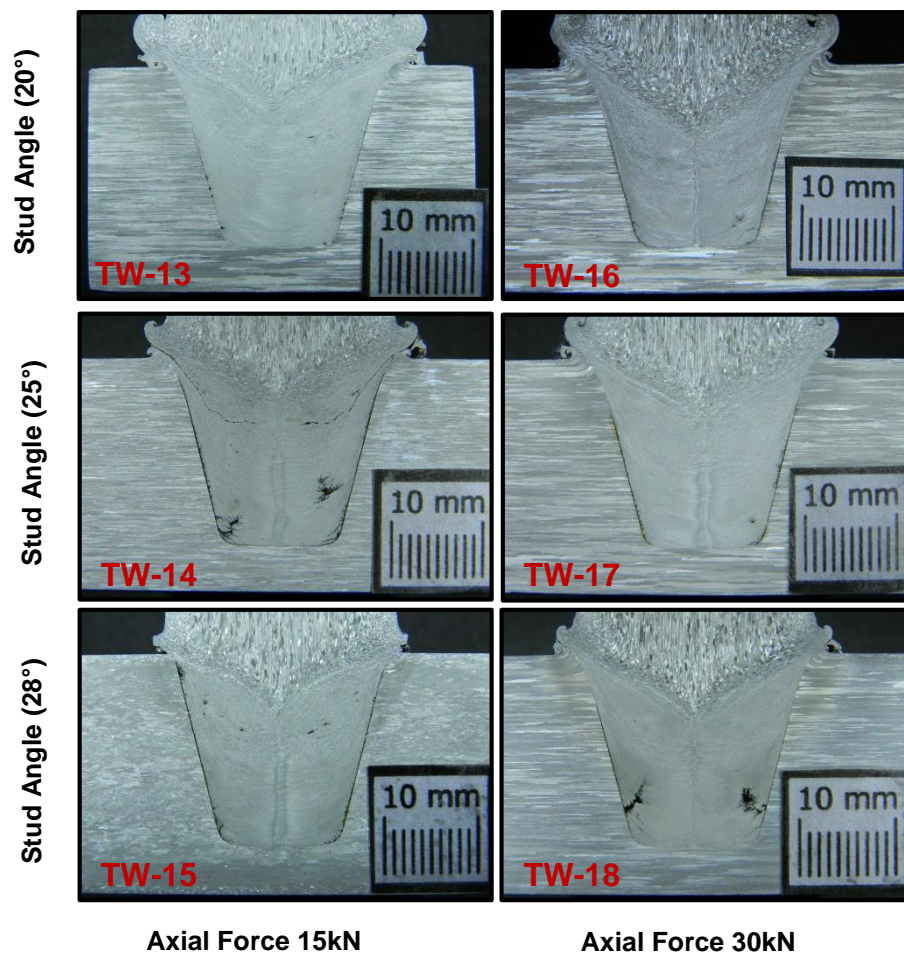


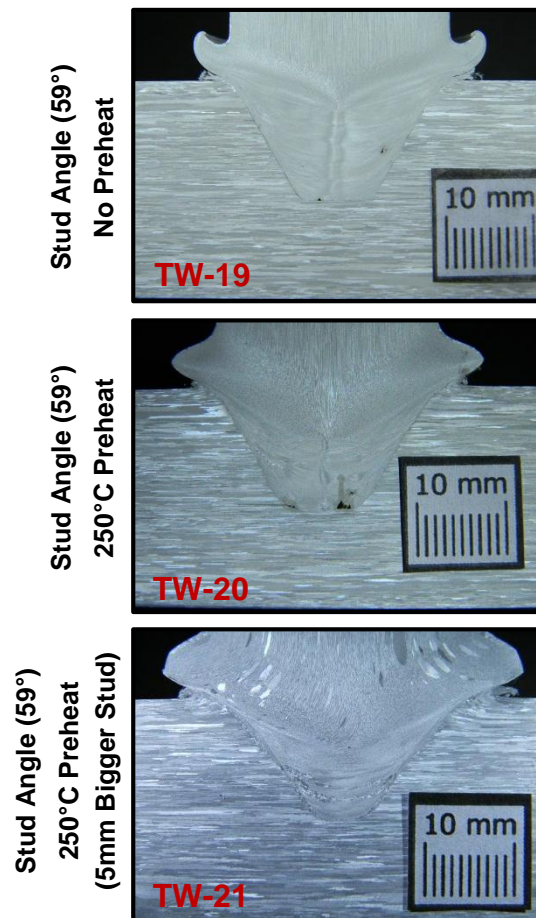


## Macrographs (Welds TW-8, TW-11 and TW-12)

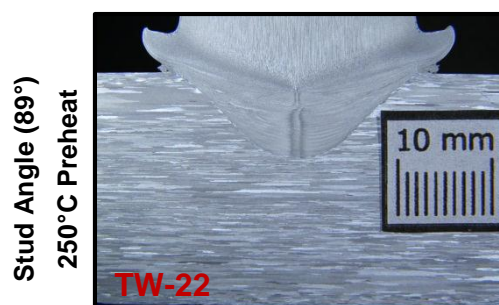


## Macrographs (Welds TW-13 to TW-18)



**Macrographs (Welds TW-19 to TW-21)**

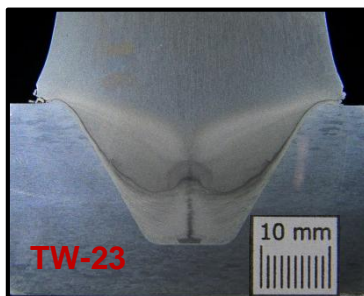
Axial Force 30kN

**Macrograph (Weld TW-22)**

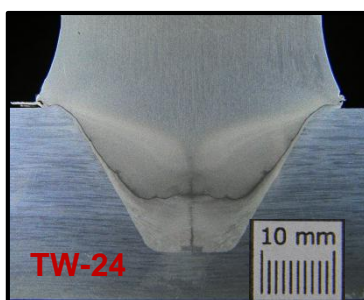
Axial Force 30kN  
(90° Hole)

Macrographs (Welds TW-19 to TW-21)

Stud Angle (55°)  
No Preheat  
No Heat Sink

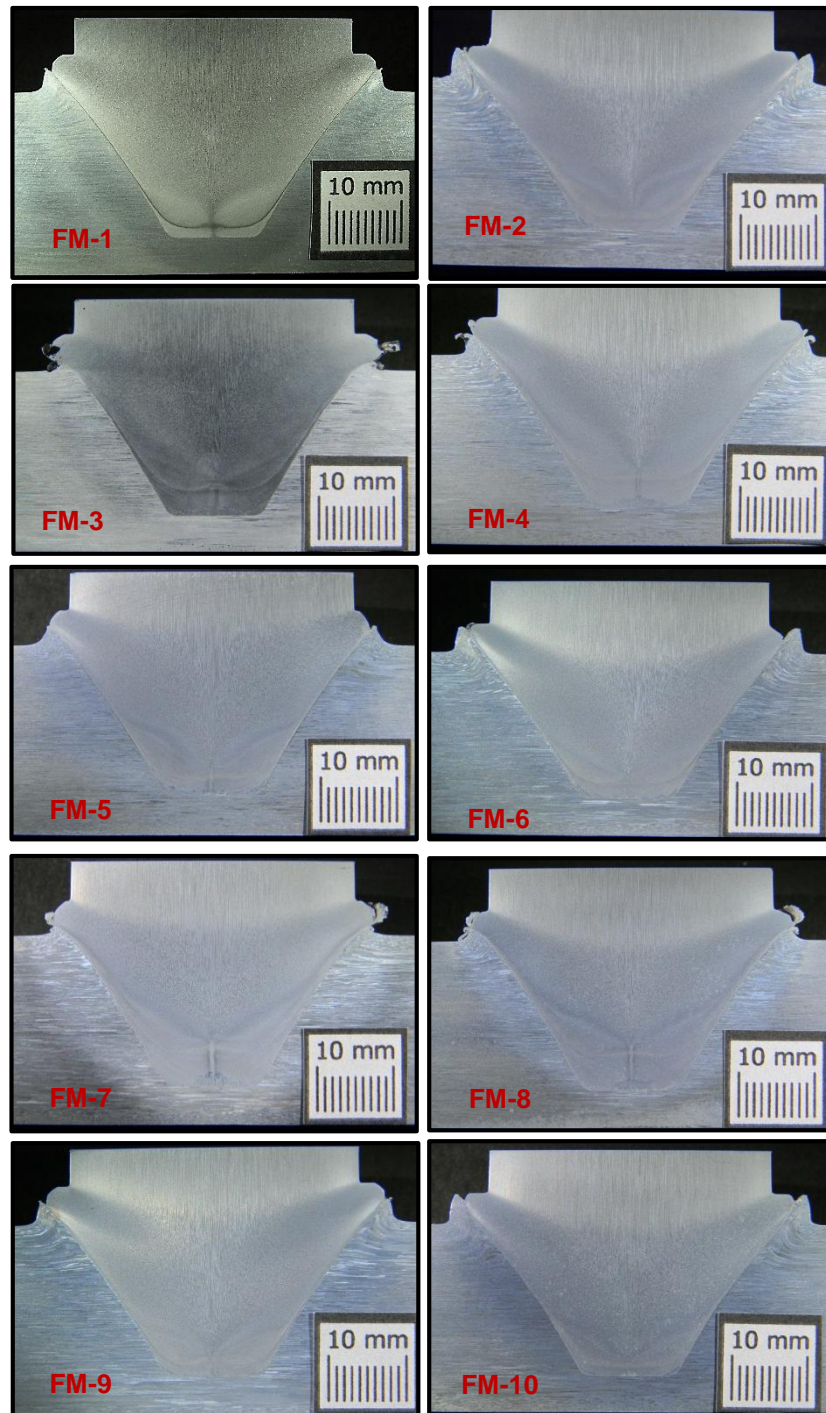


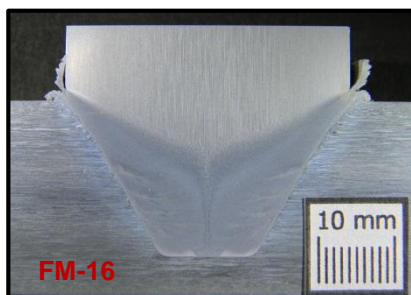
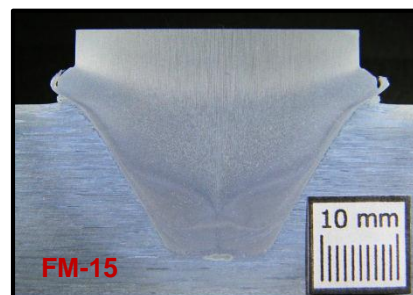
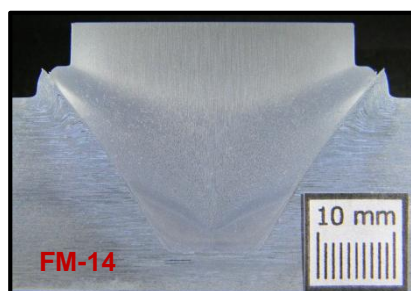
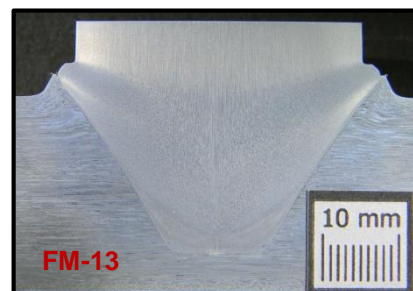
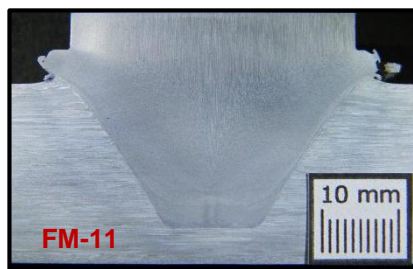
Stud Angle (55°)  
No Preheat  
Heat Sink



Axial Force Stages of 12/ 20 and 30kN

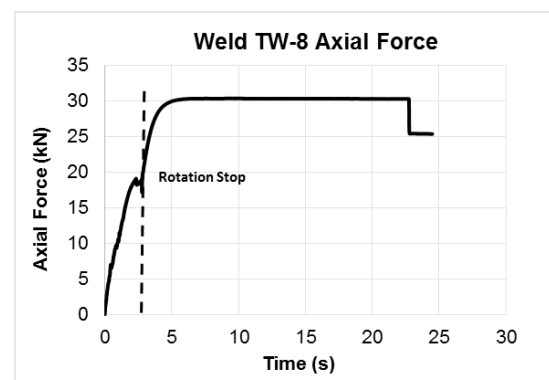
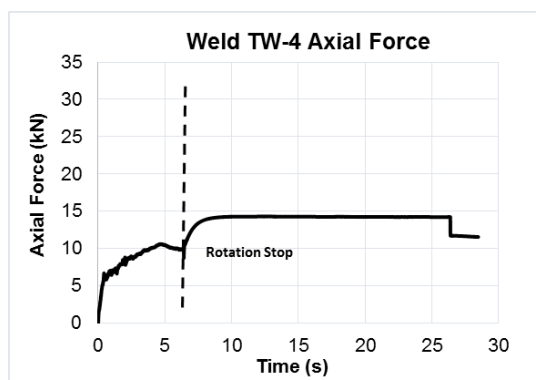
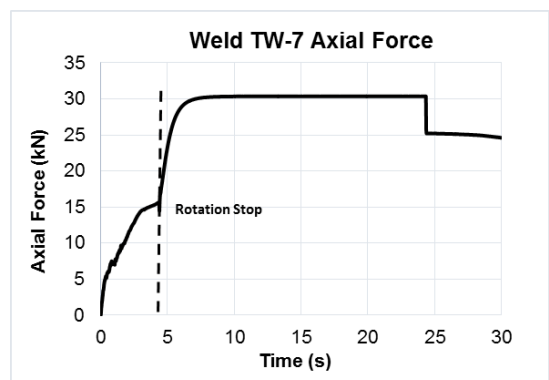
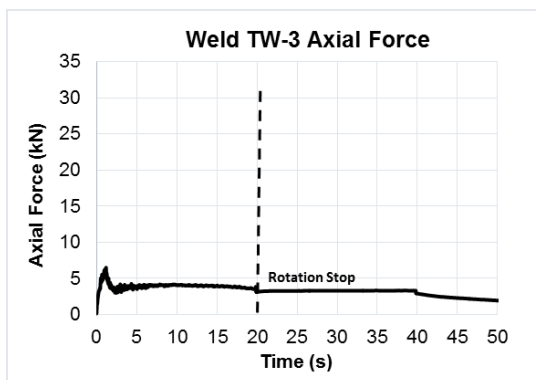
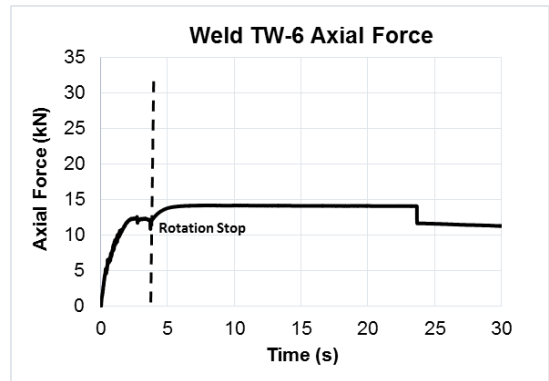
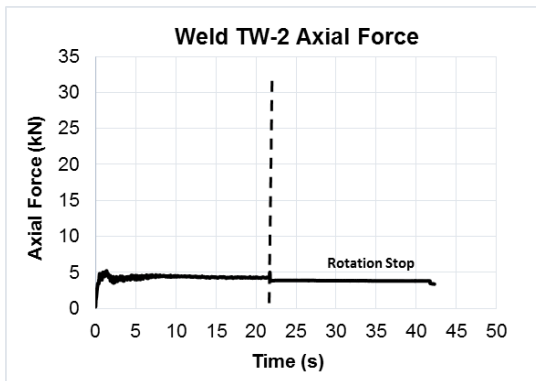
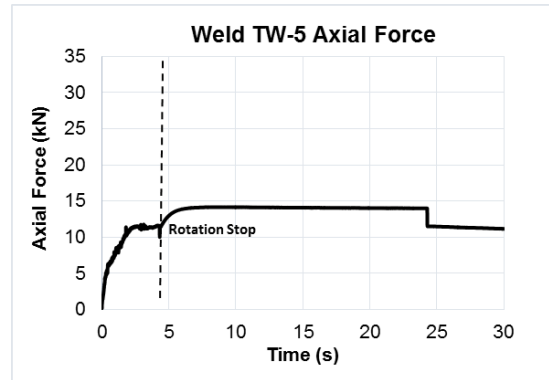
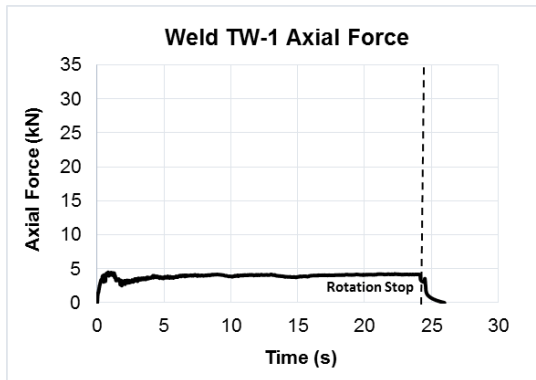
---

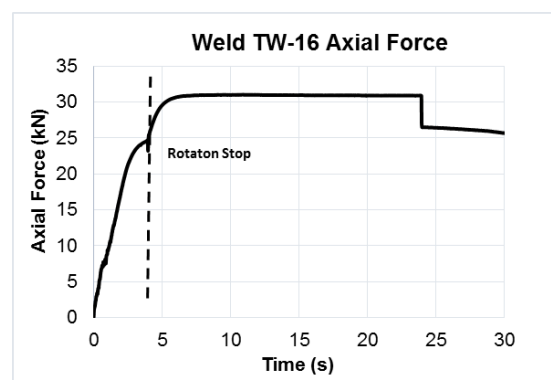
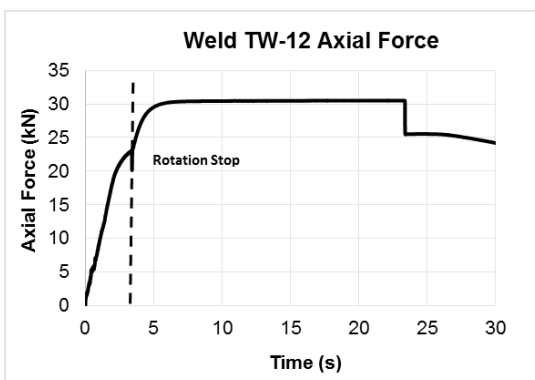
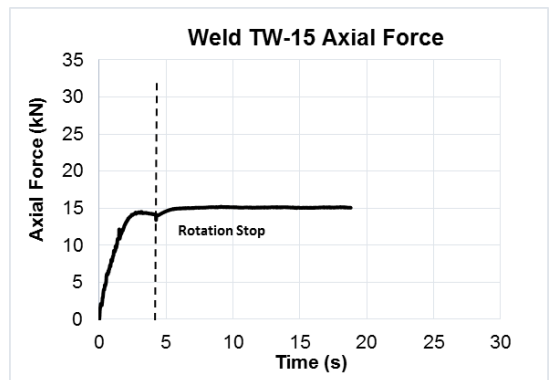
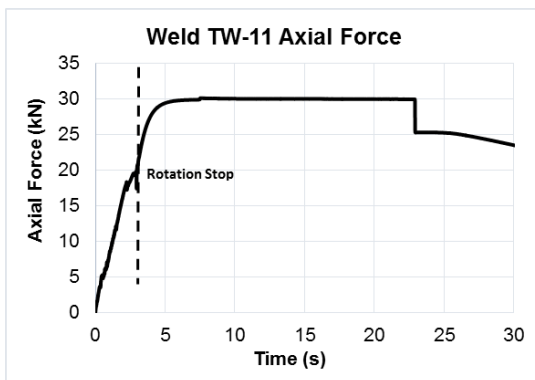
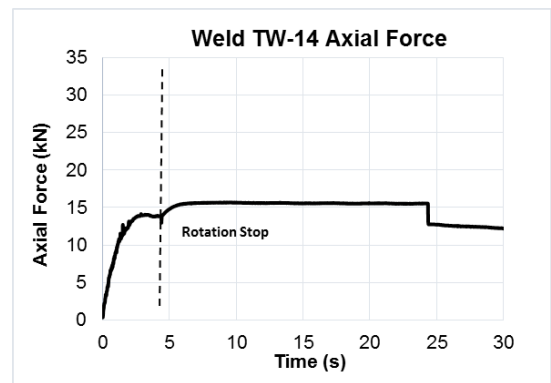
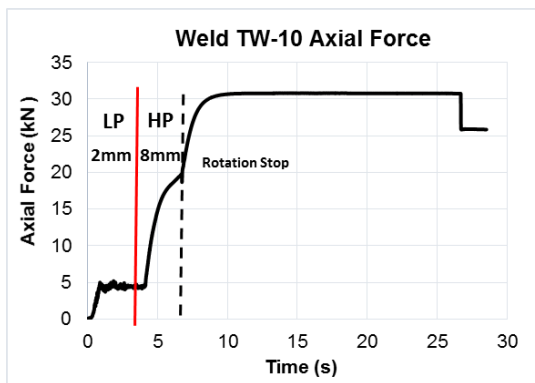
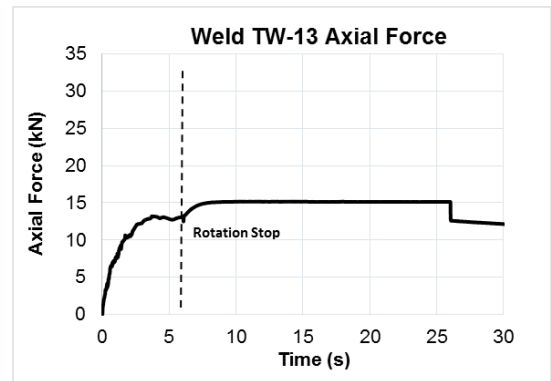
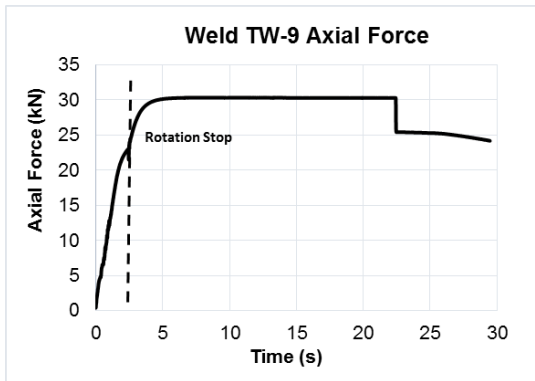
**Macrographs (Welds FM-1 to FM-16)**

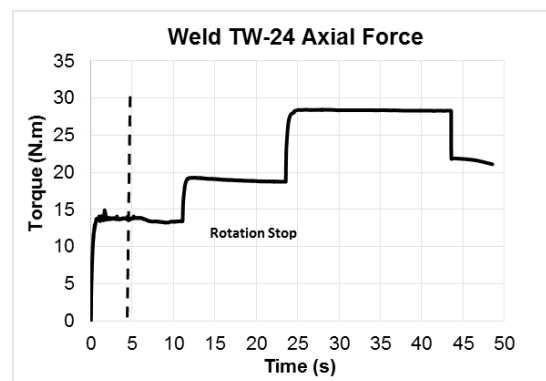
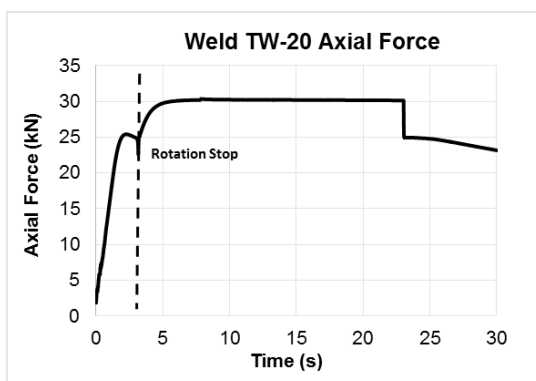
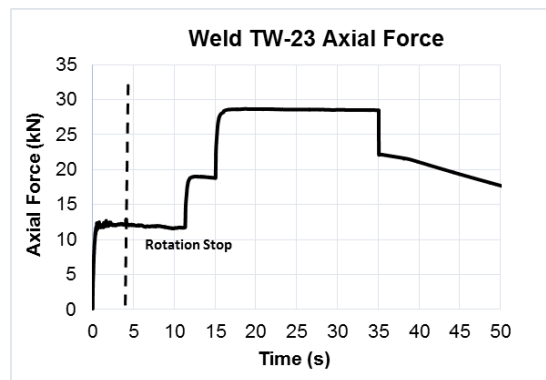
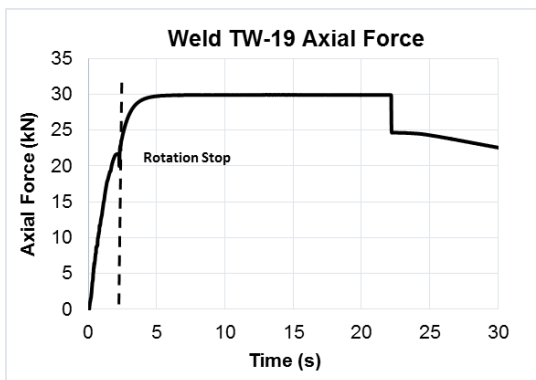
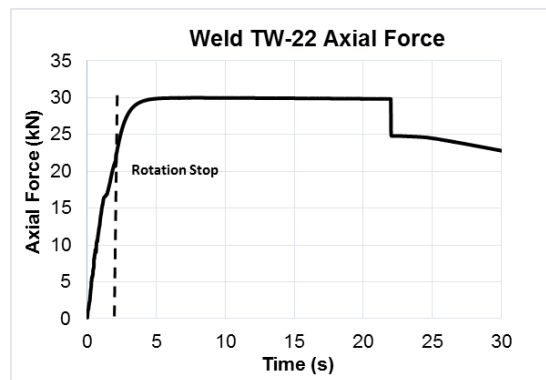
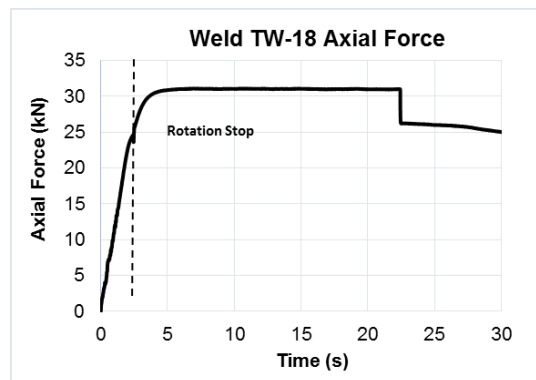
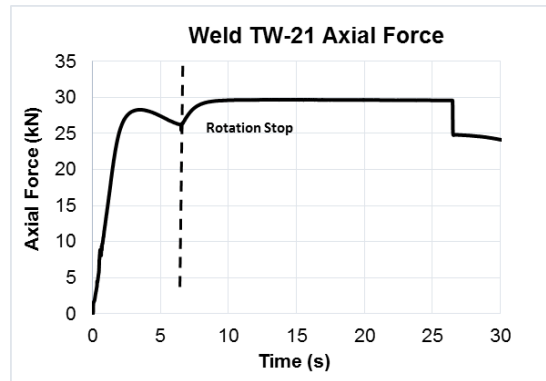
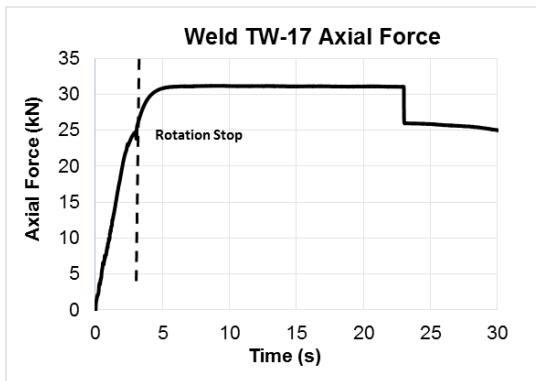


## Appendix E

## Applied Axial Force Charts for all Development Welds









## Appendix F

### Energy Input Process Torque and Axial Force Data

## Welds TW-1 to TW-10 Energy Data

Weld No:	Energy Input at 0.1s (J)	Energy Input at 0.1s (J.mm <sup>2</sup> )	Energy Input Rate at 0.1s (W/mm <sup>2</sup> )	Axial Force at 0.1s (kN)	Axial Force at 0.1s Ramp Rate (kN/s)	Time to Seizure (s)	Torque at Seizure (Nm)	Energy Input at Seizure (J)	Energy Input at Seizure (J/mm <sup>2</sup> )	Energy Input Rate at Seizure (W/mm <sup>2</sup> )	Axial Force at Seizure (kN)	Axial Force Ramp Rate at Seizure (kN/s)	Maximum Torque (PSTP) (Nm)	Time to PSTP(s)	Energy Input to PSTP (J)	Energy Input to PSTP (J/mm <sup>2</sup> )	Energy Input Rate at PSTP (W/mm <sup>2</sup> )	Axial Force at PSTP (kN)	Axial Force Ramp at PSTP (kN/s)
TW-1	162.9	2.1	20.7	1.6	16.1	0.45	12.8	1 731.8	21.0	49.0	4.0	8.9	14.6	0.5	8 548.3	7.2	14.1	4.0	7.9
TW-2	156.5	2.0	19.9	1.6	15.8	0.60	13.1	2 775.0	21.6	59.1	4.0	6.7	16.4	1.7	9 164.1	7.7	4.6	4.9	2.9
TW-3	105.3	1.3	13.4	1.6	16.2	0.50	15.2	1 877.5	19.7	47.9	4.6	9.2	30.0	1.3	10 043.8	8.4	6.7	6.1	4.9
TW-4	144.0	1.8	18.3	2.1	20.8	0.40	19.0	1 646.2	22.0	52.4	5.7	14.2	30.7	1.8	18 704.5	15.7	8.8	7.9	4.5
TW-5	162.5	2.1	20.7	2.0	19.8	0.38	18.7	1 694.6	35.4	57.5	5.2	13.9	31.7	1.4	14 437.3	12.1	8.6	8.7	6.2
TW-6	156.0	2.0	19.9	1.5	15.0	0.38	16.6	1 549.6	23.9	52.6	4.9	13.1	32.9	1.2	12 332.4	10.3	8.8	9.4	8.0
TW-7	189.4	2.4	24.1	2.1	20.6	0.35	19.2	1 905.7	24.3	69.3	5.2	14.8	33.3	1.5	15 730.1	13.2	8.9	9.3	6.3
TW-8	203.8	2.6	26.0	2.0	20.1	0.40	21.5	1 883.9	24.0	60.0	6.6	16.5	34.7	1.1	11 210.8	9.4	8.2	11.6	10.2
TW-9	128.5	1.6	16.4	2.2	22.3	0.40	19.8	1 916.5	24.4	61.0	6.0	15.1	54.1	1.0	11 510.6	9.7	10.0	11.9	12.3
TW-10	61.5	0.8	7.8	0.1	1.0	0.55	12.7	1 163.0	7.8	26.9	2.0	3.6	18.1	1.8	10 370.1	8.7	4.8	4.6	2.5

## Welds TW-1 to TW-10 Energy Data

Weld No:	Welding Time (s)	Total Energy Input (J)	Total Energy Input (J/mm <sup>2</sup> )	Total Energy Input Rate (W/mm <sup>2</sup> )	Axial Force at Plunge Depth (kN)	Energy Input at 1s (J)(W)	Energy Input at 1s (J/mm <sup>2</sup> )(W/mm <sup>2</sup> )	Axial Force at 1s (kN) (kN/s)
TW-1	24.4	110 197.0	92.4	3.8	3.1	5 332.6	4.5	4.4
TW-2	21.9	133 617.7	112.1	5.1	4.2	5 599.1	4.7	4.2
TW-3	19.9	121 077.1	101.6	5.1	3.4	8 693.4	7.3	5.6
TW-4	6.4	73 462.6	61.6	9.6	9.9	8 032.7	6.7	6.4
TW-5	4.3	49 804.1	41.8	9.7	10.0	8 760.9	7.3	7.6
TW-6	3.7	43 254.7	36.3	9.9	12.0	9 420.4	7.9	8.8
TW-7	4.4	55 792.7	46.8	10.7	15.5	8 725.6	7.3	7.0
TW-8	2.8	36 955.5	31.0	11.0	19.7	10 466.0	8.8	10.3
TW-9	2.4	38 267.5	32.1	13.2	23	12 660.0	10.6	12.4
TW-10	6.7	49 565.6	41.6	6.2	18.6	4980.5	4.2	4.5

## Welds TW-8, TW-11 and TW-12 Energy Data

Weld No:	Energy at 0.1s (J)	Energy Input at 0.1s (J/mm <sup>2</sup> )	Energy Input Rate at 0.1s (W/mm <sup>2</sup> )	Axial Force at 0.1 s (kN)	Axial Force at 0.1 s Ramp Rate (kN/s)	Time to Seizure (s)	Torque at Seizure (Nm)	Energy Input at Seizure (J)	Energy Input at Seizure (J/mm <sup>2</sup> )	Energy Input Rate at Seizure (W/mm <sup>2</sup> )	Axial Force at Seizure (kN)	Axial Force Ramp Rate at Seizure (kN/s)	Maximum Torque (PSTP) (Nm)	Time to PSTP (s)	Energy Input to PSTP (J)	Energy Input to PSTP (J/mm <sup>2</sup> )	Energy Input Rate at PSTP (W/mm <sup>2</sup> )	Axial Force at PSTP (kN)	Axial Force Ramp at PSTP (kN/s)
TW-8	203.8	2.6	26.0	2.0	20.1	0.4	21.5	1883.9	24.0	60.0	6.6	10.3	34.7	1.1	11210.8	9.4	8.2	11.6	10.2
TW-11	212.9	2.7	27.1	1.6	15.7	0.4	13.1	1279.4	16.3	46.5	3.7	8.2	41.9	1.4	15075.0	12.6	8.8	11.6	8.1
TW-12	389.6	5.0	49.6	1.6	15.8	0.1	7.0	270.2	3.4	43.0	1.4	9.0	38.9	1.4	14759.9	12.4	8.7	12.6	8.9

**Welds TW-8, TW-11 and TW-12 Energy Data**

Weld No:	Welding Time (s)	Total Energy Input (J)	Total Energy Input (J/mm <sup>2</sup> )	Total Energy Input Rate (W/mm <sup>2</sup> )	Axial Force at Plunge Depth (kN)
TW-8	2.8	36955.5	31.0	11.0	19.7
TW-11	3.0	38569.2	32.4	10.9	18.4
TW-12	3.4	43480.4	36.5	10.7	20.1

Energy Input at 1s(J)(W)	Energy Input at 1s (J/mm <sup>2</sup> )(W/mm <sup>2</sup> )	Axial Force at 1s (kN) (kN/s)
10466.0	8.8	10.3
7855.9	6.6	8.2
7618.1	6.4	9.0

## Welds TW-13 to TW-18 Energy Data

Weld No:	Energy Input at 0.1s (J)	Energy Input at 0.1s (J/mm <sup>2</sup> )	Energy Input Rate at 0.1s (W/mm <sup>2</sup> )	Axial Force at 0.1s (kN)	Axial Force at 0.1s Ramp Rate (kN/s)	Time to Seizure (s)	Torque at Seizure (Nm)	Energy Input at Seizure (J)	Energy Input at Seizure (J/mm <sup>2</sup> )	Energy Input Rate at Seizure (W/mm <sup>2</sup> )	Axial Force at Seizure (kN)	Axial Force Ramp Rate at Seizure (kN/s)	Maximum Torque (PSTP) (Nm)	Time to PSTP(s)	Energy Input to PSTP (J)	Energy Input to PSTP (J/mm <sup>2</sup> )	Energy Input Rate at PSTP (W/mm <sup>2</sup> )	Axial Force at PSTP (kN)	Axial Force Ramp at PSTP (kN/s)
TW-13	228.8	2.9	29.1	1.8	18.4	0.34	17.0	2059.5	26.2	78.3	3.8	7.6	33.8	2.1	25846.2	19.7	9.2	10.6	5.0
TW-14	189.5	2.4	24.1	2.1	21.0	0.34	16.1	1734.8	22.1	65.4	4.4	9.3	33.8	1.8	21532.8	16.4	9.1	12.2	6.8
TW-15	222.1	2.8	28.3	2.0	20.4	0.20	10.7	750.8	9.6	47.8	2.6	8.2	38.7	1.4	16811.0	12.8	9.1	10.9	7.8
TW-16	223.0	2.8	28.4	1.6	15.7	0.25	17.3	1187.2	15.1	60.5	3.4	8.8	40.8	1.6	20395.7	15.5	9.7	13.8	8.6
TW-17	229.3	2.9	29.2	1.7	17.2	0.37	16.7	2004.8	25.5	69.9	4.2	10.0	46.6	1.7	24428.2	18.6	11.1	16.7	10.0
TW-18	203.5	2.6	25.9	1.9	18.6	0.30	18.0	1645.2	20.9	69.8	4.0	11.1	45.4	1.2	16225.3	12.4	10.3	13.4	11.2

## Welds TW-13 to TW-18 Energy Data

Weld No:	Welding Time (s)	Total Energy Input (J)	Total Energy Input (J/mm <sup>2</sup> )	Total Energy Input Rate (W/mm <sup>2</sup> )	Axial Force at Plunge Depth (kN)
TW-13	6.07	82 745.7	63.0	10.4	12.7
TW-14	4.4	60 146.6	45.8	10.4	12.9
TW-15	4.24	61 366.6	46.7	11.0	13.4
TW-16	3.99	65 000.4	49.5	12.4	23.5
TW-17	3.05	51 857.3	39.5	12.9	23.8
TW-18	2.46	43 228.5	32.9	13.4	23.6

Energy Input at 1s (J)(W)	Energy Input at 1s (J/mm <sup>2</sup> )(W/mm <sup>2</sup> )	Axial Force at 1s (kN) (kN/s)
8363.4	6.4	9.6
8946.0	6.8	9.3
9312.3	7.1	8.23
9324.7	7.1	8.8
9832.4	7.5	10.0
11765.9	9.0	11.1

## Welds TW-19 to TW-21 Energy Data

Weld No:	Energy Input at 0.1s (J)	Energy Input at 0.1s (J/mm <sup>2</sup> )	Energy Input Rate at 0.1s (W/mm <sup>2</sup> )	Axial Force at 0.1s (kN)	Axial Force at 0.1s Ramp Rate (kN/s)	Time to Seizure (s)	Torque at Seizure (Nm)	Energy Input at Seizure (J)	Energy Input at Seizure (J/mm <sup>2</sup> )	Energy Input Rate at Seizure (W/mm <sup>2</sup> )	Axial Force at Seizure (kN)	Axial Force Ramp Rate at Seizure (kN/s)	Maximum Torque (PSTP) (Nm)	Time to PSTP (s)	Energy Input to PSTP (J)	Energy Input to PSTP (J/mm <sup>2</sup> )	Energy Input Rate at PSTP (W/mm <sup>2</sup> )	Axial Force at PSTP (kN)	Axial Force Ramp at PSTP (kN/s)
TW-19	81.5	1.0	10.1	0.93	9.3	0.23	15.7	725.0	9.0	39.2	2.7	11.7	42.2	0.87	12235.9	13.9	16.0	12.1	13.9
TW-20	318.5	4.0	39.7	1.67	16.7	0.11	31.9	428.1	5.3	48.5	3.2	29.1	33.4	0.71	7970.2	9.1	12.7	9.8	13.8
TW-21	474.4	5.9	59.1	1.73	17.3	0.06	12.6	270.0	3.4	56.0	1.6	26.0	46.1	0.54	7404.0	8.4	15.6	8.9	16.5



**Welds TW-19 to TW-21 Energy Data**

Weld No:	Welding Time (s)	Total Energy Input (J)	Total Energy Input (J/mm <sup>2</sup> )	Total Energy Input Rate (W/mm <sup>2</sup> )	Axial Force at Plunge Depth (kN)
TW-19	2.28	N/A	N/A	N/A	21.95
TW-20	3.24	N/A	N/A	N/A	24.2
TW-21	6.51	N/A	N/A	N/A	25.47

Energy Input at 1s(J)(W)	Energy Input at 1s (J/mm <sup>2</sup> )(W/mm <sup>2</sup> )	Axial Force at 1s (kN) (kN/s)
15040.1	17.1	13.6
14476.6	16.4	14.1
15894.3	18.1	13.7

## Weld TW-22 Energy Data

Weld No:	Energy Input at 0.1s (J)	Energy Input at 0.1s (J/mm <sup>2</sup> )	Energy Input Rate at 0.1s (W/mm <sup>2</sup> )	Axial Force at 0.1s (kN)	Axial Force at 0.1s Ramp Rate (kN/s)	Time to Seizure (s)	Torque at Seizure (Nm)	Energy Input at Seizure (J)	Energy Input at Seizure (J/mm <sup>2</sup> )	Energy Input Rate at Seizure (W/mm <sup>2</sup> )	Axial Force at Seizure (kN)	Axial Force Ramp Rate at Seizure (kN/s)	Maximum Torque (PSTP) (Nm)	Time to PSTP(s)	Energy Input to PSTP (J)	Energy Input to PSTP (J/mm <sup>2</sup> )	Energy Input Rate at PSTP (W/mm <sup>2</sup> )	Axial Force at PSTP (kN)	Axial Force Ramp at PSTP (kN/s)
TW-22	167.7	2.6	25.7	1.64	16.4	0.11	4.4	192.8	3.0	26.9	1.8	16.5	32.9	0.85	9575.6	14.6	17.2	12.3	14.5

---

## Weld TW-22 Energy Data

Weld No:	Welding Time (s)	Total Energy Input (J)	Total Energy Input (J/mm <sup>2</sup> )	Total Energy Input Rate (W/mm <sup>2</sup> )	Axial Force at Plunge Depth (kN)
TW-22	2.04	26 905	41.14	20.2	21.2

Energy Input at 1s(J)(W)	Energy Input at 1s (J/mm <sup>2</sup> )(W/mm <sup>2</sup> )	Axial Force at 1s (kN) (kN/s)
12078	18.5	14.3

## Welds TW-23 to TW-24 Energy Data

Weld No:	Energy Input at 0.1s (J)	Energy Input at 0.1s (J/mm <sup>2</sup> )	Energy Input Rate at 0.1s (W/mm <sup>2</sup> )	Axial Force at 0.1 s (kN)	Axial Force at 0.1 s Ramp Rate (kN/s)	Time to Seizure (s)	Torque at Seizure (Nm)	Energy Input at Seizure (J)	Energy Input at Seizure (J/mm <sup>2</sup> )	Energy Input Rate at Seizure (W/mm <sup>2</sup> )	Axial Force at Seizure (kN)	Axial Force Ramp Rate at Seizure (kN/s)	Maximum Torque (PSTP) (Nm)	Time to PSTP(s)	Energy Input to PSTP (J)	Energy Input to PSTP (J/mm <sup>2</sup> )	Energy Input Rate at PSTP (W/mm <sup>2</sup> )	Axial Force at PSTP (kN)	Axial Force Ramp at PSTP (kN/s)
TW-23	1285.1	9.5	94.9	5.9	58.7	0.15	23.0	2062.7	15.2	99.6	7.9	52.5	48.7	1.3	26536.3	17.6	13.2	11.9	8.9
TW-24	1326.9	9.8	98.0	5.6	56.2	0.12	37.4	1445.5	10.7	89.0	6.5	54.0	59.6	1.4	31598.1	20.9	15.2	13.7	10.0
TW-24 (Fail)	x	x	x	x	x	x	x	x	x	x	x	x	x	x	x	x	x	x	x

## Welds TW-23 to TW-24 Energy Data

Weld No:	Welding Time (s)	Total Energy Input (J)	Total Energy Input (J/mm <sup>2</sup> )	Total Energy Input Rate (W/mm <sup>2</sup> )	Axial Force at Plunge Depth (kN)
TW-23	15.1	235123.8	155.8	10.3	21.6
TW-24	23.6	344643.1	228.3	9.7	18.7
TW-24 (Fail)	41.42	529208.0	350.6	8.5	x

Energy Input at 1s (J)(W)	Energy Input at 1s (J/mm <sup>2</sup> )(W/mm <sup>2</sup> )	Axial Force at 1s (kN) (kN/s)
18320.2	12.1	11.9
20609.4	13.65	12.05
x	x	x

## Welds PT-1 to PT-4 Energy Data

Weld No:	Energy Input at 0.1s (J)	Energy Input at 0.1s (J/mm <sup>2</sup> )	Energy Input Rate at 0.1s (W/mm <sup>2</sup> )	Axial Force at 0.1 s (kN)	Axial Force at 0.1 s Ramp Rate (kN/s)	Time to Seizure (s)	Torque at Seizure/ Maximum (Nm)	Energy Input at Seizure (J)	Energy Input at Seizure (J/mm <sup>2</sup> )	Energy Input Rate at Seizure (W/mm <sup>2</sup> )	Axial Force at Seizure (kN)	Axial Force Ramp Rate at Seizure (kN/s)	Energy Input to 0.25s(J)	Energy Input to 0.25s (J/mm <sup>2</sup> )	Energy Input Rate at 0.25s (W/mm <sup>2</sup> )	Axial Force at 0.25kN (kN)	Axial Force Ramp at 0.25s (kN/s)
PT-1	1252.9	8.0	80.0	6.3	63.0	0.05	31.5	720.3	4.6	91.8	3.8	76.4	3061.2	19.5	78.0	12.3	49.1
PT-2	1043.3	6.7	66.5	7.1	71.2	0.05	25.2	536.2	3.4	68.4	4.3	86.4	2720.3	17.3	69.4	12.2	48.7
PT-3	590.9	3.8	37.7	6.7	67.4	0.13	40.8	826.8	5.3	42.2	8.5	67.8	2425.1	15.5	61.8	12.0	47.9
PT-4	722.2	4.6	46.0	6.4	64.0	0.15	38.9	958.4	6.1	40.7	7.6	50.5	2488.6	15.9	63.4	11.4	45.4

## Welds PT-1 to PT-4 Energy Data

Weld No:	Welding Time (s)	Total Energy Input (J)	Total Energy Input (J/mm <sup>2</sup> )	Total Energy Input Rate (W/mm <sup>2</sup> )	Axial Force at Plunge Depth (kN)	Ultimate Tensile Strength (kN)	Ultimate Tensile Strength (MPa)
PT-1	0.41	5304.6	33.8	82.5	12.5	11.4	45.5
PT-2	0.40	4602.3	29.3	73.3	12.2	29.4	117.2
PT-3	0.43	4300.0	27.4	63.7	12.3	20.0	79.8
PT-4	0.39	3915.2	25.0	64.0	11.5	40.7	162.4

## Welds RR-1 to RR-4 Energy Data

Weld No:	Energy Input at 0.1s (J)	Energy Input at 0.1s (J/mm <sup>2</sup> )	Energy Input Rate at 0.1s (W/mm <sup>2</sup> )	Energy Input at 1s (J)	Energy Input at 1s (J/mm <sup>2</sup> )(W/mm <sup>2</sup> )	Time to Seizure (s)	Torque at Seizure (Nm)	PSTP Maximum (Nm)	Energy Input at Seizure (J)	Energy Input at Seizure (J/mm <sup>2</sup> )	Energy Input Rate at Seizure (W/mm <sup>2</sup> )	Time to PSTP(s)	Energy Input to PSTP (J)	Energy Input to PSTP (J/mm <sup>2</sup> )	Energy Input Rate at PSTP (W/mm <sup>2</sup> )
RR-1	208.2	1.3	13.3	7402.7	4.0	0.115	19.2	85.8	267.6	1.7	14.8	2.06	34765.6	18.9	9.2
RR-2	448.0	2.9	28.6	19211.8	10.4	0.250	51.0	115.2	2302.5	14.7	58.7	1.42	31797.3	17.3	12.1
RR-3	569.8	3.6	36.3	24791.1	13.5	0.210	65.1	144.6	2298.4	14.6	69.7	1.21	32267.6	17.5	14.4
RR-4	708.8	4.5	45.2	28219.3	15.3	0.185	77.8	149.5	2192.9	14.0	75.5	1.13	32089.1	17.4	15.4



---

## Welds RR-1 to RR-4 Energy Data

Weld No:	Welding Time (s)	Total Energy Input (J)	Total Energy Input (J/mm <sup>2</sup> )	Total Energy Input Rate (W/mm <sup>2</sup> )	Stopping Time (s)	Forge Plunge	True Ramp Rate	Ultimate Tensile Strength (MPa)
RR-1	6.5	128693.4	69.9	10.7	0.2	0.8	15.2	59.0
RR-2	6.2	138463.1	75.2	12.2	0.2	0.9	45.8	126.0
RR-3	5.9	140262.5	76.2	12.8	0.2	0.8	76.4	191.2
RR-4	6.4	152304.7	82.7	13.0	0.2	0.7	112.2	195.0

## Welds FM-1 to FM-16 Energy Data

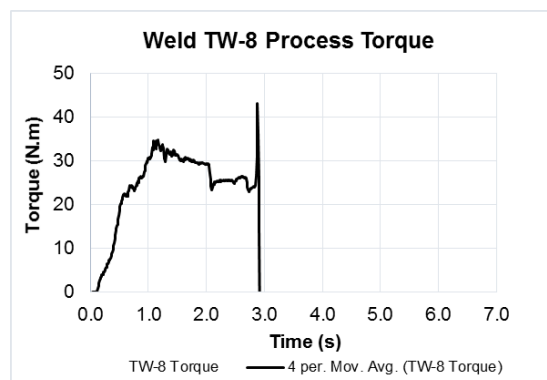
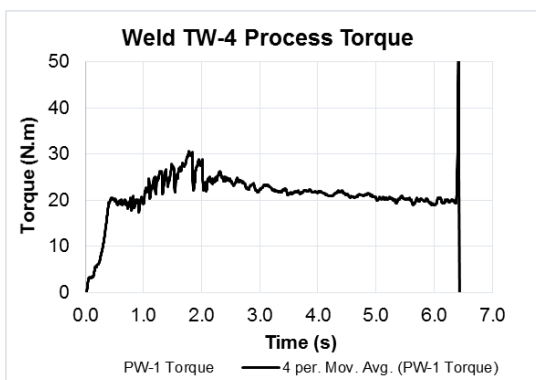
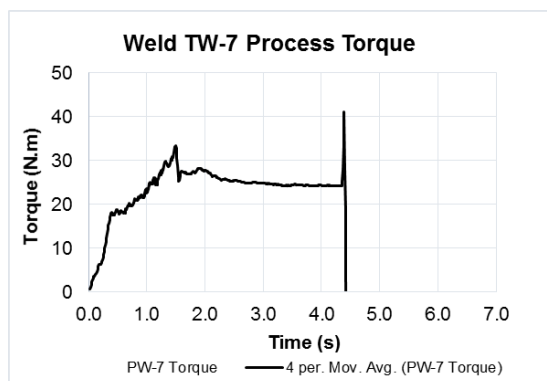
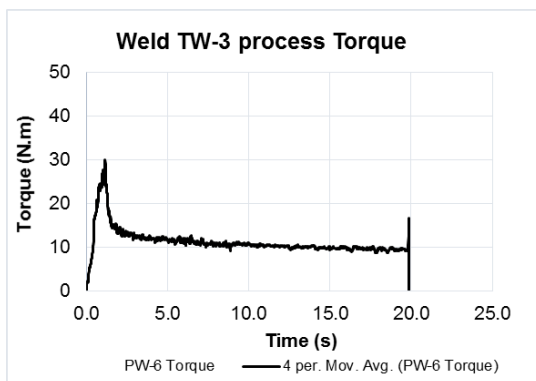
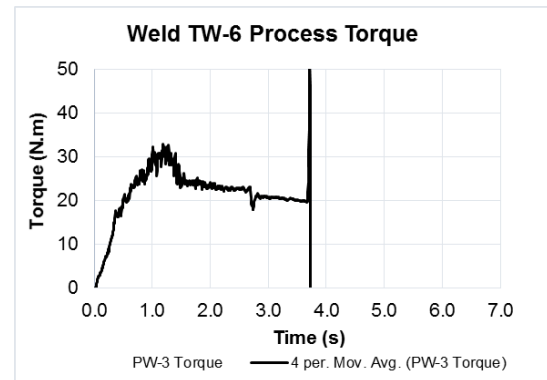
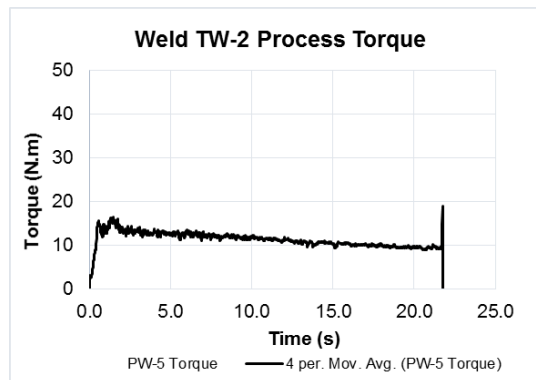
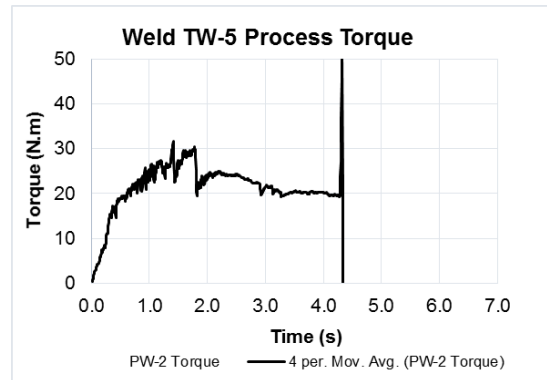
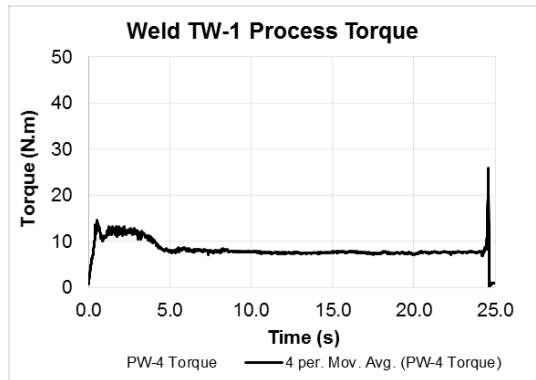
Weld No:	Energy Input at 0.1s (J)	Energy Input at 0.1s (J/mm <sup>2</sup> )	Energy Input Rate at 0.1s (W/mm <sup>2</sup> )	Energy Input at 1s (J)	Energy Input at 1s (J/mm <sup>2</sup> ) (W/mm <sup>2</sup> )	Time to Seizure (s)	Torque at Seizure (Nm)	Maximum Torque PSTPM (Nm)	Energy Input at Seizure (J)	Energy Input at Seizure (J/mm <sup>2</sup> )	Energy Input Rate at Seizure (W/mm <sup>2</sup> )	Time to PSTP(s)	Energy Input to PSTP (J)	Energy Input to PSTP (J.mm <sup>2</sup> )	Energy Input Rate at PSTP (W.mm <sup>2</sup> )
FM-1	692.5	4.4	44.1	21 676.5	11.8	0.1	39.6	51.4	812.2	5.2	41.1	1.1	23 492.1	12.8	11.9
FM-2	706.8	4.5	45.0	23 363.8	12.7	0.1	41.5	58.6	921.8	5.9	53.4	1.5	14 511.1	7.9	5.3
FM-3	569.8	3.6	36.3	24 791.1	13.5	0.2	65.1	144.6	2 298.5	14.6	69.8	1.2	32 267.6	17.5	14.4
FM-4	555.3	3.5	35.4	24 767.5	13.5	0.2	75.5	142.8	2 297.2	14.6	73.2	1.2	32 400.8	17.6	14.4
FM-5	1 008.6	6.4	64.3	26 325.8	14.3	0.1	34.0	64.3	1 008.6	6.4	64.2	0.5	10 606.8	5.8	11.9
FM-6	915.6	5.8	58.4	25 633.6	13.9	0.1	42.8	61.3	1 235.5	7.9	65.6	0.3	7 127.0	3.9	11.4
FM-7	294.7	1.9	18.8	29 211.5	15.9	0.2	79.5	184.8	1 873.8	11.9	63.6	1.0	27 485.5	14.9	15.6
FM-8	588.1	3.7	37.5	29 737.0	16.2	0.2	88.1	170.6	2 868.3	18.3	87.1	1.0	29 171.3	15.8	16.0
FM-9	555.1	3.5	35.3	23 775.7	12.9	0.1	46.3	52.4	801.0	5.1	46.4	0.4	8 925.8	4.8	11.2
FM-10	1 032.3	6.6	65.8	25 186.8	13.7	0.1	37.6	56.7	1 234.2	7.9	71.5	0.8	19 433.2	10.6	13.2
FM-11	708.8	4.5	45.2	28 219.3	15.3	0.2	77.8	149.5	2 192.9	14.0	75.5	1.1	32 089.1	17.4	15.3
FM-12	630.9	4.0	40.2	29 239.4	15.9	0.2	78.4	173.7	2 406.4	15.3	80.7	1.1	31 264.9	17.0	16.1
FM-13	1 278.5	8.1	81.5	26 421.7	14.4	0.1	39.7	59.3	1 591.5	10.1	84.5	0.6	14 399.3	7.8	13.6
FM-14	1 218.3	7.8	77.6	28 461.4	15.5	0.2	54.9	63.6	3 226.5	20.6	114.2	0.8	21 379.9	11.6	14.7
FM-15	677.8	4.3	43.2	32 189.5	17.5	0.2	89.6	181.8	2 359.6	15.0	85.9	0.9	28 361.7	15.4	17.0
FM-16	567.8	3.6	36.2	32 745.0	17.8	0.2	90.2	500.0	2 804.2	17.9	89.4	1.3	40 113.8	21.8	17.1

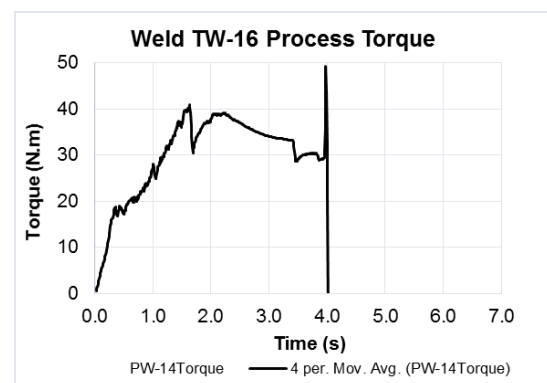
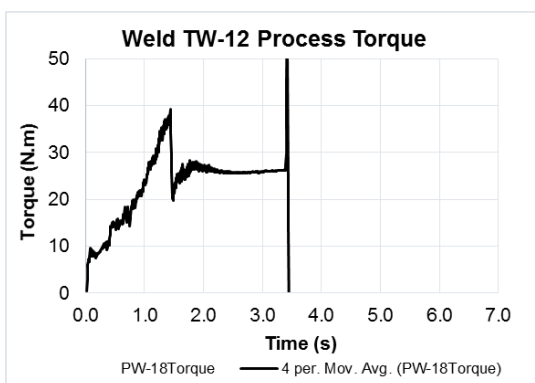
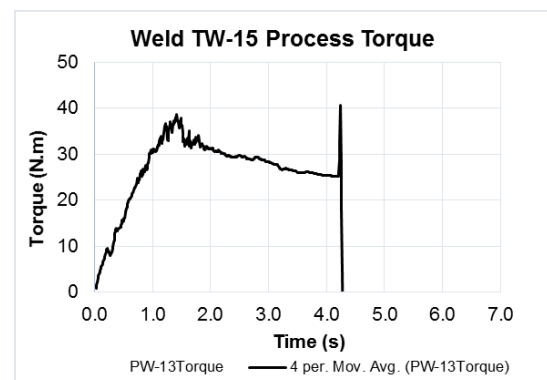
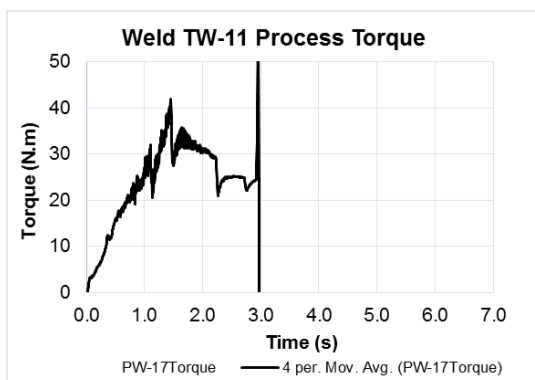
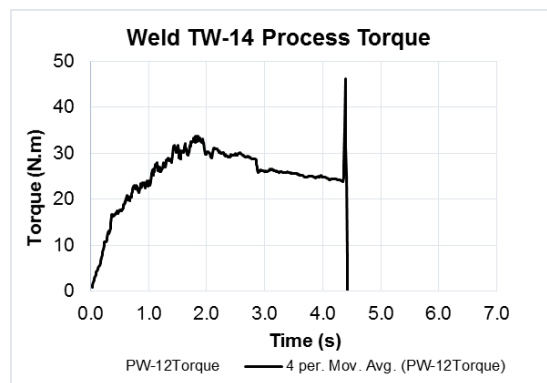
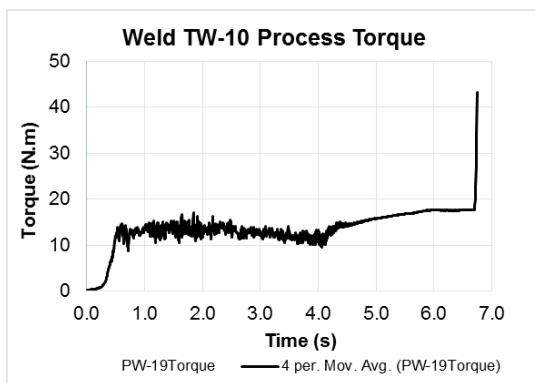
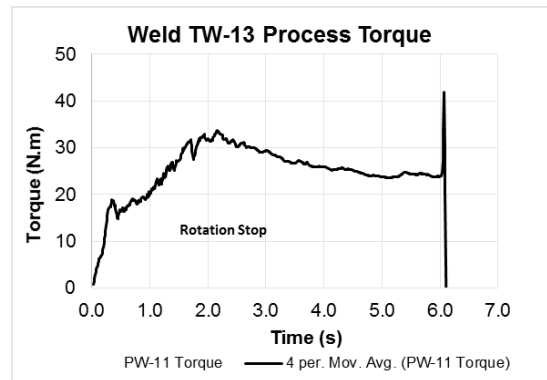
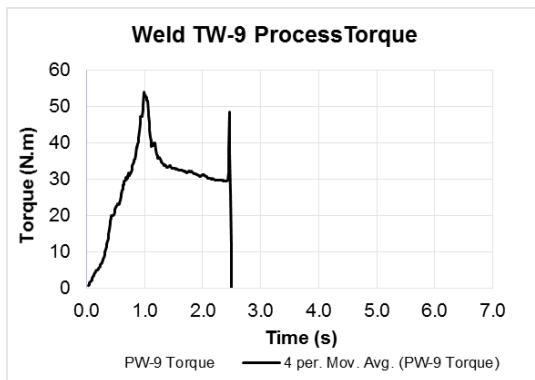
## Welds FM-1 to FM-16 Energy Data

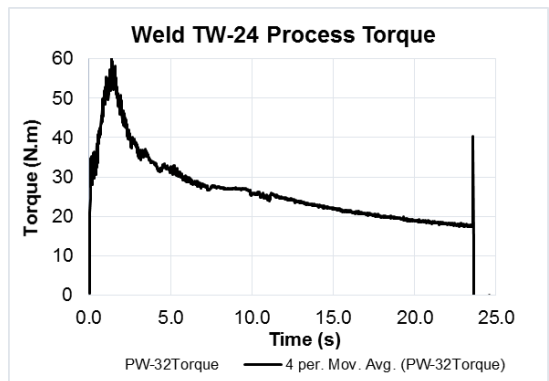
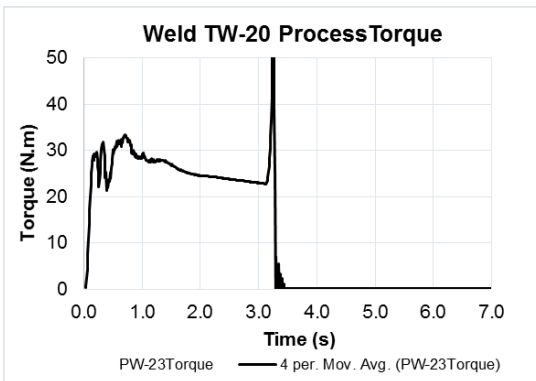
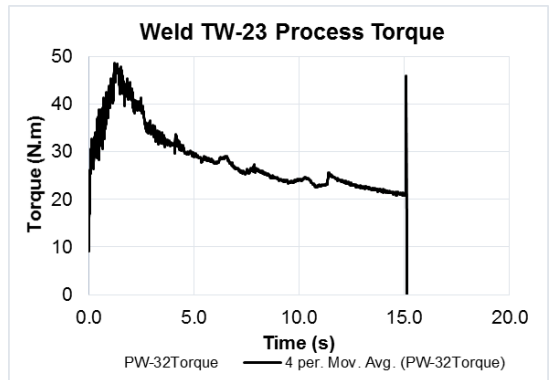
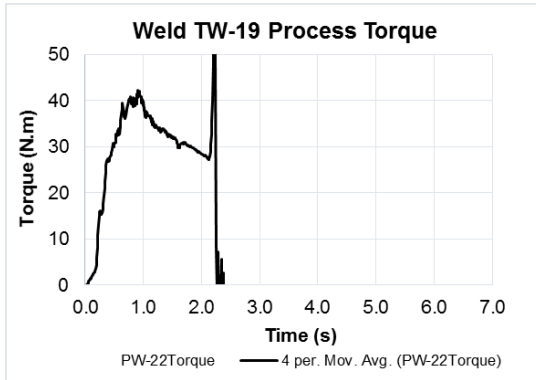
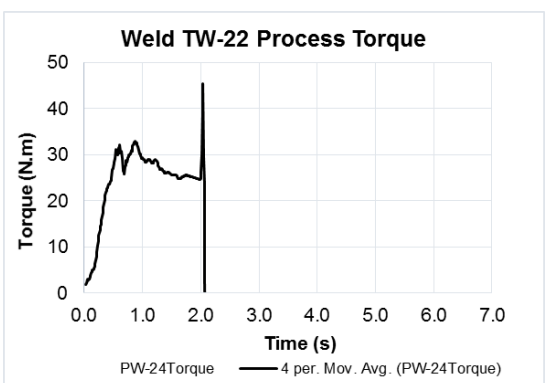
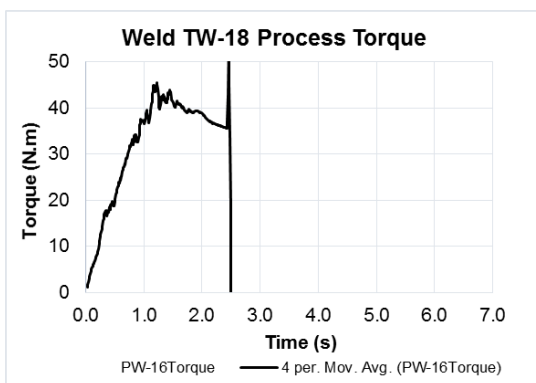
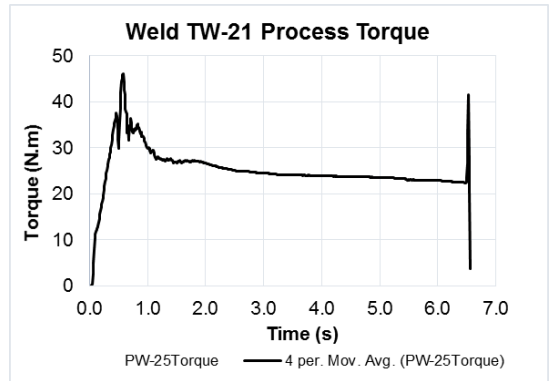
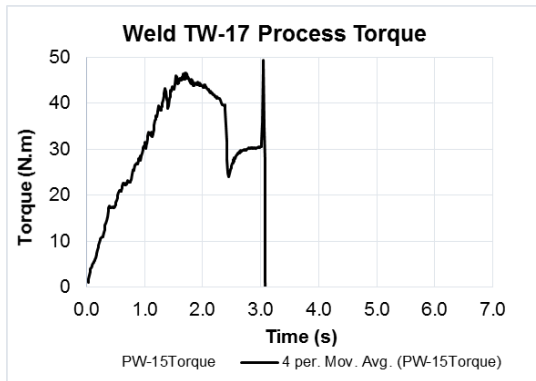
Weld No:	Welding Time (s)	Total Energy Input t (J)	Total Energy Input (J/mm <sup>2</sup> )	Total Energy Rate Input to plunge mm	Welding Time to Stop (s)	Total Energy Input to Stop (J)	Total Energy Input to Stop (J/mm <sup>2</sup> )	Total Energy Input Rate to Stop (W/mm <sup>2</sup> )	Stopping Time (s)	Plunge Depth during Stopping (mm)	Plunge Depth during Forge (mm)	Total Plunge (mm)	True Ramp Rate (KN/s)
FM-1	7.5	159 529.4	86.6	10.9	7.9	167 370.3	90.9	12.2	0.5	0.4	0.6	3.0	71.5
FM-2	4.0	102 309.0	55.6	13.8	4.5	111 239.1	60.5	13.5	0.4	0.9	0.5	3.4	70.3
FM-3	5.9	137 389.4	74.6	12.6	6.1	140 262.5	76.2	12.4	0.2	0.3	0.6	2.8	76.5
FM-4	3.5	92 404.0	50.2	14.4	3.7	95 821.0	52.0	14.1	0.2	0.5	0.6	3.0	75.5
FM-5	5.9	141 251.2	76.7	12.8	6.4	149 086.4	76.7	12.8	0.7	0.3	0.7	1.1	76.0
FM-6	3.5	102 242.4	51.0	14.7	3.9	102 242.4	55.5	14.4	0.4	0.7	0.6	2.1	75.5
FM-7	4.8	120 004.5	65.2	13.6	5.0	123 126.7	66.9	13.5	0.2	0.2	0.6	1.6	76.0
FM-8	2.8	81 297.8	44.2	15.6	3.0	84 777.7	46.1	15.3	0.2	0.3	0.6	1.6	72.1
FM-9	6.8	151 522.1	82.3	12.0	7.3	159 946.2	86.9	11.9	0.5	0.4	0.6	3.0	102.6
FM-10	4.1	105 210.8	57.1	13.7	4.5	114 252.4	62.1	14.0	0.7	0.6	0.6	1.2	69.7
FM-11	6.4	149 338.2	81.1	12.8	6.6	152 304.7	82.7	12.6	0.2	0.2	0.6	2.7	112.2
FM-12	3.2	90 860.7	49.4	15.2	3.4	94 334.6	51.2	14.9	0.2	0.4	0.6	3.0	111.9
FM-13	6.4	147 498.8	80.1	11.7	6.8	155 332.9	84.4	12.3	0.5	0.3	0.6	1.7	111.4
FM-14	3.5	96 052.9	52.2	15.1	3.9	105 377.3	57.2	14.7	0.4	0.6	0.6	1.2	110.4
FM-15	4.4	115 140.5	62.5	14.1	4.6	118 239.2	64.2	13.9	0.2	0.2	0.6	1.6	105.3
FM-16	1.4	40 113.8	21.8	15.2	1.4	40 113.8	21.8	15.2	0.0	0.0	0.3	1.1	110.4

## Appendix G

## Process Torque Charts for Process Development Welds

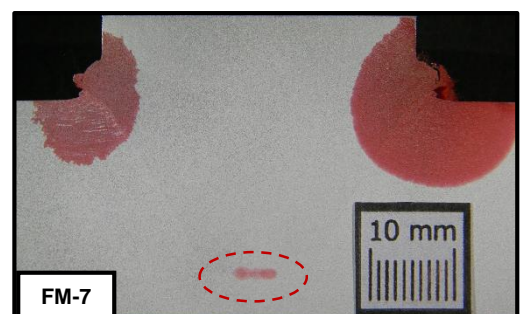
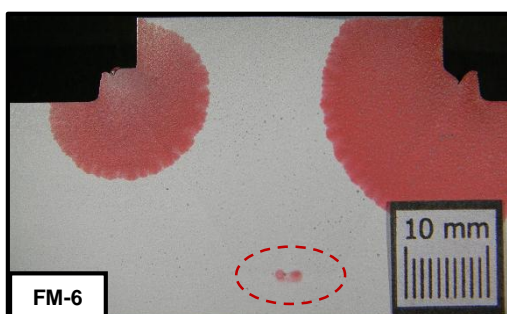
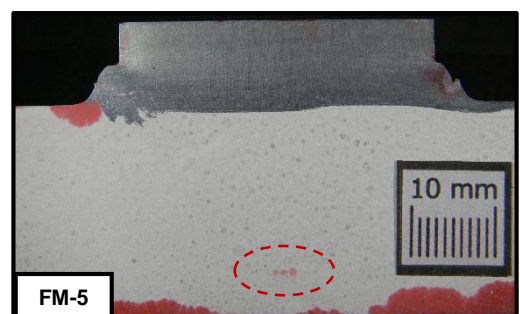
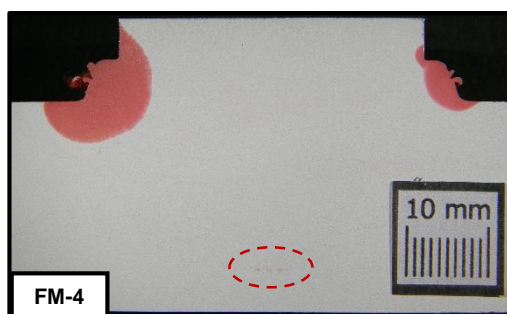
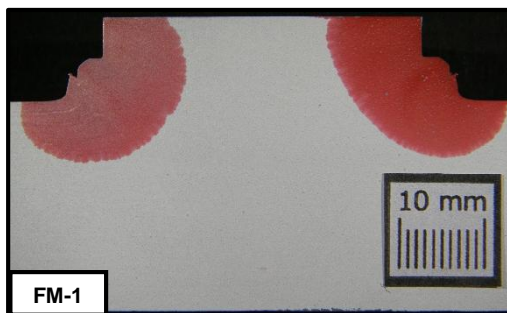
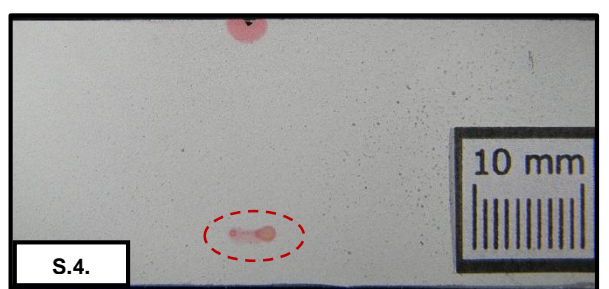
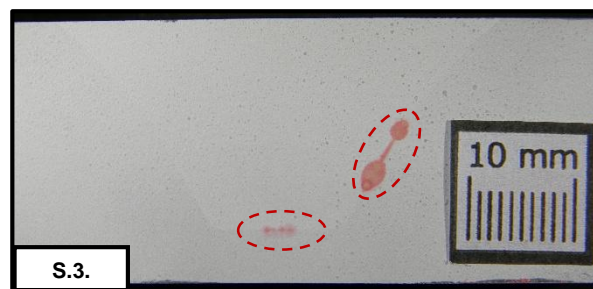
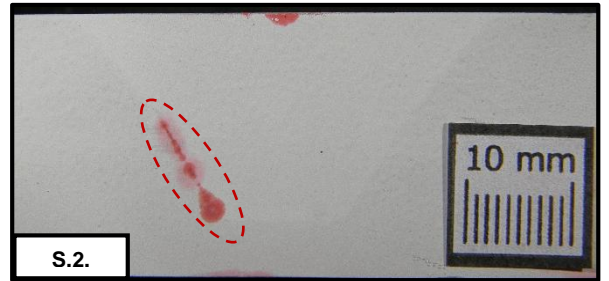
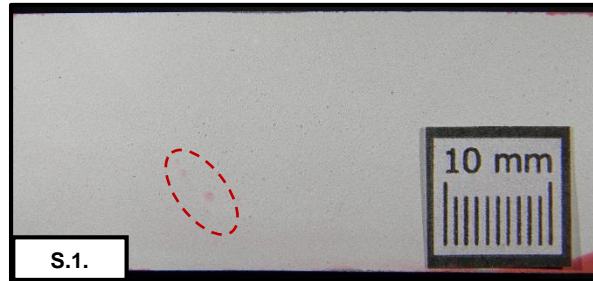


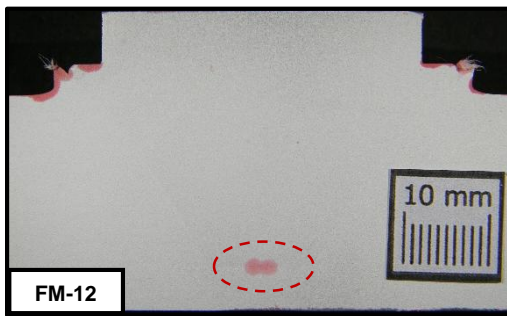
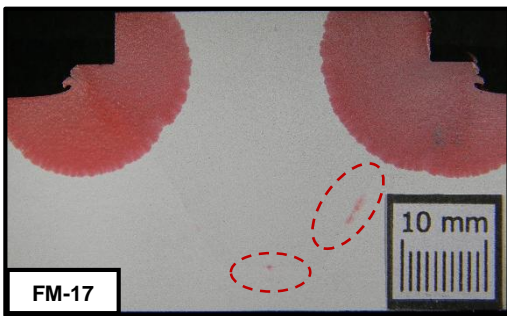
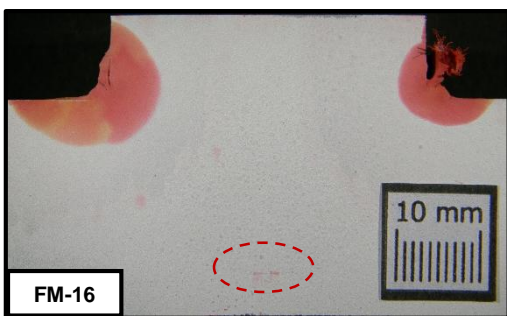
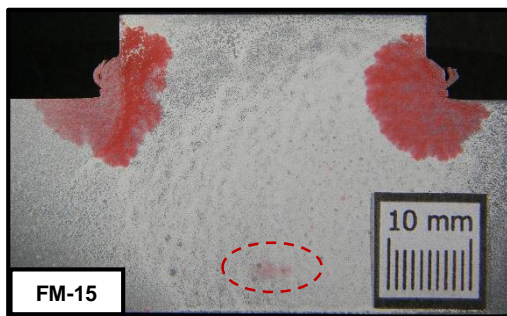
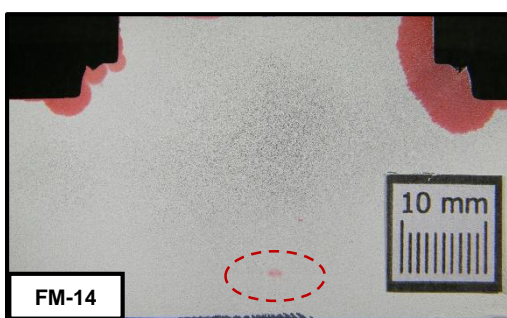
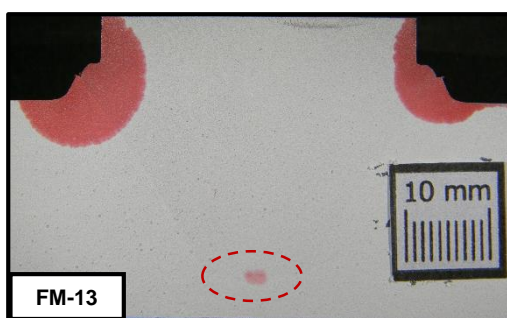
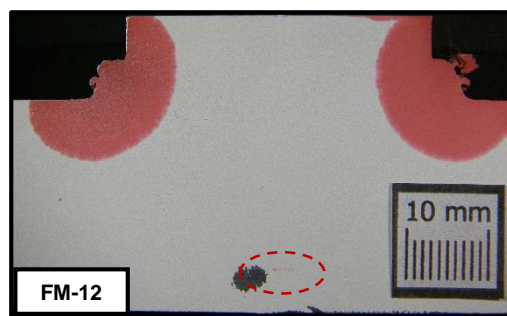
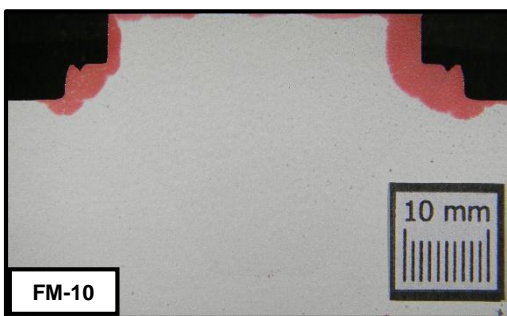
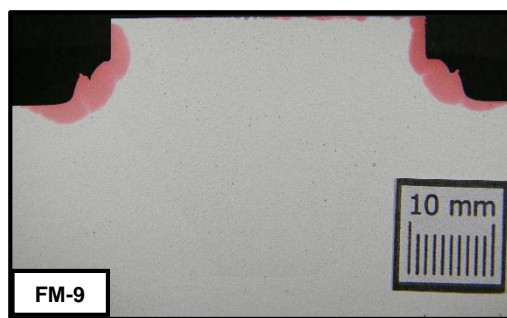
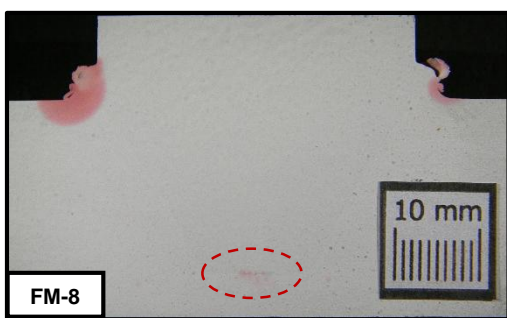




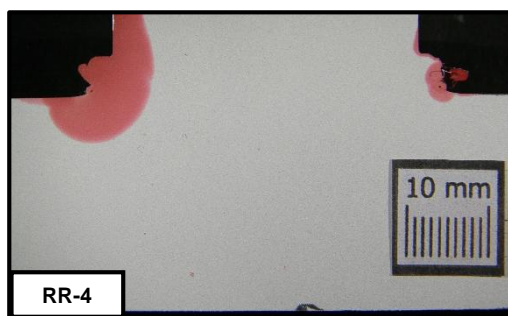
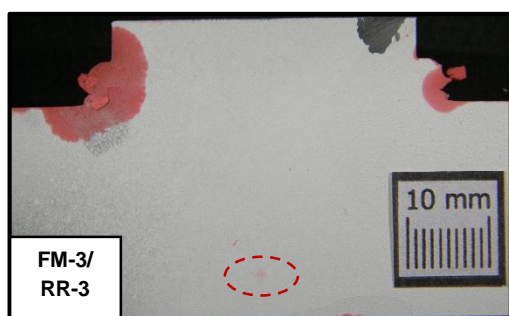
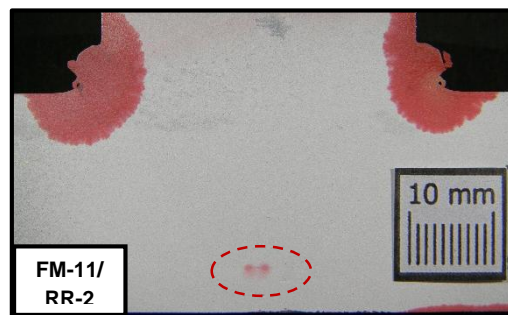
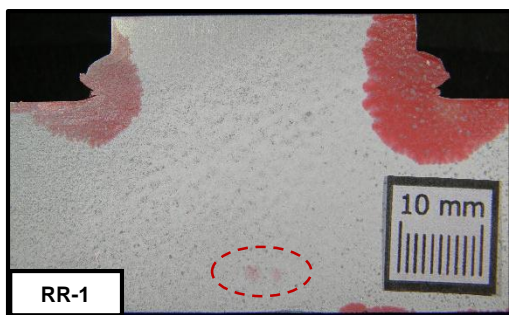
Appendix H

Dye Penetration Tests for 60° Hole Taper Angle Welds







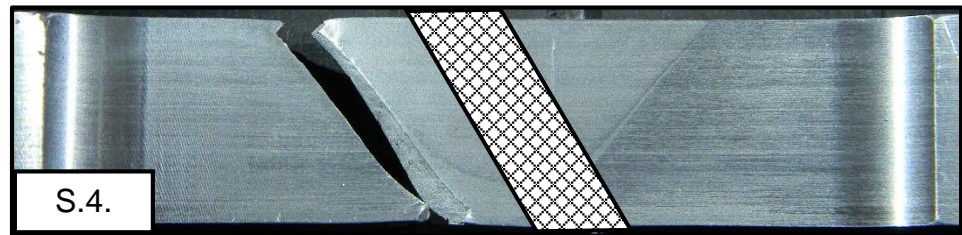
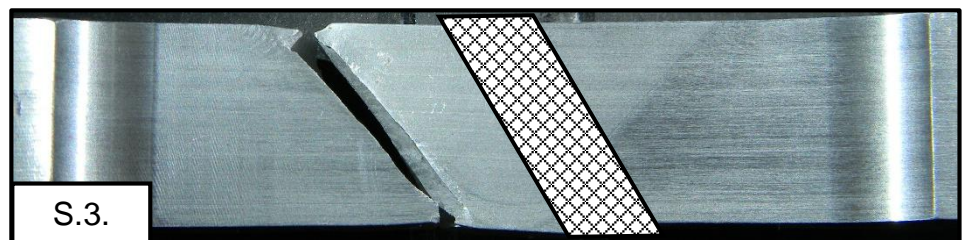
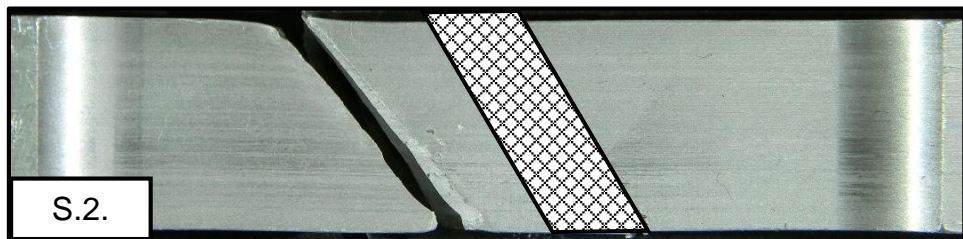
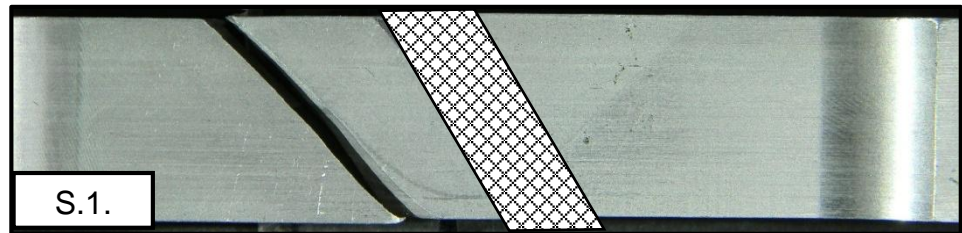


---

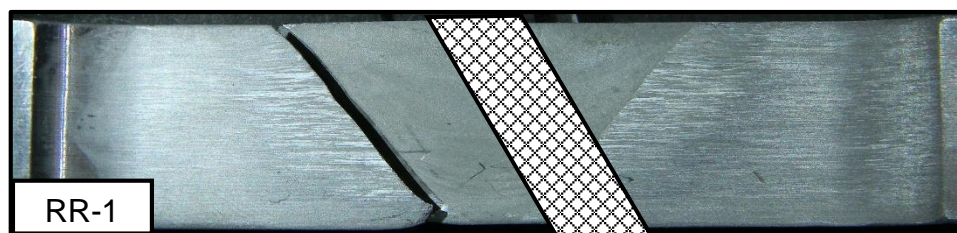
Appendix I

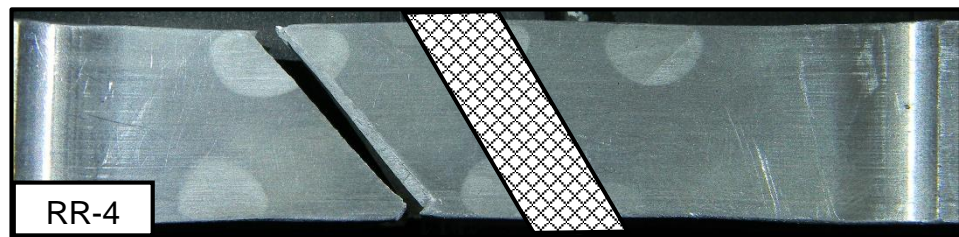
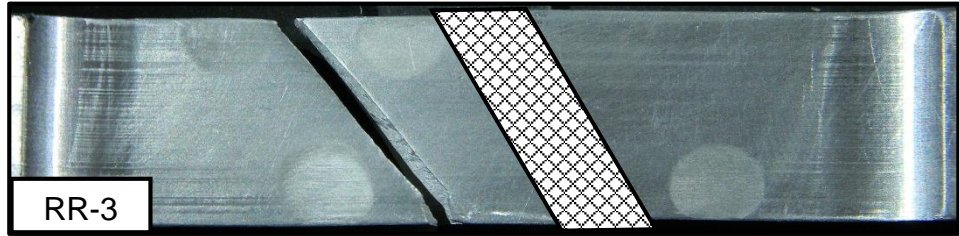
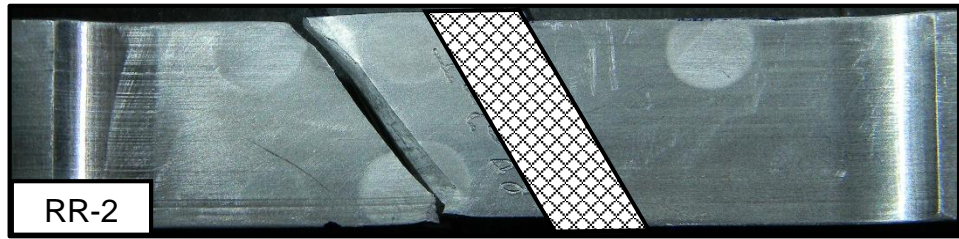
Tensile Test Fracture Modes

Welds S.1 to S.4

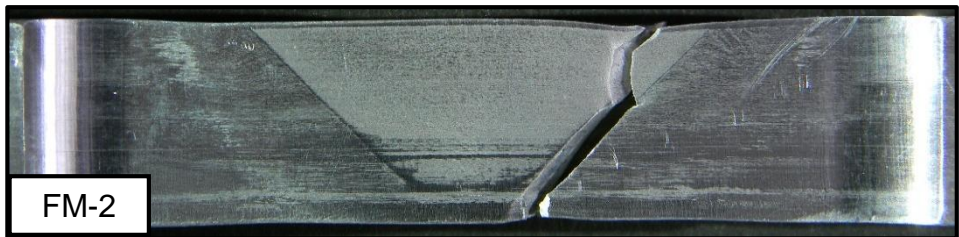


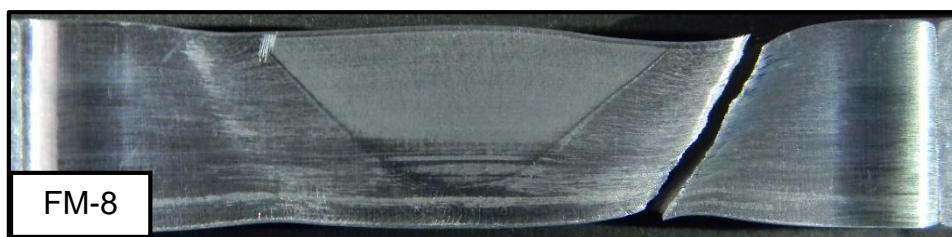
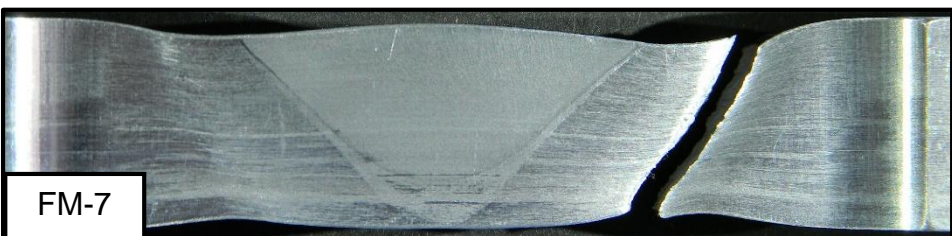
Welds RR-1 to RR-4 (Increasing Welding Force Ramp Rate)

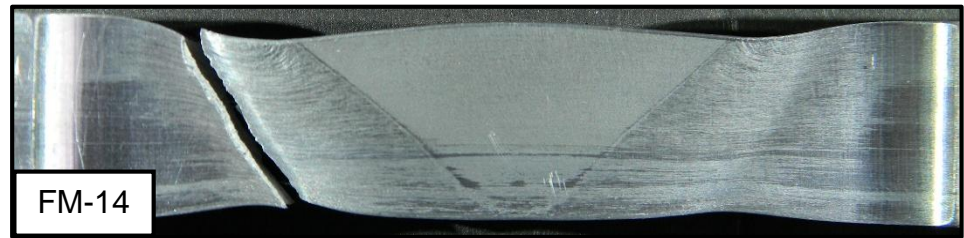




**Welds FM-1 to FM-20 (Final Weld Matrix)**

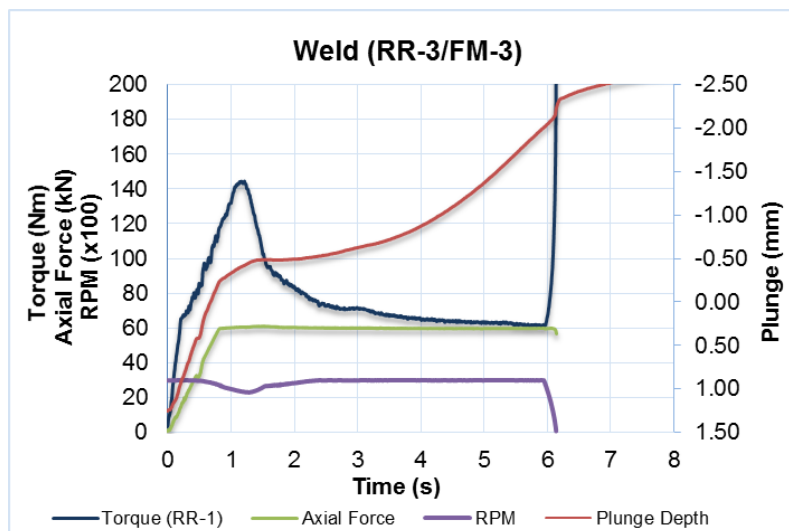
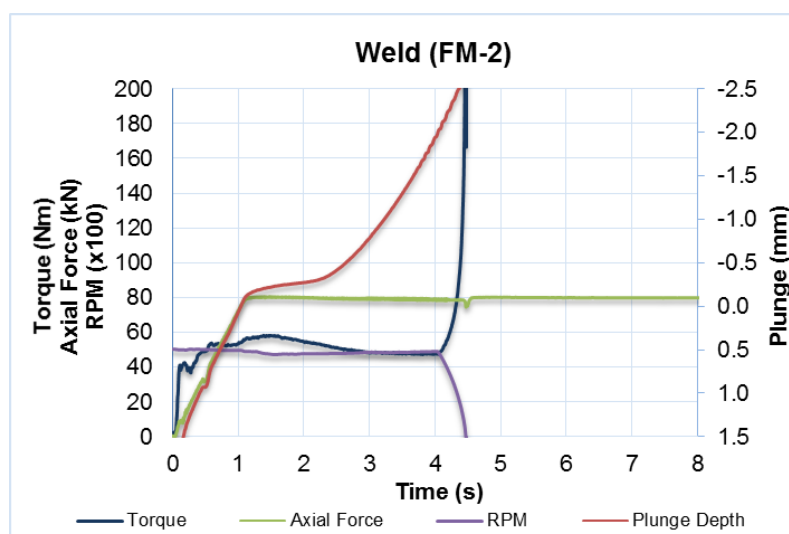
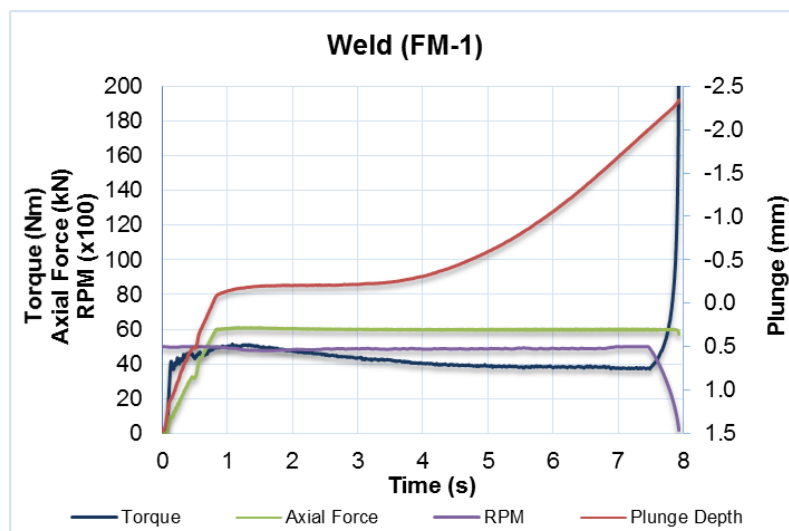


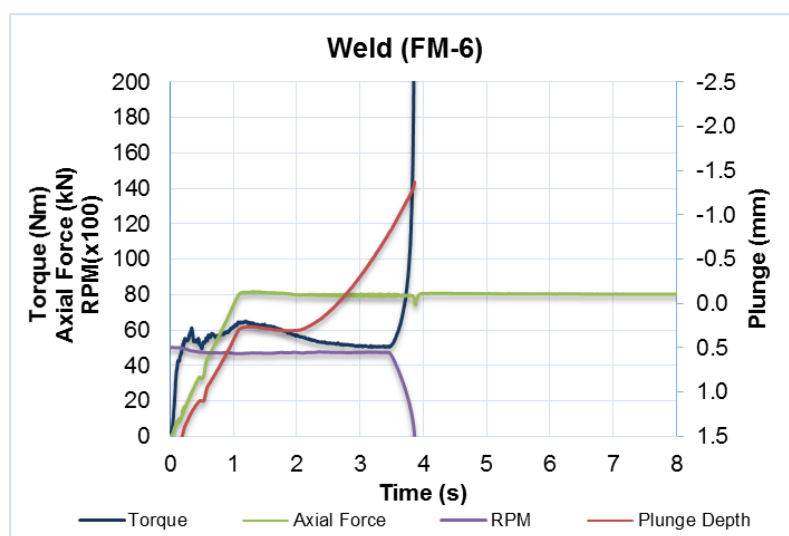
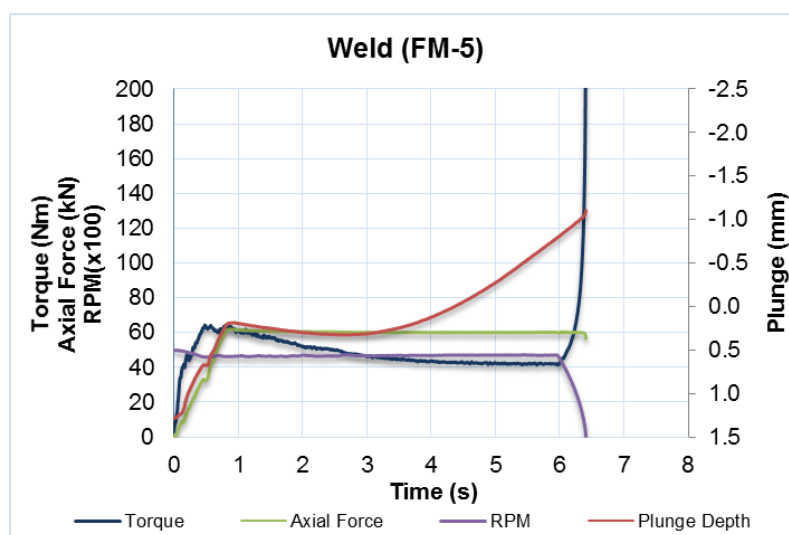
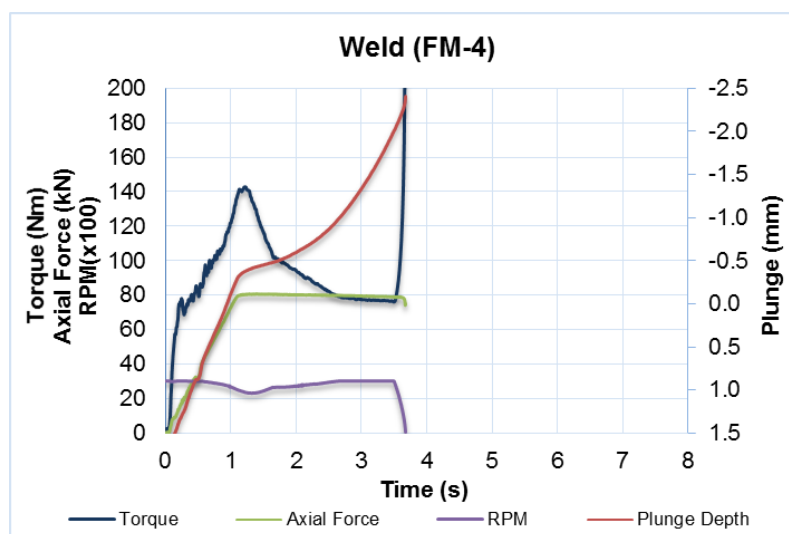


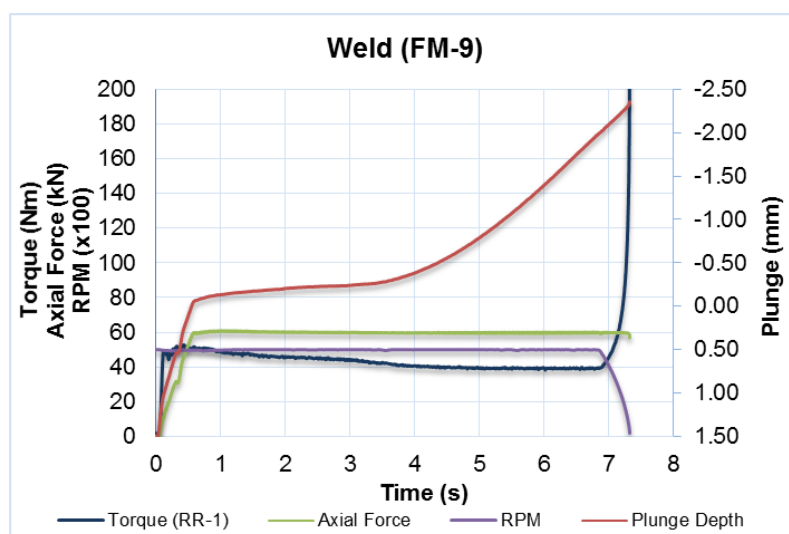
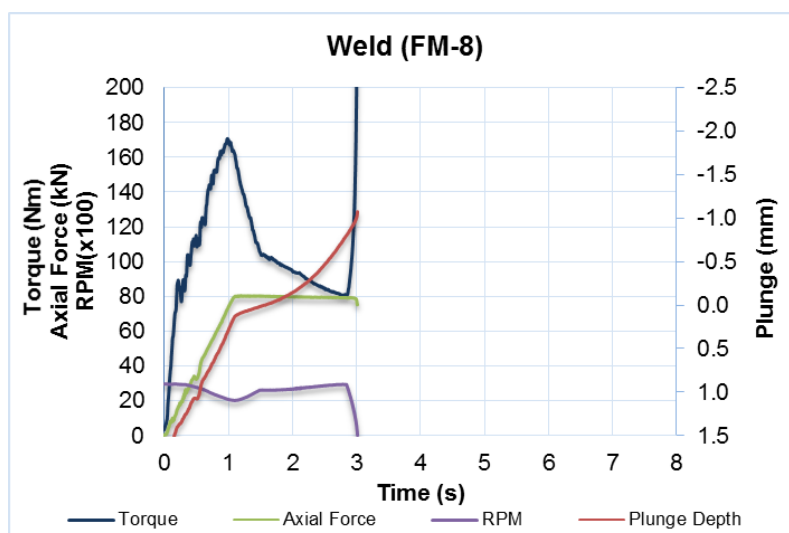
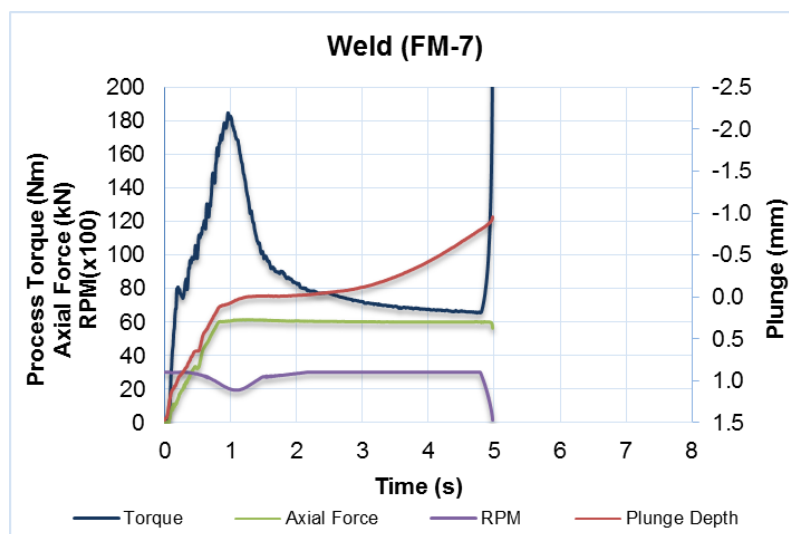


## Appendix J

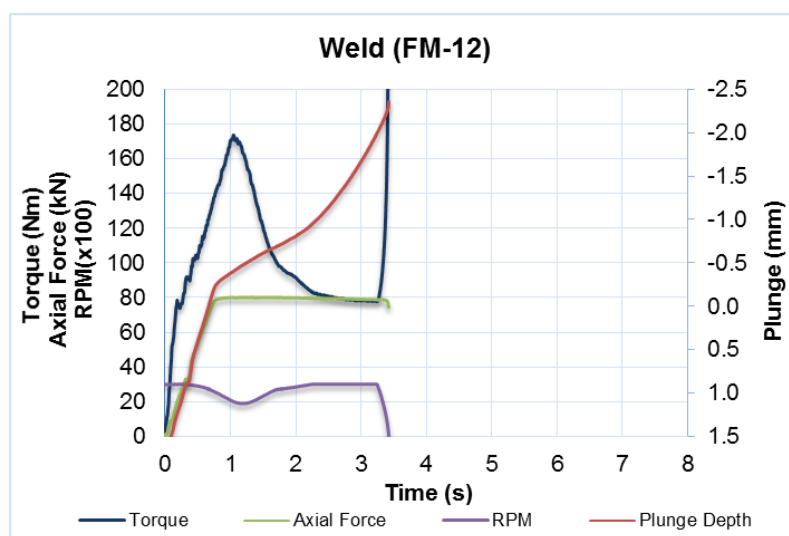
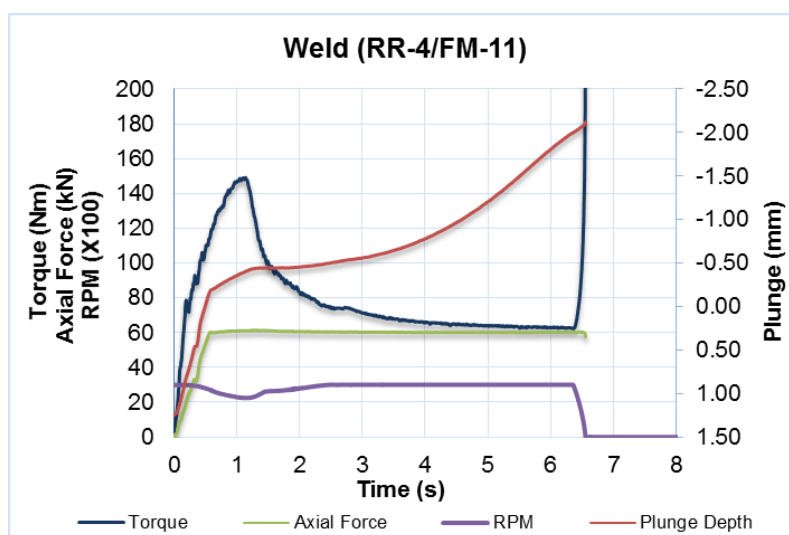
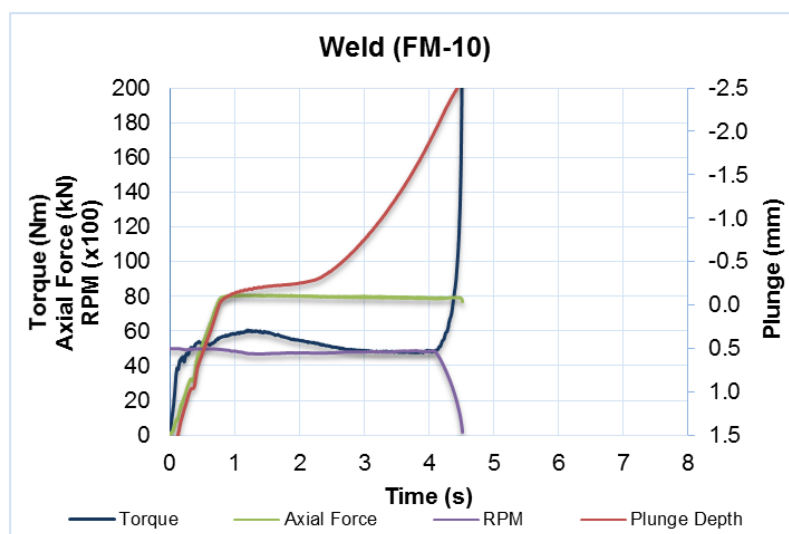
## Logged Process Data for Welds FM-1 to FM-16 and RR-1 to RR-4

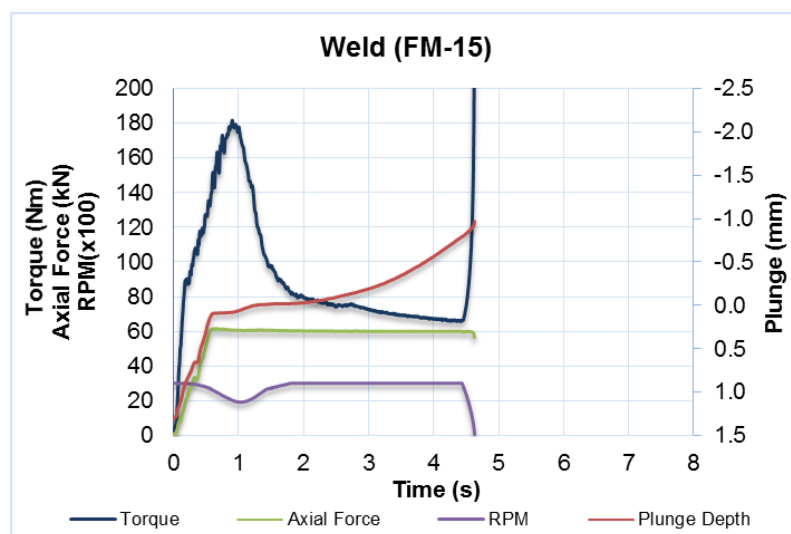
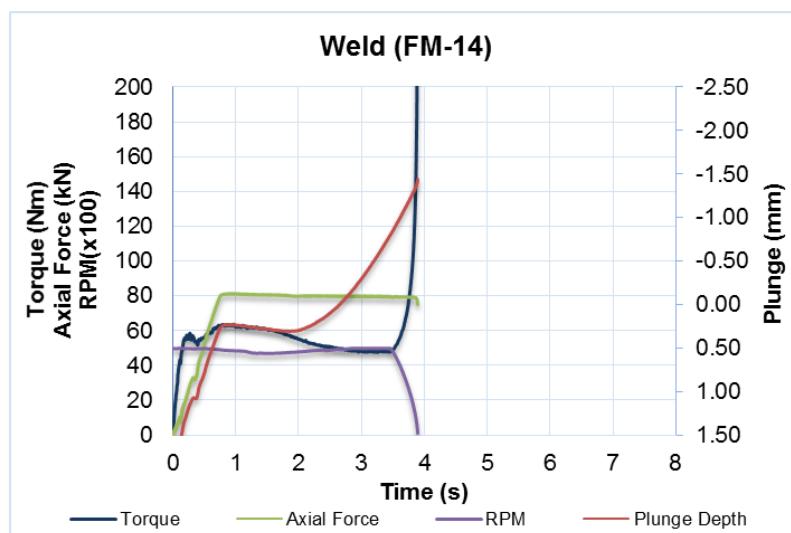
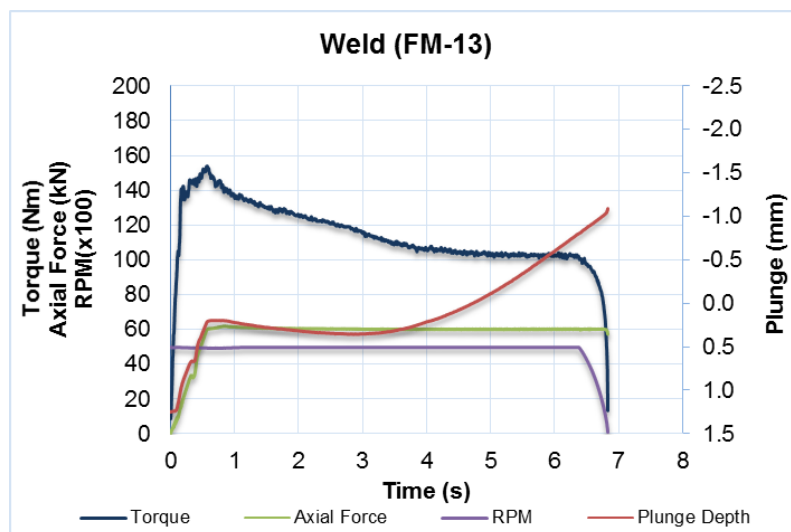


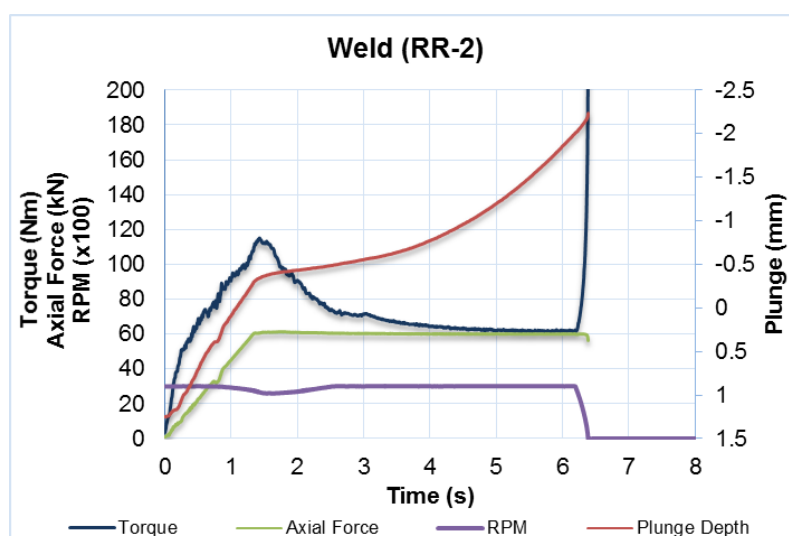
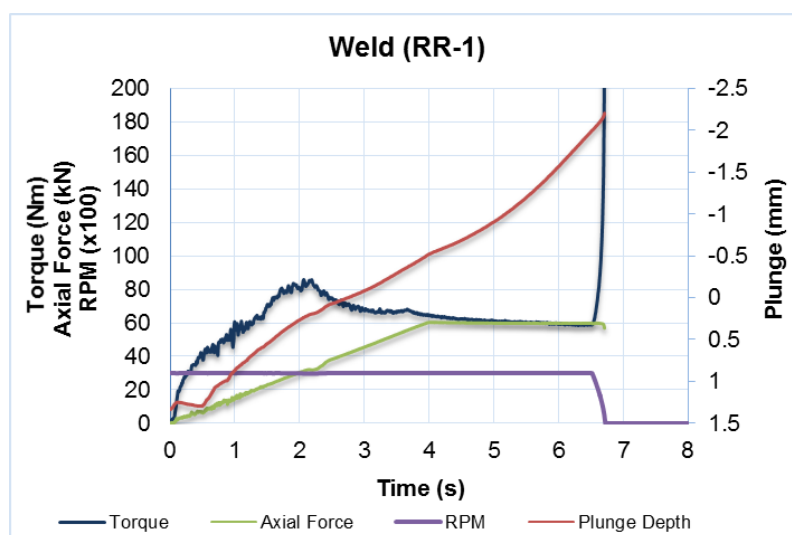
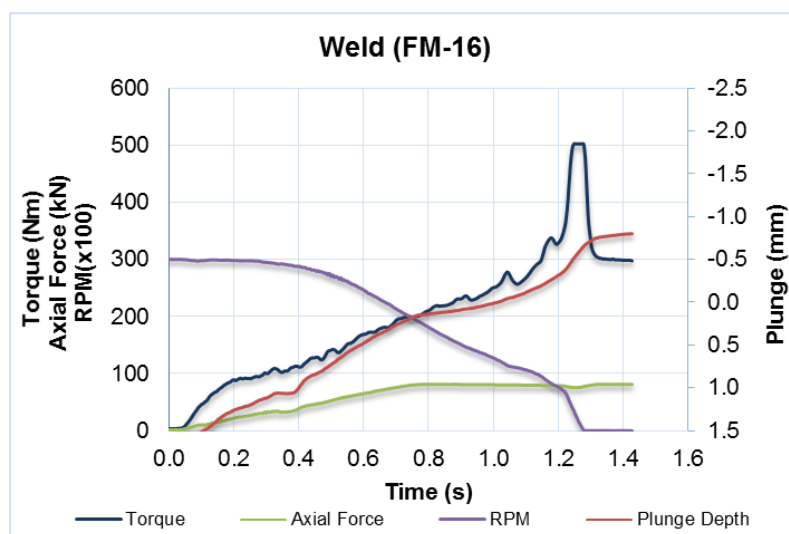


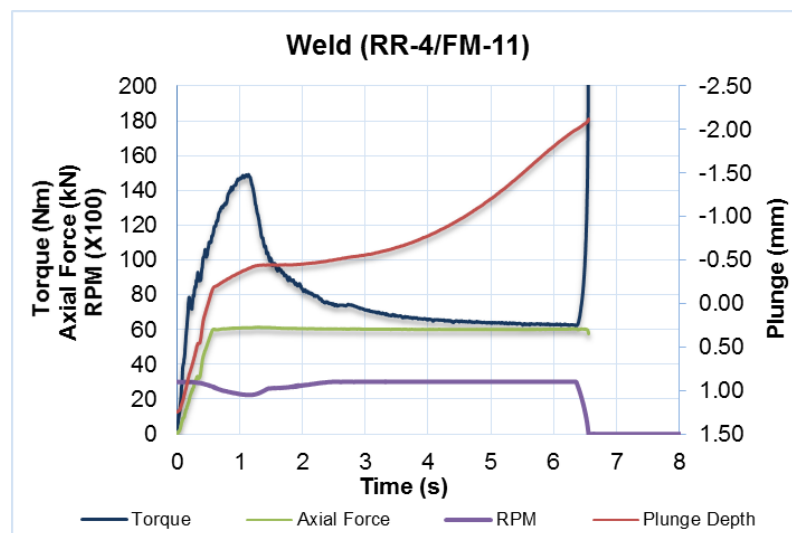
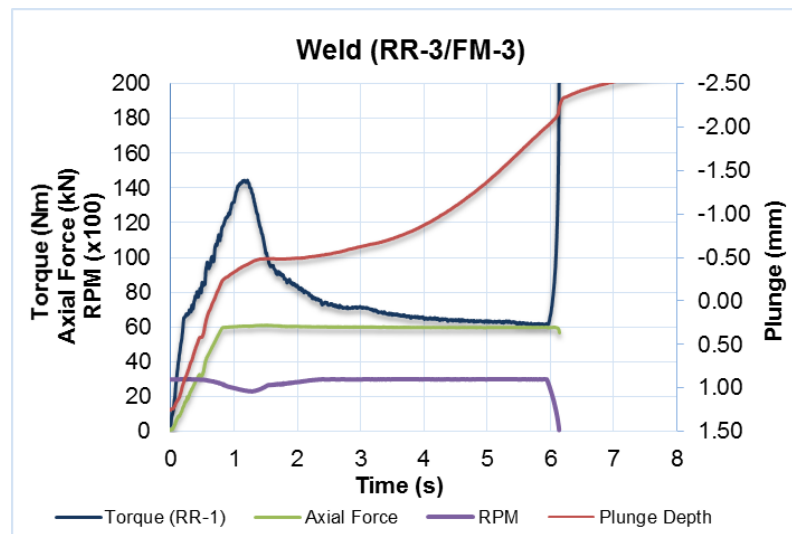






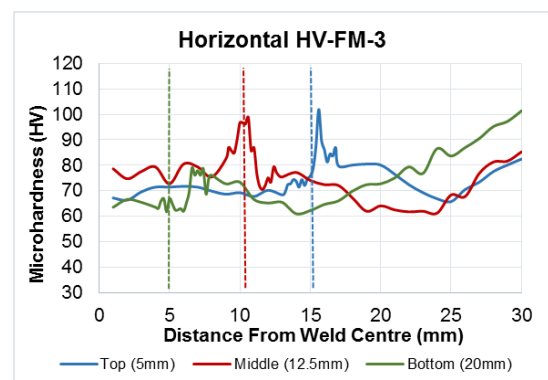
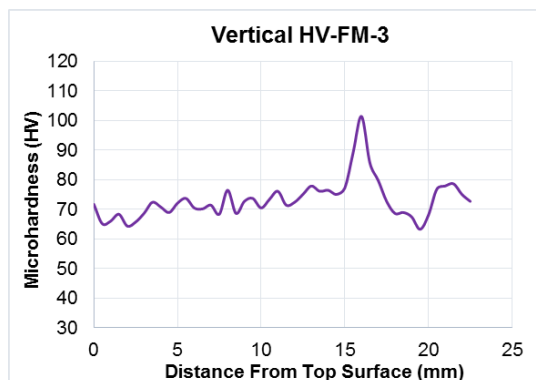
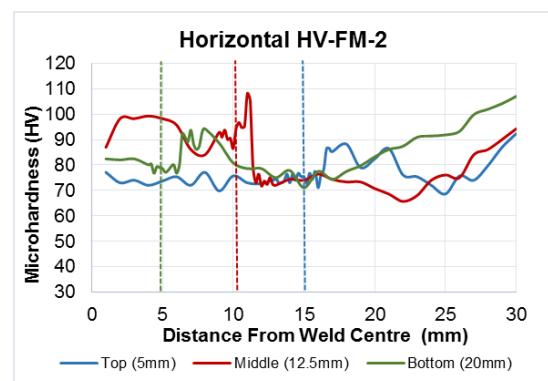
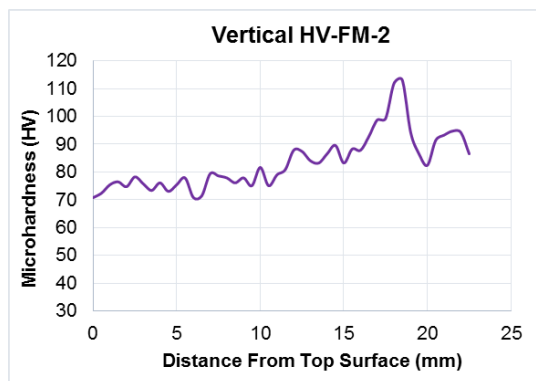
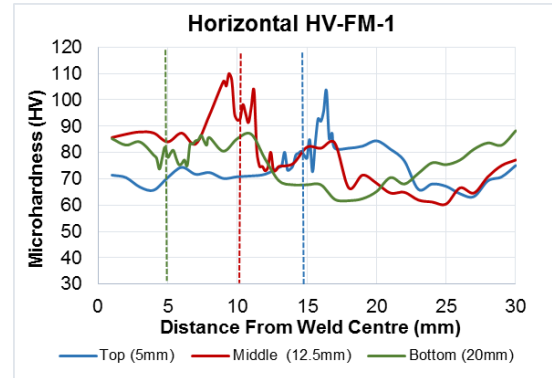
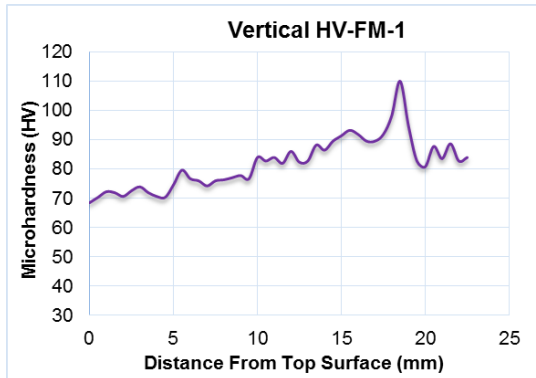


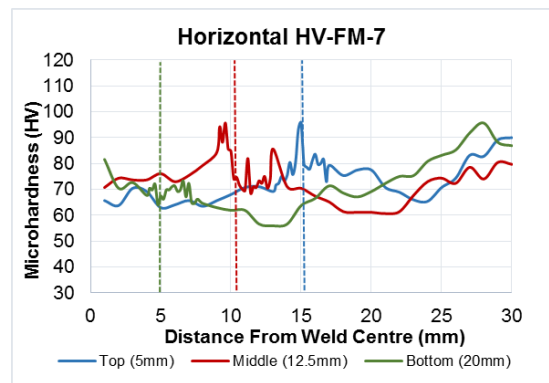
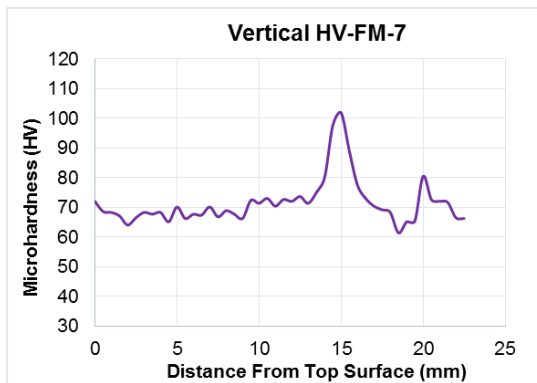
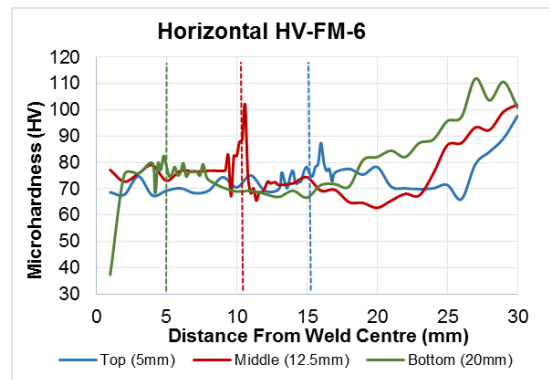
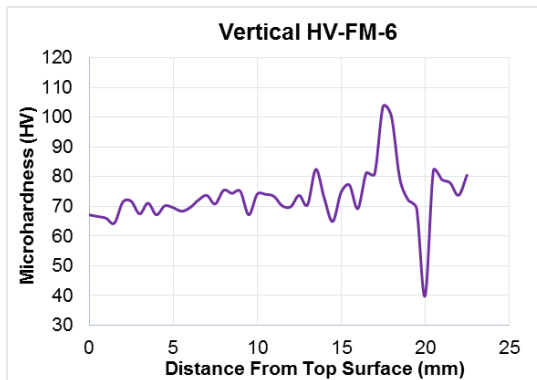
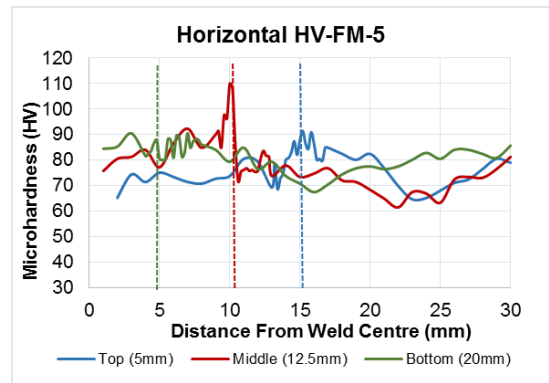
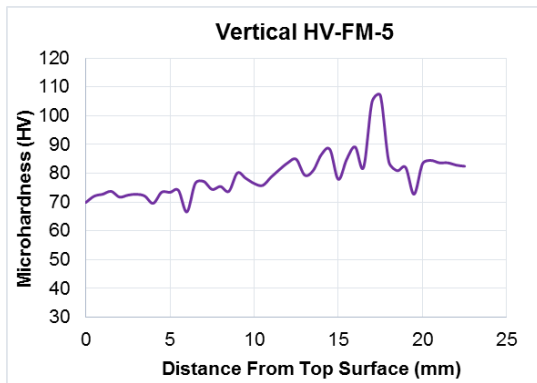
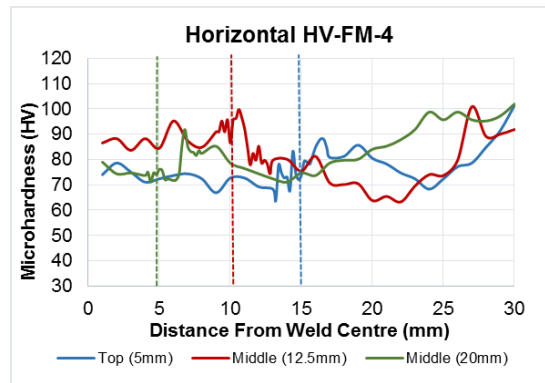
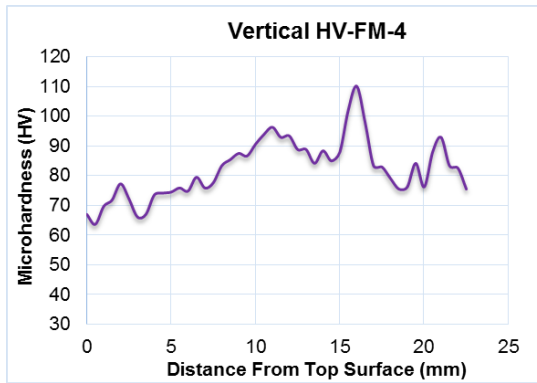


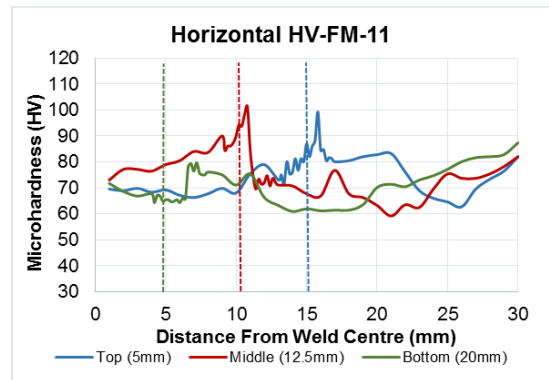
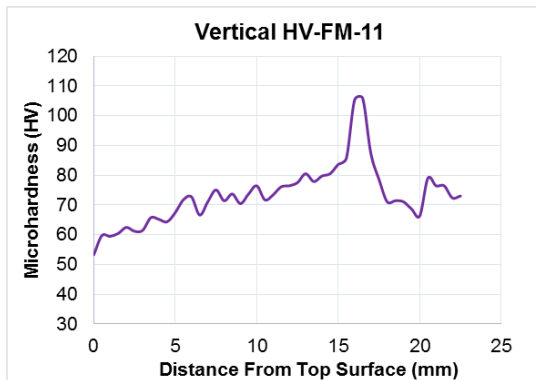
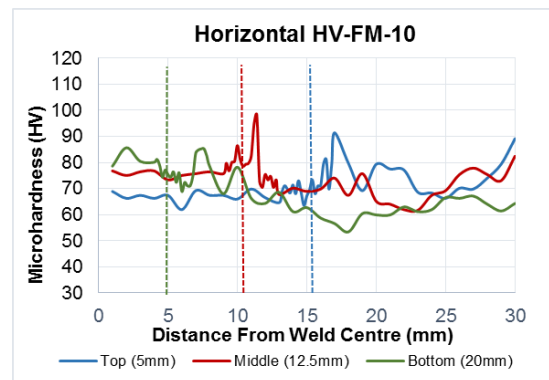
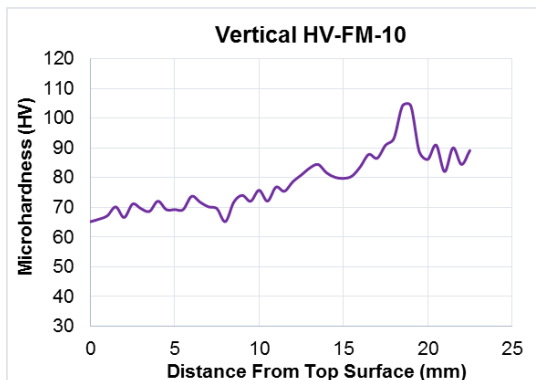
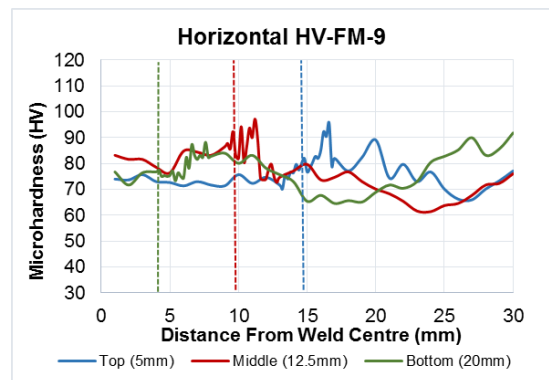
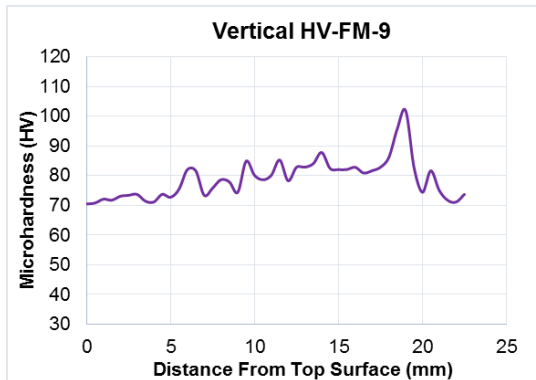
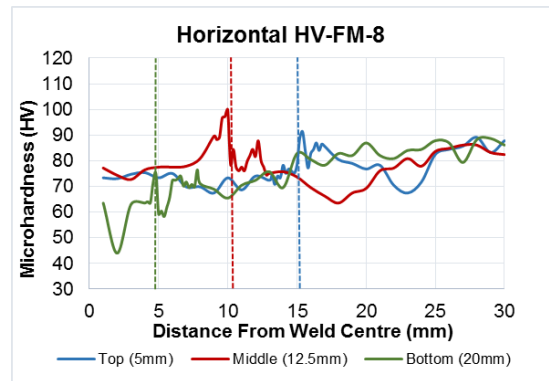
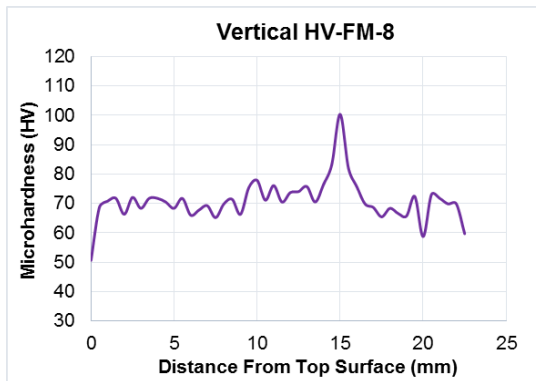


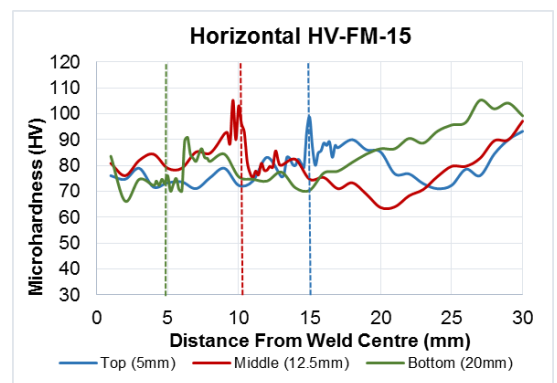
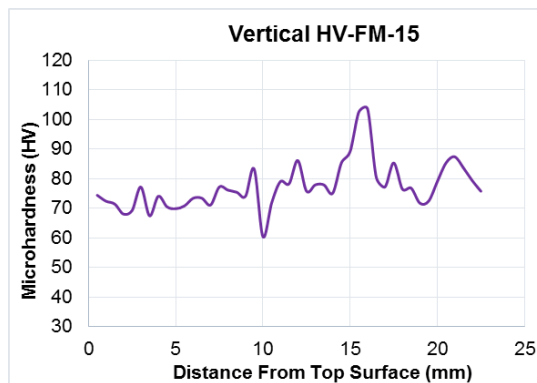
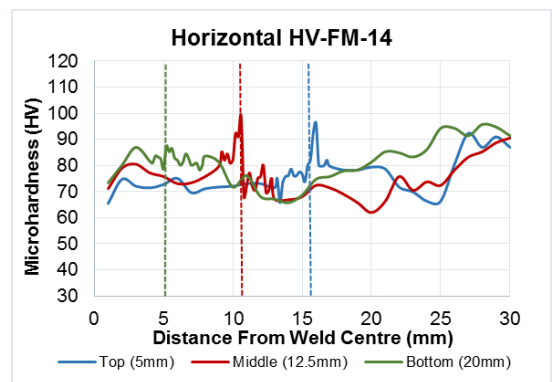
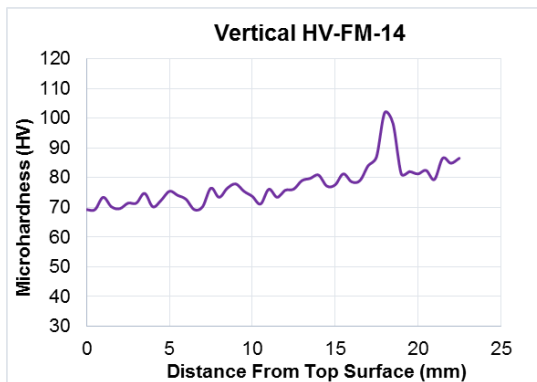
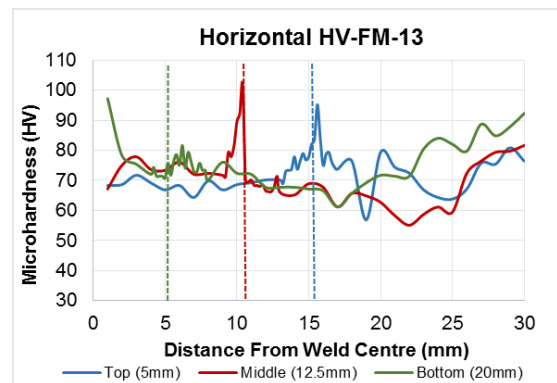
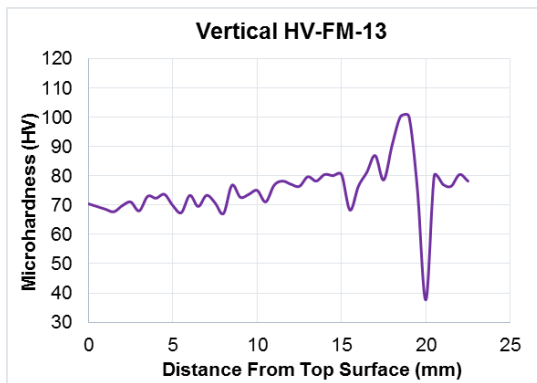
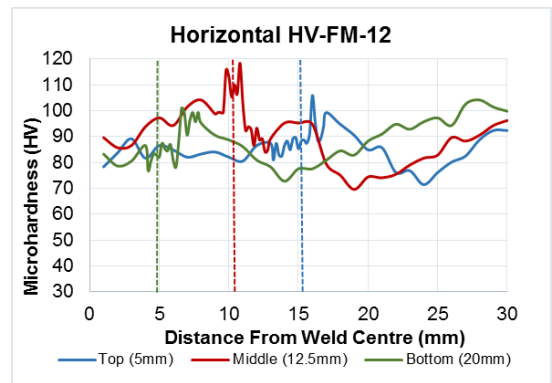
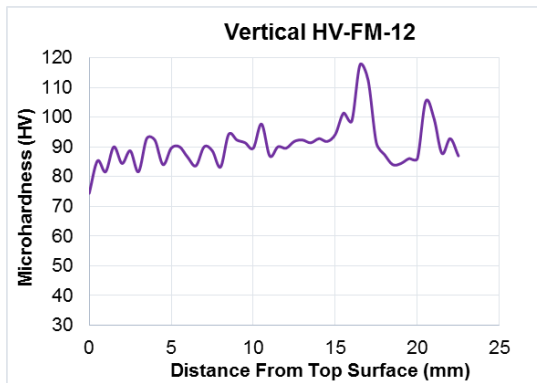
## Appendix K

## Vertical and Horizontal Microhardness Charts

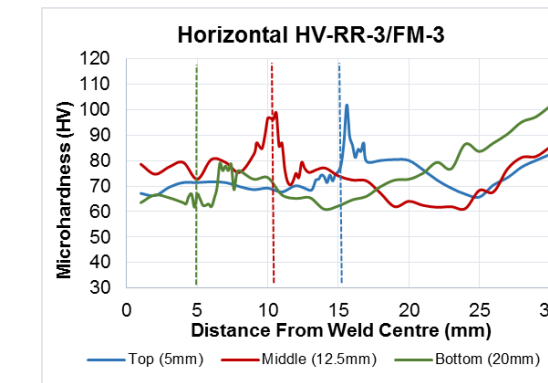
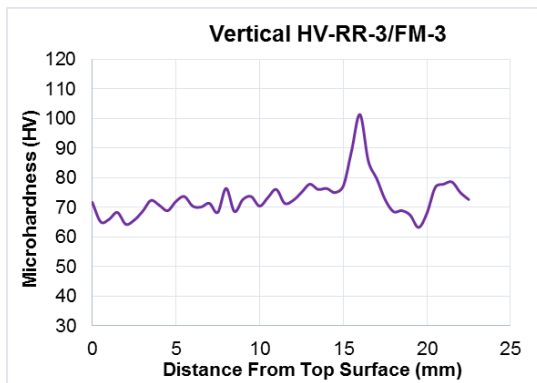
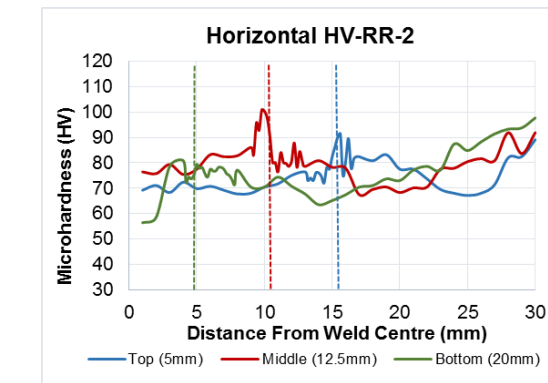
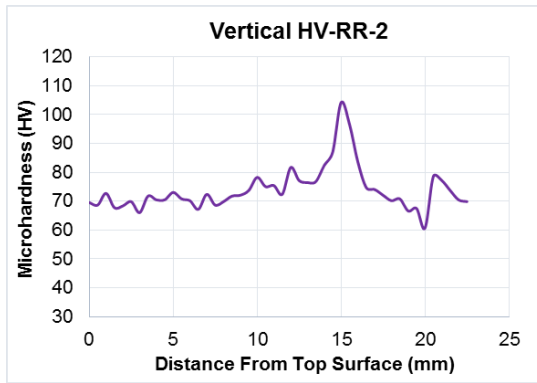
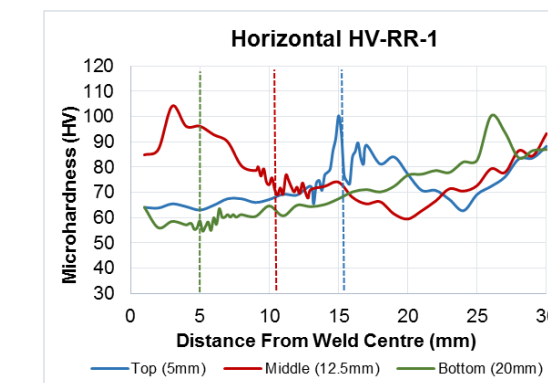
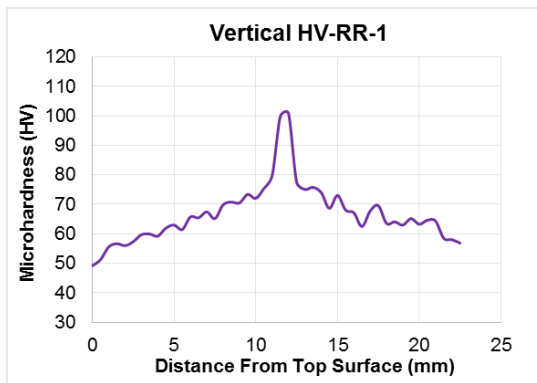
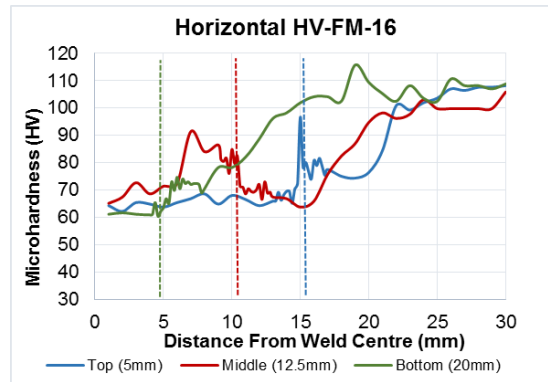
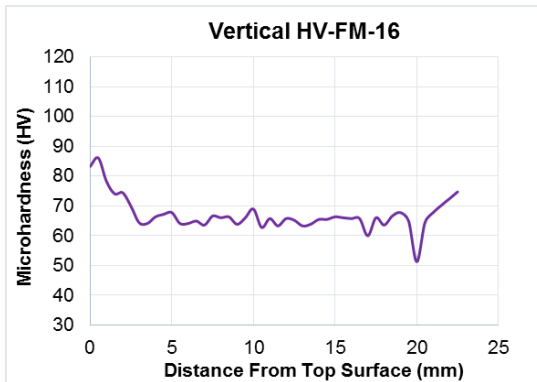


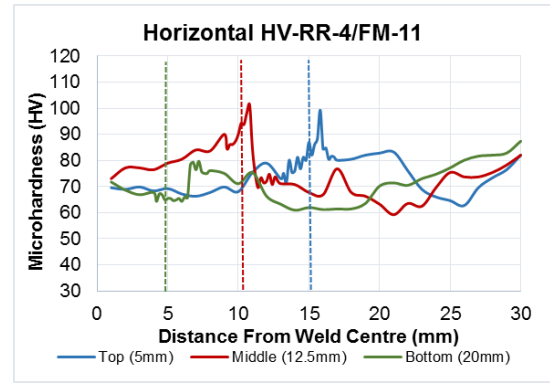
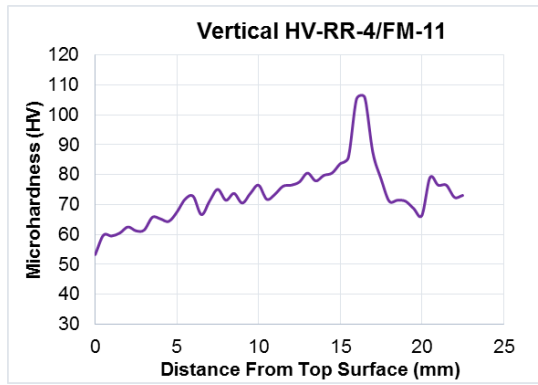






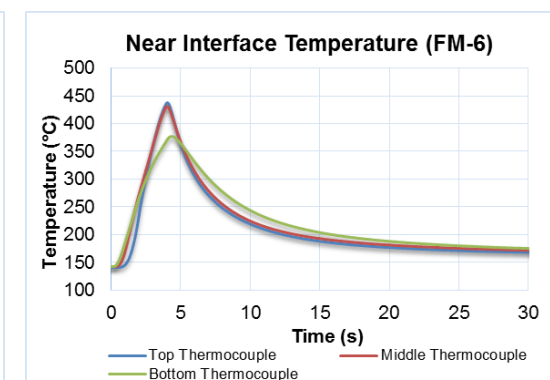
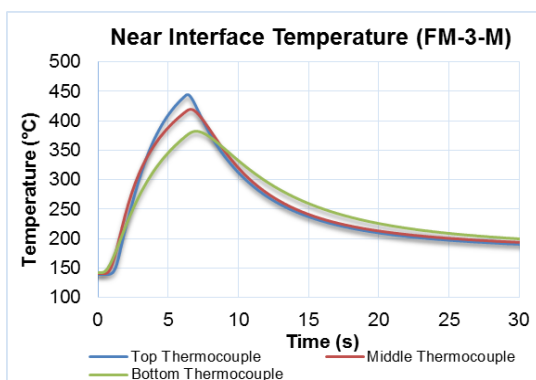
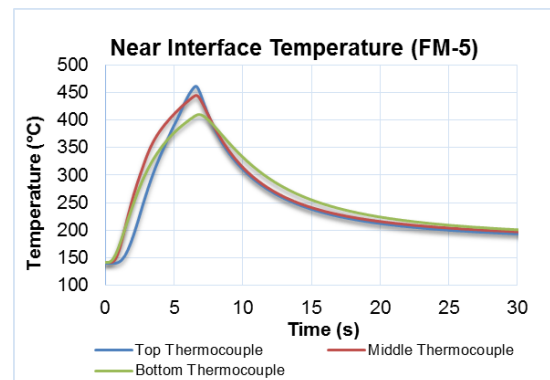
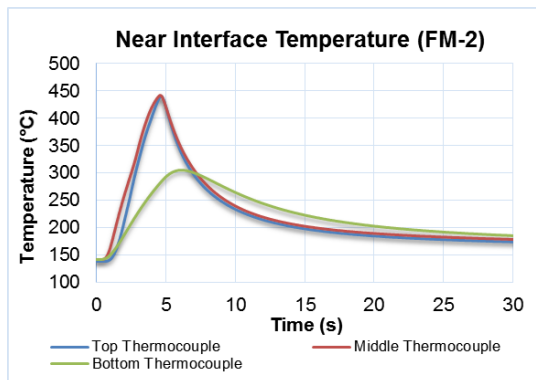
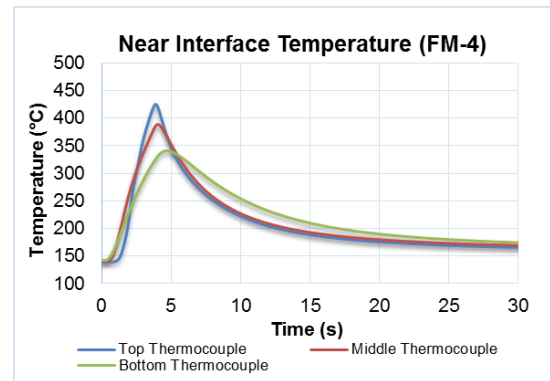
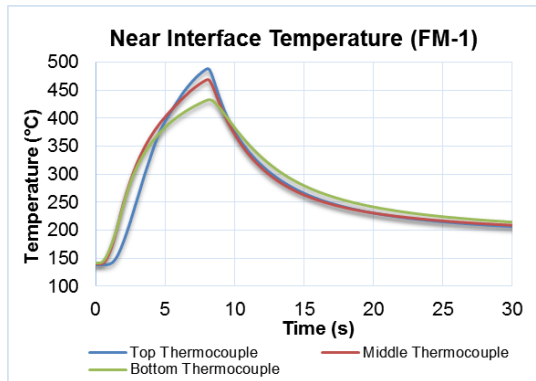


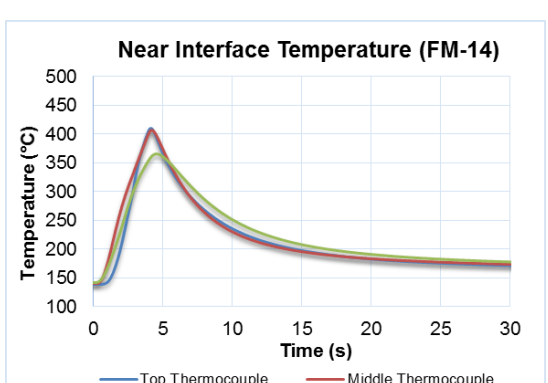
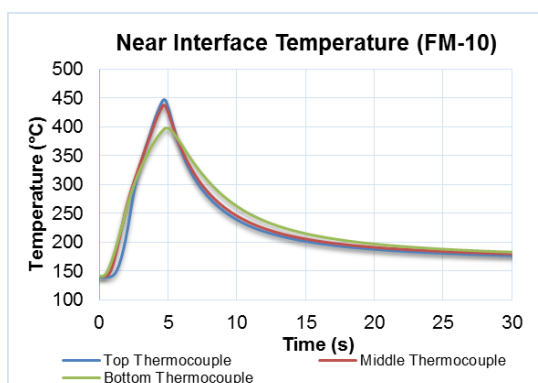
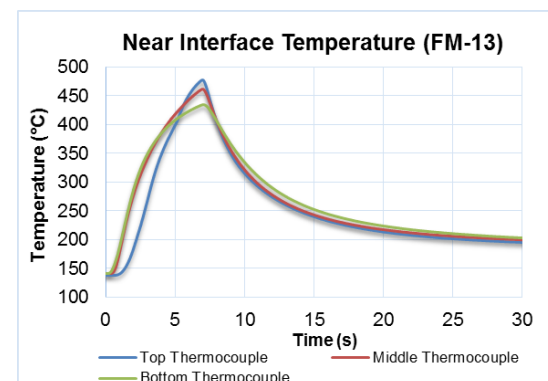
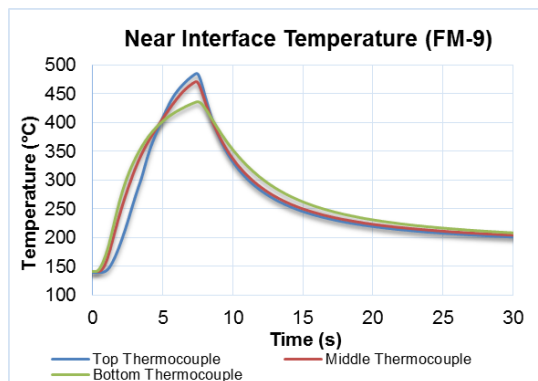
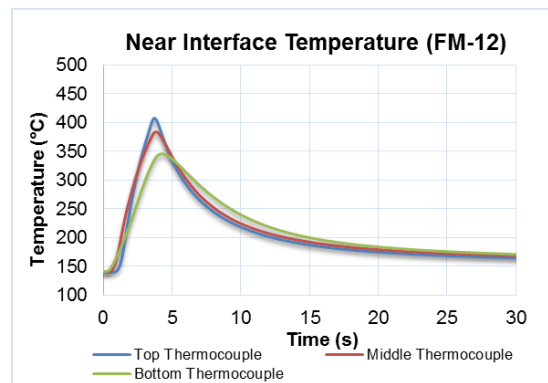
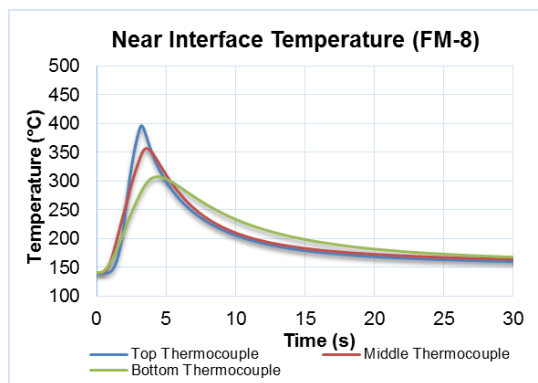
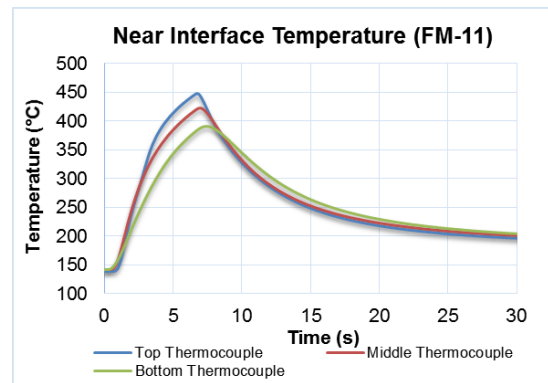
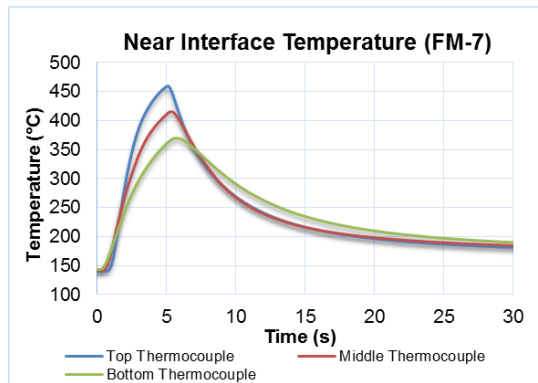


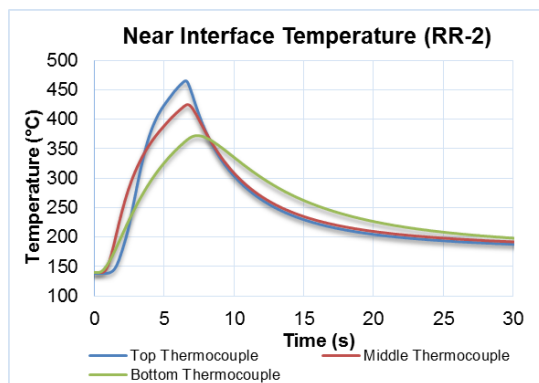
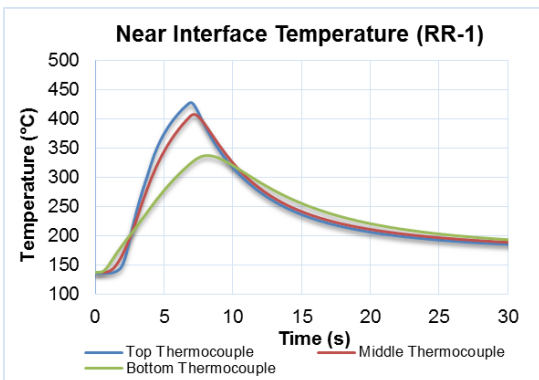
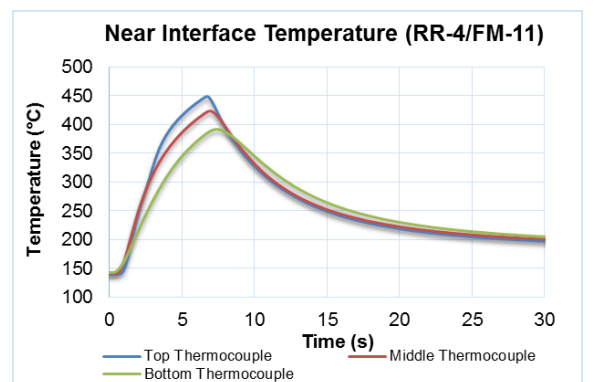
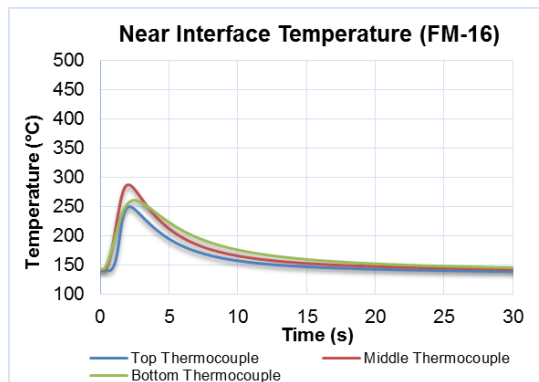
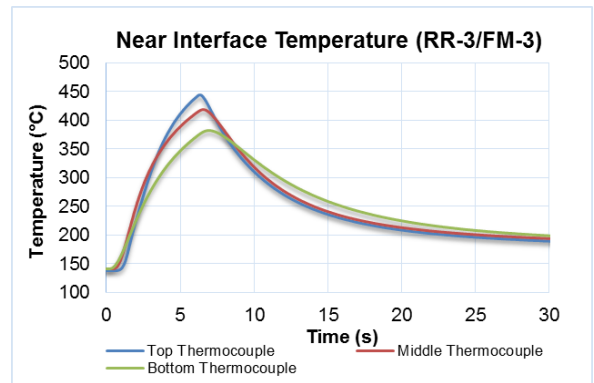
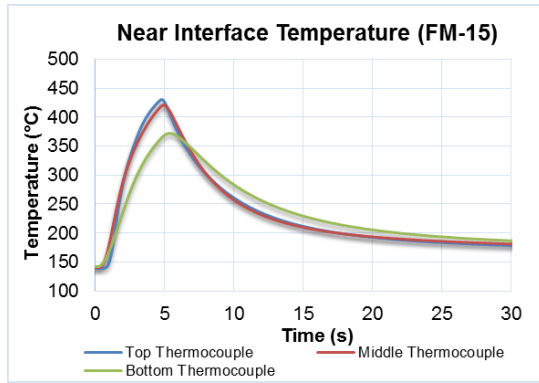


## Appendix L

## Near Interface Temperature Charts

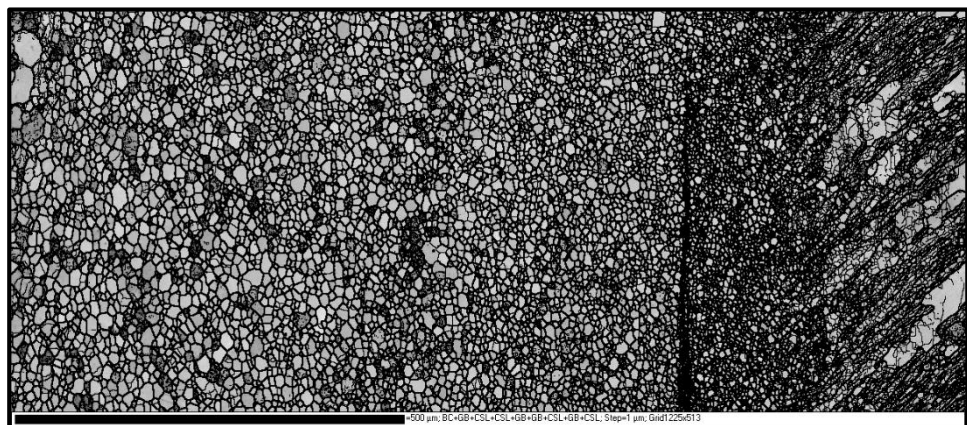
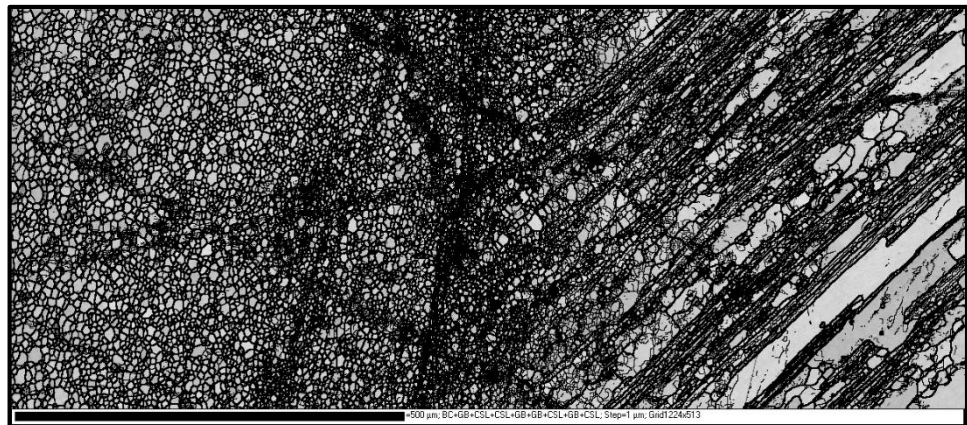
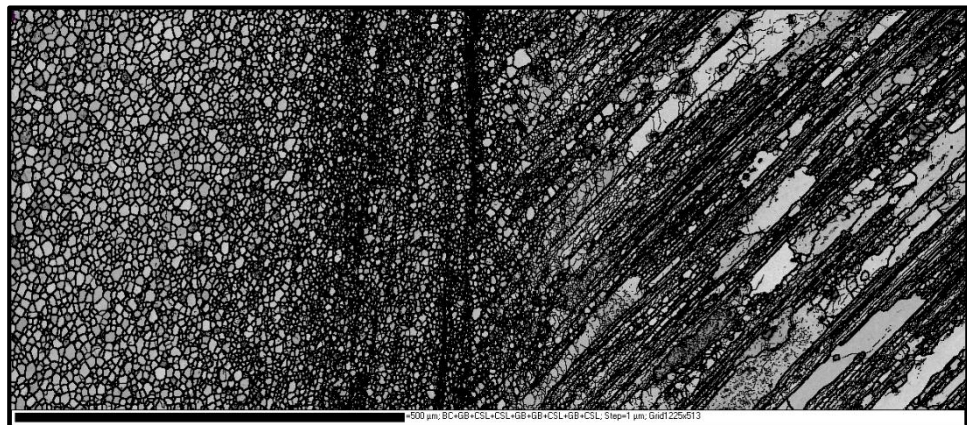
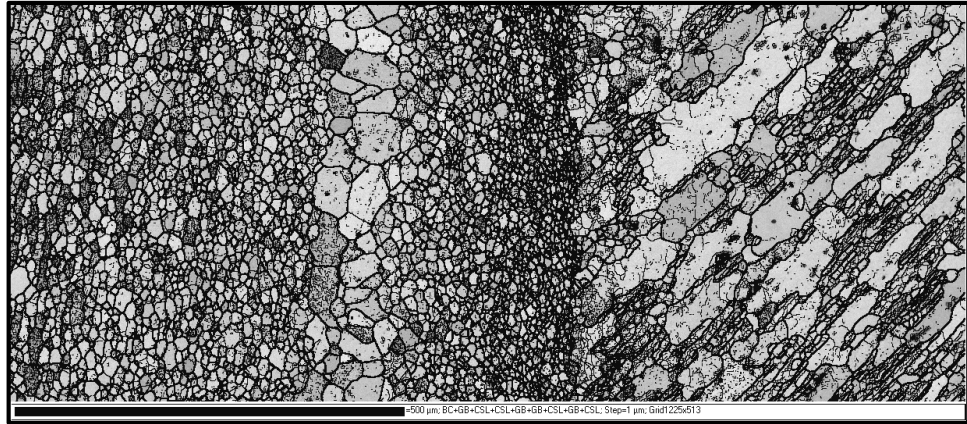




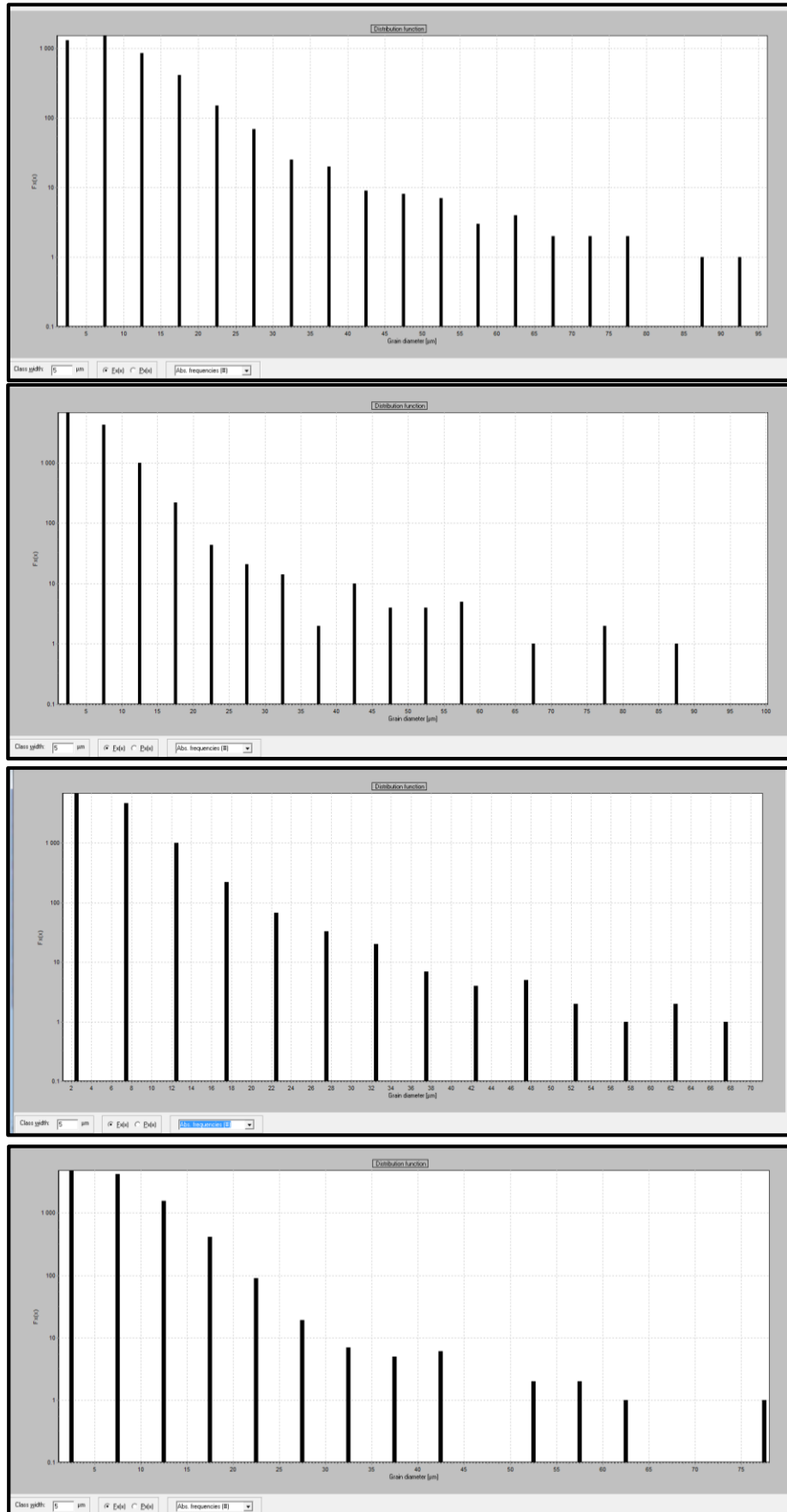


Appendix M

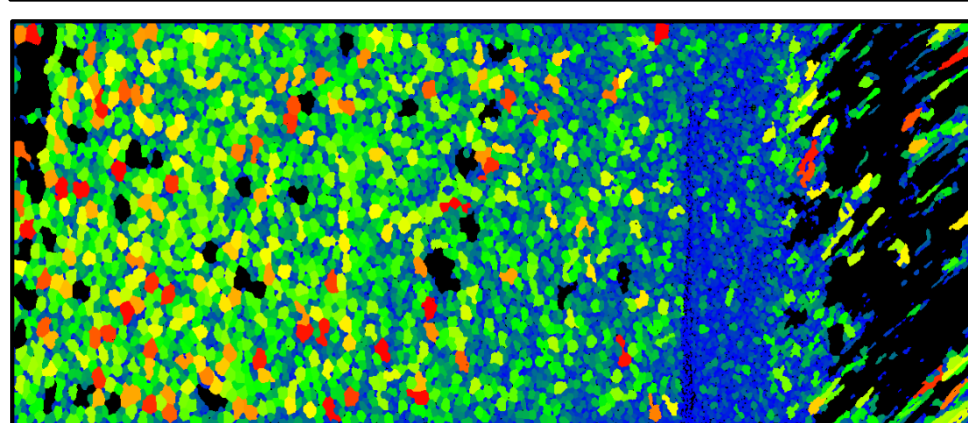
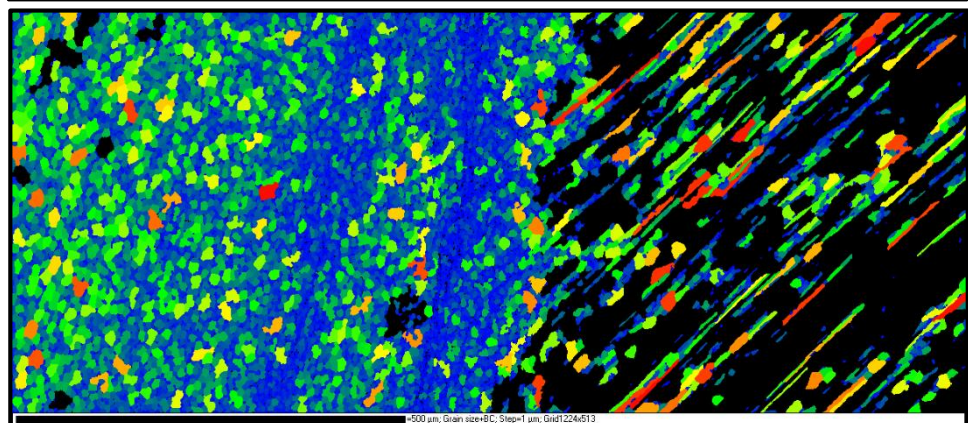
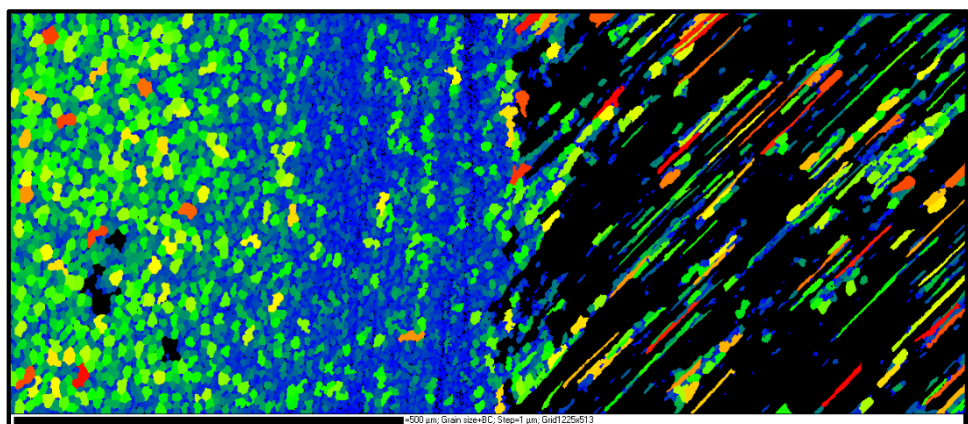
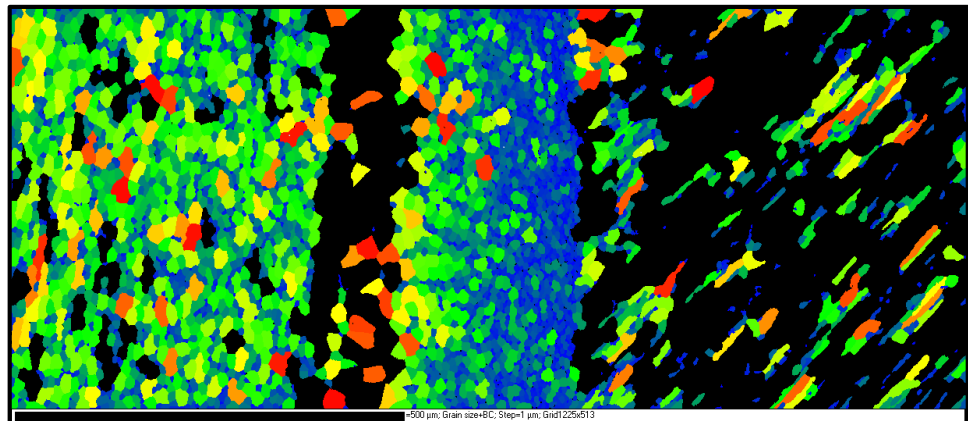
Band Contrast Maps of Welds S.1 to S.4



Grain Size Distribution Histograms of Welds S.1 to S.4

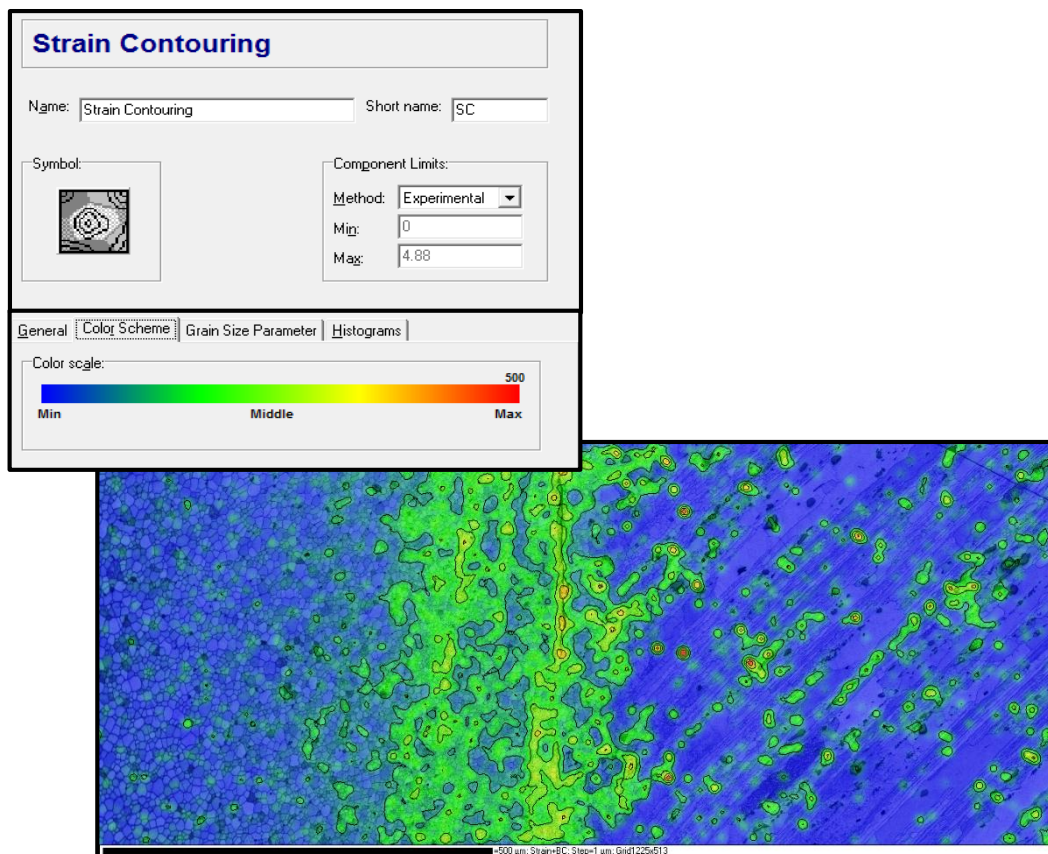
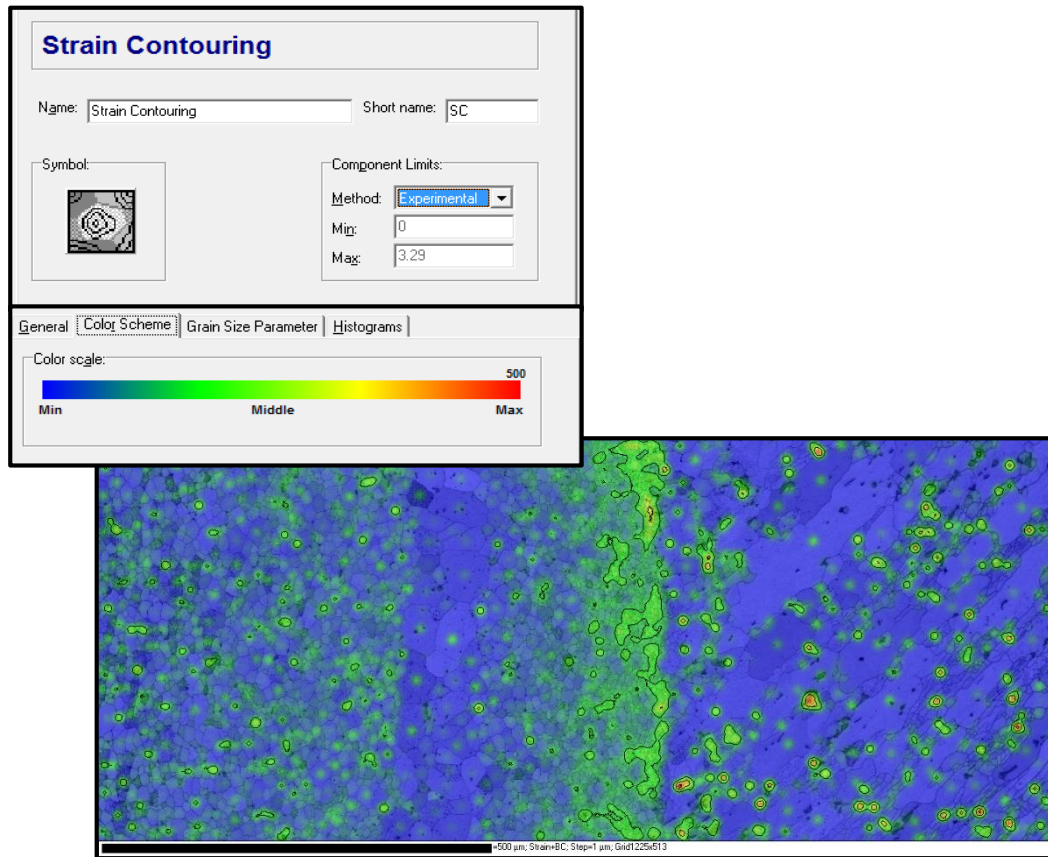


---

**Grain Size Distribution Maps of Welds S.1 to S.4**




## Residual Strain Maps of Welds S.1 to S.4 by EBSD



### Strain Contouring

Name:  Short name:

Symbol: 

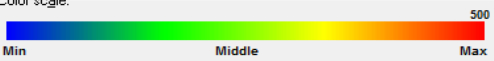
Component Limits:

Method:

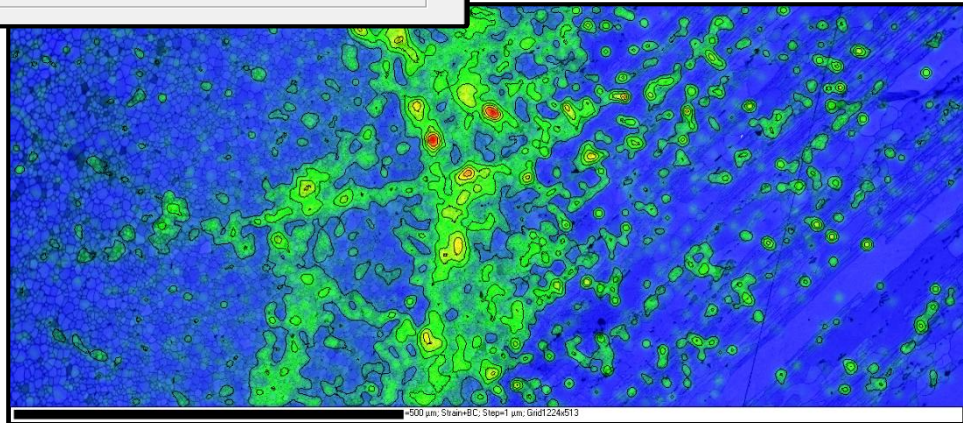
Min:

Max:

General | **Color Scheme** | Grain Size Parameter | Histograms


Color scale:  500

Min Middle Max



### Strain Contouring

Name:  Short name:

Symbol: 


Component Limits:

Method:

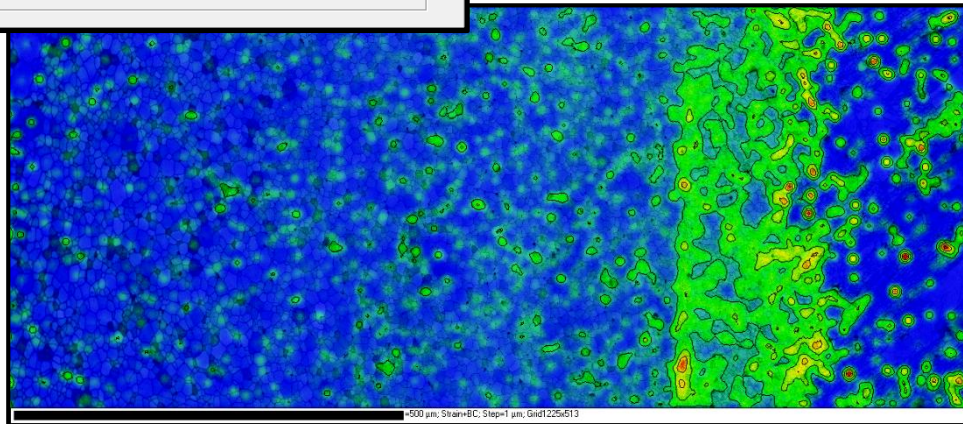
Min:

Max:

General | **Color Scheme** | Grain Size Parameter | Histograms

Color scale:  500

Min Middle Max



**Appendix N**

**Paper 1**

**D.A.G. Samuel**  
**Prof. D.G. Hattingh**  
**Prof. A. Els-Botes**

## **Characterization of Joint Integrity of Blind Friction Taper Stud Welds in the partially Supported Condition as applied to AA6082-T6**

### **Abstract**

In this study, blind tapered holes in 25mm thick AA6082-T6 plate were filled using a friction taper stud welding process. During welding, frictional torque and cycle time were recorded and used to calculate energy input into the weld. The results of these calculations showed the effect of process parameters on joint integrity with respect to input energy. Results of preliminary experiments are presented that were used for the development of a geometry process window for friction taper stud welds in aluminium alloys.

The interaction between changes in downward force and geometry were related to process energy and bonding. Process energy directly influenced weld interface bonding between the base of the hole and stud as well as side wall bonding. Experimental results showed that no good welds were achieved at low total energy input levels. Preheat was shown to increase the input energy up to the point of seizure and improve hole base diameter bonding. Hole taper angles of 60° gave good sidewall bonding when combined with the correct input process energy, achieving good sidewall bonding without the need for preheat.

## **1. Introduction**

As aluminium is used increasingly in manufacturing applications, greater demands are set on the material and weld repair procedures. This increases the need to produce high integrity, defect tolerant welds in aluminium alloys. Friction taper stud welding (FTSW) of aluminium is therefore under development as an alternative joining technique for partially supported components and more specifically, repairs on gas pipelines and filling of blind holes. Due to lack of expertise and limited published data on the topic of blind FTSW on aluminium, parameters to establish a preliminary process window for blind FTSW in AA6082-T6 had to be determined. The initial focus of the project was to determine a preliminary process window which focussed on hole and tool geometry and downward force in the partially supported welding condition.

Paula J Hartley [1] reviewed the use of through type friction taper stud welding on aluminium as used by Lockheed Martin Space systems as a defect repair procedure. The report stated a 20% strength improvement over TIG welding with improved fracture toughness [1]. K Beamish [2] researched through type friction taper stud welding of 10mm AA6082-T6. She noted the lack of literature on the topic in the public domain and attributes this to the slow uptake of the process. She investigated the effects of downward force, rotational speed, plunge depth and geometry on weld quality, with taper angles of 60° and 90° achieving 90° in a bend test. Further she found that peripheral velocity had a greater influence on weld quality than rotational speed. She documented that high downward force caused the weld interface to move up more rapidly and that excessive force induced deformation of the plug above the weld and lower surface flash [2]. Insufficient force was shown to produce a lack of bonding at the lower surface of the plate and upper surface flash [2, 6].

Mahoney et al [3] presented a method to repair voids in aluminium alloys using FTSW. The included angle of the tapered hole was 60° with 72 ridges per inch machined into the surface of the hole. In order to overcome premature shearing of the stud due to aluminium's low strength at elevated temperatures, they introduced a heat sink as part of the stud. In the study the stud was found to be thoroughly bonded to the hole and the weld nugget consisted of fine recrystallized material. The problem of poor bonding in the lower region of the weld due to reduced plasticization was overcome by using a backing plate with part of the tapered hole machined into it. This region was then machined away, leaving the fully bonded region intact.

## **1.1 Geometry Configurations**

The following summarises the hole and stud configurations known to make successful FTS welds.

Van Zyl [4] using Chromium-Molybdenum steel (10CrMo910) made blind FTSW welds using a stud and hole included angle of 15° and 20° respectively to fill a 25mm deep hole in his research on modelling of heat distribution during FTSW. Hatting et al [5] using AISI 709M40 (EN 19) made successful blind FTSW welding using the same stud and hole included angles as Van Zyl [4].

Pinheiro [6] made blind FTS welds in AZ91D – T6 Magnesium using hole included angles of 10° - 20° with base diameter combinations of 6mm and 8mm. He used a stud included angle of 10°, with hole base diameter combinations of 6mm and 8mm.

Beamish [2] made through type FTS welds in AA6082 – T6 aluminium. Due to aluminium's ability to extrude and high thermal diffusivity the stud and hole included angle used were increased in her research to 30°, 60° and 90° respectively. She found that taper angles below 90° allowed material to extrude out of the joint, therefore reducing the hydrostatic forces on the walls of the hole. When a taper angle of 90° was used the hole did not act as an extrusion die, thus increasing the force exerted on the walls of the hole, improving the bonding. She further documented that the amount of energy put into a weld and the energy input rate governs the microstructure of the weld and in turn governs its mechanical properties [2]. Further she suggests that for a through type FTSW the energy requirement will be greater than 22J/mm<sup>2</sup>.

## **2. Experimental Procedure**

Figure 1 shows the purpose built FTSW platform with the custom axial/ torsional load cell in place. It is a continuous drive system with hydraulically controlled axial motion and allows full control of rotational speed, downward force, forging force, plunge depth and forging time. Figure 2 shows a completed aluminium FTSW in the as welded condition. In application the stud is removed and the plate dressed back to provide a suitable surface finish.



**Figure 1.** FTSW Platform



**Figure 2.** Aluminium FTSW

Figure 3 shows the geometry of the hole and stud configurations used in the study, with Table 1 showing the variations of the geometry evaluated for this study. The chemical composition of the plate and stud material used in the study is given in Table 2. As stated, the greatest lack of information with regards to the FTSW of aluminium AA 6082-T6 is the effect of geometry. A test matrix was designed using fixed levels for downward force, forging force and plunge depth. The matrix used a constant forging time and two rotational speed levels. The constant parameters used in the study are given in Table 3 with the combinations tested tabulated in Table 4. The geometry selection was based on the work of Van Zyl [4], Hattingh et al [5], Pinheiro [6] and Beamish [2]. Rotational speed was chosen based on the upper limit of the welding platform and the downwards/ forging force was tested over the operating range of the welding platform. Plunge depth was estimated by analysing the clearance volume of the stud in the hole vs. the displaced material due to plunge from the work of Hattingh et al [5], Pinheiro [6] and Beamish [2].

**Table 1.** Geometry of the Tapered Stud and Hole

(a)	Stud Nose Diameter (mm)	10,9 and 6
(b)	Stud Taper Angle (°)	10~90
(c)	Hole Depth (mm)	20, 14 and 8.5
(d)	Hole Taper Angle (°)	20, 30, 60, 90
(e)	Base Hole Diameter (mm)	10, 6

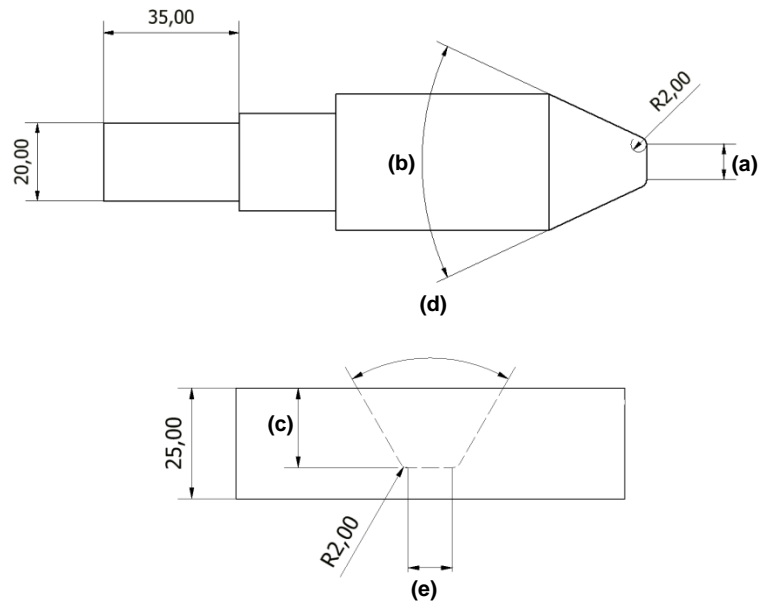


**Figure 3.** Geometry of Tapered Stud and Hole

**Table 2.** Chemical Composition of AA6082-T6 [7]

Element	Si	Fe	Cu	Mn	Mg	Zn	Ti	Cr	Al
Wt.%	0.7%	0.7-1.3%	0.1%	0.4-1%	0.6-1.2%	0.2%	0.1%	0.25%	Balance

**Table 3.** Weld Parameter Constants

Forging Time (s)	20
Rotational Speed (RPM) {PW-1~28}	5200
Rotational Speed (RPM) {PW-29}	5000
Spindle Stopping Time (ms)	500

Preliminary welds PW-1~25 were done using a control valve with a feed rate limit of 4.7mm/s. This was found to be less than the required feed rate for welding, giving a sloping applied force curve during plunging. From PW-26 onwards the valve was up-graded to a more suitable feed rate capacity. Surprisingly, although the additional feed rate improved side wall bonding, the reduced heating time of the initial interface was found to induce lack of bonding at the initial interface centre, where relative velocity is at its lowest.

During welding, frictional torque and axially applied force were recorded. This allowed for the calculation of energy input and energy input rate. Once complete, each weld was sectioned, polished and etched for macro analysis. The opposing side of the weld was used for a break out test, where it was attempted to remove the weld nugget from the plate by applying an impact load perpendicular to the stud axis. In this way a rough idea of the bonding strength



could be obtained and if failure occurred the bonded areas could be observed. Due to aluminium's high thermal diffusivity it was found that welds with good side wall and base bonding were achieved when a preheat of between 170°C and 250°C was applied to the block.

**Table 4.** Preliminary Test Matrix

	Valve Setup	Hole Depth (mm)	Stud Taper Angle (°)	Hole Taper Angle (°)	Hole Base Diameter (mm)	Stud Base Diameter (mm)	Speed (RPM)	Plunge Depth (mm)	Set Downwards Force (kN)
PW-1	Low Feed	20	10	20	10	9	5200	16	15
PW-2	Low Feed	20	15	20	10	9	5200	7.5	15
PW-3	Low Feed	20	18	20	10	9	5200	4.5	15
PW-4	Low Feed	20	10	20	10	9	5200	16	5
PW-5	Low Feed	20	15	20	10	9	5200	7.5	5
PW-6	Low Feed	20	18	20	10	9	5200	4.5	5
PW-7	Low Feed	20	10	20	10	9	5200	16	30
PW-8	Low Feed	20	15	20	10	9	5200	7.5	30
PW-9	Low Feed	20	18	20	10	9	5200	4.5	30
PW-10	Low Feed	20	15	30	10	10	5200	4.2	30
PW-11	Low Feed	20	20	30	10	9	5200	9.5	15
PW-12	Low Feed	20	25	30	10	9	5200	5	15
PW-13	Low Feed	20	28	30	10	9	5200	3.5	15
PW-14	Low Feed	20	20	30	10	9	5200	9.5	30
PW-15	Low Feed	20	25	30	10	9	5200	6	30
PW-16	Low Feed	20	28	30	10	9	5200	3.5	30
PW-17	Low Feed	20	15	20	10	9	5200	7.5	30
PW-18	Low Feed	20	15	20	10	9	5200	7.5	30
PW-19	Low Feed	20	15	20	10	9	5200	2~8	5~30
PW-20	Low Feed	20	10	20	6	6	4000	12	5
PW-21	Low Feed	20	10	20	6	6	5200	6	30
PW-22	Low Feed	14	59	60	6	6	5200	3	30
PW-23	Low Feed	14	59	60	6	6	5200	4	30
PW-24	Low Feed	8.5	89	90	6	6	5200	3	30
PW-25	Low Feed	14	59	60	6	6	5200	6	30
PW-26 (Stepped)	Low Feed	14	59	60	6	6	5200	4	30
PW-27	High Feed	20	10	20	6	6	5200	6	20
PW-28	High Feed	14	58	60	6	6	5200	6	20
PW-29	High Feed	14	58	60	6	6	5000	1~5	10~20~30

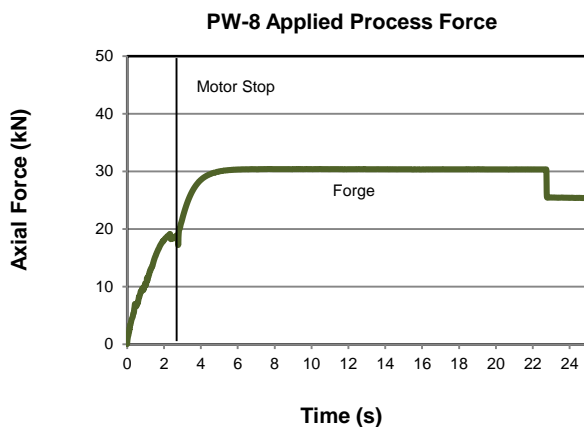


**Chart 1.** Applied Load at 4.7mm/s Feed rate

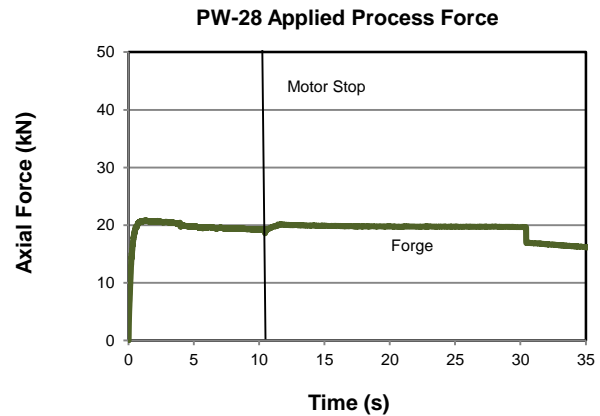


**Chart 2.** Applied Load for Up Rated System

### 3. Results.

Welds PW-1~9 were made using a 20° hole with a 10°, 15° and 18° stud angle configuration. Welds were made at three downward forces; 5, 15 and 30kN, as shown in Table 4. An example of the sloping applied downward force during plunge is given in Chart 1. All welds had reasonable bonding at the base of the hole, however 8 out of 9 had no sidewall or fillet radius bonding. All welds made at 5kN had large voids within the weld nugget as shown in Figure 4(a). Weld PW-8 had improved bonding on the sidewalls, fillet and base, Figure 4(b). However; regions of unbounded material were visible at the boundary with little or no mixing visible, giving an indistinguishable heat affected zone (HAZ).

Welds PW-11~16 used a 30° hole with a 20°, 25° and 28°stud angle. Welds were done at 15 and 30kN downwards force. Tests at 5kN were scrapped due to the large voids formed within the weld nugget. Welds showed little overall improvement, with 5 out of 6 having no side wall bonding. Weld PW-15 showed complete sidewall bonding in the upper third of the joint, showing an improvement with increased taper angles.

The effects of preheat and two stage welding were investigated using a 20° taper angle and 15° stud configuration for welds PW-17~19. With an oven temperature of 250°C, there was no noticeable improvement, with limited sidewall boding in the upper third of the weld and large voids at the fillets. With a 500°C oven preheat temperature the weld improvement was substantial. As can be seen in Figure 4 (c), there is good bonding at the base of the hole with mixing of the base materials visible. The lower third of the weld had poor sidewall

bonding, with the stud shearing at this point and the process continuing with the bottom third stationary. The upper two thirds are thoroughly bonded with no visible voids. This weld could not be broken out of the parent material, confirming good bonding in the upper region. Unfortunately, due to the high preheat requirement of a 20° hole, the upper region of the weld suffered considerable plastic deformation, making this preheat unfavourable for further analysis. The two stage weld, PW-19 had no sidewall bonding and large wall voids. This is attributed to the low energy input rate at the start of the weld, increasing the cycle time under the low downward force. This allows the stud material to soften and shear more easily, inducing premature shear of the weld nugget material, due to the low taper angle.

Welds PW-20~21 and 27 tested the geometry proposed directly by Pinheiro [6] for magnesium. The reduced stud and hole diameters, combined with the 10° stud taper angle produced welds with no sidewall bonding. In all cases the machining marks were still clearly visible; indicating little to no rubbing took place due to poorly distributed hydrostatic forces. The data at this point showed that to achieve sidewall bonding, a greater taper angle was needed. This would improve the normal force exerted on the side walls during plunge and give a greater volume of material above the weld interface of the stud. This allows heat to dissipate into a larger volume of material acting as a heat sink and increases the cross sectional area above the interface, resisting torsion.

Weld PW-22, 23 and 25 use a 60° hole taper angle and 59° stud configuration with like base diameters. PW-22 had no preheat, PW-23 was preheated to an oven temperature of 250°C and PW-25 had the same preheat procedure but utilised a 30mm stud instead of the normal 25mm, increasing the volume of material above the tapered section of the stud. No clearance between the base diameters was chosen to keep the material within the plasticized zone. This would slow material flow out of the weld zone reducing heat loss from the plate, heating of the stud and torque generated by flash above the weld interface; hence prolonging stud rotation. Figure 4(d) shows weld PW-22. The side wall and base diameter bonding are improved with Figure 4(e) showing the hole after the stud was broken out. Bonded regions are clearly visible between the machining marks, with the least bonding falling within the lower quarter, in the region of the fillet. Figure 4(f) shows weld PW-23. Large fillet voids are visible, however; more mixing of the base materials on the side walls can be seen with considerably more effort required to break out the weld nugget. Figure 4(g) shows the hole after the stud was broken out. A line of improved bonding is visible in the lower half of the weld, with no machining marks visible in the upper region. A larger plunge depth could not be used to increase the upper region bonding due to collapse of the stud material by thermal saturation. Weld PW-25 used the same setup as weld PW-23, but with a

5mm larger stud diameter. This allowed a plunge depth of 6mm to be achieved at the point of stud collapse. Figure 4(h) shows the improved sidewall, base diameter and fillet bonding. The stud could not be broken out of the base plate, indicating good bonding. However, the dynamic recrystallized portion of the weld only consisted of the lower third of the weld nugget, forming a near 45° interface line. The majority of the weld nugget is therefore not homogeneous and has uneven grain bending in the upper portion of the weld. These three welds showed that a 60° hole taper angle improved sidewall bonding and with an oven preheat of 250°C, good bonding could be archived. Further it can was concluded that a heat sink is needed to dissipate heat and prevent stud stall. Weld PW-24 used a 90° hole angle. With an oven preheat similar to PW-23 and 25, good sidewall bonding and mixing at the base is achieved, as shown in Figure 4(i). The dynamically recrystallized region consists of the majority of the weld and the interface line is predominantly flat. This showed the improvement with further increased hole angles, however is semi unpractical due to the limited depth of the hole.

At this point the feed rate of the FTSW platform was upgraded; in an effort to reduce the need for preheat of the plate. Weld PW-29 is a good example of the effect of the higher feed rate. It is a similar weld to PW-25 but used a 58° stud to allow for additional plunge depth and uses two stages of downwards force. The immediate climb to the set force reduced the time to seizure, from 0.41s to 0.09s for welds PW-25 and 29 respectively. This reduces the time allowed for the central portion of the hole to rub, generate heat and plasticize. There is therefore a characteristic central void in this region. Although the base void is still currently being addressed, the improvement with respect to side wall and fillet bonding is evident. The stud could not be removed from the plate, with no visible voids in the sidewall or fillet. The shear layer interface line was flat, with the majority of the weld consisting of dynamically recrystallized material. Further this was the first group of welds that showed a distinct HAZ. The improved frictional force reduced the time for heat energy to dissipate up the stud, prolonging premature shear.

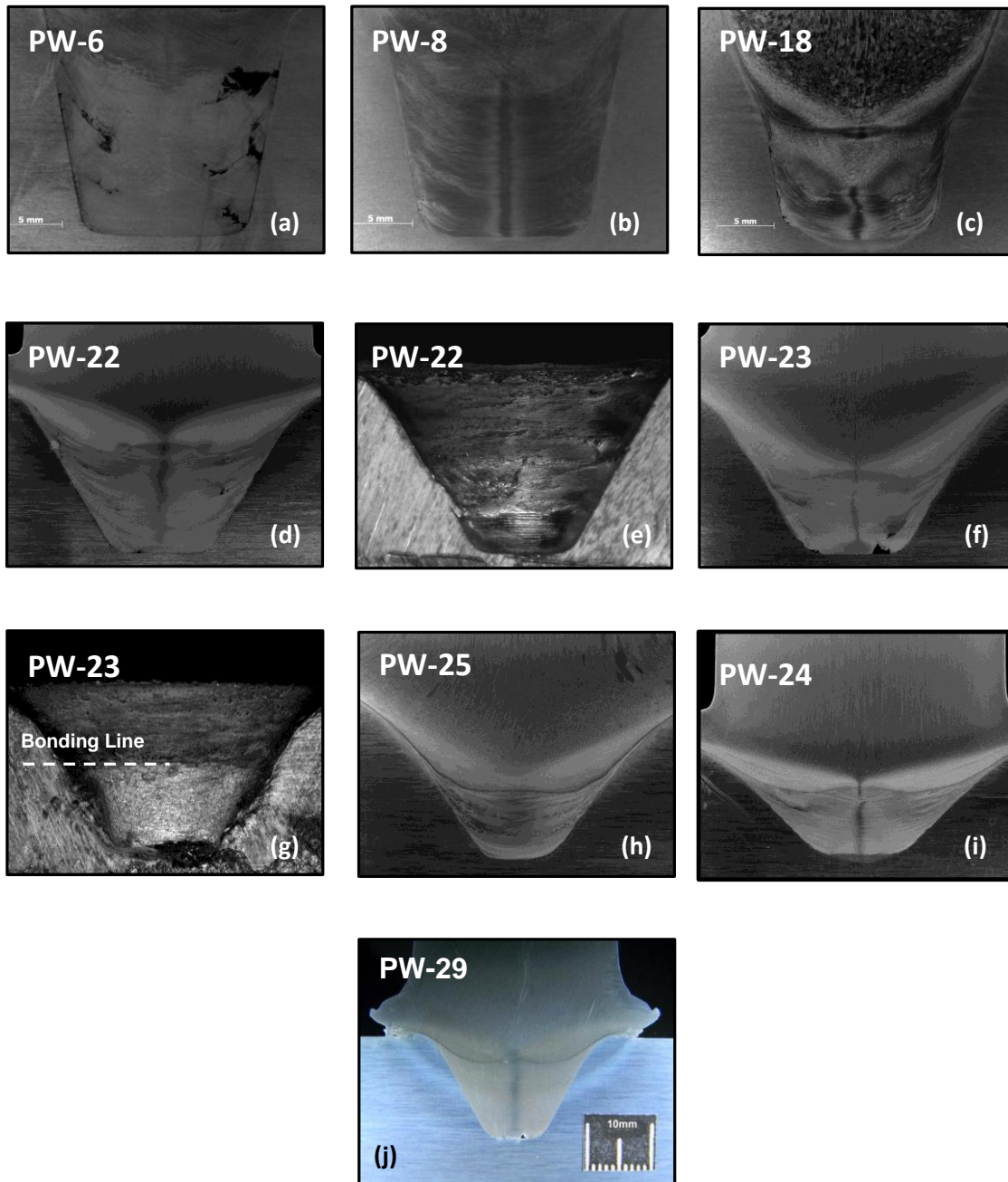


**Figure 4.** Macros of FTSW in AA 6082-T6 Aluminium

### **3.1. Energy Input Analysis**

In an effort to further understand the effects of geometry, preheat and downwards force, the energy input into each weld was analysed. All energy inputs were calculated with respect to the area of the base of the hole and also the entire hole in order to remove the effect of size between welds. As a starting point, each weld was rated in increments of 25% according to

its base hole bonding and side wall bonding. The energy trends were then analysed for correlation.

### 3.1.1. Base Diameter Bonding

The bond between the base of the hole and the stud is formed at the point of initial maximum torque, for this is when the interface is first in a state of shear [9]. From this point plunge will begin and layers of dynamically recrystallized material will be deposited above the base. The base of the hole is the coolest portion, for no heat has been added by the process at this point and the greatest amount of material surrounds it, dissipating heat away. Therefore, the greater the amount of energy that can be put into the weld per unit base hole area before plunge begins, the greater the chances of good bonding. Chart 3 shows the distribution of energy per unit base hole area vs. base diameter bonding quality, which is also tabulated in Table 5. The chart shows that welds with between 150 and 200 J/mm<sup>2</sup> had good base diameter bonding. The two welds achieving 100% base diameter bonding quality were PW-24 and 25, both with a preheat oven temperature of 250°C. The data in Table 5 shows that preheat increases the energy input up to the point of seizure by increasing the frictional torque at seizure. Welds PW-22, 23 and 25 had frictional torques of 16Nm, 32Nm and 39Nm respectively. This increases the plate temperature and improves bonding, reducing the effect of low relative velocity in the central region. The larger stud of PW-25 allowed heat to dissipate away from the interface, further prolonging plunge initiation and allowing the plate to rub and plasticize for longer.

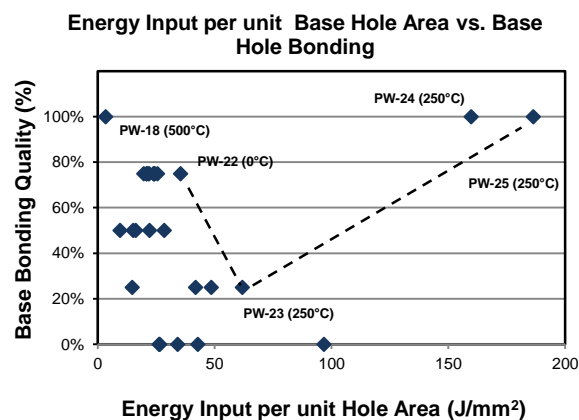


**Chart 3.** Energy Input per Unit Base Hole Area

### 3.1.2. Side Wall Bonding

The energy input into a weld before the weld interface reaches the top of the hole is used to dynamically recrystallize the weld nugget material, heat the surface of the hole and supply the energy for atomic diffusion to take place. Therefore, the greater the input energy, the greater the amount of energy available to achieve bonding. Further, the slower the interface moves up, the longer the stud/hole interface has to rub and plasticize. Chart 4 shows the total amount of input energy into each weld per unit hole area, as tabulated in Table 4. The data shows that input energy per unit hole area cannot be used as a definitive measure of weld quality, for as previously mentioned, side wall bonding is geometry dependant as shown in Chart 5. The data does however show that welds require a minimum of about 22.6J/mm<sup>2</sup> to achieve good side wall bonding when using a 90° taper angle and 75J/mm<sup>2</sup> when using a 60° taper angle, correlating with work by Beamish [2]. Welds using a hole taper angle of 60° were shown to not need preheat when an energy input of between 92 and 120 J/mm<sup>2</sup> was achieved. This energy input was achieved by using the upgraded valve, this reduced cycle time, reduced heat loss to the surrounding material and prolonged premature shearing. This shows that the more energy put into the weld, the greater the temperature of the surrounding material and the less the applied load needed to bring the surfaces into atomic distance for bonding to take place. Of the welds made using a hole taper angle of 30° or less, 72% had a side wall bonding of 25% or less, regardless of the energy input. The energy input into a weld can therefore be used to confirm a weld with good side wall bonding, once the correct geometry has been selected.

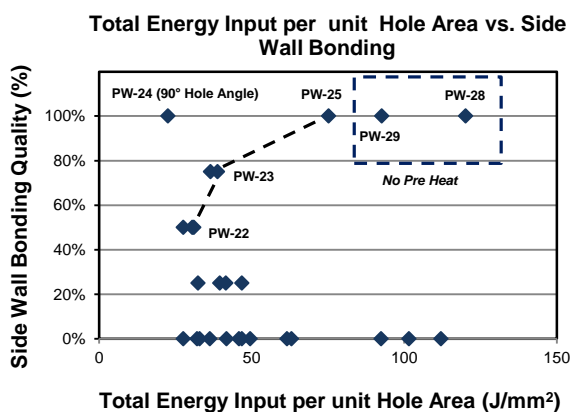


**Chart 4.** Energy Input per Unit Hole Area

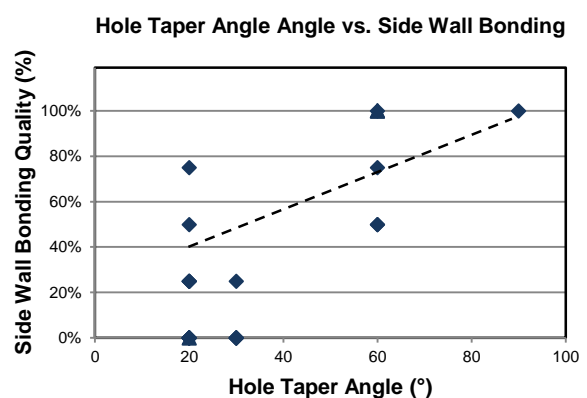


**Chart 5.** Hole Taper Angle vs. Side Wall Bonding

**Table 5. Tabulated Energy Input Data**

	Weld Time (s)	Weld Time to Seizure (s)	Total Input Energy (J)	Energy Input per unit Base Hole Area (J/mm <sup>2</sup> )	Energy Input per unit Hole Area (J/mm <sup>2</sup> )	Base Bonding (%)	Side Wall Bonding (%)	Torque at Seizure (Nm)
PW-1	6.4	0.4	73,462.63	20.96	62	75%	0%	18.95
PW-2	4.3	0.375	49,804.09	21.58	42	75%	0%	18.74
PW-3	3.68	0.375	43,254.68	19.73	36	75%	0%	16.55
PW-4	24.4	0.45	110,196.97	22.05	92	75%	0%	12.75
PW-5	21.93	0.6	133,626.98	35.45	112	75%	0%	13.07
PW-6	19.9	0.5	121,080.12	23.94	102	75%	0%	15.15
PW-7	4.38	0.35	55,792.74	24.26	47	75%	25%	19.18
PW-8	2.82	0.4	36,955.52	23.99	31	75%	50%	21.54
PW-9	2.43	0.4	38,267.45	24.40	32	75%	0%	19.77
PW-10	No Data							
PW-11	6.07	0.335	82,745.68	26.22	63	0%	0%	17.02
PW-12	4.4	0.3375	60,146.62	22.09	46	50%	0%	16.08
PW-13	4.24	0.2	61,366.64	9.56	47	50%	0%	10.7
PW-14	3.99	0.25	65,000.43	15.12	49	50%	0%	17.26
PW-15	3.05	0.365	51,857.34	25.53	39	75%	25%	16.73
PW-16	2.46	0.3	43,228.52	20.95	33	75%	0%	18
PW-17	2.96	0.35	38,569.16	16.28	32	50%	25%	13.075
PW-18	3.42	0.08	43,480.36	3.44	36	100%	75%	6.97
PW-19	6.74	0.55	49,565.62	14.8	42	25%	25%	12.72
PW-20	7.01	0.15	24,039.53	34.25	20	0%	0%	14.62
PW-21	2.48	0.125	15,842.79	42.82	13	0%	0%	16.34
PW-22	2.28	0.245	36,424.11	28.4	30	50%	50%	16.07
PW-23	3.24	0.125	46,219.83	61.86	38	25%	75%	31.93
PW-24	2.04	0.515	26,905.06	159.86	22	100%	100%	34
PW-25	6.53	0.41	89,694.87	186.46	75	100%	100%	39
PW-26 (Stepped)	2.36	0.25	32,821.92	96.8	27	0%	50%	35.19
PW-27	0.68	0.05	32,821.92	26.5	27	0%	0%	17.85
PW-28	10.46	0.1	143,183.92	48.56	120	25%	100%	36.46
PW-29	8.07	0.09	110,416.15	41.8	92	25%	100%	32.93



#### **4. Conclusion**

This study has identified geometry that allows for the FTSW of AA 6082-T6 aluminium. It has discussed hole and stud taper angles with respect to visual bond quality, identifying a 60° hole as the approximate taper angle for achieving good side wall bonding, while maintaining maximum hole depth. The effects of preheat on weld quality, energy input to seizure and energy input have been discussed and approximate values needed for a visually good weld identified. The study showed that preheat increased the amount of energy input into the weld before seizure, improving base hole bonding. The analysis of the total energy input showed that a minimum amount of energy is needed in order to have sufficient energy to dynamically recrystallize the weld nugget material, overcome dissipated energy and supply the energy required for atomic diffusion. Further, the study showed that once good geometry is identified, energy can be used to predict weld quality. A future step for this research is to analyse the interface temperature of the base and sidewalls of the hole with respect to energy, to further understand the influence of process parameters and how to predict them.

## 5. Referencing

- [1] Hartley, P.J. Friction Plug Weld Repairs for the Space Shuttle External Tanks, Welding and Metal Fabrication, September 2000.
- [2] Beamish, K. Friction taper plug welding of 10mm AA6082-T6. TWI, 2003.
- [3] Mahoney, M. W. (1999). Patent No. 8,975,406. United States Patent. M. e. (1999). Patent No. 8,975,406. United States Patent
- [4] Van Zyl, CAA. 2008. Analysis and modelling of the Temperature Distribution During the Friction Taper Stud Welding of 10CrMo910. Masters Dissertation, Nelson Mandela Metropolitan University, 2008
- [5] Hattingh DG, Bulbring DLH, Els-Botes A, James MN, Process parameters influence on performance of friction taper stud welds in AISI 4140. Materials and Design. 2011 Feb;32:3421-3430
- [6] Samuel DAG. Characterization of joint integrity of Friction Stud Welding as Applied to AISI 304L Stainless Steel. Masters Dissertation. Nelson Mandela Metropolitan University: Port Elisabeth, 2009
- [7] GKSS. Local Reinforcement of Magnesium Components by Friction Processing: Determination of Bonding Mechanisms and Assessment of Joint Properties. Pinheiro, G.A. 2008.
- [8] Aluminium Alloys-Aluminium 6082 Properties, Fabrication and Applications, Supplier Data by Aalco (Online). Available: <http://www.azom.com/Details.asp?ArticleID=2813> [Accessed 2 February 2010]
- [9] Kimura, M. Seo, K. Kusaka, M. & Fuji, A. 2003. Observation of joining phenomena in friction stage and improving friction welding method. JSME International journal, Series A/46/3: 384-390

**Appendix O**

**Paper 2**

**Development of a procedure for the filling of blind holes in thick section AA 6082-T6 Aluminium by Friction Hydro Pillar Processing**

**D.A.G. Samuel<sup>a</sup>, D.G. Hattingh<sup>a</sup>, A. Els-Botes<sup>a</sup>**

<sup>a</sup>eNtsa, Faculty of Engineering, the Built Environment & Technology, Nelson Mandela Metropolitan University, Port Elizabeth 6031, South Africa

**Abstract**

In this study, blind tapered holes in 25mm thick AA6082-T6 plate were filled by Friction Hydro Pillar Processing (FHPP). The process addresses the need to fill blind holes in thick aluminium sections for the repair of incorrectly drilled holes, friction stir welding exit holes, defects and/or cracks in aluminium components. The effects of geometry, process parameters and preheat are discussed in relationship to joint integrity and near weld interface temperature. Results of preliminary experiments are presented that were used to establish acceptable weld geometry that would allow for a defect tolerant weld. Additionally the effect of process parameters on bonding at the base of the tapered hole is presented using a parallel sided stud and tapered hole configuration. This addresses one of the pressing issues currently facing FHPP of aluminium namely the lack of bonding at the bottom of the blind hole. During welding, frictional torque, interface temperature and weld time were recorded. This data was used to calculate energy input, identifying the effect of process parameters on input energy and correlating this with sidewall bonding and near interface weld temperature. The effect of using a heat sink was investigated and is presented, with increases of 47% in total weld energy recorded. The results from the parallel FHPP show the direct influence of preheat on energy input into the weld in the first 0.1s with increases of 52% to 96% achieved. Results showed no good welds were achieved with low welding force and low total energy input levels. It was also confirmed that preheat contributes to better bonding by allowing for more frictional heat to be generated during the first stage of the process. Hole taper angles of 60° resulted in good sidewall bonding during visual evaluation when combined with high process energy input.

**Keywords:** Aluminium 6082-T6, Friction Hydro Pillar Processing, Friction Stir Welding, Friction Taper Stud Welding, Frictional Torque, Hydrostatic Forces

[darren.samuel@nmmu.ac.za](mailto:darren.samuel@nmmu.ac.za)  
eNtsa, School of Engineering  
Nelson Mandela Metropolitan University  
Summerstrand Campus (North)  
Gardham Avenue  
6031

**1. Introduction**

As aluminium is used increasingly in manufacturing applications, greater demands are set on the material. This increased the need for high integrity defect tolerant welds and repair procedures in aluminium alloys, such as plugging the exit hole of a friction stir weld (FSW), crack repair, etc. Friction hydro pillar processing (FHPP) of aluminium has been identified as a possible solution, and is under development as an alternative joining technique in blind partially supported components. The FHPP of aluminium is a relatively new process, therefore due to lack of expertise and limited published data on the topic, parameters to establish a preliminary process window for blind FTSW in AA6082-T6 had to be determined. The focus was to identify stud and hole geometry that give good sidewall and base bonding combinations. This paper presents the effect of downwards force, preheat and the effect of using a non-consumable heat sink on the FHPP of aluminium with various geometry configurations. The investigation attempts to link the effects of these parameter changes with

respect to sidewall temperature, energy input and process torque. As expected with aluminium, due to its high thermal diffusivity and low strength retention at elevated temperatures the bonding at the base of the hole forms a significant challenge. A set of parallel FHPP welds are presented that identify the conditions required to get good bonding at the base of the hole without interference. Paula J Hartley [1] reviewed the use of through type friction taper stud welding on aluminium as used by Lockheed Martin Space systems as a defect repair procedure. The report stated a 20% strength improvement over TIG welding with improved fracture toughness [1]. K Beamish [2] researched through hole type friction taper stud welding of 10mm AA6082-T6. She noted the lack of literature on the topic in the public domain and attributes this to the slow uptake of the process. Beamish investigated the effects of downward force, rotational speed, axial shortening and geometry on weld quality, with taper angles of 60° and 90° achieving 90° in a bend test. It was found that peripheral velocity had a greater influence on weld quality than rotational speed. She documented that high downward force caused the weld interface to move up more rapidly and that excessive force induced deformation of the plug [2]. Insufficient force was shown to produce a lack of bonding at the lower surface of the plate and upper surface flash [2, 6]. Mahoney et al [3] presented a method to repair voids in aluminium alloys using FTSW. The included angle of the tapered hole was 60° with 72 ridges per inch machined into the surface of the hole. In order to overcome premature shearing of the stud due to aluminium's low strength at elevated temperatures, they introduced a heat sink as part of the stud. In the study the stud was found to be thoroughly bonded to the hole and the weld nugget consisted of fine recrystallized material. The problem of poor bonding in the lower region of the weld due to reduced plasticization was overcome by using a backing plate with part of the tapered hole machined into it. This region was then machined away, leaving the bonded region intact.

## **2. Geometry Configurations**

A review of work done on FHPP was needed to gauge a starting point for the research. The following summarises the considered work identifying hole and stud geometry known to make successful tapered FHPP welds. Van Zyl [4] using Chromium-Molybdenum steel (10CrMo910) made blind FTSW welds using a stud and hole included angle of 15° and 20° respectively to fill a 25mm deep hole in his research on modelling of heat distribution during FTSW. Hattingh et al [5] using AISI 709M40 (EN 19) made successful blind FHPP welds using the same stud and hole included angles as Van Zyl [4]. Pinheiro [6] made blind FHPP welds in AZ91D – T6 Magnesium using hole included angles of 10° - 20° with base diameter combinations of 6mm and 8mm. Beamish [2] made through type FTS welds in AA6082 – T6 aluminium. Due to aluminium's ability to extrude and high thermal diffusivity the stud and hole included angle used were increased in her research to 30°, 60° and 90° respectively. She found that taper angles below 90° allowed material to extrude out of the join, therefore reducing the hydrostatic forces on the walls of the hole. When a taper angle of 90° was used the hole did not act as an extrusion die, thus increasing the force exerted on the walls of the hole. She suggests that for a through type FTSW the energy requirement will be greater than 22J/mm<sup>2</sup>.

## **3. Plunge Depth Approximation**

In order to test various geometry's, a method of keeping the consumed length sufficient to complete a weld and comparative for geometry changes was needed. Based on previous work and research by Pinheiro [6] and Hattingh et al [5], the displaced volume vs. clearance volume approximation was developed. The approximation compares the volume of consumed stud material during plunge and compares it with the volume between the unconsumed stud and hole. A displaced volume vs. clearance volume factor of 18 was found to be sufficient for preliminary work. Welds were found to be complete, without extensive stud collapse.

#### 4. Experimental Procedure

Figure 1 shows the purpose built FHPP platform with the custom axial/ torsional load cell in place. It is a continuous drive system with hydraulically controlled axial motion and allows full control of rotational speed, downward force, forging force, plunge depth and forging time. Figure 2 shows a completed aluminium FHPP weld in the as-welded condition. As a starting point geometry was investigated to identify a geometry window within which FHPP of aluminium AA 6082-T6 could be done. Once a suitable hole angle was identified, preheat of the block was investigated and parallel studs friction welded into tapered holes to investigate base bonding without the influence of the stud taper. This was necessary as geometry and process changes easily caused lock up in the first moments of rotation. Hole angles of 20°, 30°, 60° and 90° were tested with 60° proving to be the most effective without sacrificing hole depth. Figure 3 shows the geometry of the hole and stud configurations tested in the study, with Table 1 showing the variations of the geometry. The preliminary work for tapered studs was designed using fixed levels for downward force, forging force and plunge depth. The constant parameters used are given in Table 2 with the combinations tested tabulated in Table 3. The geometry selection was based on the work of Van Zyl [4], Hattingh et al [5], Pinheiro [6] and Beamish [2]. Rotational speed was chosen based on the upper limit of the welding platform and the downwards/ forging force was tested over the operating range of the welding platform. Preliminary welds PW-1 to PW-25 were done using a feed rate limit of 4.7mm/s. This was found to be less than required, giving a sloping applied force curve during plunging, giving the stud time to heat and soften. From weld PW-26 onwards the valve was upgraded to a more suitable feed rate capacity. During welding, frictional torque and axially applied force were recorded. This allowed for the calculation of energy input. Once complete, each weld was sectioned, polished and etched for macro analysis. The energy input was equated to area of the tapered hole in order to make the data comparable for different geometries. Diameter combinations of 6mm and 8mm were used with a stud included angle of 10°.

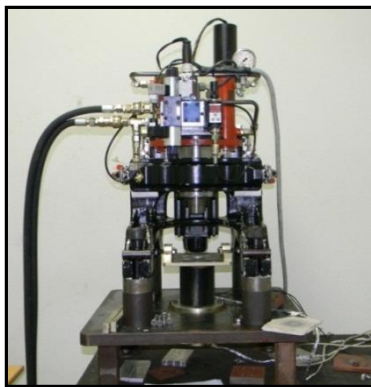


Figure 1. FTSW Platform



Figure 2. Aluminium FTSW

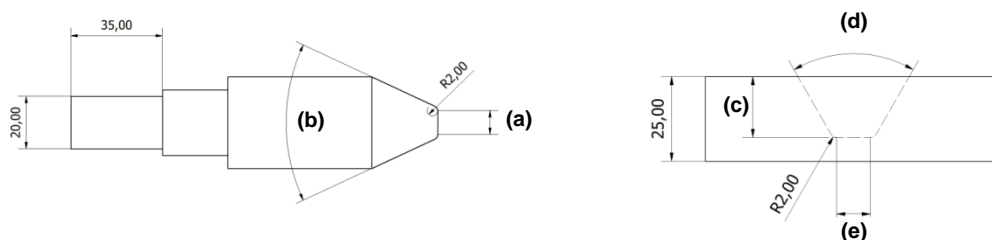


Figure 3. Geometry of Tapered Stud and Hole

**Table 1.** Geometry of the Tapered Stud and Hole

(a)	Stud Nose Diameter (mm)	10,9 and 6
(b)	Stud Taper Angle (°)	10-90
(c)	Hole Depth (mm)	20,18, 14, 8.5
(d)	Hole Taper Angle (°)	20, 30, 60, 90
(e)	Base Hole Diameter (mm)	10, 6

**Table 2.** Weld Parameter Constants

Forging Time (s)	20
Rotational Speed (RPM) {PW-1-28}	5200
Rotational Speed (RPM) {PW-29 onward}	5000
Spindle Stopping Time (Ms)	500

## 5. Results

### 5.1. Hole and Tool Geometry

The taper angles of the hole and stud were investigated first, to identify the effect on sidewall bonding. Welds PW-1to PW-9 were made using a 20° hole with a 10°, 15° and 18° stud angle configurations shown in Table 3. All welds made at 5kN had large voids within the weld nugget as shown in Figure 4(a). Weld PW-8 had improved bonding on the sidewalls, fillet and base as shown in Figure 4(b). However, regions of unbounded material were visible, giving an indistinguishable heat affected zone (HAZ). Though 5kN welds had a large total energy input, this energy was used to run the stud on top of the filled hole, not heat and bond the sidewalls. Welds PW-11to PW-16 used a 30° hole with a 20°, 25° and 28°stud angle. Tests at 5kN were abandoned due to void formation. Welds showed little overall improvement, with five out of six having no side wall bonding. Weld PW-15 showed complete sidewall bonding in the upper third of the joint, showing an improvement with increased taper angles and downwards force. Voids formed at the fillet were attributed to the low ramp up speed. The effects of preheat and two stage welding were investigated using a 20° taper angle and 15° stud configuration for welds PW-17 to PW-19. With an oven temperature of 250°C, there was no noticeable improvement. With a 500°C oven preheat temperature the weld improvement was notable as seen in Figure 4(c). Good bonding at the base of the hole with mixing of the base materials is visible. The lower third of the weld had no sidewall bonding due to insufficient hydrostatic forces and premature stud stall, with the upper two thirds thoroughly bonded. The improved bonding in the upper region is attributed to the increase in the hole taper angle by deformation due to the high preheat. Due to the high preheat requirement and the lack of bonding in the lower regions, the 20° hole taper angle proved unfavourable for further analysis. With respect to the bonding at the base of the hole, the energy input with increasing block temperature was 0.78, 2.71 and 4.96 J/mm<sup>2</sup>, with the latter giving the best base bonding, indicating the need for preheat. Welds PW-20 toPW-21 and PW-27 tested the geometry proposed by Pinheiro [6] for magnesium. The geometry produced welds with no sidewall bonding. These tests showed that to achieve sidewall bonding, a greater taper angle was needed. This would increase the normal force exerted on the side walls and give a greater volume of material above the weld interface. Heat would then dissipate into a larger volume of material, resisting shear. Weld PW-22, 23 and 25 investigated the use of a 60° hole taper and 59° stud configuration. PW-22 had no preheat, PW-23 was preheated to an oven temperature of 250°C and PW-25 had the same preheat procedure but utilised a 30mm stud instead of the normal 25mm.The 60° holes show improved side wall bonding throughout. Figure 4(d) and (e) show the improved sidewall, base diameter and fillet bonding with and without preheat. The tests showed that with preheat and a large enough stud the 60° hole angle gave good bonding. Further less preheat was needed to achieve sidewall bonding. A test was done using a 90° hole with the same preheat procedure as PW-25. As shown in Figure 4(f), excellent sidewall and base bonding was achieved. This configuration was however not perused due to the size of the exit hole needed to achieve acceptable hole depths. Based on this it was decided to use 60° as the standard taper angle for FHPP of aluminium, with geometry changes being made only to clearance and stud taper angles.

**Table 3.** Preliminary Tests

	Hole Depth (mm)	Stud Taper Angle (°)	Hole Taper Angle (°)	Hole Base Diameter (mm)	Stud Base Diameter (mm)	Speed (RPM)	Plunge Depth (mm)	Downwards Force (kN)	Preheat (°C)	Energy
PW-1	20	10	20	10	9	5200	16	15	22	1.83
PW-2	20	15	20	10	9	5200	7.5	15	22	2.07
PW-3	20	18	20	10	9	5200	4.5	15	22	1.99
PW-4	20	10	20	10	9	5200	16	5	22	2.07
PW-5	20	15	20	10	9	5200	7.5	5	22	1.99
PW-6	20	18	20	10	9	5200	4.5	5	22	1.34
PW-7	20	10	20	10	9	5200	16	30	22	2.41
PW-8	20	15	20	10	9	5200	7.5	30	22	2.60
PW-9	20	18	20	10	9	5200	4.5	30	22	1.64
PW-11	20	20	30	10	9	5200	9.5	15	22	2.91
PW-12	20	25	30	10	9	5200	5	15	22	2.41
PW-13	20	28	30	10	9	5200	3.5	15	22	2.83
PW-14	20	20	30	10	9	5200	9.5	30	22	2.84
PW-15	20	25	30	10	9	5200	6	30	22	2.92
PW-16	20	28	30	10	9	5200	3.5	30	22	2.59
PW-17	20	15	20	10	9	5200	7.5	30	250 (oven)	2.71
PW-18	20	15	20	10	9	5200	7.5	30	500 (oven)	4.96
PW-19	20	15	20	10	9	5200	2-8	5-30	22	0.78
PW-20	20	10	20	6	6	4000	12	5	22	3.18
PW-21	20	10	20	6	6	5200	6	30	22	25.59
PW-22	14	59	60	6	6	5200	3	30	22	3.36
PW-23	14	59	60	6	6	5200	4	30	22	19.43
PW-24	8.5	89	90	6	6	5200	3	30	22	5.93
PW-25	14	59	60	6	6	5200	6	30	22	19.28
PW-27	20	10	20	6	6	5200	6	20	22	40.32
PW-28	14	58	60	6	6	5200	6	20	22	39.90
PW-29	14	55	60	6	6	5000	1-5	10-20-30	22	17.86
PW-31	18	55	60	10	9	5000	0.5-2	12-20-30	22	6.93
PW-33	18	55	60	9	9	5000	0.5-1.5	12-20-30	22	20.20
PW-35	18	55	60	9	9	5000	0.5-1.5	12-20-30	22	20.86

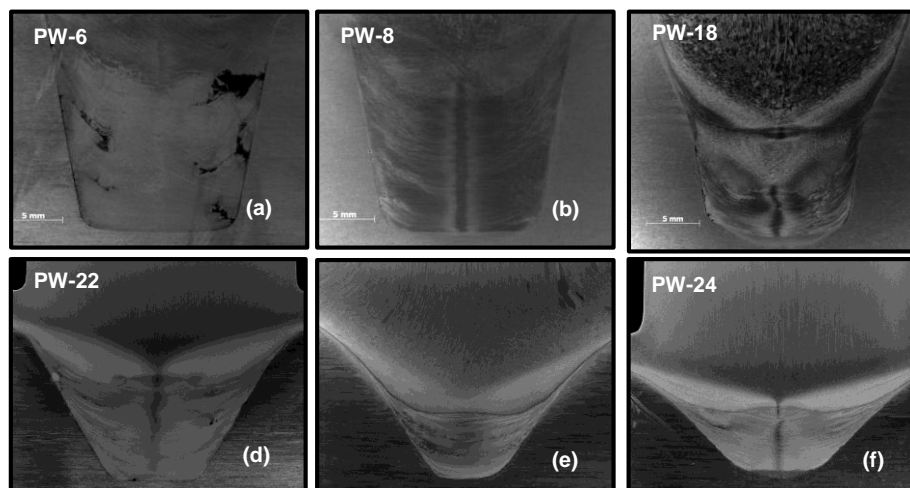


**Figure 4.** Macros of FHPF welds in AA 6082-T6 Aluminium

## 5.2. Downwards Force

The feed rate of the FHPF platform was increased in an effort to reduce the need for preheat of the plate. Weld PW-29, shown in Figure 5 is a good example of the effect of the higher feed rate. It is a similar weld to PW-25, but used a 58° stud to allow for additional plunge depth and used a two stage downwards force approach. The immediate increase to the set force reduced the time to seizure, from 0.41s to 0.09s for welds PW-25 and 29 respectively. This reduces the time allowed for the central portion (where peripheral velocity tends to zero) of the hole to rub, generate heat and plasticize which resulted in a characteristic cold forge



defect in this region. This was the first group of welds that showed a distinct HAZ. The improved frictional force reduced the time for heat energy to dissipate up the stud, prolonging premature shear. Therefore with downwards force less than required, poor sidewall bonding will occur, accompanied by voids in the fillet and weld nugget body.

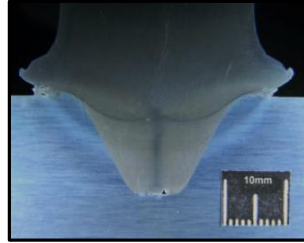


**Figure 5.** Macros of FHPP High Feed Rate Weld

### **5.3. Energy Input Analysis**

#### **5.3.1. Base Diameter and Side Wall Bonding**

The bond between the base of the hole and the stud is formed at the point of initial maximum torque, for this is when the interface is first in a state of shear [7]. From this point plunge will begin and layers of dynamically recrystallized material will be deposited above the base. The base of the hole is the coolest portion, for reason that no heat has been added by the process at this point and the greatest amount of material surrounds it. Therefore, the greater the amount of energy that can be put into the weld per unit base hole area before plunge begins, the greater the chances of good bonding. The first 0.1s of the energy put into the weld is analysed in this work to identify its effect on base bonding. The energy input into a weld before the weld interface reaches the top of the hole is used to dynamically recrystallize the weld nugget material, heat the surface of the hole and supply the energy for atomic diffusion to take place. Therefore, the greater the input energy before the hole is filled, the greater the amount of energy available to achieve bonding. Further, the slower the interface moves up, the longer the stud/hole interface has to rub and plasticize.

#### **5.3.2. Base Diameter and Side Wall Bonding with Preheat**

The effect of preheat was investigated with welds PW-22, PW-23 and PW-25. Figure 6(a) and (b) show the hole after the plate was sectioned and the stud broken out of weld PW-22 and PW-23 respectively. The Figures show that only localised bonding on the sidewalls was achieved on weld PW-22, with the machining marks still visible at the fillet. For weld PW-23, Figure 6(b) the block was preheated to an oven temperature of 250°C. The bonding in the lower region improved, with sections pulled away from the fillet and base. The dull region at the top is predominantly unbonded with only small localised bonds that were easily broken. This region was not bonded due to stud collapse as the material above the hole softened. To overcome this, a stud was constructed from a 5mm thicker rod as previously discussed. The stud could absorb more heat energy before collapse. This stud could not be removed from the hole, therefore it can be assumed that the sidewall bonding was improved. No regions with lack of bonding were visible in the weld, as shown in Figure 4(e). These welds used 3mm, 4mm and 6mm axial shortening respectively. The axial shortening was increased to 4mm to add heat as the torque had not equalised as seen in Figure 7. With preheat, equalised torque was reached more rapidly and was lower than without preheat. On visual inspection of weld PW-23, the additional 1mm produced widening of the stud due to collapse. The larger stud of PW-25 was given a 6mm axial shortening, as it was expected that the stud would take longer to collapse, therefore able to rub and plasticize in the upper

region for longer. The stud did experience collapse in the later stage of welding, however the correct applied load was maintained and more energy was put into the upper region. The energy input was analysed and tabulated in Table 4.

**Table 4.** Energy Input for 60° Holes at 4.7mm/s

Weld Number	Energy input total (J/mm <sup>2</sup> )	Energy input at 0.1s (J/mm <sup>2</sup> )	Condition
PW-22	41	3.36	Room temp 25mm stud
PW-23	52	19.43	140°C 25mm stud
PW-25	102	19.28	140°C 30mm stud

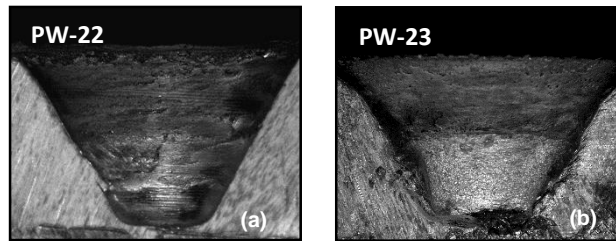


**Figure 6.** Sidewall Bonding for PW-22 and 23

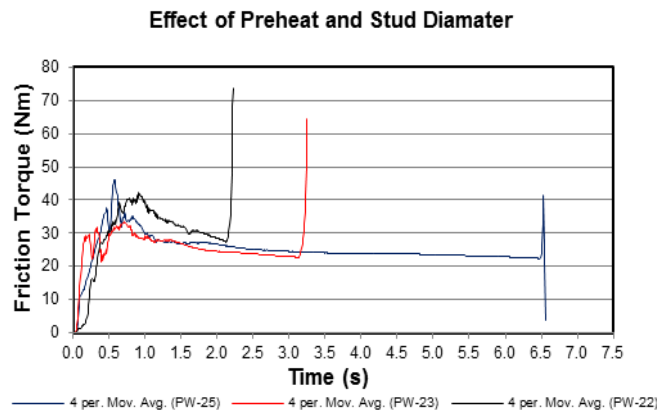


**Figure 7.** Friction Torque for Welds PW-22, 23 and 25

The energy input in the first 0.1s of the weld increased five times with preheat. As expected there was no increase in input energy in the first 0.1s with the increased stud diameter. Preheat gave only a marginal increase in the total energy put into the weld, though this did significantly improved the bonding in the lower regions. With the increase in stud diameter the total energy input into the weld doubled. With the energy input in the first 0.1s of welds PW-23 and PW-25 being the same, the additional energy was put into the region above the base of the hole.

### 5.3.3. Interface Temperature

A temperature analysis was done to evaluate the effect of clearance and the use of a heat sink on the temperature at the sidewall. Holes were drilled at the fillet, mid-point and top of the hole. Welds PW-31 and PW-33 investigate the effect of clearance and PW-35 the effect of using a heat sink. When a 1mm smaller stud was used in the 60° hole a 0.5mm increase in axial shortening was used to compensate the change in displaced volume. Though more material was displaced the maximum temperature recorded was 362°C vs. 465°C recorded with no clearance. This is caused by less material flowing out as flash; retaining more heat within the weld region, heating the block rather than the energy escaping within the flash. The welding time increased from 9.06s to 15.08s when no clearance was used and

increased further to 60.6s when a heat sink as shown in Figure 8 was fitted. This increased the maximum interface temperature to 528°C. The stud consumed slower and did not experience stud collapse in the upper regions. The sidewalls experienced further rubbing and heat generation. This was verified by the maximum torque increase of 12Nm when the heat sink was used, as heat was dissipated out the flash to the stud. The use of a heat sink can therefore be said to increase the energy input into the weld in the upper regions, as seen in Table 5. As mentioned it has no effect on the energy input during the first 0.1s of the weld, only in the total energy input. The 0.5mm clearance put in a similar total amount of energy as the volume of the hole to fill was the same. A cold forge defect can be seen in the central region of the weld at the base of the hole, shown in Figure 9(a) and (b). This is where the relative velocity is at its lowest. This is where the energy needed to keep the interface in a plasticized state was insufficient. When the conduction of heat away from the interface is higher than the generated heat, a cold forge defect is formed. Seems the heat sink and clearance has no effect on the energy input in the first 0.1s this cannot be overcome without preheat. Using a larger ramp up time could improve this; however this causes heating of the stud, inducing premature shear and stud stall, reducing side wall binding. The block will need to be preheated to overcome this.



**Figure 8.** Removable Heat Sink

**Table 5.** Energy Input for Welds Clearance and Heat Sink

Weld Number	Energy input total (J/mm <sup>2</sup> )	Energy input at 0.1s (J/mm <sup>2</sup> )	Clearance (mm)	(Temperature/ Stud Angle)
PW-31	123.26	6.93	0.5	Room (55° Stud)
PW-33	155.78	20.2	0	Room (55° Stud)
PW-35 (Heat Sink)	228.34	20.86	0	Room (55° Stud)

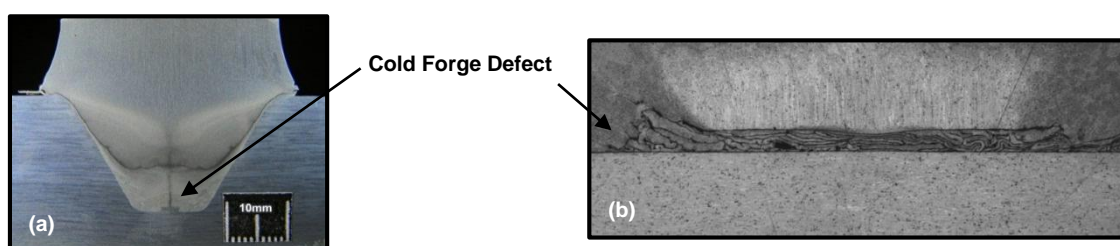


**Figure 9.** 60° FHPP Welds with Cold Forge Defect

#### 5.4. Parallel FHPP Welds

Due to aluminium's high thermal diffusivity, heat is dissipated at a rate that prohibits bonding, creating one of the largest issues facing FHPP of aluminium at the moment, lack of bonding at the base of the hole. As the stud rubs at the base of the hole during heating, microbonds are formed at the interface. Once the microbond is formed, the heat that held the bond in its plasticized state is dissipated into the backing plate. The microbonds therefore shear between the softened stud material and the bond. The stud then rubs and forms additional bonds above this, depositing layer upon layer of dynamically recrystallized material. In this

manner a tapered hole can be filled with only small locally bonded regions holding the weld nugget to the plate. A test matrix was set up to investigate only the effect of preheat and rotational speed on the bonding at the base of the hole. A 60° tapered hole was used as in welds PW-31, 33 and 35. The tapered section of the stud was machined off leaving a parallel sided stud with a 10mm base diameter and 2mm fillet. The parallel sides made it possible to focus on the effects of process parameters purely on the bonding at the base of the hole. From Table 6 it can be seen that when a weld is done using a preheat of 140°C (temperature when welding), the input energy in the first 0.1s increases. This increase in energy improves the bonding substantially. There is better mixing in the fillet as seen in Figure 10(a), (b), (e) and (f). The fracture surfaces show that without preheat the surface has a rotary smear effect, with only small traces of localised bonding as shown Figure 10(c). With preheat the entire surface is dull, with no smear effect, Figure 10(a) and (e). The sheared bonds are larger and spread over the surface of the stud, giving a 260% increase in fracture force at 5000rpm and 350% at 3000rpm. The lower rotational speed gave larger and less localised fractures. Less energy is put in per unit area, but this may be a more efficient rotational speed for the process. From this test it is clear that preheat allows more energy to be put into the weld in the first moments. Further the energy put in is not dissipated away the moment bonds are formed, but is used to form a continuous bond over surface. As seen in Figure 10(a) and (e), the central region of the fracture surface still shows an area of reduced bonding. No notable difference could be found in the time taken to reach the set axial shortening, with preheat and rotational speed changes. From this it is clear that without a stud material with a higher melting temperature, preheat is unavoidable.

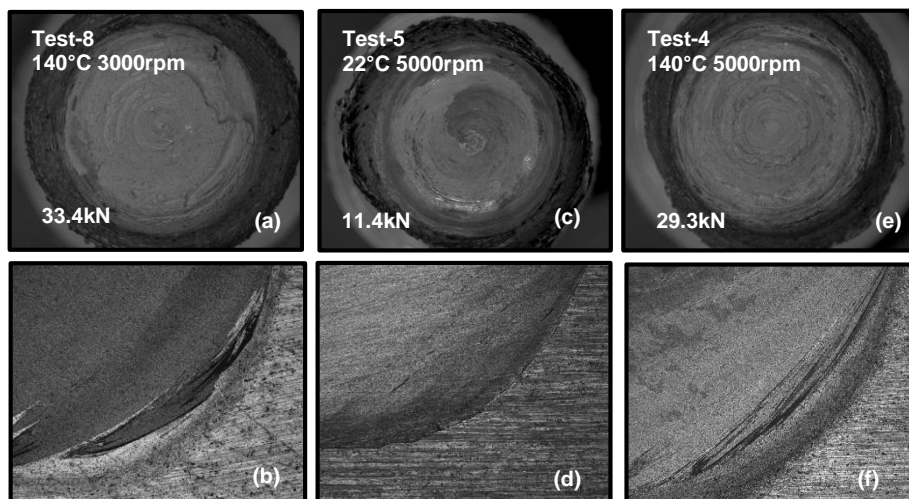


**Figure 10.** Fracture Surfaces of 60° FHPP Welds

**Table 6.** Energy Input for Parallel FHPP Welds

	Rotational Speed (rpm)	Block Temperature (°C)	Set Welding Force (kN)	Set Forge Force (kN)	Maximum Welding Force (kN)	Energy Input to 0.1s (J)	Energy Input to 0.1s (J/mm <sup>2</sup> )	Cycle time (s)	Fracture Force (kN)
Test 2	5000	22	12	30	10.7	751.9	9.57	0.44	
Test 3	5000	140	12	30	9.7	819.0	10.43	0.49	
Test 4	5000	140	25	30	12.5	898.6	10.09	0.45	29.38
Test 5	5000	22	25	30	14.3	590.3	7.52	0.47	11.40
Test 6	2400	22	25	30	13.2	344.7	4.39	0.45	
Test 7	3000	22	25	30	12.1	484.9	6.17	0.42	20.0
Test 8	3000	140	25	30	12.6	1023.5	7.82	0.39	40.7

## **6. Conclusion**

This study has identified geometry that allows for the FHPP of AA 6082-T6 aluminium. It has discussed hole and stud taper angles with respect to visual bond quality, identifying a 60° hole as the approximate taper angle for achieving good side wall bonding, while maintaining maximum hole depth. The effects of preheat on weld quality and energy input have been discussed and approximate values needed for a visually good weld highlighted. The study showed that preheat increased the amount of energy input into the weld during the first stages of the weld, improving base bonding. Though energy alone cannot be used as a definitive measure of weld quality, for bonding is geometry and preheat dependant, once good geometry is identified, energy can be used to predict weld quality. The use of a heat sink was shown to significantly increase the heat energy into the weld. As mentioned it has no effect on the energy input during the first stage of the weld, only in the total energy input. Clearance was shown to reduce interface temperature, while the use of a heat sink increased it significantly. High force ramp rates were shown to induce a cold forge defect when sufficient preheat is not applied. It was shown that with like stud and plate materials, a weld with good base bonding is not achievable without preheat due to heating of the stud material. Reduced rotational speed reduced energy input into the bottom of the weld, however 3000rpm was found to be a more efficient speed, thus improving fracture force.

## **7. Acknowledgements**

We would like to acknowledge Dr T Patterson for his input and advice on the FHPP of aluminium research at NMMU. Further, for financial assistance we would like to thank DST-LMI (Light Metals Initiative) program, NRF-IRDP program, THRIP, and NMMU RCD (Research Capacity Development).

## **8. Referencing**

- [1] Hartley, P.J. Friction Plug Weld Repairs for the Space Shuttle External Tanks, Welding and Metal Fabrication, September 2000.
- [2] Beamish, K. Friction taper plug welding of 10mm AA6082-T6. TWI, 2003.
- [3] Mahoney, M. W. (1999). Patent No. 8,975,406. United States Patent. M. e. (1999). Patent No. 8,975,406. United States Patent
- [4] Van Zyl, CAA. 2008. Analysis and modelling of the Temperature Distribution During the Friction Taper Stud Welding of 10CrMo910. Masters Dissertation, Nelson Mandela Metropolitan University, 2008
- [5] Hattingh DG, Bulbring DLH, Els-Botes A, James MN, Process parameters influence on performance of friction taper stud welds in AISI 4140. Materials and Design. 2011 Feb;32:3421-3430
- [6] Samuel DAG. Characterization of joint integrity of Friction Stud Welding as Applied to AISI 304L Stainless Steel. Masters Dissertation. Nelson Mandela Metropolitan University: Port Elisabeth, 2009
- [7] Kimura, M. Seo, K. Kusaka, M. & Fuji, A. 2003. Observation of joining phenomena in friction stage and improving friction welding method. JSME International journal, Series A/46/3: 384-390

**Appendix P**

**Paper 3**

# Characterization of Tapered Friction Stud Welding Applied to AA6082-T6

---

**D.A.G. Samuel <sup>\*,a</sup>, D.G. Hattingh<sup>a</sup>, A. Els-Botes<sup>a</sup>, A. Steuwer <sup>a,b</sup>**

<sup>a</sup> eNtsa, Faculty of Engineering, the Built Environment & Technology, Nelson Mandela Metropolitan University, Port Elizabeth 6031, South Africa.

<sup>b</sup>MAX IV Laboratory, Ole Römers Väg 1, Lund University, 22100 Lund, Sweden

## Abstract

In this study, blind tapered holes in 25mm thick AA6082-T6 heat treatable aluminium plate were filled by Friction Tapered Stud Welding. This novel process has the potential to fill blind holes in thick aluminium sections for the repair of incorrectly drilled holes, friction stir welding exit holes, defects and/or cracks in aluminium components. A set of four welds with altered welding parameters were produced and characterised extensively using Synchrotron residual stress analyses and EBSD texture maps. A link between welding force, near interface temperature and rotational speed is identified with respect to ultimate tensile strength, Vickers microhardness, and residual stress. Further, the effect of excessive peripheral velocity is identified with respect to thermal response ultimate tensile strength and residual stress data.

*Keywords:* Aluminium 6082-T6, Friction Hydro Pillar Processing, Friction Stir Welding, Friction Taper Stud Welding, Frictional Torque, Plunge Depth, Welding Force

\*Corresponding author: [darren.samuel@nmmu.ac.za](mailto:darren.samuel@nmmu.ac.za)

## 1 Introduction

As aluminium is used increasingly in engineering applications annually, greater demands are placed on the material in terms of its mechanical performance and on joined structures produced from aluminium sections [1] [2]. The increased need for superior structural integrity of the aluminium structures has driven the need to develop alternative joining and repair techniques to produce high-integrity, defect-tolerant joints. Such joints or repairs would typically be the filling of incorrectly drilled holes, crack repair or arresting and the plugging of friction stir weld (FSW) exit holes.

Friction taper stud welding (FTSW) has been identified by Nelson Mandela Metropolitan University (NMMU) as a possible solution for producing such welds in heat treatable aluminium AA6082-T6. FTSW is essentially a modified friction hydro pillar process (FHPP) technique that has been demonstrated as an alternative repair technique for the power generation industry in creep resistant steels [3] [4]. A key difference between FHPP and FTSW is that FHPP forms a pillar of dynamically recrystallized shear layers in a hole, while FTSW typically has localised dynamic recrystallization of the consumable tool at the interface, leaving a large percentage of parent tool material in the hole. Additionally there are two main types of FTSW, one that has a tapered hole through the plate, termed through type FTSW, and a second with a section of the parent plate left at the base of the hole, known as blind FTSW, which is the focus of this paper.

FTSW is a solid state joining technique that utilizes frictional heat generated through relative motion between two contacting friction surfaces to form a joint at the plasticization temperature, rather than melting as in a conventional fusion welding process [5]. During a FTSW, a tapered tool is co-axially rotated in a tapered hole, with sufficient axial force to hold the welding surfaces in intimate contact, and with sufficient peripheral velocity to generate frictional heat at the interface. As the temperature increases to the plasticization temperature, seizure of the surfaces begins, forming microbonds that are instantaneously sheared and reformed [5] [6] [7] [8]. Once the entire surface is in a state of shear, plunge begins and layers of dynamically recrystallized material are deposited one on top of the other in the hole. The welding interface will, therefore, propagate upwards as plunge progresses, until the hole is filled and a predetermined plunge depth is reached. At this point rotation is abruptly stopped and a continuous forging force is applied to consolidate the weld, forming a solid state bond at the interface [9]. The heat necessary for the FTSW is therefore provided by the conversion of mechanical input energy (Motor Power) to heat [5] [8]. A high



integrity joint is achieved without the need for multiple weld passes, shielding gasses, a large heat affected zone or an operator with advanced welding skills.

The successful adoption of this novel welding technique in an industrial environment can only be achieved by obtaining a fundamental understanding of the process. This requires that the process parameters used to make a weld be characterised in order to identify their influence on the welded joint. The focus of this paper is to identify and present the effect of axial force and rotational speed on static weld strength, Vickers microhardness, near interface temperature, residual stress and Electron Backscatter Diffraction (EBSD) texture, in a set of four welds in AA6082-T6. The investigation attempts to link the effects of process parameters to further understand their influence on the performance of the weld and what is required to identify a good weld.

## 2 Summary of Literature

Steuwer et al. [10] investigated the effect of rotational speed on residual stress in a friction stir weld (FSW) using synchrotron X-ray diffraction, using the  $\sin^2\psi$  method for calculating lattice parameters when welding AA6082 and AA5083 [10] [11]. The research showed rotational speed of the pin to have a significant effect on residual stress of the weld with changes in residual stress related to microhardness and the dissolution of precipitates. The weld zone was characterized by tensile residual stresses, balanced by compressive stresses in the parent plate [10]. Peel et al. [11] investigated the residual stress and microstructure of AA5083 friction stir welded samples using synchrotron X-ray diffraction and electron backscatter diffraction (EBSD). The work showed the recrystallized zone stretched approximately 5mm past the outer diameter of the tool, correlating with reduced microhardness results, with EBSD maps showing the softened central region to consist of reworked equiaxed grains, with no substructure [11]. Peak residual stresses were found at high traverse speeds and hence steeper thermal gradients, reducing the time for relaxing of the stresses [10]. Coelho et al. [12] used EBSD mapping to investigate the influence of microstructure on mechanical properties when friction stir welding aluminium to high strength steels. Yadav and Bauri [13] investigated the effect of FSW on microstructure and mechanical properties of aluminium and stressed the importance of understanding the microstructural evolution of both pure aluminium and aluminium alloys. The focus of the research was to develop fine grained aluminium by FSW. The state of the microstructure was investigated using EBSD inverse pole figures, with pole figures in the {111} plane used

to display preferred orientation in the weld zone [13]. The FSW process was shown to refine the grain structure from 84 $\mu$ m to 3 $\mu$ m [12] [13].

The published literature that was reviewed, has shown that the current typical residual stress and EBSD mapping research conducted on aluminium friction welds is well established for FSW, with only limited development work of aluminium FTSW done by Beamish [14], Thomas and Nicholas [15] and Mahoney et al. [16].

### **3 Material and Welding**

#### **3.1 Materials Details**

The material used in this study is AA 6082-T6, for both the plate and consumable stud. It is an Al-Si-Mg based, medium strength alloy (proof strength around 290 MPa) that is moderately heat treatable [1]. The T6 temper denotes solution heat treatment and artificially aging. It is typically used in stressed structural members and has good machinability, weld ability and formability [1] [2]. All welds were done in 25mm thick plate, with all samples taken from the same sheet, with all the studs machined from 40mm diameter round bar, all taken from the same length of material.

#### **3.2 Welding Specifications**

In this study, four welding combinations are investigated. The selection of these combinations were chosen to best investigate the influence of axial force and rotational speed on the welded joint. The forging force was kept equal to the axial force applied during welding, a 3mm plunge depth was used (as geometry did not change) and a 20s cooling time was maintained during which time a constant forging force was maintained. In all welds the plates were preheated to 200°C and allowed to cool in air to 140°C before welding was initiated. Three welds with increasing axial force and one with reduced rotational speed were done, denoted S1-S3 for increasing axial force, and S4 for reduced rotational speed. The geometry used in this study is, hole depth 20mm, hole angle 60°, stud angle 55°, hole base diameter and stud nose diameter 10mm, hole and stud corner fillet 2mm. All the welds investigated in this study were made using an axial force ramp up rate of 75kN/s.

To prevent overheating and softening of the stud material during welding, a removable steel heat sink was fitted to the shank of the stud. This stopped collapse of the stud during welding and maintained rubbing of the weld interface for the maximum time possible. Two of each weld combination were made. One sample for static tensile testing and the second for

macro investigation, microhardness testing, residual stress analysis and EBSD investigation. The samples for residual stress measurements were sent to Grenoble France to the European Synchrotron Research Facility (ESRF) for residual stress analysis prior to sectioning, polishing and etching in modified Polten's reagent for analysis.

### 3.3 Weld Characterization Methods

Optical macrographs were taken using a Nikon L110 camera after sectioning and etching in modified Poltens reagent. Tensile samples were machined according to ASTM E8M specification, to a sample height of 19mm. One millimetre was machined from the top of the plate and five from the bottom, this removed any surface defects at the top of the weld and the ligament of the parent plate at the bottom. One tensile sample was taken from each weld as shown in Figure 1. All sharp edges were broken and the UTS (Ultimate Tensile Strength) measured using an Avery 7110 DCJ tensile tester, at an extension rate of 3mm/min.

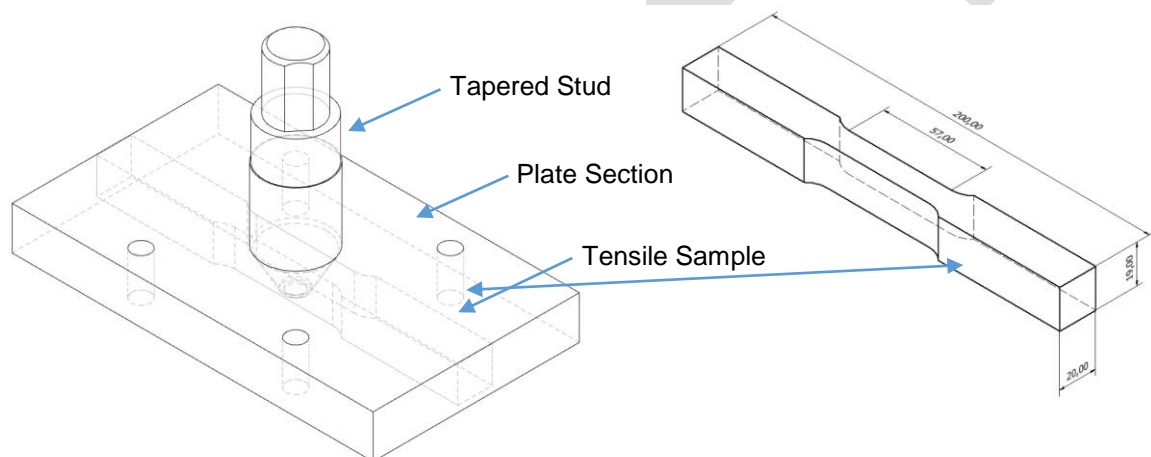


**Figure 1. Weld before machining, showing location of Tensile Sample.**

Vickers microhardness was measured using an FM – ARS 9000 automatic microhardness tester, using a 50g load. Taking the weld as symmetrical, microhardness was carried out on the right hand side of each weld. Microhardness points were taken at a spacing of 0.5mm at depths into the plate of 5mm, 12.5mm and 20mm for 50mm along the weld. Residual stress measurements were taken by Synchrotron x-ray diffraction at the same depths as the microhardness measurements, at 1mm intervals for the full 60mm plate length.

### **3.4 Synchrotron X-ray Diffraction Measurements**

The residual stress measurements of the four welds was undertaken by onbeam line ID15A at the ESRF in France, in energy dispersive mode, as described by Steuwer et al. [17]. Using two solid state detectors allows the measurement of two directions of strain simultaneously. To calculate the true lattice parameter for hoop and radial strain the following assumptions were made: the sum of all the hoop stresses weighted by area were assumed to be equal to zero due to stress balancing, the final radial stress values taken on the side of the plate were assumed to equal zero (at free surface). This was in line with work discussed and reviewed by Withers et al. [18]. This aided in establishing proper estimates for the unstrained lattice parameters. Peel et al. [11] suggests that in AA5083 the difference in microstrain between the unaffected parent material and welded sample may be as high as  $\pm 150$  microstrain, and that age hardening alloys such as AA6082-T6 alloys could expect even greater deviations due to changes in solute concentrations caused by thermal excursion expected in age hardening material, highlighting how critical the accurate calculation of lattice parameters is for the investigation [11] [10]. Assuming the strain values to be the principal strains (e.g. plain strain), the stress hoop and radial was calculated using generalised Hooke's law.

## **4 Results**

### **4.1 Microstructure**

The macrographs of welds S1 to S4 are given in Figure 2. The welds show the upper region of the tapered hole to change angle, indicating high amounts of plastic deformation of the plate, corresponding with good bonding in the upper region. All welds showed varying amounts of abnormal grain growth (AGG) at the base of the hole, initiating at the fillet. Low axial force welds (40kN) had more AGG than high axial force welds, with 80kN welds having only localised AGG at the bottom corner of the weld. Reduced rotational speed initiated a continuous band of AGG along the entire base of weld S4, corresponding with the formation of highly distortion, unstable crystallographic structures typically seen with high process torque welds.

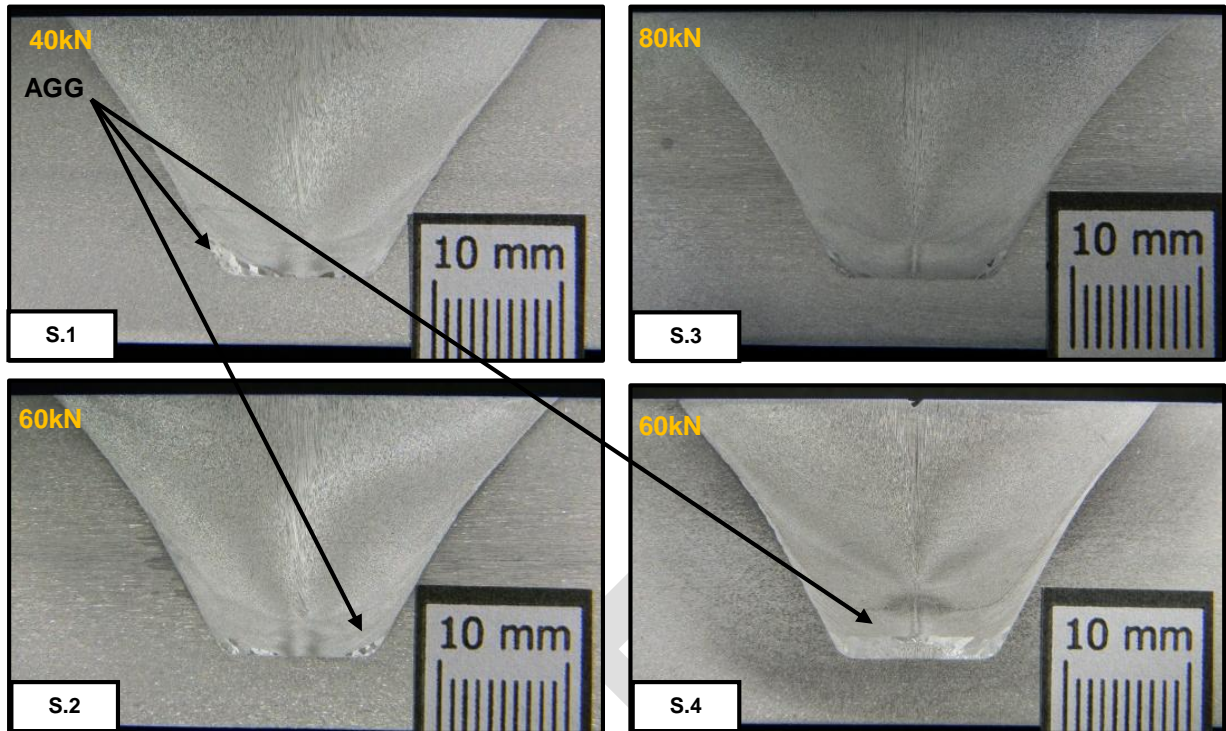


*Figure 2. Macrographs of Welds S1 to S4*

#### 4.2 Welding time

The weld combinations S1, S2, S3 and S4 had weld cycle times of 35.37s, 8.4s, 6.06s and 9.23s respectively. This shows a clear decrease in welding time with increased axial force, and a clear increase in welding time with reduced rotational speed. The increase in welding time for weld S4 was not expected, as typically reduced rotational speed increases the plunge rate in a friction welding process. Low rotational speed increases the duration of the initial heating phase of the process. Edar et al. [5] discussed that reduced rotational speed would increase the heating time of the process, therefore it is assumed that the increase in welding time is not due to reducing of plunge rate during the process, but rather a reduction in time before plunge began. This is attributed to the reduced energy input rate of low rotational speed welds. The surrounding material has less heat energy to dissipate; therefore, the weld interface at seizure will be cooler, increasing the flow stress of the material [19].

#### 4.3 Tensile Data

In order to compare the ultimate tensile strength (UTS) of the welds with parent material, a comparative reference was needed to quantify the effect of the heat cycle experienced during welding. To quantify the effect, six parent material tensile samples were prepared. Two samples had no heat treatment, two samples were heated to 200°C (the preheat

temperature) before cooling in air to room temperature and two samples were heated to 200°C, allowed to cool to 140°C in free air before being placed in an oven that was already at 500°C, and allowed to soak until temperature was reached (approximately 15 min) before free cooling in air. This was the closets representation that could be achieved in laboratory conditions to represent the thermal cycle during welding. The results given in Figure 3, gave a good indication of the achievable joint UTS that can be expected from a weld. The results show that there is a 2.8% drop in UTS due to the 200°C preheat and a 45% drop due to the 500°heat treatment process.

The recorded UTS for welds S1 to S4 is shown in Figure 3. The relationship of increasing axial force to UTS is near linear, with 80kN achieving 95% of the heat treated parent material and 52.5% of the parent material UTS. The weld done at 3000RPM (S4) achieved 24.8% higher UTS than its S2 counterpart, indicating that superior bonding was achieved at identical axial forces, with reduced rotational speed. The results show that near heat treated parent material strengths are achievable and that high axial forces promote good bonding. The UTS achieved by these development FTSW was significantly better than the 80MPa achieved by Missori and Sili [2] using Gas Metal Arc Welding (GMAW).

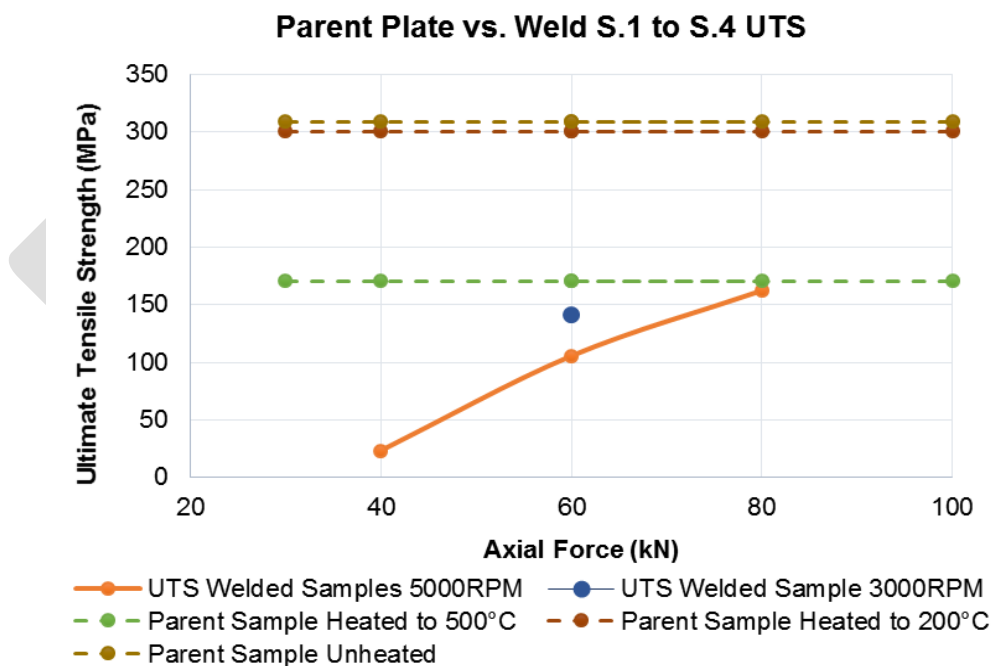


**Figure 3. Tensile Strength vs. Heat Treated Parent Plate for Welds**

The welds all failed along the bond line, with only limited and localised amounts of plastic deformation visible, as shown in Figure 4. No samples showed necking, indicating weak bonding and lack of bonding along the bond line as indicated by the dye-penetrant tests.

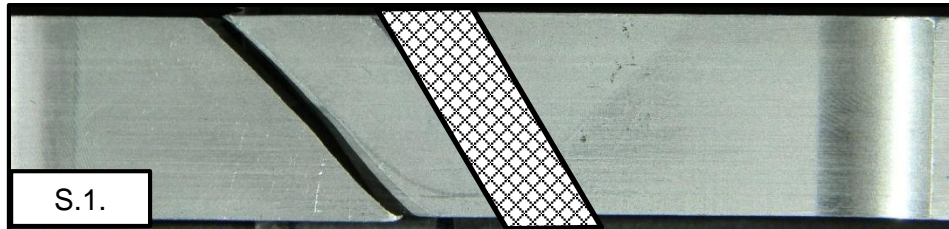


*Figure 4. Typical Fracture at Weld Interface*

#### **4.4 Near Interface Temperature**

The near interface temperature was measured by drilling into the side of the block to within 2mm of the inner sidewall of the hole. Measurements were taken at the top, middle and bottom of the hole, using N-type thermocouples at a sampling rate of 1 kHz.

The near interface temperature during welding is shown in Figure 5 for Welds S1 and S3. The recorded temperatures were comparative across all welds within the first eight seconds, with increased axial force not significantly influencing the maximum temperature. The 40kN weld achieved a marginally higher overall temperature, however, past the ten seconds welding time the additional heat was generated at the surface due to rubbing at low forces, verified by the slow cooling rate of the plate and the temperature curves running parallel from 10s onwards. Increased axial force significantly increased the temperature response in the mid region of the weld, with the time taken for the middle thermocouple to register an increase in sidewall temperature. At 80kN axial force the bottom and middle temperature response overlap as shown in Figure 5 for Weld S3. The middle region of the weld, therefore heats earlier due to increased response, allowing the mid region to be at a higher temperature for longer. This is critical as the mid region generally has the weakest bonding due to low interface heat generation and plasticization. The effect of changes in rotational speed do not appear to alter the temperature response at the bottom and middle of the weld; however, the top thermocouple responds sooner, indicating the interface moved up more rapidly, aligning with comments made by Edar et al. [5].

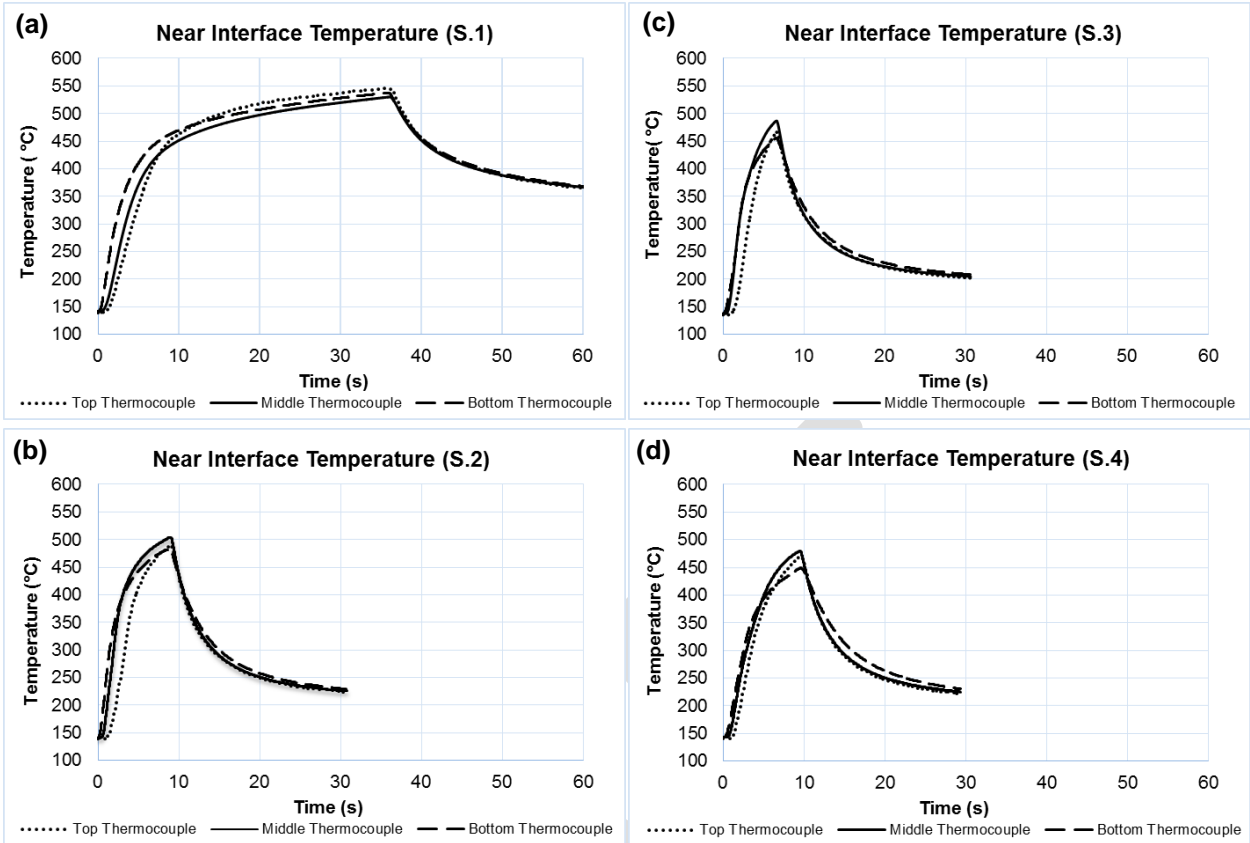


**Figure 5. Near Interface Temperature of Welds S1 to S4**

#### 4.5 Microhardness

The parent material was measured to have an average microhardness of 123HV, while the 200°C preheated sample was found to have a reduced average hardness of 116 HV, correlating with the observed 2.8% drop in UTS. The 500°C heat treated sample was found to have a reduced average hardness of 53HV, corresponding to the 44.8% drop in UTS, showing the sample to be fully annealed and highlighting the thermal sensitivity of the T6 temper. When the microhardness data is compared to that of the welded samples, the results show that increased axial force directly increases the maximum hardness within the weld zone from 70HV to 109HV, correlating with reduced welding time. This is higher than the average 60HV noted in the weld material by Missori and Sili [2] for GMAW of AA6082-T6. This shows that if appropriate processes parameters are chosen that keep the welding time to a minimum, the loss of the T6 temper is minimal due to grain refinement at the interface, corresponding with high values of hardness and hence UTS.



## 4.6 Residual Stress

Radial residual stresses were found to be relatively unaffected by changes in axial force and rotational speed, with welds typically showing 130MPa to 150MPa at the weld centre, decreasing towards zero at the edge of the plate. As expected the highest radial stresses occurred with high axial force and hence short welds.

Figure 6 (a), (b), (c) and (d) show the measured hoop stress for all weld combinations, with the intersecting vertical lines indicating the intersection of the measurement points and the sidewall of the hole. Typically the hoop stress found at the centre of the weld was between 50MPa and 150MPa, similar to the 160MPa results found by Steuwer [10]. Hoop stress for 40kN welds was found to be neutral as expected due to thermal saturation during welding. Increasing axial force is shown to increase the hoop stress in the weld zone and at the weld interface, corresponding with increased UTS. Welds S2 and S3 show a reduced hoop stress offset at the top of the hole, while weld S4 with reduced rotational speed does not have this offset. This corresponds with the reduced offset of the top thermocouple response of weld S4 when compared to weld S2 as shown in Figure 5. This shows the peripheral velocity at the top of the hole to be excessive for welds S1 to S3, as the interface rubs rather than tears as discussed by Vill [20] and Beamish [14]. The near overlapping temperature response gave near overlapping hoop stress response, cementing the link between temperature response, UTS, microhardness and hoop stress. The data also clearly shows that reduced rotational speed corresponds with reduced residual hoop stress in the centre of the weld. This decrease in residual stress was also noted by Steuwer [10] in friction stir welds.

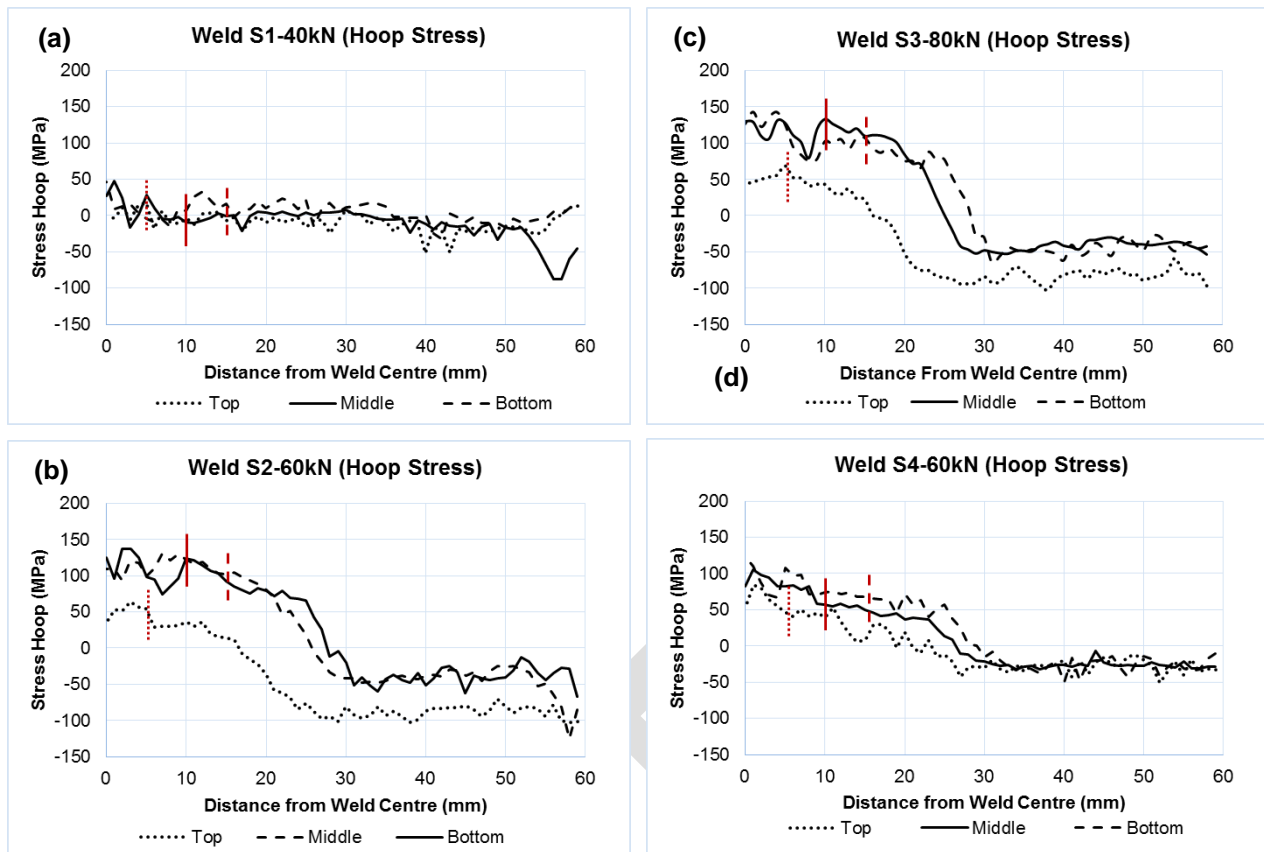


**Figure 6. Hoop Stress Charts for Welds S1 to S4**

#### 4.7 EBSD Analyses

EBSD was used to develop texture maps as a method to quantify the effect of FTSW on AA6082-T6 at a depth of 10mm along the bond line. A misorientation angle of  $8^\circ$  was identified for Welds S1 to S4 to define the grains, as this omitted the noise within the spectrum while maintaining the peaks identified as grain boundary orientations.

The Inverse Pole Figures with Band Contrast (IPF) + (BC) for welds S1 and S4 are given in Figure 8 and Figure 8 respectively. Weld S1 shows grain growth in the parent plate due to elevated weld times and a continuous band of AGG along the bond line. This indicates that the material between the stud and hole is rotating slower than the stud and that high amounts of plastic deformation occur in this region during plunge, as the difference in relative velocity induces grain deformation and hence supplies the grain boundary energy needed for grain growth. The highly deformed structure then experiences grain growth due to the extended welding time at temperature, with the grains showing no overall preferred orientation within the flash as seen in Figure 9. The AGG, lack of bonding and softening of the weld contributed to the poor static tensile performance of this weld. With increased axial force and reduced rotational speed, clear grain refinement is seen within the flash, as shown

in Figure 10. The finest grains are shown to be concentrated between the flash and stud material, at the location of the AGG in weld S1. This indicates that this is a highly strained region and if sufficient time at temperature were allowed, the fine highly stressed grains would grow and reduce the integrity of the joint. No preferred orientation was observed within the flash zone for weld S4 as shown in Figure 10, or any of the welds tested. Instead for high axial force and low rotational speed welds, preferred orientation bands between the plate and weld nugget are noted, with the flash indicating (101) orientation, the next band indicating a (001) and (111) orientation, followed by a band of grains orientated predominantly in the (111) plane. These preferred orientation bands are not noted by the pole figures as the software takes the distribution over a square region, not curved bands. These bands are considered significant as they represent the plastic flow of the material out of the hole as it migrates from the rotating stud towards the stationary plate and begins to slow while it is traveling up and out of the hole as flash. The occurrence of these bands, appears to be consistent with welds that are made at near optimum axial forces and rotational speeds, as the flash and adjacent material is sufficiently stressed to change the grain orientations, with insufficient temperature to form evenly distributed grain, maintaining weld strength.

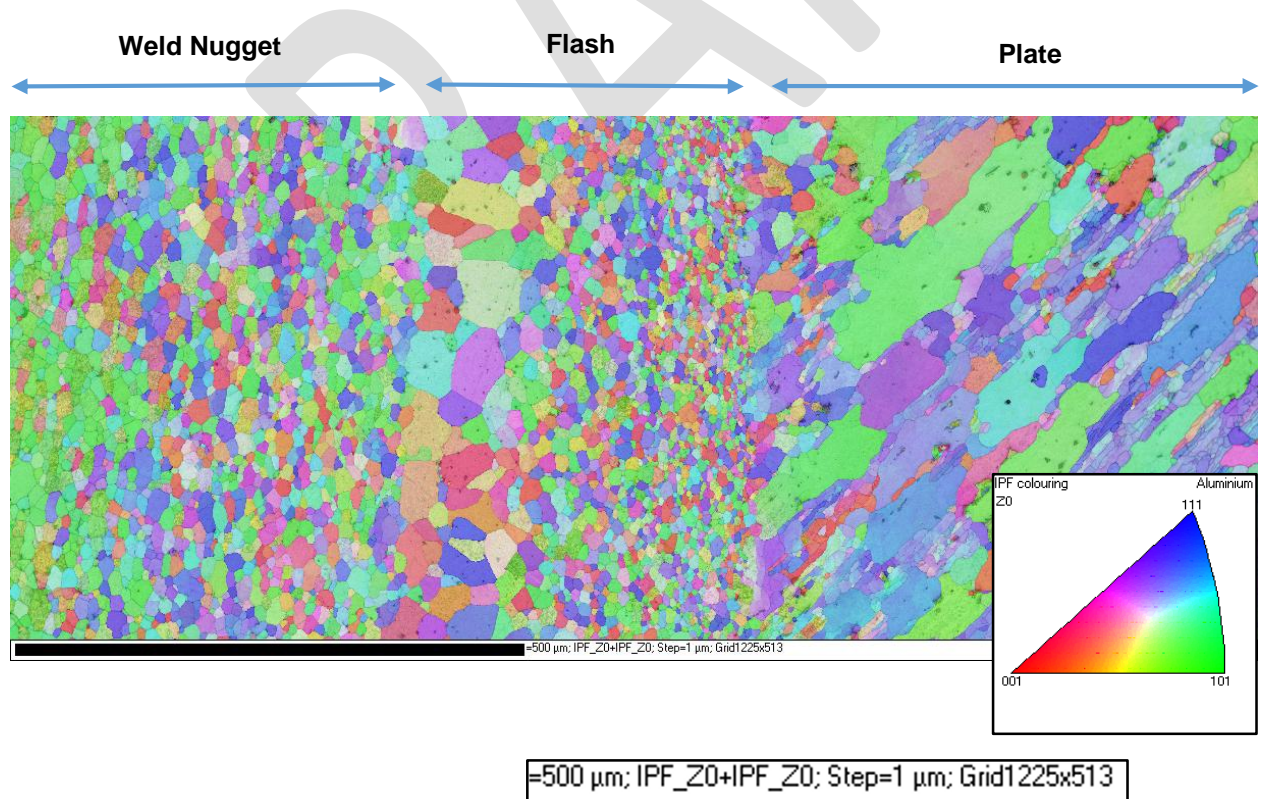


**Figure 7. IPF of Weld S1**

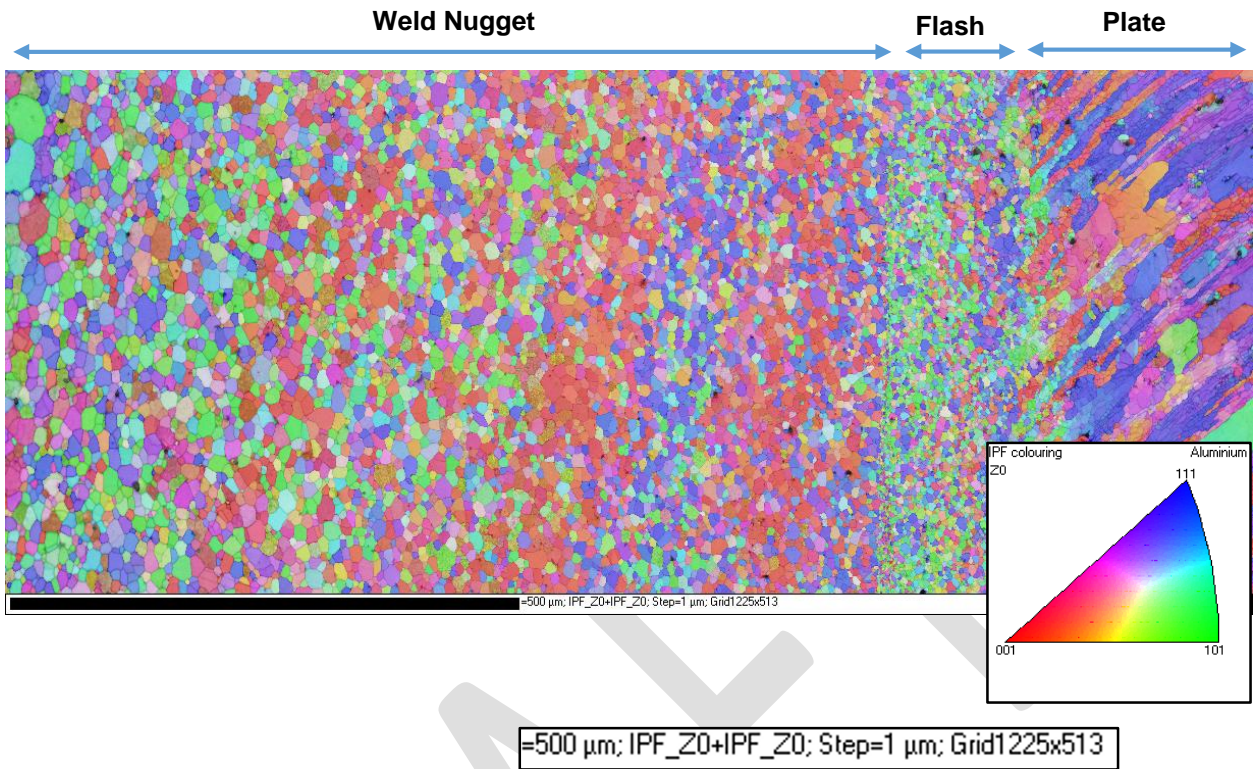


**Figure 8. EBSD inverse pole figure of Weld S4**

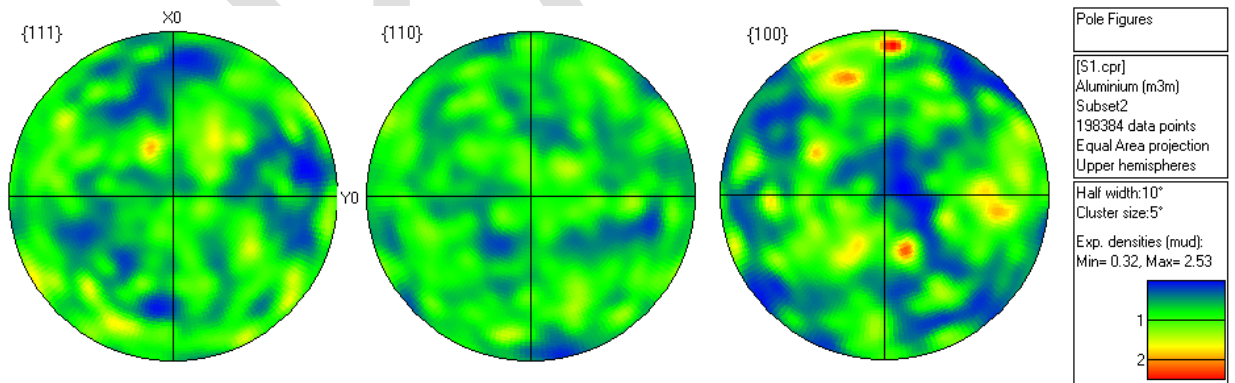


**Figure 9. Pole Figure of Weld S1 Flash Zone**

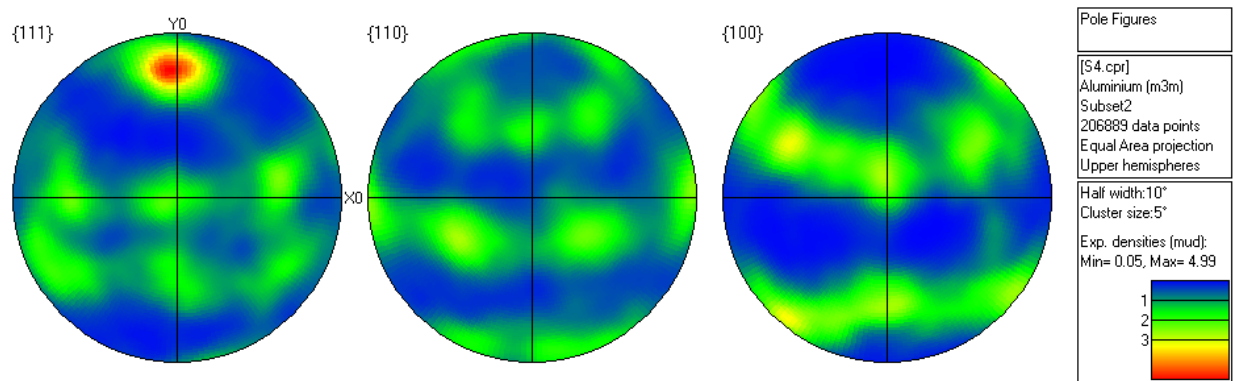


**Figure 10. Pole Figure of Weld S4 Flash Zone**

## 5 Discussion

The link between UTS, near interface temperature, microstructure, microhardness and residual stresses in friction taper stud welds of AA6082-T6 has been studied. FTSW was shown to produce joints with moderate levels of residual stress.

Welds with increased axial force were shown to have increased residual hoop stress, while low rotational speeds were found to reduce the hoop stresses within the weld zone, while maintaining high levels of static joint strength. Reduced rotational speed was shown to reduce the lag in temperature response for all three levels. Further, increased welding force was shown to reduce the thermal response lag between the bottom and middle thermocouple. This shows that the peripheral velocity of 9.94m/s in the upper region of the stud is too high for 5000RPM welds, and is significantly improved with the maximum peripheral velocity of 5.96m/s for 3000RPM welds.

Some preferred orientations noted for near ideal welding conditions in bands within the weld nugget have been observed. The temperature data shows the need for maximum plasticization of the sidewall and maximum sidewall temperature for the shortest possible time, with strong evidence that if the response of the thermocouples is near parallel and within close proximity to one another, good tensile properties are typically achieved.

The flash and weld nugget were found to consist of fine, dynamically recrystallized grains that showed changes in preferred orientation depending on the location of the grains relative to the weld centre. This correlates with high hardness values at the welding interface and elevated hoop stress in the central region of the weld.

## 6 Acknowledgements

We gratefully acknowledge Dr Jacques O' Connell who did the EBSD measurements at the Centre for High Resolution Electron Microscopy at Nelson Mandela Metropolitan University, Port Elizabeth.

## Bibliography

- [1] S. Malan and A. Paterson, Introduction to Aluminium, Aluminium Federation of South Africa, 1993.
- [2] S. Missori and A. Sili, "Mechanical behaviour of 6082T6 aluminium alloy welds," *Metallurgical Science and Technology*.
- [3] I. N. Wedderburn, Doctorate Thesis/ Development of a Creep Sample Retrieval Technique and Friction Weld Site Repair Procedure, Port Elizabeth : Nelson Mandela Metropolitan University, 2013.
- [4] D. L. Bulbring, "Characterization of Friction taper Stud Weld Properties as applied to AISI 4140 High Tensile Alloy Steel," Port Elizabeth, 2008.
- [5] P. A. Eder, P. N. Francisco, Y. A. Chen and C. d. S. Euclides, "Experimental Determination of Temperature During Rotary Friction Welding of AA1050 Aluminium with AISI 304 Stainless Steel," *J. Aerosp. Technol. Manag.*, São José dos Campos, vol. 4, no. 1, pp. 61-67, January-March 2012.
- [6] V. I. Vill, "Welding Metals By Friction," Ohio, 1960.
- [7] R. Andrews and K. Beamish, "Characterisation of and guidelines for rotary friction welding of common metallic engineering materials," The Welding Institute (TWI), Cambridge, 2005.
- [8] G. A. Pinheiro, "Local Reinforcement of Magnesium Components by Friction Processing: Determination of Bonding Mechanisms and Assessment of Joint Properties," Helmholtz, 2008.
- [9] M. N. Ahmad, M. B. Uday, H. Zuhailawati and A. B. Ismail, "Microstructure and mechanical properties of alumina-6061 aluminium alloy joined by friction welding," *Metal and Design (Elsevier)*, vol. 31, pp. 670-676, August 2009.
- [10] A. Steuwer, M. J. Peel and P. J. Withers, "Dissimilar friction stir welds in AA5083-AA6082: The effect of process parameters on residual stress," *Materials Science and Engineering*, vol. A441, pp. 187-196, 2006.
- [11] M. Peel, A. Steuwer and P. J. Withers, "Microstructure, mechanical properties and residual stresses as a function of welding speed in aluminium AA5083," *Acta Materialia*, vol. 51, pp. 4791-4801, 2003.
- [12] R. S. Coelho, A. Kostka, J. F. dos Santos and A. Kaysser-Pyzalla, "Friction-stir welding of aluminium alloy to high strength steels: Mechanical properties and their relation to microstructure," *Materials Science and Engineering*, vol. A556, pp. 175-183, 2012.

- [13] Y. Devinder and B. Ranjit, "Effect of friction processing on microstructure and mechanical properties of aluminium," *Materials Science and Engineering*, vol. A 539, pp. 85-92, 2012.
- [14] K. Beamish, "Friction taper plug welding of 10mm AA6082-T6," The Welding Institute, Cambridge, 2003.
- [15] W. M. Thomas and E. D. Nicholas, "Emerging friction joining technology for stainless steel and aluminium applications," in *Productivity Beyond 2000: IIW Asian Pacific Welding Congress*, Auckland, New Zealand, 1996.
- [16] M. Mahoney, N. Taylor, W. Bingel, F. Long, R. A. Spurling and G. S. Steele, "Method to Repair Voids in Aluminium Alloys". United States of America Patent 5,975,406, 2 November 1999.
- [17] A. Steuwer, J. R. Santisteban, P. J. Withers, L. Edwards and M. E. Fitzpatrick, "In situ determination of stresses from time-of-flight neutron transmission spectra," *Journal of applied crystallography*, vol. 36, pp. 1159-1168, 2003.
- [18] P. J. Withers, M. Preuss, A. Steuwer and W. L. Pang, "Methods for obtaining the strain-free lattice parameter when using diffraction to determine residual stress," *journal of applied crystallography*, vol. 40, pp. 891-904, 2007.
- [19] D. Samuel, Masters Disertation/ CHARACTERIZATION OF JOINT INTEGRITY OF FRICTION STUD WELDING AS APPLIED TO AISI 304L STAINLESS STEEL, Port Elizabeth: Nelson Mandela Metropolitan University, 2009.
- [20] V. I. Vill, Friction Welding of Metals, New York: Feinholds Publishing Corporation, 1962.
- [21] aalco, 2013. [Online]. Available: <http://www.azom.com/article.aspx?ArticleID=2813> . [Accessed 2 February 2010].
- [22] K. Masayuki, "Assessment of local deformation using EBSD: Quantification of local damage at grain boundaries," *Materials Characterization*, vol. 66, pp. 56-67, 2012.
- [23] D. G. Hattingh, D. L. Bulbring, A. Els-Botes and M. N. James, "Process Parameter Influence on Performance of Friction Taper Stud Welds in AISI 4140 steel," *Elsevier - Materials & Design*, vol. 32, no. 6, pp. 3421-3430, February 2011.